

Studies on C–F Activation and Radiofluorination Reactions:
Interactions of Fluorine with Boron and Silicon Lewis Acids

by
Andreas Dorian

A thesis submitted in partial fulfillment of the requirements for the degree of

Doctor of Philosophy

Department of Chemistry
University of Alberta

© Andreas Dorian, 2022

Abstract

Boron and silicon Lewis acids form strong bonds with fluorine. This ability facilitates a range of interesting reactivity. For example, small boron/silicon reagents are at the forefront of C–F activation, a field focused on cleaving one or more C–F bonds in organofluorine compounds. In addition to degradation of fluorine waste products, this field offers a compelling strategy to synthesize highly sought-after fluorinated motifs. Alternatively, boron/silicon functionalities can be introduced to bioactive small-molecules or peptides of interest. These can facilitate inclusion of the radioisotope fluorine-18, a positron emitter that enables PET imaging – an important medical tool used in the diagnosis and monitoring of several diseases.

The introductory chapter of this thesis provides a broad overview of C–F activation with boron/silicon Lewis acids. Special focus is given to reactions with trifluoromethyl arenes (ArCF_3), especially those that achieve selective single activation, resulting in the formation of valuable difluoromethyl (ArCF_2R) moieties. The second chapter describes a new method for ArCF_3 halogen-exchange, using readily available BX_3 and FeX_3 reagents. The reaction was optimized to form ArCX_3 and ArCF_2X products, and was evaluated with a variety of substrates.

The third chapter begins with a general overview of PET imaging and the synthesis of ^{18}F -labeled compounds, with a special emphasis on $[^{18}\text{F}]\text{ArCF}_3$ formation. The direct and efficient synthesis of $[^{18}\text{F}]\text{ArCF}_3$ from the corresponding non-radioactive ArCF_3 precursor remains an outstanding goal in radiochemistry. The efforts made towards the development of such a synthetic method are discussed, wherein BX_3/FeX_3 reagents were used to mediate the desired reactivity. The fourth chapter provides an overview of a radiofluorination approach termed non-canonical labeling. Some of the clinical applications of this strategy are discussed, in particular radiotracers targeting PSMA, a significant biomarker used for imaging prostate cancer. The efforts made towards the synthesis of a novel PSMA radiotracer are also described.

Preface

The majority of the second chapter was published as the following: Dorian, A.; Landgreen, E.J.; Petras, H.R.; Shepherd, J.J.; Williams, F.J. “Iron-Catalyzed Halogen Exchange of Trifluoromethyl Arenes” *Chem. Eur. J.* **2021**, *27*, 10839 – 10843 (*reused with permission from Elsevier*). The author of this thesis was responsible for all of the synthetic work in this paper, including reaction optimization, substrate scope investigations, and analytical data collection, performed under the supervision of Prof. Florence Williams. The DFT calculations were performed by E.J. Landgreen and H.R. Petras, under the supervision of Prof. James Shephard at the University of Iowa.

The work in the third and fourth chapter is unpublished, and was performed under the supervision of Prof. Ralf Schirmmacher. *Section 4.1* was adapted from the following publication: International Atomic Energy Agency. “Production and Quality Control of Fluorine-18 Labeled Radiopharmaceuticals” *IEAE-TECDOC-1968*, Vienna (**2021**), pg. 75-80 (*reused with permission from IAEA*). This section was written by the author and Carolin Jaworski, under the supervision of Prof. Schirmmacher. The project described in *Section 4.3* was initiated by the Schirmmacher/Wuest Groups (contributors include Justin Bailey and Melinda Wuest) and is a continuation of the work described in reference 281. The recent synthetic efforts were continued as a collaboration between the author and other members of the Schirmmacher Group (Lexi Gower-Fry, Yinglan Pu, Travis Kronemann, and Carolin Jaworski).

Acknowledgments

The leading acknowledgment must be given to Professor Florence Williams. The author is exceedingly thankful for the mentorship he received, and for her expertise, determination, and eternal optimism, as well as for her warm, patient, yet motivating personality, and for her tolerance of his puerility. Special gratitude is also given to Professor Ralf Schirmacher, who was willing to adopt and support the author long past what was necessary.

The author recognizes the numerous lab members he annoyed over the years. In particular, Khyati Gohil for being his partner in crime (figuratively), and fellow hoop-jumper. Zân Kazmi for being the most ridiculous human being in all of recorded history. Carolin for keeping him in check. Yinglan P. for her cheerful naiveté. Travis for his nice jogging technique. Finally, Lexi Göwer-Fry for being an extra special lab mate and supporting the author when he needed it.

Appreciation is also granted to the excellent staff within the department. Ryan Lewis for always having a couple of records lying around to chat about. The machine shop staff, in particular Paul, Dieter, and Dirk, for numerous interesting conversations. Mike Barteski for his persistent liveliness. Jason Dibbs for fixing copious broken items. The mass spectroscopy facility, especially Jing Zheng, for her help with GC-MS analysis. The NMR staff, namely Mark Miskolzie for numerous confusing, lengthy, and awkward lectures, as well as the analytical and instrumentation facilities staff, and electronics shop members. Hayley Wan and Connor P. for keeping the virulent youth in check. Anita Weiler and the chemistry office for keeping everyone organized, as well as Laura Pham and Rik T. for keeping the department running. Finally, the family of the author, for not losing their patience during his marathon of detrition.

“la lutte elle-même vers les sommets suffit à remplir un cœur d'homme; il faut imaginer Sisyphe heureux”

– Albert Camus

Table of Contents

Abstract.....	ii
Preface.....	iii
Acknowledgments.....	iv
List of Tables.....	viii
List of Figures	ix
List of Schemes.....	xi
List of Abbreviations and Symbols.....	xiv
Chapter 1: Activation of C–F Bonds by Boron and Silicon Lewis Acids.....	1
1.1 Introduction.....	1
1.1.1 Targets of C–F Activation	2
1.1.2 General Strategies for C–F Activation.....	5
1.2 Silicon Lewis Acids.....	6
1.2.1 Halogen-Exchange.....	6
1.2.2 Hydrodefluorination.....	7
1.2.3 C–F Functionalization.....	11
1.2.4 Selective Single C–F Activation.....	13
1.3 Boron Lewis Acids	14
1.3.1 Halogen-Exchange.....	14
1.3.2 Hydrodefluorination.....	16
1.3.3 C–F Functionalization.....	16
1.3.4 Selective Single C–F Activation.....	18
1.4 Conclusion and Thesis Objectives.....	21
Chapter 2: Iron-Catalyzed Halogen Exchange of Trifluoromethyl Arenes	23
2.1 Introduction.....	23
2.1.1 Iron Catalysis	23
2.1.2 Design of Experiment	24
2.2 Boryl Chloride Investigations	28
2.2.1 Reaction Screening.....	28
2.2.2 Synthesis of Trichloromethyl Arenes	29
2.2.3 Mono-Halex Design-of-Experiment.....	30

2.3 Boryl Bromide Investigations	32
2.3.1 Reaction Screening.....	32
2.3.2 Synthesis of Tribromomethyl Arenes	33
2.3.3 Mono-Halex Design-of-Experiment.....	34
2.3.4 Synthesis of Bromodifluoromethyl Arenes.....	37
2.3.5 Mechanistic Investigations	41
2.4 Boryl Iodide Investigations	42
2.4.1 Preliminary Screening.....	42
2.5 Conclusion	44
2.5.1 Future Work.....	44
2.5.2 Summary.....	45
Chapter 3: Efforts towards the Synthesis of Radiolabeled Trifluoromethyl Arenes	46
3.1 Introduction.....	46
3.1.1 Overview of PET Imaging	46
3.1.2 Fluorine-18 Production.....	48
3.1.3 Fluorine-18 Radiolabeling.....	50
3.1.4 Processing Nucleophilic Fluoride.....	52
3.2 Introduction to [¹⁸ F]R–F Synthesis.....	53
3.2.1 Electrophilic Fluorination.....	53
3.2.2 Aliphatic Nucleophilic Fluorination.....	54
3.2.3 Aromatic Nucleophilic Fluorination.....	55
3.3 Introduction to [¹⁸ F]R–CF ₃ Synthesis	57
3.3.1 Electrophilic Methods.....	57
3.3.2 Nucleophilic Methods.....	58
3.3.3 Coupling Methods	60
3.3.4 Isotopic Exchange	63
3.4 Investigations on the Synthesis of [¹⁸ F]ArCF ₃	65
3.4.1 Conditions Screening.....	65
3.4.2 Future Work.....	70
3.5 Conclusion	71

Chapter 4: Efforts towards the Synthesis of a Novel PSMA Radiotracer	72
4.1 Introduction to Non-Canonical Labeling	72
4.1.1 <i>Overview of Silicon-Mediated Radiofluorination</i>	73
4.1.2 <i>Overview of Boron-Mediated Radiofluorination</i>	74
4.1.3 <i>Overview of Aluminum-Mediated Radiofluorination</i>	75
4.2 Clinical Applications of Non-Canonical Labeling	77
4.2.1 <i>In Vivo SSTR2 Imaging</i>	77
4.2.2 <i>In Vivo GRPr Imaging</i>	79
4.2.3 <i>In Vivo Integrin Imaging</i>	79
4.2.4 <i>In Vivo PSMA Imaging</i>	81
4.3 Synthesis of a Novel PSMA-Targeting Radiotracer	88
4.3.1 <i>Radiotracer Design</i>	88
4.3.2 <i>Synthetic Progress</i>	90
4.4 Conclusion	91
Chapter 5: Summary and Conclusion	93
5.1 Thesis Summary	93
5.2 Future Directions.....	95
5.3 Conclusion	96
References	97
Appendix	109
A.1 Procedures and Characterization (Chapter 2).....	109
A.1.1 <i>General Considerations</i>	109
A.1.2 <i>Chloro-Halex Optimization</i>	110
A.1.3 <i>Bromo-Halex Optimization</i>	115
A.1.4 <i>Mono-Halex General Procedure and Scope</i>	123
A.1.5 <i>Triple-Halex General Procedure and Scope</i>	128
A.1.6 <i>Boryl Iodide Procedures</i>	130
A.2 Procedures and Characterization (Chapter 4).....	131
A.2.1 <i>General Considerations</i>	131
A.2.2 <i>PSMA Compounds</i>	131
A.3 Spectra of Reaction Mixtures and Pure Compounds	135

List of Tables

Table 2.1. Conditions investigations for boryl bromide mediated halogen-exchange.....	33
Table 2.2. Test points for the bromo-halex DOE II.....	35
Table 2.3. Summary of conditions for the halogen-exchange of 214	37
Table 2.4. Summary of reaction time optimization for electron-rich substrates.....	38
Table 2.5. GCMS analysis of products for the reaction of 237 with boron triiodide.....	44
Table 3.1. Physical parameters for a selection of positron-emitting radioisotopes.....	48
Table 4.1. Labeling and in vivo performance for different forms of DOTA-AMBF ₃ -PSMA.....	86

List of Figures

Figure 1.01. Examples of recent fluorine-containing drugs. Lasmiditan, Lascufloxacin, Nirmatrelvir	1
Figure 1.02. Price comparison of perfluoro vs partially fluorinated moieties	2
Figure 1.03. Examples of CF ₃ -containing drugs. Esaxerenone, Efavirenz, Sitagliptin	2
Figure 1.04. Representative approaches towards aryl difluoromethane synthesis.....	3
Figure 1.05. Examples of bioactive CF ₂ R compounds. Sedaxane, EVT-101, Thrombin Inhibitor	3
Figure 1.06. Transformations of ArCF ₂ X reported in the literature	4
Figure 1.07. Different conceptual approaches towards C–F activation	5
Figure 1.08. Bond dissociation energies for fluorinated methanes (kCal/mol)	5
Figure 1.09. Examples of electrophilic phosphonium species used for HDF	11
Figure 1.10. Functionalization of intermediate fluoromethyl onium salts.....	21
Figure 2.01. Summary of the reaction described in this chapter.....	23
Figure 2.02. Cytochrome-P ₄₅₀ catalyzed defluorination and concurrent hydroxylation	24
Figure 2.03. Contour plots for yield of a hypothetical reaction as a function of pH and temperature.....	25
Figure 2.04. Linear model for a 2-factor system.....	25
Figure 2.05. Second-order model for a 2-factor system	26
Figure 2.06. Full quadratic model for a 2-factor system.....	26
Figure 2.07. Illustrations of DOE designs for a 3-parameter system.....	27
Figure 2.08. Pareto chart for the chloro-halex DOE II	31
Figure 2.09. Pareto chart for the bromo-halex DOE II	35
Figure 2.10. Surface plots of ArCF ₂ Br conversion as a function of BBr ₃ and temperature.....	36
Figure 2.11. Surface plots of ArCF ₂ Br conversion as a function of time and reaction concentration.....	36
Figure 2.12. Representative HPLC trace for a halex reaction mixture	38
Figure 2.13. Analysis of ¹⁹ F NMR parameters for the reaction of triarylphosphine 231	39
Figure 2.14. Geometries and bonding for PhCF ₃ in isolation and in coordination with FeF ₃	41
Figure 2.15. Plausible mechanisms for the bromo-halex reaction.....	42
Figure 2.16. Formation of heteroleptic boron and iron complexes.....	42
Figure 2.17. Strategy for using the CF ₃ group as a masked carboxylic acid	44
Figure 3.01. Schematic depicting the operation of a PET scanner	47
Figure 3.02. Examples of fluorine-18 labeled radiotracers used for PET.....	49
Figure 3.03. Examples of nuclear reactions used for the production of fluorine-18.....	49
Figure 3.04. Examples of electrophilic radiofluorination reagents.....	50
Figure 3.05. Examples of nucleophilic radiofluorination reagents	50
Figure 3.06. Summary of strategies for molecular incorporation of fluorine-18.....	51

Figure 3.07. Summary of non-canonical radiofluorination strategies.....	51
Figure 3.08. Typical protocol used in processing aqueous fluoride-18 for radiochemistry.....	52
Figure 3.09. Acidic protocol used to form a putative iron fluoride species from aqueous fluorine-18	53
Figure 3.10. Electrophilic radiofluorination of aryl organometallic precursors	54
Figure 3.11. Metal catalyzed allylic radiofluorination.....	55
Figure 3.12. Labeled trifluoromethanes synthesized from bromodifluoromethyl precursors.....	59
Figure 3.13. Plausible scheme for the isotopic exchange of trifluoromethyl arenes.....	66
Figure 3.14. Radio-TLC analysis for the radiofluorination of a trifluoromethyl arene	69
Figure 3.15. Two-step strategy for trifluoromethyl arene radiofluorination via isotopic exchange	70
Figure 4.01. Non-canonical radiofluorination strategies	72
Figure 4.02. Overview of strategies for radiofluorination of SiFA compounds	74
Figure 4.03. Examples of common moieties used for radiometal chelation	76
Figure 4.04. Structure of labeled SiTATE.....	78
Figure 4.05. Structure of fluorine-18 AMBF ₃ -TATE.....	79
Figure 4.06. Structure of a SiFA bombesin derivative	79
Figure 4.07. Structure of leading PSMA targeting fluorine-18 radiotracers.....	83
Figure 4.08. Structure of PSMA targeting chelator-AlF radiotracers.....	84
Figure 4.09. Structure of PSMA targeting BF ₃ radiotracers	84
Figure 4.10. Structure of a PSMA targeting DOTA-AMBF ₃ radiohybrid.....	85
Figure 4.11. Conceptual example of the radiohybrid strategy	85
Figure 4.12. Structure of a PSMA targeting SiFA DOTA radiohybrid	87
Figure 4.13. PSMA targeting SiFA radiotracers.....	88
Figure 4.14. Structure of a lead PSMA targeting SiFA radiotracer.....	89
Figure 4.15. PET scans of LNCaP-mice with different PSMA targeting tracers.....	89
Figure 5.01. Summary of C–F activation strategies and products of mono-functionalization.....	93
Figure 5.02. Summary of the method developed for the halox of trifluoromethyl arenes.....	94

List of Schemes

Scheme 1.01. Base-promoted synthesis of 2-aryl quinazolines.....	4
Scheme 1.02. Dehalogenative homocoupling of a tribromomethyl arene.....	4
Scheme 1.03. Iododefluorination of alkyl fluorides using an ytterbium catalyst.....	6
Scheme 1.04. HaloDF of alkyl fluorides using an aluminum catalyst.....	7
Scheme 1.05. HDF of perfluorotoluene using silylium catalysis.....	7
Scheme 1.06. Products formed in the HDF of nonafluorohexane using silylium catalysis.....	8
Scheme 1.07. HDF catalyzed by a stabilized disilyl hydronium ion.....	8
Scheme 1.08. Cooperative mechanism of HDF with a disilyl sulfonium species.....	9
Scheme 1.09. Heterolysis of hydrosilane by a cationic ruthenium thiolate complex.....	9
Scheme 1.10. HDF of alkyl fluorides catalyzed by BCF-activated hydrosilane.....	10
Scheme 1.11. HDF of trifluoromethyl benzene with catalytic BCF and titanium-family complexes.....	10
Scheme 1.12. HDF of trifluoromethyl benzene with a phosphorous(III) catalyst.....	11
Scheme 1.13. Catalytic cycle for the silylium-catalyzed arylation of alkyl fluorides.....	12
Scheme 1.14. Mono-arylation and HDF of trifluoromethyl compounds using phosphorous(V).....	12
Scheme 1.15. Single C–F activation of ortho-silyl trifluoromethyl arenes.....	13
Scheme 1.16. Single HDF of trifluoromethylbenzene with a phosphine/silylium FLP.....	14
Scheme 1.17. Boron trihalide mediated halogen-exchange.....	14
Scheme 1.18. Boron tribromide mediated triple halogen-exchange.....	15
Scheme 1.19. Nitrogen protection strategy used in the synthesis of a triazolinone agrochemical.....	15
Scheme 1.20. Halogen-exchange using a borenium species.....	16
Scheme 1.21. C–F functionalization of 1-fluoropentane using a boron/phosphorous FLP.....	16
Scheme 1.22. HDF C–F functionalization of 1-fluoropentane using a boron/phosphorous FLP.....	16
Scheme 1.23. Functionalization of benzyl fluorides with various nucleophiles.....	17
Scheme 1.24. Conversion of trifluoromethyl arenes to diaryl ketones with boron tribromide.....	17
Scheme 1.25. Insertion of diazo esters into benzyl fluorides with boron trifluoride catalysis.....	18
Scheme 1.26. Different conditions used for the mono-halex of trifluoromethylbenzene.....	19
Scheme 1.27. Single C–F cleavage of difluoromethyl groups by a boron/phosphorous FLP.....	19
Scheme 1.28. Single C–F cleavage of trifluoromethyl arenes by a boron/pyridine FLP.....	20
Scheme 1.29. Single C–F cleavage of difluoromethyl arenes by a boron/sulfur FLP.....	20
Scheme 2.01. Example of an iron-catalyzed C–F halogen exchange.....	24
Scheme 2.02. DOE design for the synthesis of hydrazine derivatives.....	28
Scheme 2.03. Iron catalyzed halex between trifluoromethyl benzene and phenyldichloroborane.....	28
Scheme 2.04. Halex between trifluoromethyl benzene and phenyldichloroborane.....	29

Scheme 2.05. Triple chloro-halex of trifluoromethyl benzene	29
Scheme 2.06. Isolated yields of trichloromethyl derivatives produced via triple-halex	29
Scheme 2.07. Design for the chloro-halex DOE.....	30
Scheme 2.08. Design for the chloro-halex DOE II	31
Scheme 2.09. Model accuracy for the chloro-halex DOE II.....	32
Scheme 2.10. Isolated yields of tribromomethyl derivatives produced via triple-halex.....	34
Scheme 2.11. Design for the bromo-halex DOE	34
Scheme 2.12. Design for the bromo-halex DOE II.....	34
Scheme 2.13. Summary of scope investigations for the halex of trifluoromethyl arenes.....	37
Scheme 2.14. Halogen exchange with a triarylphosphine substrate	39
Scheme 2.15. Halogen exchange with a commercial insecticide flufenoxuron.....	40
Scheme 2.16. Halex of a trifluoromethyl arene with boron triiodide	43
Scheme 2.17. C–F activation of a trifluoromethyl arene with boron triiodide.....	43
Scheme 2.18. Synthesis of 2-fluoroadenine using a continuous flow protocol	45
Scheme 3.01. Electrophilic radiofluorination of an olefin FDG precursor.....	53
Scheme 3.02. Chiral organocatalytic α -radiofluorination of aldehydes.....	54
Scheme 3.03. Radiofluorination via nucleophilic substitution of an alkyl tosylate precursor	54
Scheme 3.04. Radio-deoxofluorination of a protected glucose derivative	55
Scheme 3.05. Summary of activated arene precursors used for radiofluorination.....	56
Scheme 3.06. Mechanism of arene radiofluorination from a hypervalent iodine species.....	56
Scheme 3.07. Electrophilic radiofluorination of a 1,1-difluoroolefin precursor.....	57
Scheme 3.08. Xenon difluoride mediated radiofluorination of a difluoroalkyl iodane precursor	57
Scheme 3.09. Electrophilic synthesis of labeled trifluoromethyl arenes.....	58
Scheme 3.10. Nucleophilic radiofluorination of a 1,1-difluoroolefin precursor.....	58
Scheme 3.11. Nucleophilic radiofluorination of a 1,1-difluoro-lansoprazole precursor.....	58
Scheme 3.12. Nucleophilic radiofluorination of a bromodifluoromethyl arene precursor	59
Scheme 3.13. Synthesis of radiolabeled α -trifluoromethyl carbonyl substrates	60
Scheme 3.14. Synthesis of a radiolabeled trifluoromethyl prosthetic group	60
Scheme 3.15. Summary of methods for the synthesis of radiolabeled fluoroform.....	61
Scheme 3.16. Summary of methods for nucleophilic radio-trifluoromethylation	61
Scheme 3.17. Synthesis of labeled arenes using a radio-trifluoromethyl copper(I) reagent.....	62
Scheme 3.18. Synthesis of labeled trifluoromethanes with difluorocarbene and copper(I) reagents	62
Scheme 3.19. Synthesis of a labeled trifluoromethyl sulfinate prosthetic group.....	62
Scheme 3.20. Synthesis of a labeled Umemoto trifluoromethylating reagent.....	63

Scheme 3.21. Synthesis of labeled trifluoromethyl sulfides via in situ thiolate formation.....	63
Scheme 3.22. Synthesis of labeled trifluoromethyl prosthetic groups via isotopic exchange	64
Scheme 3.23. Synthesis of radiolabeled trifluoromethyl arenes by isotopic exchange	64
Scheme 3.24. Synthesis of labeled trifluoromethanes via a gold(III) mediated fluoride rebound.....	65
Scheme 3.25. Evaluation of isotopic exchange for trifluoromethyl arene radiofluorination	66
Scheme 3.26. Synthesis of a labeled tetrafluoroborate and radio-TLC analysis.....	67
Scheme 3.27. Evaluation of a two-step process for trifluoromethyl arene radiofluorination	67
Scheme 3.28. Evaluation of acidic elution and iron-mediated trapping of fluoride-18	68
Scheme 3.29. Evaluation of iron fluoride species for trifluoromethyl arene radiofluorination	68
Scheme 3.30. Evaluation of different eluents for trifluoromethyl arene radiofluorination.....	69
Scheme 4.01. Radiofluorination of a biotin-linked trialkoxysilane	73
Scheme 4.02. Radiofluorination of a dialkylfluorosilane via isotopic exchange.....	73
Scheme 4.03. Radiofluorination of a biotin-linked phenylboronate	74
Scheme 4.04. Radiofluorination of an AMBF ₃ -rhodamine conjugate via isotopic exchange	75
Scheme 4.05. General scheme for aluminum-based radiofluorination	76
Scheme 4.06. Synthesis and radiofluorination of a SiFA octreotate conjugate	78
Scheme 4.07. Synthesis and radiofluorination of SiFA fluciclatide conjugates	80
Scheme 4.08. Radiofluorination of a cyclic RGD trifluoroborate conjugate via isotopic exchange.....	81
Scheme 4.09. Hydrolysis of the NAAG peptide and structures of related synthetic analogues	82
Scheme 4.10. Progress towards the synthesis of SiFA-Asp ₂ -QA-C ₈ -PSMA	90
Scheme 4.11. Future efforts required to complete the synthesis of SiFA-Asp ₂ -QA-C ₈ -PSMA.....	91

List of Abbreviations and Symbols

Å	Ångström
Ac	acetyl
acac	acetylacetonate
ACN	acetonitrile
A_m	molar activity
AMBF ₃	alkylammoniomethyl trifluoroborate
amu	atomic mass unit
ANOVA	analysis of variance
app.	apparent
aq.	aqueous
Ar	aryl
Asp	aspartic acid residue
AT ₁ R	angiotensin II type 1 receptor
BAr ^F ₂₀ ⁻	tetrakis(pentafluorophenyl)borate
BAr ^F ₂₄ ⁻	tetrakis(3,5-bis(trifluoromethyl)phenyl)borate
BCF	tris(pentafluorophenyl)borane
Boc	<i>tert</i> -butyloxycarbonyl
Bq	Becquerel
br.	broad
Bu	butyl
Bz	benzyl
CFC	chlorofluorocarbon
CN	cyano
conc.	concentration
conv.	conversion
CT	computed tomography
CuAAC	copper-catalyzed azide alkyne cycloaddition
CYP ₄₅₀	cytochrome P450
d	doublet

d.c.	decay-corrected
DBU	1,8-diazabicyclo[5.4.0]undec-7-ene
DCA	dichloroacetic acid
DCE	1,2-dichloroethane
DCM	dichloromethane
d.r.	diastereomeric ratio
DFT	density functional theory
diCy-18-cr-6	dicyclohexano-18-crown-6
DIPEA	N,N-diisopropylethylamine
DMF	dimethylformamide
DMSO	dimethyl sulfoxide
DOE	design of experiment
DOTA	1,4,7,10-tetraazacyclododecane-1,4,7,10-tetraacetic acid
dt	doublet of triplets
DTPA	diethylenetriamine pentaacetic acid
EDCI	1-ethyl-3-(3-dimethylaminopropyl)carbodiimide
EDG	electron donating group
ee	enantiomeric excess
EI	electron impact
eq.	equivalents
ESI	electrospray ionization
Et	ethyl
EuE	glutamate-urea-glutamate motif
EWG	electron withdrawing group
FGD	2-fluoro-2-deoxyglucose
FLP	frustrated Lewis pair
Fmoc	9-fluorenylmethoxycarbonyl
FTIR	Fourier transform infrared spectroscopy
g	gram
GC-MS	gas chromatography - mass spectrometry

GRPr	gastrin releasing peptide receptor
h	hour
Halex	halogen-exchange
HaloDF	halodefluorination
HBED	<i>N,N'</i> -di(2-hydroxybenzyl)ethylenediamine- <i>N,N'</i> -diacetic acid
HBTU	2-(1 <i>H</i> -benzotriazol-1-yl)-1,1,3,3-tetramethyluronium hexafluorophosphate
HDF	hydrodefluorination
Hex	hexanes
HFIP	1,1,1,3,3,3-hexafluoropropan-2-ol
HMDS	hexamethyldisilazane
HPLC	high performance liquid chromatography
HRMS	high-resolution mass spectrometry
HSQC	heteronuclear single quantum coherence
Hz	hertz
IE	isotopic exchange
IPA	isopropyl alcohol
IR	infrared
J	coupling constant in Hertz
K ₂₂₂	kryptofix 222 [4,7,13,16,21,24-hexaoxa-1,10-diazabicyclo[8.8.8]hexacosane]
kcal	kilocalorie
keV	kilo electronvolt
KuE	lysine-urea-glutamate motif
L	liter
LA	Lewis acid
LCMS	liquid chromatography - mass spectrometry
LG	leaving group
logD	distribution coefficient, octanol/water
logP	partition coefficient, octanol/water
m	multiplet
m/z	mass-to-charge ratio

^m CPBA	<i>meta</i> -chloroperbenzoic acid
Me	methyl
min	minute
Ms	mesyl [<i>methanesulfonyl</i>]
MTBD	7-methyl-1,5,7-triazabicyclo[4.4.0]dec-5-ene
ⁿ Bu	<i>norm</i> -butyl
n.d.c.	non-decay-corrected
NAAG	<i>N</i> -acetyl-L-aspartyl-L-glutamate
NET	neuroendocrine tumor
NFSI	<i>N</i> -fluorobenzenesulfonimide
NHC	<i>N</i> -heterocyclic carbene
NHS	<i>N</i> -hydroxysuccinimide
NMR	nuclear magnetic resonance
NODA	1,4,7-triazacyclononane-1,4-diacetic acid
NOTA	1,4,7-triazacyclononane-1,4,7-triacetic acid
nuc	nucleophile
OFAT	one-factor-at-a-time
p.i.	post injection
PC	propylene carbonate
PCC	pyridinium chlorochromate
PDFA	(triphenylphosphonio)difluoroacetate
PEG	polyethylene glycol
PET	positron emission tomography
Ph	phenyl
pKa	acid dissociation constant, $-\log$
POCOP	1,3-bis((diphenylphosphino)oxy)benzene
ppm	parts per million
PSMA	prostate specific membrane antigen
PTFE	polytetrafluoroethylene
Pyfluor	2-pyridinesulfonyl fluoride

q	quartet
QMA	quaternary methyl ammonium
R	generic organic group
r.t.	room temperature
R ²	coefficient of determination
RBF	round bottom flask
RCC	radiochemical conversion
RCY	radiochemical yield
R _f	retardation factor
RGD	arginylglycylaspartic acid
s	singlet
SCIDY	spirocyclic iodonium ylides
S _E Ar	electrophilic aromatic substitution
SET	single electron transfer
SiFA	silicon fluoride acceptor
S _N 1	nucleophilic substitution, unimolecular
S _N 2	nucleophilic substitution, bimolecular
S _N Ar	nucleophilic aromatic substitution
SPE	solid phase cartridge
SPPS	solid phase peptide synthesis
SSTr2	Somatostatin receptor type 2
SUV	standardized uptake value
SZO	sulfated zirconium oxide
t	triplet
T	temperature
^t Bu	<i>tertiary</i> -butyl
TATE	tyr ³ -octreotate
TBAF	tetrabutylammonium fluoride
TBAT	tetrabutylammonium difluorotriphenylsilicate
TBD	1,5,7-triazabicyclo[4.4.0]dec-5-ene

TBDMS	(<i>tert</i> -butyl)dimethylsilyl
TBHP	<i>tert</i> -butyl hydroperoxide
td	triplet of doublets
Tf	triflyl [<i>trifluoromethanesulfonyl</i>]
TFA	trifluoroacetic acid
TFMISO	1-(2-nitro-1 <i>H</i> -imidazol-1-yl)-3-(2,2,2-trifluoroethoxy)propan-2-ol
THF	tetrahydrofuran
THT	tetrahydrothiophene
TLC	thin layer chromatography
TMEDA	<i>N,N,N',N'</i> -tetramethylethane-1,2-diamine
TMS	trimethylsilyl
TOC	try ³ -octreotide
TON	turnover number
TPPy	2,4,6-triphenylpyridine
TRAP	1,4,7-triazacyclononane-1,4,7-tris(methylphosphinic acid propanoic acid)
Ts	tosyl [<i>4-toluenesulfonyl</i>]
UV	ultraviolet
WCA	weakly coordinating anion
%ID/g	percent injected dose per gram
°C	degrees Celsius
δ	chemical shift, parts per million
μ	micro

1.1 Introduction

Fluorine is the 13th most abundant element on earth.¹ Despite this ubiquity, organofluorine compounds are very rare in nature, and fluorine exists predominantly as fluorite, the mineral form of calcium fluoride (CaF₂). As such, organofluorine chemistry is an almost entirely synthetic field, with perhaps the first breakthrough occurring with the invention of CFC refrigerants in the 1920's (e.g. CF₂Cl₂, or Freon[®] 12).² Today, over a million tons of HF are produced annually, via the treatment of fluorite with strong acid. Despite a number of industrial applications, HF has limited usage in the laboratory due to safety and handling concerns. Alternatively, chemists prefer to use a variety of fluorine building blocks or reagents, that are often derived from HF on an industrial scale.¹

The inclusion of fluorine into a molecule allows for useful modulation of physical and chemical properties, and thus plays a critical role in molecular design. The C–F bond is characterized by a short length (1.35 Å), high polarity, and the greatest bond strength of any carbon–element single bond (> 105 kcal/mol).³ Fluorinated alkane moieties tend to have very low intermolecular forces and are rather chemically inert.⁴ This is essential to the non-stick properties of fluoropolymers such as Teflon, a prominent example of fluorine in materials chemistry.

Fluorine is ubiquitous in modern pharmaceutical and agrochemical development. An estimated 20% of marketed drugs contain fluorine, with a notable increase in recent years (43% in 2018–2019).⁵ Similarly, of the new agrochemicals from 1998–2020, fluorine was present in 53%.⁶ Substitution of a C–H bond for a C–F bond is often performed to increase metabolic stability, as C–F bonds are resistant to cleavage by oxidative enzymes.⁷ Fluorine also has a major impact on conformation, with a low lying σ^* orbital available for hyperconjugative donation. This effect, as well as changes to pK_a and lipophilicity, are frequently used to improve drug potency, permeability, and pharmacokinetics.

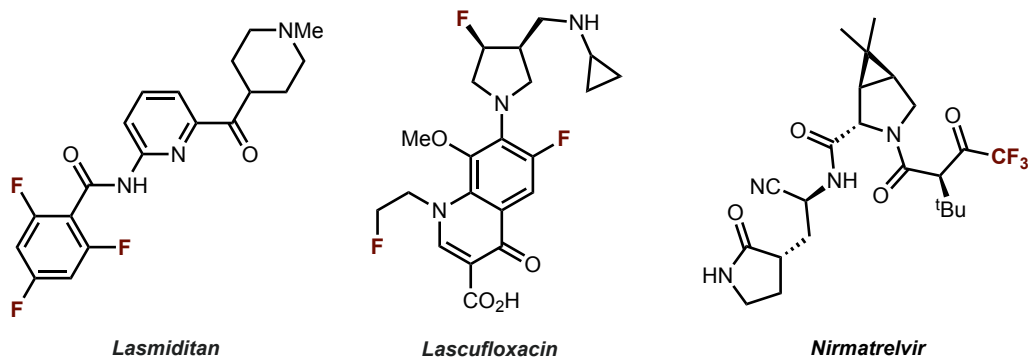


Figure 1.1. Examples of recent fluorine-containing drugs. Lasmiditan, 2019 (anti-migraine)⁸, Lascafloracin, 2019 (antibiotic)⁹, and Nirmatrelvir, 2021 (anti-viral for Covid-19)¹⁰.

Despite the various benefits of organofluorine compounds, their stability leads to serious environmental persistency problems. For example, many of the first CFC's introduced were banned under the 1986 Montreal Protocol because of their ability to deplete the ozone layer.² A variety of fluorocarbons have also been found to contribute to global warming due to their ability to act as potent greenhouse gases.¹¹ With the demand for organofluorine gases expected to grow, there is an active area of research focusing on C–F activation.¹² In addition to the potential to recycle or degrade fluoro-waste streams, C–F activation can be a powerful tool in the synthetic toolbox. In particular, selective C–F activation of polyfluorinated moieties can lead to high-value partially fluorinated intermediates (see examples in Figure 1.2).

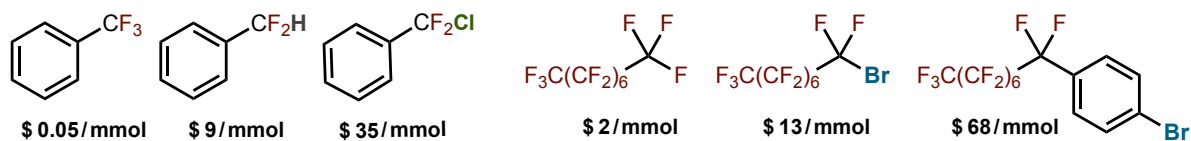


Figure 1.2. Price comparison of perfluoro vs partially fluorinated moieties¹³

1.1.1 Targets of C–F Activation

The trifluoromethyl (CF₃) group is one of the most important fluorinated moieties, particularly as an arene/heteroarene substituent (ArCF₃). The development of several new methods in the last decade to introduce of the CF₃ group has led to its ubiquity in bioactive molecules (Figure 1.3).¹⁴

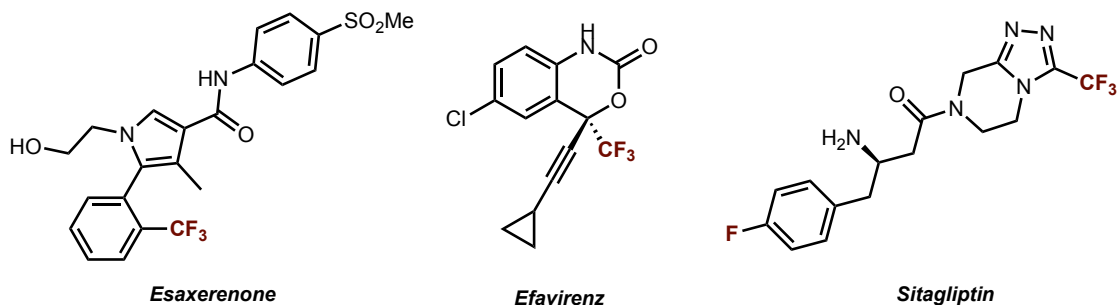


Figure 1.3. Examples of CF₃-containing drugs. Esaxerenone, 2019 (anti-hypertensive)¹⁵, Efavirenz, 1998 (anti-retroviral, essential HIV medicine)¹⁶, Sitagliptin, 2006 (anti-diabetic)¹⁷.

An appealing target of C–F activation is the direct mono-functionalization of ArCF₃.¹⁸ For example, single *hydrodefluorination* (HDF) affords a difluoromethyl arene (Figure 1.4.A), an appealing target in medicinal chemistry (see Figure 1.5 for examples). The polarized C–H bond is an effective hydrogen bond donor, allowing it to act as an isostere for various functional groups (e.g. alcohol, thiol, amine).^{19, 20} A HDF strategy to access difluoromethyl arenes offers an efficient alternative to conventional methods that rely on CF₂H building blocks, such as couplings with functionalized arenes (Figure 1.4.D), due to the ease of accessing the ArCF₃ starting material.²¹

Another enticing objective is the selective activation of ArCF_3 to form difluoromethyl derivatives (ArCF_2R), allowing access to a wide range of structural diversity from a single starting material (Figure 1.4.C). These compounds have traditionally been made via the deoxofluorination of ketones (Figure 1.4.F), using specialty electrophilic fluorinating reagents, such as α -fluoroalkylamines (NCF), or sulfur fluoride (S-F) derivatives.²² However, these reagents suffer from a number of disadvantages, such as poor atom-economy, harsh conditions/functional group incompatibility, thermal instability, high cost, and the production of hazardous byproducts.

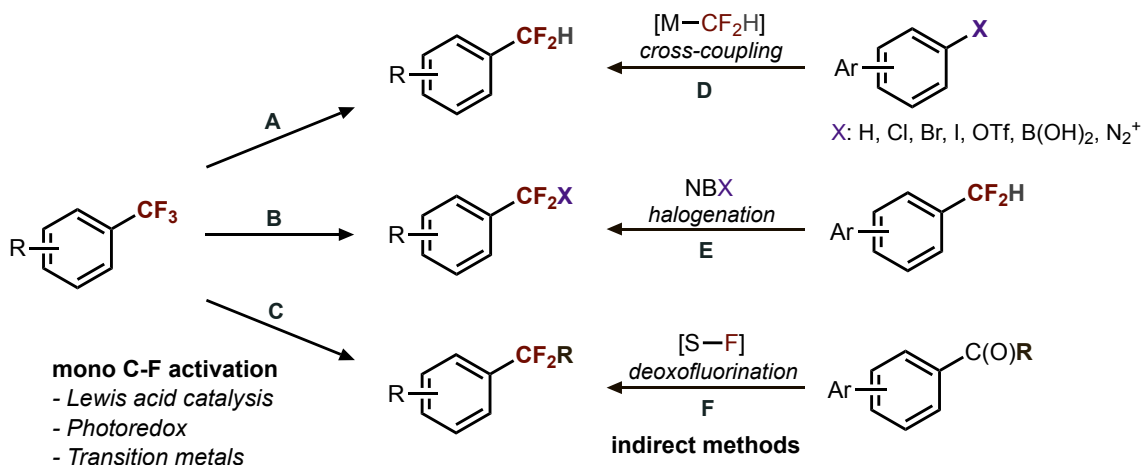


Figure 1.4. Representative approaches towards aryl difluoromethane synthesis

Finally, halodifluoromethanes (ArCF_2X) can be formed from ArCF_3 (Figure 1.4.B), via single *halogen-exchange* (halex), also termed *halodefluorination* (HaloDF).^{23, 24} In addition to unique intrinsic properties, such as increased capacity for halogen bonding, ArCF_2X compounds act as common intermediates for redox and cross-coupling reactions that generate a range of other difluoro derivatives (Figure 1.6).²⁵⁻³⁰ In the past, ArCF_2X synthesis often necessitated lengthy synthetic routes, requiring already advanced ArCF_2H starting materials (Figure 1.4.E).^{31, 32}

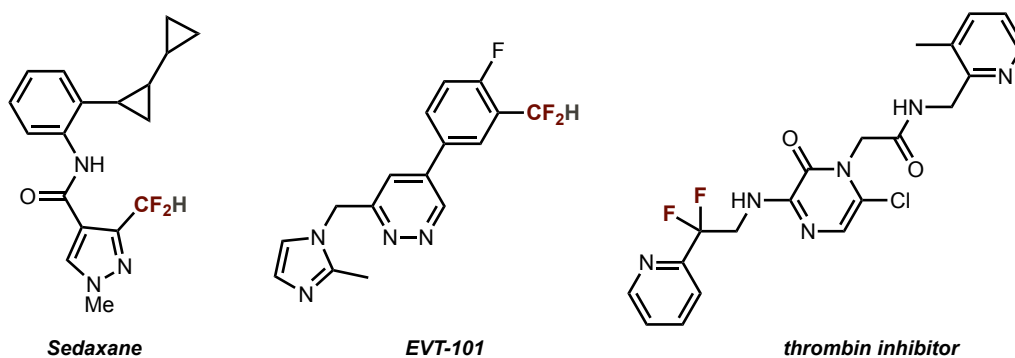


Figure 1.5. Examples of bioactive CF_2R compounds. Sedaxane, 2011 (fungicide)³³.
 EVT-101, investigational (NMDA receptor agonist)³⁴. Thrombin inhibitor, investigational.³⁵

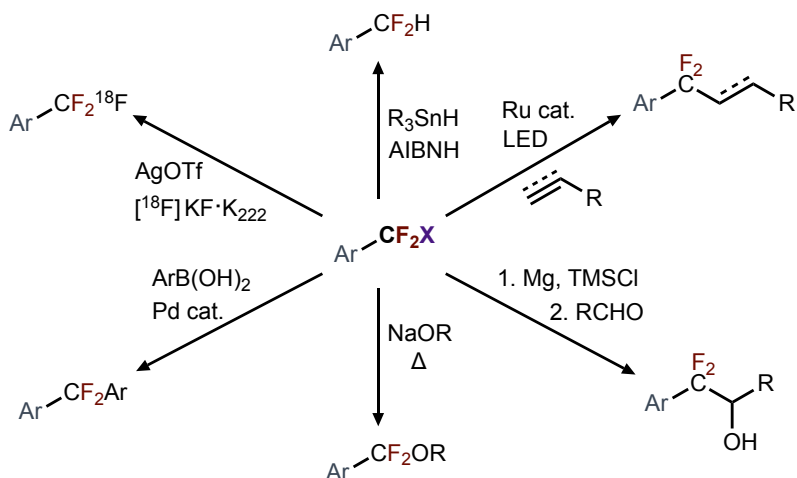
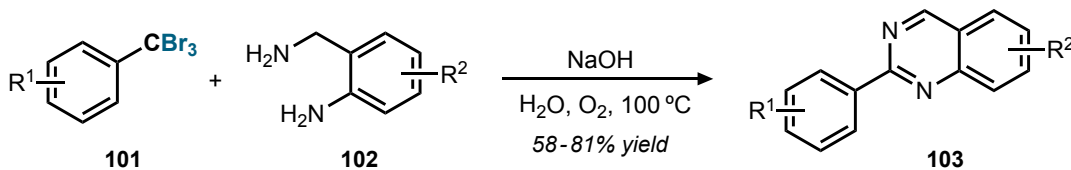


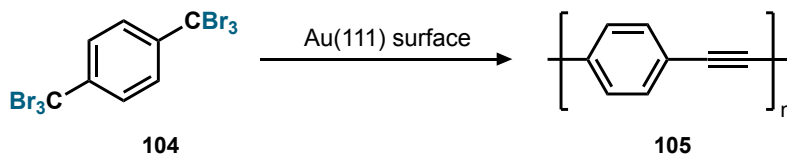
Figure 1.6. Transformations of $ArCF_2X$ ($X = Br, Cl$) reported in the literature²⁵⁻³⁰

Another useful product that can be formed from haloc with $ArCF_3$ are trihalomethyl arenes ($ArCX_3$).³⁶⁻³⁹ These can be used in a number of synthetic applications, including conversion to carboxylic acids, esters, alkynes and alkenes, and to generate heterocycles.⁴⁰⁻⁴² For example, tribromomethanes (**101**) can be coupled with aminobenzylamines (**102**) to form quinazoline products (**103**) as shown in Scheme 1.1.⁴²



Scheme 1.1. Base-promoted synthesis of 2-aryl quinazolines

In another interesting example, Xu and coworkers demonstrated the use of tribromomethyl derivatives for the on-surface formation of nanostructures. An arylene ethynylene linear wire (**105**) could be formed upon dehalogenative polymerization of the *p*-bis(tribromomethyl) benzene (**104**) starting material (Scheme 1.2).⁴¹



Scheme 1.2. Dehalogenative homocoupling of a tribromomethyl arene (yield not reported)

1.1.2 General Strategies for C–F Activation

Fluorinated organic functional groups are famously resistant to harsh chemical conditions (e.g. alkyllithium reagents, strong oxidizing conditions, etc.). Three different conceptual approaches for C–F activation have emerged, as shown in Figure 1.7.^{4, 43} Although there have been numerous developments in processes mediated by electron-rich transition metals, these are mostly applicable to aryl and vinyl C(sp²)–F bonds.⁴⁴

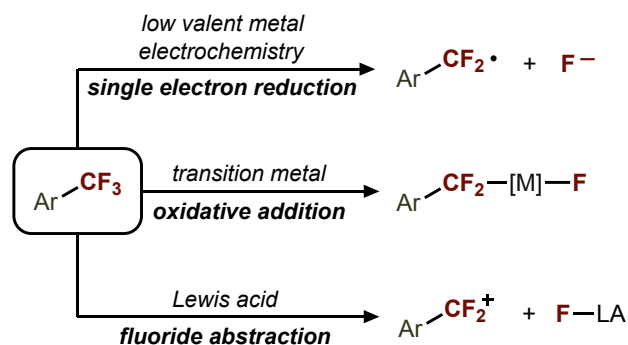


Figure 1.7. Different conceptual approaches towards C–F activation.

Single-electron reduction (SET) by a low-valent metal (typically Mg),^{45, 46} or electrochemical process^{47, 48} can be used with a number of different C–F moieties. However, these methods often have a poor substrate scope, and require excess reductant. When applied to ArCF₃, it is difficult to obtain adequate selectivity for mono-activation. This highlights the key challenge in ArCF₃ activation, in which partially defluorinated species (mono- and difluoro) tend to be more reactive than the starting trifluoride. This is a result of C–F bond strengths that decrease as the degree of fluorine substitution decreases (e.g. Figure 1.8 shows the progressive weakening of the C–F bond, as hydrogen is substituted for fluorine in tetrafluoromethane).⁴⁹

$\text{F}_3\text{C}-\text{F}$	$\text{HF}_2\text{C}-\text{F}$	$\text{H}_2\text{FC}-\text{F}$	$\text{H}_3\text{C}-\text{F}$
131	128	120	110

Figure 1.8. Bond dissociation energies for fluorinated methanes (kCal/mol)

As a result of this thermodynamic challenge, most C–F activation methods result in complete defluorination of ArCF₃. A series of recent publications have addressed this problem using photoredox catalysis to facilitate SET reduction of ArCF₃, followed by trapping with an alkene or other radical donor.⁵⁰⁻⁵³

One of the most effective strategies for activation of C(sp³)–F bonds is the use of strong main group Lewis acids, which facilitate fluoride abstraction and removal.⁵⁴ The most important of these are boron and silicon reagents, in which the formation of a strong bond with fluoride provides a thermodynamic drive (e.g. SiF₄ 166 kCal/mol⁵⁵, BF₃ 149-172 kCal/mol⁵⁶). These reagents have been applied to the

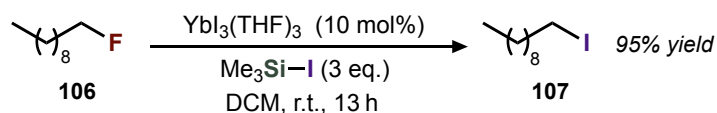
functionalization of various alkyl fluoride substrates, including ArCF₃ groups. In particular, a number of recent elegant examples have achieved *single* defluorination of ArCF₃, providing access to valuable difluorobenzyl synthons. This chapter will highlight these advances, as well as provide a general introduction to C–F activation with boron and silicon Lewis acids.

1.2 Silicon Lewis Acids

Organosilicon compounds are widely used in organic synthesis. For example, silyl hydrides (L₃Si–H) have widespread applications, such as the hydrosilylation of double bonds, whereas silyl halides (L₃Si–X) are well known for silylation of heteroatoms (O, N, etc.) and as polymer precursors. Silicon’s high fluorophilicity also makes silicon-reagents appealing for C–F activation, in particular those with high Lewis acidity (e.g. cationic silylium ions). The foremost use of silicon Lewis acids is for hydrodefluorination, with applications in halogen-exchange, and defluorinative C–C bond formation as well.

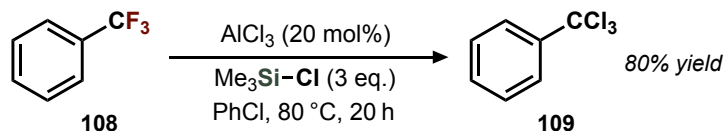
1.2.1 Halogen-Exchange

In 1981, Olah et al. showed that simple alkyl fluorides could undergo a halox reaction with an excess of TMS-iodide.⁵⁷ Efficient conversion to the alkyl iodide could be achieved with secondary or tertiary fluorides, after 16 hours at room temperature. More recently, various catalysts have been used to improve HaloDF reactions with silyl halides. Hilmersson demonstrated the halox of primary fluorides (e.g. **106**) to the corresponding iodide (**107**), using an ytterbium iodide catalyst (Scheme 1.3).⁵⁸ Mechanistic investigations suggested a two-step catalytic cycle, in which the active ytterbium catalyst is regenerated by TMS-iodide.



Scheme 1.3. Iododefluorination of alkyl fluorides using an ytterbium catalyst

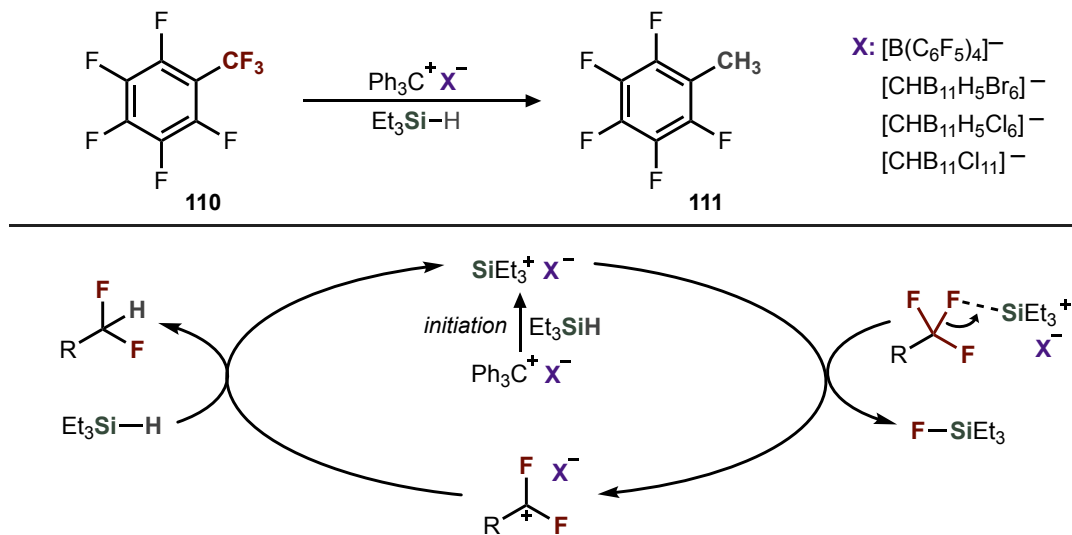
In another example, the Young Group demonstrated the ability of aluminum(III) halides to catalyze bromo- and chloroDF (Scheme 1.4), using either TMS-halide or SiCl₄ as the halide source.³⁹ The reaction was applied to both single C–F bonds (e.g. 1-fluorooctane), and to trifluoromethyl compounds (e.g. **108**). In an extension of this strategy, the Young lab showed that silyl sulfonates (e.g. TMSOMs) could be used in the functionalization of alkyl fluorides, using the boron reagent B(C₆F₅)₃ (BCF) as a catalyst (q.v. section 1.3.3).



Scheme 1.4. HaloDF of alkyl fluorides using an aluminum catalyst

1.2.2 Hydrodefluorination

Hydrodefluorination is the most important area of silicon-mediated C–F activation. Hydrosilanes are readily available, making them appealing stoichiometric reagents to undergo HDF, via an overall Si–H/C–F metathesis process. Mechanistically, this proceeds via a silylium ion (tricoordinate silicon cation) intermediate,⁵⁹ formed via the addition of a cationic *activator* species (e.g. trityl salt), and stabilized by a weakly coordinating anion (WCA, X[−]). This strategy was pioneered by the Ozerov Group,^{60–64} illustrated by the example shown in Scheme 1.5, depicting the selective defluorination of the CF₃ group in perfluorotoluene (**110**). The silylium species abstracts a fluoride ion to generate a carbocation intermediate, which then reacts with stoichiometric hydrosilane to form the HDF product, and regenerate the silylium catalyst.

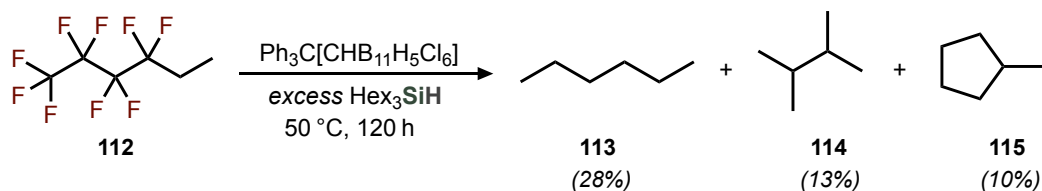


Scheme 1.5. HDF of perfluorotoluene using silylium catalysis

Initial investigations utilized the tetraarylborate anion [B(C₆F₅)₄][−] as the WCA, but found its efficiency was limited, due to decomposition in the reaction medium, providing TON ≤ 126.⁶⁰ *Turnover number* (TON) is a useful metric for quantifying catalyst efficiency, defined by the moles of product formed, divided by the moles of catalyst/activator used. Vast improvements were observed when halogenated carboranes [CHB₁₁X₁₁][−] were used as the WCA. For example, utilizing Ph₃C[CHB₁₁H₅Cl₆] as an activator, pentafluorotoluene **111** could be obtained in 86% yield, with a TON of 1250. This reaction illustrates the typical selectivity for LA mediated C–F activation, in which all three C(sp³)–F bonds are defluorinated, but the C(sp²)–F bonds remain intact, likely due to the

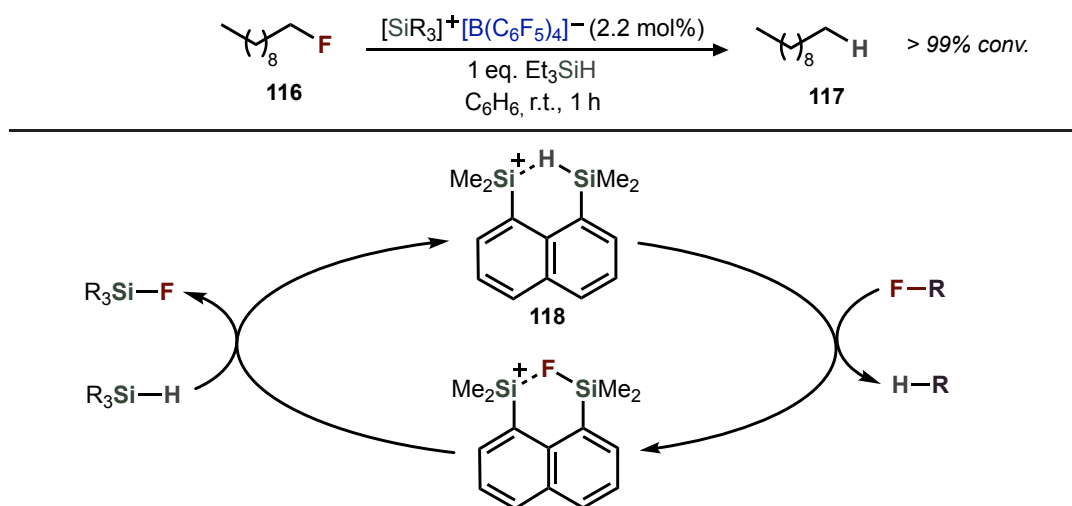
relative instability of the aryl cation. In a recent modification of this strategy, surface-catalysis was employed to effect HDF, using an SZO surface functionalized with triisopropylsilyl groups.⁶⁵

A frequent problem with silylium HDF is the potential for isomerization or Friedel-Crafts reactivity, arising from carbocation intermediates. For example, nonafluorohexane **112** could undergo HDF under forcing conditions, but afforded a range of rearrangement and cyclization products (Scheme 1.6).⁶¹



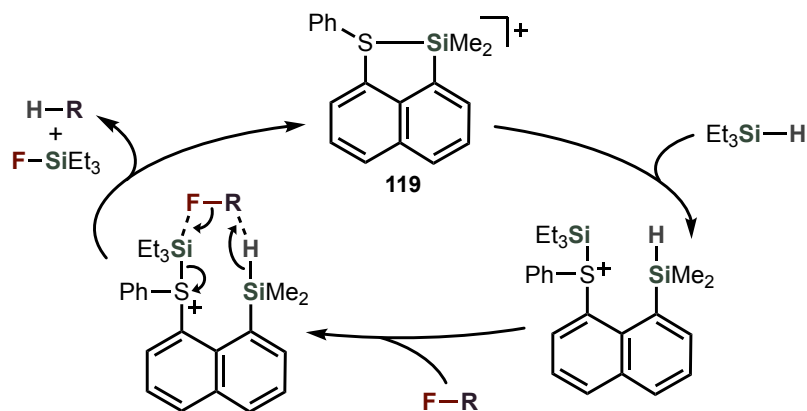
Scheme 1.6. Products formed in the HDF of nonafluorohexane using silylium catalysis

As an alternative to trityl salt activators, specially-designed stabilized silylium cations can be used directly as catalysts in HDF reactions. For example, Müller and coworkers introduced a series of silicon-ions based on a 1,8-naphthalenyl backbone, such as **118** (Scheme 1.7).⁶⁶⁻⁶⁸ After C–F abstraction and formation of the HDF product **117**, the active catalyst is regenerated via reaction with a stoichiometric hydrosilane reagent. In addition to silyl hydronium ion **118**, Müller synthesized related fluoronium, arenium, and chalconium silyl ions, all of which proved to have similar catalytic activity.



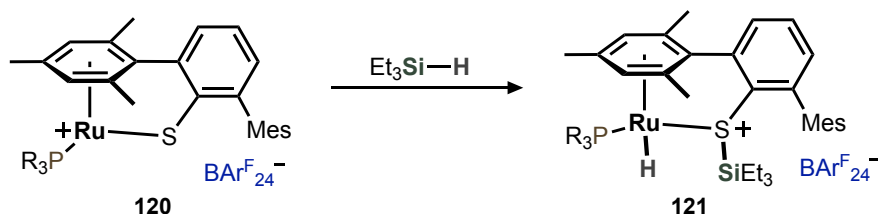
Scheme 1.7. HDF catalyzed by a stabilized disilyl hydronium ion

Interestingly, silyl-chalconium species (e.g. **119**) appears to operate by a different cooperative mechanism (Scheme 1.8).⁶⁶ This mechanism begins with Si–H heterolysis, in which hydride is transferred to the cationic silicon, and the triethylsilyl fragment is abstracted by the basic sulfur. A concerted σ -bond metathesis with the alkyl fluoride then affords the product, and regenerates the catalyst. This proposal was supported by observation that more Lewis basic chalcogens improved catalyst performance, and by the lack of rearrangement products formed.



Scheme 1.8. Cooperative mechanism of HDF with a disilyl sulfonium species

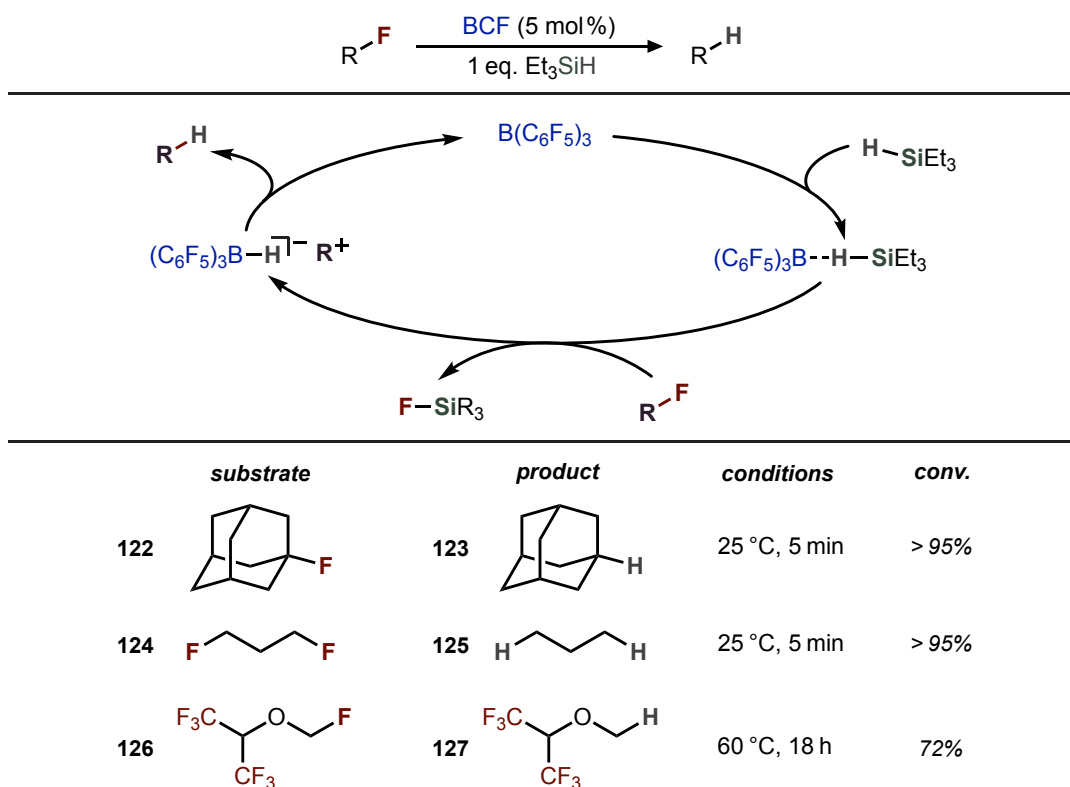
An analogous cooperative mechanism is thought to occur with Oestreich's cationic ruthenium(II) thiolate complex (Scheme 1.9).⁶⁹ Addition of hydrosilane to the complex results in transfer of the silyl fragment to sulfur, and hydride transfer to the ruthenium center. ¹H NMR studies were performed to provide evidence for formation of the ruthenium(II) hydride species **121**. Oestreich demonstrated the ability of this catalytic system to hydrodefluorinate various trifluoromethyl anilines.⁷⁰



Scheme 1.9. Heterolysis of hydrosilane by a cationic ruthenium thiolate complex

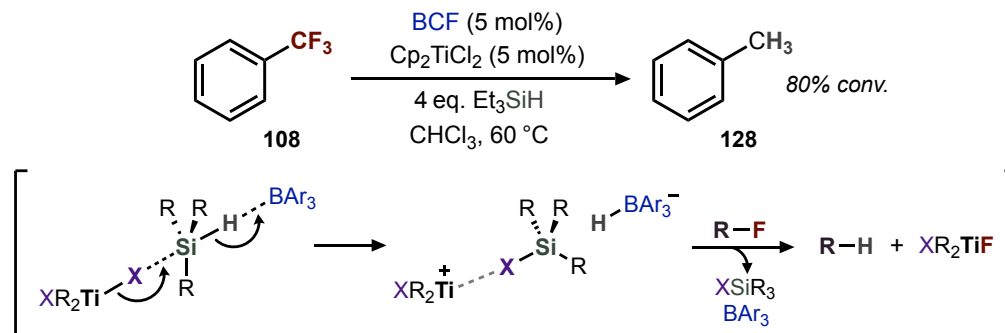
Yet another mechanistic scheme occurs with certain Lewis acids, in which interaction with the hydrosilane occurs via an η^1 -coordination of the hydride bond. Although the silicon center does not form a discrete positive charge, it is sufficiently activated to abstract fluoride. This type of pathway is illustrated in Scheme 1.10, in which BCF is used as a catalytic LA.⁷¹ As the silicon abstracts fluoride, the hydride is completely transferred to BCF, forming a borohydride species. The borohydride then transfers hydride to the carbenium ion, forming the HDF product and regenerating the BCF catalyst.

The reactivity of this system is lower than those based on silylium ions. For example, while the primary fluoride in **126** undergoes HDF, the two CF₃ groups remain intact, and the oxygen heteroatom is tolerated. This is in contrast to very strong acids, such as silyliums, which are poisoned via coordination with any heteroatoms that are present. An analogous hydrosilane activation pathway was also suggested for the related Lewis acid Al(C₆F₄)₃,⁷² as well as for a cationic iridium(III) POCOP pincer complex developed by Brookhart and coworkers.^{73, 74}



Scheme 1.10. HDF of alkyl fluorides catalyzed by BCF-activated hydrosilane

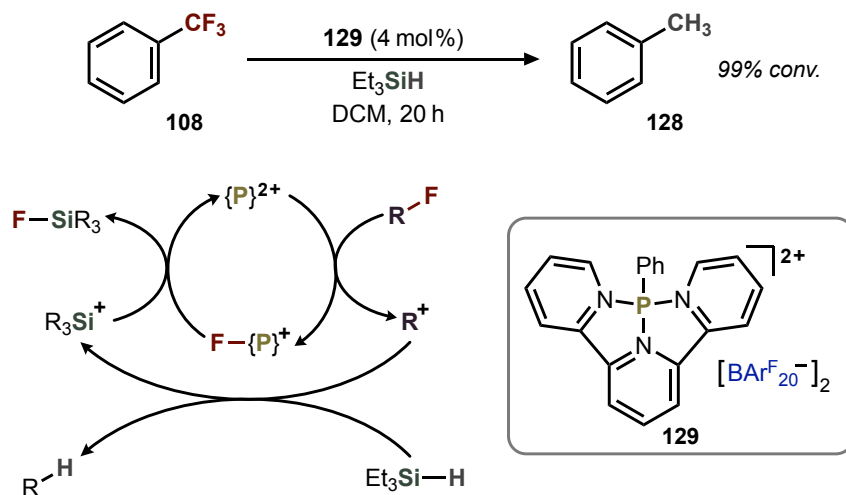
In a recent example, Lamač and coworkers demonstrated that the addition of a catalytic group 4 (Ti, Zr, Hf) complex (e.g. TiX_2R_2) to BCF/ Et_3SiH creates a more reactive system that can react with CF_3 groups (Scheme 1.11).⁷⁵ In addition to η^1 -activation of the Si–H bond by BCF, the authors propose a simultaneous halide abstraction by the silicon center, forming a cationic metal complex that acts as the active species that performs C–F abstraction.



Scheme 1.11. HDF of trifluoromethyl benzene with catalytic BCF and titanium-family complexes

Lewis acids based on other elements can also be combined with hydrosilane to affect HDF, such as the electrophilic phosphorus(III) dication (**129**) reported by Stephan and coworkers (Scheme 1.12).⁷⁶ The phosphorus acid does not act as an *initiator* of a silylium cycle, but rather acts as a catalyst, initiating the cycle by directly abstracting fluoride. The resulting carbocation is reduced by the

hydrosilane, generating a silylium species, which in turn abstracts fluoride from the phosphorous center, regenerating the catalyst.



Scheme 1.12. HDF of trifluoromethyl benzene with a phosphorous(III) catalyst

Stephan and others have developed a number of other electron-deficient phosphorus compounds, used in conjunction with hydrosilane for HDF, with some examples shown in Figure 1.9 (counterions omitted for clarity, $[\text{BAR}^{\text{F}}_{20}]^-$).⁷⁷

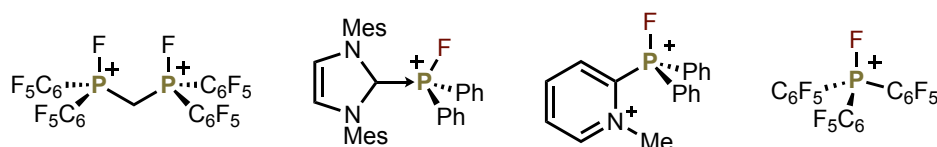
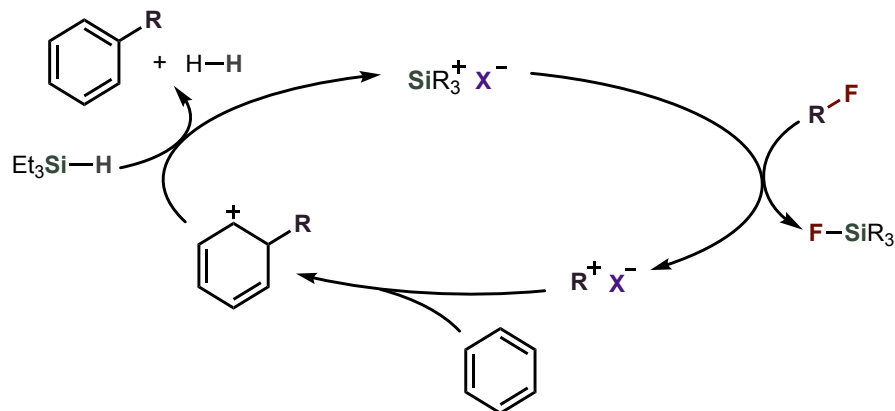
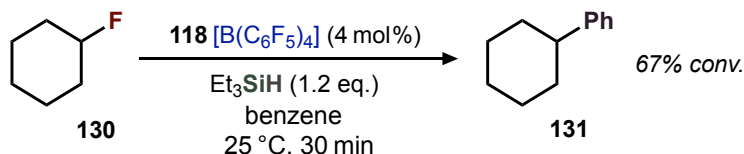


Figure 1.9. Examples of electrophilic phosphonium species used for HDF

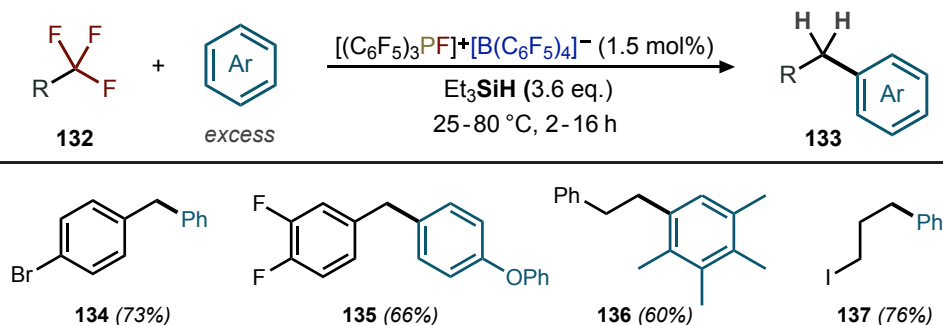
1.2.3 C–F Functionalization

Alternative to HDF, various methods employ a nucleophilic species to trap carbocation intermediates, facilitating C–F bond functionalization. For example, the hydrogen-bridged disilylation discussed above (**118**) was also used to functionalize primary/secondary alkyl fluorides, such as fluorocyclohexane **130** (Scheme 1.13).⁷⁸ The resulting carbenium undergoes a $\text{S}_{\text{E}}\text{Ar}$ reaction with a suitable arene, followed by quenching of the arenium with hydrosilane, releasing dihydrogen and the arylated product. Divergent reactivity was still a problem however, with the observation of di- and trialkylated arenes, as well as rearrangement products.



Scheme 1.13. Catalytic cycle for the silylium-catalyzed arylation of alkyl fluorides

In a similar manner, Stephan demonstrated the arylation of RCF_3 substrates with an electrophilic phosphorus catalyst (Scheme 1.14).⁷⁹ A range of both ArCF_3 (**134**, **135**) and alkyl- CF_3 (**136**, **137**) substrates were reported, with generally high yield and selectivity (see abbreviated scope). Similarly, a number of different arenes could be used (*p*-xylene, toluene, mesitylene, 1,1-biphenyl, etc.).

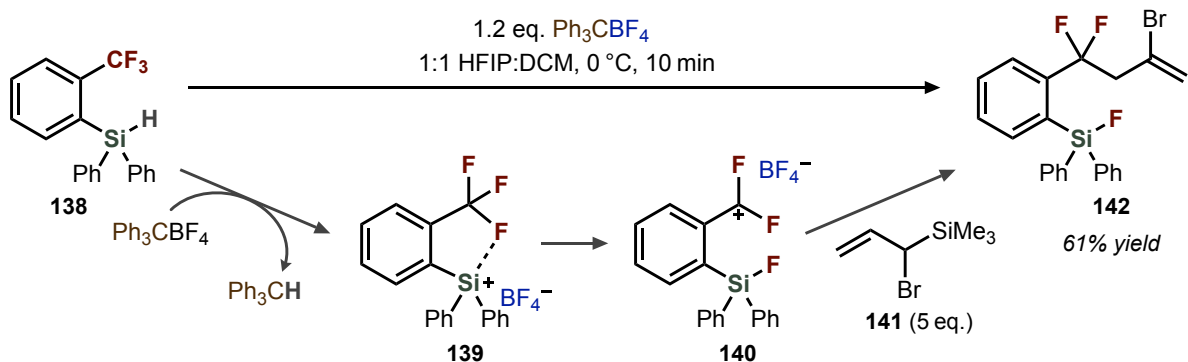


Scheme 1.14. Mono-arylation and HDF of trifluoromethyl compounds using a phosphorous(V) catalyst

Under these conditions, 1° alkyl fluorides such as 1-fluorohexane, underwent extensive rearrangements, indicating $\text{S}_{\text{N}}1$ reactivity is still operative. However, no isomerization was observed with alkyl- CF_3 substrates. The authors postulate this is a result of arylation occurring first, leading to a conformationally more robust difluorobenzyl cation, which then undergoes rapid HDF. In addition to RCF_3 substrates, benzyl fluorides were likewise shown to undergo arylation, or to couple with allylsilanes to form homoallylic aryl alkenes.⁸⁰

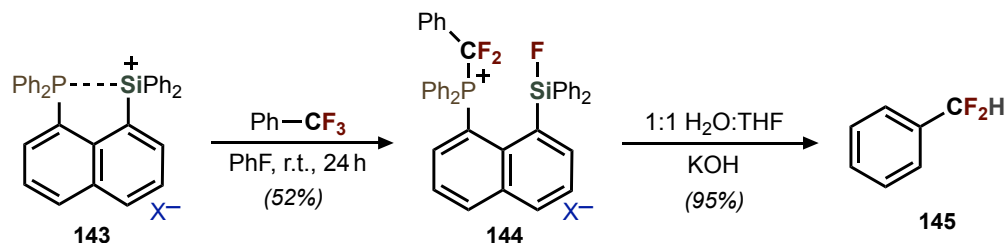
1.2.4 Selective Single C–F Activation

Hosoya and coworkers reported a clever design to achieve mono-selective defluorination of ArCF_3 , tethering a hydrosilane ortho to the CF_3 group (Scheme 1.15).⁸¹ A silylium (**139**) is formed upon treatment with a trityl cation precatalyst, which subsequently performs single *intramolecular* fluoride abstraction. Nucleophilic addition to the carbocation (**140**) then forms the ArCF_2R product. Alternatively, a mechanism with concerted hydride abstraction and C–F bond cleavage is also plausible. The original scope of allylsilane nucleophiles (e.g. **141**) was later expanded to include a range of other halides.⁸² Further, the use of a Ph_3CX precatalyst (X : Cl, Br, OTf) allowed for direct formation of ArCF_2X products, in good-to-excellent yields. Although quite efficient, this method has poor generality, utilizing only specific pre-functionalized arenes, and requiring an additional removal step if the ortho-silane is not desired in the final molecule.



Scheme 1.15. Single C–F activation of ortho-silyl trifluoromethyl arenes

A powerful approach for defluorination is the use of Frustrated Lewis Pairs (FLPs).⁸³ An FLP is a Lewis acid/base combination, in which steric conflict prevents formation of a traditional Lewis adduct. This allows the acid and base to retain their individual reactivities, thereby offering unique selectivity advantages in C–F chemistry. As in other LA mediated processes, fluoride abstraction affords a carbocation intermediate. However, the base component of the FLP is able to coordinate (*trap*) this cation, rendering it inactive towards further reactivity. This was first illustrated by Stephan and coworkers with phosphine/silylium FLP **143** (Scheme 1.16).⁸⁴ The *intramolecular* nature of the FLP was thought to be advantageous, allowing for rapid trapping of the PhCF_2^+ species to afford **144**. Treatment with base then affects C–P cleavage, affording ArCF_2H **145**. Importantly, this example was the first application of FLP chemistry to selective ArCF_3 activation, with the drawback that a stoichiometric amount of the sensitive silylium FLP is required.



Scheme 1.16. Single HDF of trifluoromethylbenzene with a phosphine/silylium FLP.

1.3 Boron Lewis Acids

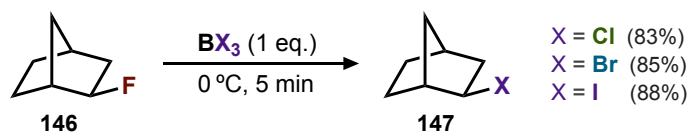
Boron compounds have long been utilized for the cleavage of strong bonds in synthetic organic chemistry, particularly alkoxy aryl ethers. More recently, boronic and borinic acids have been utilized as catalysts to direct reactivity, or to pre-activate bonds for functionalization. These chemistries take advantage of boron compounds' fast on/off ligand binding kinetics. As such, boron Lewis acids rapidly settle at the thermodynamically preferred location, leading to exceptional chemoselectivity.

Less well developed is the development of chemoselectivity in reactions where boron acts to directly drive bond cleavage, rather than act as a catalyst. Previous work in the Williams Group has begun to explore selectivity profiles of heteroleptic boryl halides in the context of C–O activation. This led to a method with improved regio- and chemoselectivities in dialkyl ether functionalizations.

Boron compounds are also important in the growing area of C–F activation, both as catalytic species, and as stoichiometric reagents. Whereas silicon excels in the area of HDF, boron complexes are often the first choice for halex reactivity. Additionally, electrophilic boron species frequently serve as the Lewis acid partner in FLP chemistry.

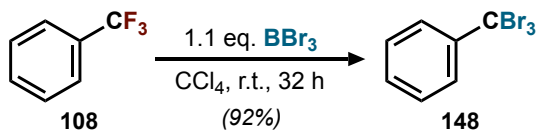
1.3.1 Halogen-Exchange

Boron trihalides (BX_3) are particularly useful for halex reactivity. They are widely available, inexpensive, and form gaseous BF_3 under defluorination conditions. Barrio and coworkers were the first to report on their use for alkyl fluoride halex in 1995 (Scheme 1.17).⁸⁵ For example, norbornyl fluoride (**146**) could be efficiently converted to the corresponding alkyl halide (**147**) using BX_3 (X: Cl, Br, I). Similar yields (78–94 %) could be obtained for 1°, 2°, 3° alkyl mono-fluorides, although some rearrangement chemistry was observed with 1° substrates, such as 1-fluoroheptane.



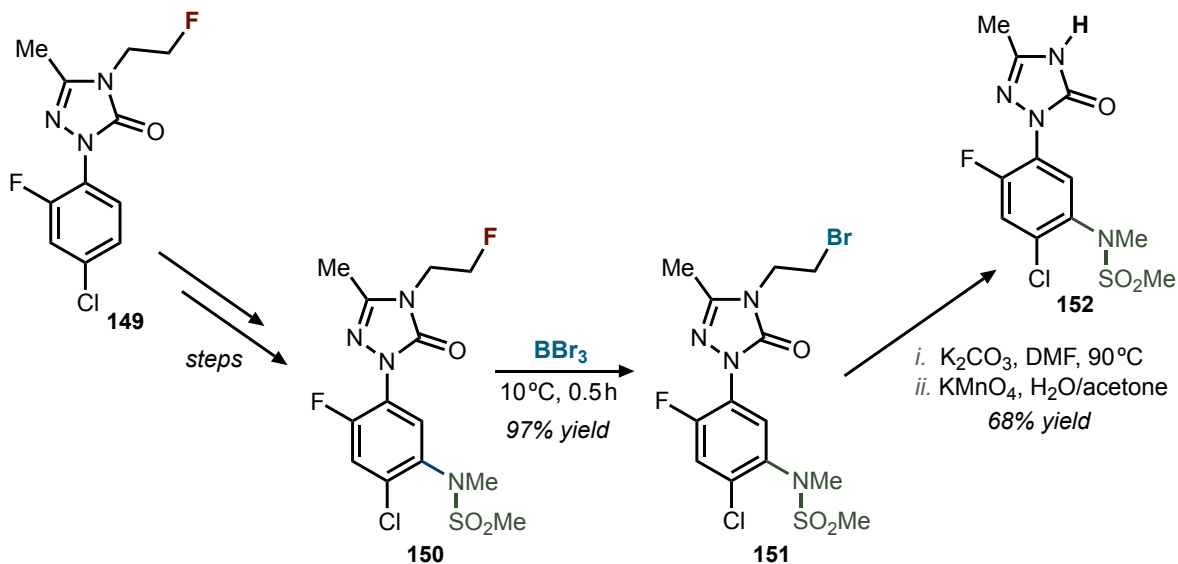
Scheme 1.17. Boron trihalide mediated halogen-exchange

Prakash and Olah evaluated BBr_3 halex with a more robust trifluoromethyl substrate (**108**), demonstrating conversion to the tribromomethane **148** (Scheme 1.18).²³ However, this transformation necessitated an extended 32-hour reaction time, and the problematic use of carbon tetrachloride (highly regulated due to toxicity and environmental concerns). Chen et al. used the same conditions to report a short substrate scope, although only simple arenes were used (single halogen or alkyl substituents).³⁷



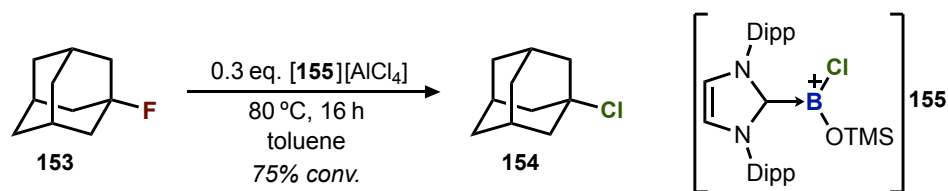
Scheme 1.18. Boron tribromide mediated triple halogen-exchange

Theodoridis used these precedents to conceive a method for nitrogen protection, using the 2-fluoroethyl group.⁸⁶ He demonstrated this strategy in the synthesis of an aryl triazolone (152) agrochemical (Scheme 1.19). The protected compound **149** underwent a number of synthetic transformations to introduce the sulfonamide moiety (**150**), without interference from the inert fluoroethyl group. Deprotection could then be initiated by BBr_3 halex, to provide the alkyl bromide (**151**). Elimination to form the olefin, followed by oxidative cleavage then affords the free nitrogen. Although an interesting strategy, the number of synthetic steps required for deprotection is a disadvantage, and this method has seen little uptake in the synthetic community.



Scheme 1.19. Nitrogen protection strategy used in the synthesis of a triazolone agrochemical

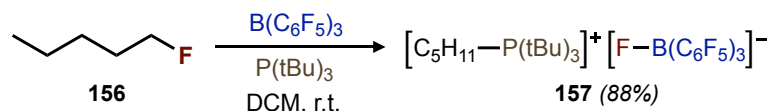
Rivard and coworkers reported a rare example utilizing a cationic boron complex for C–F activation.⁸⁷ They synthesized an NHC-ligated oxoborenum cation (**155**), which proved capable at effecting halogen-exchange with fluoroadamantane **153** (Scheme 1.20). Interestingly, cationic boron complexes are rarely used for C–F activation, unlike their silicon counterparts.



Scheme 1.20. Halogen-exchange using a borenium species

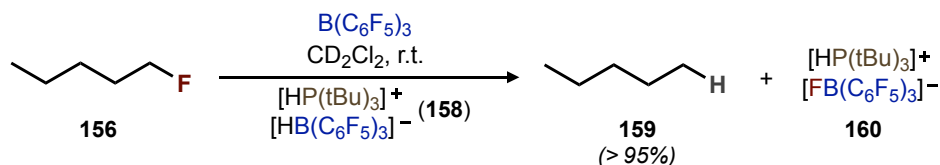
1.3.2 Hydrodefluorination

The Stephan Group was the first to demonstrate the use of FLP chemistry for C–F activation, with a short series of alkyl fluorides, including adamantyl–, cyclohexyl–, and pentylfluoride (**156**), as shown in Scheme 1.21.⁷¹ They utilized an *intermolecular* phosphine/borane FLP in stoichiometric amounts, with reactivity driven by the fluorophilicity of BCF, which has a Lewis acidity in-between that of BF₃ and BCl₃. The reaction led to salt products (e.g. **157**) containing a fluoroborate anion and alkylphosphonium cation.



Scheme 1.21. C–F functionalization of 1-fluoropentane using a boron/phosphorous FLP

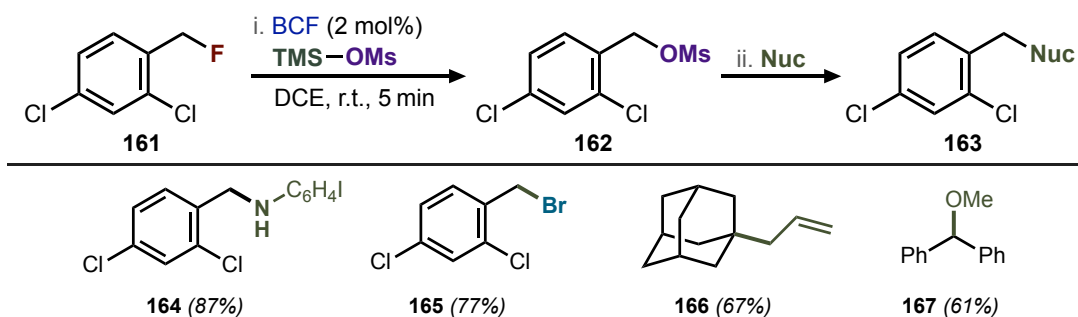
This FLP can also be used to split H₂ (another important application of FLP chemistry), to afford hydridoborate phosphonium salt **158**.⁸⁸ Stoichiometric addition of this salt to 1-fluoropentane (**156**), along with one equivalent of neutral BCF, results in HDF and the formation of pentane (**159**), in an overall B–H/C–F metathesis process (Scheme 1.22).



Scheme 1.22. HDF C–F functionalization of 1-fluoropentane using a boron/phosphorous FLP

1.3.3 C–F Functionalization

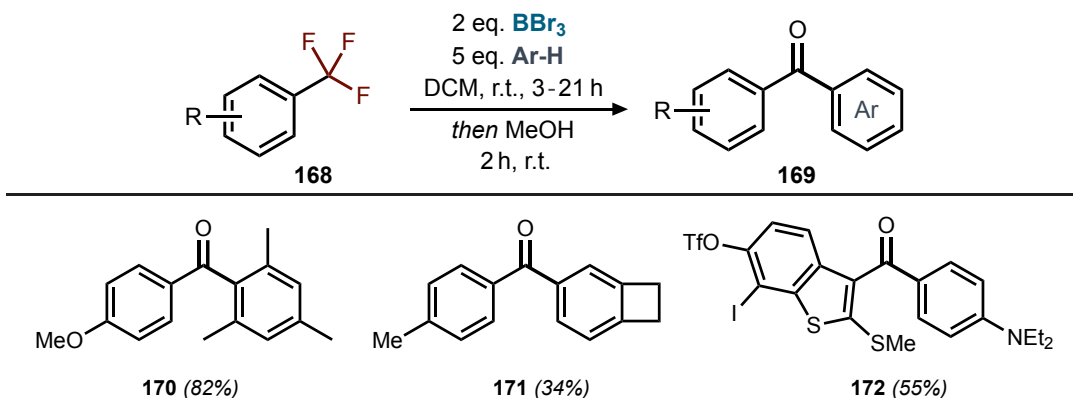
The Young Group formulated a two-step strategy to substitute benzyl fluorides (e.g. **161**) with various nucleophiles (Scheme 1.23).⁸⁹ The BCF catalyst facilitates fluoride abstraction, with subsequent transfer to a stoichiometric silane, affording a benzyl mesylate (or triflimide) intermediate **162**. The pseudo-stable mesylate intermediate can then be functionalized with a suitable nucleophile. The silyl mesylate proved much more effective than the analogous iodasilane, which proceeded much slower for both the C–F activation step and subsequent substitution.



Scheme 1.23. Functionalization of benzyl fluorides with various nucleophiles

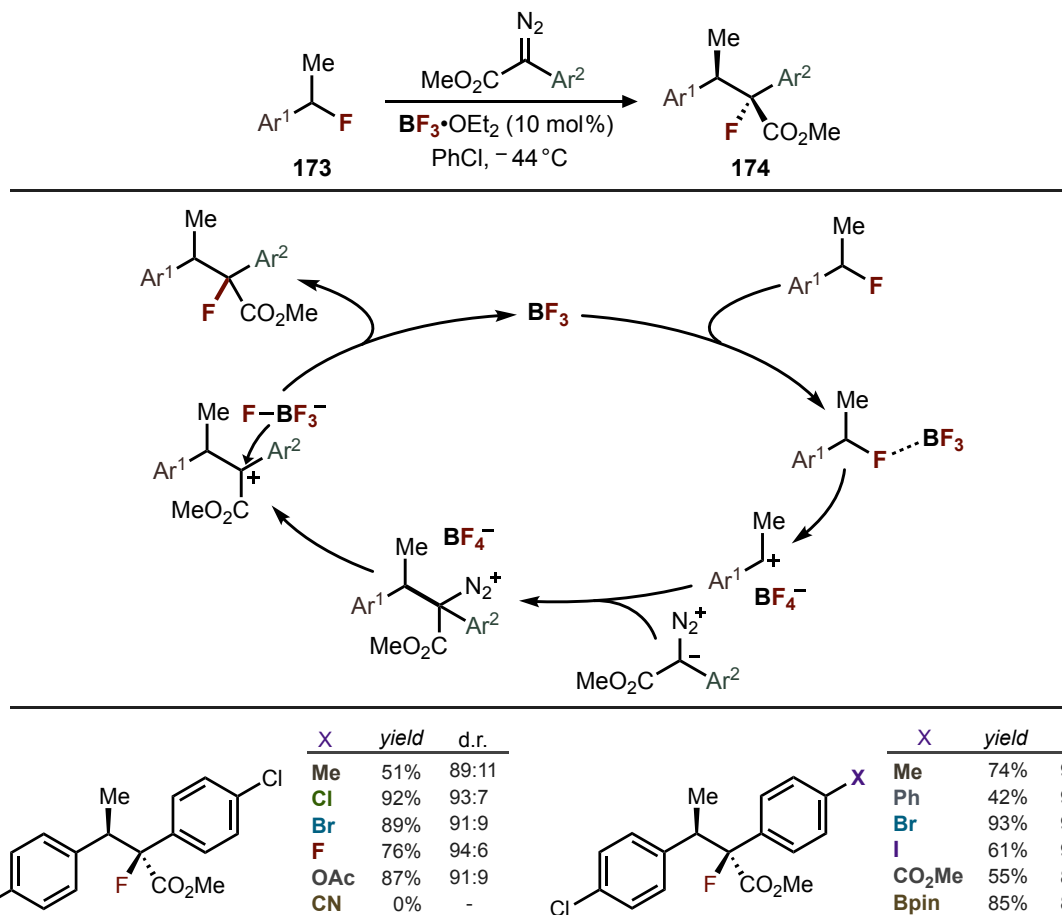
Partitioning C–F activation and functionalization into separate steps was key to the success of this method. It allowed for substitution with amines, alcohols, and other nucleophilic species that are incompatible with strong Lewis acids such as BCF.

Hosoya and Yoshida demonstrated that ArCF_3 substrates (**168**) could be converted to diaryl ketones (**169**), using BBr_3 (Scheme 1.24).⁹⁰ The reaction proceeds via an ArCBr_3 intermediate, and is thought to then undergo acyl bromide formation upon the addition of methanol, followed by Friedel-Crafts acylation with the arene. Various substrates were explored, including functionalized benzothiophenes (e.g. **172**). Alternatively, in the absence of the arene, alcohol addition affords the corresponding ester.



Scheme 1.24. Conversion of trifluoromethyl arenes to diaryl ketones with boron tribromide

Yasuda and Nishimoto disclosed a one-carbon elongation of benzyl fluorides **173** with diazoesters by employing BF_3 catalysis (Scheme 1.25).⁹¹ This formal C–F insertion process affords the homobenzyl fluoride **174** with high levels of diastereoselectivity. The proposed mechanism, evaluated with DFT calculations, begins with abstraction of fluoride by BF_3 , forming the benzylic cation. Attack by the nucleophilic diazo carbon then forms a diazonium species, and subsequent extrusion of N_2 affords a homobenzyl cation. Finally, C–F bond formation mediated by BF_4^- affords the product and regenerated catalyst BF_3 . This C–F cleavage/reformation process can be described as a *fluoride-rebound*, reminiscent of a mechanism observed by Toste and coworkers upon the treatment of Au(III)-CF_3 complexes with BCF.⁹²



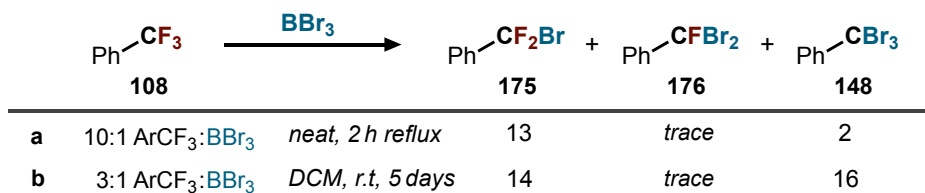
Scheme 1.25. Insertion of diazo esters into benzyl fluorides with boron trifluoride catalysis

The diastereoselectivity originates in the C–F reformation step, proceeding via the conformation which minimizes Ar¹/Ar² steric repulsions, affording most products with diastereomeric ratios in the range of 85:15 – 95:5. A variety of para-substituted benzyl fluorides proceeded in moderate-to-high yield, with the exception of those containing strong EWG's (e.g. CN). Various electron-deficient diazo esters were also competent in the reaction, whereas electron-rich diazo esters required addition in excess, given their propensity to dimerize in solution.

1.3.4 Selective Single C–F Activation

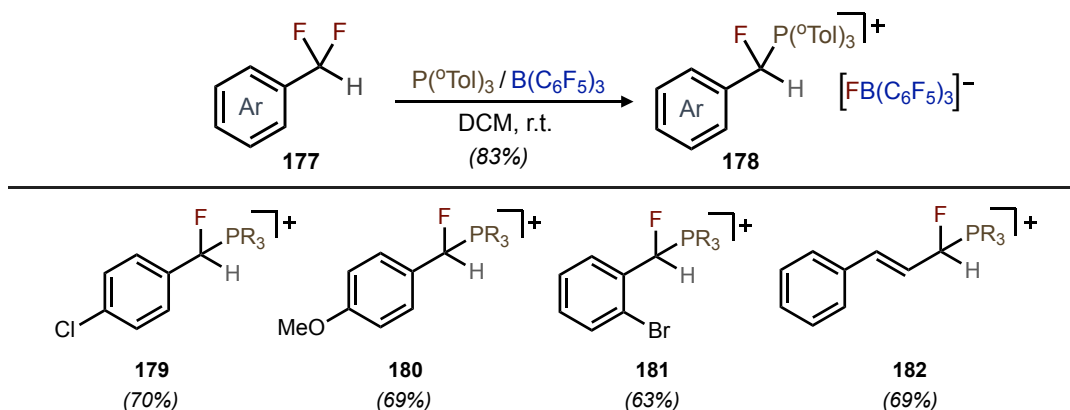
In order to achieve a *single* halex with PhCF₃ **108**, Prakash and Olah modified the conditions of the BBr₃ reaction (Scheme 1.26).²³ Good selectivity for the mono-bromide **175** could be obtained with a large excess of PhCF₃ **108** (entry a), although fairly aggressive refluxing conditions were required. With more BBr₃, reflux could be avoided (entry b), but a 5-day reaction was required, and the selectivity for CF₂Br **175** was diminished. Despite the low yields, these conditions have been used

almost exclusively by other researchers to make ArCF₂Br compounds. No mechanistic investigations or a substrate scope were explored.



Scheme 1.26. Different conditions used for the mono-halex of trifluoromethylbenzene

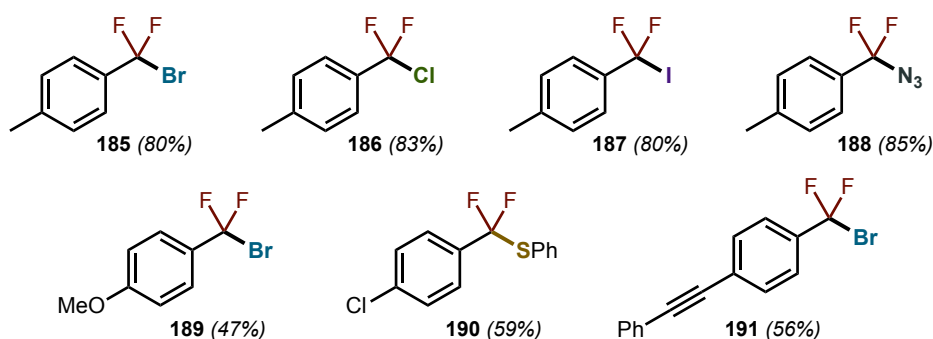
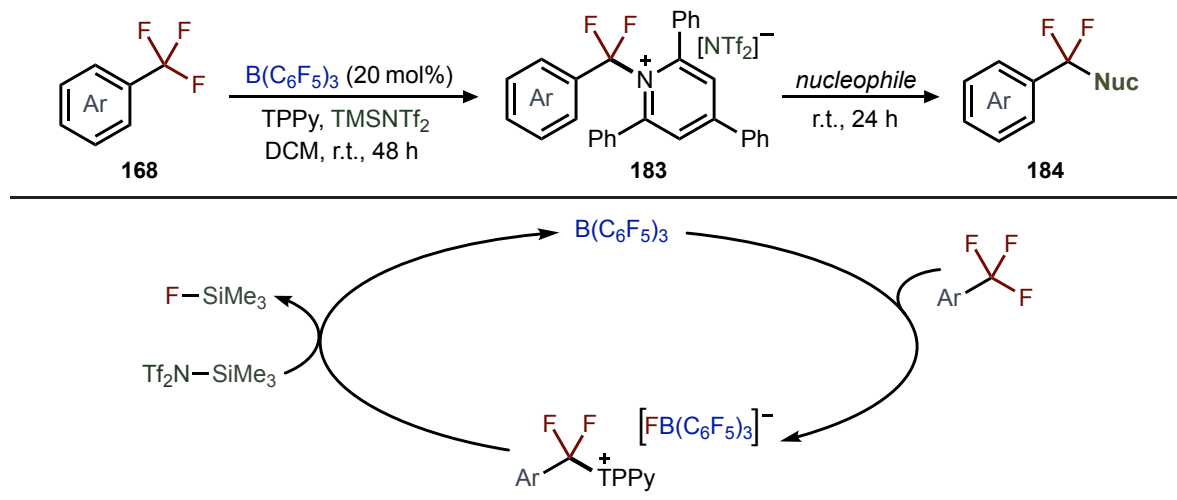
C–F activation was realized using an *intermolecular* FLP by Young and coworkers (Scheme 1.27).⁹³ Combining BCF with a bulky phosphine base proved an effective FLP combination for the defluorination of *gem*-difluoromethylenes (e.g. **177**). The resulting stable phosphonium/borate salt **178** could be isolated for a variety of substrates (see examples below, isolated yields shown).



Scheme 1.27. Single C–F cleavage of difluoromethyl groups by a boron/phosphorous FLP

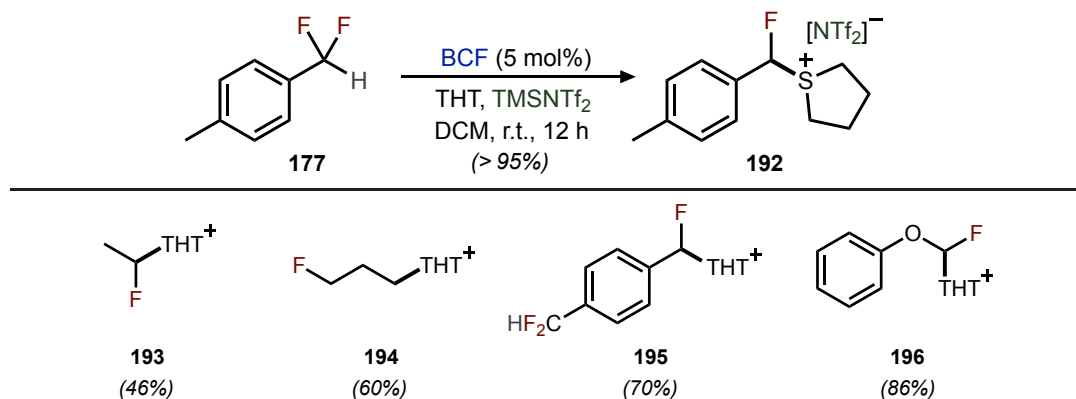
Young extended this work to use catalytic amounts of BCF, with the addition of a trimethylsilyl triflimide additive (TMS-NTf₂), as shown in Scheme 1.28 (NMR yields shown).⁹⁴ The triflimide acts to regenerate BCF from the fluoroborate anion, thermodynamically driven by the formation of Me₃SiF gas. The stability of the intermediate phosphonium salts necessitated the need to examine alternative FLP base partners, that could more easily allow for subsequent nucleophilic substitution.

The nitrogen base 2,4,6-triphenylpyridine (TPPy) was found to be an effective base partner, allowing for facile substitution of the intermediate salt **183** with a range of nucleophiles. For example, treatment of intermediates (**183**) with tetrabutylammonium halides afforded the corresponding ArCF₂X compound (**185-187**, **189**, **191**). Electron-poor arenes (e.g. **190**) tended to slow the C–F activation, often necessitating increased temperatures (60 °C in DCE). Conversely, with arenes containing electron-donating groups (e.g. **189**), the first C–F activation step was quite rapid, but the resulting TPPy salt was less stable, and could begin to decompose before addition of the nucleophile.



Scheme 1.28. Single C–F cleavage of trifluoromethyl arenes by a boron/pyridine FLP

Additional screening revealed the effectiveness of using sulfur bases, in particular tetrahydrothiophene (THT).⁹⁵ For example, 4-difluoromethyl toluene **177** could be converted to the THT salt **192** with high efficiency (Scheme 1.29). This was applied to a range of other substrates, including non-benzylic alkyl fluorides (e.g. **193**, **194**, **196**). Further, there were rare examples of activation of equivalent *distal* C–F bonds, such as in **194** and **195**.



Scheme 1.29. Single C–F cleavage of difluoromethyl arenes by a boron/sulfur FLP

The scope of derivatizations was also expanded, for both trifluoro- and difluoromethyl starting materials. A summary of methods used by the Young Group for salt (TPPy, THT, or PR_3) derivatization is shown in Figure 1.10.⁹³⁻⁹⁵ In addition to nucleophilic addition, photoredox and Suzuki couplings afford alkyl and aryl fluoromethylenes respectively. Alkyl phosphonium salts are known to react with carbonate, facilitating nucleophilic transfer of one of the alkyl groups. As such, treatment of difluorobenzyl phosphonium ($\text{ArCF}_2\text{PR}_3^+$) with Cs_2CO_3 enables reaction with benzaldehyde to afford α -fluoroalcohols. Alternatively, KOH addition to phosphonium salts affords the formal HDF product. Finally, with RCF_2H starting materials, phosphonium salt formation, deprotonation, and a subsequent Wittig reaction produces α -fluorostyrenes.

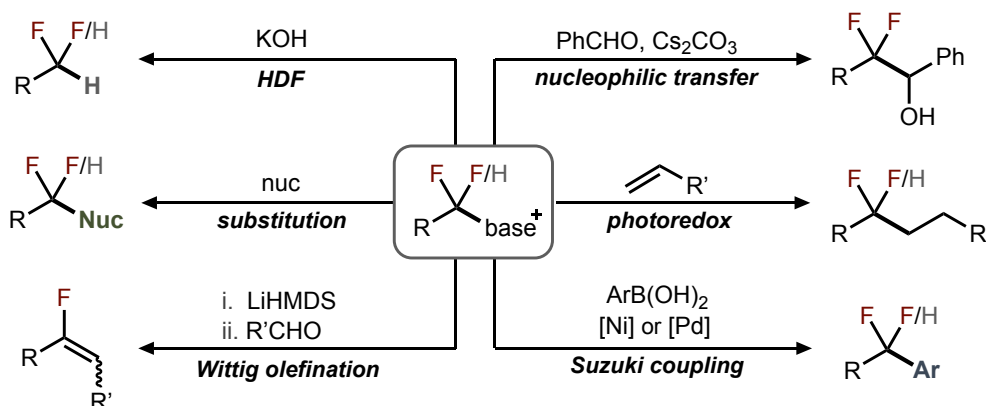


Figure 1.10. Functionalization of intermediate fluoromethyl onium salts

The cumulation of C–F activation methods developed by Young and coworkers represented a major advance in the field. However, one disadvantage of these methods is their inherent complexity, requiring rigorously dry conditions and specialty reagents (e.g. TMS-NTf_2). As such, it remains to be seen if these methodologies will see significant uptake in the chemical community for synthesis of ArCF_2R and ArCHFR compounds.

1.4 Conclusion and Thesis Objectives

The captivating and fruitful properties of organofluorine compounds have led to numerous impacts in the pharmaceutical, agrochemical, and materials science fields. As fluorinated functional groups become more common, so too does the search for new methods to functionalize C–F bonds. This strategy has important implications for the degradation of environmentally persistent industrial fluorocarbons. In addition, C–F activation offers a unique approach to access high-value fluorinated motifs. This chapter focused on recent methods that employ boron and silicon Lewis acids for the activation of $\text{C}(\text{sp}^3)\text{–F}$ bonds. These methods are similar to those that use aluminum or acidic transition-metal complexes, and are complementary to photoredox and other reductive processes.

Reactions with trifluoromethyl arenes (ArCF_3) were discussed extensively. Although there are a number of useful transformations involving triple defluorination of ArCF_3 , one of the most appealing goals is single activation of ArCF_3 . The resulting difluoromethyl (CF_2R , CF_2X , CF_2H) products are highly desirable, but have been traditionally difficult to access. A number of elegant methods have been used to produce these moieties. However, many of these methods require either pre-functionalization of the ArCF_3 (e.g. ortho-silane), or sensitive reagents/methods (e.g. FLP chemistry), that are not always attractive for routine synthesis or large-scale procedures.

Chapter 2 aims to address some of these drawbacks, building upon the BX_3 halox reactions reported by Barrio, and Olah, wherein slow reactivity was observed with ArCF_3 substrates (*vide supra*). This limitation motivated investigations into catalysts for halogen-exchange. In addition, there was an incentive to improve the selectivity for ArCF_2X formation via *single* halox, given the utility of such products. The ultimate development of a new method utilizing FeX_3 reagents is described, as well as investigations into the mechanism of catalytic activation, and the synthesis of ArCF_2X or ArCX_3 products from an assortment of ArCF_3 substrates.

Chapter 3 gives an overview of PET imaging, an important medical tool for the diagnosis and monitoring of several diseases. There is a particular focus on the radionuclide fluorine-18, one of the leading PET radioisotopes, and the different radiofluorination strategies used for its incorporation to biomolecules of interest. One notable goal in radiofluorination, yet to be achieved by any existing methods, is the efficient synthesis of ^{18}F ArCF_3 directly from the corresponding ArCF_3 precursor. The efforts towards development of such a method are described in this chapter, with the hypothesis that the BX_3/FeX_3 method developed in Chapter 2, could facilitate ArCF_3 halox with ^{18}F fluoride.

Chapter 4 expands upon a group of radiofluorination strategies referred to as *non-canonical labeling*, and some of their applications in the development of clinical candidates for PET imaging. In particular, there has been a major impetus to develop new tracers targeting PSMA, a biomarker that can facilitate monitoring of prostate cancer and other tumors. As such, a novel PSMA radiotracer was designed in the Schirmacher Group, and the ongoing efforts towards its synthesis are also described in this chapter.

2.1 Introduction

As described in the previous chapter, an appealing target for the functionalization of C–F bonds is the conversion to higher halide C–X bonds (X = Cl, Br, I), a process termed *halodefluorination* (HaloDF).^{39, 57, 58, 85, 96-99} These larger halides are versatile synthetic handles, with heightened reactivity over the parent fluoride.

Halex reactions on fluorinated substrates are typically performed with stoichiometric early valent metal halides (TiX₄, MoCl₅), or p-block metalloid halides (BX₃, AlX₃, R₃SiX).⁵⁴ These halide reagents provide the necessary thermodynamic drive through formation of a strong fluoride bond. However, challenging substrates often require additional catalysts to avoid high temperatures and long reaction times.

This chapter describes work performed within the Williams Group, in which iron catalysts were utilized to facilitate ArCF₃ halex with boron trihalides (Figure 2.1). To the knowledge of the author, this reaction constitutes the first example of halex reaction with mechanistic evidence for iron coordination and direct activation of a C–F bond. Although Barrio previously disclosed BX₃ mediated halex, only mono-fluoroalkane starting materials were used.⁸⁵ Whereas when a trifluoromethyl substrate (PhCF₃) was subjected to BBr₃ by Olah and Prakash, forcing conditions were required, and poor selectivity for *single* halex was observed (q.v. *section 1.3.4*).²³ The present work builds upon these reports, examining the benefit of halex catalysts, and the ability of various ArCF₃ substrates to undergo the halex reaction.

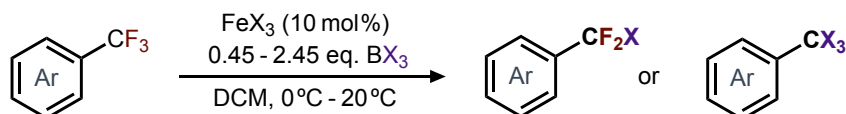


Figure 2.1. Summary of the reaction described in this chapter

2.1.1 Iron Catalysis

Iron, being a low-cost high abundance metal, has been surprisingly absent in catalytic defluorination development. The potential of iron catalysis in this field is nevertheless exemplified in the activity of enzymes such as Horseradish peroxidase, Methane monooxygenase and Cytochrome P450s, all employing iron-based catalytic motifs, which perform catalytic defluorination along with oxygenation (e.g. Figure 2.2).^{100, 101}

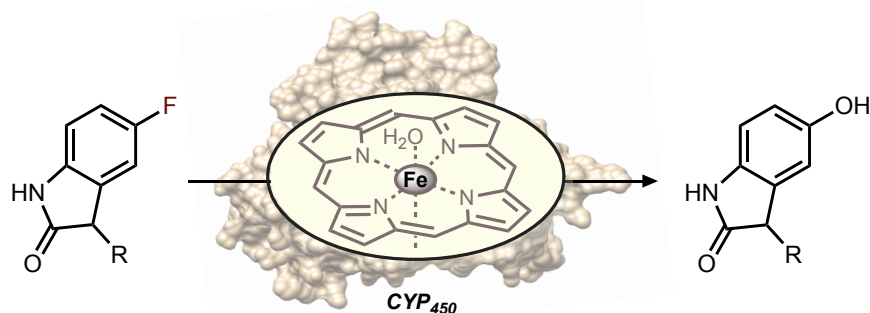
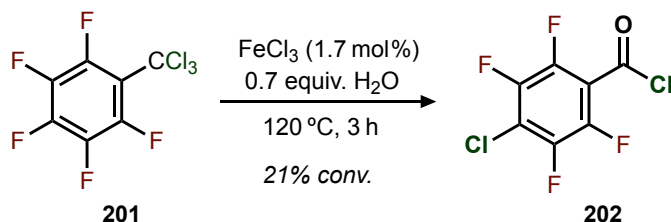


Figure 2.2. Cytochrome-P450 catalyzed defluorination and concurrent hydroxylation

In the organic synthesis literature, there appears to be only one example of iron-catalyzed defluorination, in which FeCl_3 is used to catalyze the chlorination of pentafluorobenzene **201** (Scheme 2.1).¹⁰² Given the relevance in biological systems, and apparent under-utilization in the C–F activation literature, the ability of iron compounds to catalyze C–F halogen exchange reactions was examined.



Scheme 2.1. Example of an iron-catalyzed C–F halogen exchange

2.1.2 Design of Experiment

Design-of-Experiment (DOE) is a powerful statistical method, frequently used for optimization of complex processes, such as chemical reactions.^{103, 104} Traditional reaction optimization typically relies on the *one-factor-at-a-time* (OFAT) approach – each reaction factor (e.g. temperature, concentration, time, etc.) is individually and sequentially evaluated. However, a major drawback to this approach is that it does not consider *interaction effects* between factors.

This problem is illustrated in a hypothetical reaction shown in Figure 2.3, in which two factors are manipulated to identify a maximum yield. An example OFAT optimization could begin by fixing $T = 0^\circ\text{C}$, then varying the pH – indicating max yield at $\text{pH} = 7.0$. Next, at a fixed $\text{pH} = 7.0$, temperature is varied until a maximum at 15°C is identified. This implies an optimum of 58% yield at $\{T = 15^\circ\text{C}, \text{pH} = 7.0\}$, failing to identify a true optimum of 95% yield at $\{T = 40^\circ\text{C}, \text{pH} = 5.2\}$, and account for the complexity of the system, in which there is a strong temperature/pH interaction effect.

DOE utilizes a range of factor combinations (e.g. DOE test points: ▲ in Figure 2.3). Regression analysis is used to generate a mathematical model of a reaction outcome (e.g. yield) as a function of the defined factors.¹⁰⁵ As such, the entire *reaction space* encompassed by the test points is evaluated,

allowing for prediction of the true local optimum. The relative importance of each factor, as well as any interaction effects, is determined using *analysis of variance* (ANOVA).

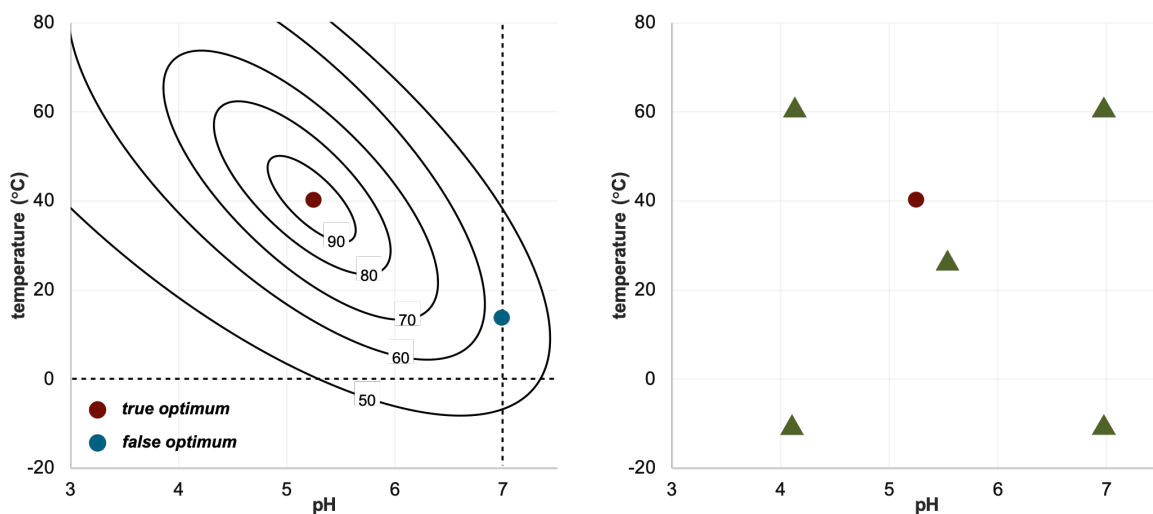


Figure 2.3. Contour plots for yield of a hypothetical reaction as a function of pH and temperature. *OVAT approach* (left). *DOE design* (right).

DOE allows for creation of a *soft model* – a local empirical approximation, in contrast to a hard-physiochemical model (e.g. DFT, rate theory, etc.), that can be difficult to apply in complex systems (and rarely incorporates interaction effects). The following illustrations depict a 2-factor reaction (e.g. temperature, pH), although the same principles can be applied to multi-factor systems. Figure 2.4 shows the equation for a linear model ($\beta_n = \text{constant}$), as well as a geometric interpretation which appears as a *plane*. These linear equation terms are referred to as the *main effects* of the model.

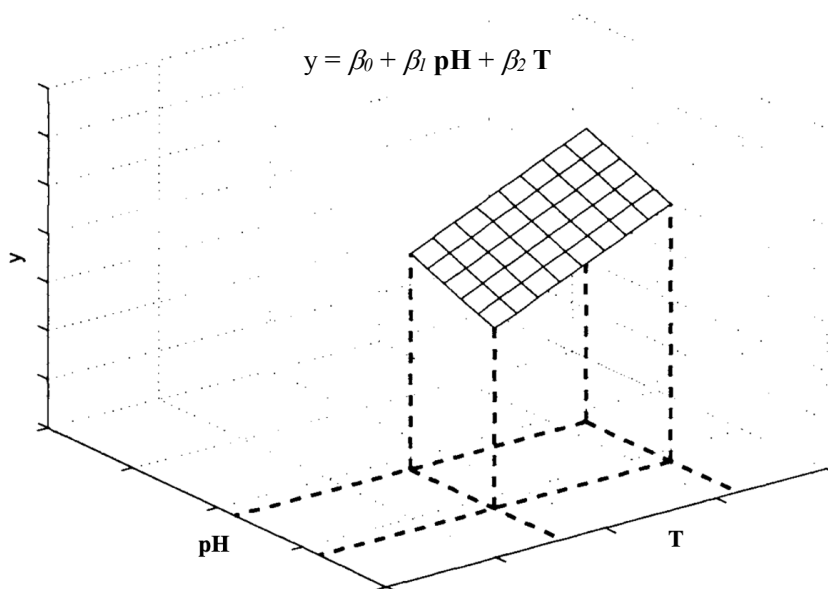


Figure 2.4. Linear model for a 2-factor system.¹⁰⁶

When a strong interaction effect is present, a linear model is insufficient, and a *cross-product* term must be added, producing a second-order model (Figure 2.5). The degree of interaction is described by the cross-product coefficient (β_3), geometrically appearing as a *twisted-plane*. Finally, the most sophisticated models include quadratic terms (Figure 2.6), necessary when a system contains significant curvature (non-linearity).

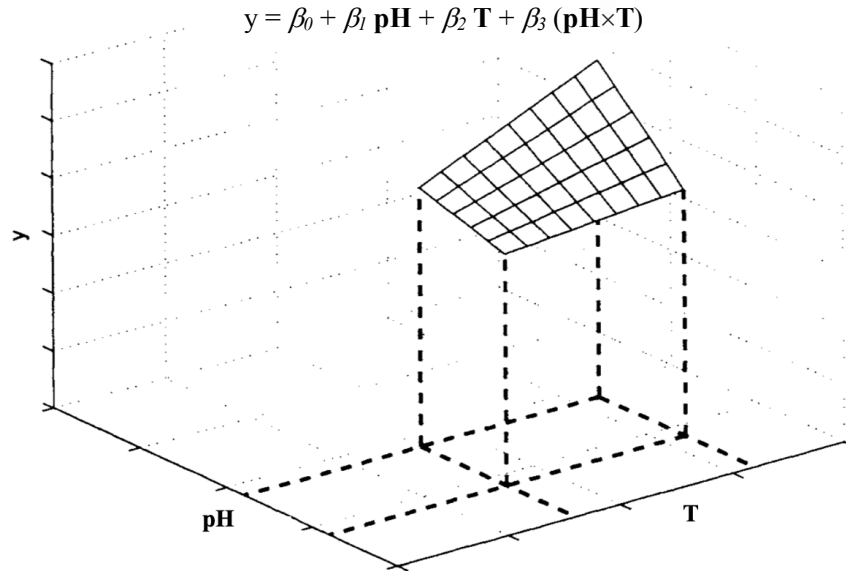


Figure 2.5. Second-order model for a 2-factor system.¹⁰⁶

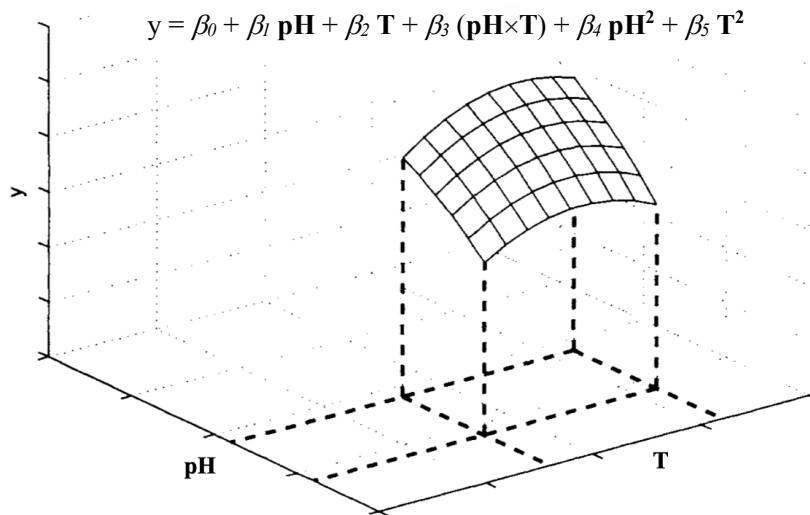


Figure 2.6. Full quadratic model for a 2-factor system.¹⁰⁶

Although any of the terms discussed above are available for incorporation to the model (for each factor), only the most significant terms are ultimately included. This is as result of a technique called *stepwise regression*, in which either the most significant variable is added, or the least significant one

removed, during each step of the iterative model building process. This prevents *over-fitting* – when a model contains too many terms and starts fitting noise, losing the ability to predict future data points.

In order to quantify how well the data fits the model, a number of statistics are evaluated. Namely, standard R^2 values are examined, as well as a cross-validation test called $R^2_{\text{predicted}}$. This is calculated systematically by removing a data point, regenerating the regression model, then testing how well the new model fits the removed data point. $R^2_{\text{predicted}}$ is always lower than R^2 , but if it is significantly lower, this may be an indication of an over-fit model. Examination of distribution of residuals as a function of reaction order, can reveal the presence of any systematic experimental error that may be present.

A number of different DOE designs can be employed, visualized below for 3-factor systems (Figure 2.7). In a *full factorial* design, two values are chosen for each factor (high/low level), and every combination of high/low is performed (spheres in Figure 2.7), along with a center point. This design is effective for linear systems and for providing a general picture of factor influence. It can often be simplified to a *fractional factorial*, which reduces the number of experiments, but still spans the entire reaction space. A *response surface* design provides the most fine-tuned model, and is especially necessary when significant curvature is present (i.e. when quadratic terms are significant). It encompasses all points used in a full factorial, along with additional axial points centered at the face of the design cube (see red spheres in Figure 2.7).

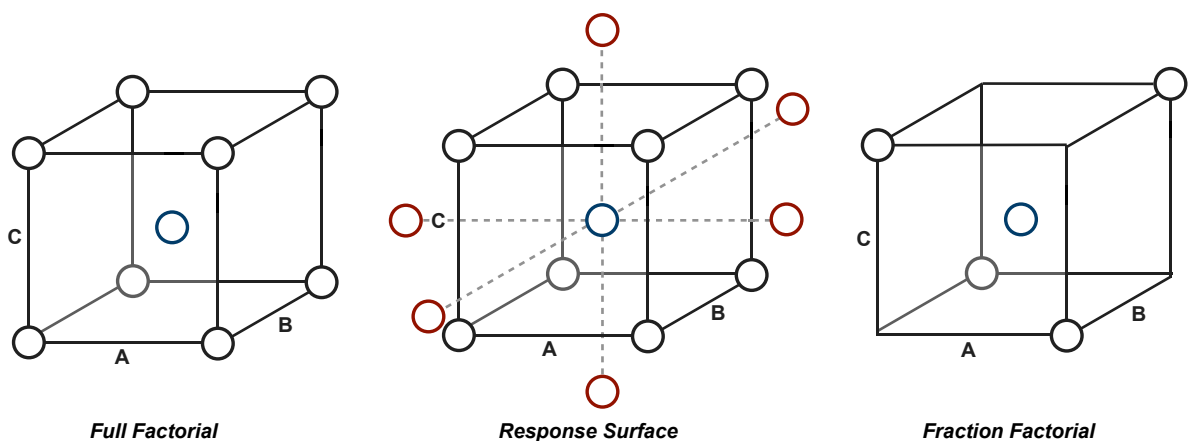
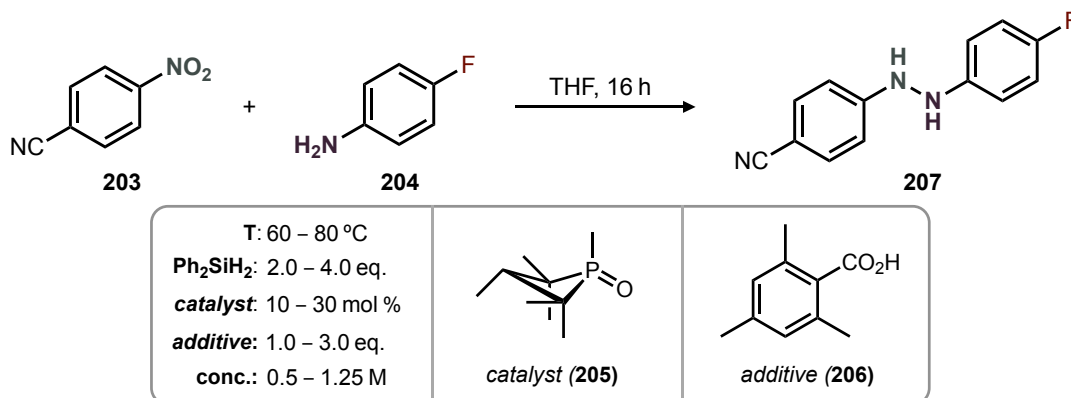


Figure 2.7. Illustrations of DOE designs for a 3-parameter system

The advantages of DOE are well recognized in process science and engineering, where it is frequently used.¹⁰⁵ Although less popular in academic chemistry, examples of DOE optimizations are becoming more common. In an example from the Radosevich Group, a 5-factor half fractional DOE (2^{5-1}) was used to identify reaction sensitivity with regard to each factor.¹⁰⁷ The reaction utilizes a hydrosilane to reduce the P(V) catalyst to P(III) *in situ*, as well as a carboxylic acid additive that acts to donate a proton during an azo reduction step. Thus, equivalents of the additive, the hydrosilane, and the catalyst were chosen as factors for investigation, as well as standard reaction parameters,

temperature and concentration (Scheme 2.2). Key factors were found to be concentration, and temperature/silane and additive/silane interaction effects. Ultimately, the DOE aided in identifying an optimum reaction yield (86%), and validation of the overall reaction robustness.

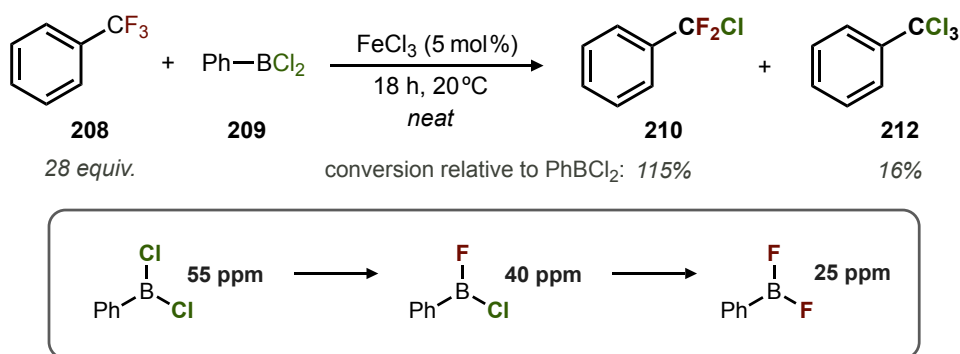


Scheme 2.2. DOE design for the synthesis of hydrazine derivatives

2.2 Boryl Chloride Investigations

2.2.1 Reaction Screening

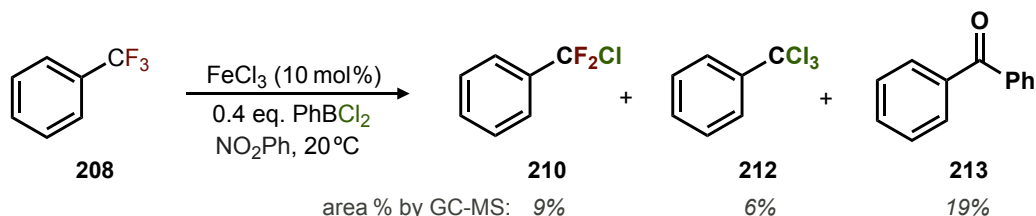
HaloDF work in the Williams Group was initiated by the discovery that ferric chloride could catalyze a halalex reaction between trifluoromethyl benzene (**208**) and phenyldichloroborane (**209**), with only trace conversion observed in the absence of ferric chloride (Scheme 2.3). With **208** in heavy excess, the PhBCl₂ was completely consumed, as indicated by reaction monitoring with ¹¹B NMR spectroscopy. After workup, the GC-MS and ¹⁹F NMR spectra revealed formation of both the mono-chloro product **210** and the trichloromethyl compound **212**.



Scheme 2.3. Iron catalyzed halalex between trifluoromethyl benzene and phenyldichloroborane, with *in situ* ¹¹B NMR monitoring

A quick screening revealed the comparable activity of other Lewis acids catalysts: FeBr₃, FeF₃, AlCl₃, InCl₃, and SbCl₅. Different boryl chlorides could also undergo the halalex: BCl₃, chlorocatecholborane, as well as other boryl halides BBr₃, BI₃ (*vide infra*). Further optimization of the chloro-

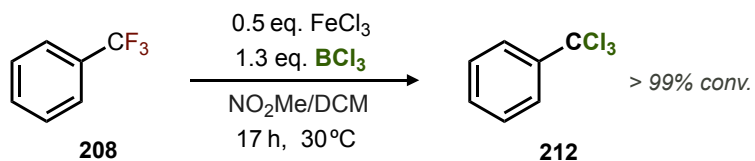
halex with PhBCl₂ led to the identification of nitrobenzene as a suitable solvent, allowing for reduction of the excess **208**. However, significant amounts of benzophenone (**213**) were observed, indicating the presence of an off-target cross-coupling pathway (Scheme 2.4). To avoid this, the boryl chloride was switched to the readily-available and inexpensive reagent, BCl₃. The solvent was also changed to nitromethane, which was found to be ideal for dissolving high loadings of FeCl₃.



Scheme 2.4. Halex between trifluoromethyl benzene and phenyldichloroborane.

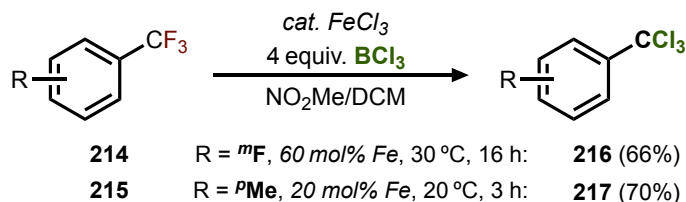
2.2.2 Synthesis of Trichloromethyl Arenes

As discussed in Chapter 1, trihalomethyl arenes are useful in a number of synthetic applications. With high iron loadings (50 mol%), and a slightly elevated temperature, the trifluoromethyl compound **208** was completely consumed after 5 hours, affording trichloromethyl benzene **212** as sole product by GC-MS (Scheme 2.5). Nitromethane was used in conjunction with DCM, which is present in the BCl₃ commercial reagent (overall 5:3 NO₂Me/DCM, [PhCF₃] = 0.31 M).



Scheme 2.5. Triple chloro-halex of trifluoromethyl benzene

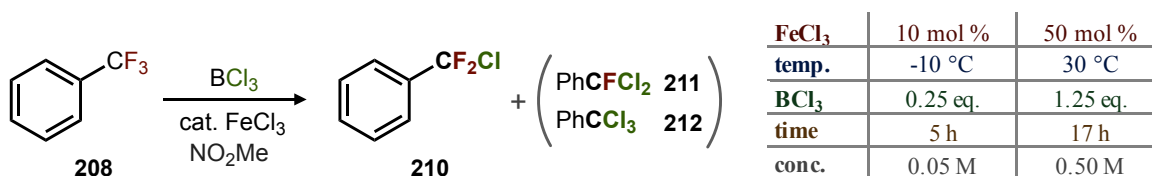
Evaluation with other trifluoromethyl derivatives revealed a distinct effect of aryl substitution. Meta-fluoro substrate **214** required more forcing conditions (increase to 4 equivalents BCl₃) to achieve full conversion (Scheme 2.6). On the other hand, with the electron rich *para*-methyl arene (**215**), the reaction proceeded much quicker, and was complete after only 3 hours at room temperature.



Scheme 2.6. Isolated yields of trichloromethyl derivatives produced via triple-halex

2.2.3 Mono-Halex Design-of-Experiment

With conditions for triple-halex in hand, an intriguing possibility remained to optimize the reaction for *single* halogen-exchange, and produce the valuable mono-chloro derivative (**210**) as the major product (q.v. *section 1.1.1*). However, this is an inherently challenging problem, given the ability of the mono-chloro product to undergo further halex reactivity (*over-reaction*). A DOE strategy (*vide supra*) was deemed well-suited to further explore and optimize this reaction.



Scheme 2.7. Design for the chloro-halex DOE

The BCl₃ halex reaction was analyzed with a response surface design (Scheme 2.7), using the following five factors: FeCl₃ loading, temperature (T), BCl₃ equivalents (B), reaction time (t), and concentration of ArCF₃ in the reaction (M). After the specified time, an aqueous workup was performed to prevent further reactivity. The organic fraction was then analyzed with GC-MS to verify the identity of the products formed, and ¹⁹F NMR spectroscopy to quantify the amount of chlorodifluoromethane species **210** (as well as **211** and **208**) using an internal standard. The conversion values for **210** were used as the response for the model.

Figure 2.8 depicts the most important factors, based on their *standardized effect* (a t-statistic quantifying the statistical significance of each effect). This revealed strong quadratic effects for both temperature and concentration, with optimal values corresponding the maxima of the paraboloid surface shown in Figure 2.9 (*left*). However, these factors did not have any significant interaction effects with the three other variables. As such, temperature and molarity were kept at fixed values in the ensuing investigations.

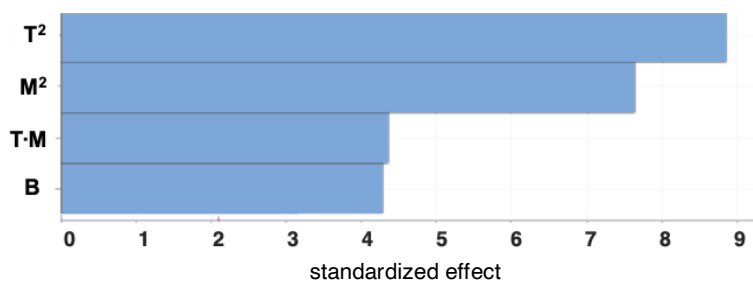


Figure 2.8. Pareto chart for the chloro-halex DOE

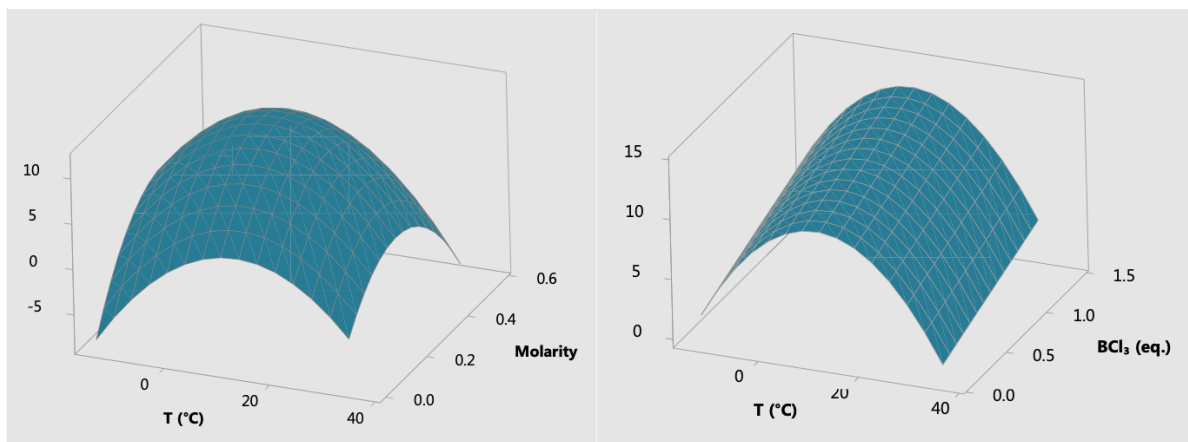
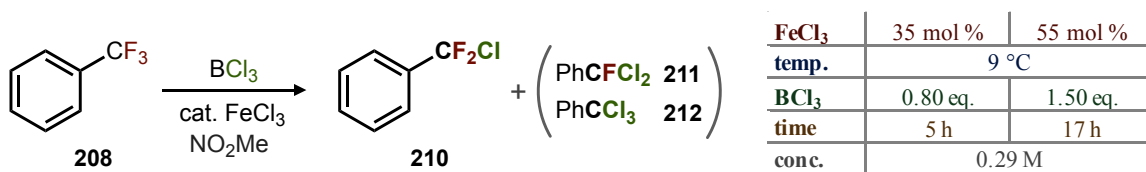


Figure 2.9. Surface plots from the DOE model

A second response surface DOE was performed to hone in on optimal conditions, using a narrower range of the three remaining factors (Scheme 2.8). The high-level for BCl_3 amount was also increased, as the first DOE model implied that this may be beneficial (see positive slope in Figure 2.9 right).



Scheme 2.8. Design for the chloro-halex DOE II

The model was fit with an R^2 value of 95%, identifying time as the most critical factor, followed by FeCl_3 loading, with a minimal contribution from the amount of BCl_3 (Figure 2.10). The predicted conditions for maximum conversion are shown in Scheme 2.9. Empirical evaluation of these conditions shows good agreement between the DOE model, and the experimental value of 17% PhCF_2Cl (product distribution includes 4% PhCFCl_2 and 75% PhCF_3).

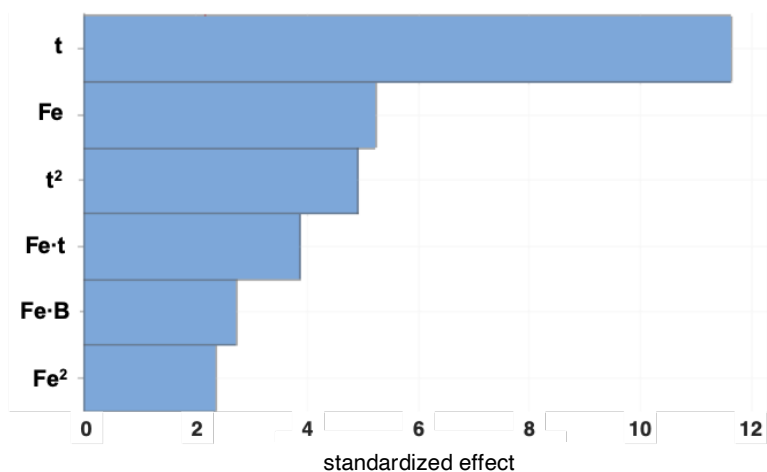
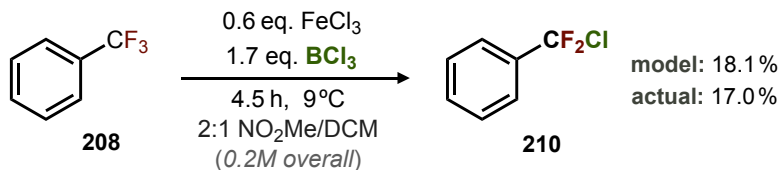


Figure 2.8. Pareto chart for the chloro-halex DOE II



Scheme 2.9. Model accuracy for the chloro-halex DOE II

In summary, a new protocol for BCl_3 halex was developed, using catalytic FeCl_3 , and providing ArCCl_3 or ArCF_2Cl products. There remained motivation to evaluate the catalysis of $\text{B}-\text{Br}$ halex, and potentially improve the sluggish reactivity of BBr_3 with ArCF_3 observed by Olah and Prakash (*vide supra*).²³ In addition, the halex products ($\text{ArCF}_2\text{Br}/\text{ArCBr}_3$) are perhaps more appealing for subsequent derivatization, given the greater leaving group ability of bromine versus chlorine.

2.3 Boryl Bromide Investigations

2.3.1 Reaction Screening

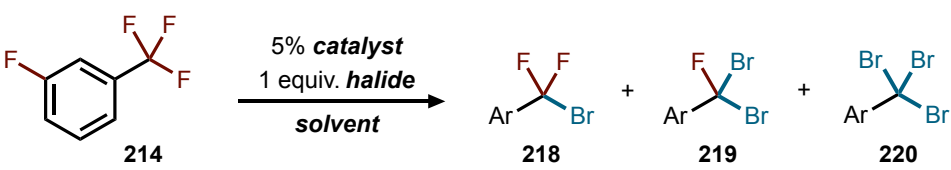
As with BCl_3 , a variety of halophilic Lewis acids were screened for the ability to catalyze BBr_3 halex reactions (Table 2.1). The meta-fluoro derivative (**214**) was used for screening, allowing for facile determination of conversion by ^{19}F NMR spectroscopy, using the *m*-fluoro group as a reporter. In the absence of a catalyst, the known background reaction provides mono-bromide compound **218** at 7% conversion (entry 1).²³

While silver(I), copper(I), iron(0) and iron(II) showed no improvements on C–F exchange efficiencies (entries 2-5), iron(III) and gallium(III) compounds accelerated the halex process (entries 6-10), generating tribrominated product **220** in 83–91% conversion. Interestingly, the identity of the halide on the Fe(III) center did not significantly affect the reaction, although could lead to mixed halide transfer (e.g. entry 6, trace ArCF_2Cl formed).

Ensuing investigations were performed with ferric fluoride. Solvent selection proved important (entries 11-13), likely due to the varying solubility of the ferric fluoride reagent. However, it should be noted that the iron complex showed a distinct increase in solubility upon boryl halide addition (*see* Figure 6.11), and that the reaction performed similarly with different ferric halides. Use of hexanes led to poor solubilization, whereas in nitromethane, coordination with BBr_3 was observed in the ^{11}B NMR spectrum, and was suspected to mitigate reactivity.

Different boryl bromides were also competent in the halex reaction (entries 14-15), although these reactions were slow relative to those with BBr_3 . Tribromomethyl arene **220** could be formed as the sole product, using excess BBr_3 and an extended reaction time (entry 16). Consistent with their relative Lewis acid strengths, BBr_3 was noticeably more reactive than BCl_3 , still able to undergo halex at -10°C (entry 17).

Table 2.1. Conditions investigations for boryl bromide mediated halogen-exchange

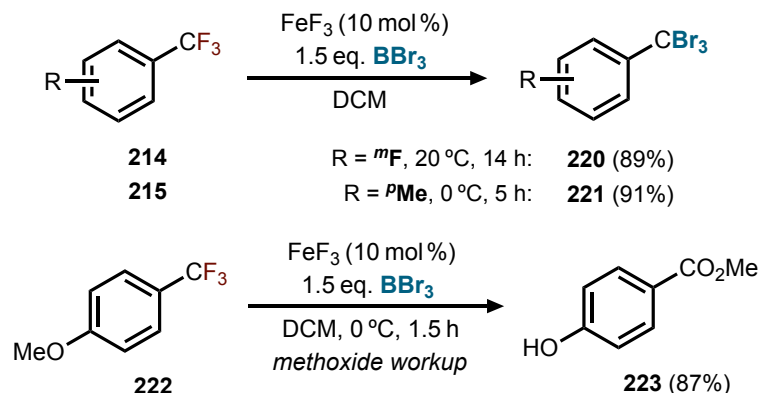


entry	catalyst	halide	solvent	218 (%)	220 (%)	C-F _{total} (%) ^a
1	–	BBr ₃	DCM	7	nd.	7
2	AgBr	BBr ₃	DCM	8	nd.	9
3	CuI	BBr ₃	DCM	7	nd.	8
4	Fe(CO) ₅	BBr ₃	DCM	7	nd.	8
5	FeCl ₂	BBr ₃	DCM	6	nd.	7
6	FeCl ₃	BBr ₃	DCM	4	89	272
7	FeBr ₃	BBr ₃	DCM	5	83	256
8	FeF ₃	BBr ₃	DCM	5	83	255
9	Fe(OTf) ₃	BBr ₃	DCM	tr.	91	273
10	Ga(OTf) ₃	BBr ₃	DCM	tr.	83	249
11	FeF ₃	BBr ₃	heptane	tr.	nd.	tr.
12	FeF ₃	BBr ₃	PhCl	14	tr.	27
13	FeF ₃	BBr ₃	MeNO ₂	nd.	nd.	nd.
14 ^b	FeF ₃	Me ₂ BBr	DCM	21	35	128
15 ^b	FeF ₃	(cat)BBr	DCM	tr.	nd.	tr.
16 ^c	FeF ₃	BBr ₃	DCM	nd.	95	284
17 ^d	FeF ₃	BBr ₃	DCM	12	nd.	15

Reactions performed at 1.0 mmol scale, 0.2 M molarity, 20 °C, and 5 hours. Conversions determined by ¹⁹F NMR (relative to 4-fluorotoluene internal standard). **219** was trace in all entries (< 3% conversion). *Cat* = catechol. *nd.* = not detected. *Tr.* = trace. [a] C-F_{total} refers to the molar fraction of C–F bonds converted to C–X bonds. [b] 3 eq. R₂BBr used. [c] 10 mol% FeF₃, 1.5 eq. BBr₃, 14 h. [d] Performed at –10°C.

2.3.2 Synthesis of Tribromomethyl Arenes

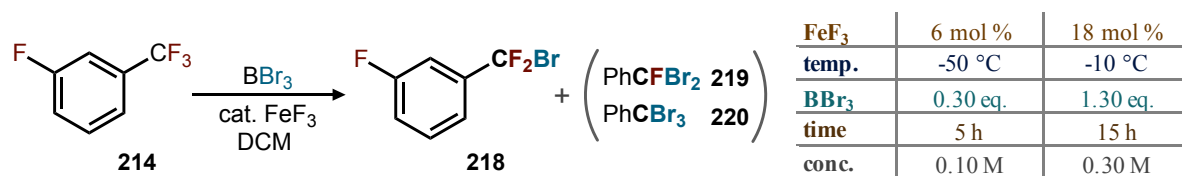
Using the optimized conditions, the tribromo compound **220** could be isolated after a standard aqueous workup (without the need for additional purification), in 89% yield (Scheme 2.10). As in the chloro-halex, *p*-methyl substrate **215** proved much more reactive than *m*-fluoride **214**, with a reduced reaction time and temperature. Substitution with a stronger electron-donating methoxy group (**222**) increase reactivity further, with full defluorination achieved after 1.5 hours (along with cleavage of the methyl ether). This increased arene electron-density is also thought to have accelerated the rapid hydrolysis/ methanolysis of the tribromomethane that occurred during workup, affording the methyl ester **223**.



Scheme 2.10. Isolated yields of tribromomethyl derivatives produced via triple-halex

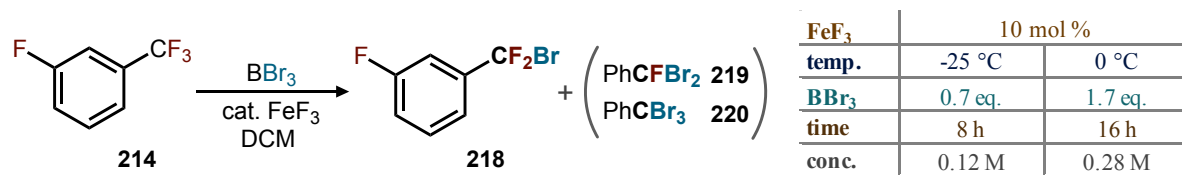
2.3.3 Mono-Halex Design-of-Experiment

As with the chloro-halex, tuning the reaction to target *single* bromo-halex was an appealing challenge. Temperature was anticipated to be a critical, given the observation that lower temperatures provided a higher ArCF_2Br product ratio (Table 2.1, entry 17). A fractional factorial DOE was designed with *m*-fluoro substrate **214** and the same 5 factors as the chloro-DOE, with conversion to ArCF_2Br **218** as the response (Scheme 2.11). The levels for catalyst loading and temperature were somewhat lower than with BCl_3 , a result of the increased reactivity of BBr_3 .



Scheme 2.11. Design for the bromo-halex DOE

Unlike the chloro-halex, no terms containing FeF_3 loading were significant for model inclusion. This is likely a result of sparing FeF_3 solubility in the reaction mixture, preventing any reaction acceleration with increasing catalyst loadings. The loading was consequently fixed at 10% for the ensuing set of experiments (Scheme 2.12). A second DOE was performed, using a *response surface* design to examine the role of non-linear effects and hone in on optimal conditions for conversion to **218**.



Scheme 2.12. Design for the bromo-halex DOE II

Evaluation of data normality and fit parameters of $R^2 = 77\%$ and $R^2_{\text{predicted}} = 50\%$, indicated a well-fitted model for ArCF₂Br conversion. Additionally, lack of any trend in the residuals as a function of reaction order, indicated the model was free of systematic error. In order to further cross-validate the model, a few testing points (not used for model generation), ranging throughout the reaction space, were chosen and performed experimentally. The conversion values were then compared to those predicted by the model, showing overall good agreement (Table 2.2).

Table 2.2. Test points for the bromo-halex DOE II

temp. (°C)	BBr ₃ (eq.)	time (h)	conc. (M)	ArCF ₂ Br (%)	
				model	actual
-3	0.45	6	0.32	25.2	26.5
-9	1.70	13	0.32	19.0	14.4
-9	1.70	16	0.32	19.0	15.4
3	1.40	7	0.10	8.9	9.7
-13	1.95	15	0.32	19.4	21.1
-13	1.50	14	0.25	18.2	22.9

The relative importance of each factor is shown in the Pareto chart below (Figure 2.9). Indeed, temperature was found to be a vital factor, both as a linear term (T), and as a quadratic (T²). The non-linear effect of temperature, as well as the significant T/BBr₃ interaction effect can be seen in the response surface shown below (Figure 2.10).

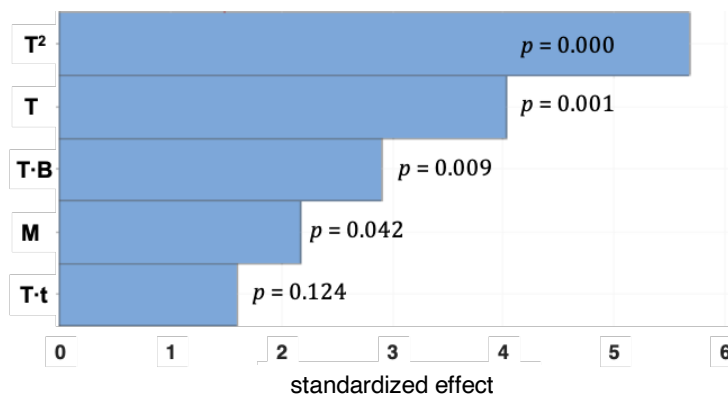


Figure 2.9. Pareto chart for the bromo-halex DOE II

Interestingly, time was not a highly significant variable to the model, as shown by the shallow slope in Figure 2.11. These results suggest that optimal conversion is more complex than identifying a time point where a statistical mixture of products favors formation of ArCF₂Br **218**.

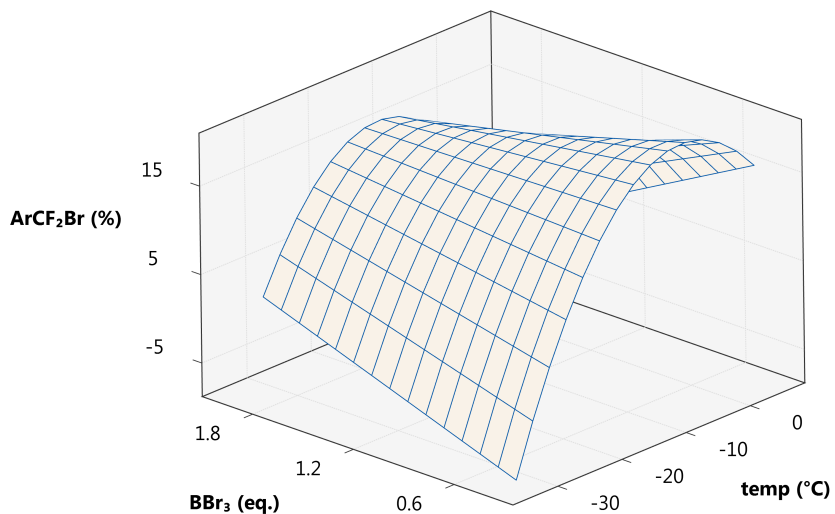


Figure 2.10. Surface plots of ArCF₂Br conversion as a function of BBr₃ equivalents and temperature (constants: $t = 12$ h, conc. = 0.2 M).

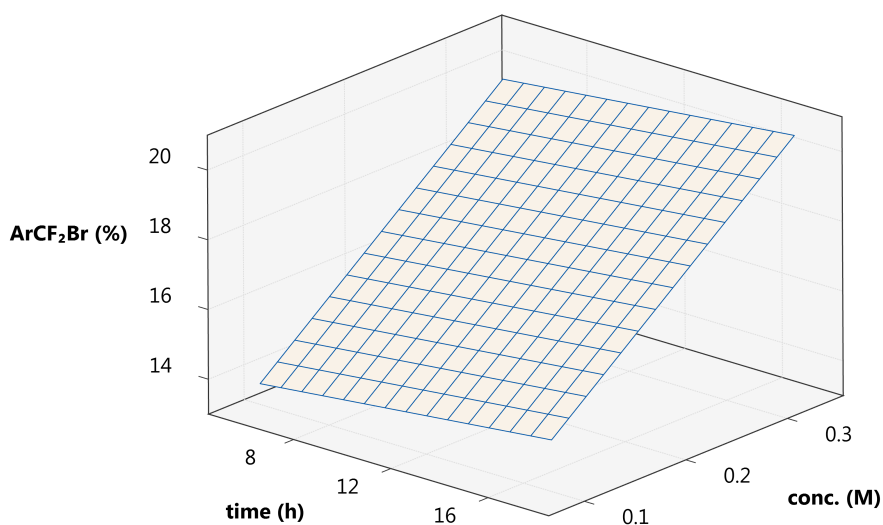


Figure 2.11. Surface plots of ArCF₂Br conversion as a function of time and reaction concentration (constants: BBr₃ = 1.2 eq., $T = 12.5$ °C).

The DOE model predicted conditions for a maximum conversion to ArCF₂Br **218** of 25%. Experimentally, these conditions resulted in 27% conversion, slightly outperforming the model (Table 2.3, entry 3). The model could also be used to identify the conditions that gave the best selectivity for **218**, shown in entry 4. For comparison, entries 1–2 utilize conditions reported by Olah and Prakash (q.v. section 1.3.4).²³

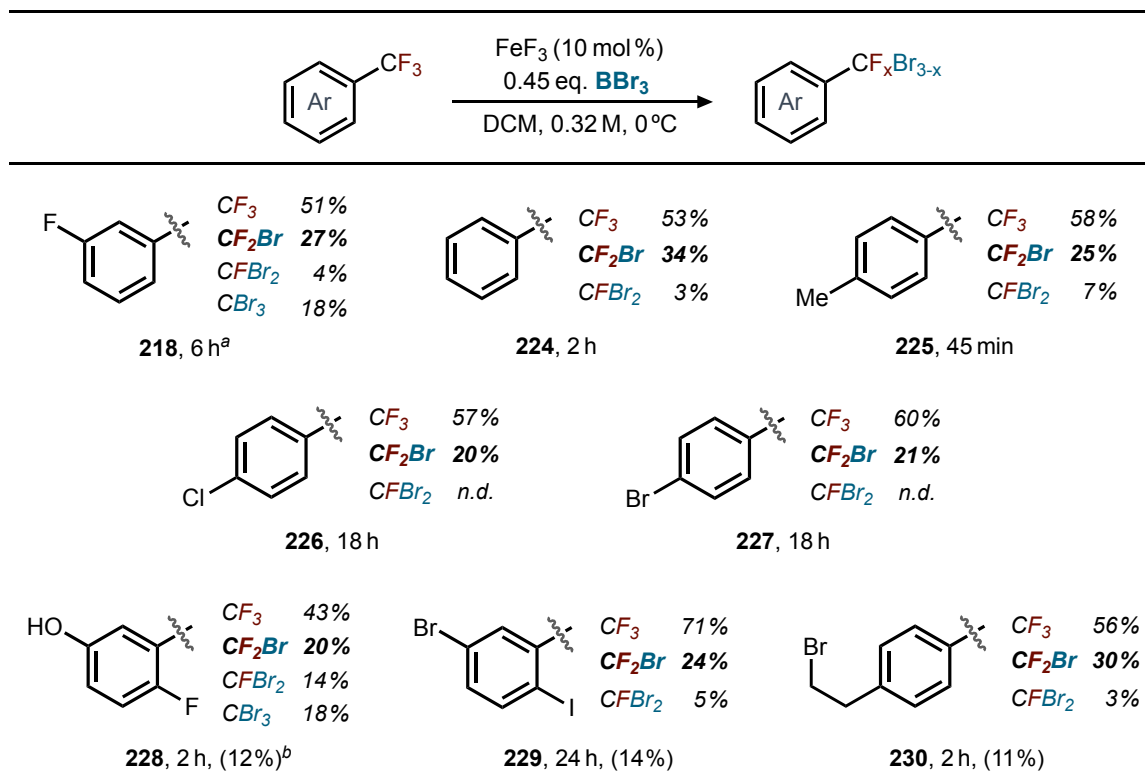
Table 2.3. Summary of conditions for the halogen-exchange of **214**

entry	ArCF ₃ :BBr ₃	conditions	218 (%)	219 (%)	220 (%)
			ArCF ₂ Br	ArCFBr ₂	ArCBr ₃
1	10:1	neat, reflux, 2 h	13	4	3
2	3:1	DCM, 0.1 M, r.t, 5 days	12	1	22
3	2.2:1	10 mol% FeF ₃ , DCM, 0.32 M, -3 °C, 6 h	27	4	18
4	4:1	10 mol% FeF ₃ , DCM, 0.32 M, -17 °C, 6 h	16	3	1

2.3.4 Synthesis of Bromodifluoromethyl Arenes

Given optimized reaction parameters for *m*-fluoro substrate **214**, it was sought to apply conditions favoring ArCF₂Br formation to a selection of ArCF₃ substrates, as shown in Scheme 2.13. The product distribution (quantified with ¹⁹F NMR spectroscopy), indicated that ArCF₂Br was the major product in all cases, with the majority of remaining material accounted for by the ArCF₃ starting material.

Scheme 2.13. Summary of scope investigations for the halox of trifluoromethyl arenes



0.40 mmol scale. Conversions determined by ¹⁹F NMR (relative to 4-fluorotoluene internal standard), isolated yields of the CF₂Br product in parentheses. [a] Performed at -3 °C. [b] 1.45 eq. BBr₃ used.

Qualitative analysis of small-molecule substrates **224–227** (for which volatility affected isolated yields) was performed with GC-MS, confirming the presence of CF₃, CF₂Br, CFBr₂, and CBr₃

compounds. For heavier substrates **228–230**, **232**, **234**, the mixture was purified using preparatory reverse-phase HPLC. The spectra typically showed four closely-clustered peaks, corresponding to the same four-component product distribution as above (Figure 2.12). The ArCF₂Br product (previously unknown) could be successfully isolated for these substrates, allowing for full characterization.

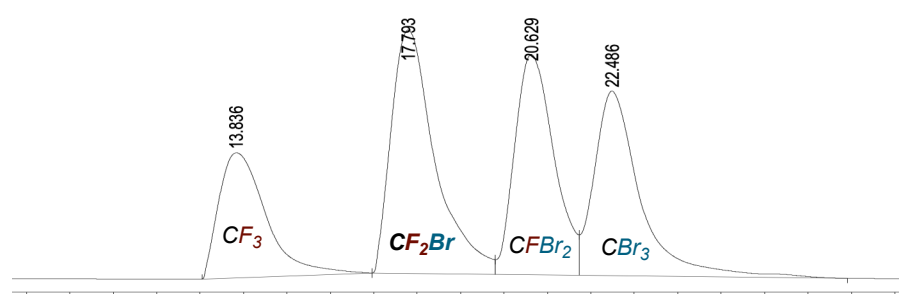


Figure 2.12. Representative HPLC trace for a halox reaction mixture (compound **228**)

Generally, only the reaction time had to be adjusted to account for differences between substrates, with more rapid reactivity observed for electron-rich arenes. For example, with alkyl-substituted arene **230**, six hours lead to poor ArCF₂Br conversion (*via over-reaction*), and only when the time was reduced to two hours was the conversion satisfactory (Table 2.4). Two hours was also effective for moderately electron-neutral substrates **224** and **228**, whereas the reaction time was further reduced to 45 minutes for *para*-methyl substrate **225**. Conversely, substrates containing electron-withdrawing groups **226**, **227**, **229** required much longer reaction times of 18 or 24 hours. For substrates containing Lewis basic functionalities (**228**, **231**, **233**), an additional equivalent of BBr₃ was added at the outset, in anticipation of its coordination and subsequent deactivation by the basic group.

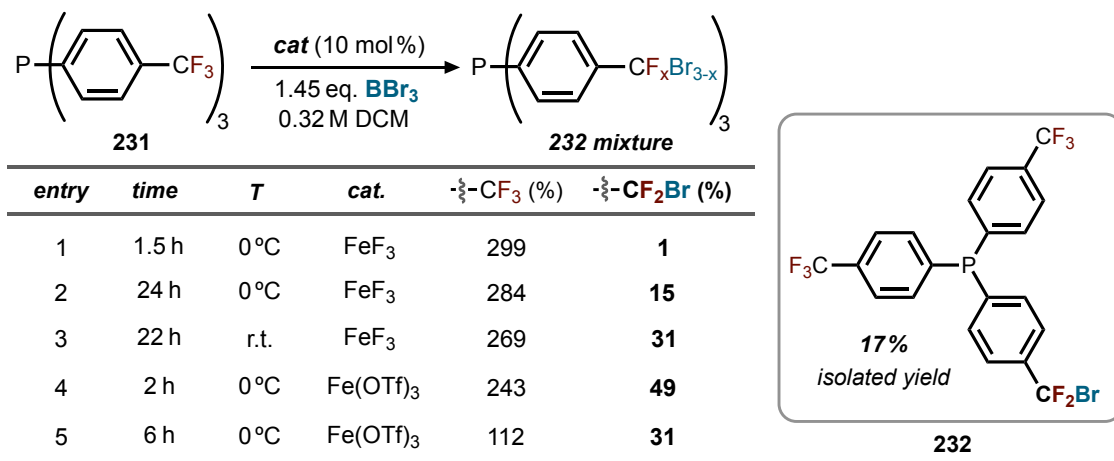
Table 2.4. Summary of reaction time optimization for electron-rich substrates

Compound 230				Compound 225			
<i>time</i>		ArCF ₃ (%)	ArCF ₂ Br (%)	<i>time</i>		ArCF ₃ (%)	ArCF ₂ Br (%)
6 h	<i>standard conditions</i>	58	11	90 min	<i>standard conditions</i>	56	4
4 h		57	12	45 min		58	25
2 h		56	30	30 min		83	15

The halox reaction was also applied to a triarylphosphine substrate (**231**), containing three CF₃ groups (Scheme 2.14). The initial experiments were analyzed with ³¹P NMR spectroscopy (entry 1), which indicated substantial formation of phosphine oxide products (~26 ppm). The remaining experiments included a freeze-thaw-degas cycle to remove oxygen from the reaction mixture, which successfully kept the phosphine oxide levels to < 10%.

A plethora of different products/intermediates can be envisioned during the progressive conversion of the 3×CF₃ starting material **231** (*19 possible intermediates*). The reaction mixture spectra (¹⁹F NMR) were carefully examined in the vicinity of the starting material CF₃ peak (**A**), as shown in Figure 2.13.

A reasonable supposition was made that the two new peaks (**B**, **C**) also correspond to CF₃ groups, given the < 1 ppm shift from peak **A** (by comparison, CF₂Br undergoes a ~19 ppm shift). However, the identities of peak **B/C** were not clear, possibly corresponding to any of the 19 intermediates (or their phosphine oxides). In addition, each of **A**, **B**, **C** may arise from overlapping peaks of different intermediates. Indeed, the CF₃ peaks of both starting material (**231**) and product (**232**) are indistinguishable and both corresponding to **A**. Thus, rather than quantifying particular species, the total CF₃ amount was determined using the sum of peaks **A–C**.



Scheme 2.14. Halogen exchange with a triarylposphine substrate

The CF₂Br region was integrated analogously, grouping together overlapping or closely-clustered peaks (**X**, **Y**, **Z**). Thus, although the exact amount of **232** (relative to other CF₂Br products) could not be determined, this quantitation strategy was effective for providing a general illustration of reaction behavior, and facilitated optimization studies.

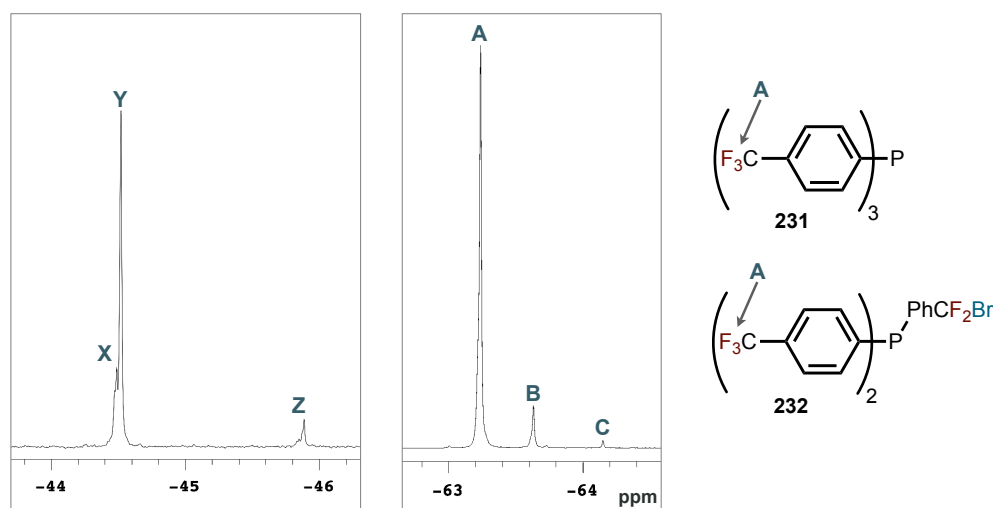
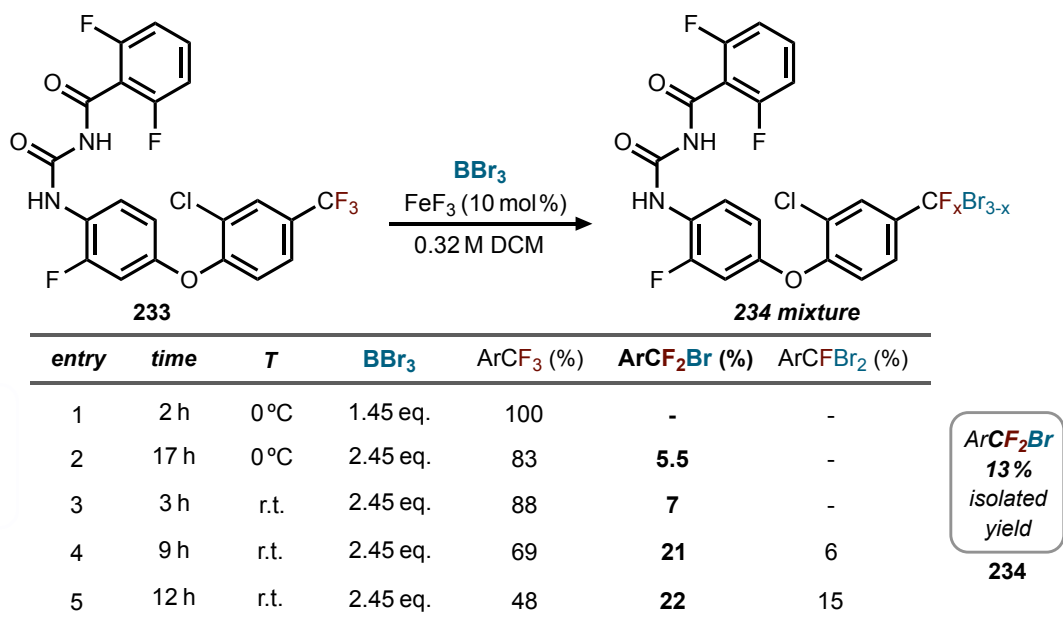


Figure 2.13. Analysis of ¹⁹F NMR parameters for the reaction of triarylposphine 231

Formation of the CF₂Br moiety was fairly slow at 0 °C, even after 24 hours (entry 2). Moderate improvement could be achieved by increasing the reaction temperature (entry 3). However, even more effective was the substitution of FeF₃ with Fe(OTf)₃, providing optimal conversion after 2 hours at 0 °C (entry 4), with 6 hours leading to *over-reaction* (entry 5). Using these optimal conditions, the mono-CF₂Br product (**232**) could be successfully isolated in 17% yield.

The final substrate examined was a commercial insecticide flufenoxuron **233** (Scheme 2.15). No reaction was observed with 1.45 equivalents of BBr₃ (entry 1), so it was increased by a further equivalent, given the presence of multiple sites with the potential to coordinate BBr₃. With 2.45 equivalents, the ArCF₂Br product was observed (entry 2), but only with an increase to room temperature were satisfactory conversions obtained (entries 4, 5). Despite the complexity of this substrate, functional group tolerance was excellent in these reactions, with ¹⁹F NMR quantitation of the CF₃/CF₂Br/CFBr₂ species accounting for >85–95% of the product distribution, indicating that minimal decomposition had occurred. Purification of the reaction mixture from entry 5, led to successful isolation of the ArCF₂Br compound **234** in 13% yield.



Scheme 2.15. Halogen exchange with a commercial insecticide flufenoxuron

In summary, substrates with substitution at *ortho*, *meta*, and *para* positions, including halides, alkyl, and hydroxy groups, were all well tolerated, with similar conversions to the desired ArCF₂Br product. The reaction displayed excellent chemoselectivity for C(sp₃)–F bonds, with no apparent reactivity at aryl C(sp₂)–F, or other C(sp₂)–X, bonds. The reaction with flufenoxuron **233** demonstrated tolerance of the diaryl ether, aryl C–Cl bond, and benzoylurea moieties. With substrate **230**, there was no evidence of Friedel-Crafts alkylation or byproducts arising from other possible cationic pathways due to activation of the alkyl bromide side chain.

2.3.5 Mechanistic Investigations

At the outset of mechanistic investigations, both heterogeneous and homogeneous catalysis appeared plausible in this system. Theoretical calculations were used to evaluate the viability of a homogeneous process, given the high degree of solubilization of the iron complexes in the presence of the boron trihalide reagents.[†] Should a homogeneous process appear reasonable, these calculations could shed light on the potential role of an iron catalyst in the mechanism.

Unrestricted Kohn-Sham density functional theory (B3LYP/6-31G**),^{108, 109} was used to study coordination energies between PhCF₃ (**208**), BBr₃, and FeF₃ in dimeric and trimeric orientations. The lowest dimeric coordination energy observed was between PhCF₃ and FeF₃ at -7.6 kcal/mol, and was predicted to stretch the coordinated C–F bond by approximately 0.1 Å (Figure 2.14 *right*). For comparison, the optimized structure of free PhCF₃ was obtained, showing a slight elongation of the C–F bond perpendicular to the phenyl ring, perhaps due to a stereoelectronic effect involving π -donation into the $\sigma_{\text{C-F}}^*$ (Figure 2.14 *left*). However, this effect is relatively small (~ 0.003 Å) compared to that of FeF₃ coordination.

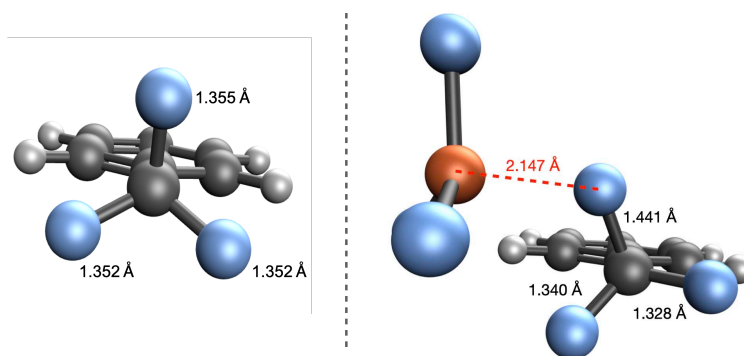


Figure 2.14. Geometries and bonding for PhCF₃ in isolation (*left*) and in coordination with FeF₃ (*right*)

The binding energy of BBr₃ to PhCF₃ was also calculated, and in contrast to FeF₃, was predicted to be uphill by 7.0 kcal/mol. ¹⁹F NMR experiments support these calculations and provide evidence for solution activation of the C–F bond. The fluorine signal in PhCF₃ is shifted downfield by 2.5 ppm in the presence of FeCl₃, whereas BCl₃ only elicits a downfield shift of 0.2 ppm (CD₂Cl₂).

The lowest energy trimers (PhCF₃, BBr₃ and FeF₃) have interactions dominated by PhCF₃ and FeF₃ binding, with the lowest energy trimer at -0.78 kcal/mol relative to the monomers. Therefore, while iron activation of the BBr₃ remains a valid mechanistic possibility, calculations and NMR experiments suggest that direct interaction of iron with PhCF₃ is energetically favorable and weakens the C–F bond.

[†] Calculations performed by the Shepherd Lab (University of Iowa)

Dimers of iron halides (Fe_2F_6 and Fe_2Cl_6) were also evaluated for their coordinating affinity for either the PhCF_3 substrate or the boron trihalide (BBr_3 and BCl_3). These calculations suggest that binding to monomeric species (FeX_3) is more favorable than binding to a dimeric iron cluster (Fe_2X_6).

Figure 2.15 shows plausible mechanisms based on these data. The nucleophilic bromide is likely delivered from a boron halide complex, as the identity of the boron halide reagent determines the major halex product. Subsequent transfer of the fluoride from the iron to the boron center is required for the process to be exergonic overall (1st Br exchange: -25.7 kcal/mol),¹¹⁰ and this is corroborated by the experimental observations of gas evolution (BF_3) and a disappearance of the ^{11}B NMR signal. This experiment also highlights that ligand exchange between FeF_3 and BBr_3 is facile under the reaction conditions, so heteroleptic iron complexes likely play an important mechanistic role.

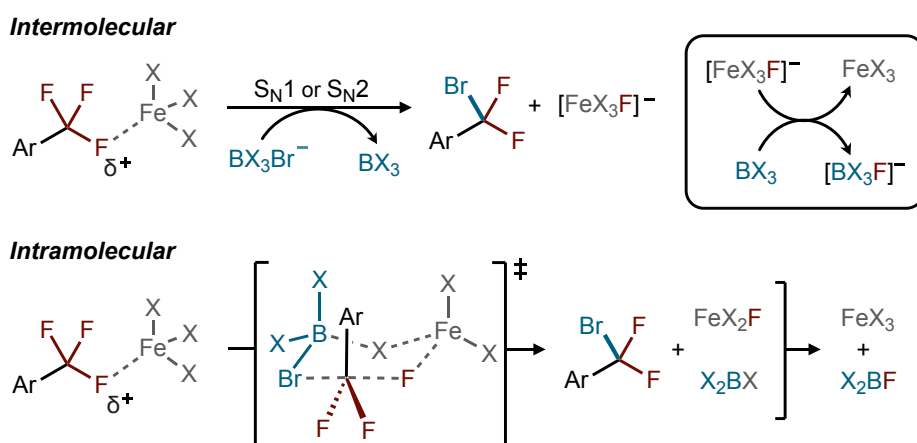


Figure 2.15. Plausible mechanisms for the bromo-halex reaction.

To test this hypothesis, FeF_3 was combined with an equimolar amount of BBr_3 in an NMR tube, containing a sealed $\text{BF}_3:\text{OEt}_2$ capillary internal standard (Figure 2.16). After one hour, ^{19}F NMR showed a series of new peaks and the ^{11}B NMR spectra showed a 32% reduction in the BBr_3 peak relative to internal standard. This substantiates the suggestion that ligand exchange and the formation of heteroleptic complexes can occur.

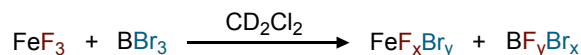


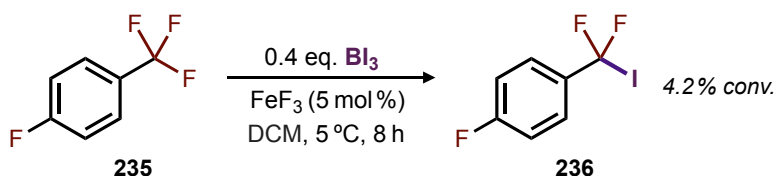
Figure 2.16. Formation of heteroleptic boron and iron complexes

2.4 Boryl Iodide Investigations

2.4.1 Preliminary Screening

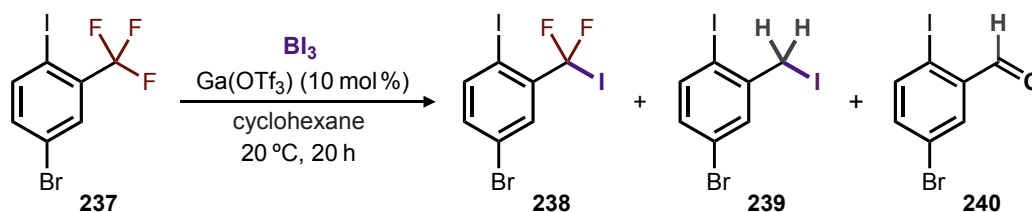
Iodine compounds are attractive intermediates for further functionalization, given the excellent leaving-group ability of iodine. As such, extension of the halex reaction to include boron triiodide is currently under investigation, and some preliminary results are presented herein.

The hallex reactivity of BI₃ was evaluated using *p*-fluoro substrate **235**, allowing for facile monitoring by ¹⁹F NMR spectroscopy, via the *p*-fluoro reporter. The conditions initially evaluated were similar to those optimized for BBr₃ hallex. However, this only resulted in trace conversion to ArCF₂I **236**, with mostly starting material remaining (Scheme 2.16). Increasing BI₃ to 1.4 equivalents allowed for complete consumption of the starting material. However, **236** was absent from the ¹⁹F NMR spectrum, and the formation of numerous new peaks indicated that a complex mixture was present.



Scheme 2.16. Hallex of a trifluoromethyl arene with boron triiodide

The next approach was evaluation of Ga(OTf)₃ as the catalyst, given its positive performance in an earlier screening (q.v. Table 2.1). Indeed, Ga(OTf)₃ appeared similarly effective for BI₃ hallex, especially with cyclohexane as the solvent. Initial inspection of crude ¹⁹F NMR and GC-MS spectra showed clean conversion to a limited number of products, in contrast to the complex mixture observed with FeX₃ catalysts. As such, these conditions were further evaluated with dihaloarene **237**, using varying amounts of BI₃ (Scheme 2.17). The resulting reaction mixtures were then analyzed with GC-MS (Table 2.5).



Scheme 2.17. C–F activation of a trifluoromethyl arene with boron triiodide

At low BI₃ loadings, GCMS indicated that the hallex product **238** was major, and this result was corroborated by the ¹⁹F NMR spectrum (entry 1). Interestingly, higher amounts of BI₃ resulted in the formation of two unexpected products, benzyl iodide **239**, and benzaldehyde **240**. Iodocyclohexane was also observed, indicating that the cyclohexane solvent plays a non-innocent role in this reaction, and is plausibly the source of hydrogen in the formation of **239/240**. The oxygen in **240** is likely incorporated during the aqueous workup via hydrolysis of an ArCl₂H species.

The final reaction mixture was separated with column chromatography (entry 3), affording pure benzyl iodide **239** (23 % yield) and benzaldehyde **240** (40 % yield). The identity of these products was then confirmed by NMR and HRMS analysis.

Table 2.5. GCMS analysis of products for the reaction of **237** with boron triiodide

entry	conditions	237 ArCF ₃	238 ArCF ₂ I	239 ArCH ₂ I	240 ArCHO
1	0.33 eq. BI ₃	65	24	7	3
2	1.05 eq. BI ₃	20	4	73	3
3	1.25 eq. BI ₃	1	0	53	42

* area-percent of starting material derived products

2.5 Conclusion

2.5.1 Future Work

Additional studies on the synthesis of ArCX₃ compounds would be a natural area for expansion, given the fairly small scope initially examined. In addition to ArCF₃ groups, there is interest in applying the iron-catalyzed halox method to alkyl-CF₃ and perfluoroalkane substrates, which tend to be particularly inert and challenging to functionalize.

There is also potential to expand upon the derivatization reactions of both ArCX₃ and ArCF₂X products. In particular, the development of *one-pot* methods would be beneficial, allowing for efficient and rapid conversion of a CF₃ moiety to a different functionality. For example, the CF₃ group could be used as a *masked carboxylic acid* in multi-step synthetic routes. Such a strategy is illustrated in Figure 2.17, where an ArCF₃ starting material is used, and is then subjected to various reaction conditions as the synthesis proceeds. The inert CF₃ group would have a minimal effect on these reactions, whereas a more sensitive carboxylic acid could cause interference, or undergo side-reactions. Upon completion of the synthesis, triple-halex of the CF₃ moiety, followed by *in situ* hydrolysis, would afford the carboxylic acid compound.

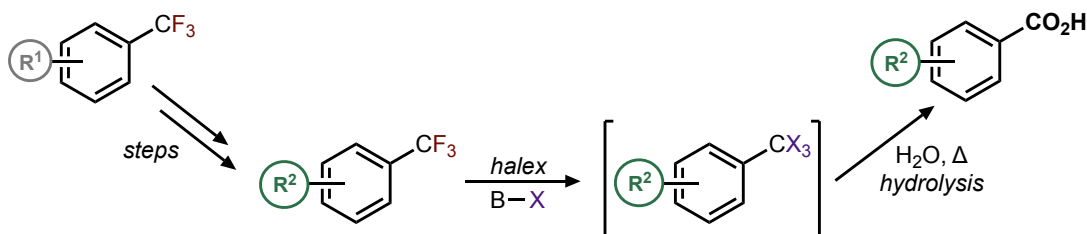
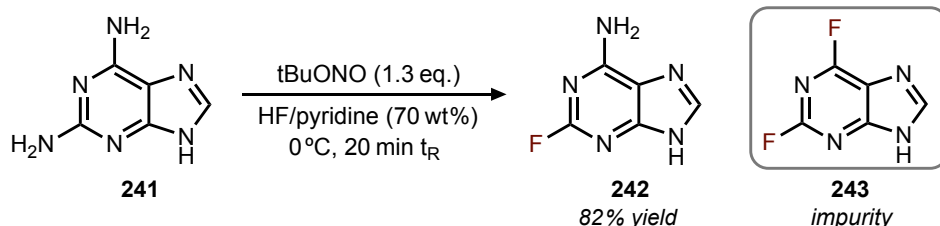


Figure 2.17. Strategy for using the CF₃ group as a masked carboxylic acid

Another area for future investigation is the synthesis of ArCF₂X products using continuous flow chemistry.¹¹¹ This approach is known to offer advantages in reactions with challenging selectivity profiles. For example, a flow process was successfully employed in the synthesis of 2-fluoroadenine **242** (Scheme 2.18).¹¹² The inherent challenge of this method is preventing further reaction of the product **242**, which contains an additional reactive amino group. Indeed, the batch synthesis was

hindered by significant formation of the difluoro impurity **243**, with increasing amounts formed upon scale-up. Flow systems minimize extra reaction time experienced by the product after it has formed, decreasing undesired further reactivity. In this example, the flow protocol produced high-purity **242**, with low amounts of **243**, obviating the need for chromatographic purification, resulting in a > 10% yield improvement over the batch process. Similarly, the challenge of halox-mediated ArCF₂X synthesis is the continual reactivity of the product, suggesting that this reaction is a good candidate for translation to a continuous flow protocol.



Scheme 2.18. Synthesis of 2-fluoroadenine using a continuous flow protocol

There are numerous areas for expansion in the boron triiodide reaction. Future studies will involve optimization of this reaction to target a single product, as well as experiments to provide insight into the mechanism. To probe the possibility of radical behavior, a trapping experiment may facilitate detection of reactive intermediate species. An experiment with deuterated cyclohexane would also be of interest, and could confirm the source of hydrogen in **239/240** if the corresponding deuterated analogues were formed. Given the sensitive nature of this reaction towards water, it would be valuable to evaluate bench-top versus glove-box protocols, as well as the effect of adding a known amount of water to the reaction. Ultimately, this reaction is envisioned to be a powerful strategy for the late-stage unmasking of stable CF₃ groups, to much more reactive benzyl iodide or benzaldehyde moieties. These reaction conditions are currently an area of active investigation in the Williams Group.

2.5.2 Summary

This chapter described a new method for boryl halide mediated halogen-exchange, utilizing ferric halides as catalysts. Initially developed conditions favored full exchange of trifluoromethyl arenes with BCl₃ and BBr₃, providing ArCX₃ products. DOE proved to be a powerful tool for process optimization, and was successfully employed to study the reaction in the context of *single* halogen-exchange. A substrate scope of ArCF₂Br products was performed, with successful application to electron-deficient and electron-rich arenes, showing good functional group tolerance. These reactions are eminently practical, using inexpensive, readily-available reagents and run at convenient temperatures. Notably, mechanistic insight from computational analyses suggests that ferric halides may be direct activators of the C–F bond, which has important implications for future C–F activation methods development.

3.1 Introduction

Positron Emission Tomography (PET) is an important medical tool for the diagnosis and monitoring of various pathologies, such as cancer, heart disease, and brain disorders.¹¹³ It is a leading technique in nuclear imaging, a branch of medicine utilizing *radiotracers* – pharmaceuticals labeled with a radioactive isotope. In particular, PET requires a positron (β^+) emitting radioisotope, an important example being fluorine-18 (^{18}F), which has been the subject of major research in recent years.¹¹⁴⁻¹¹⁸

This chapter provides a general overview of PET imaging, as well as ^{18}F labeling procedures and synthetic methods, with an emphasis on $[^{18}\text{F}]\text{ArCF}_3$ synthesis. Given the prevalence of ArCF_3 moieties in bioactive compounds, the formation of $[^{18}\text{F}]\text{ArCF}_3$ has been an appealing target in radiochemistry.¹¹⁷ However, most of these methods are indirect, and it remains an outstanding goal to efficiently synthesize $[^{18}\text{F}]\text{ArCF}_3$ *directly* from the unlabeled ArCF_3 precursor (i.e. an isotopic exchange halex reaction).

As the BX_3 and FeX_3 conditions described in the previous chapter were found to facilitate halex, it was reasoned that combining these reagents with ^{18}F could affect the direct formation of $[^{18}\text{F}]\text{ArCF}_3$. The research efforts undertaken towards this goal are discussed in this chapter. Although some positive results were observed, further investigation is required to develop an efficient radiolabeling method.

3.1.1 Overview of PET Imaging

PET is an invaluable tool for non-invasive *in vivo* imaging.¹¹³ However, a sophisticated workflow is required to facilitate PET, starting with the production of a β^+ emitting isotope by a cyclotron. Incorporation of this radioisotope into a bioactive compound of interest affords a radiotracer, which then is purified and injected into the subject. The subject is placed into a PET scanner, which depicts the radiotracer's 3-dimensional localization within the body. The PET scan can provide functional molecular information via the visualization of physiological and metabolic processes in real-time. As such, PET is a powerful tool for medical diagnosis, particularly in oncology,¹¹⁹ cardiology,¹²⁰ and neurology,¹²¹ as well as for the drug development process.¹²² It provides complementary information to structural imaging techniques (e.g. CT), often allowing for disease identification at an early (presymptomatic) stage of development.

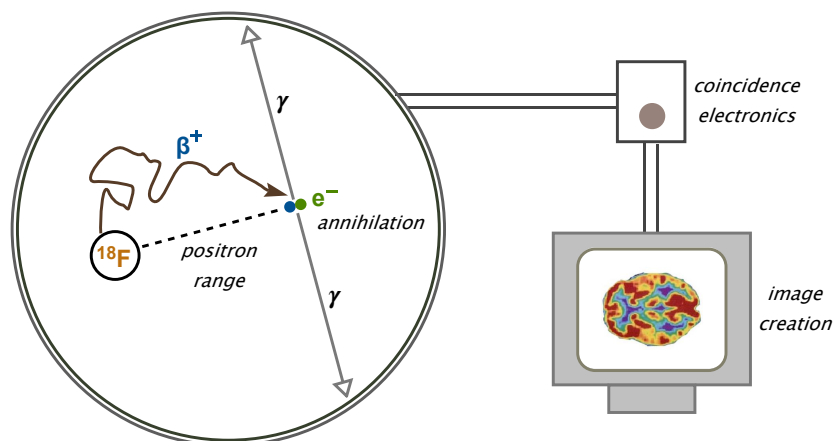
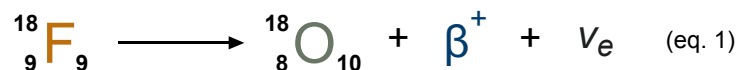


Figure 3.1. Schematic depicting the operation of a PET scanner

The physical principles of PET are summarized in Figure 3.1, using the radioisotope ^{18}F as an example.¹²³⁻¹²⁵ β^+ emission occurs as a result of nuclear instability, caused by an excess number of protons. The unstable nucleus undergoes a *proton-to-neutron* transformation, with concurrent emission of a positron (*positive electron*) antiparticle to maintain charge balance, along with a neutral neutrino (ν_e) particle. β -decay is stochastic, with a continuous energy spectrum for the emitted positron. The remaining energy balance for each emission is accounted for by the neutrino, such that the total decay energy is a constant for a particular isotope. In the example of ^{18}F , the nucleus is proton-rich, containing one less neutron than the stable ^{19}F isotope. Thus, β^+ emission occurs as ^{18}F is transmuted into ^{18}O (equation 1).



After emission, the β^+ undergoes deceleration along a short erratic path, before colliding with an electron present in the surrounding medium. This collision results in *annihilation* – the process of particle/antiparticle combination. The two particles cease to exist as all of their mass is converted to energy, resulting in the emission of two equal energy γ -photons (511 keV) at 180° from each other.

The PET scanner contains a circular array of scintillation detectors, which utilize a technique called *coincidence detection* to determine the location of emission. A *response line* is only acquired when two photons are detected simultaneously at opposite sides of the chamber. Acquisition of a large number of response lines can then be used to construct an image depicting the spatial location of radioactivity.

PET is an extremely sensitive technique, requiring only nanomolar to picomolar amounts of radiotracer. As such, perturbation to biological systems is minimal, and pharmacological effects are typically negligible. A variety of radionuclides have been used for PET imaging, differentiated by a number of important parameters, as shown in Table 3.1.¹²⁵

Table 3.1. Physical parameters for a selection of positron-emitting radioisotopes

nuclide	half-life (min)	mean energy (MeV)	β^+ decay
^{18}F	110	0.25	97%
^{11}C	20.3	0.39	99%
^{13}N	10	0.49	100%
^{15}O	2	0.74	100%
^{124}I	60192	0.81	25%
^{68}Ga	68	0.84	89%
^{64}Cu	762	0.28	59%

Half-life dictates the amount of time available for synthetic manipulations, purification, and injection following production of the radioisotope. This becomes a limiting factor for short-lived nuclides, particularly ^{13}N and ^{15}O , and to some degree for ^{11}C , ^{68}Ga , and ^{18}F as well. On the other hand, contamination and waste-stream management are concerns for long-lived isotopes (^{124}I , ^{64}Cu). Additionally, these may give patients unnecessary radiation exposure after completion of the imaging, especially if the clearance of the radiopharmaceutical is slow.

The average positron energy is a key parameter, determining the average distance travelled by the positron before annihilation, known as the *positron range* (typically 1–4 mm). The larger this range, the greater the loss in spatial resolution, and as such, isotopes with a lower positron energy are favored for PET. Finally, isotopes that decay primarily by β^+ emission are preferred, in contrast to those that undergo a high proportion of electron capture, an alternative decay mode for some proton-rich nuclei.

Carbon-11 has a long history of use in biological sciences, and has been the most readily-available β^+ emitter for many years, as well as the leading PET isotope.¹²⁶ In addition to the favorable properties discussed above, it is biogenic in nature, and can be incorporated into many biological compounds without changing the structure. However, the properties of ^{18}F are arguably superior, and as such, ^{18}F has been the focus of major research efforts in the last decade.¹¹⁴⁻¹¹⁸

3.1.2 Fluorine-18 Production

A key advantage of ^{18}F is its low β^+ energy, resulting in a mean range of 0.6 mm in water, thereby leading to excellent PET image resolution.¹²⁵ In addition, the 110 minute half-life is long enough to facilitate radiolabeling, *in vivo* studies, and even transportation to remote PET facilities. The prevalence of fluorine in pharmaceuticals is highly beneficial for their translation to ^{18}F analogues, allowing for the tracer to be chemically identical with the parent compound. Unlike many radiometals, ^{18}F is typically incorporated into the tracer via a strong covalent bond. The C–F bond is more resistant to metabolic oxidation and hydrolysis than the corresponding C–H bond, leading to high stability *in*

vivo.⁷ It is crucial to prevent tracer breakdown *in vivo*, as this results in the release of ^{18}F anions, which tend to accumulate in calcium-rich fluorophilic bones, leading to increased noise in the PET image.

The most important PET tracer is [^{18}F] FDG, a glucose analogue containing a fluorine in place of the 2-hydroxy (see Figure 3.2).¹²⁷ [^{18}F] FDG is used to study changes to glucose metabolism, facilitating the visualization of tumors and other cellular pathologies. It is a critical tool in oncology, and the development of clinical PET centers is largely owed to [^{18}F] FDG. Another example of a clinical tracer is the dopaminergic compound, [^{18}F] 6-fluoro-L-DOPA, used to monitor changes in dopamine metabolism, allowing for detection of various malignancies, such as neuroendocrine and pancreatic cancers.¹²⁸ Fluorine-18 is typically incorporated as an alkyl or aryl C–F, but some examples of CF_3 inclusion are also known, for example in the hypoxia imaging agent [^{18}F] FTMISO.¹²⁹

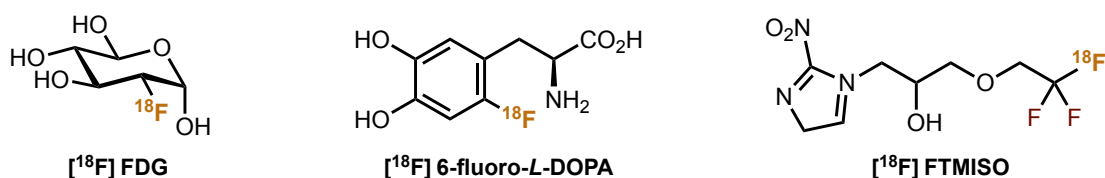


Figure 3.2. Examples of fluorine-18 labeled radiotracers used for PET

As with most β -emitters, ^{18}F is produced in a cyclotron facility, using accelerated particles to bombard a particular target.¹²³ It can be produced as aqueous fluoride (F^-) or as fluorine gas (F_2). To produce gaseous fluorine, a target containing oxygen-18 and inert carrier gas (krypton) is bombarded with high energy protons (Figure 3.3.A). The ^{18}O undergoes a (p,n) reaction, in which the high energy proton collides with the nucleus, kicking out a neutron. A small amount of non-radioactive (carrier) F_2 is added to capture the ^{18}F , facilitating formation of [^{18}F] F_2 . This method has mostly replaced another gas-phase method in which ^{20}Ne is bombarded with deuterons ($^{20}\text{Ne}(d,\alpha)^{18}\text{F}$). Alternatively, a target of ^{18}O labeled water can be bombarded to afford an aqueous [^{18}F] F^- (Figure 3.3.B).

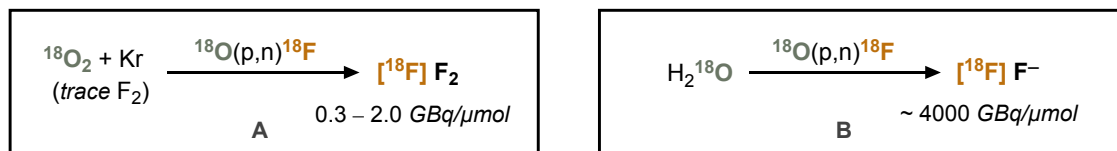


Figure 3.3. Examples of nuclear reactions used for the production of fluorine-18

These methods differ significantly in *molar activity* (A_m) of the ^{18}F produced.¹³⁰ This quantity is typically measured in units of GBq per μmol , with higher values corresponding to a higher $^{18}\text{F} / ^{19}\text{F}$ ratio. The becquerel (Bq) is the standard unit for radioactivity, corresponding to one nuclear decay per second (dps). ^{18}F can never be obtained near the maximum theoretical molar activity, as there are numerous unavoidable sources for ^{19}F contamination (^{18}O water target, seals, transfer lines, synthetic apparatus, reagents, etc.).

Aqueous $[^{18}\text{F}]\text{F}^-$ is typically preferred over $[^{18}\text{F}]\text{F}_2$, as it is obtained with 2–3 orders of magnitude higher molar activity, and is easier to handle than as a highly reactive fluorine gas. Bergman and Solin reported an alternative “*post-target*” method to indirectly produce $[^{18}\text{F}]\text{F}_2$ with higher activity, starting by substituting CH_3I with $[^{18}\text{F}]\text{F}^-$ to afford $[^{18}\text{F}]\text{CH}_3\text{F}$.¹³¹ Subjecting $[^{18}\text{F}]\text{CH}_3\text{F}$ to an electric discharge effects atomization, and trapping with carrier fluorine gas affords $[^{18}\text{F}]\text{F}_2$ at up to 55 GBq/ μmol .

The cyclotron produced ^{18}F is often derivatized to form a secondary reagent, allowing for different reactivity profiles. This is usually the case with $[^{18}\text{F}]\text{F}_2$, as it is rather difficult to handle, and is very reactive, often resulting in poor regio- and chemoselectivity. Figure 3.4 depicts some of the common derivatives of $[^{18}\text{F}]\text{F}_2$, which also act as sources of electropositive fluorine.¹³²⁻¹³⁸

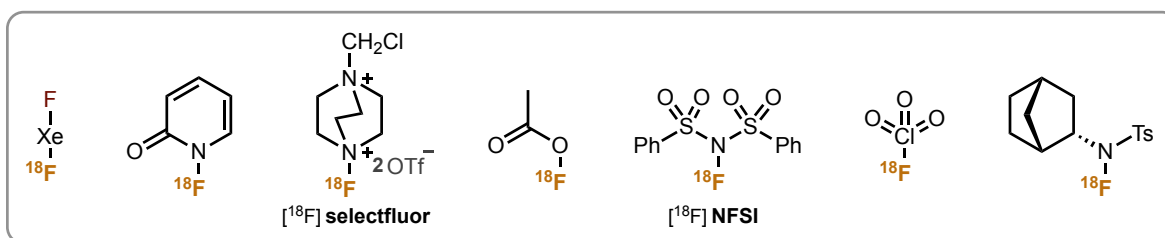


Figure 3.4. Examples of electrophilic radiofluorination reagents

On the other hand, anionic $[^{18}\text{F}]\text{F}^-$ is more often used without any derivatization. Some secondary reagents do exist however, shown in Figure 3.5. For example, $[^{18}\text{F}]$ acyl fluorides can be generated as an anhydrous gas, beneficial for very water sensitive reactions,¹³⁹ whereas $[^{18}\text{F}]\text{TBAF}$ is typically used to aid in solubility. The Doyle lab developed Pyfluor as a thermally-stable, easy-to-handle solid for deoxofluorination, as well as the ^{18}F analogue $[^{18}\text{F}]\text{Pyfluor}$.¹⁴⁰

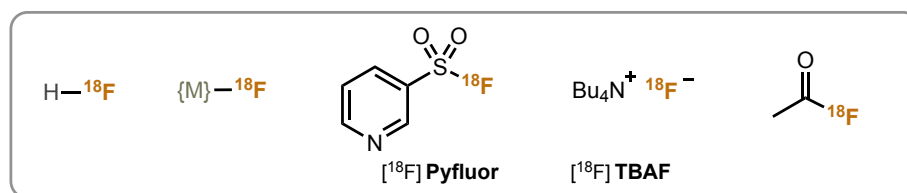


Figure 3.5. Examples of nucleophilic radiofluorination reagents

3.1.3 Fluorine-18 Radiolabeling

Figure 3.6. depicts an overview of the general strategies for introduction of ^{18}F to a molecule of interest (referred to as the *precursor*).¹¹⁸ Nucleophilic $[^{18}\text{F}]$ fluoride sources are typically used for *nucleophilic fluorination* of electron-deficient substrates, via leaving group substitution. On the other hand, electropositive ^{18}F sources undergo *electrophilic fluorination*, often reacting with a carbon-based nucleophile in the precursor (olefin, enolate, organometallic, etc.). A final strategy is the use of *prosthetic groups* – small fragments containing preinstalled ^{18}F , which are then coupled to the

precursor using a robust conjugation strategy (e.g. active-ester addition, click chemistry, etc.).¹⁴¹ This approach offers the advantage that the challenging ^{18}F bond formation step occurs on a simple prosthetic molecule, obviating any stability/selectivity concerns that can arise in direct precursor labeling. This strategy is particularly useful when the precursor is a sensitive biological molecule, such as a peptide or protein.

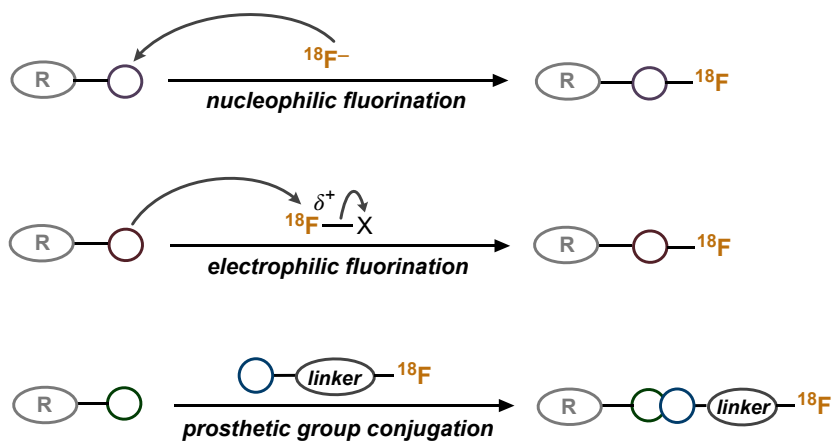


Figure 3.6. Summary of strategies for molecular incorporation of fluorine-18

Another important group of methods for ^{18}F labeling have emerged, referred to as *non-canonical labeling* (Figure 3.7).¹⁴² These are a subset of nucleophilic fluorination, which involve the binding of ^{18}F to a heteroatom group present in the precursor, namely moieties based on boron, silicon, or aluminum atoms (see Chapter 4 for more details).

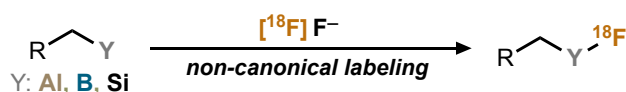


Figure 3.7. Summary of non-canonical radiofluorination strategies

Radiochemical methods are typically evaluated by an important parameter termed *radiochemical yield* (RCY).¹⁴³ This quantity refers to the amount of radioactivity present in the final radioactive compound, as a percentage of the starting activity. In other words, it is a yield relative to the limiting reagent, which in radiofluorination is always ^{18}F (\sim picomolar quantities). Since ^{18}F is continuously decaying, longer synthetic procedures lead to lower values. However, RCY is usually *decay-corrected* (d.c.) – adjusting the value to as if no decay had occurred, allowing for time-independent comparisons. If RCY is not adjusted, it is specified *non-decay-corrected* (n.d.c.).

When discussing a single radiochemical step (e.g. single reaction), the term *radiochemical conversion* (RCC) is used.¹⁴⁴ In addition, methods can be classified as *no-carrier-added* (n.c.a.) or *carrier-added* (c.a.), referring to whether a source of non-radioactive ^{19}F has been actively added.¹³⁰

3.1.4 Processing Nucleophilic Fluoride

A key challenge in performing reactions with the fluoride anion is ensuring that it has a high nucleophilicity. However, $[^{18}\text{F}]\text{F}^-$ is produced as an acidic aqueous solution, wherein the fluoride is extensively solvated by water, limiting its ability to be an effective nucleophile. As such, nearly all ^{18}F reactions involve removal of water using a workflow of the type shown in Figure 3.8.¹²³ The majority of water, as well as trace radiometal impurities, are removed as the ^{18}F solution is passed through a quaternary methyl ammonium (QMA) cartridge, a small ion-exchange column. Water passes freely through, but $[^{18}\text{F}]\text{F}^-$ is retained as it exchanges with the free anions ($\text{X}: \text{Cl}^-$ or HCO_3^-) and binds to stationary NR_4^+ groups.

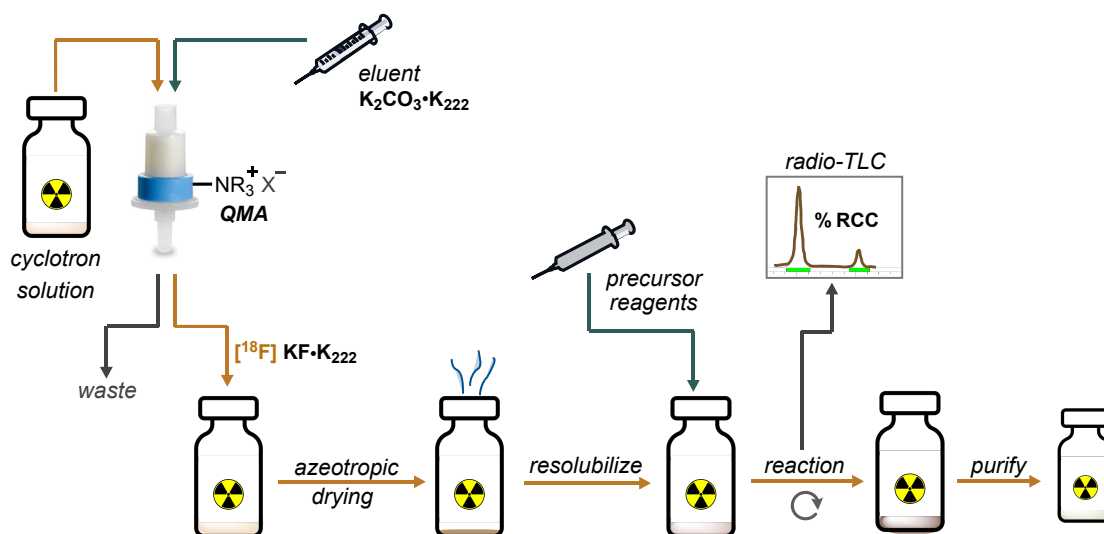


Figure 3.8. Typical protocol used in processing aqueous fluoride-18 for radiochemistry

The ^{18}F can subsequently be freed from the QMA using an *elution solution*. This is typically an inorganic salt dissolved in a polar organic solvent (plus minimal water for solubility). This salt facilitates anion exchange, and provides a counterion for the eluted fluoride. The most common mixture is K_2CO_3 and K_{222} dissolved in $\text{ACN}/\text{H}_2\text{O}$, which produces $[^{18}\text{F}]\text{KF} \cdot \text{K}_{222}$ upon elution. K_{222} is a crown-ether cryptand that acts as phase-transfer reagent – binding K^+ and facilitating KF solubility in organic media and the nucleophilicity of F^- . Similar phase-transfer properties are found in tetraalkylammonium salts, such as $\text{Bu}_4\text{N}^+\text{HCO}_3^-$, which produces $[^{18}\text{F}]\text{TBAF}$ upon elution.

The next step is removal of residual water by azeotropic drying, typically at 110°C , sometimes aided by a stream of dry gas. Two-to-three cycles of heating to dryness, followed by dry solvent addition (usually ACN) are performed. The carbonate/bicarbonate base added in the previous step is critical to keep ^{18}F in the fluoride form, and prevent loss of activity as volatile $[^{18}\text{F}]\text{HF}$.

The necessary reagents can then be added, and the reaction monitored with radio-TLC. With standard silica TLC plates, unreacted $[^{18}\text{F}]\text{F}^-$ stays at the baseline, and can be differentiated from a labeled

organic compound which would typically have a higher R_f . Finally, the labeled product is purified, typically with radio-HPLC, which monitors radioactivity and UV absorbance in parallel. The RCY is calculated relative to the starting activity of the cyclotron solution used, thereby encompassing all steps of the workflow.

Although a number of alternations/improvements have been suggested, few have seen widespread acceptance into this standard protocol, in which operational simplicity and quickness are of principal importance. One interesting example from Sanford and Scott utilized acidic solution to elute the $[^{18}\text{F}] \text{F}^-$ from the QMA (Figure 3.9).¹⁴⁵ Combining the eluent with an iron compound ($\text{Fe}(\text{acac})_3$), followed by heating under pressure, led to the formation of a putative $[^{18}\text{F}]$ “FeF” species (FeFX_2), preventing loss of volatile $[^{18}\text{F}] \text{HF}$ during a subsequent drying step. This species was demonstrated to be effective for the opening of hindered epoxides to form $[^{18}\text{F}]$ fluorohydrins.

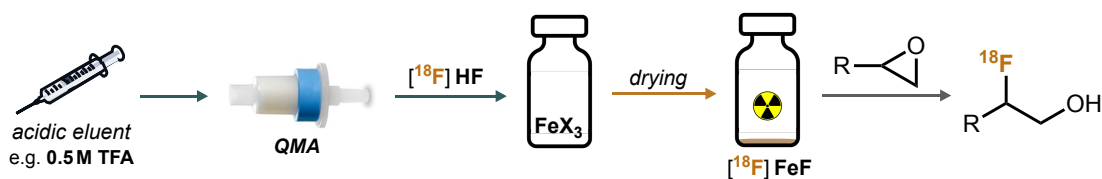
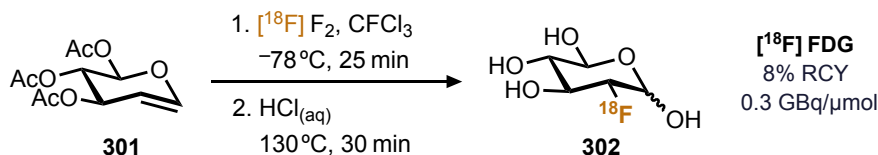


Figure 3.9. Acidic protocol used to form a putative iron fluoride species from aqueous fluorine-18

3.2 Introduction to $[^{18}\text{F}] \text{R-F}$ Synthesis

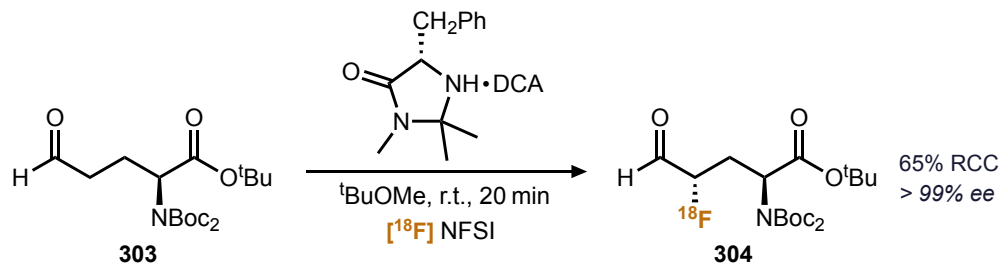
3.2.1 Electrophilic Fluorination

The challenges of using $[^{18}\text{F}] \text{F}_2$ are illustrated in the following example, depicting the first synthesis of $[^{18}\text{F}] \text{FDG}$ (**302**) from an olefin precursor **301** (Scheme 3.1).¹⁴⁶ In addition to requiring cryogenic conditions, the product (**302**) is formed in a low yield of 8% RCY, along with the unwanted axial-fluorine epimer in 3% RCY.



Scheme 3.1. Electrophilic radiofluorination of an olefin FDG precursor

Alternatively, derivatized reagents have tempered reactivity, and can often facilitate room temperature reactions. For example, the $[^{18}\text{F}] \text{NFSI}$ reagent was reported to perform α -radiofluorination of aldehydes (e.g. **303**), facilitated by a chiral organocatalyst (Scheme 3.2).¹⁴⁷ The fluorinated products (e.g. **304**) could be subsequently oxidized and deprotected to afford $[^{18}\text{F}]$ fluoro amino acids. $[^{18}\text{F}] \text{NFSI}$ is also able to act as source of ^{18}F radicals, as documented by Britton and coworkers, who described a reaction with carbo-centered radical species.¹⁴⁸



Scheme 3.2. Chiral organocatalytic α -radiofluorination of aldehydes

Fluoroarenes can also be formed using electrophilic ^{18}F sources, typically with organometallic precursors, such as aryl stannanes or boronic acids (Figure 3.10).¹¹⁵ This fluorodemetalation strategy is more effective with electron-rich rings, and for example, was used in the synthesis of [^{18}F] 6-fluoro-L-DOPA.¹⁴⁹

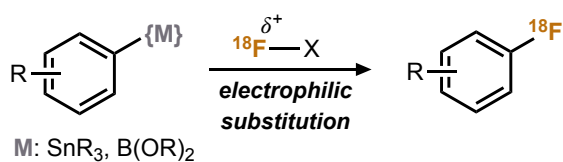
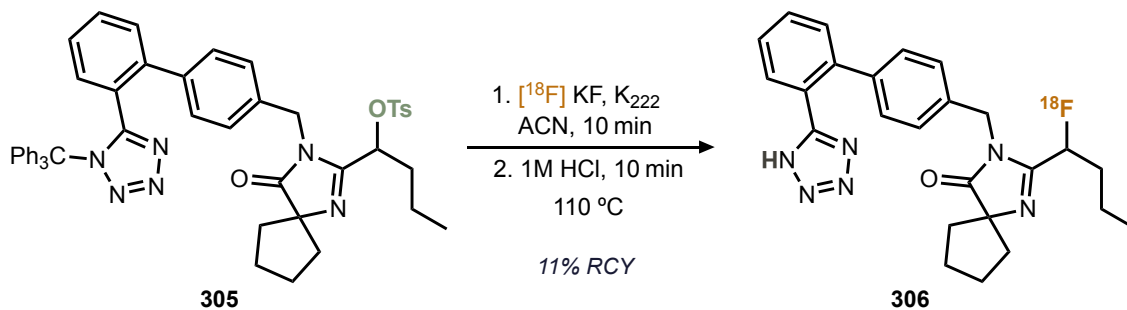


Figure 3.10. Electrophilic radiofluorination of aryl organometallic precursors

3.2.2 Aliphatic Nucleophilic Fluorination

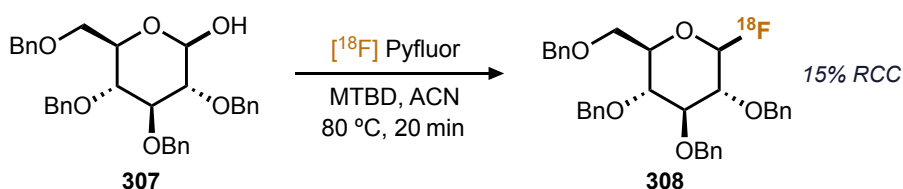
The most common method to form [^{18}F] alkyl fluorides is via substitution of a precursor with a suitable leaving group. This strategy is highlighted in the following example, describing the synthesis of a radiolabeled analogue of the AT_1R antagonist Irbesartan (Scheme 3.3).¹⁵⁰ Substitution of the protected tosylate precursor **305** using standard conditions (K_2CO_3 , K_{222}), followed by N-deprotection, readily affords [^{18}F] fluoro-Irbesartan **306** in moderate radiochemical yield.



Scheme 3.3. Radiofluorination via nucleophilic substitution of an alkyl tosylate precursor

Alcohols normally require conversion to a sulfonyl leaving group (e.g. OTs, OMs), before fluoride substitution can be performed. However, the recently reported deoxofluorination reagent [^{18}F] Pyfluor obviates the need for prefunctionalization.¹⁴⁰ For example, Doyle and coworkers demonstrated the

direct conversion of a protected glucose precursor (**307**) with [^{18}F] Pyfluor, affording protected [^{18}F] FDG **308** (Scheme 3.4).



Scheme 3.4. Radio-deoxofluorination of a protected glucose derivative

Sergeev and coworkers reported an interesting example in which aqueous [^{18}F] fluoride is used directly in the substitution of alkyl tosylate precursors.¹⁵¹ A TiO_2 catalyst was found to adsorb the [^{18}F] fluoride, activating it for the reaction, although high temperatures were still required (130 °C). O'Hagan and coworkers demonstrated the ability of fluorinase enzymes to catalyze radiofluorination, reporting [^{18}F] fluoride substitution with the biological molecule *S*-adenosyl-L-methionine.¹⁵²

Transition metals can also be used to facilitate radiofluorination, offering an alternative to conventional substitution conditions that require basic conditions and high temperature. For example, the Gouverneur and Nguyen Groups have reported allylic fluorination methods using iridium and palladium catalysis (Figure 3.11), whereas [^{18}F] cobalt and iron fluorides have been found to affect epoxide ring opening (see Figure 3.9).¹⁵³⁻¹⁵⁵

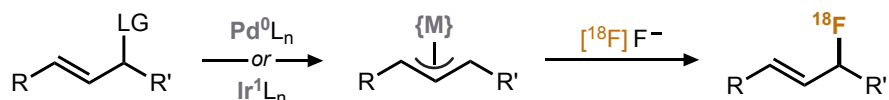


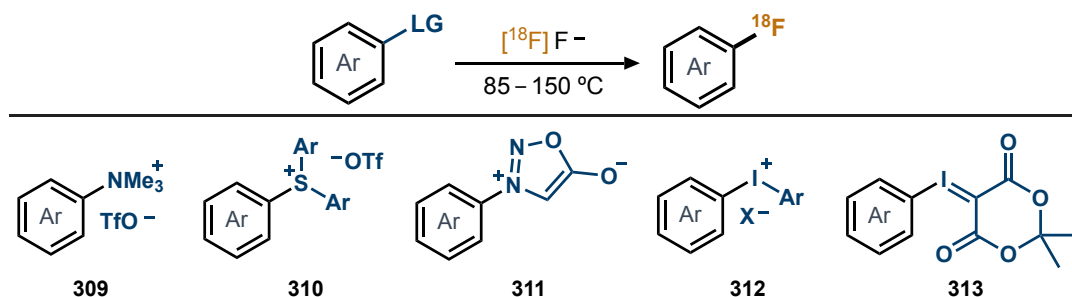
Figure 3.11. Metal catalyzed allylic radiofluorination

3.2.3 Aromatic Nucleophilic Fluorination

Fluorine-18 can be readily introduced into a target arene using substitution ($\text{S}_{\text{N}}\text{Ar}$) chemistry (Scheme 3.5).¹¹⁵ However, the arene precursor typically requires an electron-withdrawing activating group, or use of an electron-deficient heteroarene, such as pyridine. In order to surmount these scope limitations, an ongoing area of research is focused on identifying novel active leaving groups, beyond standard halides and pseudohalides.

Early attempts to use aryl diazonium salts or aryl triazenes for radiofluorination had limited success (Balz-Schiemann and Wallach reactions, respectively). On the other hand, triarylsulfonium salts (**310**) have been found to be appealing precursors for $\text{S}_{\text{N}}\text{Ar}$.¹⁵⁶ When the two auxiliary arenes (i.e. those that form the Ar_2S leaving group) are both phenyls, the target arene must be electron-deficient to obtain good chemoselectivity. However, the use of *p*-methoxyphenyls as auxiliary arenes leads to good

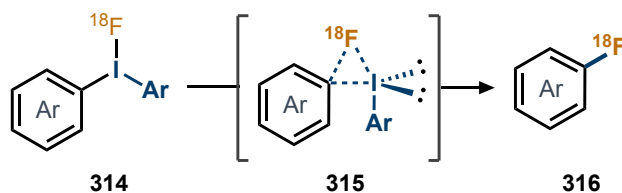
selectivity for more neutral target arenes.¹⁵⁷ *N*-arylsydnonones (**311**) were also found to be excellent leaving groups for aromatic substitution, albeit only with electron-deficient arenes.¹⁵⁸



Scheme 3.5. Summary of activated arene precursors used for radiofluorination

Ritter, Hooker and coworkers developed an elegant method to radiofluorinate phenols directly, using a diaryl-imidazolium to activate the oxygen.¹⁵⁹ Inclusion of a ruthenium catalyst facilitated this reaction with electron-rich phenols, via the formation of a η^6 - π -complex.¹⁶⁰

Perhaps the most important class of precursors are those utilizing an iodine(III) moiety.¹⁶¹ In particular, diaryliodonium salts (**312**) are well-known, and have been used as precursors for a number of clinical PET tracers.¹⁶² With unsymmetrical iodoniums, the more electron-deficient arene of the pair undergoes substitution preferentially. As such, 2-thiophene was introduced as an effective auxiliary arene, imparting good regioselectivity for a number of target arenes.¹⁶³ Alternatively, Sanford and coworkers found that copper(I) mediates the radiofluorination of diaryliodoniums, and that mesitylene was an effective auxiliary under these conditions.^{164, 165} Mechanistically, the iodine(III) compounds are thought to first react with fluoride to form a trigonal bipyramidal fluoro iodide species **314** (Scheme 3.6).¹⁶⁶ Transfer of fluoride to the arene, via a 3-membered transition state (**315**), results in formation of the aryl fluoride product (**316**).



Scheme 3.6. Mechanism of arene radiofluorination from a hypervalent iodine species

More recently, aryl iodonium ylides (e.g. **313**) have been found to offer excellent regioselectivity and high RCC for both electron-rich and electron-poor arenes.¹⁶⁷ A number of spirocyclic iodonium ylides (SCIDYs) have also been reported, containing cyclo- butyl, pentyl, hexyl, as well as adamantyl rings in place of the two methyl groups in **313**.^{168, 169}

Another distinct grouping of methods for [¹⁸F] aryl fluoride formation are transition-metal mediated reactions.¹⁷⁰ Most frequently, such reactions utilize copper complexes and aryl boronic acids/esters or

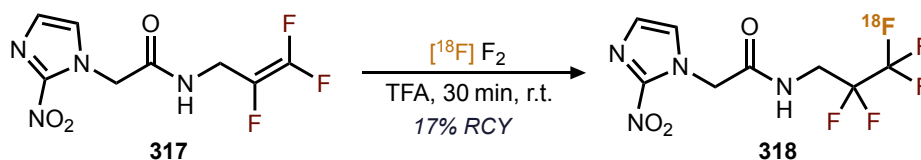
aryl stannanes as precursors. The Ritter Group has also reported oxidative radiofluorinations using Ni(II) or cationic Pd(IV) complexes.^{171, 172}

3.3 Introduction to [¹⁸F] R–CF₃ Synthesis

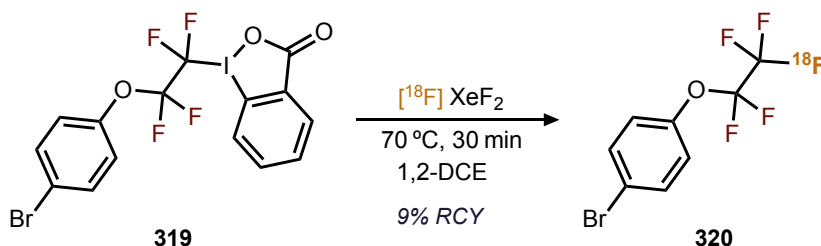
This section will describe some examples of [¹⁸F] trifluoromethane synthesis, highlighting the different conceptual strategies that are used. As previously discussed (q.v. *section 1.1*), the CF₃ group is rapidly increasing in ubiquity in bioactive compounds. However, [¹⁸F] RCF₃ are difficult to synthesize efficiently, and often require multi-step routes. This chemistry is arguably under-explored, and methods often cannot achieve high molar activities. One plausible contribution to this is the occurrence of undesired ¹⁸F/¹⁹F isotopic exchange reactions, leading to reduced molar activity.

3.3.1 Electrophilic Methods

The goal of achieving high molar activity [¹⁸F] RCF₃ compounds is poorly met by electrophilic reagents, which have their own specific activity limitations. As such, electrophilic methods are fairly uncommon (Scheme 3.7, 3.8). In the few reported examples, typical precursors are 1,1-difluoroolefins (e.g. **317**),¹⁷³ or substrates that provide access to difluoromethyl anion synthons (e.g. **319**).¹⁷⁴ The synthesis of hypoxia tracer [¹⁸F] EF5 (**318**) and [¹⁸F] perfluoroethyl substrate **320** proceeded in low-to-moderate radiochemical yields, and molar activities were not reported.^{173, 174}



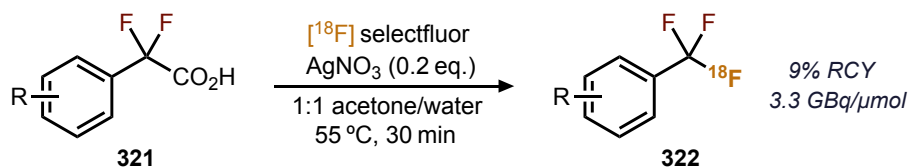
Scheme 3.7. Electrophilic radiofluorination of a 1,1-difluoroolefin precursor



Scheme 3.8. Xenon difluoride mediated radiofluorination of a difluoroalkyl iodane precursor

Somewhat more attractive conditions were reported by Gouverneur and coworkers, utilizing difluoroacetic acid derivatives (**321**) as precursors (Scheme 3.9).¹⁷⁵ A silver catalyst effects decarboxylative radiofluorination of **321**, using the [¹⁸F] selectfluor reagent, which is stable under

aqueous conditions. However, the [^{18}F] ArCF_3 (**322**) products were obtained in fairly low molar activities of no more than 3.3 GBq/ μmol .

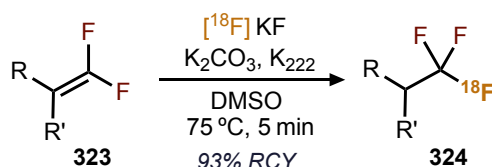


Scheme 3.9. Electrophilic synthesis of labeled trifluoromethyl arenes

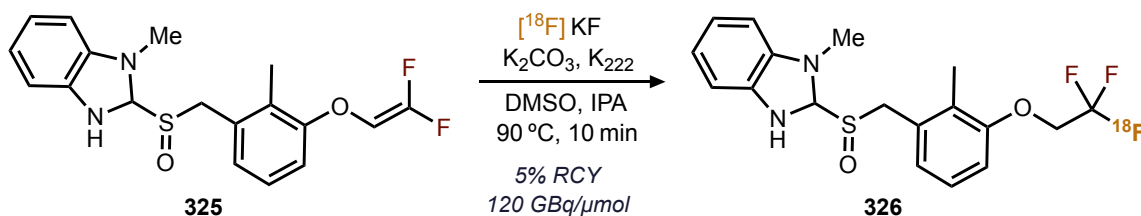
An alternative to [^{18}F] F_2 derivatives, is the use of [^{18}F] F^- with a stoichiometric oxidant, providing sources of electrophilic or radical ^{18}F *in situ*. For example, aryl difluoromethanes (ArCF_2H) could undergo radical C–H fluorination to afford the corresponding [^{18}F] ArCF_3 using [^{18}F] F^- and a manganese(III) salen precatalyst, and iodosobenzene as the oxidant.¹⁷⁶

3.3.2 Nucleophilic Methods

Among the most common methods for [^{18}F] RCF_3 synthesis are nucleophilic addition and substitution reactions. For example, 1,1-difluoroolefins (**323**) undergo addition with fluoride to afford the corresponding trifluoride **324** (Scheme 3.10), with trace water acting as the source for the vicinal proton.¹⁷⁷ This strategy was recently applied in the synthesis of a clinical PET candidate (**326**), aimed at detecting tau aggregation in the brain, a potentially powerful tool to advance understanding of neurodegenerative disorders (Scheme 3.11).¹⁷⁸ The [^{18}F] lansoprazole derivative (**326**) was labeled in low yield, but with high molar activity, facilitating first-in-human studies.



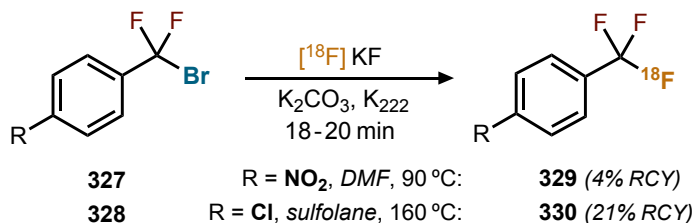
Scheme 3.10. Nucleophilic radiofluorination of a 1,1-difluoroolefin precursor



Scheme 3.11. Nucleophilic radiofluorination of a 1,1-difluoro-lansoprazole precursor

Substitution can also be performed using a difluoromethyl moiety appended to a leaving group. For example, bromodifluoromethyl arenes (**327**, **328**) undergo fluorination to afford [^{18}F] ArCF_3 in moderate-to-low RCY (Scheme 3.12).^{179, 180} Substitution of the chloro analogue (ArCF_2Cl) is also

possible, although somewhat harsher conditions are required (220 °C, Sb₂O₃).¹⁸¹ An exception is 2-CF₂Cl indoles, which can be efficiently labeled under metal-free conditions at 85 °C.¹⁸²



Scheme 3.12. Nucleophilic radiofluorination of a bromodifluoromethyl arene precursor

This strategy using CF₂Br precursors has been employed for the synthesis of various bioactive aryl- and heteroaryl [¹⁸F] CF₃ compounds, such as those shown in Figure 3.12 (labeling conditions in brackets).¹⁸³⁻¹⁸⁵ Low-to-moderate molar activities were obtained in these examples, sufficient to perform preclinical animal studies.

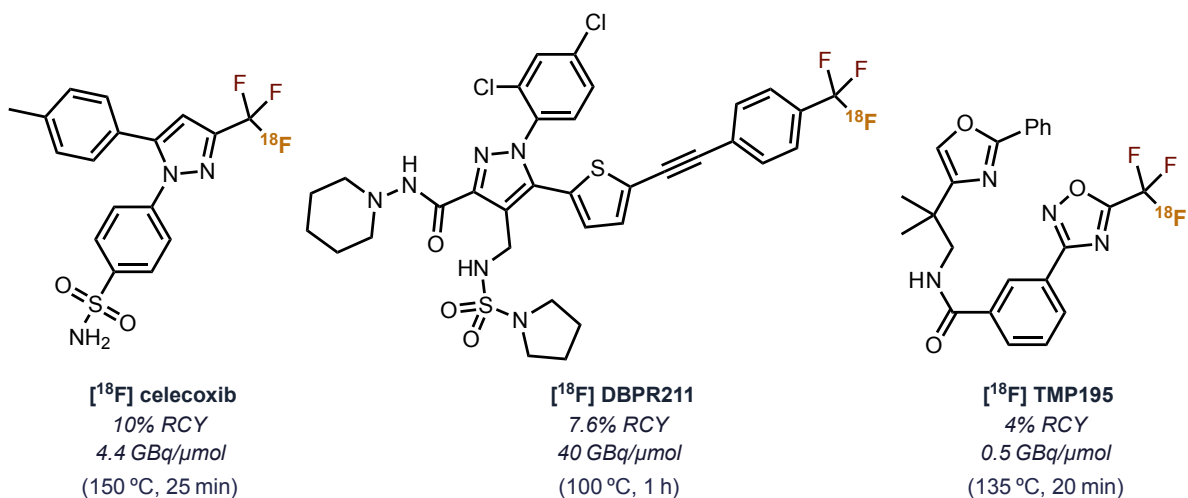
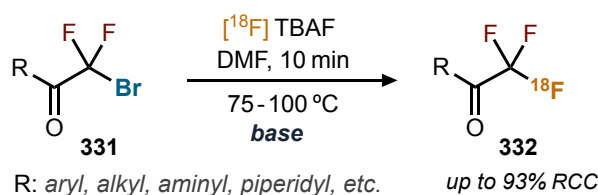


Figure 3.12. Labeled trifluoromethanes synthesized from bromodifluoromethyl precursors

Gouverneur and coworkers investigated alternatives to avoid the high temperatures typically required for rapid ArCF₂Br substitution with [¹⁸F] F⁻. They found that addition of silver(I) triflate was rather effective, allowing the reaction to proceed in 20 minutes at room temperature for a range of ArCF₂Br substrates (10 examples, up to 80% RCC).¹⁸⁶ The same lab demonstrated that AgOTf could also be used to facilitate [¹⁸F] ArOCF₃ / ArSCF₃ formation from CF₂Br precursors, under mild conditions (60 °C, 20 minutes).¹⁸⁷

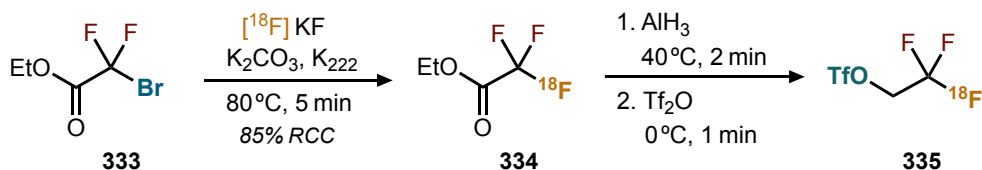
Substrates containing a CF₂Br group vicinal to a carbonyl (**331**) are also effective [¹⁸F] CF₃ precursors (Scheme 3.13). The Szabó Group reported a number of such examples, finding that the addition of a nitrogenous base (DBU or TBD) was necessary to achieve a high RCC.^{188, 189} In another aliphatic example, [¹⁸F] 2-aminoethyl CF₃ substrates were synthesized via an oxidative fluoro-

desulfurization reaction with a thioester or trithioorthoester precursor.^{190, 191} After ¹⁸F incorporation, carrier HF-pyridine was added to facilitate full fluorination and formation of [¹⁸F]EtCF₃ product.



Scheme 3.13. Synthesis of radiolabeled α -trifluoromethyl carbonyl substrates

Nucleophilic substitution has also been used to prepare CF₃ containing prosthetic groups (Scheme 3.14). For instance, radiofluorination of ester derivative **333**, followed by reduction and triflation, affords [¹⁸F] 2-trifluoroethyl triflate **335**.¹⁹² This prosthetic group can subsequently be incorporated into a complex molecule via substitution of the triflate leaving group.

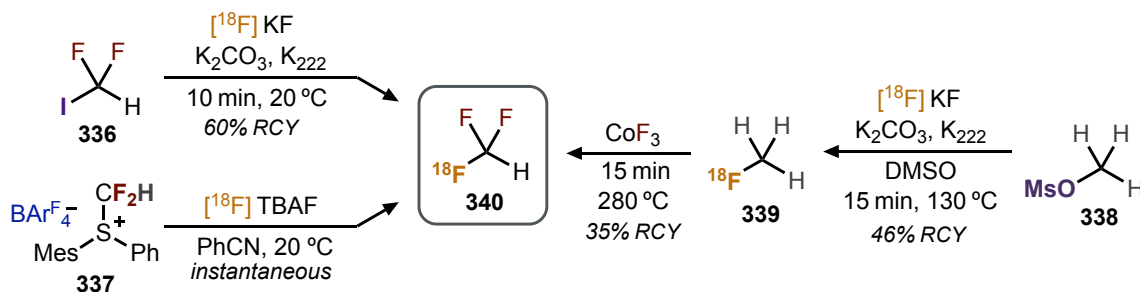


Scheme 3.14. Synthesis of a radiolabeled trifluoromethyl prosthetic group

3.3.3 Coupling Methods

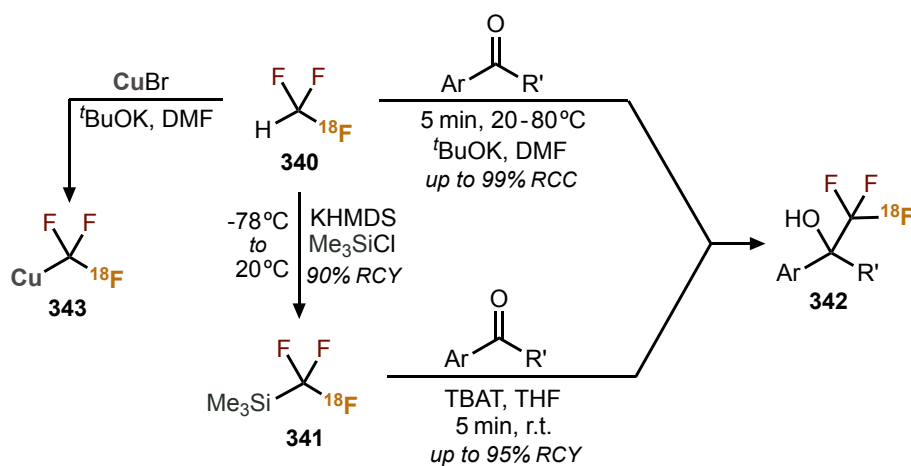
The last few decades have seen a wealth of new methods for direct CF₃ incorporation. The source of CF₃ is often one of many specialty group transfer reagents, that can be a source of nucleophilic, electrophilic, or radical CF₃. Formation of ¹⁸F analogues of these reagents is challenging, and typically utilizes CF₂ building blocks to form [¹⁸F]CF₃ reagents.

Perhaps the simplest difluoro building block is difluoroiodomethane **336**. Vugts and coworkers showed that it could undergo substitution with fluoride to produce [¹⁸F] fluoroform **340** (Scheme 3.15).^{193, 194} Despite being a difficult to handle gas that must be trapped at low temperature and purified by distillation, [¹⁸F] fluoroform is a common intermediate in various synthetic methods. It is also readily formed using the active difluoromethyl sulfonium reagent **337**.¹⁹⁵ Alternatively, Pike and coworkers showed that a two-step process, starting with substitution of mesylate **338**, followed by C–H fluorination, produces [¹⁸F] fluoroform **340** in high molar activity (averaging 38 GBq/ μ mol).¹⁹⁶



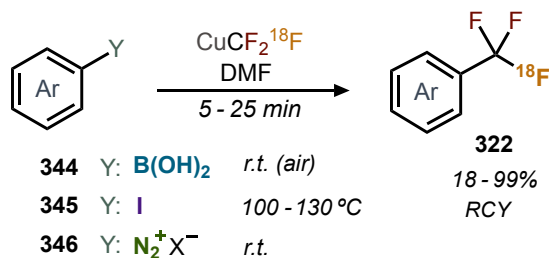
Scheme 3.15. Summary of methods for the synthesis of radiolabeled fluoroform

$[^{18}\text{F}]$ fluoroform (**340**) is an effective source of nucleophilic CF_3 (Scheme 3.16). For example, under basic conditions it undergoes addition to aldehydes/ketones to form $[^{18}\text{F}]$ α -(trifluoromethyl)benzyl alcohols **342** (18 examples).¹⁹³ Alternatively, **340** can be converted into the ^{18}F analogue of the Ruppert-Prakash reagent (**341**), a common trifluoromethylating reagent in organic chemistry.¹⁹⁴ This reagent adds to aldehydes/ketones under mild conditions, requiring only an activator (TBAT), rather than strong base, to form benzyl alcohols **342** (13 examples).



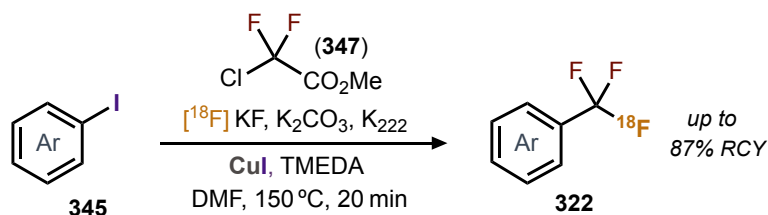
Scheme 3.16. Summary of methods for nucleophilic radio-trifluoromethylation

$[^{18}\text{F}]$ fluoroform (**340**) can also be converted to $[^{18}\text{F}]$ CuCF_3 (**343**) via addition of strong base in the presence of a copper(I) species.^{195, 196} $[^{18}\text{F}]$ CuCF_3 (**343**) is well-suited to undergo coupling with a suitable arene precursor (e.g. ArX) to form $[^{18}\text{F}]$ ArCF_3 , drawing upon a number of well-established methods in organic chemistry.¹⁹⁷ For example, the trifluoromethylation of various aryl boronic acids (**344**), aryl iodides (**345**), and aryl diazonium salts (**346**) has been reported by the groups of Pannecoque and Pike (Scheme 3.17).^{195, 196}



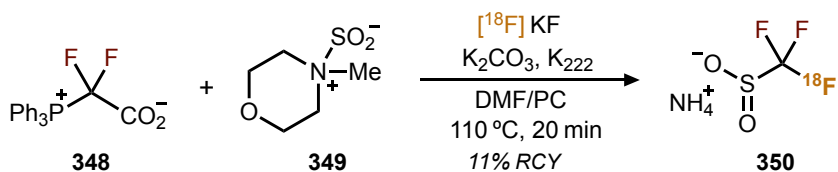
Scheme 3.17. Synthesis of labeled arenes using a radio-trifluoromethyl copper(I) reagent

An alternative strategy is the generation of $[\text{F}^{18}]\text{CuCF}_3$ *in situ*, rather than pre-forming it in a separate vessel. This was successfully applied to the trifluoromethylation of a range of aryl and heteroaryl iodides **345** as shown in Scheme 3.18.¹⁹⁸ This approach utilizes a difluorocarbene ($:\text{CF}_2$) precursor, methyl chlorodifluoroacetate (**347**), as a CF_2 building block. In the presence of CuI and a ligand (TMEDA), **347** undergoes decomposition to form MeI , CO_2 , and $:\text{CF}_2$ which readily reacts with $[\text{F}^{18}]\text{F}^-$ and copper(I) to form $[\text{F}^{18}]\text{CuCF}_3$. These synthetic conditions were successfully employed to synthesize tracers for small-animal PET studies – a nucleoside analogue $[\text{F}^{18}]\text{trifluridine}$ for cancer imaging,¹⁹⁹ and $[\text{F}^{18}]\text{PTTP}$ for the imaging of inflammation.²⁰⁰ These *one-pot* methods have only been demonstrated with iodo arenes, which require high temperatures to react. The more reactive aryl boronic acids would likely interfere with the *in situ* formation of $[\text{F}^{18}]\text{CuCF}_3$.



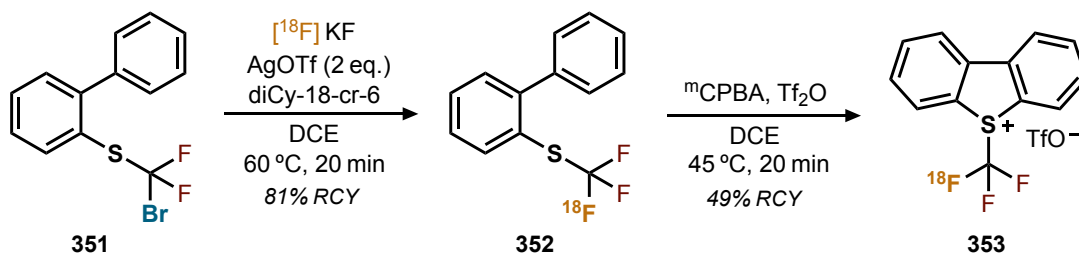
Scheme 3.18. Synthesis of labeled trifluoromethanes with difluorocarbene and copper(I) reagents

Examples of radical $[\text{F}^{18}]\text{CF}_3$ reagents have been reported, such as the sulfinate **350** reported by Gouverneur and coworkers (Scheme 3.19).²⁰¹ This reagent is also formed via a difluorocarbene, formed upon the thermal decarboxylation of PDFA (**348**), followed by trapping with $[\text{F}^{18}]\text{F}^-$ and an SO_2 source **349**. The sulfinate (**350**) was successfully employed for the radical trifluoromethylation of tyrosine and tryptophan residues in native peptides, in the presence of a stoichiometric oxidant (TBHP) and an iron(III) salt.



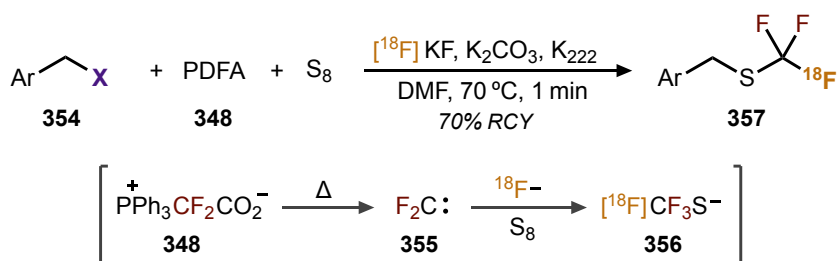
Scheme 3.19. Synthesis of a labeled trifluoromethyl sulfinate prosthetic group

In another example, the [¹⁸F]Umemoto reagent (**353**), a source of electrophilic CF₃, was synthesized (Scheme 3.20).²⁰² Substitution of ArCF₂Br (**351**) afforded [¹⁸F] trifluoromethyl sulfane **352**, which underwent an ^mCPBA-mediated oxidative cyclization to form **353**. This reagent (**353**) was found to effectively label a number of peptide substrates, reacting with cysteine residues to form [¹⁸F] RSCF₃.



Scheme 3.20. Synthesis of a labeled Umemoto trifluoromethylating reagent

[¹⁸F]RSCF₃ compounds can also be formed via *trifluoromethylthiolation* as shown in Scheme 3.21. Liang and coworkers showed PDFA-derived difluorocarbene (**355**) reacts with octasulfur (S₈) and [¹⁸F] F⁻ to produce a nucleophilic thiolate species **356**.²⁰³ The thiolate then can undergo substitution with a heterobenzyl halide precursor (**354**) to afford the CF₃ thioether product (**357**). This protocol was later expanded to the [¹⁸F] trifluoromethylthiolation of α -bromo ketones/esters, by the addition of a copper(I) promoter (proceeding via a putative [¹⁸F]CuSCF₃ intermediate).²⁰⁴

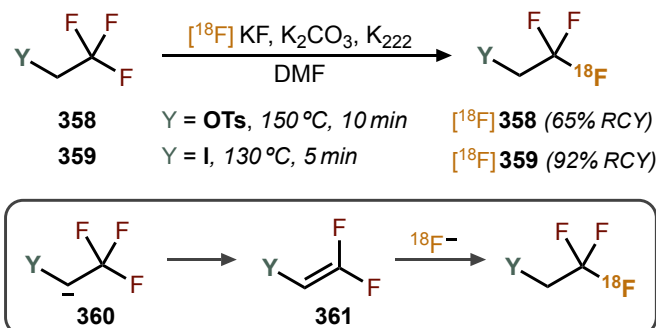


Scheme 3.21. Synthesis of labeled trifluoromethyl sulfides via in situ thiolate formation

3.3.4 Isotopic Exchange

Isotopic exchange (¹⁹F/¹⁸F) is fairly uncommon for [¹⁸F]RCF₃ synthesis, and for C–F compounds in general. In addition to the challenges of breaking the C–F bond, these methods are often especially hard-pressed to produce high molar activity products. Unlike other methods, in which excess starting precursor can be separated, the ¹⁹F compound simply dilutes the ¹⁸F product, lowering molar activity. However, isotopic exchange offers some appealing advantages, namely that no specially functionalized precursor is required. Rather, the target CF₃ molecule can be used directly as the precursor, offering a direct and straightforward approach.

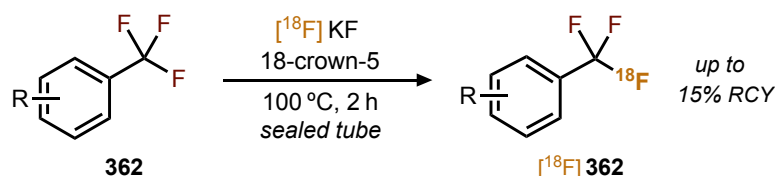
This isotopic exchange strategy was used in the preparation of CF_3 prosthetic groups ^{18}F **358**, **359** (Scheme 3.22).¹²⁹ The mechanism is thought to proceed by α -deprotonation to form **360**. This anion eliminates fluoride to form difluoroalkene **361**, which reforms ^{18}F CF_3 upon addition of ^{18}F fluoride.



Scheme 3.22. Synthesis of labeled aliphatic trifluoromethyl prosthetic groups via isotopic exchange

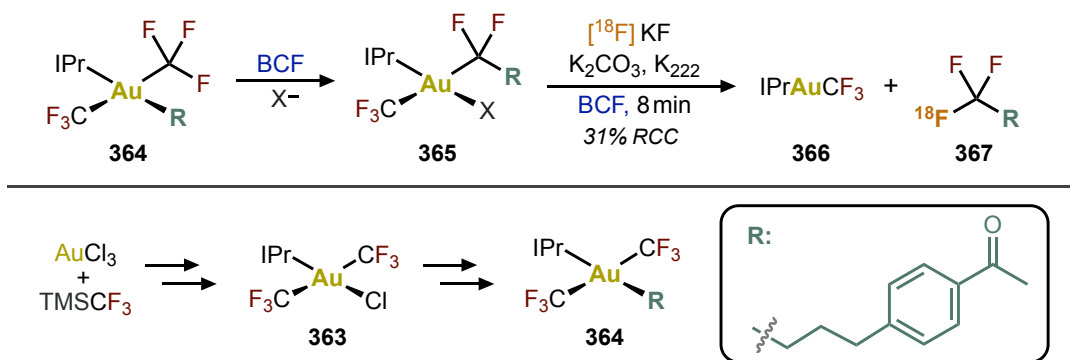
Comparable results were obtained with similar aliphatic CF_3 compounds, including various inhalation anesthetics (isoflurane, sevoflurane, etc.).²⁰⁵⁻²⁰⁷ Although radiochemical conversions were high with most substrates, the products tended to have very low molar activities.

The only example of substrates without α -protons are from a short 1979 symposium abstract documenting the isotopic exchange of aryl trifluoromethanes **362**, including benzothiazole, phenothiazine, and uracil heteroarenes (Scheme 3.23).²⁰⁸ However, few details are given and molar activities were not reported. The method is not ideal, utilizing fairly harsh conditions, and a very long reaction time.



Scheme 3.23. Synthesis of radiolabeled trifluoromethyl arenes by isotopic exchange

In a recent example, the Toste Group described a multi-step route to aliphatic ^{18}F CF_3 groups, in which C–F abstraction and reintroduction occur in distinct steps, termed a *fluoride rebound* mechanism (a formal isotopic exchange).⁹² This method utilizes a CF_3 gold(III) complex (**364**), which undergoes C–F cleavage upon treatment with BCF (Scheme 3.24). The resulting cationic difluoro intermediate proceeds with migratory insertion of the R-group to form difluoromethyl substrate **365**. This substrate is primed for radiofluorination, with the inclusion of ^{18}F F^- and subsequent reductive elimination leading to the trifluoro product (**367**) and a reduced gold(I) species (**366**).



Scheme 3.24. Synthesis of labeled trifluoromethanes via a gold(III) mediated fluoride rebound

Although radiochemical yields were moderate (12–31% RCY) for the three examples reported, each required a unique synthetic route. After proceeding through common intermediate **363**, a functional handle was introduced to the gold center, allowing for each R group to be constructed in a *de novo* fashion. Thus, although an elegant strategy, this method is arguably limited by its complexity and lack of generality.

3.4 Investigations on the Synthesis of [¹⁸F] ArCF₃

As described above, there has been relatively little progress in the development of isotopic exchange methods for trifluoromethyl compounds (ArCF₃ in particular). However, this remains a very appealing goal. The ability to directly use a CF₃ starting material, without the need for complex derivatization to a functionalized difluoro substrate, would be very powerful and would expedite the synthesis of ¹⁸F-analogues of existing bioactive CF₃ compounds.

This section describes the efforts towards adapting the ArCF₃ substitution conditions described in Chapter 2, into a radiochemical method. Given the ability of these conditions to cleave the C–F bond, it was reasoned that this may facilitate conditions wherein isotopic exchange is kinetically viable. Alternatively, a two-step method was envisioned, with an initial halogen exchange to form ArCF_{n-3}Br_n species *in situ*, followed by addition of [¹⁸F]F⁻ to facilitate nucleophilic substitution.

3.4.1 Conditions Screening

Various attempts to effect isotopic exchange using standard elution conditions were performed. This involved elution of 300–700 MBq ¹⁸F with a solution of K₂CO₃ (~3 mg, 20 μmol) and K₂₂₂ (~15 mg, 40 μmol) in 4:1 ACN:H₂O (1 mL), followed by azeotropic drying at 110 °C (2–3 cycles of 2 mL ACN addition and evaporation to dryness). The dry residue was resuspended in a reaction solvent, and this stock solution was then added into vials containing the ArCF₃ mixture (0.01–0.04 mmol scale). The 2-

bromoethyl substituted ArCF_3 substrate **368** was used, as it had previously been found to have a high reactivity, and its higher boiling point prevented evaporative losses.

Isotopic exchange was envisioned to occur as depicted in Figure 3.13, initiated by the binding of an acidic iron species to fluorine. Substitution could then occur with either free $^{18}\text{F}^-$, or a nucleophilic $^{18}\text{F}^- \text{BX}_3^-$ species, to furnish the radiofluorine product. The FeX_3 and BX_3 species would likely be heteroleptic in nature, given the propensity for ligand exchange to occur (q.v. *section 2.3.5*). Additionally, incorporation of BBr_3 to the reaction mixture would result in halox reactivity with ArCF_3 , further complicating the distribution of ligands ($^{18}\text{F}/\text{F}/\text{Br}$) between the FeX_3 , BX_3 , and $\text{ArCF}_{3-n}\text{X}_n$ species.

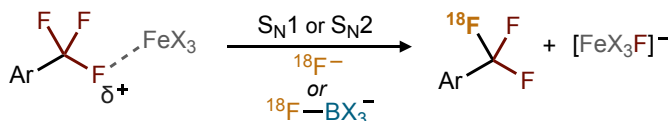


Figure 3.13. Plausible scheme for the isotopic exchange of trifluoromethyl arenes

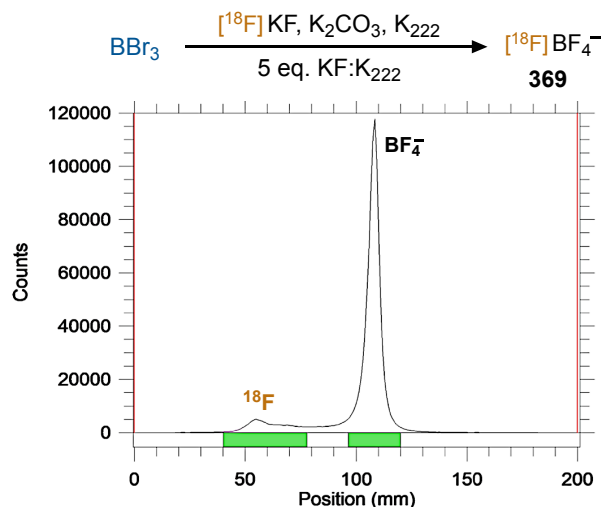
Initial attempts, which involved simply combining ArCF_3 (**368**) with FeF_3 and ^{18}F fluoride, followed by stirring at room temperature, were unsuccessful at producing any ^{18}F **368** (Scheme 3.25, entry 1). The addition of various Lewis acids to this mixture proved similarly ineffectual, including both boryl bromides and fluorides (entries 2–7).



entry	reagents	time	RCC
1	0.3 eq. FeF_3	20 min	0%
2	0.3 eq. FeF_3 , 1 eq. BF_3OEt_2	20 min	0%
3	0.3 eq. FeF_3 , 1 eq. PhBF_2	20 min	0%
4	0.3 eq. FeF_3 , 1 eq. AgOTf	20 min	0%
5	0.3 eq. FeF_3 , 0.3 eq. BBr_3	30 min	0%
6	0.3 eq. $\text{Fe}(\text{OTf})_3$, 0.3 eq. BBr_3	30 min	0%
7	0.3 eq. $\text{Fe}(\text{OTf})_3$, ^{18}F 369	1 h	0%

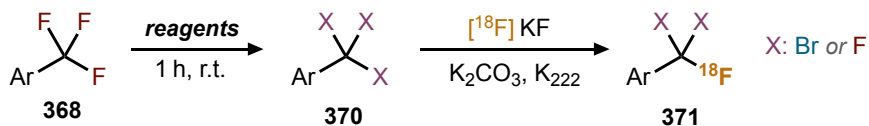
Scheme 3.25. Evaluation of isotopic exchange for trifluoromethyl arene radiofluorination

The last entry (7) utilized a putative $^{18}\text{F}^- \text{BF}_4^-$ species (**369**) that was first formed in a separate flask, via addition of $^{18}\text{F}^-$ to BBr_3 , along with excess carrier fluoride (Scheme 3.26). Paper TLC could successfully distinguish free $^{18}\text{F}^-$ from $^{18}\text{F}^- \text{BF}_4^-$ as shown by the radio-TLC spectrum below. A curcumin stain corroborated the presence of the putative boron species near the solvent front. However, this species **369** was also unsuccessful at effecting isotopic exchange to produce ^{18}F **368**.



Scheme 3.26. Synthesis of a labeled tetrafluoroborate and radio-TLC analysis

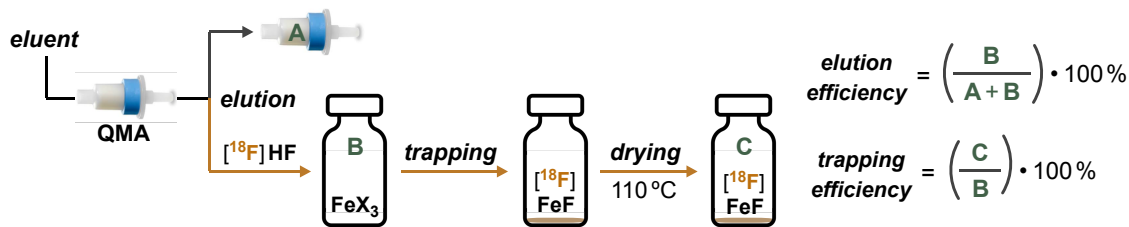
In the next attempts, the ArCF_3 , FeF_3 , and BBr_3 reagents were pre-combined to effect formation of $\text{ArCF}_{3-n}\text{Br}_n$ intermediates (**370**), as shown in Scheme 3.27. The $[^{18}\text{F}]\text{F}^-$ solution was then added to the same reaction vessel. A fairly high temperature and extended reaction time were required to achieve trace conversion to the presumptive species **371** (entry 2).



entry	reagents	solvent	temperature	time	RCC
1	0.3 eq. FeF_3 , 0.3 eq. BBr_3	DCM	50 °C	2 h	0%
2	0.1 eq. FeF_3 , 0.5 eq. BBr_3	DCE	110 °C	2 h	1%

Scheme 3.27. Evaluation of a two-step process for trifluoromethyl arene radiofluorination

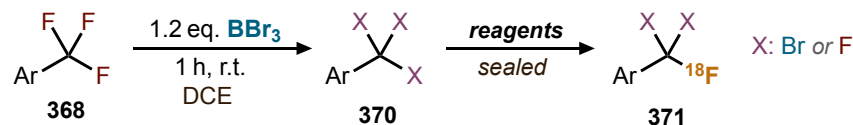
One hypothesis explaining these low conversions is that K_2CO_3 is incompatible with the reaction conditions that foster halogen reactivity. Inspired by the work of Sanford and coworkers (q.v. section 3.1.4), alternative acidic elution methods were evaluated (Scheme 3.28). The eluent (1 mL) was combined with FeBr_3 (5–10 mg) to effect formation of a putative $[^{18}\text{F}]\text{FeFX}_2$ species (hence written “ FeF^+ ”), thereby preventing loss of $[^{18}\text{F}]\text{HF}$ during the azeotropic drying step. Elution efficiency, which quantifies the fraction of $[^{18}\text{F}]\text{F}^-$ that is removed from the QMA, was high with various acidic eluents (entries 1–4). Trapping efficiency was initially low (entry 1), indicating limited $[^{18}\text{F}]\text{FeF}$ formation, relative to $[^{18}\text{F}]\text{HF}$ losses. Variable improvements were observed by heating the eluted $[^{18}\text{F}]\text{HF}$ solution with FeBr_3 in a sealed vessel before proceeding with the drying step (entries 2–4). The process was evaluated without the azeotropic drying step, removing water by flushing the QMA with dry NO_2Me before acidic elution (entries 5–6). Although this approach reduced losses of volatile $[^{18}\text{F}]\text{HF}$, the elution efficiencies were lower.



entry	elution	efficiency	trapping	efficiency
1	HCl / H ₂ O (conc.)	97%	FeBr₃	23%
2	FeBr₃ / NO ₂ Me (0.03 M)	85%	80 °C, 10 min, <i>sealed</i>	27%
3	TFA / 4:1 ACN:H ₂ O (0.05 M)	98%	FeBr₃ , 100 °C, 10 min, <i>sealed</i>	48%
4	TFA / NO ₂ Me (0.05 M)	86%	FeBr₃ , 110 °C, 10 min, <i>sealed</i>	19%
5	flush, then TFA / NO ₂ Me	57%	FeBr₃ , <i>no drying</i>	–
6	flush, then 370 , FeF ₃ , DCE	62%	<i>no drying</i>	–

Scheme 3.28. Evaluation of acidic elution and iron-mediated trapping of fluoride-18

The [¹⁸F] FeF species produced were then evaluated for their ability to facilitate conversion of ArCF_{n-3}Br_n species **370** to radio-fluorinated species **371**. This proved unsuccessful, with no conversion observed after heating **370** in a sealed vessel for an extended time with any of the [¹⁸F] FeF species (Scheme 3.29). Using the **370** reaction mixture itself for elution was moderately efficient, but also failed to produce any product **371**.

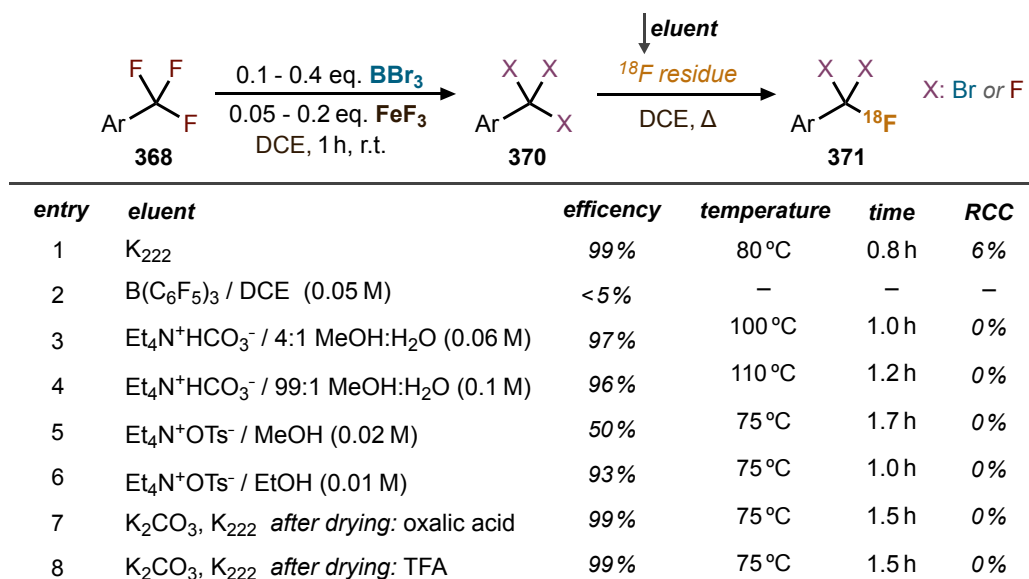


entry	reagents	temperature	time	RCC
1	[¹⁸ F] FeF residue (entry c)	90 °C	1.2 h	0%
2	[¹⁸ F] FeF residue (entry d)	100 °C	1.5 h	0%
3	[¹⁸ F] FeF / HF mixture (entry e)	100 °C	1.5 h	0%
4	[¹⁸ F] “F ⁻ ” mixture (entry f)	90 °C	1.5 h	0%

Scheme 3.29. Evaluation of iron fluoride species for trifluoromethyl arene radiofluorination

The lack of success with acidic elution prompted a return to more conventional elution conditions (Scheme 3.30). Elution was highly efficient with K₂₂₂ in ACN/H₂O in the absence of K₂CO₃ (entry 1). When the dry residue was combined with a mixture of ArCF_{3-n}Br_n (**370**), a significantly improved conversion of 6% was observed (Figure 3.14). However, the dry residue contained < 1% of the eluted activity, indicating near complete loss of activity as [¹⁸F] HF in the drying step beforehand. This experiment confirms that K₂CO₃ inhibits the formation of **371**. Further screening was performed, with the aim of identifying a less basic eluent that would not interfere with acidic halox reactivity, while also limiting activity losses from [¹⁸F] HF formation.

An organic solution of BCF proved incapable of eluting ^{18}F from the QMA (entry 2). On the other hand, tetraethylammonium carbonate solutions resulted in very high elution efficiencies (entries 3–4). It was reasoned that the reduced basicity of HCO_3^- vs CO_3^{2-} may serve to cause less interference in the ^{18}F -halex. However, the reaction of the dried ^{18}F -residue with **370** failed to produce any of the desired ^{18}F ArCF_3 product (**371**).



Scheme 3.30. Evaluation of different eluents for trifluoromethyl arene radiofluorination

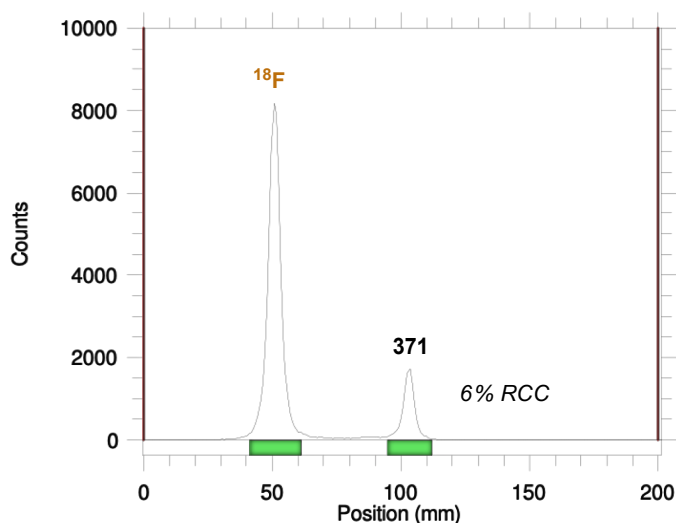


Figure 3.14. Radio-TLC analysis for the radiofluorination of a trifluoromethyl arene (entry 1)

Containing an even less basic anion, tetraethylammonium tosylate was subsequently evaluated for elution. A solution in methanol was only moderately effective (entry 5), with a significant improvement upon switching to ethanol (entry 6). An alternative protocol was also evaluated, beginning with

standard K_{222}/K_2CO_3 elution and subsequent azeotropic drying. A small amount of protic acid was then added to neutralize the K_2CO_3 , before proceeding with the desired hallex reaction (entries 7–8). Unfortunately, none of these approaches resulted in conversion to product **371**.

3.4.2 Future Work

The experiment without K_2CO_3 demonstrates the feasibility of this radiofluorination strategy. However, significant research is still required to develop this approach into an efficient and workable method. Further examination of different eluent mixtures may reveal one that is compatible with the hallex reactivity. In addition, new solvents could be evaluated, especially those with higher boiling points that would allow for increased reaction temperatures to be readily accessed. Although some of the reactions were performed at temperatures above solvent boiling point (*sealed vessel reactions*), this presents some challenges. For example, with very small-scale or concentrated reactions, complete loss of liquid solvent can occur. Thus, identifying a high-boiling solvent that is compatible with hallex reactivity would be beneficial.

An alternative possibility is to explore is a two-step approach, in which the $ArCF_3$ undergoes complete defluorination, and the resulting $ArCBr_3$ product is isolated and purified (Figure 3.15). In the next step, $AgOTf$ mediated fluorination (*vide supra*) could be performed, with the advantage that $ArCBr_3$ would be more reactive than $ArCF_2Br$. Excess carrier fluoride could then be added to complete rapid reformation of $ArCF_3$.

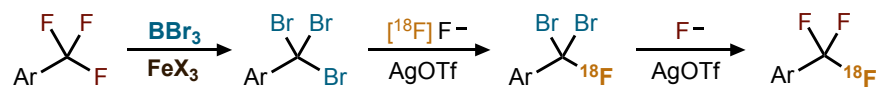


Figure 3.15. Two-step strategy for trifluoromethyl arene radiofluorination via formal isotopic exchange

More investigations into the direct isotopic exchange are also warranted (as per Scheme 3.25). High temperatures could be examined, as well as different iron(III) acids. To confirm that the reaction is indeed forming the desired $[^{18}F]ArCF_3$ product, radio-HPLC analysis would also be required. This would also act to purify the product, and allow for specific activity determination. Further, a range of other CF_3 substrates could be examined.

3.5 Conclusion

The full potential of PET imaging is arguably only beginning to be appreciated. The ability to non-invasively probe the distribution and activity of a compound *in vivo* is extremely powerful. Fluorine-18 has emerged as one of the most effective radioisotopes for PET imaging, as a result of its favorable imaging and half-life properties. However, there are a number of unique challenges in this field, including the development of robust and efficient radiolabeling methods.

This chapter summarized the major strategies used for ^{18}F introduction, with special focus on the synthesis of $[^{18}\text{F}]\text{ArCF}_3$ groups. These are attractive substrates, given the ubiquity of ArCF_3 groups in pharmaceutical chemistry. However, the chemistry in this area is limited, with considerable potential for the development of novel methods. A particular objective that has yet to be realized is the efficient synthesis of $[^{18}\text{F}]\text{ArCF}_3$ through isotopic exchange.

This chapter discussed the efforts made towards developing a new method for direct $[^{18}\text{F}]\text{ArCF}_3$ formation. This approach aimed to extend the BX_3/FeX_3 conditions discussed in the second chapter into a radiochemical method. A preliminary positive result was observed, demonstrating the feasibility of this method. However, more research is required to further explore these conditions and develop a complete radiolabeling methodology.

Chapter 4: Efforts towards the Synthesis of a Novel PSMA Radiotracer

4.1 Introduction to Non-Canonical Labeling

As mentioned in the previous chapter, a particular group of radiofluorination methods termed *non-canonical labeling* have recently emerged (Figure 4.1). These reactions utilize nucleophilic $[^{18}\text{F}]\text{F}^-$, which binds to a heteroatom moiety that has been incorporated into the precursor, namely a functionality based on a boron, silicon, or aluminum atom (*non-canonical moiety*).

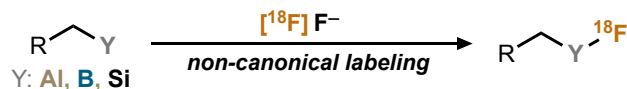


Figure 4.1. Non-canonical radiofluorination strategies

The advantage of this approach is that labeling conditions are exceedingly mild. Labeling often occurs readily at room temperature, without a need for the high temperatures (70 – 220 °C) that are required for $[^{18}\text{F}]\text{C}-\text{F}$ formation. Formation of a strong heteroatom-fluoride bond is the driving force for these methods. This reactivity is similar to C–F activation chemistry, except that the heteroatom mediates inclusion of fluorine to a molecule-of-interest, rather than its removal. However, some of the challenges include the synthetic attachment of the non-canonical moiety to a target precursor, as well as the stability of the heteroatom-fluoride bond *in vivo*.

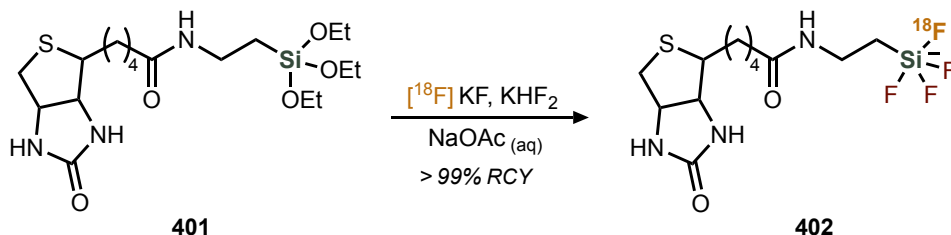
Despite early work from the 1960s,^{209, 210} these methods have only received major research interest in the last 15 years.^{211, 212} There are two general reaction categories utilizing boron and silicon moieties: fluorine displacement of a leaving group (*LG*) from the heteroatom, and isotopic exchange (*IE*) of a ^{19}F precursor with ^{18}F fluoride. Distinctly, aluminum-mediated methods are based on the formation of an $[^{18}\text{F}]\text{Al}-\text{F}$ species, and its chelation by a radiotracer target.

This chapter gives an overview of each of these strategies. In addition, their application in the design of clinical radiotracer candidates is discussed, with special focus on those targeting PSMA, an important biomarker for imaging prostate cancer. The synthesis of a novel PSMA radiotracer designed in the Schirmmacher Group is also described.

To design a clinical radiotracer, an existing bioactive scaffold is typically used, with distal inclusion of the non-canonical moiety. Although these moieties facilitate efficient radiolabeling, a number of other critical parameters can be altered by their introduction, such as lipophilicity (logP), binding affinity (K_D), and stability. The tracer must ultimately be evaluated in preclinical (e.g. mouse models) and clinical studies to evaluate biodistribution, and accumulation in the target tissue (e.g. tumor uptake). This is quantified by units of *injected-dose-per-gram* (%ID/g), calculated from the activity concentration in the particular tissue (Bq/g), as a fraction of the total injected activity (Bq).

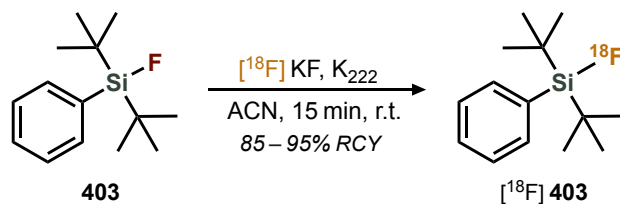
4.1.1 Overview of Silicon-Mediated Radiofluorination

In 1985, Rosenthal et al. found that chlorotrimethylsilane could undergo substitution to form [^{18}F] fluorotrimethylsilane, with high efficiency (80% RCY).²¹³ However, *in vivo* studies showed rapid bone-uptake of radioactivity, indicating fast hydrolysis of the ^{18}F from the silicon moiety. In 2005, Perrin and co-workers reported the labeling of a biotin-linked alkyl triethoxysilane **401**, using carrier-added fluoride (KHF_2) under aqueous conditions, forming the [^{18}F] tetrafluorosilicate product **402** in near quantitative radiochemical yield (Scheme 4.1).²¹⁴



Scheme 4.1. Radiofluorination of a biotin-linked trialkoxysilane

Shortly after, Schirmacher and coworkers showed that a dialkylfluorosilane compound **403**, termed a *silicon-fluoride acceptor* (SiFA) compound, could undergo isotopic exchange to generate the radiofluoride analogue [^{18}F] **403** (Scheme 4.2).²¹⁵ An alternative *leaving group* approach was reported by Choudhry and co-workers, who showed rapid substitution of *t*-butyldiphenylmethoxysilane to form [^{18}F] *t*-butyldiphenylfluorosilane, with aqueous [^{18}F] F^- at room temperature.²¹⁶ The two *tert*-butyl groups on the silicon were found impart the necessary stability towards hydrolysis, albeit at the cost of an appreciable increase in lipophilicity.²¹⁷



Scheme 4.2. Radiofluorination of a dialkylfluorosilane via isotopic exchange

Since these pioneering reports, there have been numerous innovations in SiFA radiolabeling methods, both within the *IE* strategy, and the *LG* strategy, in which a variety of different silicon leaving groups have been explored (Figure 4.2).²¹⁸ Both approaches are able to deliver labeled compounds in high RCY, with moderate-to-high molar activities in the range of 25–225 GBq/ μmol . One benefit of *IE* is that it typically proceeds at room temperature, whereas the *LG* methods require elevated temperatures, potentially limiting their application towards sensitive biomolecules. In addition, *IE* tends not to produce side products, and the ^{18}F product is chemically identical to the ^{19}F starting material. Thus, purification can be performed rapidly using a solid phase cartridge (SPE), whereas *LG*

methods typically require HPLC purification to separate the ^{18}F product from the chemically distinct starting material.

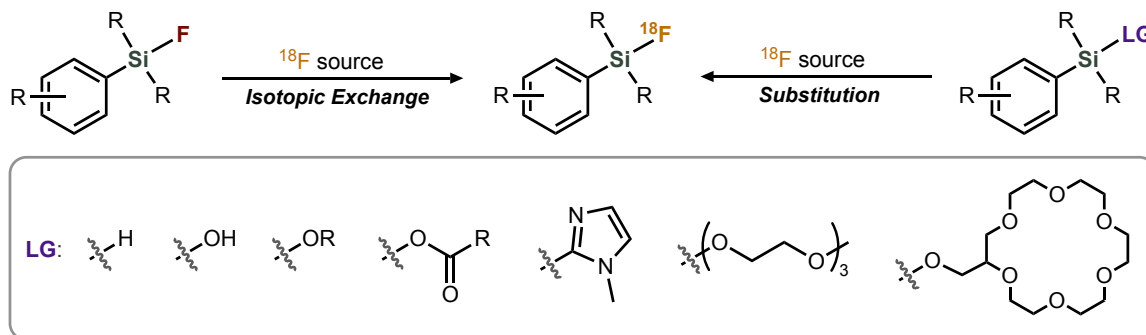
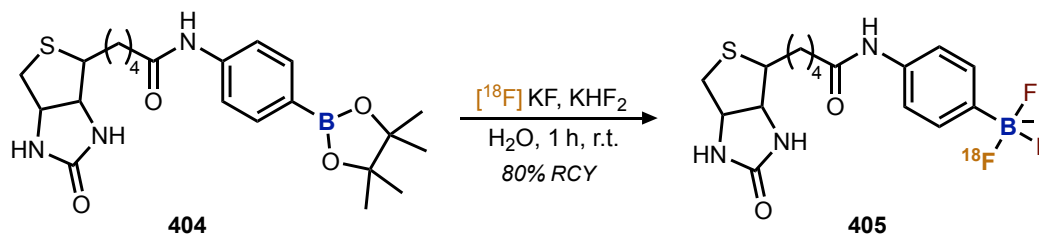


Figure 4.2. Overview of strategies for radiofluorination of SiFA compounds

The principal disadvantage of the SiFA moiety is its high lipophilicity. Introduction of SiFA to a small molecule has a major effect on its physicochemical properties, typically worsening biodistribution and overall pharmacological performance (leads to rapid hepatobiliary clearance). It is often necessary to counter the lipophilicity increase by introducing polar auxiliaries, such as PEG linkers, aspartic acid residues, carbohydrates, or quaternary ammonium salts. Much of the SiFA labeling work has focused on peptides, which are typically large enough to tolerate addition of the SiFA moiety and retain their biological activity. Since various peptide receptors are upregulated in many cancers, there has been a major focus on radiolabeling tumor-homing peptides for PET imaging.

4.1.2 Overview of Boron-Mediated Radiofluorination

As previously discussed, boron forms very strong bonds with fluorine. In the early 1960s, initial attempts were made to incorporate ^{18}F into small molecules via binding to a boron moiety.^{219, 220} In recent years, this strategy has been pioneered by the Perrin Group.²²¹ In an initial report in 2005, they documented the efficient radiolabeling of aryl boronic ester **404** using aqueous $[\text{}^{18}\text{F}]\text{F}^-$, along with carrier KHF_2 , resulting in an easily isolable $[\text{}^{18}\text{F}]$ aryltrifluoroborate precipitate **405** (Scheme 4.3).²¹⁴



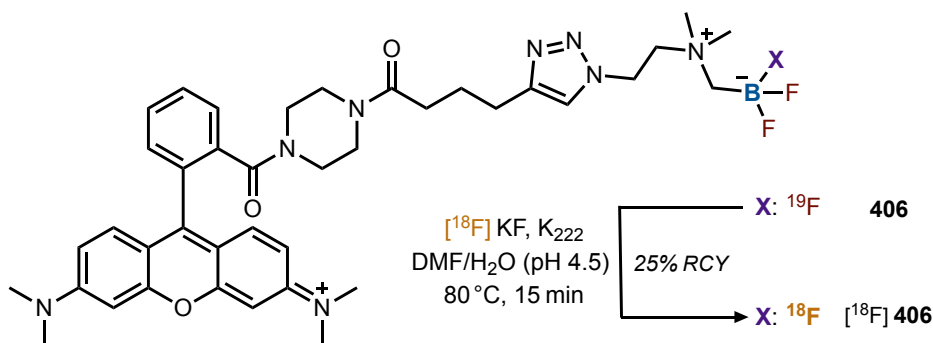
Scheme 4.3. Radiofluorination of a biotin-linked phenylboronate

For *in vivo* applications, Perrin and coworkers studied the hydrolytic stability of ArBF_3 substrates at physiological pH and found that they were reasonably stable after 60 minutes, without any significant

release of ^{18}F anions.²²² This work countered the common belief that radiofluorination cannot occur in aqueous media, due to the attenuated reactivity of highly solvated ^{18}F anions.

As with SiFA compounds, isotopic exchange has emerged as a viable approach for [^{18}F] trifluoroborates synthesis. The mild reaction conditions (pH ~2, room temperature), and minimal side-product formation, lead to facile purification, without the need for HPLC.^{222, 223} The weakness of this methodology lies in the problematic, pH-independent hydrolysis of the ArBF_3 group to the corresponding boronic acid, and the concurrent release of $^{18}\text{F}^-$ anions.²²⁴ Perrin and coworkers found that there is a simple linear correlation between the rate of ArBF_3 hydrolysis and the $\text{p}K_a$ of the corresponding carboxylic acid, allowing for predictable design of trifluoroborate precursors.²²⁵

A major improvement to trifluoroborate stability was achieved with the design of a new moiety containing a quaternary ammonium linker, referred to as an *alkylammoniomethyltrifluoroborate* (AMBF_3).²²⁶ This was demonstrated using non-dried ^{18}F solution to synthesize [^{18}F] **406**, a rhodamine-linked AMBF_3 , achieving an A_m of 150 $\text{GBq}/\mu\text{mol}$ (Scheme 4.4). Compound [^{18}F] **406** showed minimal hydrolysis in 37 °C human serum after 150 minutes, as well as excellent *in vivo* stability in mice models, with minimal bone uptake.

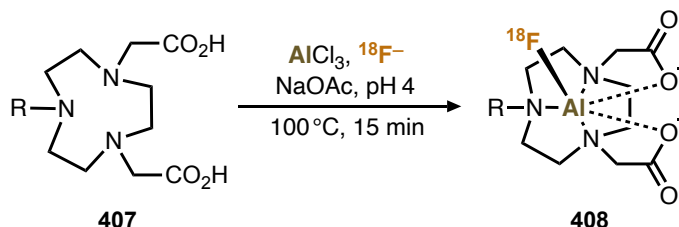


Scheme 4.4. Radiofluorination of an AMBF_3 -rhodamine conjugate via isotopic exchange

4.1.3 Overview of Aluminum-Mediated Radiofluorination

Aluminum mediated radiofluorination methods are based on chelation, similar to established methods with gallium-68, another well-studied positron emitting radionuclide.²¹² The general mechanism involves the *in situ* formation of a [^{18}F] AlF^{2+} cation. This requires buffering to pH 4, as too acidic conditions result in [^{18}F] HF formation, and too basic in the formation of insoluble aluminum hydroxides.²²⁷⁻²²⁹ The [^{18}F] AlF^{2+} species then binds to the precursor via a chelating moiety. An example is shown in Scheme 4.5, in which complex **408** is formed upon coordination of [^{18}F] AlF^{2+} with cyclic chelator **407**.²³⁰ Advantages of this approach include compatibility in aqueous medium, as well as a straightforward one-step labeling procedure. In general, the highest radiochemical yields are

obtained by keeping the final reaction volume small and buffer solutions concentrated. A slight excess of the chelating substrate over the aluminum species is also beneficial, as is the addition of an organic co-solvent, such as ethanol or acetonitrile.²³¹



Scheme 4.5. General scheme for aluminum-based radiofluorination

The negatively charged oxygens in the chelating moiety (carboxylates) are crucial to ensure a stable aluminum(III) complex is formed. The ionic character of these interactions is essential and affinity is linearly dependent on the basicity of the coordinating moieties.^{227, 232} The Al–F bond is robust, with a strength of ~160 kCal/mol, leading to high stability *in vivo*, and good biological compatibility.²³³⁻²³⁶

A summary of chelating moieties is shown in Figure 4.3. *DTPA* derivatives have long been known to form stable complexes with group 13 atoms, serving as inspiration for the first chelation studies with [¹⁸F] AlF species.²³⁷ However, it was found that a peptide-*DTPA* complex with [¹⁸F] AlF lacked the necessary stability in water and human serum.²³⁸ Attempts with cyclic chelators such as *DOTA* and hexadentate *NOTA* derivatives (*written* *NOTA*₍₆₎), such as *SCN-Bz-NOTA*, lead to low RCY.

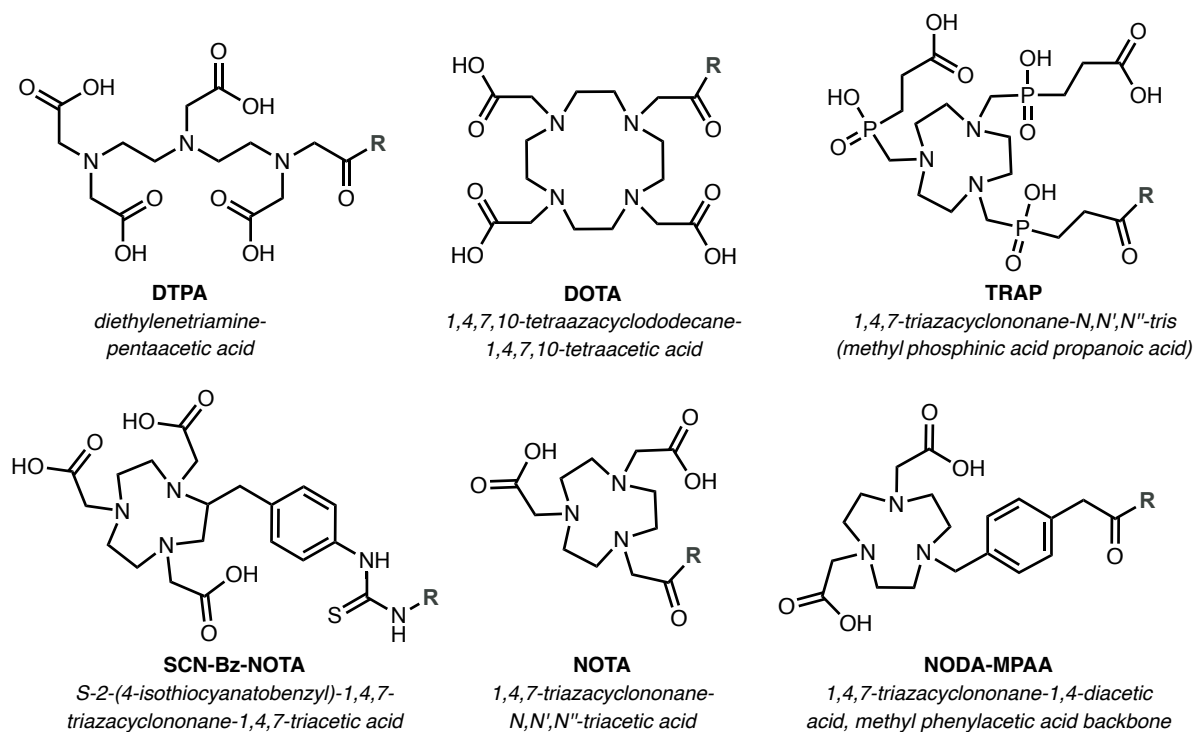


Figure 4.3. Examples of common moieties used for radiometal chelation

Labeling efficiency could be significantly improved using chelators bearing a 3*N*, 2*O* configuration, such as in *NODA-MPAA*, or pentadentate *NOTA* derivatives (*NOTA*₍₅₎). In this configuration, there remains a free coordination site for fluoride binding, leading to the formation of a stable octahedral complex.²³⁹ In contrast, the extra coordination site in hexadentate derivatives disrupts the aluminum-fluoride bonding, and favors chelate formation of with aluminum alone (as an Al³⁺ complex).

4.2 Clinical Applications of Non-Canonical Labeling

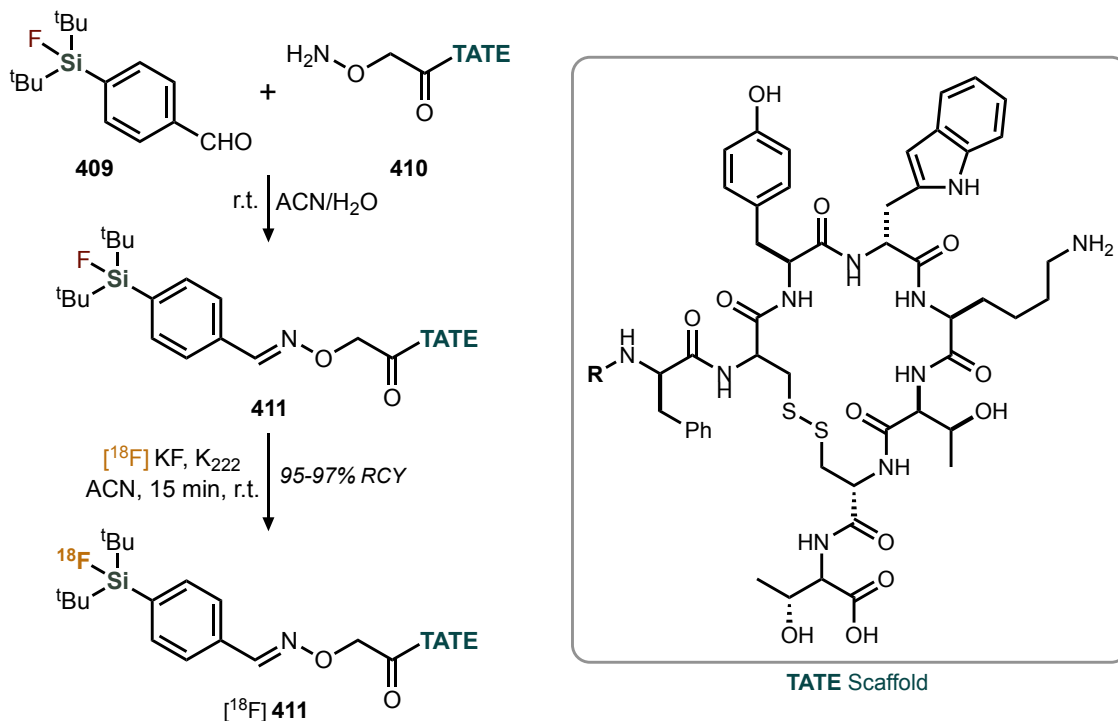
4.2.1 *In Vivo* SSTR2 Imaging

A prominent target in clinical imaging is the somatostatin type-2 receptor (*SSTR2*). It is overexpressed in many tumors, and in particular, is targeted to facilitate PET imaging of neuroendocrine tumors (NET). As such, various synthetic analogues of the native ligand somatostatin have been developed. The most common for radiotracer development are try³-octreotide (*TOC*), and tyr³-octreotate (*TATE*), which is used in the current clinical standard ⁶⁸Ga-DOTA-TATE (NetSpot[®]). This compound uses the radionuclide ⁶⁸Ga, which has some disadvantages compared to ¹⁸F.

Fluorine-18 has a lower positron energy (0.64 vs 1.90 MeV), leading to higher resolution images. It also has a longer half-life (110 vs 68 minutes), providing more time for the preparation, transport, and injection of the radiotracer. In addition, large multi-dose batches of ¹⁸F can be easily produced in a cyclotron facility, whereas ⁶⁸Ga is produced in low dosages from a generator system.

Schirmacher and coworkers initially demonstrated conjugation of a SiFA moiety (**409**) to an amino-oxy functionalized TATE derivative (**411**), followed by isotopic exchange to form SiFA-TATE [¹⁸F] **411** in 95% RCY (Scheme 4.6).²¹⁵ However, the increase in lipophilicity imparted by the SiFA group lead to substantial hepatobiliary excretion and non-specific binding in a rat tumor model, making [¹⁸F] **411** unsuitable for PET imaging.

The increase in lipophilicity could be counteracted by introducing polar auxiliaries, including a dimethylammonium moiety linked to the SiFA arene, termed a SiFAlin group. These additions resulted in the development of the current clinical lead [¹⁸F] SiFAlin-Glc-Asp₂-PEG₁-TATE (**412**), which can be producing using isotopic exchange in 53 % RCY and 44–63 GBq/μmol A_m (Figure 4.4).²⁴⁰ Preclinical studies in tumor-bearing mice showed favourable performance of **412**, with improved tumor accumulation at 60 minutes post-injection over ⁶⁸Ga-DOTATATE (18.5 vs 14.1 %ID/g).²⁴¹ Bone uptake was minimal, and high tumor-to-blood and tumor-to-muscles ratios were observed (> 55 and > 210 respectively).



Scheme 4.6. Synthesis and radiofluorination of a SiFA octreotate conjugate

The first clinical evaluation of **412** (renamed [^{18}F]SiTATE) was recently published, wherein it was evaluated for the imaging of NET, relative to [^{68}Ga]DOTA-TOC.²⁴²⁻²⁴⁴ Although uptake was slightly higher in the liver, spleen, and adrenal glands, and much higher in the kidneys, **412** also showed very good tumor uptake, greater than [^{68}Ga]DOTA-TOC in almost all tumor lesions. Overall, image quality was comparable between the two tracers, indicating that **412** represents a viable alternative for NET imaging.

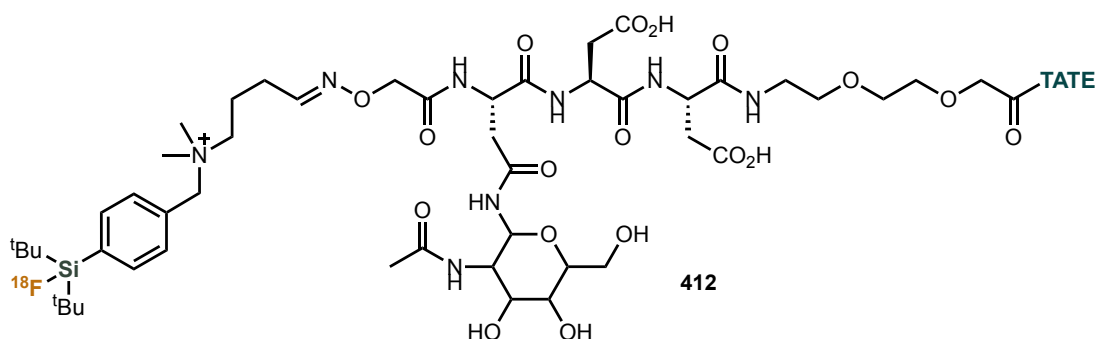


Figure 4.4. Structure of labeled SiTATE

The AMBF₃ moiety developed by Perrin and coworkers was also combined with tyr³-octreotate to develop a candidate for NET imaging. This compound, [^{18}F] AMBF₃-TATE (**413**), was synthesized via isotopic exchange under aqueous conditions in 20–25% RCY, with a A_m of 111 GBq/ μmol (Figure 4.5).²⁴⁵ Preclinical studies confirmed that **413** binds to *SSTR* receptors, and that clearance from non-

targeted tissue is rapid. An outstanding safety profile was observed, with no adverse effects observed upon treatment with a 1000-fold clinical dose.²⁴⁶ A clinical study on the effectiveness of **413** to image NET is ongoing.

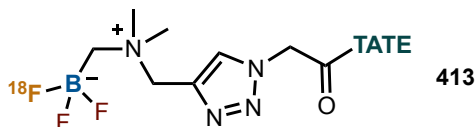


Figure 4.5. Structure of fluorine-18 AMBF₃-TATE

4.2.2 In Vivo GRPr Imaging

The imaging of Gastrin-Releasing Peptide receptors (*GRPr*) is important in the diagnosis of several cancers, particularly prostate cancer, utilizing radiolabeled analogues of bombesin-type peptides. The latest SiFA conjugates with bombesin have also included polar auxiliaries to counterbalance the lipophilicity, such as the cysteic acid containing derivative (**414**) reported by the Ametamay Group (Figure 4.6).²⁴⁷ However, despite improvements from the first generation of SiFA derivatives (without polar auxiliaries),²⁴⁸ **414** was found to have poor tumor uptake and significant hepatobiliary clearance.

Wängler and coworkers evaluated SiFA bombesin analogues with added PEG chains, along with carbohydrates and other acidic residues.²⁴⁹ However, these compounds had high liver accumulation, and were unsuccessful in imaging the target tumors. These issues might be alleviated by introducing the SiFAlin moiety, but no such bombesin analogue has been reported to date.

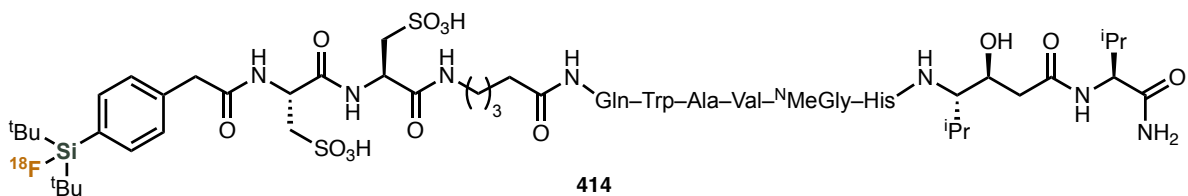
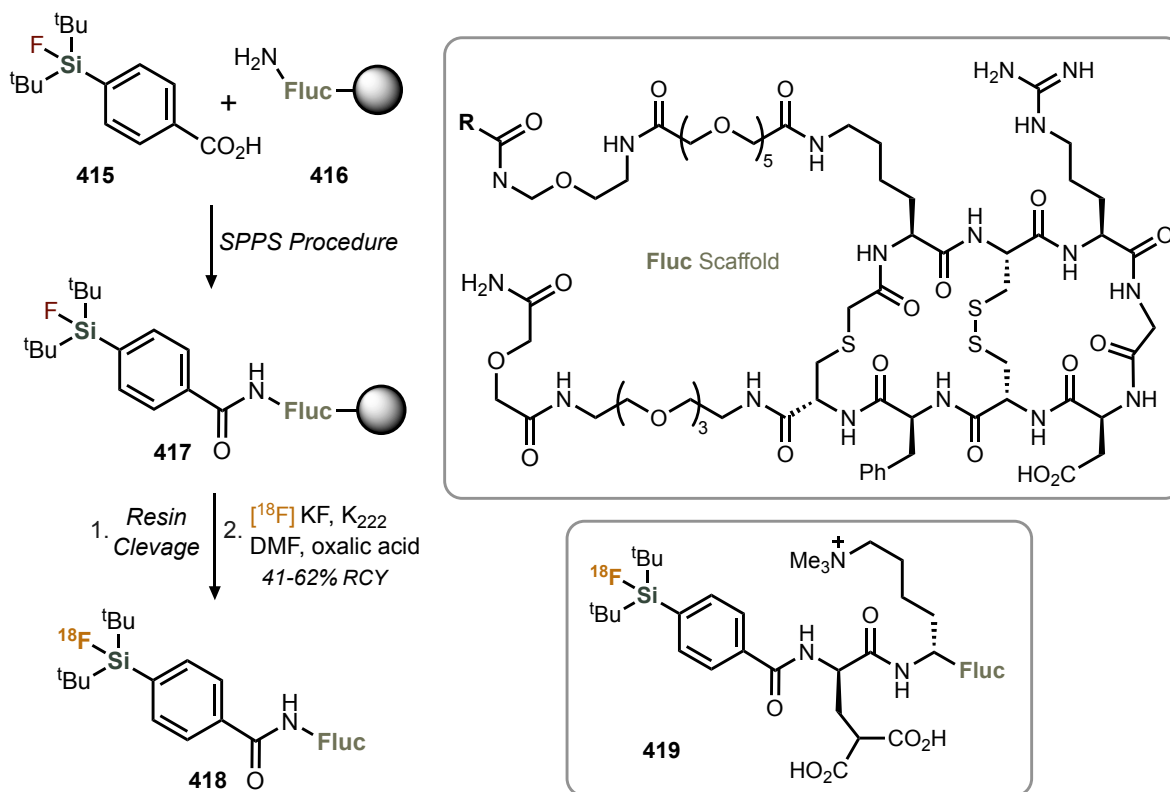


Figure 4.6. Structure of a SiFA bombesin derivative

4.2.3 In Vivo Integrin Imaging

Angiogenesis is a fundamental process in the growth and metastasis of many cancer types. Integrin glycoproteins, in particular $\alpha_v\beta_3$ and $\alpha_v\beta_5$ are highly upregulated in vascular endothelial cells during this process, and as such, are important targets in oncological imaging.²⁵⁰ These are targeted by various probes containing the *arginine-glycine-aspartic acid* (*RGD*) amino acid motif, a prominent example of which is the bicyclic *RGD* compound Fluciclatide.²⁵¹ Wängler and coworkers demonstrated that the SiFA group could be readily incorporated into the Fluciclatide scaffold. SiFA carboxylic acid **415** was readily incorporated at the end of a solid-phase peptide synthetic sequence, under standard Fmoc

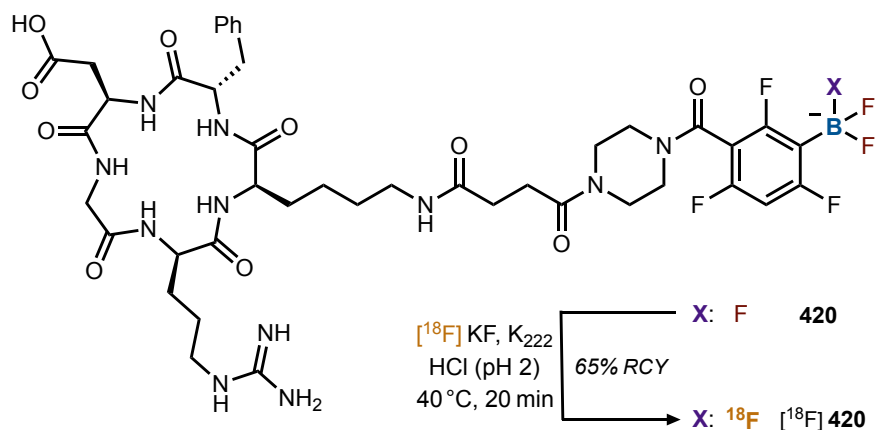
conditions (Scheme 4.7).²⁴⁹ Resin cleavage, and subsequent radiofluorination produced tracer **418**, with molar activities of up to 60 GBq/ μ mol. As with other SiFA tracers, introduction of polar auxiliaries was vital to ensure favorable pharmacokinetics, exemplified by compound **419**. This tracer showed encouraging tumor uptake at U87MG tumor-bearing mice (5.3 %ID/g), as well as favorable biodistribution, and rapid blood clearance.



Scheme 4.7. Synthesis and radiofluorination of SiFA fluciclatide conjugates

Perrin and coworkers utilized the boron-based strategy to label a dimeric cyclic *RGD* peptide, labeling an arylborimidine precursor with carrier-added $[^{18}\text{F}]\text{F}^-$ to form an $[^{18}\text{F}]\text{ArBF}_3$ tracer.²⁵² Alternatively, an alkyne-linked arylborimidine can first undergo radiofluorination to form $[^{18}\text{F}]\text{ArBF}_3$, followed by CuAAC conjugation with an azide-linked *RGD* peptide to form the tracer.²⁵³

Isotopic exchange of trifluoroborates has also been used to radiolabel *RGD* peptides. The Perrin group used this approach to label a dimeric cyclic *RGD* under acidic conditions, achieving the ArBF_3 product $[^{18}\text{F}]\text{420}$ in 65% RCY, with a very high A_m of 518 GBq/ μ mol (Scheme 4.8).²⁵⁴ This radiotracer was administered to U87MG tumor bearing mice, but was found to have somewhat low tumor uptake of 2.0 %ID/g at 30 minutes post injection, and a moderate tumor-to-muscle ratio of 3.9.



Scheme 4.8. Radiofluorination of a cyclic RGD trifluoroborate conjugate via isotopic exchange

The [^{18}F] AIF strategy was also applied to the labeling of RGD peptides. Cheng and coworkers reported the synthesis of labeled cyclic RGD dimer, combined with a NOTA moiety (AIF-NOTA-RGD₂).²⁵⁵ This radiochemistry showed improved efficiency relative to previous methods for RGD dimer synthesis, and promising in vivo stability. Further modifications were made to this scaffold, such as addition of PEG-linkers between the RGD and NOTA moieties, resulting in the development of Alfatide I and Alfatide II. These have been investigated in a number of clinical trials, showing their potential to become useful tools for the early detection and monitoring of various cancers.

4.2.4 In Vivo PSMA Imaging

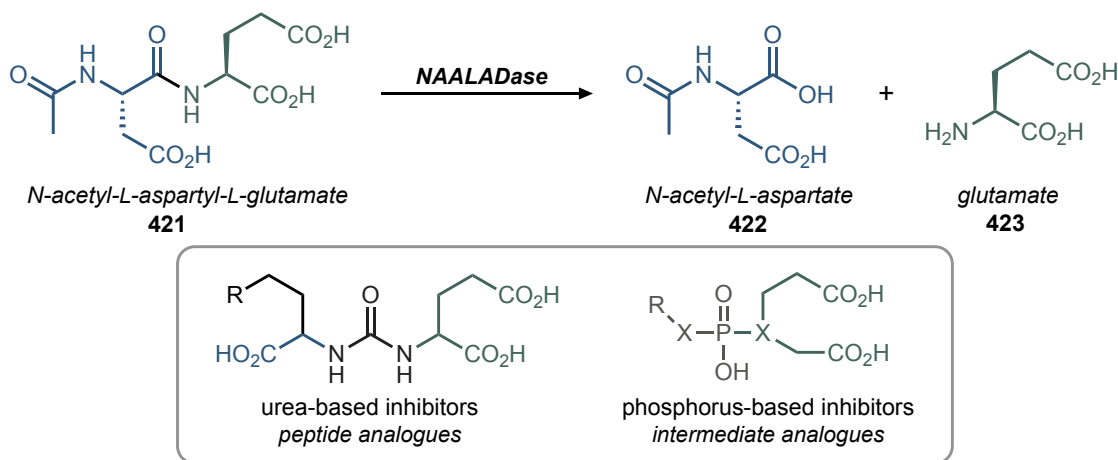
Prostate cancer is one of the most prevalent cancers in men, and leads to circa 3 million deaths each year.²⁵⁶ Although the discovery of *prostate-specific-antigen* (PSA) has improved early diagnosis and treatment, it fails to account for the heterogenous nature of prostate cancer, which can range from localized and slow growing, to highly aggressive and metastatic.^{257, 258} In addition, established imaging strategies are limited in their ability to evaluate metastatic progression, and thus determine which of numerous treatment options are warranted.²⁵⁹ These problems demonstrate the need to develop new diagnostic tools for monitoring prostate cancer.

In 1987, a new antigenic marker was discovered, a transmembrane protease termed *prostate-specific membrane antigen* (PSMA), also known as *glutamate carboxypeptidase type II* (GCPII).²⁶⁰ Almost all prostate cancers show significant PSMA overexpression, up to 1000-fold over healthy cells, with levels directly correlating with the progression of the disease.^{261, 262} These are ideal properties for a biomarker, and as such, there has been significant focus on the development of PSMA-targeting radiotracers, for either imaging or therapeutic applications.^{263, 264} In addition, the PSMA complex undergoes cellular internalization upon binding of the ligand, contributing to the high tumor retention of targeting radiotracers.²⁶⁵

Elevated PSMA expression has also been observed in other solid tumors, offering further clinical potential.²⁶⁶ However, PSMA is found in some healthy tissues, including cells of the nervous system, the small bowel, as well as the kidneys, and the salivary glands, the latter two of which often account for the majority of off-target uptake with PSMA tracers.^{264, 267}

Structurally, PSMA consists of an intracellular, transmembrane, and extracellular domain. The extracellular domain contains the active site, which is comprised of two pockets.²⁶⁸ The S1' pocket is involved in the binding of a glutamate residue in native ligands, whereas the other pocket S1 is more flexible and is less selective in its binding mode. This active site also contains two zinc ions, which bind to the ligand and aid in cleavage of the peptide bond.

PSMA is also known as *N-acetyl-alpha-linked acidic dipeptidase* (NAALADase), as it acts to cleave NAAG (**421**) to liberate acetylaspartate (**422**) and glutamate (**423**) in the central nervous system (Scheme 4.9). This is an important process in neurological signaling, as glutamate is the primary excitatory neurotransmitter. However, excessive glutamate can lead to neuronal damage and is associated with various neurodegenerative diseases.²⁶⁹ The first inhibitors were developed in this context, with the potential to provide a neuroprotective effect.²⁷⁰ A series of analogues were developed based either on NAAG (urea compounds), or the tetrahedral intermediate that is formed during NAAG hydrolysis in the active site (phosphates, phosphonates, phosphoramidates), as shown in Scheme 4.9.



Scheme 4.9. Hydrolysis of the NAAG peptide and structures of related synthetic analogues

Modern PSMA-targeting agents continue to utilize one of these two binding motifs, and have been used to form various bioconjugates, including antibodies, antibody-drug conjugates, toxin conjugates, and photodynamic therapy conjugates.²⁶³ In the radiotracer context, there are numerous examples under clinical investigation, utilizing a range of different isotopes, chiefly gallium-68 (e.g. ⁶⁸Ga-PSMA-11) and fluorine-18 (see leading examples in Figure 4.7).²⁷¹ These established ¹⁸F-tracers utilize tradition methods for radiofluorination, and as such, there has been recent focus on applying non-canonical methods to PSMA tracer design, given the advantages they offer (*vide supra*).

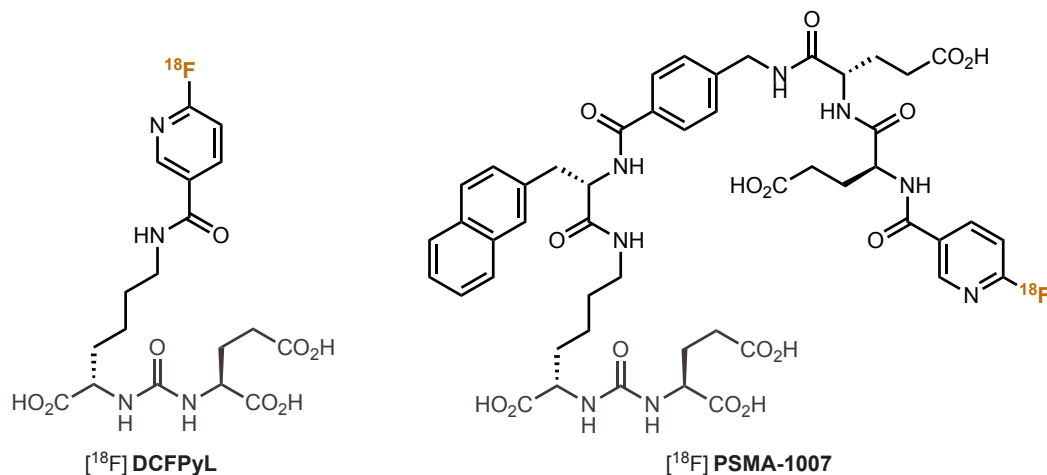


Figure 4.7. Structure of leading PSMA targeting fluorine-18 radiotracers

The aluminum strategy was first non-canonical approach to be applied to PSMA targeting, given the similarity to already existing tracers for radiometal chelation. Malik et al. demonstrated proof-of-principle in 2012, designing a NOTA derivative based on the *lysine-urea-glutamate* (KuE) scaffold (see Figure 4.8).²⁷² The tracer, $[^{18}\text{F}]$ AIF-NOTA₍₅₎-DUPA-Pep, was synthesized in a high RCY of 83%, although no follow-up biological studies were performed.

A subsequent tracer incorporated the acyclic chelator *HBED*, resulting in $[^{18}\text{F}]$ AIF-PSMA-11 (Figure 4.8). This was inspired by previous *HBED* tracer ^{68}Ga -PSMA-11, which exhibited strong chelation with Ga^{3+} ions. Incorporation of $[^{18}\text{F}]$ AIF²⁺ was fairly efficient, with optimal yields occurring at lower temperatures (49% RCY at 35°C). Production-scale optimization on automated synthesis units affords 18 – 21% n.d.c. RCY, and high molar activities of 120 – 544 GBq/μmol. *In vitro* studies were performed using a human prostate carcinoma cell line LNCaP, finding that binding affinity K_D was comparable to the ^{68}Ga -analogue (10.3 vs 12.6 nM). Tumor uptake was also comparable (10.8 % ID/g) in a tumor-bearing mice study, as were the typical high values for kidney, bladder, and salivary gland uptake. Slight bone uptake was observed, indicating formation of free fluoride and hydrolysis of the $[^{18}\text{F}]$ AIF species. However, this did not have any impact on tumor uptake or visualization.

In a recent example, a new radiotracer $[^{18}\text{F}]$ AIF-PSMA-BCH was reported, along with preclinical data, as well as a pilot clinical study (11 patients).²⁷³ The manual synthesis was moderately efficient, with an RCY of 32%, and molar activities of 13 – 19 GBq/μmol. Both *in vitro* and *in vivo* studies suggested good tracer stability. Good tumor uptake of 7.9 %ID/g was observed, along with typical off-target accumulation (kidneys, salivary glands). The detectability of tumor lesions in the clinical study was also found to be good, indicating promise for further investigation.

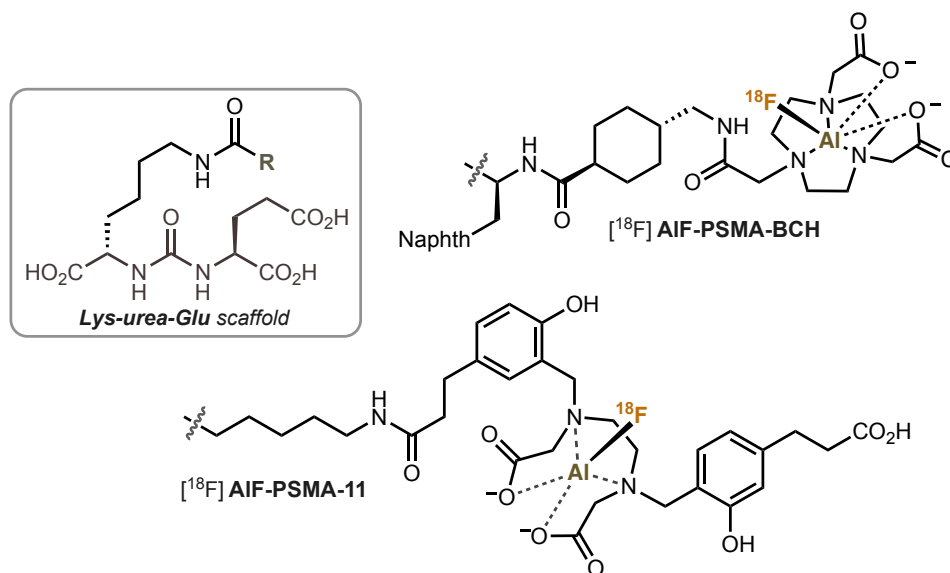


Figure 4.8. Structure of PSMA targeting chelator-AlF radiotracers

In 2019, the Perrin Group designed a series of eight trifluoroborate PSMA-ligands, also based on the *KuE* scaffold (select examples in Figure 4.9), and screened their labeling performance, as well as a number of *in vitro* and *in vivo* parameters.²⁷⁴ Binding affinities (K_D) were determined using LNCaP cells, and biodistributions values were obtained using LNCaP-xenograft bearing mice. The structures contained either the AMBF₃ moiety (e.g. **424**) or a pyridinium-BF₃ scaffold (e.g. **426**). The smaller unelaborated structures, such as **424** and **426**, displayed low relative affinities ($K_D = 12 - 28$ nM), whereas introduction of a naphthylalanine-tranexamic acid motif (**425**) led to improved affinities ($K_D < 2$ nM). The best affinity of 0.22 nM was obtained in an extended analogue of **425**, containing two glutamate-triazole-AMBF₃ motifs (**427**, not shown).

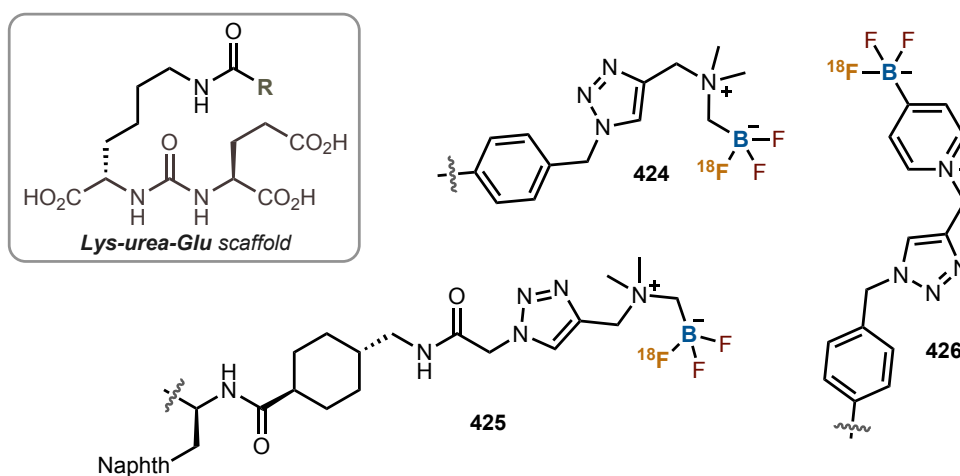


Figure 4.9. Structure of PSMA targeting BF₃ radiotracers

All eight analogues were obtained after HPLC purification in moderate yield (4 – 16 % RCY n.d.c.) and high A_m (56 – 278 GBq/ μ mol). They all showed normal high renal uptake, and good tumor uptake in the biodistribution studies, with the highest obtained for **427** at 16.7 %ID/g. This compound also displayed low hepatobiliary clearance, and overall low background activity, identifying it as the lead compound for future research. High hepatobiliary clearance is problematic as it often leads to poor tumor uptake, and hinders detection of small lesions in the pelvis and liver.

In the following year, Perrin and coworkers reported another *KuE* analogue, containing a DOTA moiety (DOTA-AMBF₃-PSMA) that can be labeled in two distinct ways (Figure 4.10).²⁷⁵ Incorporation of ¹⁸F can occur via the AMBF₃ moiety, whereas various radiometals can be incorporated by DOTA chelation. As such, this tracer can form a *theranostic pair*,²⁷⁶ two chemically identical compounds, but containing differing radionuclides (isotopologues), illustrated by the example in Figure 4.11.

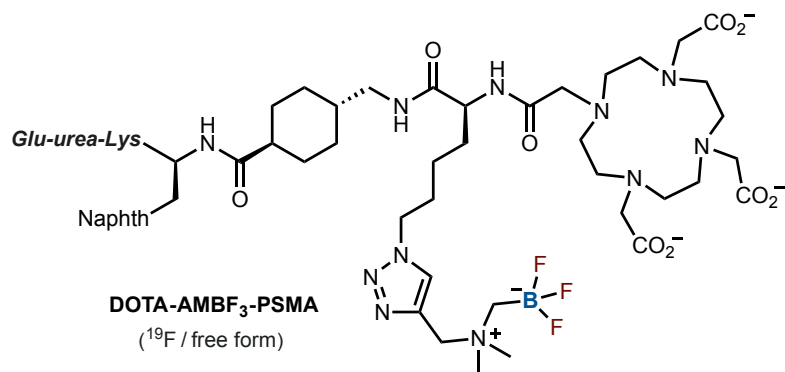


Figure 4.10. Structure of a PSMA targeting DOTA AMBF₃ radiohybrid

In this example, compound **A** could be formed by chelation of non-radioactive lutecium (^{nat}Lu), and isotopic exchange to incorporate ¹⁸F, forming a compound suitable for PET imaging. Conversely, compound **B** could be labeled with ¹⁷⁷Lu, thereby acting as a therapeutic agent via the emission of α -particles that kill the surrounding cells. Since **A/B** would exhibit identical *in vivo* behavior, imaging with species **A** also provides the exact biodistribution profile of **B**. This strategy allows for therapeutic targeting and dosimetry to be tuned to a specific patient, offering exciting precision in the field of personalized medicine.

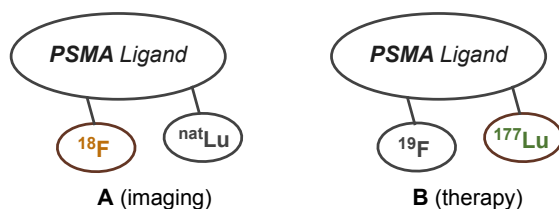


Figure 4.11. Conceptual example of the radiohybrid strategy

Alternatively, two β^+ emitters could be used to form an identical *imaging pair*, for instance $^{nat}\text{Ga}/^{18}\text{F}$ and $^{68}\text{Ga}/^{19}\text{F}$. This offers extra synthetic flexibility, allowing either isotope to be used for labeling, easing the challenge that the target isotope is not always available in every radiopharmaceutical facility at all times. More generally, these compounds that are able incorporate two different radionuclides can be classified as *radiohybrid* ligands.

The DOTA-AMBF₃-PSMA compound was first evaluated for binding affinity, showing no significant difference from previous analogues at 9.3 nM.²⁷⁵ Various radionuclide combinations were synthesized and evaluated in LNCaP-xenograft bearing mice, summarized in Table 4.1. Yields and molar activities varied, but were unoptimized, and proved sufficient for this preliminary study. Tumor uptake was good in all cases, supporting the feasibility of theranostic strategies for PSMA imaging. In addition, the metal-free complex (^{18}F /free) showed low liver uptake, indicating that, regardless of radiohybrid applications, either bound or unbound DOTA appears to act as an effective polar auxiliary.

Table 4.1. Labeling and *in vivo* performance for different forms of DOTA-AMBF₃-PSMA

nuclide pair	RYC (%)	molar activity (GBq/ μmol)	tumor uptake (%ID/g)
^{18}F /free	1.0	137	10.6
$^{18}\text{F}/^{nat}\text{Cu}$	2.7	178	14.3
$^{nat}\text{F}/^{64}\text{Cu}$	10	3.3	11.6
$^{nat}\text{F}/^{177}\text{Lu}$	41	348	11.2

A similar radiohybrid strategy was employed by the Wester Group, synthesizing a series of five tracers containing with both a SiFA group and a chelator moiety (rhPSMA-5 to -10).²⁷⁷ The PSMA-binding motif was comprised of either the *KuE* motif (*vide supra*) or the analogous *EuE* scaffold (*as in* rhPSMA-7), and either a DOTA or TRAP chelator (Figure 4.12). The *EuE* compounds showed improved affinities (IC_{50}) over those containing the *KuE* motif, with values of 2.5 – 4.5 nM. Notably, there was no appreciable difference in binding affinity between the gallium-chelate and free form of each inhibitor. Similarly, additional *in vitro* studies showed comparable levels of receptor internalization between each form, with slightly higher values for the metal-free species.

Each of the *EuE* compounds was labeled with gallium-68 (ca. 60% RCY, 59 GBq/ μmol) and evaluated in LNCaP tumor-bearing mice, showing good tumor uptake, comparable with the clinical standards (7 – 12 % ID/g). Undesired liver uptake and ensuing hepatobiliary clearance were also minimal, correlating with other examples in which cyclic chelator moieties act as effective polar auxiliaries. Indeed, logP values were between –2.0 to –3.5, corresponding to a marked increase in hydrophilicity relative to typical SiFA compounds.

The rhPSMA-7 compound was identified as a lead, and the free [^{18}F] rhPSMA-7 was synthesized for *in vivo* comparison with the [^{68}Ga] ^{19}F -rhPSMA-7 analogue. Although biodistribution was similar

between the two species, the free [^{18}F] rhPSMA-7 species showed somewhat higher renal uptake and lower tumor uptake (5.5 vs 8.6 %ID/g), despite being slightly favored in the *in vitro* studies (with a higher degree of internalization). Although somewhat ambiguous, these results seem to indicate the benefit of gallium inclusion. Interestingly, the gallium complexes were also less lipophilic than the free complexes.

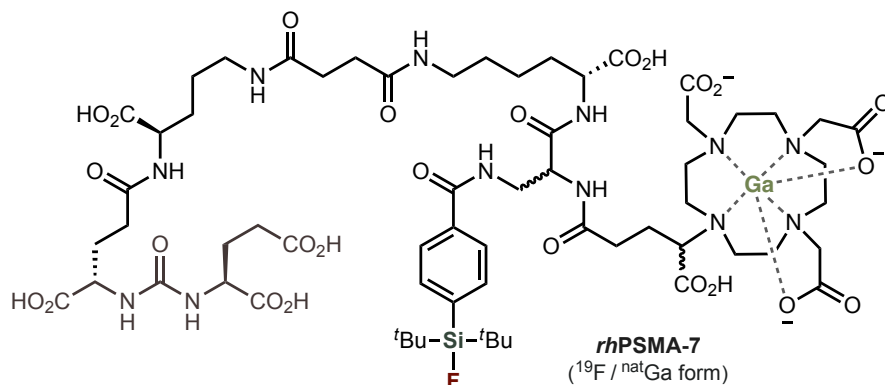


Figure 4.12. Structure of a PSMA targeting SiFA DOTA radiohybrid

Subsequently, clinical studies were performed with [^{18}F] $^{\text{nat}}\text{Ga}$ -rhPSMA-7, which was optimized for production on an automated synthesis unit, with an average of 49% RCY and 291 GBq/ μmol A_m .²⁷⁸ Biodistribution in healthy subjects was similar to preclinical observations, and allowed for determination of radiation dosimetry. Studies on prostate cancer patients showed that [^{18}F] Ga-rhPSMA-7 had a similar ability to detect metastatic lesions as an established tracer [^{68}Ga] PSMA-11.

In these initial studies, [^{18}F] Ga-rhPSMA-7 was present as a mixture of four stereoisomers (Figure 4.12). The individual isomers were synthesized to compare their *in vivo* performance, identifying modest advantages for the isomer referred to as rhPSMA-7.3 (**R** at the SiFA arm, **S** at the DOTA arm), showing high tumor uptake with minimal increase in kidney, liver, and blood uptake.²⁷⁹ As such, ^{18}F -rhPSMA-7.3 is currently being evaluated in phase III clinical trials, with initial results suggesting it is superior for determining metastasis in newly diagnosed prostate cancer.²⁸⁰

Schirmacher, Wuest, and colleagues also designed a series of PSMA-targeting tracers that incorporated the SiFA group to the *lysine-urea-glutamate* (KuE) scaffold (select examples in Figure 4.13).²⁸¹ The first analogue (**428**) integrated a SiFA moiety via a simple oxime ether linkage, and was found have moderate lipophilicity ($\text{LogD}_{7.4} = -1.0$) and receptor affinity ($\text{IC}_{50} = 106 \text{ nM}$). Introduction of a PEG₄ linker (**427**) lead to a slight improvement of LogD, but decreased binding potency 5-fold. As a result of their hydrophobic nature, these compounds showed very high liver/intestine uptake in LNCaP-bearing mice, resulting in favored hepatobiliary clearance and low tumor uptake. To combat these issues, the authors introduced a series of polar auxiliaries, with the aim of reducing the hydrophobicity imparted by the SiFA motif.

Introduction of sulfonamide linkers proved ineffective at improving LogD values. On the other hand, introduction of one-to-three aspartic acids residues, along with a PEG₃ chain (e.g. **429**), had a major impact on hydrophilicity, reducing the LogD_{7.4} values to circa -3.1. However, only the analogues containing two-or-three aspartic acid residues were found to have improved tumor uptake, and showed a shift away from hepatobiliary clearance to a primarily renal pathway. The Asp₂ compound **428** was recognized as the lead, showing a tumor uptake of 5.6 % ID/g.

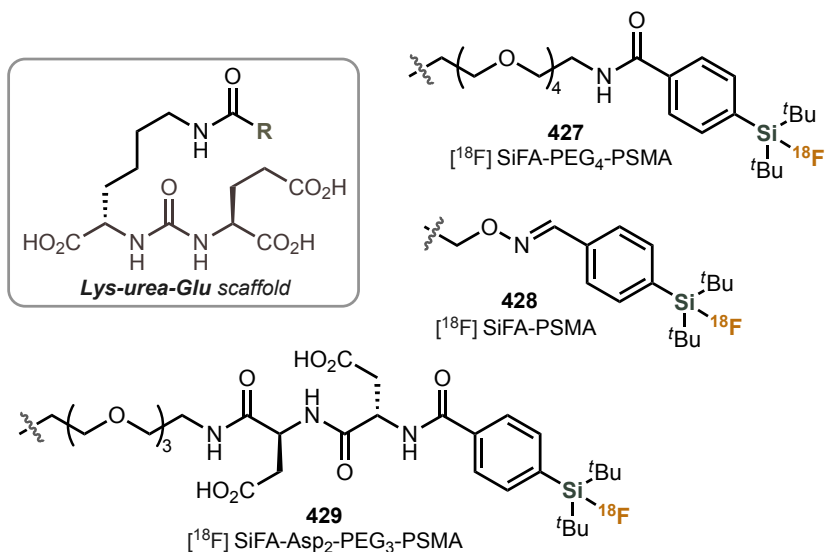


Figure 4.13. PSMA targeting SiFA radiotracers

A new labeling protocol was also reported, allowing for the manual synthesis of **429** in > 70 % RCY, with an A_m of 86 GBq/ μmol . The standard procedure (q.v. section 3.1.4) was adapted such that only $\sim 1/10$ of the eluent solution is used to elute the ^{18}F (termed the *four-drop-method*). Elution efficiency remained high (>80%), relying on the fact that the ^{18}F is largely trapped at the top of the QMA during passage of the ^{18}F -cyclotron solution, and can thus be recovered efficiently by reversing the direction of flow before passage of the eluent. The leading advantage of this method is that it keeps the amount of base eluted to a minimum and increases consistency, thereby assuaging the need to perform a pH adjustment after the azeotropic drying is complete. This subsequently allows for low precursor loading (10 nmol), facilitating the formation of high molar activity products.

4.3 Synthesis of a Novel PSMA-Targeting Radiotracer

4.3.1 Radiotracer Design

Although the initial evaluation of SiFA-Asp₂-PEG₃-PSMA (**429**) was fairly positive, there remained opportunities for improvement. An intriguing possibility was the inclusion of a polar dimethylammonium motif to a PSMA tracer, given the improvements observed upon its introduction

to octreotate analogues. Paradoxically, previous tracers seemed to benefit from the inclusion of a hydrophobic naphthylalanine-tranexamic acid motif (e.g. **425**), adjacent to the *KuE* scaffold. A new tracer was designed to incorporate both of these elements, while maintaining the diaspartic acid scaffold present in the previous lead compound (**429**). An 8-carbon linker was introduced adjacent to the *KuE*, as a simple mimic of the hydrophobic tranexamic motif, while a quaternary ammonium moiety was placed adjacent to the Asp₂ to maintain hydrophilicity (Figure 4.14).

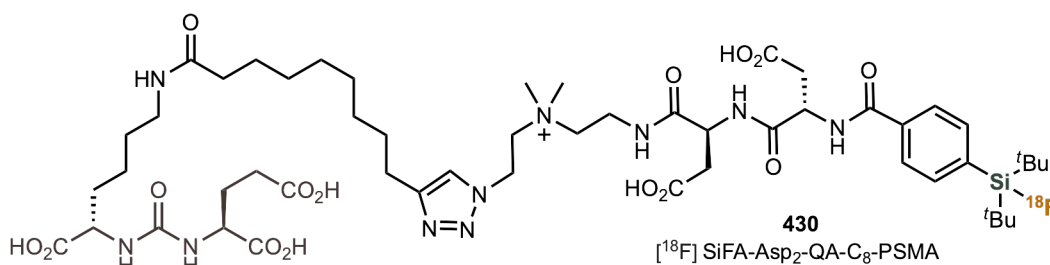


Figure 4.14. Structure of a lead PSMA targeting SiFA radiotracer

This compound SiFA-Asp₂-QA-C₈-PSMA (**430**) was previously synthesized on a trace scale in the Schirmacher Group to perform preliminary biological evaluation (*unpublished*). Excitingly, this compound **430** showed significant improvements over previous analogues, with a tumor uptake in LNCaP-bearing mice of 9.6%ID/g. This is depicted by the PET images shown in Figure 4.15, wherein the LNCaP tumor is somewhat visible with the Asp₂ compound **429**, but strongly visible with the new compound **430**. By comparison, the tumor is not visible in the first-generation compounds (**428**, **427**), which only show diffuse abdominal uptake (intestines).

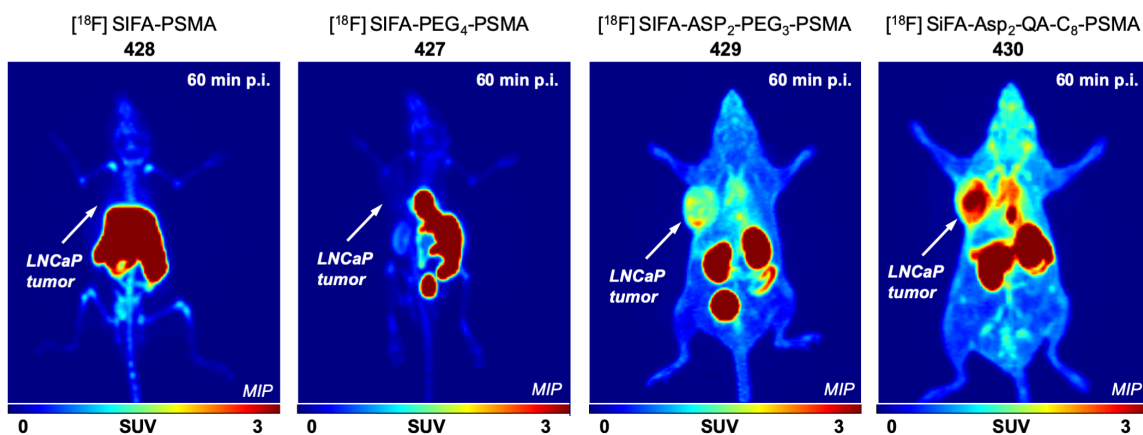


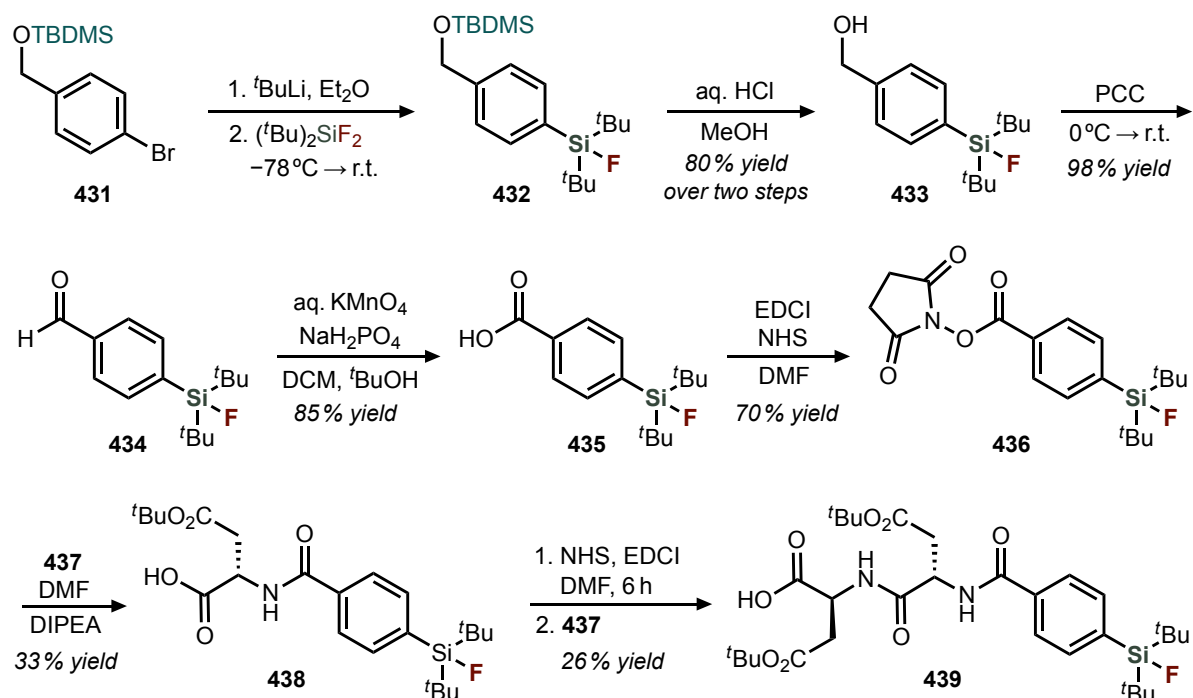
Figure 4.15. PET scans of LNCaP-mice with different PSMA targeting tracers

It therefore became an important goal to synthesize a larger batch of **430** (~200 mg), to enable further *in vivo* evaluations, as well as *in vitro* studies, such as determination of binding affinity and cellular internalization. This required the synthesis of multiple building blocks, starting on a multi-gram scale, as presented below in Scheme 4.10.

4.3.2 Synthetic Progress

The synthesis began with introduction of the SiFA motif, following protocols previously established in the Schirmmayer Group.^{243, 282} Lithium-halogen exchange was performed with aryl bromide **431**, facilitating *in situ* formation of the corresponding aryl lithium species. Addition to the silyl fluoride reagent (^tBu)₂SiF₂ resulted in the formation of SiFA arene **432**, isolated in 82% yield after column purification. However, this decreased to approximately 50% yield upon scale-up from 0.5 to 4.5 g, as a result of difficult separation between the starting material and product on a large-scale silica column.

Acidic deprotection of the silyl protecting group in **432** afforded SiFA alcohol **433**. Stepwise oxidation to the corresponding aldehyde (**434**), and subsequent carboxylic acid (**435**) proceeded efficiently. The carboxylic acid was then activated with EDCI, followed by coupling with *N*-hydroxysuccinimide to afford active ester **436** (~900 mg).

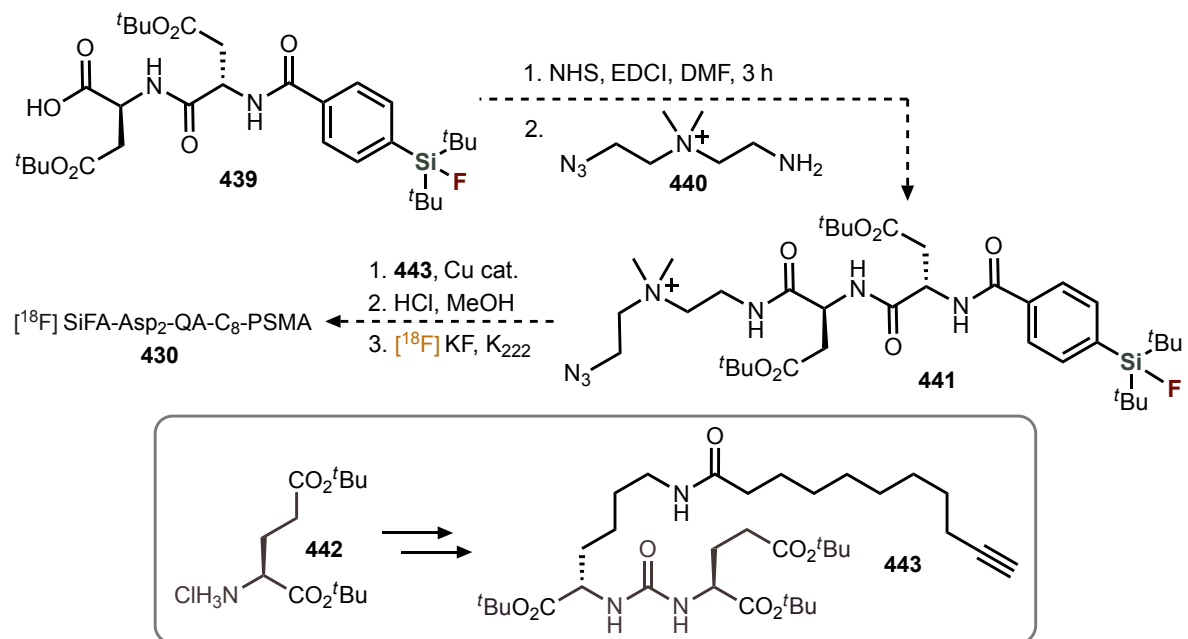


Scheme 4.10. Progress towards the synthesis of SiFA-Asp₂-QA-C₈-PSMA

Amidation was then achieved via the addition of *t*-butyl protected aspartic acid **437** (L-Asp(O^tBu)-OH) to the NHS-ester **436**, in the presence of base. However, the reaction proved difficult to push to completion, and often stalled before all the starting material was consumed. As such, the product **438** was isolated in fairly low yield after column purification. The second amidation was performed via a two-step method, starting with activation of the free carboxylic acid with EDCI/NHS, followed by addition of aspartic acid **437**. Purification could not be performed on silica, requiring reverse-phase

preparatory HPLC to afford the product **439** in a low yield of 26%. Further optimization of the HPLC method is anticipated to improve this yield.

The route to complete of the synthesis of **430** is depicted in Scheme 4.11. An additional amide coupling with the quaternary ammonium fragment **440** would afford species **441**. This azide-containing species could act as a partner for a CuAAC (*click*) reaction. The alkyne partner for this reaction **443**, containing the *KuE* scaffold, can be readily synthesized from amino acid building blocks. After azide-alkyne coupling, treatment of the resulting product with aqueous acid would affect universal deprotection of the *t*-butyl esters to reveal free carboxylic acids. Finally, radiofluorination via isotopic exchange of the SiFA moiety would afford the final radiotracer **430**.



Scheme 4.11. Future efforts required to complete the synthesis of SiFA-Asp₂-QA-C₈-PSMA

4.4 Conclusion

Since the seminal reports in the mid-2000s, non-canonical labeling strategies for fluorine-18 incorporation have grown substantially. Initial drawbacks of these methods included insufficient ^{18}F -bond stability *in vivo*, and significant changes to pharmacological behavior imparted by the non-canonical group. Major advances from the application of new chelator moieties have addressed these issues for aluminum methods. Boron/silicon methods have benefited from modulating the groups surrounding the heteroatom, and via introduction of polar auxiliaries, with numerous developments in both the leaving group and isotopic exchange approaches.

The simplicity and practicality of these methods for labeling and purification represent a major advantage over the classical C–F bond forming reactions. As such, the use of these methods to label peptides are becoming more common, with many examples of integration into clinical imaging candidates. This includes the imaging of important cancer biomarkers, such as *SSTr2* and *GRPr* receptors, *integrin* glycoproteins, and *PSMA* membrane receptors. The latter is a critical marker able to identify the progression of prostate cancer, and has been a prevalent tracer target in recent years.

PSMA analogues incorporating a non-canonical moiety have been thoroughly investigated by the networks of Perrin, Wester, and Schirrmacher. The initial compounds disclosed by the Schirrmacher Group suffered from a number of limitations, including low tumor uptake and high hepatobiliary clearance in tumor-bearing mouse studies, although moderate improvement was observed upon introduction of a diaspartic acid motif. To further improve these properties, an aliphatic linker and quaternary ammonium salt were incorporated to the tracer design, and the resulting compound SiFA-Asp₂-QA-C₈-PSMA was found to have excellent performance during preliminary *in vivo* evaluation.

As such, a higher-scale synthesis of this compound was undertaken to achieve greater quantities to facilitate further *in vivo* and *in vitro* evaluations. Moderate synthetic progress was made, with the completion of seven synthetic steps. To finish the tracer synthesis, three additional synthetic steps are required, followed by a radiofluorination step, utilizing the SiFA moiety to perform isotopic exchange. This compound is a promising candidate for clinical evaluation, with the potential to be a transformative tool in the diagnosis of prostate cancer and related pathologies.

5.1 Thesis Summary

Organofluorine compounds have long fascinated chemists for their unique physical properties, and have found numerous applications in the pharmaceutical, agrochemical, and materials science fields. In addition to the various developments for introducing fluorinated moieties, there has been much recent attention on C–F activation, chemistry designed to target the cleavage of C–F bonds. This offers a valuable tool for degrading environmentally harmful fluorine waste streams, as well as a singular strategy for accessing complex fluorinated functionalities. For example, mono-functionalization of the ubiquitous ArCF_3 moiety affords a range of valuable difluoromethane compounds (Figure 5.1), as highlighted in the opening chapter.

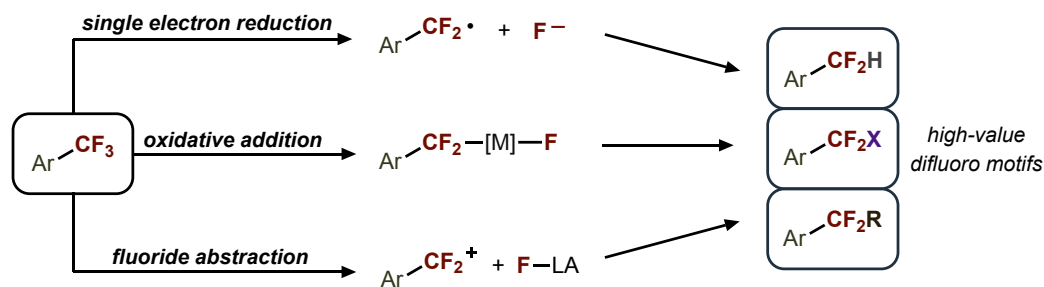


Figure 5.1. Summary of C–F activation strategies and products of mono-functionalization

A wealth of different strategies have been used for C–F activation, such as electrochemistry, photoredox, transition-metal mediated methods, and the exciting field of Lewis acid activation. The latter was highlighted by the description of several recent cutting-edge examples in the opening chapter, with leading work from the groups of Oestreich, Stephan, and Young. Acidic boron and silicon reagents are forefront in this area, driving reactivity via the formation of strong bond with fluorine. C–F activation remains a hot topic in organic chemistry, and will likely continue to see exciting new developments in the years to come.

Although initiated by a serendipitous discovery, the appeal of achieving C–F activation of ArCF_3 moieties became readily apparent within the Williams Group. The ability of ferric halides to catalyze ArCF_3 halogen-exchange of was investigated experimentally, and through computational studies which suggest that the iron species is the direct activator of the C–F bond. This platform was used to readily synthesize ArCX_3 products, whereas targeting ArCF_2X products necessitated the use of a *design-of-experiment* approach for optimization (Figure 5.2). This highlighted the utility of DOE for organic methods development, wherein it has seen relatively little uptake.

This method is rather practical, utilizing low-cost and readily available reagents, without the need for any delicate techniques or equipment. As with many of the precedents for C–F functionalization,

the use for an acidic boron reagent was the driving force for this reactivity. The synthesis of ArCF_2X products was found to run smoothly with a range of functionalized substrates, including the agrochemical flufenoxuron. It is envisioned that this method will find use in medicinal chemistry, given its potential to facilitate late-stage diversification. Although moderately yielding, much of the product distribution was accounted for by the starting material, which can be recovered after the reaction.

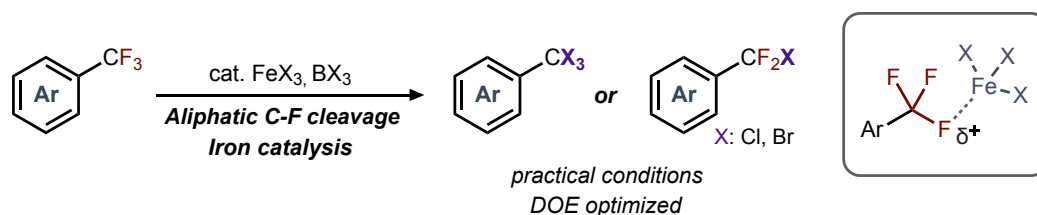


Figure 5.2. Summary of the method developed for the halox of trifluoromethyl arenes

The central role of PET in modern medical imaging was discussed, as well as the increasingly important role of the ^{18}F isotope, which has a number of intrinsic advantages over other β^+ emitters. As a result, the development of new radiofluorination methods have garnered much recent interest. An attractive goal is the radiosynthesis of $[^{18}\text{F}] \text{ArCF}_3$ substrates, given the increasing prevalence of the CF_3 moiety in pharmaceuticals. However, literature reports on the direct formation of $[^{18}\text{F}] \text{CF}_3$ moieties via isotopic exchange have been minimal, and necessitated the use of harsh conditions. As such, this area was deemed worthy of further study, with the aim of achieving mild conditions for CF_3 isotopic exchange.

Screening reactions were performed using BX_3/FeX_3 reagents, wherein these would drive the initial C–F abstraction, along with potential to participate in the redelivery of an ^{18}F anion. Effecting the desired reactivity with these conditions proved rather challenging, with the majority of conditions generating zero-value conversions. However, a single preliminary encouraging result was observed, indicating that this approach may be feasible.

The fourth chapter provided a discourse on non-canonical labeling, a class of methods that are also contingent on the formation of a strong fluorine bond with boron, silicon (or aluminum) moieties. However, rather than using these elements for defluorination, they are incorporated to a bioactive compound, as a handle that facilitates rapid ^{18}F -incorporation. There are various clinical candidates containing non-canonical moieties, namely those targeting cancer biomarkers to facilitate tumor imaging. In particular, the PSMA receptor has been an attractive target for tracer development, and the synthetic efforts towards a new compound SiFA-Asp₂-QA-C₈-PSMA were described. Excellent performance in initial *in vivo* studies suggest that this compound is a promising candidate for imaging prostate cancer.

5.2 Future Directions

The ArCF₃ halogen-exchange work was the first incursion into C–F activation by the Williams Group, and is anticipated to serve as a foundational study to guide continued investigations in this area. One potential opportunity is to expand the scope of ArCX₃ synthesis, which was not central to this work. Another appealing avenue for investigation is the development of *one-pot* methods, combining the formation of ArCX₃ / ArCF₂X products with a subsequent reaction. For example, one could envision the rapid conversion of ArCF₃ to the corresponding ArCO₂H, proceeding via an ArCX₃ intermediate that is hydrolyzed *in situ*.

A potential approach to improve the yield of the ArCF₂X products, is to apply this reaction to a continuous flow system, as these are known to facilitate selectivity control in reactions with a complex kinetic profile.¹¹¹ The preliminary boron triiodide studies revealed intriguing divergent reactivity, with the potential to form benzyl iodide or benzaldehyde products, which are well-suited to undergo addition of nucleophilic species. As such, this method has the potential to facilitate late-stage unmasking of the inert CF₃ group and facilitate further reactivity. The application of these methods to alkyl-CF₃ substrates or perfluoroalkanes is also of interest, given their propensity to be unreactive or sluggish under most conditions.

In the [¹⁸F] ArCF₃ investigations, a greater examination of eluent mixtures could allow for identification of conditions compatible with halox reactivity. For example, application of the *four-drop-method* may avoid the issues of K₂CO₃ shutting down reactivity. Upon achieving a protocol for efficiently introducing dry ¹⁸F to the halox reaction mixture, various parameters can be altered for optimization, including reaction temperature, solvent, and ratio of ¹⁸F-to-precursor.

A fairly straightforward scheme has been established to complete the synthesis of SiFA-Asp₂-QA-C₈-PSMA. Biological studies will then be performed, including *in vitro* studies to determine binding affinity and cellular internalization, as well as *in vitro* mouse-studies to further evaluate biodistribution and tumor uptake. If results are positive, clinical studies will ultimately be performed, first on healthy volunteers, followed by prostate cancer patients. The radiofluorination step will also require optimization to ensure the product is formed with high molar activity and radiochemical purity.

5.3 Conclusion

An underlying theme of this thesis has been the use of boron or silicon moieties to control the reactivity of fluoride or organofluorine species. These heteroatoms evidently have a special role in the fluorine chemistry field, yet are quite diverse in the type of reaction that they can perform. Their functions range from catalytic initiators, active catalytic species, FLP partners, intramolecular fluoride abstractors, to participators in the new bond-forming step, with the ability to facilitate various C–F functionalizations, such as hydrodefluorination, halogen-exchange, and defluorinative C–C formation. A diverse set of boron and silicon reagents are also often readily-available and inexpensive.

Even in thermodynamically neutral reactions, such as isotopic exchange, boron/silicon moieties tend to have low activation energies for the addition of fluoride. These proceed via an *addition-elimination* pathway, in which the high C–F bond strength lowers the energy of intermediate, thereby lowering the energy barrier of the reaction. As such, attachment of these heteroatom moieties into a target bioactive molecule facilitates the rapid kinetics for inclusion of ^{18}F by isotopic exchange. Given their expansive role in fluorine chemistry, boron and silicon moieties will no doubt continue to play a key role in the future developments in this field.

References

1. Caron, S., *Org. Process Res. Dev.* **2020**, *24*, 470-480.
2. Dolbier, W.R., *J. F. Chem.* **2005**, *126*, 157-163.
3. O'Hagan, D., *Chem. Soc. Rev.* **2008**, *37*, 308-319.
4. Burdeniuc, J.; Jedlicka, B.; Crabtree, R.H., *Chem. Ber.* **1996**, *130*, 145-154.
5. Inoue, M.; Sumii, Y.; Shibata, N., *ACS Omega* **2020**, *5*, 10633-10640.
6. Ogawa, Y.; Tokunaga, E.; Kobayashi, O.; Hirai, K.; Shibata, N., *iScience* **2020**, *23*, 101467-101490.
7. Gillis, E.P.; Eastman, K.J.; Hill, M.D.; Donnelly, D.J.; Meanwell, N.A., *J. Med. Chem.* **2015**, *58*, 8315-8359.
8. Li, H.; Sheeran, J.W.; Kouvcchinov, D.; Clausen, A.M.; Crouch, I.T.; Bio, M.M.; Fang, Y.-Q.; Frank, S.A.; Johnson, M.D.; Kerr, M.S., *J. Org. Chem.* **2022**, *87*, 2045-2054.
9. Rusu, A.; Lungu, I.-A.; Moldovan, O.-L.; Tanase, C.; Hancu, G., *Pharmaceutics* **2021**, *13*, 1289-1326.
10. Nocentini, A.; Capasso, C.; Supuran, C.T., *Expert Opin. Drug Discov.* **2022**, 1-11.
11. Shine, K.P.; Sturges, W.T., *Science* **2007**, *315*, 1804-1805.
12. Sovacool, B.K.; Griffiths, S.; Kim, J.; Bazilian, M., *Renew. Sust. Energ. Rev.* **2021**, *141*, 110759-110814.
13. Prices from Sigma-Aldrich. sigmaaldrich.com/CA/en (accessed 25-April-2022).
14. Alonso, C.; Martinez de Marigorta, E.; Rubiales, G.; Palacios, F., *Chem. Rev.* **2015**, *115*, 1847-1935.
15. Arai, K.; Homma, T.; Morikawa, Y.; Ubukata, N.; Tsuruoka, H.; Aoki, K.; Ishikawa, H.; Mizuno, M.; Sada, T., *Eur. J. Pharmacol.* **2015**, *761*, 226-234.
16. Patel, M.; Ko, S.S.; McHugh, R.J.; Markwalder, J.A.; Srivastava, A.S.; Cordova, B.C.; Klabe, R.M.; Erickson-Viitanen, S.; Trainor, G.L.; Seitz, S.P., *Bioorg. Med. Chem. Lett.* **1999**, *9*, 2805-2810.
17. Lyseng-Williamson, K.A., *Drugs* **2007**, *67*, 587-597.
18. Jaroschik, F., *Chem. Eur. J.* **2018**, *24*, 14572-14582.
19. Zafrani, Y.; Saphier, S.; Gershonov, E., *Future Med. Chem.* **2020**, *12*, 361-365.
20. Zafrani, Y.; Yeffet, D.; Sod-Moriah, G.; Berliner, A.; Amir, D.; Marciano, D.; Gershonov, E.; Saphier, S., *J. Med. Chem.* **2017**, *60*, 797-804.
21. Sap, J.B.I.; Meyer, C.F.; Straathof, N.J.W.; Iwumene, N.; am Ende, C.W.; Trabanco, A.A.; Gouverneur, V., *Chem. Soc. Rev.* **2021**, *50*, 8214-8247.
22. Ni, C.; Hu, M.; Hu, J., *Chem. Rev.* **2015**, *115*, 765-825.
23. Prakash, G.K.S.; Hu, J.; Simon, J.; Bellew, D.R.; Olah, G.A., *J. F. Chem.* **2004**, *125*, 595-601.
24. Gupta, R.; Young, R.D., *Synthesis* **2022**, *54*, 1671-1683.
25. Yoshida, M.; Morinaga, M.; Iyoda, M., *J. F. Chem.* **1994**, *68*, 33-38.
26. Sumino, S.; Uno, M.; Fukuyama, T.; Ryu, I.; Matsuura, M.; Yamamoto, A.; Kishikawa, Y., *J. Org. Chem.* **2017**, *82*, 5469-5474.

27. Guidotti, J.; Wakselman, C.; Metz, F.; Tordeux, M., *Synlett* **2004**, 1759-1762.
28. Guidotti, J.; Schanen, V.; Tordeux, M.; Wakselman, C., *J. F. Chem.* **2005**, *126*, 443-447.
29. Gu, J.-W.; Guo, W.-H.; Zhang, X., *Org. Chem. Front.* **2015**, *2*, 38-41.
30. Verhoog, S.; Pfeifer, L.; Khotavivattana, T.; Calderwood, S.; Collier, T.; Wheelhouse, K.; Tredwell, M.; Gouverneur, V., *Synlett* **2015**, *27*, 25-28.
31. He, J.; Pittman, C.U., *Synth. Commun.* **1999**, *29*, 855-862.
32. Hass, A.; Spitzer, M.; Lieb, M., *Chem. Ber.* **1988**, *121*, 1329-1340.
33. Zeun, R.; Scalliet, G.; Oostendorp, M., *Pest Manag. Sci.* **2013**, *69*, 527-534.
34. Regan, M.C.; Zhu, Z.; Yuan, H.; Myers, S.J.; Menaldino, D.S.; Tahirovic, Y.A.; Liotta, D.C.; Traynelis, S.F.; Furukawa, H., *Nat. Commun.* **2019**, *10*, 321-331.
35. Burgey, C.S.; Robinson, K.A.; Lyle, T.A.; Sanderson, P.E.J.; Lewis, S.D.; Lucas, B.J.; Krueger, J.A.; Singh, R.; Miller-Stein, C.; White, R.B.; Wong, B.; Lyle, E.A.; Williams, P.D.; Coburn, C.A.; Dorsey, B.D.; Barrow, J.C.; Stranieri, M.T.; Holahan, M.A.; Sitko, G.R.; Cook, J.J.; McMasters, D.R.; McDonough, C.M.; Sanders, W.M.; Wallace, A.A.; Clayton, F.C.; Bohn, D.; Leonard, Y.M.; Detwiler, T.J.; Lynch, J.J.; Yan, Y.; Chen, Z.; Kuo, L.; Gardell, S.J.; Shafer, J.A.; Vacca, J.P., *J. Med. Chem.* **2003**, *46*, 461-473.
36. Henne, A.L.; Newman, M.S., *J. Am. Chem. Soc.* **1938**, 1697-1698.
37. Chen, H.; Yin, J.; Lin, Y., *Chem. Papers.* **2009**, *63*, 92-96.
38. Dankert, F.; Deubner, H.L.; Müller, M.; Buchner, M.R.; Kraus, F.; von Hänisch, C., *Z. Anorg. Allg. Chem.* **2020**, *646*, 1501-1507.
39. Goh, K.K.K.; Sinha, A.; Fraser, C.; Young, R.D., *RSC Adv.* **2016**, *6*, 42708-42712.
40. Liu, H.; Kondo, S.-i.; Takeda, N.; Unno, M., *Eur. J. Inorg. Chem.* **2009**, 1317-1319.
41. Sun, Q.; Yu, X.; Bao, M.; Liu, M.; Pan, J.; Zha, Z.; Cai, L.; Ma, H.; Yuan, C.; Qiu, X.; Xu, W., *Angew. Chem. Int. Ed.* **2018**, *57*, 4035-4038.
42. Chatterjee, T.; Kim, D.I.; Cho, E.J., *J. Org. Chem.* **2018**, *83*, 7423-7430.
43. Amii, H.; Uneyama, K., *Chem. Rev.* **2009**, *109*, 2119-2183.
44. Ahrens, T.; Kohlmann, J.; Ahrens, M.; Braun, T., *Chem. Rev.* **2015**, *115*, 931-972.
45. Utsumi, S.; Katagiri, T.; Uneyama, K., *Tetrahedron* **2012**, *68*, 1085-1091.
46. Munoz, S.B.; Ni, C.; Zhang, Z.; Wang, F.; Shao, N.; Mathew, T.; Olah, G.A.; Prakash, G.K.S., *Eur. J. Org. Chem.* **2017**, *2017*, 2322-2326.
47. Clavel, P.; Léger-Lambert, M.-P.; Biran, C.; Serein-Spirau, F.; Bordeau, M.; Roques, N.; Marzouk, H., *Synthesis* **1999**, *5*, 829-834.
48. Clavel, P.; Lessene, G.; Biran, C.; Bordeau, M.; Roques, N.; Trévin, S.; de Montauzon, D., *J. F. Chem.* **2001**, *107*, 301-310.
49. Lemal, D.M., *J. Org. Chem.* **2004**, *69*, 1-11.
50. Wang, H.; Jui, N.T., *J. Am. Chem. Soc.* **2018**, *140*, 163-166.
51. Vogt, D.B.; Seath, C.P.; Wang, H.; Jui, N.T., *J. Am. Chem. Soc.* **2019**, *141*, 13203-13211.

52. Chen, K.; Berg, N.; Gschwind, R.; Konig, B., *J. Am. Chem. Soc.* **2017**, *139*, 18444-18447.
53. Luo, Y.-C.; Tong, F.-F.; Zhang, Y.; He, C.-Y.; Zhang, X., *J. Am. Chem. Soc.* **2021**, *143*, 13971-13979.
54. Stahl, T.; Klare, H.F.T.; Oestreich, M., *ACS Catal.* **2013**, *3*, 1578-1587.
55. Walsh, R., *J. Chem. Soc. Faraday Trans. 1* **1983**, *79*, 2233-2248.
56. Grant, D.J.; Dixon, D.A., *J. Phys. Chem. A* **2009**, *113*, 777-787.
57. Olah, G.A.; Narang, S.C.; Field, L.D., *J. Org. Chem.* **1981**, *46*, 3727-3728.
58. Janjetovic, M.; Ekebergh, A.; Traff, A.M.; Hilmersson, G., *Org. Lett.* **2016**, *18*, 2804-2807.
59. Walker, J.C.L.; Klare, H.F.T.; Oestreich, M., *Nat. Rev. Chem.* **2020**, *4*, 54-62.
60. Scott, V.J.; Çelenligil-Çetin, R.; Ozerov, O.V., *J. Am. Chem. Soc.* **2005**, *127*, 2852-2853.
61. Douvris, C.; Ozerov, O.V., *Science* **2008**, *321*, 1188-1190.
62. Gu, W.; Haneline, M.R.; Douvris, C.; Ozerov, O.V., *J. Am. Chem. Soc.* **2009**, *131*, 11203-11212.
63. Douvris, C.; Nagaraja, C.M.; Chen, C.-H.; Foxman, B.M.; Ozerov, O.V., *J. Am. Chem. Soc.* **2010**, *132*, 4946-4953.
64. Press, L.P.; McCulloch, B.J.; Gu, W.; Chen, C.-H.; Foxman, B.M.; Ozerov, O.V., *Chem. Commun.* **2015**, *51*, 14034-14037.
65. Culver, D.B.; Conley, M.P., *Angew. Chem. Int. Ed.* **2018**, *57*, 14902-14905.
66. Kordts, N.; Künzler, S.; Rathjen, S.; Sieling, T.; Großekappenberg, H.; Schmidtman, M.; Müller, T., *Chem. Eur. J.* **2017**, *23*, 10068-10079.
67. Lühmann, N.; Hirao, H.; Shaik, S.; Müller, T., *Organometallics* **2011**, *30*, 4087-4096.
68. Panisch, R.; Bolte, M.; Müller, T., *J. Am. Chem. Soc.* **2006**, *128*, 9676-9682.
69. Omann, L.; Königs, C.D.F.; Klare, H.F.T.; Oestreich, M., *Acc. Chem. Res.* **2017**, *50*, 1258-1269.
70. Stahl, T.; Klare, H.F.T.; Oestreich, M., *J. Am. Chem. Soc.* **2013**, *135*, 1248-1251.
71. Caputo, C.B.; Stephan, D.W., *Organometallics* **2012**, *31*, 27-30.
72. Chen, J.; Chen, E.Y.-X., *Angew. Chem. Int. Ed.* **2015**, *54*, 6842-6846.
73. Yang, J.; White, P.S.; Schauer, C.K.; Brookhart, M., *Angew. Chem. Int. Ed.* **2008**, *47*, 4141-4143.
74. Yang, J.; Brookhart, M., *Adv. Synth. Catal.* **2009**, *351*, 175-187.
75. Dunlop, D.; Pinkas, J.; Horáček, M.; Žilková, N.; Lamač, M., *Dalton. Trans.* **2020**, *49*, 2771-2775.
76. Chitnis, S.S.; Krischer, F.; Stephan, D.W., *Chem. Eur. J.* **2018**, *24*, 6543-6546.
77. Bayne, J.M.; Stephan, D.W., *Chem. Eur. J.* **2019**, *25*, 9350-9357.
78. Lühmann, N.; Panisch, R.; Müller, T., *Appl. Organomet. Chem.* **2010**, *24*, 533-537.
79. Zhu, J.; Pérez, M.; Caputo, C.B.; Stephan, D.W., *Angew. Chem. Int. Ed.* **2016**, *55*, 1417-1421.
80. Zhu, J.; Pérez, M.; Stephan, D.W., *Angew. Chem. Int. Ed.* **2016**, *55*, 8448-8451.
81. Yoshida, S.; Shimomori, K.; Kim, Y.; Hosoya, T., *Angew. Chem. Int. Ed.* **2016**, *55*, 10406-10409.
82. Idogawa, R.; Kim, Y.; Shimomori, K.; Hosoya, T.; Yoshida, S., *Org. Lett.* **2020**, *22*, 9292-9297.

83. Stephan, D.W., *Acc. Chem. Res.* **2015**, *48*, 306-316.
84. Mallov, I.; Ruddy, A.J.; Zhu, H.; Grimme, S.; Stephan, D.W., *Chem. Eur. J.* **2017**, *23*, 17692-17696.
85. Namavari, M.; Satyamurthy, N.; Barrio, J.R., *J. F. Chem.* **1995**, *72*, 89-93.
86. Theodoridis, G., *Tetrahedron Lett.* **1998**, *39*, 9365-9368.
87. Swarnakar, A.K.; Hering-Junghans, C.; Ferguson, M.J.; McDonald, R.; Rivard, E., *Chem. Eur. J.* **2017**, *23*, 8628-8631.
88. Ullrich, M.; Lough, A.J.; Stephan, D.W., *Organometallics* **2010**, *29*, 3647-3654.
89. Jaiswal, A.K.; Prasad, P.K.; Young, R.D., *Chem. Eur. J.* **2019**, *25*, 6290-6294.
90. Ikeda, M.; Matsuzawa, T.; Morita, T.; Hosoya, T.; Yoshida, S., *Chem. Eur. J.* **2020**, *26*, 12333-12337.
91. Wang, F.; Nishimoto, Y.; Yasuda, M., *J. Am. Chem. Soc.* **2021**, *143*, 20616-20621.
92. Levin, M.D.; Chen, T.Q.; Neubig, M.E.; Hong, C.M.; Theulier, C.A.; Kobylanskii, I.J.; Janabi, M.; O'Neil, J.P.; Toste, F.D., *Science* **2017**, *356*, 1272-1276.
93. Mandal, D.; Gupta, R.; Young, R.D., *J. Am. Chem. Soc.* **2018**, *140*, 10682-10686.
94. Mandal, D.; Gupta, R.; Jaiswal, A.K.; Young, R.D., *J. Am. Chem. Soc.* **2020**, *142*, 2572-2578.
95. Gupta, R.; Mandal, D.; Jaiswal, A.K.; Young, R.D., *Org. Lett.* **2021**, *23*, 1915-1920.
96. Mizukami, Y.; Song, Z.; Takahashi, T., *Org. Lett.* **2015**, *17*, 5942-5945.
97. Matsubara, K.; Ishibashi, T.; Koga, Y., *Org. Lett.* **2009**, *11*, 1765-1768.
98. Terao, J.; Begum, S.A.; Shinohara, Y.; Tomita, M.; Naitoh, Y.; Kambe, N., *Chem. Commun.* **2007**, 855-857.
99. San Filippo Jr., J.; Sowinski, A.F.; Romano, L.J., *J. Org. Chem.* **1975**, *40*, 3295-3296.
100. Wang, Y.; Liu, A., *Chem. Soc. Rev.* **2020**, *49*, 4906-4925.
101. Amaya, G.M.; Durandis, R.; Bourgeois, D.S.; Perkins, J.A.; Abouda, A.A.; Wines, K.J.; Mohamud, M.; Starks, S.A.; Daniels, R.N.; Jackson, K.D., *Chem. Res. Toxicol.* **2018**, *31*, 570-584.
102. Shipilov, A.I.; Kolpashchikova, L.A.; Igumnov, S.M., *Russ. J. Org. Chem.* **2003**, *39*, 975-978.
103. Murray, P.M.; Bellany, F.; Benhamou, L.; Bučar, D.-K.; Tabor, A.B.; Sheppard, T.D., *Org. Biomol. Chem.* **2016**, *14*, 2373-2384.
104. Design and Optimization in Organic Synthesis. In *Data Handling in Science and Technology*, Carlson, R.; Carlson, J. E., Eds. Elsevier: 2005; Vol. 24.
105. Weissman, S.A.; Anderson, N.G., *Org. Process Res. Dev.* **2015**, *19*, 1605-1633.
106. Reprinted from "Design and Optimization in Organic Synthesis: Chapter 3. In *Data Handling in Science and Technology*, Carlson, R.; Carlson, J. E., Eds. Elsevier: 2005; Vol. 24, pp 27-66." with permission from Elsevier.
107. Li, G.; Miller, S.P.; Radosevich, A.T., *J. Am. Chem. Soc.* **2021**, *143*, 14464-14469.
108. Becke, A.D., *J. Chem. Phys.* **1993**, *98*, 1372-1377.
109. Rassolov, V.A.; Ratner, M.A.; Pople, J.A.; Redfern, P.C.; Curtiss, L.A., *J. Comput. Chem.* **2001**, *22*, 976-984.

110. Bartlett, R.J.; Musiał, M., *Rev. Mod. Phys.* **2007**, *79*, 291-352.
111. Plutschack, M.B.; Pieber, B.; Gilmore, K.; Seeberger, P.H., *Chem. Rev.* **2017**, *117*, 11796-11893.
112. Salehi Marzijarani, N.; Snead, D.R.; McMullen, J.P.; Lévesque, F.; Weisel, M.; Varsolona, R.J.; Lam, Y.; Liu, Z.; Naber, J.R., *Org. Process Res. Dev.* **2019**, *23*, 1522-1528.
113. Ametamey, S.M.; Honer, M.; Schubiger, P.A., *Chem. Rev.* **2008**, *108*, 1501-1516.
114. Brooks, A.F.; Topczewski, J.J.; Ichiishi, N.; Sanford, M.S.; Scott, P.J.H., *Chem. Sci.* **2014**, *5*, 4545-4553.
115. Preshlock, S.; Tredwell, M.; Gouverneur, V., *Chem. Rev.* **2016**, *116*, 719-766.
116. Bratteby, K.; Shalgunov, V.; Herth, M.M., *ChemMedChem.* **2021**, *16*, 2612-2622.
117. Francis, F.; Wuest, F., *Molecules.* **2021**, *26*, 6478-6503.
118. Jacobson, O.; Kiesewetter, D.O.; Chen, X., *Bioconjugate Chem.* **2015**, *26*, 1-18.
119. Gallamini, A.; Zwarthoed, C.; Borra, A., *Cancer* **2014**, *6*, 1821-1889.
120. Werner, R.A.; Chen, X.; Rowe, S.P.; Lapa, C.; Javadi, M.S.; Higuchi, T., *Trends Cardiovasc. Med.* **2020**, *30*, 11-19.
121. Zimmer, L.; Luxen, A., *NeuroImage* **2012**, *61*, 363-370.
122. Matthews, P.M.; Rabiner, E.A.; Passchier, J.; Gunn, R.N., *Br. J. Clin. Pharmacol.* **2012**, *73*, 175-186.
123. *Production and Quality Control of Fluorine-18 Labelled Radiopharmaceuticals*. International Atomic Energy Agency: Vienna, 2021.
124. Pimlott, S.L.; Sutherland, A., *Chem. Soc. Rev.* **2011**, *40*, 149-162.
125. Conti, M.; Eriksson, L., *EJNMMI Phys.* **2016**, *3*, 8-25.
126. Scott, P.J.H., *Angew. Chem. Int. Ed.* **2009**, *48*, 6001-6004.
127. Rigo, P.; Paulus, P.; Kaschten, B.J.; Hustinx, R.; Bury, T.; Jerusalem, G.; Benoit, T.; Foidart-Willems, J., *Eur. J. Nucl. Med* **1996**, *23*, 1641-1674.
128. Pretze, M.; Wängler, C.; Wängler, B., *Biomed. Res. Int.* **2014**, *2014*, 674063-674063.
129. Suehiro, M.; Yang, G.; Torchon, G.; Ackerstaff, E.; Humm, J.; Koutcher, J.; Ouerfelli, O., *Bioorg. Med. Chem.* **2011**, *19*, 2287-2297.
130. de Goeij, J.J.M.; Bonardi, M.L., *J. Radioanal. Nucl. Chem.* **2005**, *263*, 13-18.
131. Bergman, J.; Solin, O., *Nucl. Med. Biol.* **1997**, *24*, 677-683.
132. Chirakal, R.; Firna, G.; Schrobilgen, G.J.; McKay, J.; Garnett, E.S., *Int. J. Appl. Radiat. Isot.* **1984**, *35*, 401-404.
133. Jewett, D.M.; Potocki, J.F.; Ehrenkauf, R.E., *J. F. Chem.* **1984**, *24*, 477-484.
134. Teare, H.; Robins, E.G.; Årstad, E.; Luthra, S.K.; Gouverneur, V., *Chem. Commun.* **2007**, 2330-2332.
135. Ehrenkauf, R.E.; MacGregor, R.R., *Int. J. Appl. Radiat. Isot.* **1983**, *34*, 613-615.
136. Oberdorfer, F.; Hofmann, E.; Maier-Borst, W., *Int. J. Rad. Appl. Instrum. Part A.* **1988**, *39*, 685-688.

137. Teare, H.; Robins, E.G.; Kirjavainen, A.; Forsback, S.; Sandford, G.; Solin, O.; Luthra, S.K.; Gouverneur, V., *Angew. Chem. Int. Ed.* **2010**, *49*, 6821-6824.
138. Satyamurthy, N.; Bida, G.T.; Phelps, M.E.; Barrio, J.R., *Int. J. Rad. Appl. Instrum. Part A.* **1990**, *41*, 733-738.
139. Jiang, H.; DeGrado, T., *J. Nucl. Med.* **2014**, *55*, 161-161.
140. Nielsen, M.K.; Ugaz, C.R.; Li, W.; Doyle, A.G., *J. Am. Chem. Soc.* **2015**, *137*, 9571-9574.
141. van der Born, D.; Pees, A.; Poot, A.J.; Orru, R.V.A.; Windhorst, A.D.; Vugts, D.J., *Chem. Soc. Rev.* **2017**, *46*, 4709-4773.
142. Krishnan, H.S.; Ma, L.; Vasdev, N.; Liang, S.H., *Chem. Eur. J.* **2017**, *23*, 15553-15577.
143. Coenen, H.H.; Gee, A.D.; Adam, M.; Antoni, G.; Cutler, C.S.; Fujibayashi, Y.; Jeong, J.M.; Mach, R.H.; Mindt, T.L.; Pike, V.W.; Windhorst, A.D., *Nucl. Med. Biol.* **2017**, *55*, v-xi.
144. Herth, M.M.; Ametamey, S.; Antuganov, D.; Bauman, A.; Berndt, M.; Brooks, A.F.; Bormans, G.; Choe, Y.S.; Gillings, N.; Häfeli, U.O.; James, M.L.; Kopka, K.; Kramer, V.; Krasikova, R.; Madsen, J.; Mu, L.; Neumaier, B.; Piel, M.; Rösch, F.; Ross, T.; Schibli, R.; Scott, P.J.H.; Shalgunov, V.; Vasdev, N.; Wadsak, W.; Zeglis, B.M., *Nucl. Med. Biol.* **2021**, *93*, 19-21.
145. Verhoog, S.; Brooks, A.F.; Winton, W.P.; Viglianti, B.L.; Sanford, M.S.; Scott, P.J.H., *Chem. Commun.* **2019**, *55*, 6361-6364.
146. Ido, T.; Wan, C.-N.; Casella, V.; Fowler, J.S.; Wolf, A.P.; Reivich, M.; Kuhl, D.E., *J. Label. Comp. Radiopharm.* **1978**, *14*, 175-183.
147. Buckingham, F.; Kirjavainen, A.K.; Forsback, S.; Krzyczmonik, A.; Keller, T.; Newington, I.M.; Glaser, M.; Luthra, S.K.; Solin, O.; Gouverneur, V., *Angew. Chem. Int. Ed.* **2015**, *54*, 13366-13369.
148. Nodwell, M.B.; Yang, H.; Čolović, M.; Yuan, Z.; Merkens, H.; Martin, R.E.; Bénard, F.; Schaffer, P.; Britton, R., *J. Am. Chem. Soc.* **2017**, *139*, 3595-3598.
149. Namavari, M.; Bishop, A.; Satyamurthy, N.; Bida, G.; Barrio, J.R., *Int. J. Rad. Appl. Instrum. Part A.* **1992**, *43*, 989-996.
150. Hoffmann, M.; Chen, X.; Hirano, M.; Arimitsu, K.; Kimura, H.; Higuchi, T.; Decker, M., *ChemMedChem.* **2018**, *13*, 2546-2557.
151. Sergeev, M.E.; Morgia, F.; Lazari, M.; Wang, C.; van Dam, R.M., *J. Am. Chem. Soc.* **2015**, *137*, 5686-5694.
152. Deng, H.; Cobb, S.L.; Gee, A.D.; Lockhart, A.; Martarello, L.; McGlinchey, R.P.; O'Hagan, D.; Onega, M., *Chem. Commun.* **2006**, 652-654.
153. Topczewski, J.J.; Tewson, T.J.; Nguyen, H.M., *J. Am. Chem. Soc.* **2011**, *133*, 19318-19321.
154. Hollingworth, C.; Hazari, A.; Hopkinson, M.N.; Tredwell, M.; Benedetto, E.; Huiban, M.; Gee, A.D.; Brown, J.M.; Gouverneur, V., *Angew. Chem. Int. Ed.* **2011**, *50*, 2613-2617.
155. Benedetto, E.; Tredwell, M.; Hollingworth, C.; Khotavivattana, T.; Brown, J.M.; Gouverneur, V., *Chem. Sci.* **2013**, *4*, 89-96.
156. Mu, L.; Fischer, C.R.; Holland, J.P.; Becaud, J.; Schubiger, P.A.; Schibli, R.; Ametamey, S.M.; Graham, K.; Stellfeld, T.; Dinkelborg, L.M.; Lehmann, L., *Eur. J. Org. Chem.* **2012**, *2012*, 889-892.

157. Sander, K.; Gendron, T.; Yiannaki, E.; Cybulska, K.; Kalber, T.L.; Lythgoe, M.F.; Årstad, E., *Sci. Rep.* **2015**, *5*, 9941-9946.
158. Narayanam, M.K.; Ma, G.; Champagne, P.A.; Houk, K.N.; Murphy, J.M., *Angew. Chem. Int. Ed.* **2017**, *56*, 13006-13010.
159. Neumann, C.N.; Hooker, J.M.; Ritter, T., *Nature* **2016**, *534*, 369-373.
160. Beyzavi, H.; Mandal, D.; Strebl, M.G.; Neumann, C.N.; D'Amato, E.M.; Chen, J.; Hooker, J.M.; Ritter, T., *ACS Cent. Sci.* **2017**, *3*, 944-948.
161. Pike, V.W., *J. Label. Comp. Radiopharm.* **2018**, *61*, 196-227.
162. Chun, J.-H.; Lu, S.; Lee, Y.-S.; Pike, V.W., *J. Org. Chem.* **2010**, *75*, 3332-3338.
163. Ross, T.L.; Ermert, J.; Hocke, C.; Coenen, H.H., *J. Am. Chem. Soc.* **2007**, *129*, 8018-8025.
164. Ichiishi, N.; Brooks, A.F.; Topczewski, J.J.; Rodnick, M.E.; Sanford, M.S.; Scott, P.J.H., *Org. Lett.* **2014**, *16*, 3224-3227.
165. McCammant, M.S.; Thompson, S.; Brooks, A.F.; Krska, S.W.; Scott, P.J.H.; Sanford, M.S., *Org. Lett.* **2017**, *19*, 3939-3942.
166. Lee, Y.-S.; Chun, J.-H.; Hodošček, M.; Pike, V.W., *Chem. Eur. J.* **2017**, *23*, 4353-4363.
167. Cardinale, J.; Ermert, J.; Humpert, S.; Coenen, H.H., *RSC Adv.* **2014**, *4*, 17293-17299.
168. Rotstein, B.H.; Stephenson, N.A.; Vasdev, N.; Liang, S.H., *Nat. Commun.* **2014**, *5*, 4365-4372.
169. Rotstein, B.H.; Wang, L.; Liu, R.Y.; Patteson, J.; Kwan, E.E.; Vasdev, N.; Liang, S.H., *Chem. Sci.* **2016**, *7*, 4407-4417.
170. Mossine, A.; Makaravage, K.; Ichiishi, N.; Brooks, A.; Miller, J.; Sanford, M.; Scott, P., *J. Nucl. Med.* **2016**, *57*, 1-2.
171. Lee, E.; Kamlet, A.S.; Powers, D.C.; Neumann, C.N.; Boursalian, G.B.; Furuya, T.; Choi, D.C.; Hooker, J.M.; Ritter, T., *Science* **2011**, *334*, 639-642.
172. Lee, E.; Hooker, J.M.; Ritter, T., *J. Am. Chem. Soc.* **2012**, *134*, 17456-17458.
173. Dolbier, W.R.; Li, A.-R.; Koch, C.J.; Shiue, C.-Y.; Kachur, A.V., *Appl. Radiat. Isot.* **2001**, *54*, 73-80.
174. Gruber, S.; Ametamey, S.M.; Schibli, R., *Chem. Commun.* **2018**, *54*, 8999-9002.
175. Mizuta, S.; Stenhagen, I.S.R.; O'Duill, M.; Wolstenhulme, J.; Kirjavainen, A.K.; Forsback, S.J.; Tredwell, M.; Sandford, G.; Moore, P.R.; Huiban, M.; Luthra, S.K.; Passchier, J.; Solin, O.; Gouverneur, V., *Org. Lett.* **2013**, *15*, 2648-2651.
176. Carroll, L.; Evans, H.L.; Spivey, A.C.; Aboagye, E.O., *Chem. Commun.* **2015**, *51*, 8439-8441.
177. Riss, P.J.; Aigbirhio, F.I., *Chem. Commun.* **2011**, *47*, 11873-11875.
178. Kramer, V.; Brooks, A.F.; Haeger, A.; Kuljis, R.O.; Rafique, W.; Koeppe, R.A.; Raffel, D.M.; Frey, K.A.; Amaral, H.; Scott, P.J.H.; Riss, P.J., *ACS Chem. Neurosci.* **2020**, *11*, 427-435.
179. Das, M.K.; Mukherjee, J., *Appl. Radiat. Isot.* **1993**, *44*, 835-842.
180. Hammadi, A.; Crouzel, C., *J. Label. Comp. Radiopharm.* **1993**, *33*, 703-710.
181. Angelini, G.; Speranza, M.; Shiue, C.Y.; Wolf, A.P., *J. Chem. Soc. Chem. Comm.* **1986**, 924-925.

182. Bock, L.; Schultheiß, S.K.; Maschauer, S.; Lasch, R.; Gradl, S.; Prante, O.; Zard, S.Z.; Heinrich, M.R., *Eur. J. Org. Chem.* **2021**, 2021, 6258-6262.
183. Turkman, N.; Liu, D.; Pirola, I., *Sci. Rep.* **2021**, 11, 10668-10678.
184. Prabhakaran, J.; Underwood, M.D.; Parsey, R.V.; Arango, V.; Majo, V.J.; Simpson, N.R.; Van Heertum, R.; Mann, J.J.; Kumar, J.S.D., *Bioorg. Med. Chem.* **2007**, 15, 1802-1807.
185. Chang, C.-P.; Huang, H.-L.; Huang, J.-K.; Hung, M.-S.; Wu, C.-H.; Song, J.-S.; Lee, C.-J.; Yu, C.-S.; Shia, K.-S., *Bioorg. Med. Chem.* **2019**, 27, 216-223.
186. Verhoog, S.; Pfeifer, L.; Khotavivattana, T.; Calderwood, S.; Collier, T.L.; Wheelhouse, K.; Tredwell, M.; Gouverneur, V., *Synlett* **2016**, 27, 25-28.
187. Khotavivattana, T.; Verhoog, S.; Tredwell, M.; Pfeifer, L.; Calderwood, S.; Wheelhouse, K.; Lee Collier, T.; Gouverneur, V., *Angew. Chem. Int. Ed.* **2015**, 54, 9991-9995.
188. Gómez, A.B.; Cortés González, M.A.; Lübcke, M.; Johansson, M.J.; Halldin, C.; Szabó, K.J.; Schou, M., *Chem. Commun.* **2016**, 52, 13963-13966.
189. Meyer, D.N.; Cortés González, M.A.; Jiang, X.; Johansson-Holm, L.; Pourghasemi Lati, M.; Elgland, M.; Nordeman, P.; Antoni, G.; Szabó, K.J., *Chem. Commun.* **2021**, 57, 8476-8479.
190. Josse, O.; Labar, D.; Georges, B.; Grégoire, V.; Marchand-Brynaert, J., *Bioorg. Med. Chem.* **2001**, 9, 665-675.
191. Cheguillaume, A.; Gillart, J.; Labar, D.; Grégoire, V.; Marchand-Brynaert, J., *Bioorg. Med. Chem.* **2005**, 13, 1357-1367.
192. Johnström, P.; Stone-Elander, S., *J. Label. Comp. Radiopharm.* **1995**, 36, 537-547.
193. van der Born, D.; Herscheid, J.D.M.; Orru, R.V.A.; Vugts, D.J., *Chem. Commun.* **2013**, 49, 4018-4020.
194. Pees, A.; Vosjan, M.J.W.D.; Vasdev, N.; Windhorst, A.D.; Vugts, D.J., *Chem. Commun.* **2021**, 57, 5286-5289.
195. Ivashkin, P.; Lemonnier, G.; Cousin, J.; Grégoire, V.; Labar, D.; Jubault, P.; Pannecoucke, X., *Chem. Eur. J.* **2014**, 20, 9514-9518.
196. Yang, B.Y.; Telu, S.; Haskali, M.B.; Morse, C.L.; Pike, V.W., *Sci. Rep.* **2019**, 9, 14835-14845.
197. Li, G.B.; Zhang, C.; Song, C.; Ma, Y.D., *Beilstein J. Org. Chem.* **2018**, 14, 155-181.
198. Huiban, M.; Tredwell, M.; Mizuta, S.; Wan, Z.; Zhang, X.; Collier, T.L.; Gouverneur, V.; Passchier, J., *Nat. Chem.* **2013**, 5, 941-944.
199. King, A.; Doepner, A.; Turton, D.; Ciobota, D.M.; Da Pieve, C.; Wong Te Fong, A.-C.; Kramer-Marek, G.; Chung, Y.-L.; Smith, G., *Org. Biomol. Chem.* **2018**, 16, 2986-2996.
200. Fu, Z.; Lin, Q.; Hu, B.; Zhang, Y.; Chen, W.; Zhu, J.; Zhao, Y.; Choi, H.S.; Shi, H.; Cheng, D., *J. Nucl. Med.* **2019**, 60, 930-936.
201. Kee, C.W.; Tack, O.; Guibbal, F.; Wilson, T.C.; Isenegger, P.G.; Imiołek, M.; Verhoog, S.; Tilby, M.; Boscutti, G.; Ashworth, S.; Chupin, J.; Kashani, R.; Poh, A.W.J.; Sosabowski, J.K.; Macholl, S.; Plisson, C.; Cornelissen, B.; Willis, M.C.; Passchier, J.; Davis, B.G.; Gouverneur, V., *J. Am. Chem. Soc.* **2020**, 142, 1180-1185.
202. Verhoog, S.; Kee, C.W.; Wang, Y.; Khotavivattana, T.; Wilson, T.C.; Kersemans, V.; Smart, S.; Tredwell, M.; Davis, B.G.; Gouverneur, V., *J. Am. Chem. Soc.* **2018**, 140, 1572-1575.

203. Zheng, J.; Wang, L.; Lin, J.-H.; Xiao, J.C.; Liang, S.H., *Angew. Chem. Int. Ed.* **2015**, *54*, 13236-13240.
204. Zheng, J.; Cheng, R.; Lin, J.-H.; Yu, D.-H.; Ma, L.; Jia, L.; Zhang, L.; Wang, L.; Xiao, J.-C.; Liang, S.H., *Angew. Chem. Int. Ed.* **2017**, *56*, 3196-3200.
205. Kilbourn, M.R.; Subramanian, R., *J. Label. Comp. Radiopharm.* **1990**, *28*, 1355-1361.
206. Aigbirhio, F.I.; Pike, V.W.; Waters, S.L.; Makepeace, J.; Tanner, R.J.N., *J. Chem. Soc. Chem. Comm.* **1993**, 1064-1065.
207. Satter, M.R.; Martin, C.C.; Oakes, T.R.; Christian, B.F.; Nickles, R.J., *Appl. Radiat. Isot.* **1994**, *45*, 1093-1100.
208. Ido, T.; Irie, T.; Kasida, Y., *J. Label. Comp. Radiopharm.* **1979**, *16*, 153-154.
209. Gens, T.A.; Wethongton, J.A.; Brosi, A.R., *J. Phys. Chem.* **1958**, *62*, 1593-1593.
210. Poole, R.T.; Winfield, J.M., *J. Chem. Soc. Dalton Trans.* **1976**, 1557-1560.
211. Bernard-Gauthier, V.; Bailey, J.J.; Liu, Z.; Wängler, B.; Wängler, C.; Jurkschat, K.; Perrin, D.M.; Schirmmayer, R., *Bioconjugate Chem.* **2016**, *27*, 267-279.
212. Fersing, C.; Bouhlef, A.; Cantelli, C.; Garrigue, P.; Lisowski, V.; Guillet, B., *Molecules.* **2019**, *24*, 2866-2907.
213. Rosenthal, M.S.; Bosch, A.L.; Nickles, R.J.; Gatley, S.J., *Int. J. Appl. Radiat. Isot.* **1985**, *36*, 318-319.
214. Ting, R.; Adam, M.J.; Ruth, T.J.; Perrin, D.M., *J. Am. Chem. Soc.* **2005**, *127*, 13094-13095.
215. Schirmmayer, R.; Bradtmöller, G.; Schirmmayer, E.; Thews, O.; Tillmanns, J.; Siessmeier, T.; Buchholz, H.G.; Bartenstein, P.; Wängler, B.; Niemeyer, C.M.; Jurkschat, K., *Angew. Chem. Int. Ed.* **2006**, *45*, 6047-6050.
216. Choudhry, U.; Martin, K.E.; Biagini, S.; Blower, P.J., *Nucl. Med. Commun.* **2006**, *27*, 293-293.
217. Höhne, A.; Yu, L.; Mu, L.; Reiher, M.; Voigtmann, U.; Klar, U.; Graham, K.; Schubiger, P.A.; Ametamey, S.M., *Chem. Eur. J.* **2009**, *15*, 3736-3743.
218. Bernard-Gauthier, V.; Wängler, C.; Schirmmayer, E.; Kostikov, A.; Jurkschat, K.; Wängler, B.; Schirmmayer, R., *Biomed. Res. Int.* **2014**, *2014*, 454503-454523
219. Askenasy, H.M.; Laor, Y.; Anbar, M.; Lewitus, Z.; Kosary, I.Z.; Guttmann, S., *Am. J. Roentgenology* **1962**, *88*, 350-354.
220. Entzian, W.; Aronow, S.; Soloway, A.H.; Sweet, W.H., *J. Nucl. Med.* **1964**, *5*, 542-550.
221. Perrin, D.M., *Acc. Chem. Res.* **2016**, *49*, 1333-1343.
222. Li, Z.; Chansaenpak, K.; Liu, S.; Wade, C.R.; Conti, P.S.; Gabbaie, F.P., *Medchemcomm.* **2012**, *3*, 1305-1308.
223. Liu, Z.; Lin, K.-S.; Benard, F.; Pourghiasian, M.; Kiesewetter, D.O.; Perrin, D.M.; Chen, X., *Nat. Protoc.* **2015**, *10*, 1423-1432.
224. Ting, R.; Harwig, C.W.; Lo, J.; Li, Y.; Adam, M.J.; Ruth, T.J.; Perrin, D.M., *J. Org. Chem.* **2008**, *73*, 4662-4670.
225. Liu, Z.; Chao, D.; Li, Y.; Ting, R.; Oh, J.; Perrin, D.M., *Chem. Eur. J.* **2015**, *21*, 3924-3928.

226. Liu, Z.B.; Pourghiasian, M.; Radtke, M.A.; Lau, J.; Pan, J.H.; Dias, G.M.; Yapp, D.; Lin, K.S.; Benard, F.; Perrin, D.M., *Angew. Chem. Int. Ed.* **2014**, *53*, 11876-11880.
227. Farkas, E.; Fodor, T.; Kalman, F.K.; Tircso, G.; Toth, I., *React. Kinet. Mech. Cat.* **2015**, *116*, 19-33.
228. Nemes, J.; Toth, I.; Zekany, L., *J. Chem. Soc. Dalton Trans.* **1998**, 2707-2713.
229. Martin, R.B., *Biochem. Bioph. Res. Co.* **1988**, *155*, 1194-1200.
230. Allott, L.; Da Pieve, C.; Turton, D.R.; Smith, G., *React. Chem. Eng.* **2017**, *2*, 68-74.
231. Laverman, P.; McBride, W.J.; Sharkey, R.M.; Eek, A.; Joosten, L.; Oyen, W.J.G.; Goldenberg, D.M.; Boerman, O.C., *J. Nucl. Med.* **2010**, *51*, 454-461.
232. Andre, J.P.; Macke, H.; Kaspar, A.; Kunnecke, B.; Zehnder, M.; Macko, L., *J. Inorg. Biochem.* **2002**, *88*, 1-6.
233. Martin, R.B., *Coordin. Chem. Rev.* **1996**, *149*, 23-32.
234. Smith, G.E.; Sladen, H.L.; Biagini, S.C.G.; Blower, P.J., *Dalton. Trans.* **2011**, *40*, 6196-6205.
235. Antonny, B.; Chabre, M., *J. Bio. Chem.* **1992**, *267*, 6710-6718.
236. Li, L., *Crit. Rev. Oral. Biol. M.* **2003**, *14*, 100-114.
237. Scheinberg, D.A.; Strand, M.; Gansow, O.A., *Science* **1982**, *215*, 1511-1513.
238. McBride, W.J.; Sharkey, R.M.; Karacay, H.; D'Souza, C.A.; Rossi, E.A.; Laverman, P.; Chang, C.H.; Boerman, O.C.; Goldenberg, D.M., *J. Nucl. Med.* **2009**, *50*, 991-998.
239. D'Souza, C.A.; McBride, W.J.; Sharkey, R.M.; Todaro, L.J.; Goldenberg, D.M., *Bioconjugate Chem.* **2011**, *22*, 1793-1803.
240. Litau, S.; Niedermoser, S.; Vogler, N.; Roscher, M.; Schirmacher, R.; Fricker, G.; Wängler, B.; Wängler, C., *Bioconjugate Chem.* **2015**, *26*, 2350-2359.
241. Niedermoser, S.; Chin, J.; Wängler, C.; Kostikov, A.; Bernard-Gauthier, V.; Vogler, N.; Soucy, J.P.; McEwan, A.J.; Schirmacher, R.; Wängler, B., *J. Nucl. Med.* **2015**, *56*, 1100-1105.
242. Ilhan, H.; Lindner, S.; Todica, A.; Cyran, C.C.; Tiling, R.; Auernhammer, C.J.; Spitzweg, C.; Boeck, S.; Unterrainer, M.; Gildehaus, F.J.; Böning, G.; Jurkschat, K.; Wängler, C.; Wängler, B.; Schirmacher, R.; Bartenstein, P., *Eur. J. Nucl. Med. Mol. Imaging.* **2020**, *47*, 870-880.
243. Lindner, S.; Wängler, C.; Bailey, J.J.; Jurkschat, K.; Bartenstein, P.; Wängler, B.; Schirmacher, R., *Nat. Protoc.* **2020**, *15*, 3827-3843.
244. Wängler, C.; Niedermoser, S.; Chin, J.; Orchowski, K.; Schirmacher, E.; Jurkschat, K.; Iovkova-Berends, L.; Kostikov, A.P.; Schirmacher, R.; Wängler, B., *Nat. Protoc.* **2012**, *7*, 1946-1955.
245. Liu, Z.; Pourghiasian, M.; Benard, F.; Pan, J.; Lin, K.S.; Perrin, D.M., *J. Nucl. Med.* **2014**, *55*, 1499-1505.
246. Lau, J.; Pan, J.; Rousseau, E.; Uribe, C.F.; Seelam, S.R.; Sutherland, B.W.; Perrin, D.M.; Lin, K.S.; Bénard, F., *EJNMMI Res.* **2020**, *10*, 25-35.
247. Dialer, L.O.; Selivanova, S.V.; Muller, C.J.; Muller, A.; Stellfeld, T.; Graham, K.; Dinkelborg, L.M.; Kramer, S.D.; Schibli, R.; Reiher, M.; Ametamey, S.M., *J. Med. Chem.* **2013**, *56*, 7552-7563.

248. Höhne, A.; Mu, L.; Honer, M.; Schubiger, P.A.; Ametamey, S.M.; Graham, K.; Stellfeld, T.; Borkowski, S.; Berndorff, D.; Klar, U.; Voigtmann, U.; Cyr, J.E.; Friebe, M.; Dinkelborg, L.; Srinivasan, A., *Bioconjug. Chem.* **2008**, *19*, 1871-1879.
249. Lindner, S.; Michler, C.; Leidner, S.; Rensch, C.; Wängler, C.; Schirmacher, R.; Bartenstein, P.; Wängler, B., *Bioconjugate Chem.* **2014**, *25*, 738-749.
250. Ley, K.; Rivera-Nieves, J.; Sandborn, W.J.; Shattil, S., *Nat. Rev. Drug Discov.* **2016**, *15*, 173-183.
251. Debordeaux, F.; Chansel-Debordeaux, L.; Pinaquy, J.B.; Fernandez, P.; Schulz, J., *Nucl. Med. Biol.* **2018**, *62-63*, 31-46.
252. Li, Y.; Liu, Z.B.; Lozada, J.; Wong, M.Q.; Lin, K.S.; Yapp, D.; Perrin, D.M., *Nucl. Med. Biol.* **2013**, *40*, 959-966.
253. Li, Y.; Liu, Z.B.; Wang, M.; Lozada, J.; Lin, K.S.; Yapp, D.; Benard, F.; Perrin, D., *Biopolymers* **2013**, *100*, 242-242.
254. Liu, Z.B.; Li, Y.; Lozada, J.; Wong, M.Q.; Greene, J.; Lin, K.S.; Yapp, D.; Perrin, D.M., *Nucl. Med. Biol.* **2013**, *40*, 841-849.
255. Liu, S.L.; Liu, H.G.; Jiang, H.; Xu, Y.D.; Zhang, H.; Cheng, Z., *Eur. J. Nucl. Med. Mol. Imaging.* **2011**, *38*, 1732-1741.
256. Ferlay, J.; Colombet, M.; Soerjomataram, I.; Dyba, T.; Randi, G.; Bettio, M.; Gavin, A.; Visser, O.; Bray, F., *Eur. J. Cancer* **2018**, *103*, 356-387.
257. Mazaris, E.; Tsiotras, A., *Nephrourol Mon.* **2013**, *5*, 792-800.
258. Saini, S., *Cell. Oncol. (Dordr.)* **2016**, *39*, 97-106.
259. Turkbey, B.; Albert, P.S.; Kurdziel, K.; Choyke, P.L., *Am. J. Roentgenol.* **2009**, *192*, 1471-1480.
260. Horoszewicz, J.S.; Kawinski, E.; Murphy, G.P., *Anticancer Res.* **1987**, *7*, 927-935.
261. Kawakami, M.; Nakayama, J., *Cancer Res.* **1997**, *57*, 2321-2324.
262. Bostwick, D.G.; Pacelli, A.; Blute, M.; Roche, P.; Murphy, G.P., *Cancer* **1998**, *82*, 2256-2261.
263. Wüstemann, T.; Haberkorn, U.; Babich, J.; Mier, W., *Med. Res. Rev.* **2019**, *39*, 40-69.
264. Eiber, M.; Fendler, W.P.; Rowe, S.P.; Calais, J.; Hofman, M.S.; Maurer, T.; Schwarzenboeck, S.M.; Kratochwil, C.; Herrmann, K.; Giesel, F.L., *J. Nucl. Med.* **2017**, *58*, 67-76.
265. Liu, H.; Rajasekaran, A.K.; Moy, P.; Xia, Y.; Kim, S.; Navarro, V.; Rahmati, R.; Bander, N.H., *Cancer Res.* **1998**, *58*, 4055-4060.
266. Backhaus, P.; Noto, B.; Avramovic, N.; Grubert, L.S.; Huss, S.; Bögemann, M.; Stegger, L.; Weckesser, M.; Schäfers, M.; Rahbar, K., *Eur. J. Nucl. Med. Mol. Imaging.* **2018**, *45*, 860-877.
267. Silver, D.A.; Pellicer, I.; Fair, W.R.; Heston, W.D.; Cordon-Cardo, C., *Clin. Cancer. Res.* **1997**, *3*, 81-85.
268. Bařinka, C.; Rovenska, M.; Mlochova, P.; Hlouchova, K.; Plechanovova, A.; Majer, P.; Tsukamoto, T.; Slusher, B.S.; Konvalinka, J.; Lubkowski, J., *J. Med. Chem.* **2007**, *50*, 3267-3273.
269. Tilleux, S.; Hermans, E., *J. Neurosci. Res.* **2007**, *85*, 2059-2070.
270. Zhou, J.; Neale, J.H.; Pomper, M.G.; Kozikowski, A.P., *Nat. Rev. Drug Discov.* **2005**, *4*, 1015-1026.

271. Neels, O.C.; Kopka, K.; Liolios, C.; Afshar-Oromieh, A., *Cancer* **2021**, *13*, 6255-6279.
272. Malik, N.; Zlatopolskiy, B.; Machulla, H.-J.; Reske, S.N.; Solbach, C., *J. Label. Comp. Radiopharm.* **2012**, *55*, 320-325.
273. Liu, T.L.; Liu, C.; Xu, X.X.; Liu, F.; Guo, X.Y.; Li, N.; Wang, X.J.; Yang, J.H.; Yang, X.; Zhu, H.; Yang, Z., *J. Nucl. Med.* **2019**, *60*, 1284-1292.
274. Kuo, H.T.; Lepage, M.; Lin, K.S.; Pan, J.; Zhang, Z.; Liu, Z.; Pryyma, A.; Zhang, C.; Merckens, H.; Roxin, A.; Perrin, D.; Benard, F., *J. Nucl. Med.* **2019**, *60*, 1160-1166.
275. Lepage, M.L.; Kuo, H.-T.; Roxin, Á.; Huh, S.; Zhang, Z.; Kandasamy, R.; Merckens, H.; Kumlin, J.O.; Limoges, A.; Zeisler, S.K.; Lin, K.-S.; Bénard, F.; Perrin, D.M., *Chembiochem.* **2020**, *21*, 943-947.
276. Shende, P.; Gandhi, S., *J. Drug Deliv. Sci. Technol.* **2021**, *64*, 102594-102604.
277. Wurzer, A.; Di Carlo, D.; Schmidt, A.; Beck, R.; Eiber, M.; Schwaiger, M.; Wester, H.J., *J. Nucl. Med.* **2020**, *61*, 735-742.
278. Wurzer, A.; Di Carlo, D.; Herz, M.; Richter, A.; Robu, S.; Schirrmacher, R.; Mascarin, A.; Weber, W.; Eiber, M.; Schwaiger, M.; Wester, H.-J., *EJNMMI Radiopharm. Chem.* **2021**, *6*, 4-19.
279. Wurzer, A.; Parzinger, M.; Konrad, M.; Beck, R.; Günther, T.; Felber, V.; Färber, S.; Di Carlo, D.; Wester, H.-J., *EJNMMI Res.* **2020**, *10*, 149-159.
280. Langbein, T.; Wang, H.; Rauscher, I.; Krönke, M.; Knorr, K.; Wurzer, A.; Schwamborn, K.; Maurer, T.; Horn, T.; Haller, B.; Wester, H.J.; Eiber, M., *J. Nucl. Med.* **2022**, *63*, 263440-263469.
281. Bailey, J.J.; Wuest, M.; Wagner, M.; Bhardwaj, A.; Wängler, C.; Wängler, B.; Valliant, J.F.; Schirrmacher, R.; Wuest, F., *J. Med. Chem.* **2021**, *64*, 15671-15689.
282. Iovkova, L.; Wangler, B.; Schirrmacher, E.; Schirrmacher, R.; Quandt, G.; Boening, G.; Schurmann, M.; Jurkschat, K., *Chem. Eur. J.* **2009**, *15*, 2140-2147.
283. McAtee, R.C.; Beatty, J.W.; McAtee, C.C.; Stephenson, C.R.J., *Org. Lett.* **2018**, *20*, 3491-3495.
284. Bermejo Góme, A.; González, M.A.C.; Lübcke, M.; Johansson, M.J.; Schou, M.; Szabó, K.J., *J. F. Chem.* **2017**, *194*, 51-57.
285. Saito, K.; Umi, T.; Yamada, T.; Suga, T.; Akiyama, T., *Org. Biomol. Chem.* **2017**, *15*, 1767-1770.
286. Yang, H.-M.; Liu, M.-L.; Tu, J.-W.; Miura-Stempel, E.; Campbell, M.G.; Chuang, G.J., *J. Org. Chem.* **2020**, *85*, 2040-2047.
287. Zhou, N.; Wang, L.; Thompson, D.W.; Zhao, Y., *Org. Lett.* **2008**, *10*, 3001-3004.

Appendix

A.1 Procedures and Characterization (Chapter 2)

A.1.1 General Considerations

Reactions were performed in glass test-tubes (16x100mm) that were fitted with a stir bar and rubber septum, and then flame-dried under high vacuum. Solid reagents were weighed directly into the test tube, via temporary removal of the septum. Reactions were kept under a static dry nitrogen atmosphere, and all liquid reagent additions were performed using standard Schlenk techniques. Dichloromethane (DCM) was obtained from a LC Technology Solutions SP-1 solvent purification system. Nitromethane was stored over CaH₂ and distilled under nitrogen prior to use. All other reagents were obtained commercially and used without additional purification. Temperature control was achieved using a Neslab CryoCool (CC-65) immersion cooler, or an ice bath for 0 °C.

GC-MS spectra were obtained using a Bruker Scion TQ 456 System. HRMS spectra were obtained from a Kratos Analytical MS50G EI-MS. FTIR spectra were obtained using a Thermo Nicolet 8700 with an attached continuum microscope. HPLC purification was performed using an Agilent 1260 preparatory system, with a C8 Zorbax column (PrepHT, 21.2 x 150 mm, 7 μm). NMR spectra were obtained using one of the following Varian (Agilent) spectrometers: MR DD2 400 MHz, VNMRS 500 MHz, VNMRS 600 MHz, VNMRS 700 MHz.

NMR chemical shifts (δ) are reported in ppm, and are referenced to residual protonated solvent in ¹H NMR (7.26 ppm for CHCl₃), deuterated solvent in ¹³C NMR (77.06 ppm for CDCl₃), or internal standard in ¹⁹F NMR (-161.64 ppm for C₆F₆ in CDCl₃) or (-119.5 ppm for *p*-FPhCH₃ in DCM/CDCl₃). Coupling constants (*J*) are reported in Hertz (Hz). The following splitting pattern abbreviations are used: *doublet* (d), *triplet* (t), *quartet* (q), *doublet of triplets* (dt), *triplet of doublets* (td), *multiplet* (m), *apparent* (app.), *broad* (br). Carbon multiplicities were determined from HSQC, using the following abbreviations: C = *no attached hydrogens*, CH = *one attached hydrogen*, CH₂ = *two attached hydrogens*, CH₃ = *three attached hydrogens*.

Reaction conversions calculated from ¹⁹F NMR spectra are reported to one decimal place. To validate this level of precision, a general baseline deviation error was calculated based on integration values of the baseline. Three spectral regions (3000 Hz): left of peaks, center of the spectra, and right of the peaks, were evaluated in four different representative ¹⁹F NMR experiments (with *internal standard integral* = 100). The average baseline error was calculated to be $6.6 \pm 2.2 \times 10^{-4}$ integration per Hz, with no significant difference between the spectra examined (ANOVA, *p* = 0.163). When applied to the ArCF₂Br peak, this translates to an error of $0.12 \pm 0.04\%$ for ArCF₂Br conversion.

Using this higher level of precision for ¹⁹F NMR derived conversions was deemed beneficial for use in DOE analysis, in particular, due to the presence of many low value numbers. It is readily

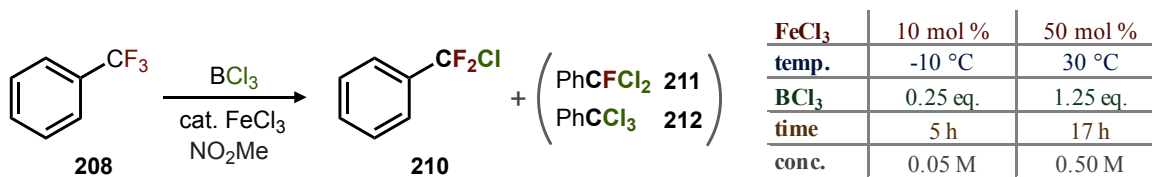
acknowledged that workup procedures (separate from NMR precision), likely produce an additional 1-2% error. Nevertheless, the combined effects of these errors were small enough (or systematic enough) to provide good fits for the DOE analysis.

DOE experiments were created and analyzed using Minitab 19 software. In the DOE models described below, the reagent amounts shown in brackets correspond to the high and low values of the model. Model fitting utilized stepwise regression, in which terms were added to maintain a hierarchy at each step. In other words, if a higher order term (i.e. T²) is included, then so is the respective lower order term (i.e. T). Standard R² and R²-adjusted analyses were performed, as well as a leave-one-out analysis (referred to as R²-predicted), which is calculated as follows.

$$R^2(\text{pred}) = 1 - \frac{\text{PRESS}}{\text{SS Total}} = 1 - \frac{\sum_{i=1}^n \left(\frac{e_i}{1-h_i} \right)^2}{\sum_{i=1}^n (y_i - \bar{y})^2}$$

y_i = i^{th} observed response value
 \bar{y} = mean response
 n = number of observations
 e_i = i^{th} residual
 h_i = i^{th} diagonal element of $X(X'X)^{-1}X'$
 X = design matrix

A.1.2 Chloro-Halex Optimization



Scheme A.1. Design for the chloro-halex DOE

A 5-factor *Fractional Factorial* DOE (2⁵⁻¹) was performed (with 4 center points), followed by augmentation with 10 axial points ($\alpha = 1.2$), forming a *Response Surface Design*. Reaction vessels were charged with ferric chloride (5 mg, 50 mg), nitromethane (1.25 mL, 12.3 mL), and α,α,α -trifluorotoluene **208** (75.5 μ L, 0.615 mmol). After adjusting the mixture to the target temperature, boron trichloride (1M in DCM) was added (155 μ L, 770 μ L). Additional DCM was added (615 μ L) such that the total DCM volume was equal to 770 μ L. After the target reaction time, C₆F₆ was added directly to the mixture (20 μ L). An aliquot was taken and combined with equal parts CDCl₃ in an NMR tube. Immediate analysis with ¹⁹F NMR showed PhCF₃ **208** (-62.8 ppm), PhCF₂Cl **210** (-48.6 ppm) and PhCFCl₂ **211** (-52.6 ppm), which were quantified relative to the C₆F₆ internal standard (-161.6 ppm). DOE regression analysis was performed using stepwise regression ($\alpha=0.05$).

Table A.1. Raw data and statistical analysis for the chloro-halex DOE

Raw Data

FeCl ₃ (%)	temp. (°C)	BCl ₃ (eq.)	time (h)	conc. (M)	CF ₂ Cl (%)	FeCl ₃ (mol)	temp. (°C)	BCl ₃ (eq.)	time (h)	conc. (M)	CF ₂ Cl (%)
5.0	-10	0.25	5	0.50	0.6	50.0	30	0.25	17	0.05	0.7
50.0	-10	0.25	5	0.05	0.0	5.0	-10	1.25	17	0.50	8.3
5.0	30	0.25	5	0.05	0.0	50.0	-10	1.25	17	0.05	1.5
50.0	30	0.25	5	0.50	1.2	5.0	30	1.25	17	0.05	4.3
5.0	-10	1.25	5	0.05	0.0	50.0	30	1.25	17	0.50	0.0
50.0	-10	1.25	5	0.50	7.0	0.5	10	0.75	11	0.28	8.6
5.0	30	1.25	5	0.50	0.0	54.5	10	0.75	11	0.28	11.3
50.0	30	1.25	5	0.05	7.9	27.5	-14	0.75	11	0.28	0.6
5.0	-10	0.25	17	0.05	0.0	27.5	34	0.75	11	0.28	0.4
50.0	-10	0.25	17	0.50	5.6	27.5	10	0.15	11	0.28	4.0
5.0	30	0.25	17	0.50	1.5	27.5	10	1.35	11	0.28	14.7
27.5	10	0.75	11	0.28	15.1	27.5	10	0.75	3.8	0.28	8.2
27.5	10	0.75	11	0.28	14.4	27.5	10	0.75	18.2	0.28	13.5
27.5	10	0.75	11	0.28	14.0	27.5	10	0.75	11	0.00	0.4
27.5	10	0.75	11	0.28	13.6	27.5	10	0.75	11	0.55	3.1

Analysis of Variance

Source	DF	Adj SS	Adj MS	F _{value}	P _{value}
Model	10	830.9	83.1	27.6	0.000
Blocks	1	94.3	94.3	31.4	0.000
Linear	5	82.4	16.5	5.5	0.003
FeCl ₃	1	8.1	8.1	2.7	0.117
temp	1	3.1	3.1	1.0	0.323
BCl ₃	1	55.0	55.0	18.3	0.000
time	1	6.9	6.9	2.3	0.147
conc	1	9.2	9.2	3.1	0.096
Square	2	642.5	321.2	106.9	0.000
temp*temp	1	235.0	235.0	78.2	0.000
conc*conc	1	175.0	175.0	58.2	0.000
2-Way	2	86.6	43.3	14.4	0.000
FeCl ₃ *time	1	29.5	29.5	9.8	0.005
temp*conc	1	57.1	57.1	19.0	0.000
Error	19	57.1	3.0		
Lack-of-Fit	16	55.8	3.5	8.1	0.055
Pure Error	3	1.3	0.4		
Total	29	888.1			

Coded Coefficients

Term	Coef	SE _{coeff}	T _{value}	P _{value}
Constant	12.17	0.559	21.8	0.000
FeCl ₃ (A)	0.66	0.399	1.64	0.117
temp (B)	-0.41	0.399	-1.02	0.323
BCl ₃ (C)	1.71	0.399	4.28	0.000
time (D)	0.60	0.399	1.51	0.147
conc (E)	0.70	0.399	1.75	0.096
temp*temp	-6.45	0.729	-8.84	0.000
conc*conc	-5.56	0.729	-7.63	0.000
FeCl ₃ *time	-1.36	0.433	-3.13	0.005
temp*conc	-1.89	0.433	-4.36	0.000

Regression Parameters

S	R ²	R ² (adj)	R ² (pred)
1.73	94%	90%	85%

Regression Equation

$$CF_2Cl = -7.1 + 0.14A + 0.42B + 3.4C - 0.38D + 68E - 0.016B^2 - 110E^2 - 0.010AD - 0.42BE$$

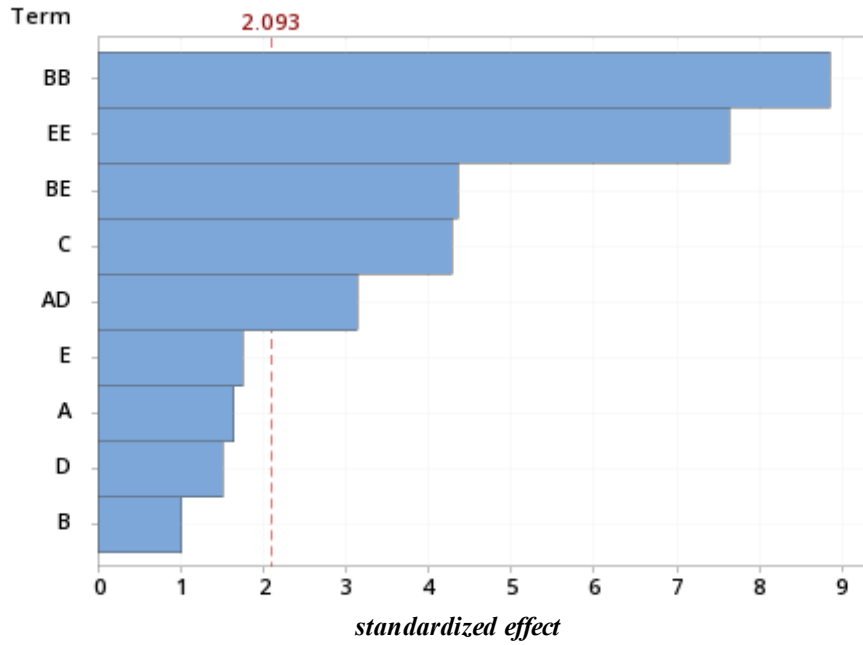


Figure A.1. Full Pareto chart for the chloro-halex DOE

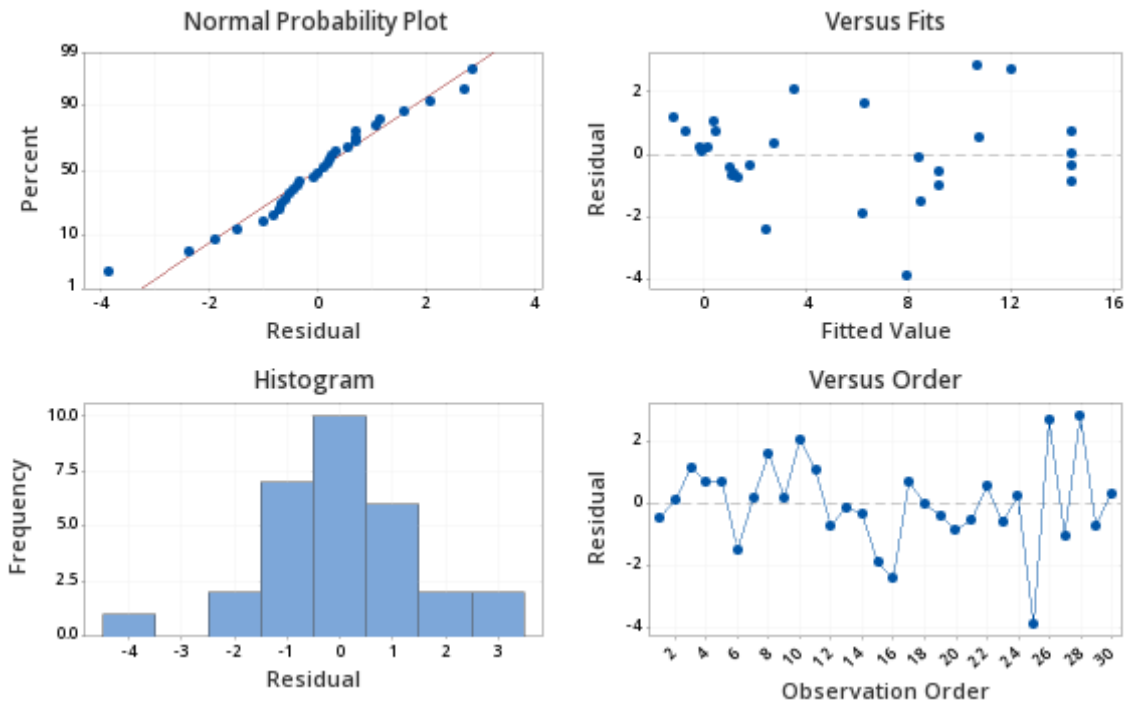
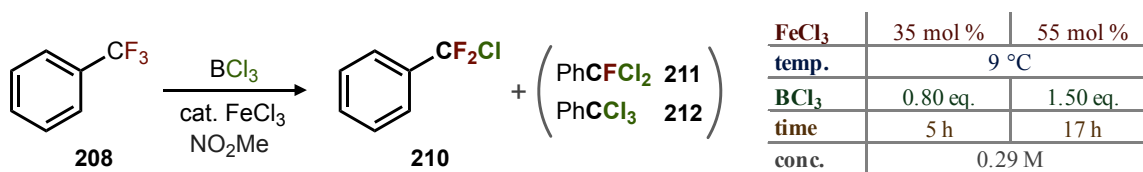


Figure A.2. Residual plots for the chloro-halex DOE



Scheme A.2. Design for the chloro-halex DOE II

A 3-factor *Response Surface* DOE was performed (4 center points, axial points at $\alpha = 1.63$). Vessels were charged with ferric chloride (44.0 mg, 69.0 mg), nitromethane (2.65 mL), and α,α,α -trifluorotoluene **208** (95 μ L, 0.77 mmol). After adjusting the mixture to the 9 °C, boron trichloride (1M in DCM) was added (620 μ L, 1160 μ L). Additional DCM was added (710 μ L, 170 μ L) such that the total DCM volume was equal to 1330 μ L. After the desired time, the mixture was slowly quenched by adding a few drops of water. The mixture was transferred to a separatory funnel containing sat. NaHCO₃ solution (15 mL), brine (15 mL) and DCM (20 mL). The test tube was rinsed forward with 5 mL water and 10 mL DCM. The DCM layer was removed, and the aqueous layer washed with additional DCM (20 mL). The combined organic layers were then filtered through a bed of Na₂SO₄, into a beaker, followed by the addition of 100 μ L of 4-fluorotoluene. After stirring well, an aliquot was taken and combined with equal parts CDCl₃ in an NMR tube. Analysis with ¹⁹F NMR showed PhCF₃ **208** (−62.8 ppm), PhCF₂Cl **210** (−48.6 ppm) and PhCFCl₂ **211** (−52.6 ppm), quantified relative to the 4-fluorotoluene internal standard (−119.5 ppm). Regression analysis was performed using stepwise regression ($\alpha=0.05$), in which terms were added to maintain a hierarchical model at each step.

Table A.2. Raw data and statistical analysis for the chloro-halex DOE II

Raw Data

FeCl ₃ (%)	temp. (°C)	BCl ₃ (eq.)	time (h)	conc. (M)	CF ₂ Cl (%)	FeCl ₃ (%)	temp. (°C)	BCl ₃ (eq.)	time (h)	conc. (M)	CF ₂ Cl (%)
35.0	9	0.8	7.0	0.29	16.3	45.0	9	1.2	11.0	0.29	13.8
55.0		0.8	7.0		14.3	45.0		1.2	11.0		13.0
35.0		1.5	7.0		12.2	28.7		1.2	11.0		15.7
55.0		1.5	7.0		14.8	61.3		1.2	11.0		8.3
35.0		0.8	15.0		11.6	45.0		0.6	11.0		15.2
55.0		0.8	15.0		1.6	45.0		1.7	11.0		13.7
35.0		1.5	15.0		9.4	45.0		1.2	4.5		17.8
55.0		1.5	15.0		5.2	45.0		1.2	17.5		1.2
45.0		1.2	11.0		13.5	45.0		1.2	11.0		11.8
45.0		1.2	11.0		14.3	45.0		1.2	11.0		15.5

Analysis of Variance

Source	DF	Adj ss	Adj MS	Fvalue	Pvalue
Model	7	386.1	55.2	30.5	0.000
Linear	3	294.0	98.0	54.3	0.000
FeCl ₃	1	49.5	49.5	27.4	0.000
BCl ₃	1	1.6	1.6	0.9	0.362
time	1	242.9	242.9	134.5	0.000
Square	2	51.3	25.6	14.2	0.001
FeCl ₃ *FeCl ₃	1	10.2	10.2	5.6	0.035
time*time	1	43.7	43.7	24.2	0.000
2-Way	2	40.9	20.5	11.3	0.002
FeCl ₃ *BCl ₃	1	13.5	13.5	7.5	0.018
FeCl ₃ *time	1	27.4	27.4	15.2	0.002
Error	12	21.7	1.8		
Lack-of-Fit	8	13.9	1.7	0.9	0.585
Pure Error	4	7.7	1.9		
Total	19	407.8			

Coded Coefficients

Term	Coef	SE _{coeff}	Tvalue	Pvalue
Constant	13.8	0.468	29.4	0.000
FeCl ₃ (A)	-1.93	0.368	-5.23	0.000
BCl ₃ (B)	-0.35	0.368	-0.95	0.362
time (C)	-4.27	0.368	-11.6	0.000
FeCl ₃ *FeCl ₃	-0.88	0.369	-2.37	0.035
time*time	-1.81	0.369	-4.92	0.000
FeCl ₃ *BCl ₃	1.30	0.475	2.74	0.018
FeCl ₃ *time	-1.85	0.475	-3.89	0.002

Regression Parameters

S	R ²	R ² (adj)	R ² (pred)
1.34	95%	92%	81%

Regression Equation

$$CF_2Cl = 0.20 + 0.68A + 18B + 3.5C - 0.11C^2 - 0.0088A^2 + 0.37AB - 0.046AC$$

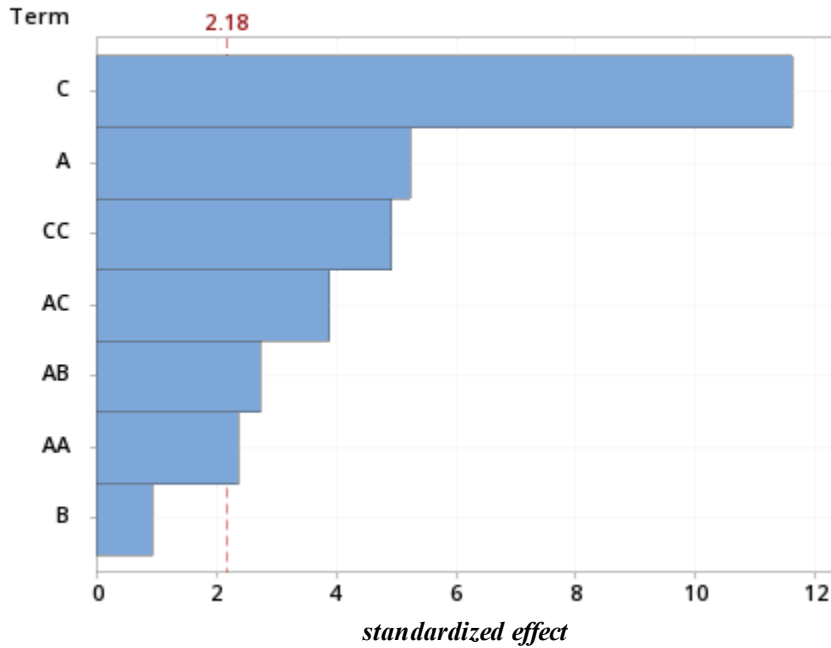


Figure A.3. Full Pareto chart for the chloro-halex DOE II

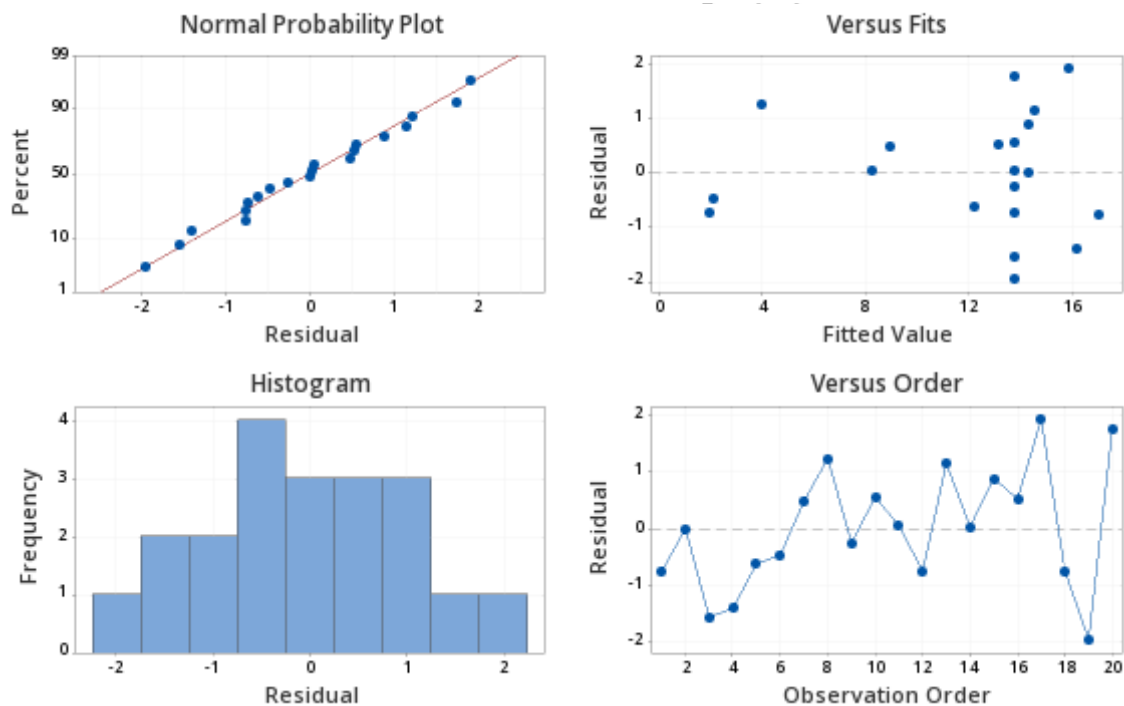
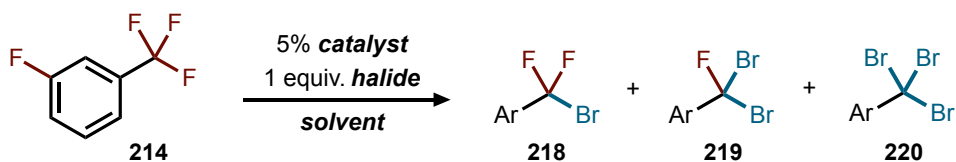


Figure A.4. Residual plots for the chloro-halex DOE II



Figure A.5. Representative images of the chloro-halex reaction

A.1.3 Bromo-Halex Optimization



Scheme A.3. Bromo-halex reaction screening investigations

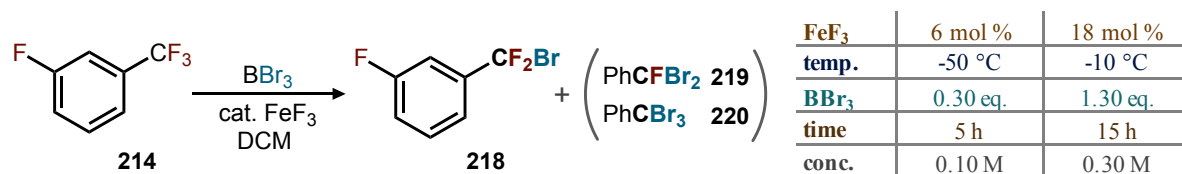
Reaction vessels were charged with the metal catalyst (0.05 mmol), followed by the reaction solvent (5 mL, 0.2M) and 3-fluoro(trifluoromethyl)benzene **214** (126 μ L, 1.00 mmol). The boryl halide reagent was slowly added, and the mixture stirred at the target temperature for the designated time. The mixture

was quenched by adding 2–3 mL DCM and a few drops of water (fuming observed). The mixture was then transferred to a separatory funnel containing saturated aqueous NaHCO₃ (20 mL), brine (20 mL) and DCM (20 mL). The test tube was rinsed-forward with 15 mL water and 15 mL DCM. The DCM layer was removed, and the aqueous layer washed with additional DCM (20 mL). The combined organic layers were then filtered through a bed of Na₂SO₄ into a beaker, followed by a DCM wash. The internal standard (100 μ L 4-fluorotoluene) was then added to the beaker, and the solution was stirred well, before an aliquot was taken and combined with equal parts CDCl₃ in an NMR tube. Analysis with ¹⁹F NMR showed ArCF₃ **214** (–63.3 ppm CF₃, –111.5 ppm ^mF), ArCF₂Br **218** (–44.5 ppm CF₂, –111.5 ppm ^mF), ArCFBr₂ **219** (–54.4 ppm CF, –111.8 ppm ^mF) and ArCBr₃ **220** (–112.5 ppm ^mF) which were quantified relative to the 4-fluorotoluene internal standard (–119.5 ppm).

Table A.3. Reaction details for bromo-halex screening investigations

	temp	time	solvent	metal catalyst		boryl halide			¹⁹ F NMR Conv. (%)				C-F _{total}
				reagent	amount	reagent	mmol	amount	214	218	219	220	
1	20 °C	5 h	DCM	-	-	BBr ₃	1.0	96.5 μ L	89.3	7.1	0.1	0.0	7
2	20 °C	5 h	DCM	AgBr	9.4 mg	BBr ₃	1.0	96.5 μ L	87.7	7.6	0.7	0.0	9
3	20 °C	5 h	DCM	CuI	9.5 mg	BBr ₃	1.0	96.5 μ L	88.2	7.3	0.5	0.0	8
4	20 °C	5 h	DCM	Fe(CO) ₅	6.6 μ L	BBr ₃	1.0	96.5 μ L	88.7	7.3	0.5	0.0	8
5	20 °C	5 h	DCM	FeCl ₂	6.3 mg	BBr ₃	1.0	96.5 μ L	81.2	5.9	0.7	0.0	7
6	20 °C	5 h	DCM	FeCl ₃	8.1 mg	BBr ₃	1.0	96.5 μ L	4.3	3.8	0.3	89.2	272
7	20 °C	5 h	DCM	FeBr ₃	14.8 mg	BBr ₃	1.0	96.5 μ L	7.3	6.1	0.9	82.6	256
8	20 °C	5 h	DCM	FeF ₃	5.6 mg	BBr ₃	1.0	96.5 μ L	5.5	4.7	0.5	83.1	255
9	20 °C	5 h	DCM	Fe(OTf) ₃	25.2 mg	BBr ₃	1.0	96.5 μ L	0.8	0.5	0.5	90.6	273
10	20 °C	5 h	DCM	Ga(OTf) ₃	25.8 mg	BBr ₃	1.0	96.5 μ L	1.5	0.3	0.0	82.9	249
11	20 °C	5 h	heptane	FeF ₃	5.6 mg	BBr ₃	1.0	96.5 μ L	92.5	0.9	0.0	0.0	1
12	20 °C	5 h	PhCl	FeF ₃	5.6 mg	BBr ₃	1.0	96.5 μ L	82.8	14.1	3.2	2.3	27
13	20 °C	5 h	MeNO ₂	FeF ₃	5.6 mg	BBr ₃	1.0	96.5 μ L	96.7	0.0	0.0	0.0	0
14	20 °C	5 h	DCM	FeF ₃	5.6 mg	Me ₂ BBr	3.0	293 μ L	42.5	20.8	1.0	35.2	128
15	20 °C	5 h	DCM	FeF ₃	5.6 mg	(cat)BBr ^b	3.0	596 mg	92.8	0.7	0.0	0.0	1
16	20 °C	14 h	DCM	FeF ₃	11.3 mg	BBr ₃	1.5	145 μ L	0.0	0.0	0.0	94.6	284
17	-10 °C	5 h	DCM	FeF ₃	5.6 mg	BBr ₃	1.0	96.5 μ L	83.8	11.8	1.5	0.0	15

^[a] C-F_{total} = [CF₂Br] + 2×[CFBr₂] + 3×[CBr₃] ^[b] B-bromocatechol borane.



Scheme A.4. Design for the bromo-halex DOE

A 5-factor *Fractional Factorial* DOE (2^{5-1}) was performed (3 center points). Reaction vessels were charged with ferric fluoride (4.3 mg, 12.9 mg), DCM (2.1 mL, 6.4 mL), and 3-fluoro(trifluoromethyl)benzene **214** (80 μ L, 0.63 mmol). The mixture was placed in a -78 °C bath, before the addition of boron tribromide (18.5 μ L, 79.5 μ L). The mixture was transferred to a bath at the target reaction temperature. After the desired reaction time, the mixture was quenched by adding 2–3 mL DCM and a few drops of water (fuming is expected). The mixture was then slowly transferred to a separatory funnel containing saturated NaHCO₃ solution (15 mL), brine (15 mL) and DCM (20 mL). The test tube was rinsed forward with 5 mL water and 10 mL DCM. The DCM layer was removed, and the aqueous layer washed with additional DCM (20 mL). The combined organic layers were then filtered through a bed of NaSO₄, into a beaker, followed by the addition of 100 μ L of 4-fluorotoluene. The solution was stirred well, before an aliquot was taken and combined with equal parts CDCl₃ in an NMR tube. Analysis with ¹⁹F NMR showed ArCF₃ **214** (-63.2 ppm CF₃, -111.5 ppm ^mF), ArCF₂Br **218** (-44.5 ppm CF₂, -111.5 ppm ^mF), ArCFBr₂ **219** (-54.4 ppm CF, -111.8 ppm ^mF) and ArCBr₃ **220** (-112.5 ppm ^mF) which were quantified relative to the 4-fluorotoluene internal standard (-119.5 ppm). DOE regression analysis was performed using stepwise regression ($\alpha=0.05$), in which terms were added to maintain a hierarchical model at each step.

Table A.4. Raw data and statistical analysis for the bromo-halex DOE

Raw Data

FeF₃ (%)	temp. (°C)	BBr₃ (eq.)	time (h)	conc. (M)	CF₂Br (%)	FeF₃ (%)	temp. (°C)	BBr₃ (eq.)	time (h)	conc. (M)	CF₂Br (%)
6	-50	0.3	5	0.30	0.6	6	-10	0.3	15.0	0.30	22.3
18	-50	0.3	5	0.10	0.9	18	-10	0.3	15.0	0.10	11.0
6	-10	0.3	5	0.10	1.7	6	-50	1.3	15.0	0.30	5.2
18	-10	0.3	5	0.30	8.4	18	-50	1.3	15.0	0.10	7.5
6	-50	1.3	5	0.10	1.4	6	-10	1.3	15.0	0.10	24.2
18	-50	1.3	5	0.30	2.1	18	-10	1.3	15.0	0.30	18.7
6	-10	1.3	5	0.30	14.5	12	-30	0.8	10.0	0.20	3.7
18	-10	1.3	5	0.10	12.4	12	-30	0.8	10.0	0.20	4.0
6	-50	0.3	15	0.10	0.3	12	-30	0.8	10.0	0.20	4.7
18	-50	0.3	15	0.30	1.5						

Analysis of Variance

Source	DF	Adj ss	Adj MS	Fvalue	Pvalue
Model	6	896.4	149.4	13.63	0.000
Linear	4	805.6	201.4	18.37	0.000
temp	1	548.7	548.7	50.06	0.000
BBr ₃	1	96.5	96.5	8.81	0.012
time	1	148.2	148.2	13.52	0.003
conc.	1	12.1	12.1	1.10	0.315
2-Way	2	90.8	45.4	4.14	0.043
temp*time	1	55.1	55.1	5.03	0.045
BBr ₃ *conc.	1	35.7	35.7	3.26	0.096
Error	12	131.5	11.0		
Curvature	1	43.7	43.7	5.48	0.039
Lack-of-Fit	9	87.3	9.70	36.82	0.027
Pure Error	2	0.53	0.26		
Total	18	1028			

Coded Coefficients

Term	Coef	SE _{coeff}	Tvalue	Pvalue
Constant	7.64	0.8	10.1	0.000
FeF ₃ (A)	-	-	-	-
temp (B)	5.86	0.8	7.1	0.000
BBr ₃ (C)	2.46	0.8	3.0	0.012
time (D)	3.04	0.8	3.7	0.003
conc (E)	0.87	0.8	1.1	0.315
temp*time	1.86	0.8	2.2	0.045
BBr ₃ *conc	-1.49	0.8	-1.8	0.096

Statistical Summary

S	R ²	R ² _(adj)	R ² _(pred)
3.31	87%	81%	68%

Regression Equation

$$\text{ArCF}_2\text{Br} = -5.7 + 0.11\mathbf{B} + 11\mathbf{C} + 1.2\mathbf{D} + 33\mathbf{E} - 0.019\mathbf{BD} - 30\mathbf{CE}$$

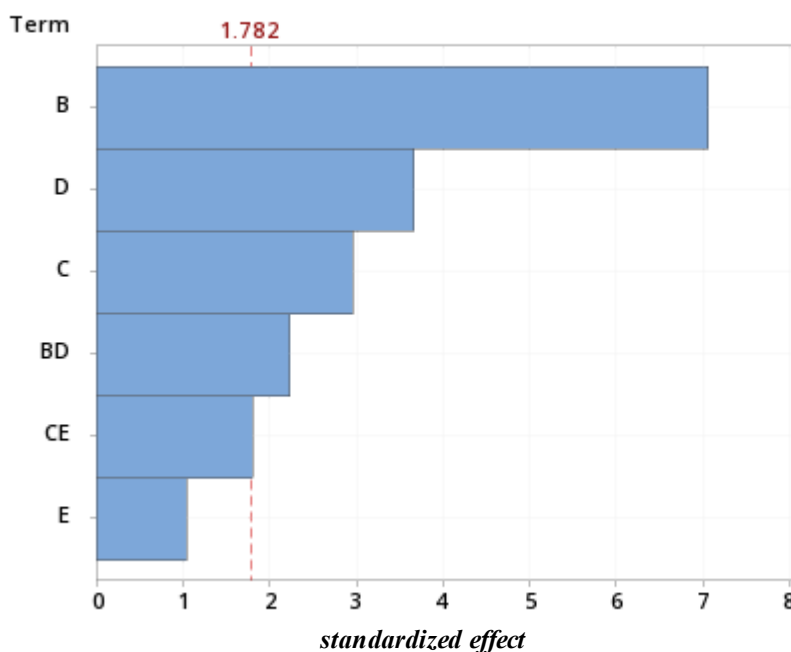


Figure A.6. Full Pareto chart for the bromo-halex DOE

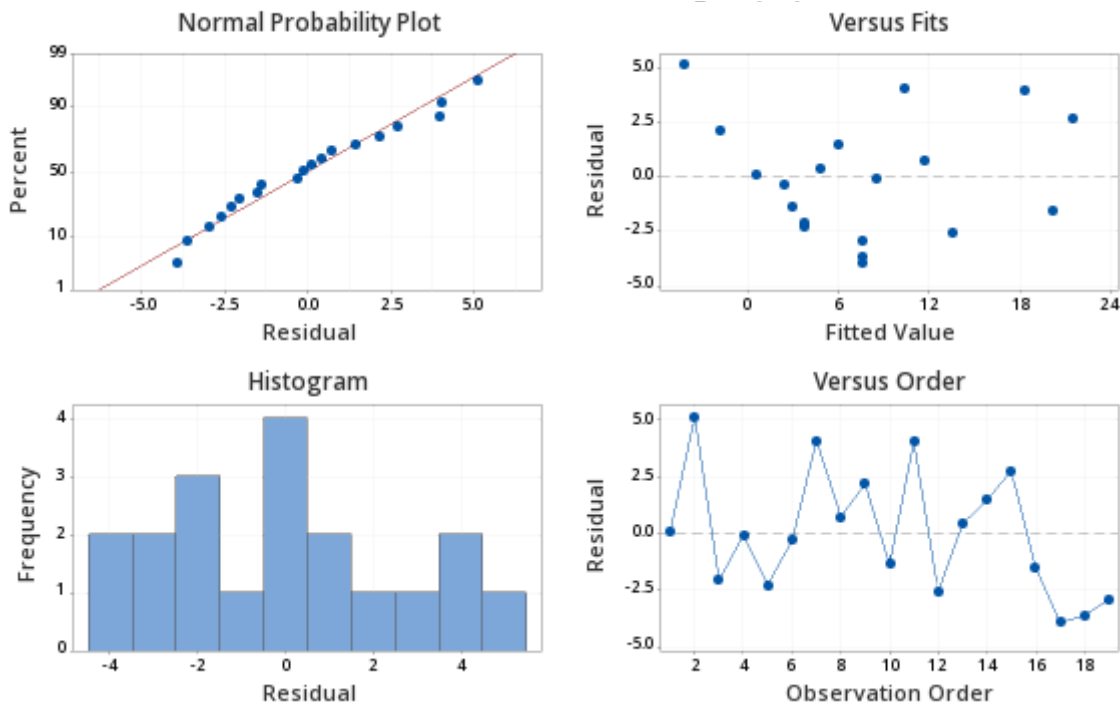
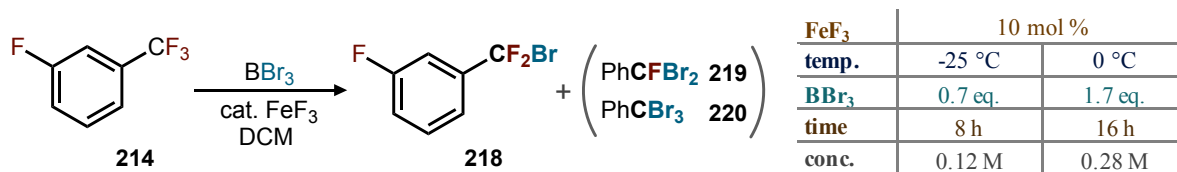


Figure A.7. Residual plots for the bromo-halex DOE



Scheme A.5. Design for the bromo-halex DOE II

A 4-factor *Response Surface* DOE was performed (4 center points, axial points at $\alpha = 1.5$). Reaction vessels were charged with ferric fluoride (7.2 mg), DCM (2.3 mL, 5.3 mL), and 3-fluoro(trifluoromethyl)benzene **214** (80 μL , 0.63 mmol). The mixture was placed in a $-78\text{ }^\circ\text{C}$ bath, before the addition of boron tribromide (43 μL , 104 μL). The mixture was transferred to a bath at the target reaction temperature. After the desired reaction time, the mixture was quenched by adding 2–3 mL DCM and a few drops of water (fuming is expected). The mixture was then slowly transferred to a separatory funnel containing saturated NaHCO_3 solution (15 mL), brine (15 mL) and DCM (20 mL). The test tube was rinsed forward with 5 mL water and 10 mL DCM. The DCM layer was removed, and the aqueous layer washed with additional DCM (20 mL). The combined organic layers were then filtered through a bed of NaSO_4 , into a beaker, followed by the addition of 100 μL of 4-fluorotoluene. The solution was stirred well, before an aliquot was taken and combined with equal parts CDCl_3 in an NMR tube. Analysis with ^{19}F NMR showed ArCF_3 **214** (-63.3 ppm CF_3 , -111.5 ppm ${}^m\text{F}$), ArCF_2Br

218 (–44.5 ppm CF₂, –111.5 ppm ^mF), ArCFBr₂ **219** (–54.4 ppm CF, –111.8 ppm ^mF) and ArCBr₃ **220** (–112.5 ppm ^mF) which were quantified relative to the 4-fluorotoluene internal standard (–119.5 ppm). DOE regression analysis was performed using stepwise regression ($\alpha=0.15$).

Table A.5. Raw data and statistical analysis for the bromo-halex DOE II

Raw Data

FeF ₃ (%)	temp. (°C)	BBr ₃ (eq.)	time (h)	conc. (M)	CF ₂ Br (%)
10	-25	0.70	8	0.12	1.9
	0	0.70	8	0.12	20.4
	-25	1.70	8	0.12	4.7
	0	1.70	8	0.12	13.1
	-25	0.70	16	0.12	1.6
	0	0.70	16	0.12	18.3
	-25	1.70	16	0.12	5.2
	0	1.70	16	0.12	0.1
	-13	1.20	6	0.20	9.7
	-13	1.20	18	0.20	22.4
	-13	1.20	12	0.08	13.8
	-13	1.20	12	0.32	20.6
	-13	1.20	12	0.20	18.8
	-13	1.20	12	0.20	20.7

FeF ₃ (%)	temp. (°C)	BBr ₃ (eq.)	time (h)	conc. (M)	CF ₂ Br (%)
10	-25	0.70	8	0.28	5.3
	0	0.70	8	0.28	20.1
	-25	1.70	8	0.28	c
	0	1.70	8	0.28	15.6
	-25	0.70	16	0.28	5.5
	0	0.70	16	0.28	17.7
	-25	1.70	16	0.28	11.9
	0	1.70	16	0.28	13.5
	-31	1.20	12	0.20	4.1
	6	1.20	12	0.20	2.4
	-13	0.45	12	0.20	15.8
	-13	1.95	12	0.20	18.2
	-13	1.20	12	0.20	17.2
	-13	1.20	12	0.20	20.4

Analysis of Variance

Source	DF	Adj SS	Adj MS	F _{value}	P _{value}
Model	7	1084.5	154.9	9.29	0.000
Linear	4	365.8	91.4	5.49	0.004
temp	1	270.4	270.4	16.22	0.001
BBr ₃	1	14.8	14.8	0.89	0.358
time	1	1.8	1.8	0.11	0.747
conc.	1	78.8	78.8	4.73	0.042
Square	1	535.4	535.4	32.12	0.000
temp*temp	1	535.4	535.4	32.12	0.000
2-Way	2	183.3	91.7	5.5	0.013
temp*BBr ₃	1	140.4	140.4	8.42	0.009
temp*time	1	42.9	42.9	2.57	0.124
Error	20	333.4	16.7		
Lack-of-Fit	17	325.6	19.2	7.34	0.063
Pure Error	3	7.8	2.6		
Total	27	1417.9			

Coded Coefficients

Term	Coef	SE _{coef}	T _{value}	P _{value}
Constant	17.4	1.18	14.7	0.000
temp (A)	3.63	0.90	4.03	0.001
BBr ₃ (B)	-0.85	0.90	-0.94	0.358
time (C)	0.30	0.90	0.33	0.747
conc (D)	1.96	0.90	2.17	0.042
temp*temp	-6.94	1.22	-5.67	0.000
temp*BBr ₃	-2.96	1.02	-2.90	0.009
temp*time	-1.64	1.02	-1.60	0.124

Regression Parameters

S	R ²	R ² (adj)	R ² (pred)
4.08	77%	68%	50%

Regression Equation

$$\text{ArCF}_2\text{Br} = 22 + 0.14\text{A} + 7.6\text{B} + 0.34\text{C} + 25\text{D} - 0.044\text{A}^2 - 0.47\text{AB} - 0.033\text{AC}$$

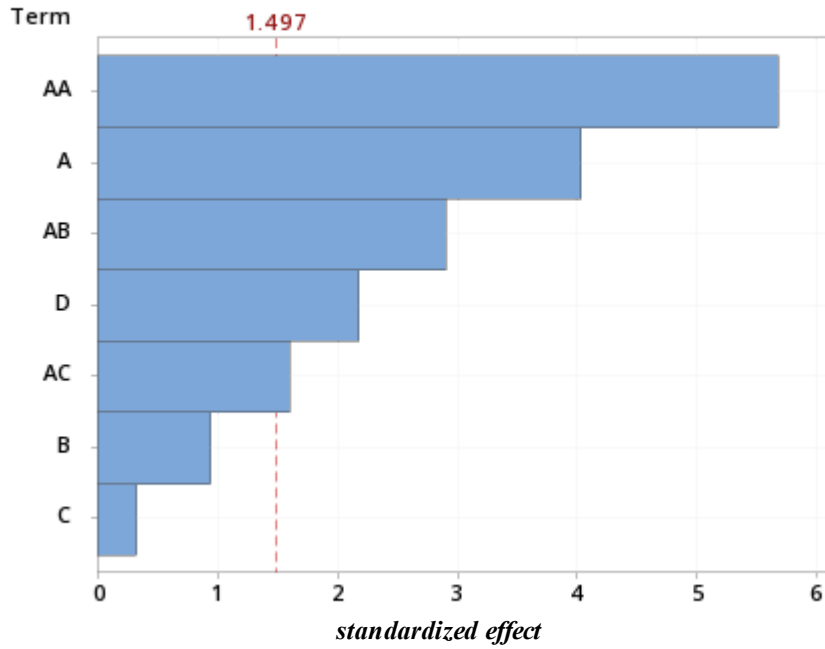


Figure A.8. Full Pareto chart for the bromo-halex DOE II

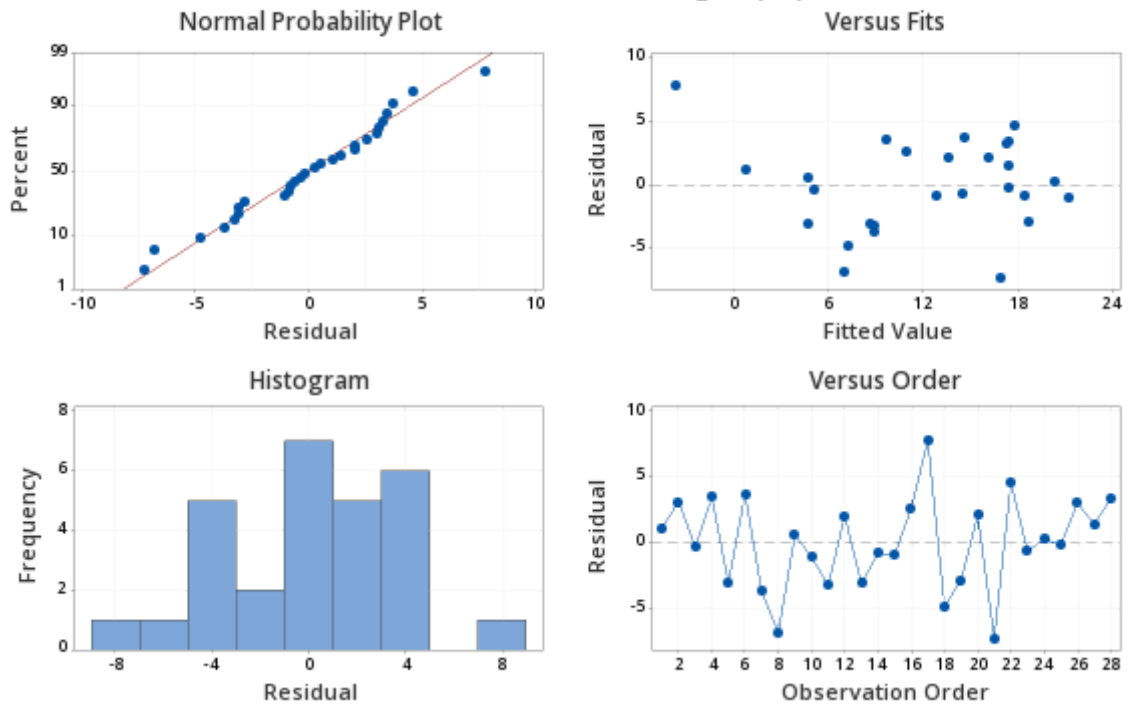


Figure A.9. Residual plots for the bromo-halex DOE II

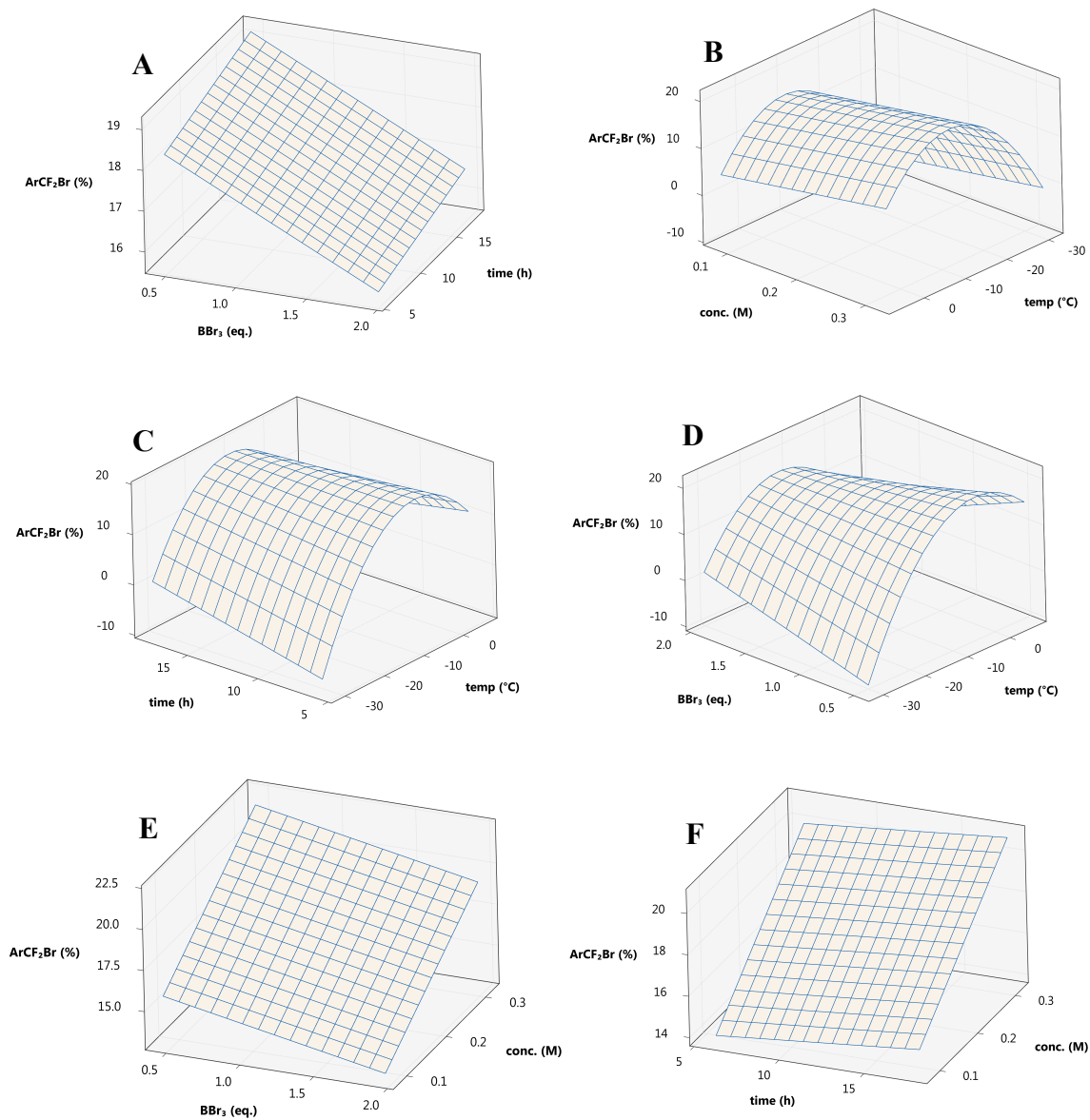


Figure A.10. Complete set of surface plots for bromo-halex DOE II



Figure A.11. Representative images of the bromo-halex reaction

A.1.4 Mono-Halex General Procedure and Scope

The reaction vessel was charged with FeX_3 catalyst, then dry *solvent*. It was adjusted to temperature T , and the $ArCF_3$ reagent was added, followed by BX_3 (three cycles of freeze-thaw-degas included for substrate **232**). After stirring for time t , the mixture was quenched by slow addition of H_2O at $0\text{ }^\circ\text{C}$ (fuming expected). It was transferred to a separatory funnel containing aq. $NaHCO_3$ (15 mL), brine (15mL) and DCM (20 mL). The test tube was rinsed forward with 5 mL H_2O and 10 mL DCM. The DCM layer was removed, and the aqueous washed with additional DCM (20 mL). The combined organics were filtered through Na_2SO_4 , followed by 4-fluorotoluene addition (100 μL). After stirring well, an aliquot was combined with equal parts $CDCl_3$ in an NMR tube. Conversion to $ArCF_2X$ was quantified by ^{19}F NMR spectroscopy (376 MHz), relative to 4-fluorotoluene (-119.5 ppm). Conversion values are the average of a set of duplicate runs.

Table A.6. Experimental details for the synthesis of halodifluoromethyl compounds

product	FeX_3	solvent	$ArCF_3$	BX_3	T	t	conv. (%)	yield	
								mass	(%)
210	75 mg $FeCl_3$ (0.6 eq.)	2.65 mL NO_2Me	95.0 μL (0.77 mmol)	1.3 mL BCl_3 <i>IM in DCM</i> (1.7 eq.)	$9\text{ }^\circ\text{C}$	4.5 h	17%	-	
218	7.2 mg FeF_3 (0.1 eq.)	2.0 mL DCM	80.0 μL (0.63 mmol)	27.5 μL BBr_3 (0.45 eq.)	$-3\text{ }^\circ\text{C}$	6 h	27%	-	
224	4.5 mg FeF_3 (0.1 eq.)	1.25 mL DCM	49.0 μL (0.40 mmol)	17.5 μL BBr_3 (0.45 eq.)	$0\text{ }^\circ\text{C}$	2 h	34%	-	
225	4.5 mg FeF_3 (0.1 eq.)	1.25 mL DCM	56.0 μL (0.40 mmol)	17.5 μL BBr_3 (0.45 eq.)	$0\text{ }^\circ\text{C}$	45 min	25%	-	
226	4.5 mg FeF_3 (0.1 eq.)	1.25 mL DCM	53.5 μL (0.40 mmol)	17.5 μL BBr_3 (0.45 eq.)	$0\text{ }^\circ\text{C}$	18 h	20%	-	
227	4.5 mg FeF_3 (0.1 eq.)	1.25 mL DCM	56.0 μL (0.40 mmol)	17.5 μL BBr_3 (0.45 eq.)	$0\text{ }^\circ\text{C}$	18 h	21%	-	
228	4.5 mg FeF_3 (0.1 eq.)	1.25 mL DCM	50.0 μL (0.40 mmol)	56 μL BBr_3 (1.45 eq.)	$0\text{ }^\circ\text{C}$	2 h	20%	24 mg	12%
229	4.5 mg FeF_3 (0.1 eq.)	1.25 mL DCM	140.5 mg (0.40 mmol)	17.5 μL BBr_3 (0.45 eq.)	$0\text{ }^\circ\text{C}$	24 h	24%	47 mg	14%
230	4.5 mg FeF_3 (0.1 eq.)	1.25 mL DCM	68.0 μL (0.40 mmol)	17.5 μL BBr_3 (0.45 eq.)	$0\text{ }^\circ\text{C}$	2 h	30%	27 mg	11%
234	4.5 mg FeF_3 (0.1 eq.)	1.25 mL DCM	195.5 mg (0.40 mmol)	56 μL BBr_3 (2.45 eq.)	$20\text{ }^\circ\text{C}$	12 h	22%	57 mg	13%
232	20 mg $Fe(OTf)_3$ (0.1 eq.)	1.25 mL DCM	186.5 mg (0.40 mmol)	56 μL BBr_3 (1.45 eq.)	$0\text{ }^\circ\text{C}$	2 h	-	71 mg	17%

Table A.7. Summary of ^{19}F NMR shifts and product distributions for halodifluoromethyl mixtures

		δ (ppm)	conversion (%)					δ (ppm)	conversion (%)		
			run 1	run 2	mean				run 1	run 2	mean
210	ArCF ₃	-63.1	78.7	70.3	74.5	218	ArCF ₃	-63.3, -111.6	43.8	57.3	50.5
	ArCF ₂ X	-48.9	15.9	17.9	16.9		ArCF ₂ X	-44.5, -111.6	28.4	25.2	26.8
	ArCFX ₂	-52.9	3.3	5.0	4.2		ArCFX ₂	-54.5, -112.0	3.9	3.8	3.9
	ArCX ₃	-	-	-	-		ArCX ₃	-112.6	19.6	16.8	18.2
224	ArCF ₃	-63.1	50.5	55.8	53.1	228	ArCF ₃	-62.2, -126.8	48.2	37.2	42.7
	ArCF ₂ X	-43.9	34.6	34.2	34.4		ArCF ₂ X	-45.1, -124.1	22.0	17.3	19.7
	ArCFX ₂	-53.5	2.8	2.3	2.5		ArCFX ₂	-55.4, -119.0	14.1	13.5	13.8
	ArCX ₃	-	-	-	-		ArCX ₃	-112.3	15.3	21.5	18.4
225	ArCF ₃	-62.7	47.5	68.8	58.2	230	ArCF ₃	-62.9	55.5	56.4	55.9
	ArCF ₂ X	-42.9	25.1	24.4	24.7		ArCF ₂ X	-43.6	28.4	31.0	29.7
	ArCFX ₂	-52.5	9.8	5.0	7.4		ArCFX ₂	-53.1	2.5	2.6	2.5
	ArCX ₃	-	-	-	-		ArCX ₃	-	-	-	-
226	ArCF ₃	-63.0	58.0	55.2	56.6	232*	-CF ₃	-63.4	235	252	243
	ArCF ₂ X	-44.2	20.3	20.2	20.2		-CF ₂ X	-44.7	46.8	50.2	48.5
	ArCFX ₂	-	0.0	0.0	0.0		-CFX ₂	-	-	-	-
	ArCX ₃	-	-	-	-		-CX ₃	-	-	-	-
227	ArCF ₃	-63.2	61.2	58.1	59.7	234†	ArCF ₃	-62.7	47.7	47.3	47.5
	ArCF ₂ X	-44.4	21.6	20.9	21.3		ArCF ₂ X	-43.6	22.0	22.5	22.3
	ArCFX ₂	-	0.0	0.0	0.0		ArCFX ₂	-53.7	15.1	15.5	15.3
	ArCX ₃	-	-	-	-		ArCX ₃	-	-	-	-
229	ArCF ₃	-63.6	75.1	66.8	70.9						
	ArCF ₂ X	-46.7	22.7	25.3	24.0						
	ArCFX ₂	-50.1	3.7	6.0	4.8						
	ArCX ₃	-	-	-	-						

* conversions refer to combined total of overlapping or closely-clustered peaks for each CF_x moiety

† species also contain Ar-F peaks (-111.3, -125.5 ppm)

Substrates **210**, **218**, **224**, **225**, **226**, **227** were also analyzed with GC-MS, confirming the presence of ArCF₃, ArCF₂X, ArCFX₂, and ArCX₃ compounds. The synthesis of **218** was scaled-up, and the product isolated by distillation. Duplicate runs (0.40 mmol) for **228**, **229**, **230**, **232**, **234** were combined (0.80 mmol total) before using preparatory reverse-phase HPLC for purification. Spectra typically contained four clustered peaks, also corresponding to the ArCF₃, ArCF₂X, ArCFX₂, and ArCX₃ compounds, allowing for isolation and characterization of the ArCF₂Br product.

Large Scale Synthesis of Compound 218

A flame-dried 50 mL RBF was charged with ferric fluoride (113 mg, 1.0 mmol, 0.10 eq.), followed by dichloromethane (31 mL, 0.32M). The mixture was cooled to 0 °C, and 3-fluoro(trifluoromethyl) benzene **214** was added (1.26 mL, 10.0 mmol), followed by the dropwise addition of BBr₃ (434 μL, 4.5 mmol, 0.45 eq.). After 4 hours, the mixture was diluted with ~10 mL DCM and quenched by adding water dropwise at 0 °C (significant fuming). The mixture was transferred to a separatory funnel containing aq. saturated NaHCO₃ solution (30 mL), brine (30 mL) and DCM (50 mL). The RBF was rinsed forward with 10 mL water and 20 mL DCM. The DCM layer was removed, and the aqueous layer washed with additional DCM (40 mL). The combined organic layers were dried over NaSO₄ and filtered. ¹⁹F NMR revealed the following *relative* product ratio: 50 % *ArCF*₃ (**214**), 24 % *ArCF*₂Br (**218**), 5 % *ArCF*Br₂ (**219**), 21 % *ArC*Br₃ (**220**). The DCM was gently evaporated using a rotovap (T < 20 °C, using mild vacuum). The resulting oil was purified using a Hickman still apparatus, using mild vacuum and heating, affording a high purity (>95%) fraction of **218** (127 mg, 6%).

3-(bromodifluoromethyl)-1-fluoro-benzene (218). Colorless oil. ¹H NMR (CDCl₃, 500 MHz): δ 7.43 (m, 2H), 7.32 (dt, 1H, *J* = 9.0 Hz, 2.5 Hz), 7.19 (t, 1H, *J* = 8.3 Hz) ppm. ¹³C NMR (CDCl₃, 126 MHz): δ 162.3 (C, d, *J*_{CF} = 248.7 Hz), 140.2 (C, td, *J*_{CF} = 24.5 Hz, 7.8 Hz), 130.6 (CH, d, *J*_{CF} = 8.0 Hz), 120.1 (CH, app. q, *J*_{CF} = 13.3 Hz), 118.4 (CH, d, *J*_{CF} = 20.9 Hz), 117.2 (C, td, *J*_{CF} = 303.9 Hz, 2.8 Hz), 112.0 (CH, dt, *J*_{CF} = 24.5 Hz, 5.3 Hz) ppm. ¹⁹F NMR (CDCl₃, 376 MHz): δ -44.1 (s, 2F), -110.6 (m, 1F) ppm. HRMS (EI, C₇H₄F₃Br, M⁺): calcd.: 223.9448, found: 223.9448. FTIR (cast film): 3074, 2925, 2853, 1589, 1483, 1434, 1242, 1135, 700 cm⁻¹.

Identification of Volatile Compounds

Known compounds **210**²⁸³, **224**²³, **225**⁹⁴, **226**²⁹, **227**²⁸⁴ matched their respective reported ¹⁹F NMR spectra. Product identity was verified with GC-MS, which was performed using the following method:

column: Zebron ZB-5MS (30m x 0.25cm), 0.25μm film
injection: 1 μL, (50:1 split)
gradient: 50 °C to 300 °C gradient (20 min). 300 °C (8 min)
mass range: 35 – 500 amu

Isolation of Heavy Compounds

The DCM solution produced after workup was gently concentrated under vacuum. The resulting residue was taken up in 3-5 mL acetonitrile, and divided into 3–6 portions for injection into a preparative-HPLC, allowing for separation of the ArCF₂Br compound from the other components.

method A: 40 min gradient 58% ACN (H₂O) to 66% ACN (H₂O), 30mL/min, C8 column. **(229)**

method B: 30 min gradient 50% ACN (H₂O) to 85% ACN (H₂O), 30mL/min, C8 column. **(230)**

method C: 35 min gradient 78% ACN (H₂O) to 85% ACN (H₂O), 30mL/min, C8 column. **(232)**

method D: 35 min gradient 30% ACN (H₂O) to 50% ACN (H₂O), 30mL/min, C8 column. **(228)**

method E: 40 min gradient 55% ACN (H₂O) to 75% ACN (H₂O), 30mL/min, C8 column. **(234)**

After combining the desired fractions from each injection, the solution was partially concentrated under vacuum to reduce the amount of acetonitrile present. The solution was transferred to a separatory funnel along with DCM (~150 mL) and solid NaCl was then added until the aqueous layer became saturated. The organic phase was separated, and the aqueous layer was washed with additional DCM (2 × 75 mL). The organic layers were combined, dried over NaSO₄ and filtered, then evaporated under vacuum to afford the pure ArCF₂Br compound.

3-(bromodifluoromethyl)-4-fluoro-1-phenol (228). Yellow oil (24 mg, 12%). HPLC (*method D*) R.T. = 17.8 min. ¹H NMR (CDCl₃, 500 MHz): δ 7.05 (t, 1H, *J* = 9.5 Hz), 6.99 (dd, 1H, *J* = 5.8 Hz, 3.1 Hz), 6.93 (dt, 1H, *J* = 8.9 Hz, 3.4 Hz), 4.28 (br. s, 1H). ¹³C NMR (CDCl₃, 126 MHz): δ 152.9 (C, dt, *J*_{CF} = 249.0 Hz, 3.4 Hz), 151.2 (C, d, *J*_{CF} = 2.3 Hz), 126.2 (C, td, *J*_{CF} = 24.6 Hz, 12.4 Hz), 119.8 (CH, d, *J*_{CF} = 8.0 Hz), 118.2 (CH, d, *J*_{CF} = 23.0 Hz), 114.0 (C, td, *J*_{CF} = 303.9 Hz, 2.2 Hz), 111.9 (CH, t, *J*_{CF} = 6.4 Hz) ppm. ¹⁹F NMR (CDCl₃, 376 MHz): δ -44.5 (d, 2F, *J* = 15.0 Hz), -122.8 (m, 1F) ppm. **HRMS** (EI, C₇H₄OF₃Br, M⁺): calcd.: 239.9398, found: 239.9395. **FTIR** (cast film): 3388, 3081, 2930, 2856, 1602, 1503, 1303, 1228, 1109, 952, 836, 774 cm⁻¹.

4-bromo-2-(bromodifluoromethyl)-1-iodobenzene (229). Beige solid (47 mg, 14%). HPLC (*method A*) R.T. = 13.8 min. ¹H NMR (CDCl₃, 700 MHz): δ 7.88 (d, 1H, *J* = 8.4 Hz), 7.75 (d, 1H, *J* = 2.4 Hz), 7.26 (dd, 1H, *J* = 8.4, 2.4 Hz) ppm. ¹³C NMR (CDCl₃, 176 MHz): δ 143.9 (CH), 141.1 (C, t, *J*_{CF} = 23.1 Hz), 135.3 (CH), 128.9 (CH, t, *J*_{CF} = 8.6 Hz), 122.5 (C), 115.9 (C, t, *J*_{CF} = 305.5 Hz), 89.6 (C, t, *J*_{CF} = 2.7 Hz) ppm. ¹⁹F NMR (CDCl₃, 376 MHz): δ -46.3 (s, 2F) ppm. **HRMS** (EI, C₇H₃Br₂F₂I, M⁺): calcd.: 409.7614, found: 409.7613. **FTIR** (cast film): 3090, 2924, 1571, 1551, 1456, 1377, 1275, 1232, 906, 870, 752 cm⁻¹.

1-(bromodifluoromethyl)-4-(2-bromoethyl)-benzene (230). Yellow oil (27 mg, 11%). HPLC (*method B*) R.T. = 11.7 min. $^1\text{H NMR}$ (CDCl_3 , 700 MHz): δ 7.57 (d, 2H, $J = 8.4$ Hz), 7.31 (d, 2H, $J = 8.4$ Hz), 3.58 (t, 2H, $J = 7.4$ Hz), 3.22 (t, 2H, $J = 7.4$ Hz) ppm. $^{13}\text{C NMR}$ (CDCl_3 , 176 MHz): δ 142.4 (C), 136.9 (C, t, $J_{\text{CF}} = 23.7$ Hz), 129.0 (CH), 124.7 (CH, t, $J_{\text{CF}} = 5.0$ Hz), 118.4 (C, t, $J_{\text{CF}} = 303.9$ Hz), 38.9 (CH_2), 32.1 (CH_2) ppm. $^{19}\text{F NMR}$ (CDCl_3 , 376 MHz): δ -43.0 (s, 2F) ppm. **HRMS** (EI, $\text{C}_9\text{H}_8\text{F}_2\text{Br}_2$, M^+): calcd.: 311.8961, found: 311.8954. **FTIR** (cast film): 3043, 3015, 2966, 2852, 1615, 1418, 1277, 1055, 884 cm^{-1} .

4-(bromodifluoromethyl)phenyl bis[4-(trifluoromethyl)phenyl]phosphine (232). Yellow oil (71 mg, 17%). HPLC (*method C*) R.T. = 14.5 min. $^1\text{H NMR}$ (CDCl_3 , 700 MHz): δ 7.64 (d, 4H, $J = 8.0$ Hz), 7.61 (d, 2H, $J = 7.6$ Hz), 7.42 (app. t, 4H, $J_{\text{HH}}, J_{\text{PH}} = 7.6$ Hz), 7.38 (app. t, 2H, $J_{\text{HH}}, J_{\text{PH}} = 7.8$ Hz) ppm. $^{13}\text{C NMR}$ (CDCl_3 , 176 MHz): δ 140.3 (C, d, $J_{\text{CP}} = 14.3$ Hz), 139.7 (C, d, $J_{\text{CP}} = 14.0$ Hz), 139.1 (C, t, $J_{\text{CF}} = 24.0$ Hz), 134.0 (CH, d, $J_{\text{CP}} = 19.9$ Hz), 133.9 (CH, d, $J_{\text{CP}} = 19.9$ Hz), 131.6 (C, q, $J_{\text{CF}} = 32.6$ Hz), 125.7 (CH, dq, $J_{\text{CP}} = 7.3$ Hz, $J_{\text{CF}} = 3.7$ Hz), 124.8 (CH, dt, $J_{\text{CP}} = 7.0$ Hz, $J_{\text{CF}} = 5.0$ Hz), 123.9 (C, q, $J_{\text{CF}} = 272.5$ Hz), 117.9 (C, t, $J_{\text{CF}} = 303.9$ Hz) ppm. $^{19}\text{F NMR}$ (CDCl_3 , 376 MHz): δ -44.2 (s, 2F), -62.9 (s, 6F) ppm. $^{31}\text{P NMR}$ (CDCl_3 , 162 MHz): δ -6.0 (s) ppm. **HRMS** (EI, $\text{C}_{21}\text{H}_{12}\text{BrF}_8\text{P}$, M^+): calcd.: 525.9732, found: 525.9741. **FTIR** (cast film): 3043, 1607, 1398, 1169, 1132, 1017, 889, 701 cm^{-1} .

N-[4-[2-chloro-4-(bromodifluoromethyl)phenoxy]-2-fluorophenyl]aminocarbonyl]-2,6-difluorobenzamide (234). Off-white solid (57 mg, 13%). HPLC (*method E*) R.T. = 20.1 min. $^1\text{H NMR}$ (CDCl_3 , 700 MHz): δ 10.68 (s, 1H), 9.56 (s, 1H), 8.00 (t, 1H, $J = 8.9$ Hz), 7.74 (d, 1H, $J = 2.3$ Hz), 7.51 (tt, 1H, $J = 8.5$ Hz, 6.3 Hz), 7.47 (dd, 1H, $J = 8.6$ Hz, 2.3 Hz), 7.03 (t, 2H, $J = 8.2$ Hz), 6.99 (d, 1H, $J = 8.5$ Hz), 6.85 (dd, 1H, $J = 10.9$ Hz, 2.7 Hz), 6.77 (ddd, 1H, $J = 8.9$ Hz, 2.6 Hz, 1.2 Hz) ppm. $^{13}\text{C NMR}$ (CDCl_3 , 176 MHz): δ 162.1 (C), 160.1 (C, dd, $J_{\text{CF}} = 256.0$, 6.0 Hz), 154.9 (C), 153.5 (C, d, $J_{\text{CF}} = 248.8$ Hz), 152.2 (C, d, $J_{\text{CF}} = 9.8$ Hz), 150.9 (C), 134.5 (C, t, $J_{\text{CF}} = 24.7$ Hz), 133.7 (CH, t, $J_{\text{CF}} = 10.5$ Hz), 127.4 (CH, t, $J_{\text{CF}} = 5.2$ Hz), 125.4 (C), 124.4 (CH, t, $J_{\text{CF}} = 5.1$ Hz), 123.1 (CH, d, $J_{\text{CF}} = 2.0$ Hz), 122.2 (C, d, $J_{\text{CF}} = 10.7$ Hz), 119.1 (CH), 116.9 (C, t, $J_{\text{CF}} = 303.8$ Hz), 114.7 (CH, d, $J_{\text{CF}} = 3.4$ Hz), 112.4 (CH, dd, $J_{\text{CF}} = 21.6$, 3.7 Hz), 112.2 (C, t, $J_{\text{CF}} = 18.1$ Hz), 106.9 (CH, d, $J_{\text{CF}} = 22.4$ Hz) ppm. $^{19}\text{F NMR}$ (CDCl_3 , 376 MHz): δ -43.1 (s, 2F), -110.2 (s, 2F), -124.2 (s, 1F) ppm. **HRMS** (ESI, $\text{C}_{21}\text{H}_{11}\text{BrClF}_5\text{N}_2\text{O}_3$, $(\text{M}+\text{Na})^+$): calcd.: 547.9562, found: 547.9565. **FTIR** (cast film): 3234, 3134, 2966, 1701, 1626, 1599, 1555, 1492, 1289, 1260, 1068, 918, 797 cm^{-1} .

A.1.5 Triple-Halex General Procedure and Scope

A flamed-dried reaction vessel was charged with FeX_3 catalyst, followed by dry *solvent*. It was adjusted to target temperature T , and the $ArCF_3$ reagent was added (1.0 mmol, 1 eq.). The BX_3 reagent was then added, and the mixture stirred for the specified reaction time t .

Table A.8. Experimental details for the synthesis of various trihalomethanes

product	FeX_3	solvent	$ArCF_3$	BX_3	T	t	yield	
							mass	(%)
215	97.5 mg FeCl ₃ (0.6 eq.)	1.0 mL NO ₂ Me	126 μ L	4 mL BCl ₃ (4 eq.)	30 °C	16 h	141 mg	66%
216	32.5 mg FeCl ₃ (0.2 eq.)	1.0 mL NO ₂ Me	140 μ L	4 mL BCl ₃ (4 eq.)	20 °C	3 h	146 mg	70%
220	11.3 mg FeF ₃ (0.1 eq.)	3.1 mL DCM	126 μ L	145 μ L BBr ₃ (1.5 eq.)	20 °C	14 h	307 mg	89%
221	11.3 mg FeF ₃ (0.1 eq.)	3.1 mL DCM	140 μ L	145 μ L BBr ₃ (1.5 eq.)	0 °C	5 h	313 mg	91%
223	11.3 mg FeF ₃ (0.1 eq.)	3.1 mL DCM	147 μ L	145 μ L BBr ₃ (1.5 eq.)	0 °C	1.5 h	133 mg	87%

Isolation of Compounds

The mixture was quenched with H₂O, added dropwise at 0 °C (fuming is expected). It was then transferred to a separatory funnel containing saturated aq. NaHCO₃ (15 mL), brine (15 mL) and DCM (20 mL). The test tube was rinsed forward with 5 mL H₂O and 10 mL DCM. The DCM layer was separated, and the aqueous layer washed with additional DCM (20 mL). The combined organic layers were dried over Na₂SO₄. The solution was concentrated with a rotovap, followed by drying under high vacuum for 1–3 hours. No further purification was required.

3-fluoro-1-(trichloromethyl)benzene (215). Orange-brown oil (141 mg, 66%). ¹H NMR (CDCl₃, 700 MHz): δ 7.73 (dd, 1H, J = 8.1, 1.4 Hz), 7.65 (dt, 1H, J = 10.0, 2.2 Hz), 7.42 (td, 1H, J = 8.2, 5.8 Hz), 7.14 (td, 1H, J = 8.2, 2.2 Hz) ppm. ¹³C NMR (CDCl₃, 176 MHz): δ 162.1 (C, d, J_{CF} = 247.7 Hz), 146.4 (C, d, J_{CF} = 7.6 Hz), 130.1 (CH, d, J_{CF} = 8.1 Hz), 121.3 (CH, d, J_{CF} = 3.1 Hz), 117.4 (CH, d, J_{CF} = 21.3 Hz), 113.3 (CH, d, J_{CF} = 25.2 Hz), 96.3 (C) ppm. ¹⁹F NMR (CDCl₃, 376 MHz): δ -111.3 (d, 1F, J = 6.4 Hz) ppm. HRMS (EI, C₇H₄FCl₃, M⁺): calcd.: 211.9363, found: 211.9360. FTIR (cast film): 3079, 1593, 1487, 1439, 1249, 1141, 809, 777, 752 cm⁻¹.

4-methyl-1-(trichloromethyl)benzene (216). Characterization is consistent with the literature.²⁸⁵ Yellow oil (146 mg, 70%). ¹H NMR (CDCl₃, 700 MHz): δ 7.82 (d, 2H, *J* = 8.6 Hz), 7.23 (d, 2H, *J* = 8.7 Hz), 2.40 (s, 3H) ppm. ¹³C NMR (CDCl₃, 176 MHz): δ 141.7 (CH), 140.7 (CH), 129.0 (CH), 125.5 (CH), 97.8 (C), 21.1 (CH₃) ppm.

3-fluoro-1-(tribromomethyl)benzene (220). Clear orange oil (307 mg, 89%). ¹H NMR (CDCl₃, 700 MHz): δ 7.80 (ddd, 1H, *J* = 8.1, 2.2, 0.8 Hz), 7.73 (dt, 1H, *J* = 10.3, 2.3 Hz), 7.37 (td, 1H, *J* = 8.3, 5.9 Hz), 7.06 (tdd, 1H, *J* = 8.1, 2.5, 0.8 Hz) ppm. ¹³C NMR (CDCl₃, 176 MHz): δ 161.6 (C, d, *J*_{CF} = 247.9 Hz), 149.0 (C, d, *J*_{CF} = 7.6 Hz), 129.6 (CH, d, *J*_{CF} = 7.9 Hz), 122.4 (CH, d, *J*_{CF} = 2.5 Hz), 117.1 (CH, d, *J*_{CF} = 21.0 Hz), 114.3 (CH, d, *J*_{CF} = 25.5 Hz), 33.9 (C, s) ppm. ¹⁹F NMR (CDCl₃, 376 MHz): δ -111.6 (d, 1F, *J* = 7.1 Hz) ppm. HRMS (EI, C₇H₄FBr₃, M⁺): calcd.: 345.7827, found: 345.7823. FTIR (cast film): 3074, 1588, 1483, 1434, 1273, 1242, 1135, 725, 701 cm⁻¹.

4-methyl-1-(tribromomethyl)benzene (221). Characterization is consistent with the literature.⁴² Beige solid (313 mg, 91%). ¹H NMR (CDCl₃, 700 MHz): δ 7.90 (d, 2H, *J* = 8.6 Hz), 7.20 (d, 2H, *J* = 8.3 Hz), 2.41 (s, 3H) ppm. ¹³C NMR (CDCl₃, 176 MHz): δ 144.5 (C), 140.5 (C), 128.6 (CH), 126.4 (CH), 36.2 (C), 21.1 (CH₃) ppm.

Isolation of Compound 223

The mixture was quenched by slowly adding 10 mL of methanol at 0°C, followed by potassium hydroxide (1 g). The mixture was stirred at room temperature for 1 hour, before being concentrated to dryness under vacuum. The resulting residue was taken up in DCM (40 mL) and brine (30 mL), and transferred to a separatory funnel. The mixture was adjusted to ~ pH 4, using 2M HCl. The DCM layer was removed, and the aqueous layer washed with additional DCM (30 mL). The combined organic layers were dried over Na₂SO₄. Removal of the solvent under vacuum afforded compound **223** as a white powder. No further purification was required.

Methyl 4-hydroxybenzoate (223). Characterization is consistent with the literature.²⁸⁶ White solid (133 mg, 87%). ¹H NMR (CDCl₃, 600 MHz): δ 7.94 (d, 2H, *J* = 8.4 Hz), 6.89 (d, 2H, *J* = 8.4 Hz), 6.48 (br. s, 1H), 3.90 (s, 3H). ¹³C NMR (CDCl₃, 151 MHz): δ 167.5, 160.3, 132.0, 122.3, 115.3, 52.1 ppm.

A.1.6 Boryl Iodide Procedures

A flamed-dried reaction vessel was charged with gallium triflate *catalyst*, followed by dry *solvent*. It was adjusted to target temperature *T*, and the *ArCF₃* reagent **237** (5-bromo-2-iodo-trifluoromethylbenzene) was added (1.0 mmol, 1 eq.). The *BI₃* reagent was then added, and the mixture stirred for the specified reaction time *t*.

Table A.9. Experimental details for the boron triiodide reaction

entry	cat.	solvent	ArCF ₃ (237)	BI ₃	<i>T</i>	<i>t</i>	239		240	
							mass	(%)	mass	(%)
1	21 mg Ga(OTf) ₃ (0.1 eq.)	1.6 mL cyclo- hexane (0.25 M)	140.5 mg	52 mg (0.33 eq.)	20 °C	20 h	-	-	-	-
2				165 mg (1.05 eq.)			-	-	-	-
3				196 mg (1.25 eq.)			38 mg	23%	50 mg	40%

After the specified time, the mixture was quenched with H₂O, added dropwise at 0 °C (fuming is expected). It was then transferred to a separatory funnel containing saturated aq. NaHCO₃ (15 mL), brine (15 mL) and hexane (20 mL). The test tube was rinsed forward with 5 mL H₂O and 10 mL hexane. The hexane layer was separated, and washed with a saturated aq. Na₂S₂O₃ solution. The combined aqueous layers were washed with additional hexane (20 mL). The combined organic layers were dried over Na₂SO₄. A small (ca. 0.5 mL) aliquot was taken for GC-MS analysis. The solution was concentrated with a rotovap, followed by drying under high vacuum for 1–3 hours. TLC analysis (1% EtOAc in hexanes) revealed the presence of starting material ArCF₃ **237** (*R_f* = 0.60), ArCF₂I **238** (*R_f* = 0.57), ArCH₂I **239** (*R_f* = 0.40), and ArCHO **240** (*R_f* = 0.07). The mixture in entry 3 was purified using a silica gel column (0% → 5% EtOAc in hexane), affording pure **239** and **240**.

5-bromo-2-(iodomethyl)-1-iodobenzene (239). Off-white solid (38 mg, 23%). ¹H NMR (CDCl₃, 500 MHz): δ 7.65 (d, *J* = 8.0 Hz, 1H), 7.59 (d, *J* = 2.5 Hz, 1H), 7.06 (dd, *J* = 8.5, 2.0 Hz, 1H), 4.47 (s, 2H) ppm. ¹³C NMR (CDCl₃, 126 MHz): δ 143.6, 141.5, 132.6, 132.5, 122.9, 97.7, 10.4 ppm. HRMS (EI, C₇H₅I₂Br, M⁺): calcd.: 421.7664, found: 421.7653.

5-bromo-2-iodo-benzaldehyde (240). Characterization is consistent with the literature.²⁸⁷ Off-white solid (50 mg, 40%). ¹H NMR (CDCl₃, 500 MHz): δ 9.99 (s, 1H), 7.99 (d, *J* = 2.5 Hz, 1H), 7.81 (d, *J* = 8.0 Hz, 1H), 7.41 (dd, *J* = 8.5, 2.5 Hz, 1H) ppm. ¹³C NMR (CDCl₃, 126 MHz): δ 194.3, 141.9, 138.3, 136.4, 133.2, 123.5, 98.3 ppm.

A.2 Procedures and Characterization (Chapter 4)

A.2.1 General Considerations

Moisture-sensitive reactions were performed with oven-dried glassware, while maintaining a static dry argon atmosphere, using purchased anhydrous solvents. Reagents and solvents were obtained commercially and used without additional purification. Flash chromatography was performed using EDM Millipore 60 40–63 μm silica gel. TLC was performed on glass-backed plates of silica 60 F₂₅₄.

NMR spectra were obtained using one of the following Agilent spectrometers: MR DD2 400 MHz, VNMRS 500 MHz, VNMRS 700 MHz. NMR chemical shifts (δ) are reported in ppm, and are referenced to residual protonated solvent in ¹H NMR (7.26 ppm for CHCl₃), deuterated solvent in ¹³C NMR (77.06 ppm for CDCl₃). Coupling constants (*J*) are reported in Hertz (Hz), with abbreviations: *doublet* (d), *triplet* (t), *quartet* (q), *doublet of triplets* (dt), *multiplet* (m), *apparent* (app.), *broad* (br).

HPLC purification was performed using an Agilent 1220 system, with a C18(2) Luna column (10 \times 250 mm, 5 μm , 100 Å), a flowrate of 3 mL/min, and the following solvent mixture (*Method F*):

0–5 min: 70% A \rightarrow 85% A	<i>Solvent A</i> : 0.05% TFA in ACN.
5–35 min: isocratic 85% A	<i>Solvent B</i> : H ₂ O.

A.2.2 PSMA Compounds

The synthesis was performed following the route delineated in reference 281.

Synthesis of Compound 433

Compound **431** (660 mg, 2.2 mmol) was added to a flame-dried RBF, followed by dry diethyl ether (13 mL). The solution was then cooled to -80°C . A 1.7 M *tert*-butyl lithium solution in pentane (2.7 mL, 4.6 mmol, 2.1 eq.) was then slowly added via syringe, and the mixture stirred for 30 minutes at -80°C . This solution was then transferred via cannula to a second RBF containing di(*tert*-butyl)difluorosilane (0.51 g, 2.6 mmol, 1.2 eq.) in diethyl ether (10 mL) at -80°C . The reaction mixture was allowed to warm slowly to room temperature over 12 hours, and was then quenched by via addition of saturated aq. NaCl solution (10 mL). The organic layer was separated and the aqueous layer extracted with diethyl ether (3 \times 25 mL). The combined organic layers were dried over NaSO₄, and then concentrated *in vacuo*, affording a yellowish oil (**432**). This oil was dissolved in methanol (19 mL) and 0.5 mL concentrated HCl was added. The mixture was stirred at room temperature for 21 hours. The mixture was concentrated *in vacuo*, then reconstituted in diethyl ether (20 mL) and washed with a saturated aq. NaHCO₃ (20 mL). The organic layer was separated and the aqueous layer washed with additional ether (3 \times 20 mL). The combined organics were dried over NaSO₄, and then

concentrated *in vacuo*. The resulting oil was dried overnight under high-vacuum, affording **433** as an off-white solid (474 mg, 80 %).

4-(di-tert-butylfluorosilyl)benzyl alcohol. $^1\text{H NMR}$ (CDCl_3 , 400 MHz): δ 7.61 (d, 2H, $J = 7.9$ Hz), 7.34 (d, 2H, $J = 7.9$ Hz), 4.59 (s, 2H), 3.29 (s, 1H), 1.08 (s, 18H) ppm. $^{13}\text{C NMR}$ (CDCl_3 , 126 MHz): δ 142.2, 134.3 (d, $J_{\text{CF}} = 4.4$ Hz), 133.0 (d, $J_{\text{CF}} = 13.8$ Hz), 126.2, 65.2, 27.4, 20.3 (d, $J_{\text{CF}} = 12.2$ Hz) ppm. $^{19}\text{F NMR}$ (CDCl_3 , 469 MHz): δ -188.9 (s, 1F) ppm. Characterization is consistent with the literature.²⁸²

Synthesis of **Compound 434**

SiFA alcohol **433** (1.08 g, 3.95 mmol) was dissolved in dry DCM (20 mL) in an RBF and cooled to 0 °C. A solution of pyridinium chlorochromate (2.15 g, 10.0 mmol, 2.5 eq.) in dry DCM (50 mL) was slowly added, and the mixture stirred for 30 minutes at 0 °C and an additional 2.2 hours at room temperature. The mixture was added to a short silica pad ($\sim 3 \times 8$ cm), and the RBF rinsed with diethyl ether (3×35 mL), which was then added to the silica pad (leaving black gum material remaining). The ether was eluted through the pad, and the resulting solution was concentrated *in vacuo*, affording **434** as a brown solid (1.04 g, 98 %).

4-(di-tert-butylfluorosilyl)benzaldehyde. $^1\text{H NMR}$ (CDCl_3 , 498 MHz): δ 10.04 (s, 1H), 7.88 (d, 2H, $J = 7.8$ Hz), 7.79 (d, 2H, $J = 7.7$ Hz), 1.07 (s, 18H) ppm. $^{13}\text{C NMR}$ (CDCl_3 , 126 MHz): δ 192.5, 142.2 (d, $J_{\text{CF}} = 13.4$ Hz), 137.0, 134.5 (d, $J_{\text{CF}} = 4.4$ Hz), 128.4, 27.2, 20.3 (d, $J_{\text{CF}} = 12.2$ Hz) ppm. Characterization is consistent with the literature.²⁴⁴

Synthesis of **Compound 435**

The SiFA aldehyde **434** (1.04 g, 3.87 mmol) was added to an RBF, and dissolved in *t*-butanol (22.5 mL), DCM (2.5 mL), and 1.25 M $\text{NaH}_2\text{PO}_4 \cdot \text{H}_2\text{O}$ buffer (15 mL). Aqueous 1 M KMnO_4 (22 mL) was then added at room temperature, and the mixture stirred for 25 minutes. It was quenched by the addition of saturated aqueous Na_2SO_3 solution (15 mL), and conc. HCl was then added until the purple color disappeared. The resulting solution was extracted with diethyl ether (3×200 mL), and the combined organic layers dried over NaSO_4 and then concentrated *in vacuo*, to afford **435** as a white solid (0.93 g, 85 %).

4-(di-tert-butylfluorosilyl)benzoic acid. $^1\text{H NMR}$ (CDCl_3 , 400 MHz): δ 8.09 (d, 2H, $J = 8.1$ Hz), 7.74 (d, 2H, $J = 8.1$ Hz), 1.07 (s, 18H) ppm. $^{13}\text{C NMR}$ (CDCl_3 , 101 MHz): δ 172.1, 141.3 (d, $J_{\text{CF}} = 13.7$ Hz), 134.1 (d, $J_{\text{CF}} = 4.4$ Hz), 130.2, 129.0 (d, $J_{\text{CF}} = 1.0$ Hz), 27.3 (d, $J_{\text{CF}} = 1.1$ Hz), 20.3 (d, $J_{\text{CF}} = 12.3$ Hz) ppm. Characterization is consistent with the literature.²⁸²

Synthesis of **Compound 436**

N-hydroxysuccinimide (413 mg, 3.59 mmol, 1.6 eq.) was added to an RBF. A solution of SiFA benzoic acid **435** (628 mg, 2.22 mmol) in DMF (10 mL) was subsequently added, followed by EDCI (538 mg, 2.80 mmol, 1.25 eq.). The reaction was stirred at room temperature for 18 hours. The addition of water (8 mL), led to formation of a precipitate, which was collected by filtration, and rinsed with addition water (10 mL). The filtrate was extracted with diethyl ether (200 mL). The organic layer was washed with saturated NaCl solution (100 mL), then dried over NaSO₄, and concentrated *in vacuo*, to afford **436** as a white shiny solid (584 g, 70 %).

5-dioxopyrrolidin-1-yl 4-(di-tert-butylfluorosilyl)benzoate. ¹H NMR (CDCl₃, 400 MHz): δ 8.13 (d, 2H, *J* = 8.0 Hz), 7.77 (d, 2H, *J* = 8.4 Hz), 2.92 (s, 4H), 1.07 (s, 18H) ppm. ¹³C NMR (CDCl₃, 176 MHz): δ 169.2, 162.0, 142.9 (d, *J*_{CF} = 13.7 Hz), 134.3 (d, *J*_{CF} = 4.2 Hz), 129.2, 126.0, 27.2, 25.7, 20.2 (d, *J*_{CF} = 11.6 Hz) ppm. ¹⁹F NMR (CDCl₃, 376 MHz): δ -188.5 (s, 1F) ppm. Characterization is consistent with the literature.²⁸²

Synthesis of **Compound 438**

SiFA compound **436** (582 mg, 1.54 mmol) was combined with H-L-Asp(O^tBu)-OH **437** (322 mg, 1.69 mmol, 1.1 eq.) in an RBF, along with DMF (19 mL) and DMSO (1 mL). Hünig's base (92 μL, 0.54 mmol, 0.35 eq.) was then slowly added, and the mixture stirred at room temperature for 20 hours. The mixture was concentrated *in vacuo* to circa ½ the original volume. The residual solution was then combined with brine (150 mL) and extracted with DCM (3×150 mL). The combined organics dried over NaSO₄, and concentrated *in vacuo*, to afford a crude yellow oil, which was then purified by column chromatography (2.8×11 cm silica column), using a gradient of 100% hexanes → 100% ethyl acetate. The combined fractions were concentrated *in vacuo*, affording **438** as a white powder (232 mg, 33 %). *R*_F (6% MeOH in DCM) = 0.20.

(S)-4-(tert-butoxy)-2-(4-(di-tert-butylfluorosilyl)benzamido)-4-oxobutanoic acid. ¹H NMR (CDCl₃, 700 MHz): δ 7.80 (d, 2H, *J* = 7.7 Hz), 7.69 (d, 2H, *J* = 7.0 Hz), 7.41 (d, 1H, *J* = 7.0 Hz), 5.07 (app. s, 1H), 3.07 (app. d, 1H, *J* = 14.7 Hz), 2.89 (app. d, 1H, *J* = 16.8 Hz), 1.44 (s, 9H), 1.04 (s, 18H) ppm. ¹³C NMR (CDCl₃, 176 MHz): δ 175.0, 170.7, 167.5, 138.9 (d, *J*_{CF} = 13.4 Hz), 134.3, 134.3 (d, *J*_{CF} = 4.2 Hz), 126.2, 82.3, 49.2, 37.2, 28.0, 27.3, 20.2 (d, *J*_{CF} = 12.0 Hz) ppm. Characterization is consistent with the literature.²⁸¹

Synthesis of Compound 439

SiFA compound **438** (270 mg, 0.60 mmol) and *N*-hydroxysuccinimide (84 mg, 0.73 mmol, 1.2 eq.) were combined in an RBF, and dissolved in DMF (10 mL). EDCI (100 mg, 0.64 mmol, 1.1 eq.) was then added, and the mixture stirred at room temperature for 6 hours. The reagent H-L-Asp(O^tBu)-OH **437** (135 mg, 0.71 mmol, 1.2 eq.) was added, followed by stirring at room temperature for 14 hours. The reaction mixture was co-evaporated with toluene to provide an off-white syrup. The syrup was dissolved in diethyl ether (50 mL), resulting in the formation of white precipitate, which was removed by filtration. The organic filtrate solution was washed with 10% aqueous NH₄Cl (50 mL), water (50 mL), and brine (50 mL). The combined aqueous layers were extracted with DCM (3 × 50 mL). The combined organics were dried over NaSO₄, filtered, and concentrated *in vacuo*, to afford a crude yellow oil. The crude was purified using reverse-phase HPLC (*method F*), affording **439** as a white powder (95 mg, 26%). R.T. = 15.6 min.

(S)-4-(tert-butoxy)-2-((S)-4-(tert-butoxy)-2-(4-(di-tert-butylfluorosilyl)benzamido)-4-oxo-butanamido)-4-oxobutanoic acid. ¹H NMR (CDCl₃, 500 MHz): δ 7.82 (d, 2H, *J* = 8.0 Hz), 7.74 (d, 1H, *J* = 8.0 Hz), 7.70 (d, 1H, *J* = 8.0 Hz), 7.67 (d, 1H, *J* = 8.0 Hz), 5.06 (m, 1H), 4.84 (dt, 1H, *J* = 7.5, 4.4 Hz), 3.00 (dd, 1H, *J* = 16.7, 4.2 Hz), 2.97 (dd, 1H, *J* = 17.0, 4.5 Hz), 2.74 (dd, 1H, *J* = 17.3, 4.7 Hz), 2.70 (dd, 1H, *J* = 16.7, 6.2 Hz), 1.47 (s, 9H), 1.38 (s, 1H), 1.06 (s, 18H) ppm. ¹³C NMR (CDCl₃, 126 MHz): δ 172.2, 171.8, 170.9, 170.3, 167.3, 139.0 (d, *J*_{CF} = 13.7 Hz), 134.3 (d, *J*_{CF} = 4.4 Hz), 134.3, 126.1, 82.5, 82.4, 49.8, 48.9, 37.0, 36.7, 28.1, 28.0, 27.3, 20.3 (d, *J*_{CF} = 12.1 Hz) ppm. ¹⁹F NMR (CDCl₃, 376 MHz): δ -188.6 (s, 1F) ppm. Characterization is consistent with the literature.²⁸¹

A.3 Spectra of Reaction Mixtures and Pure Compounds

Figure A.12. ^{19}F NMR spectrum of compound **210** reaction I (CDCl_3 , 376.3 MHz)

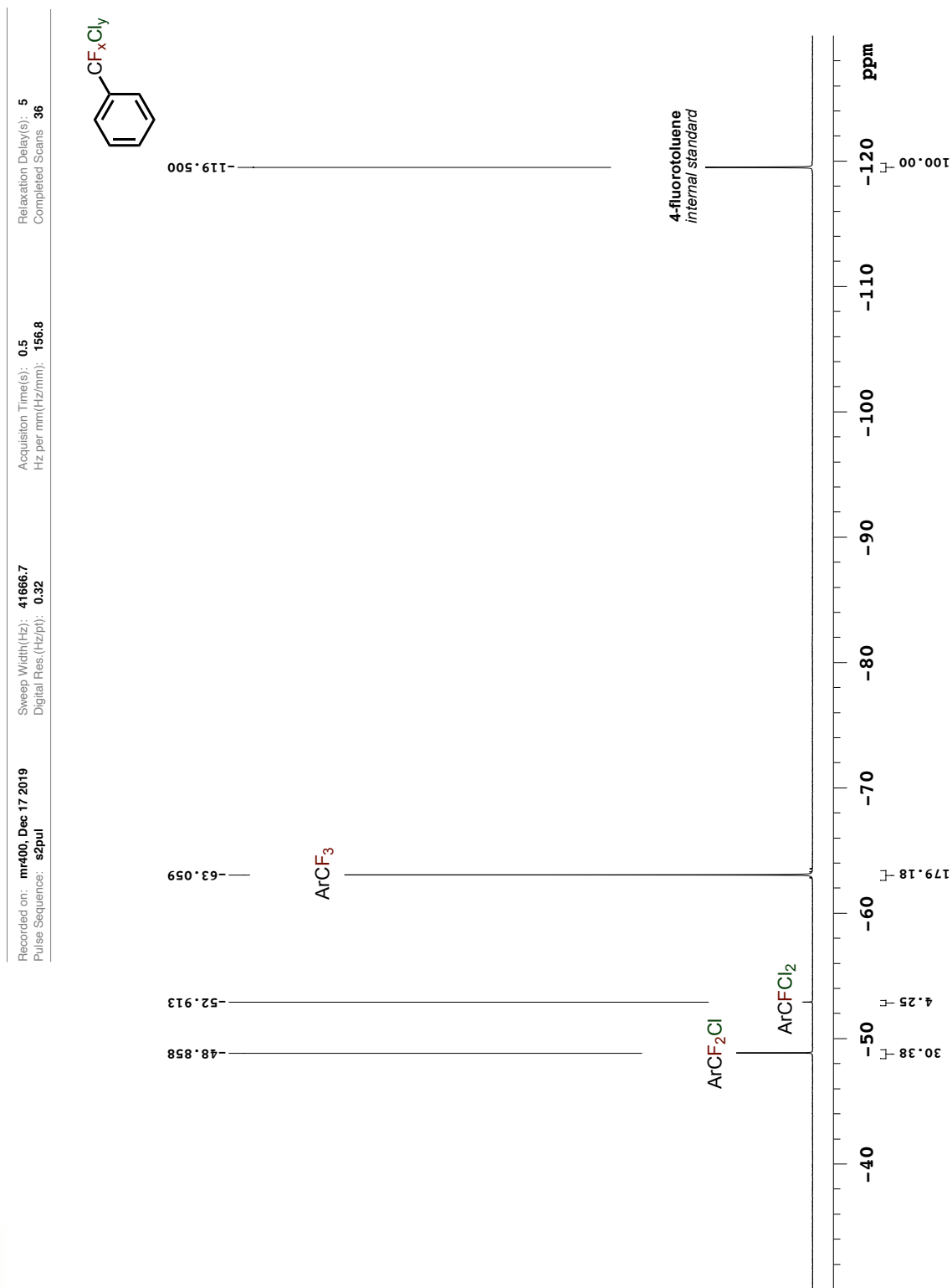


Figure A.13. ^{19}F NMR spectrum of compound **210** reaction II (CDCl_3 , 376.3 MHz)

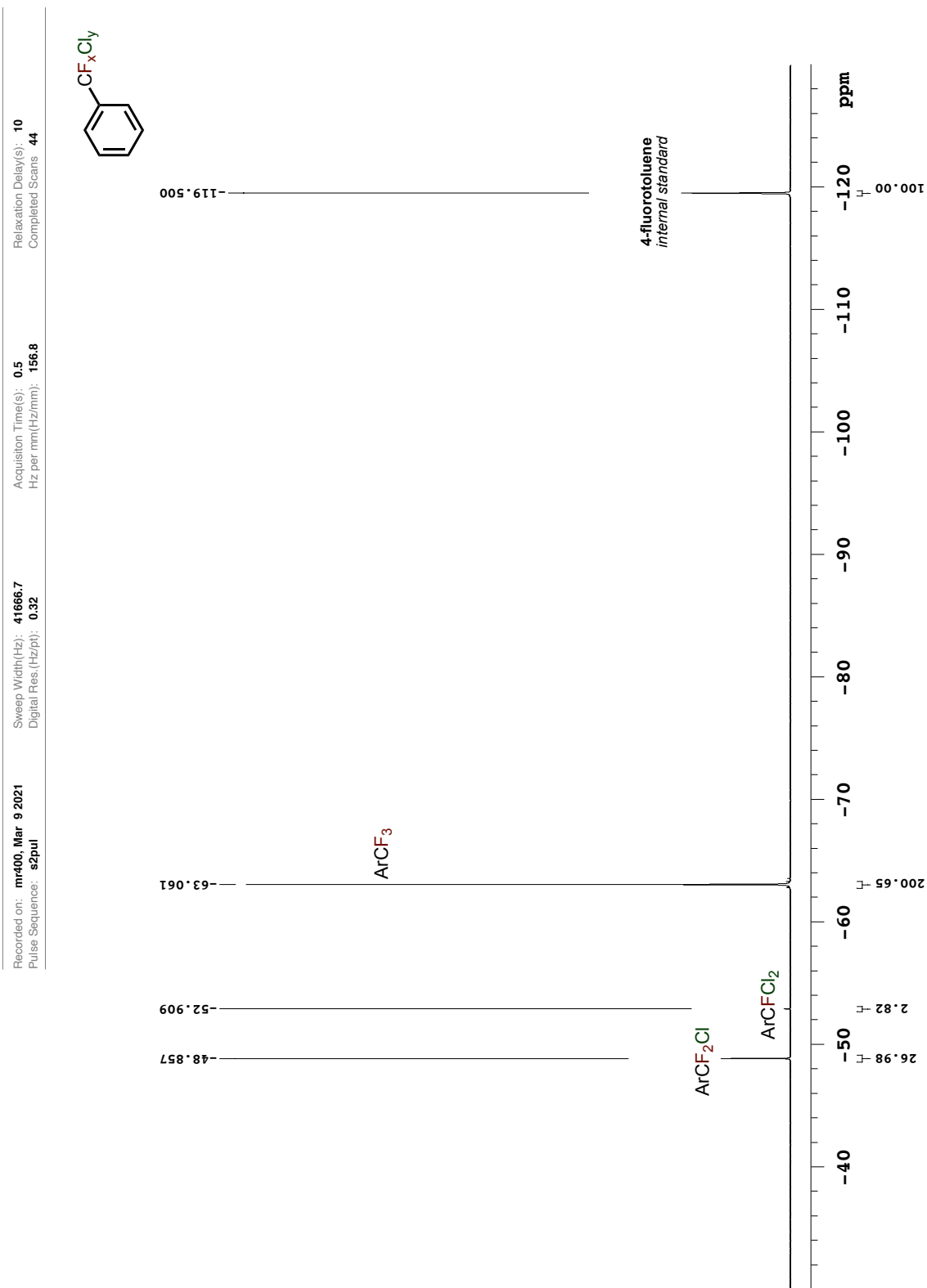


Figure A.14. ^{19}F NMR spectrum of compound **218** reaction I (CDCl_3 , 376.3 MHz)

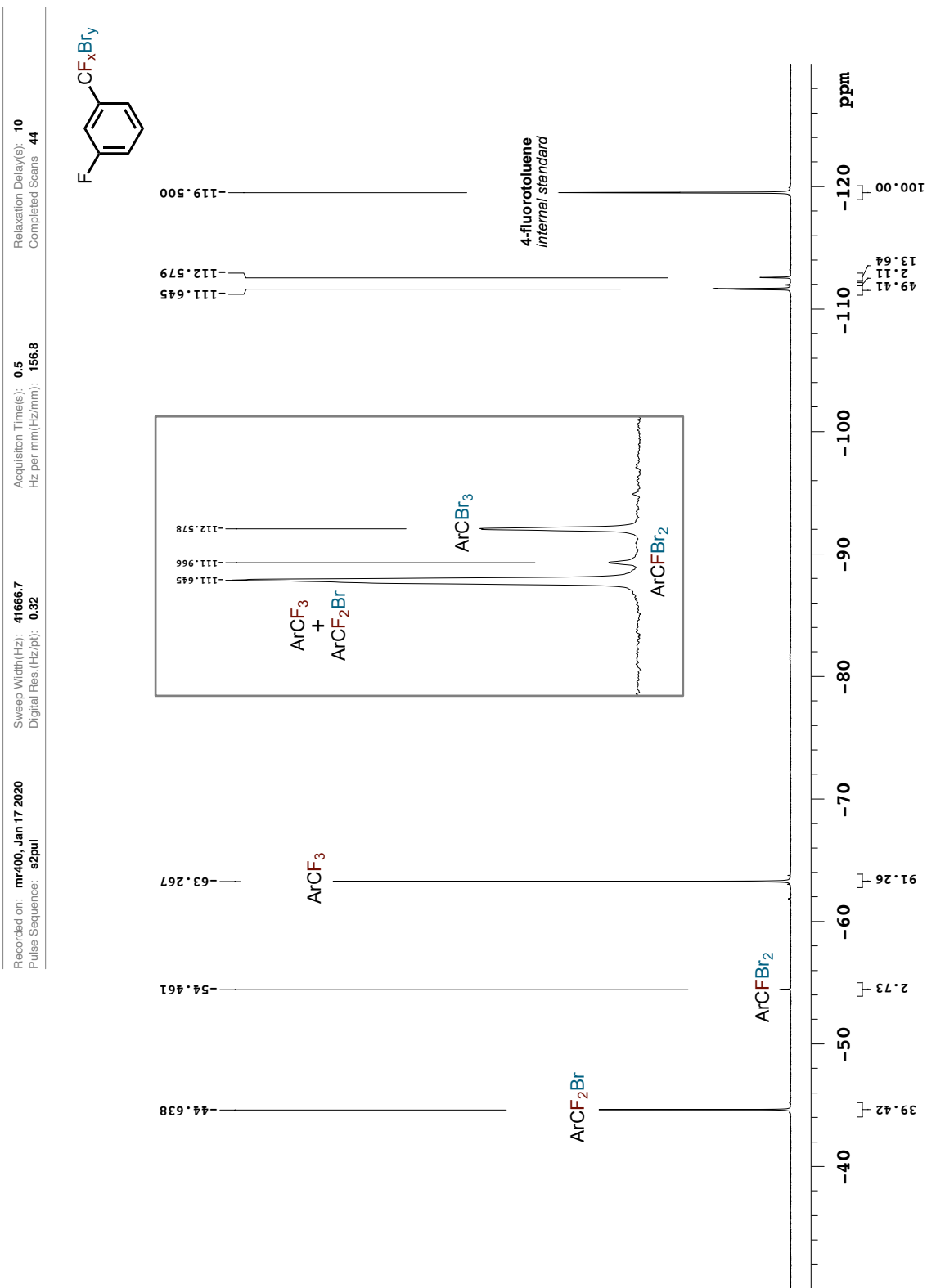


Figure A.15. ^{19}F NMR spectrum of compound **218** reaction II (CDCl_3 , 376.3 MHz)

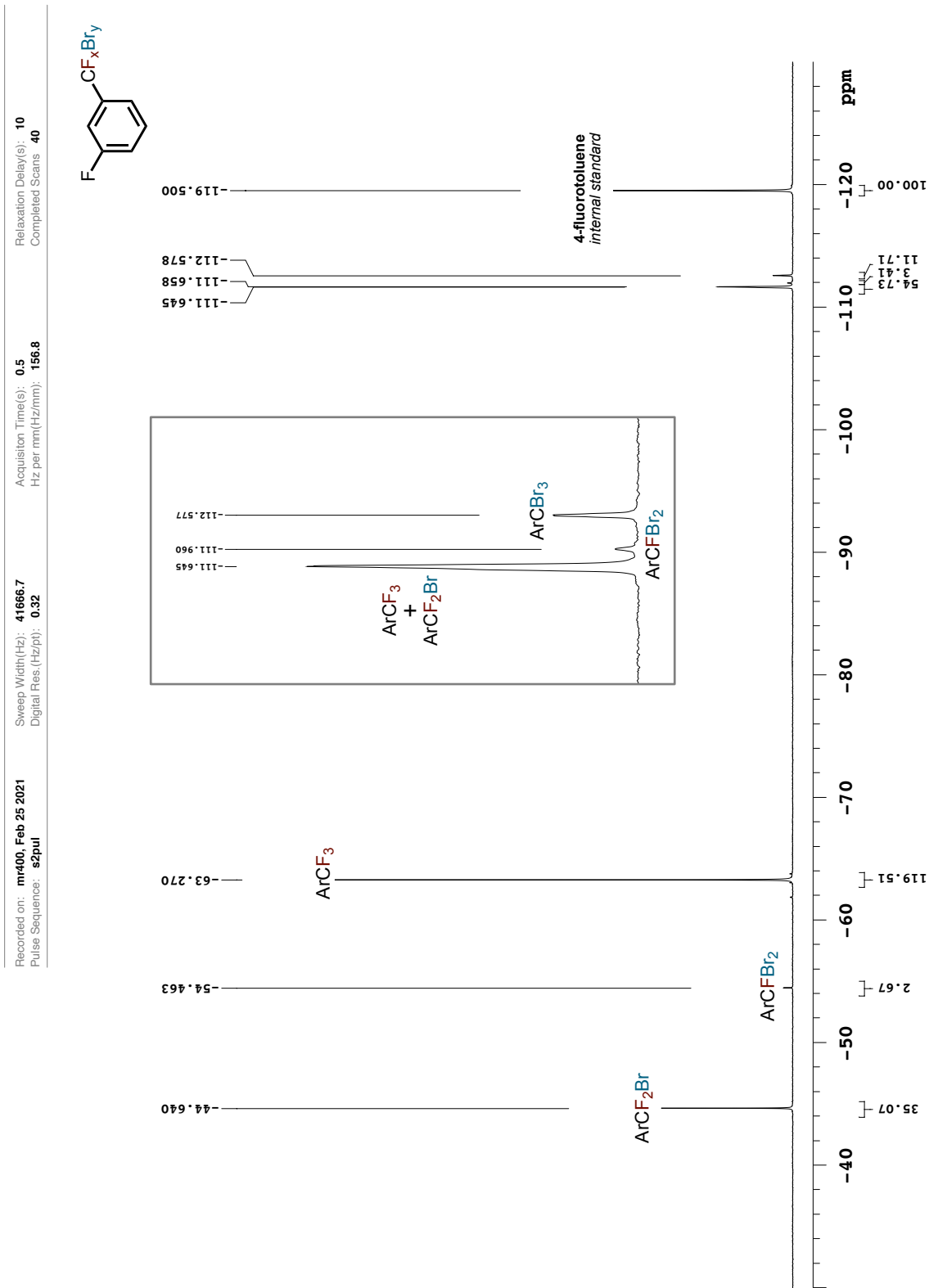


Figure A.16. ^{19}F NMR spectrum of compound **224** reaction I (CDCl_3 , 376.3 MHz)

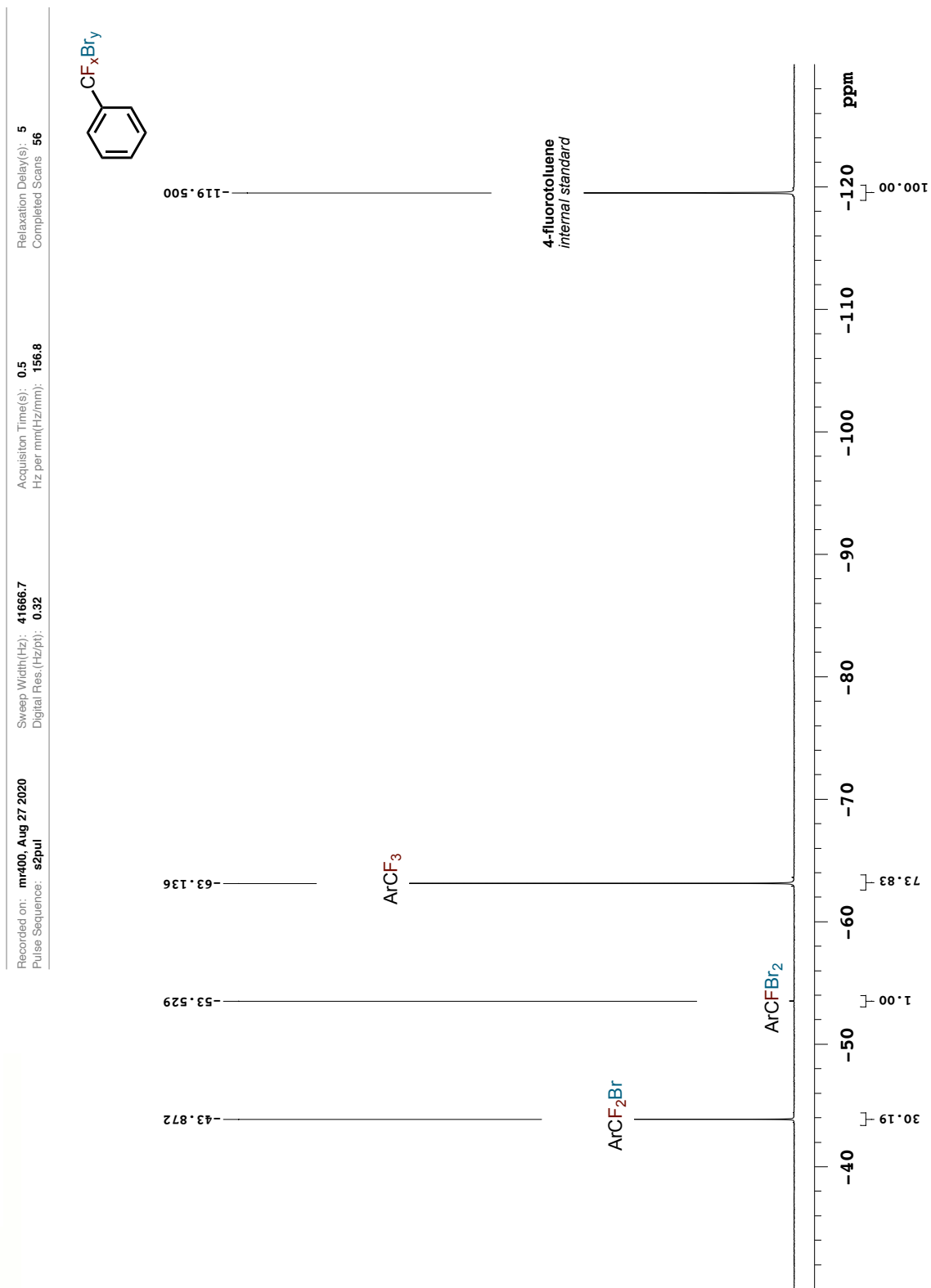


Figure A.17. ^{19}F NMR spectrum of compound **224** reaction II (CDCl_3 , 376.3 MHz)

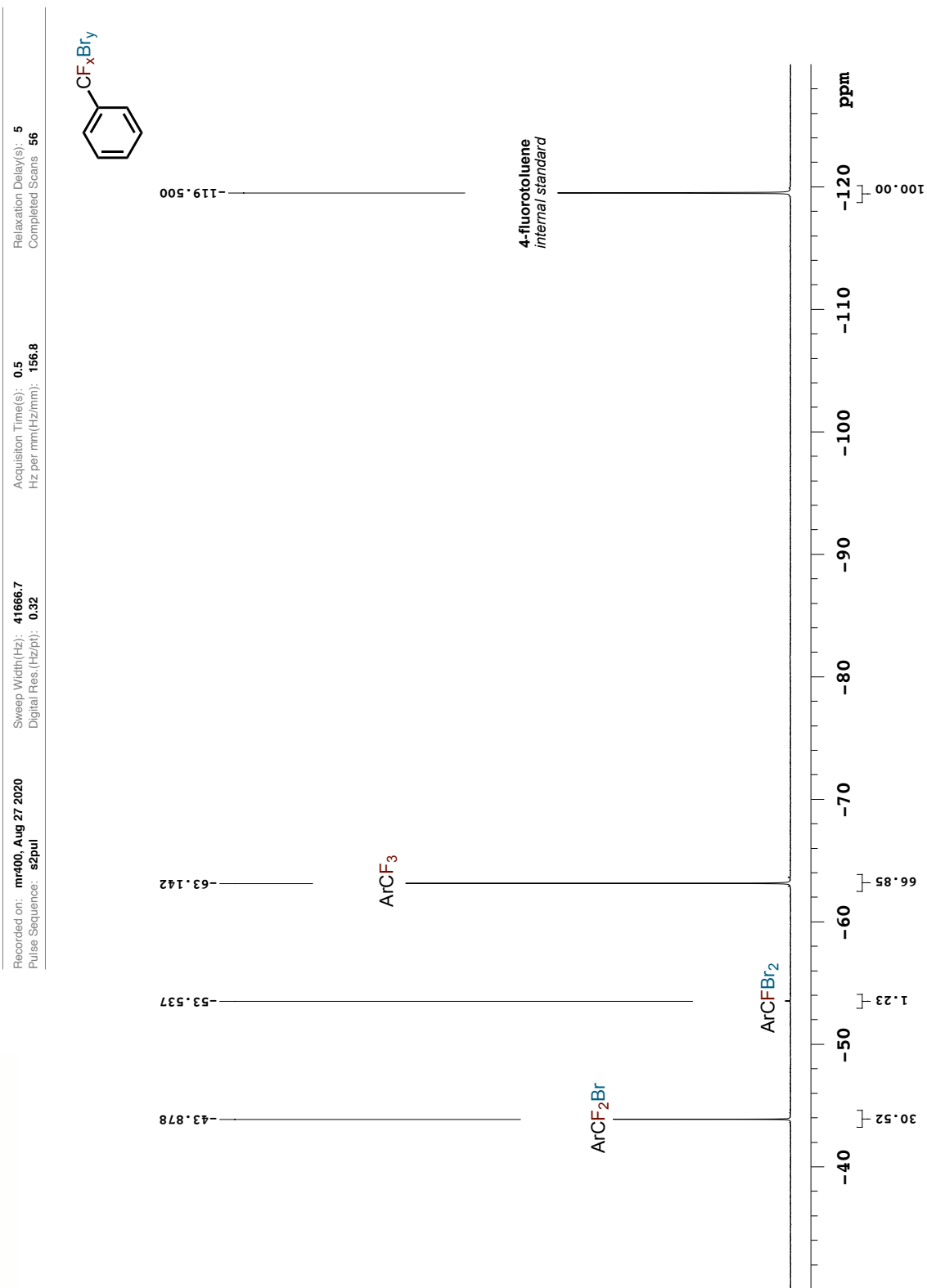


Figure A.18. ^{19}F NMR spectrum of compound 225 reaction I (CDCl_3 , 376.3 MHz)

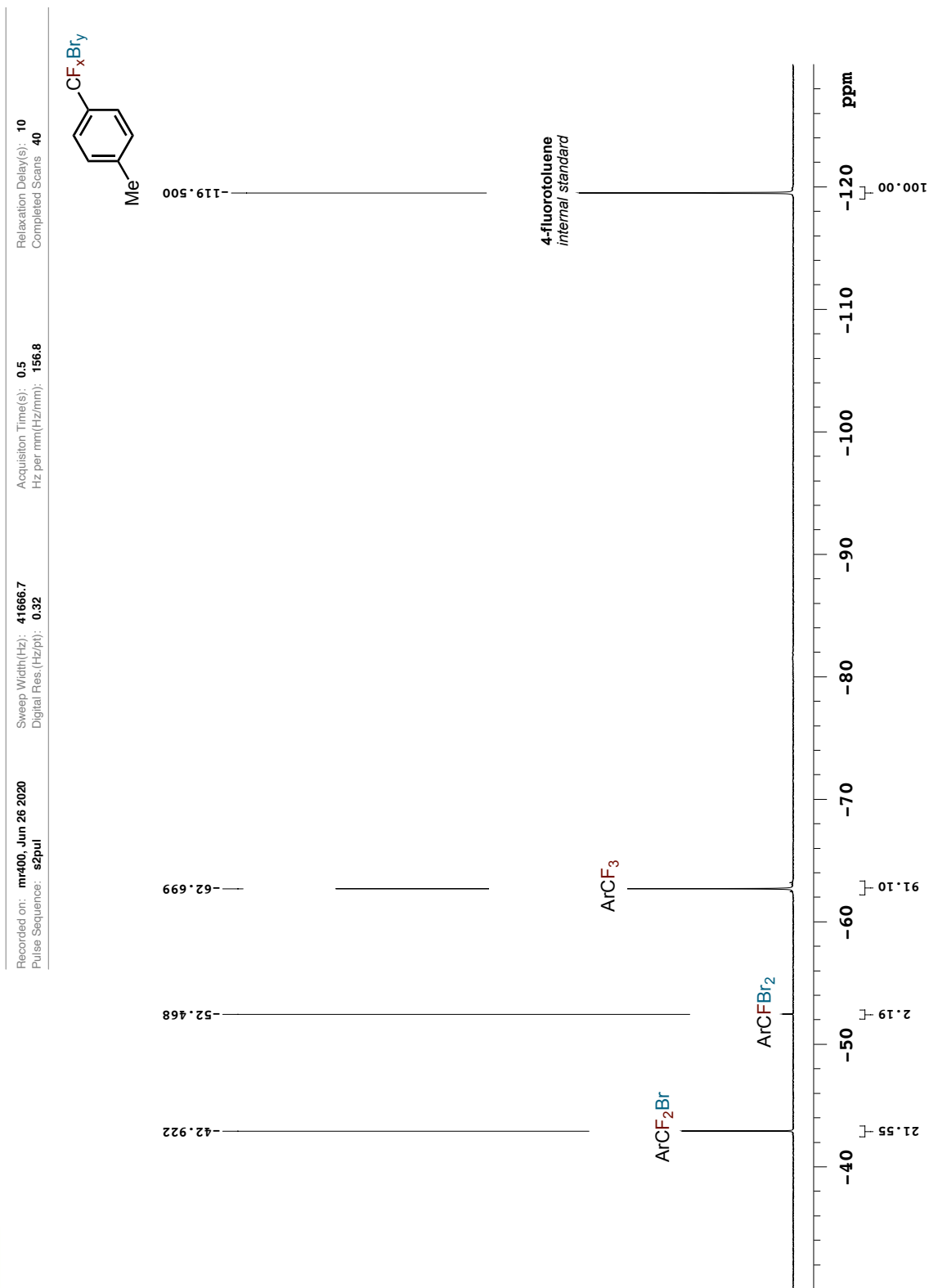


Figure A.19. ^{19}F NMR spectrum of compound **225** reaction II (CDCl_3 , 376.3 MHz)

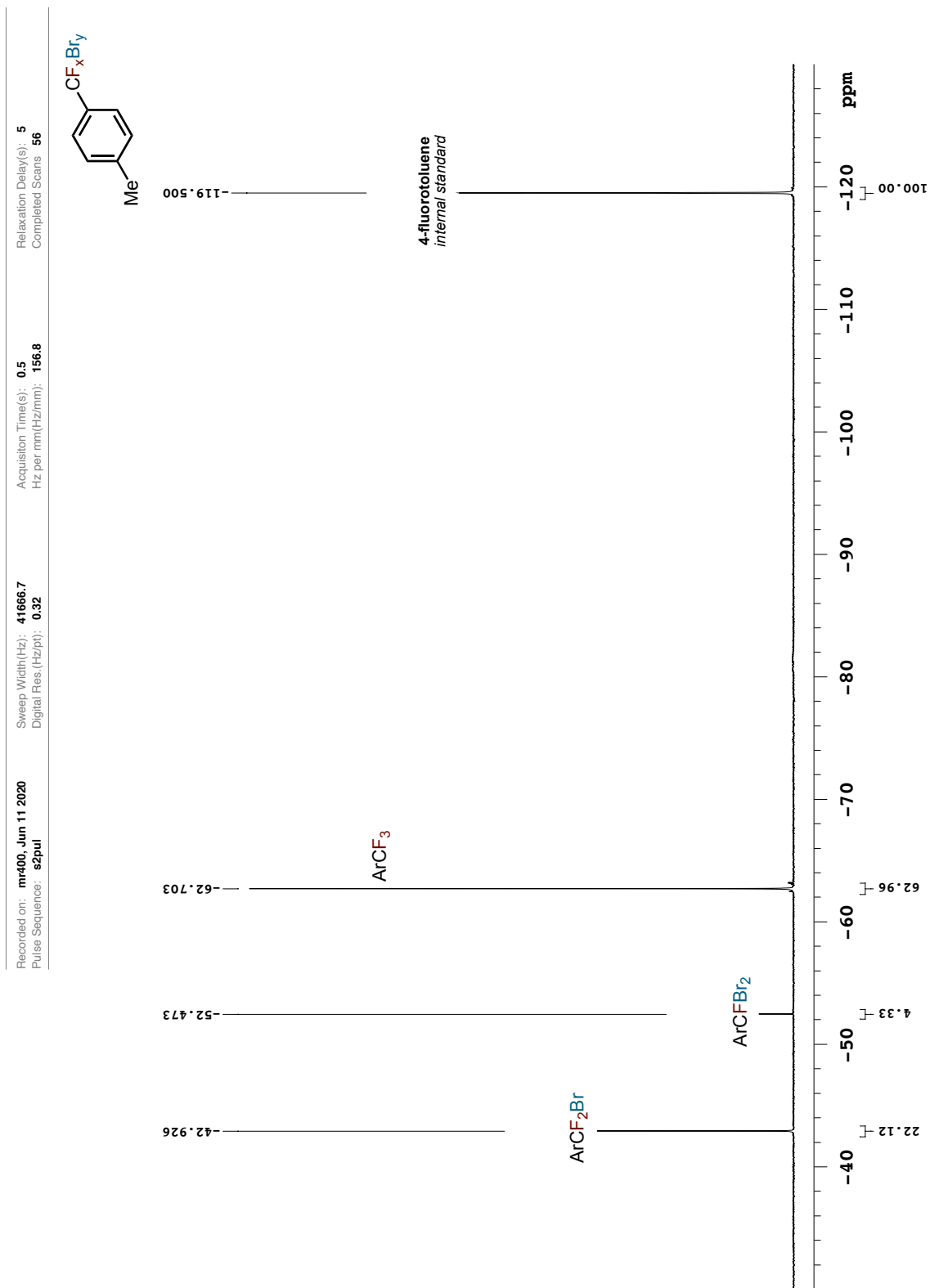


Figure A.20. ^{19}F NMR spectrum of compound **226** reaction I (CDCl_3 , 376.3 MHz)

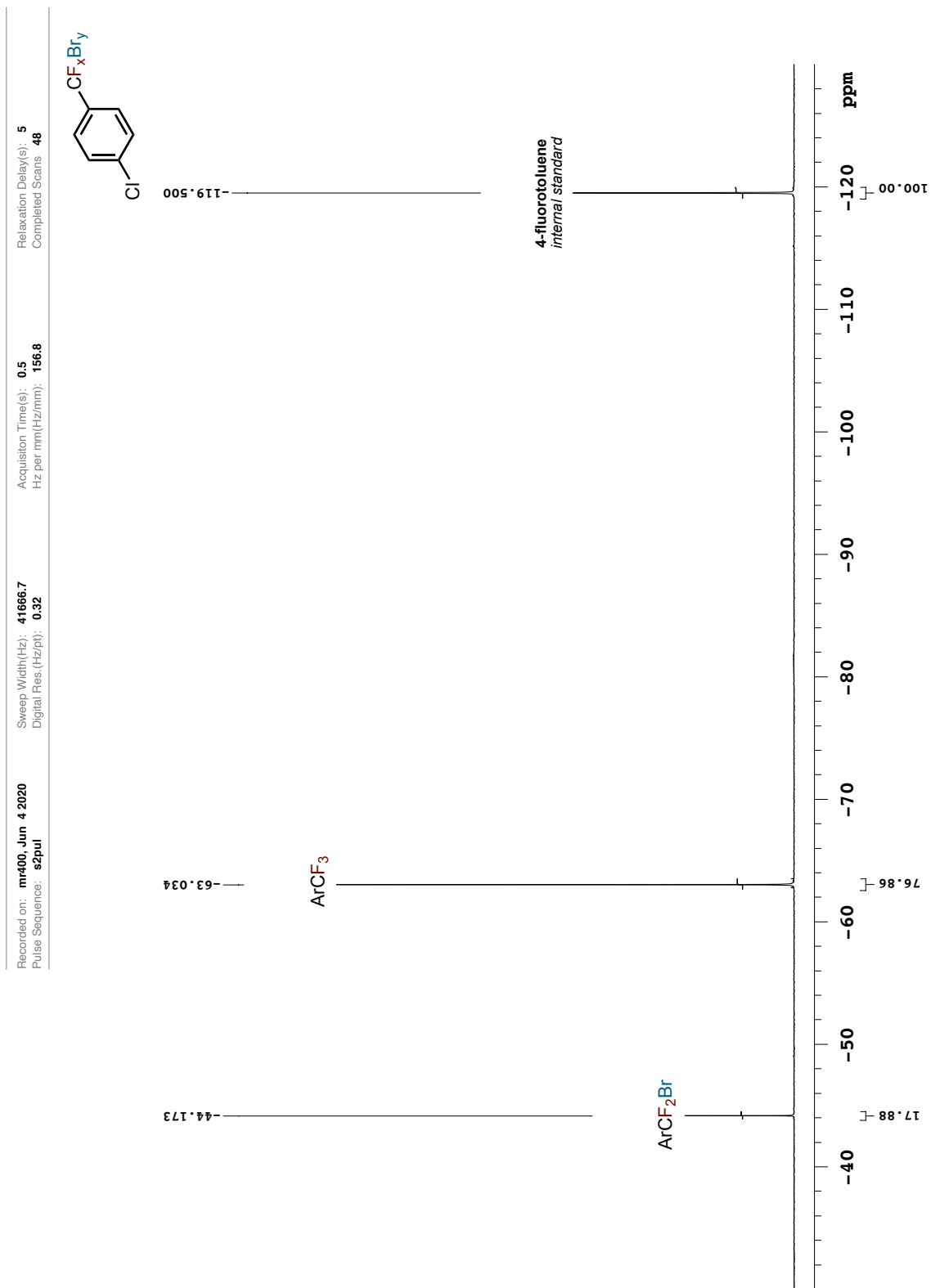


Figure A.21. ^{19}F NMR spectrum of compound **226** reaction II (CDCl_3 , 376.3 MHz)

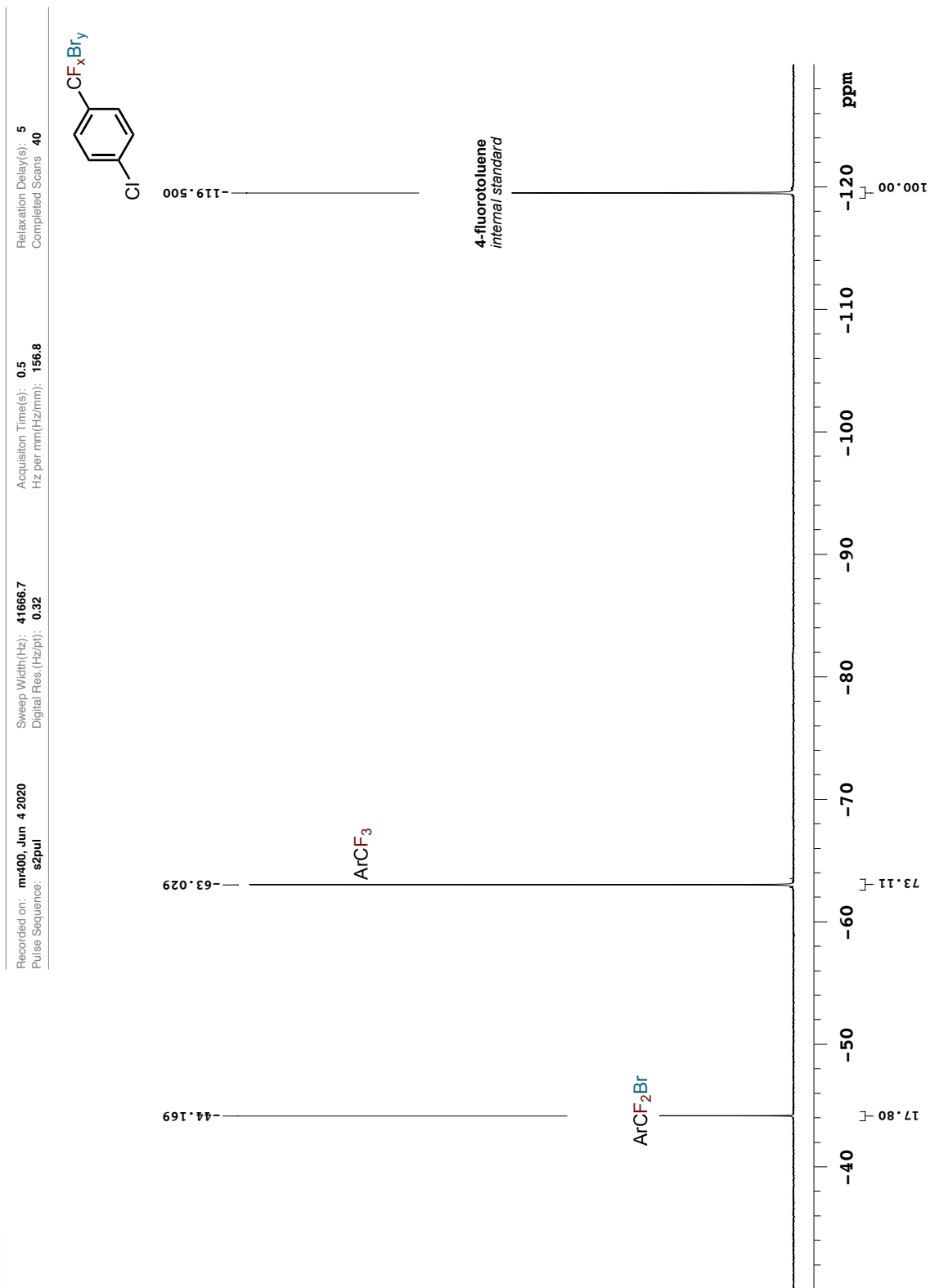


Figure A.22. ^{19}F NMR spectrum of compound **227** reaction I (CDCl_3 , 376.3 MHz)

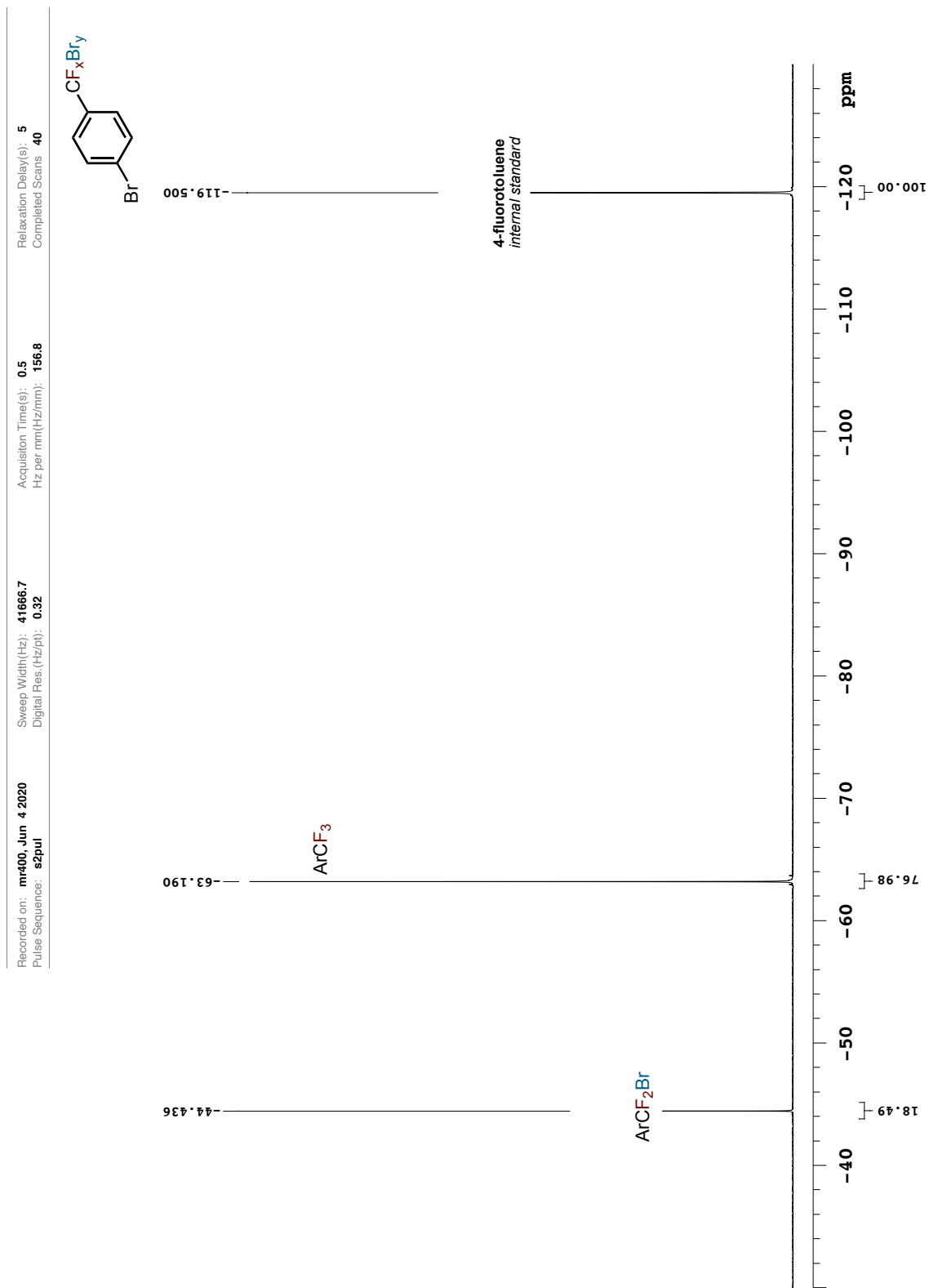


Figure A.23. ^{19}F NMR spectrum of compound **227** reaction II (CDCl_3 , 376.3 MHz)

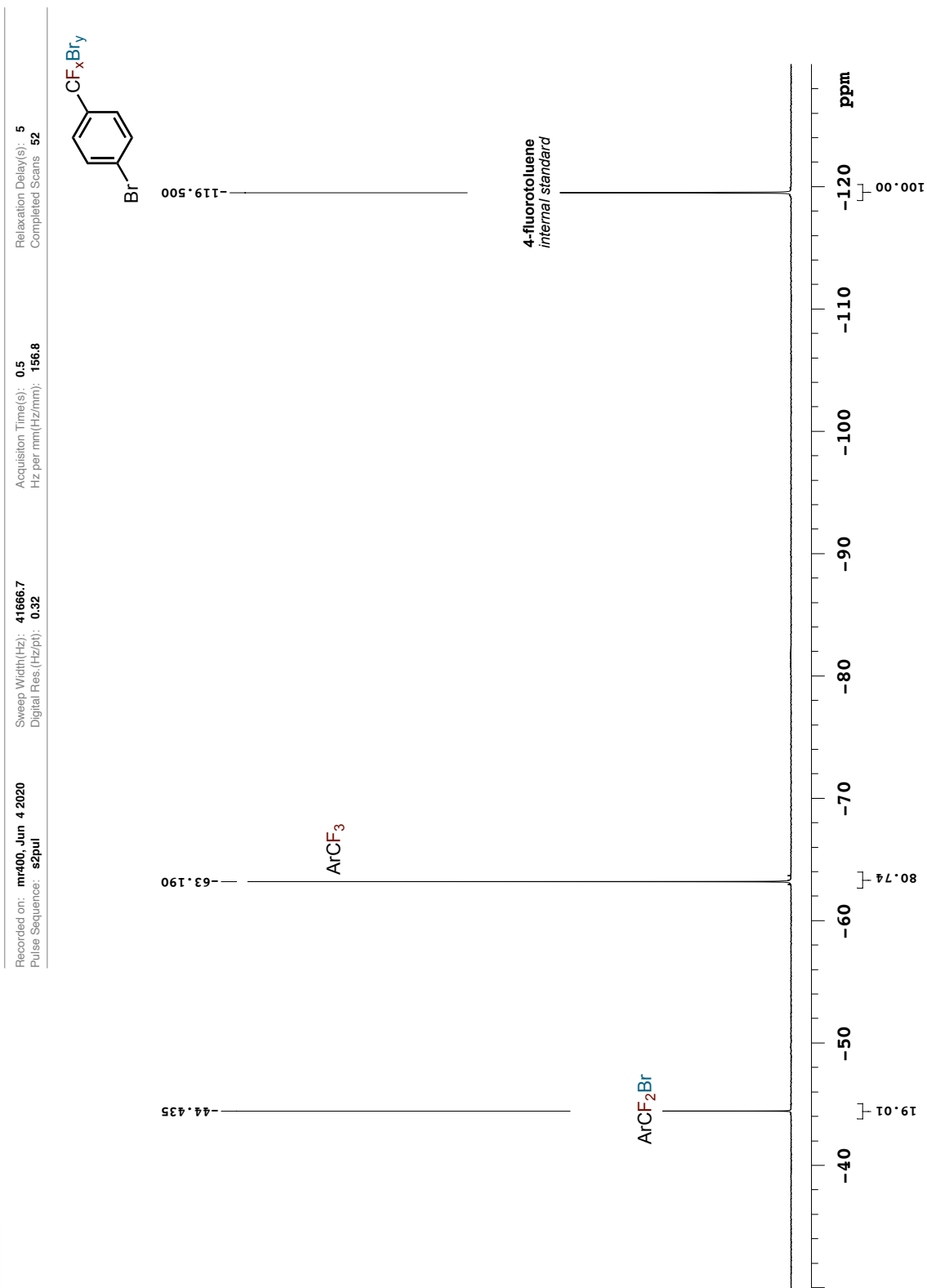


Figure A.24. ^{19}F NMR spectrum of compound **228** reaction I (CDCl_3 , 376.3 MHz)

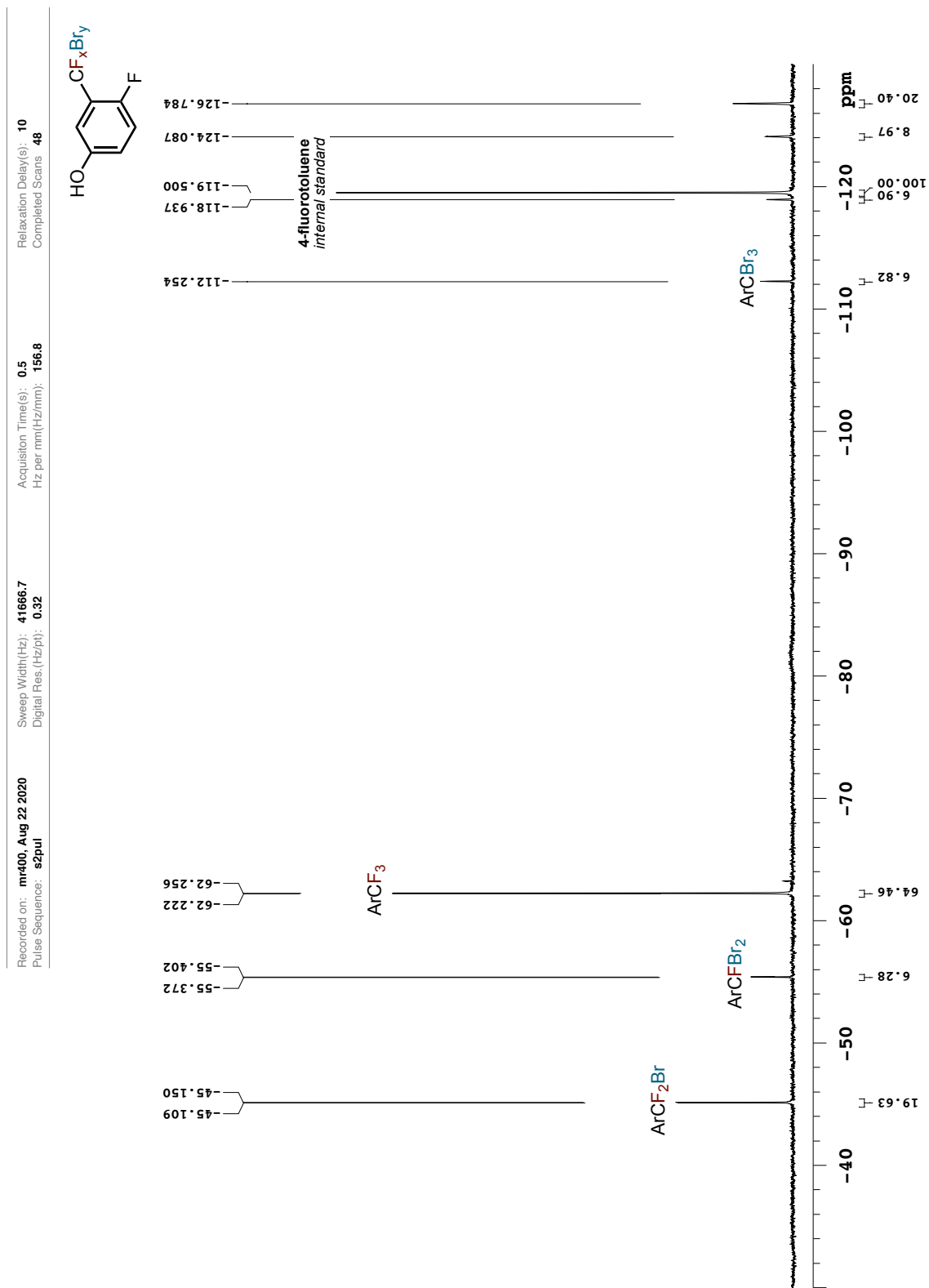


Figure A.25. ^{19}F NMR spectrum of compound **228** reaction II (CDCl_3 , 376.3 MHz)

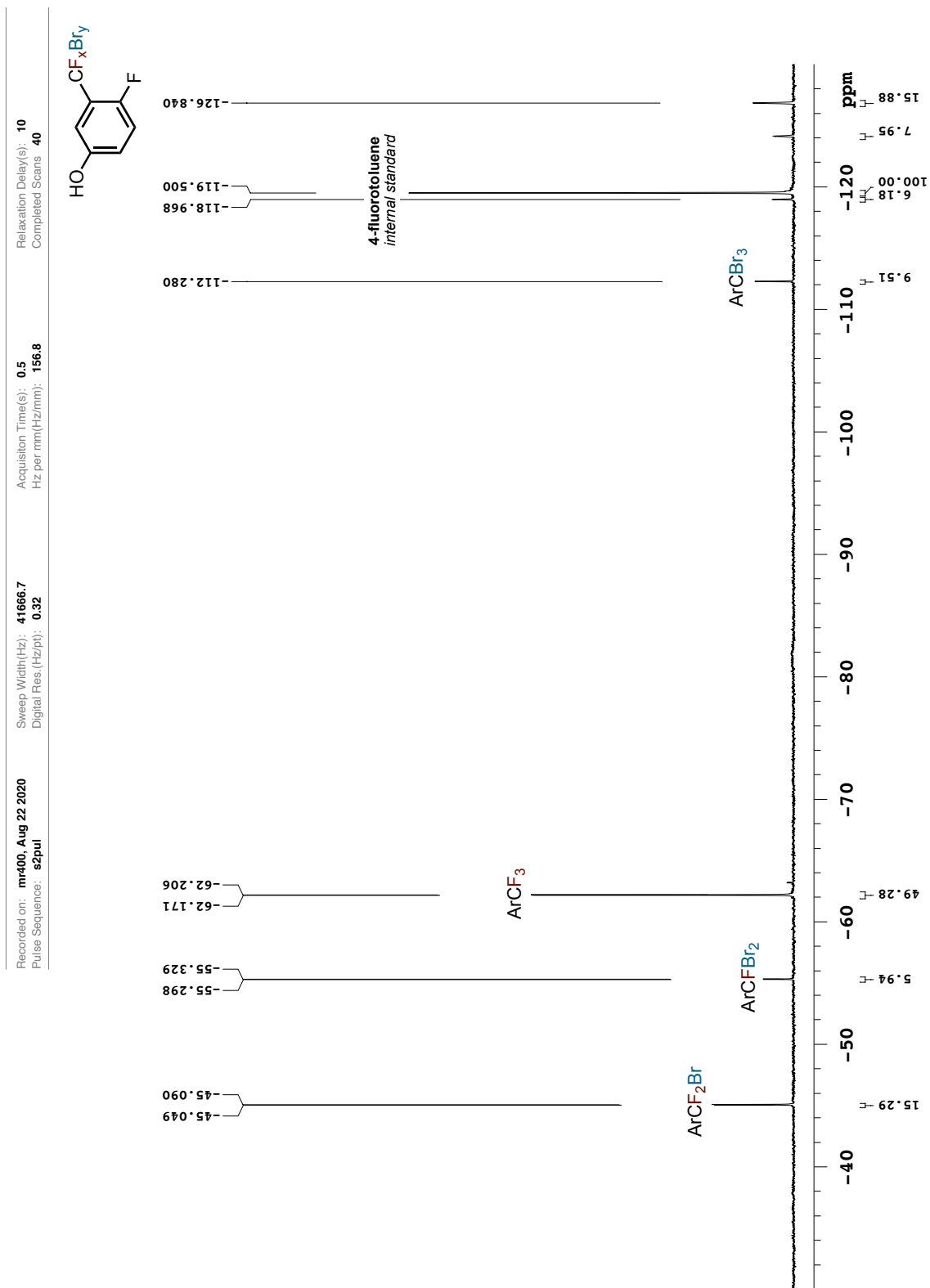


Figure A.26. ^{19}F NMR spectrum of compound **229** reaction I (CDCl_3 , 376.3 MHz)

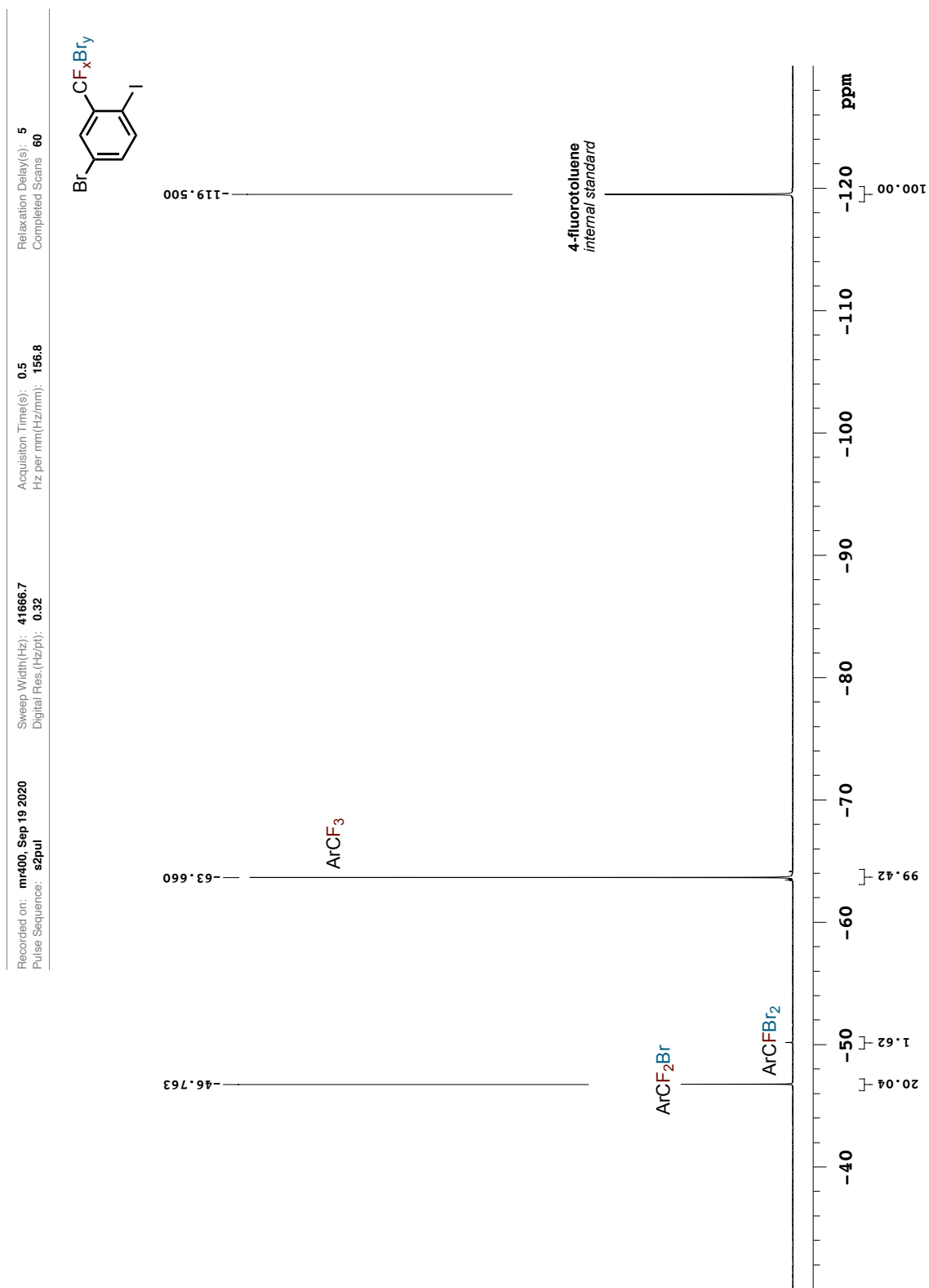


Figure A.27. ^{19}F NMR spectrum of compound **229** reaction II (CDCl_3 , 376.3 MHz)

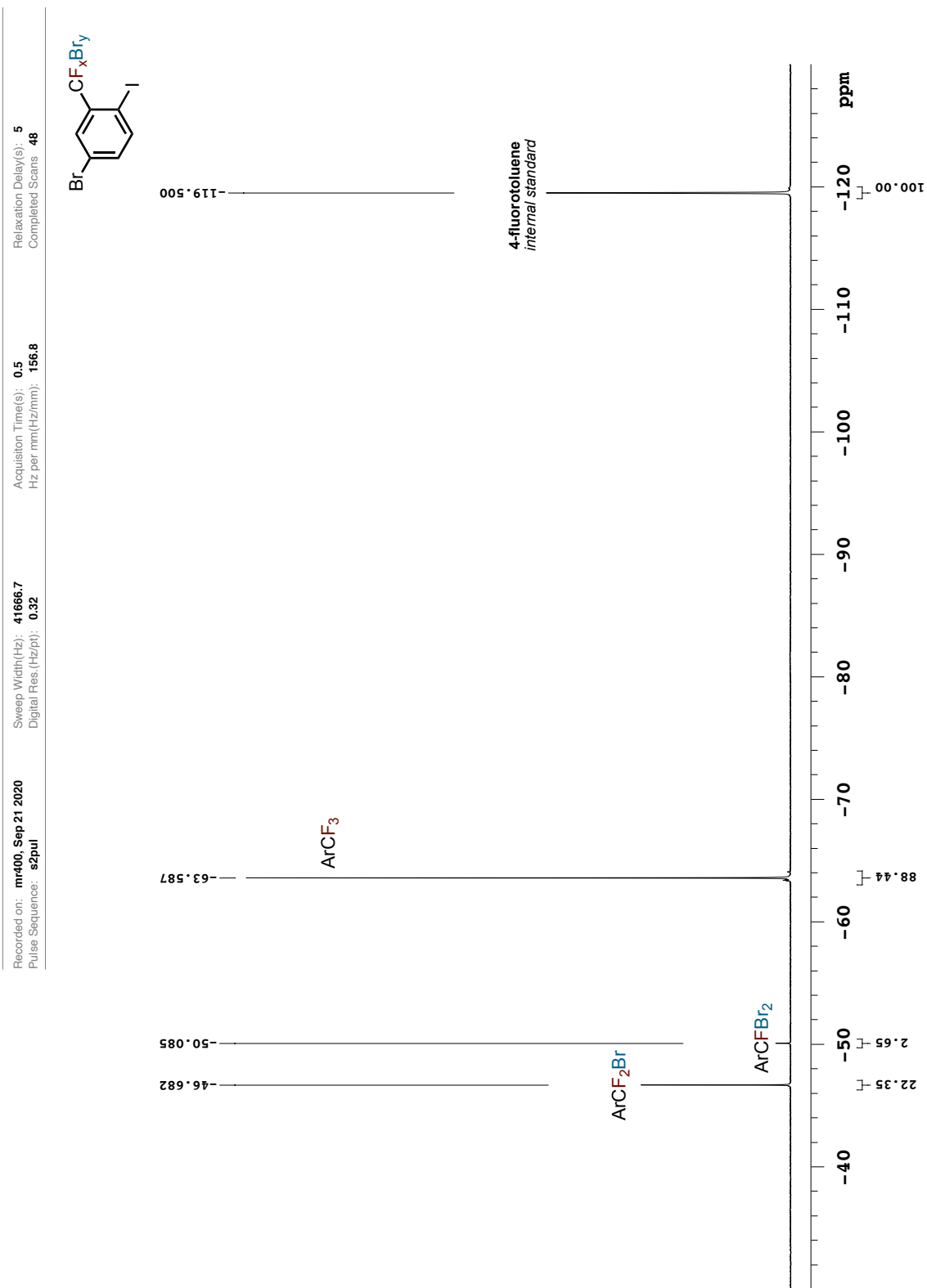


Figure A.28. ^{19}F NMR spectrum of compound **230** reaction I (CDCl_3 , 376.3 MHz)

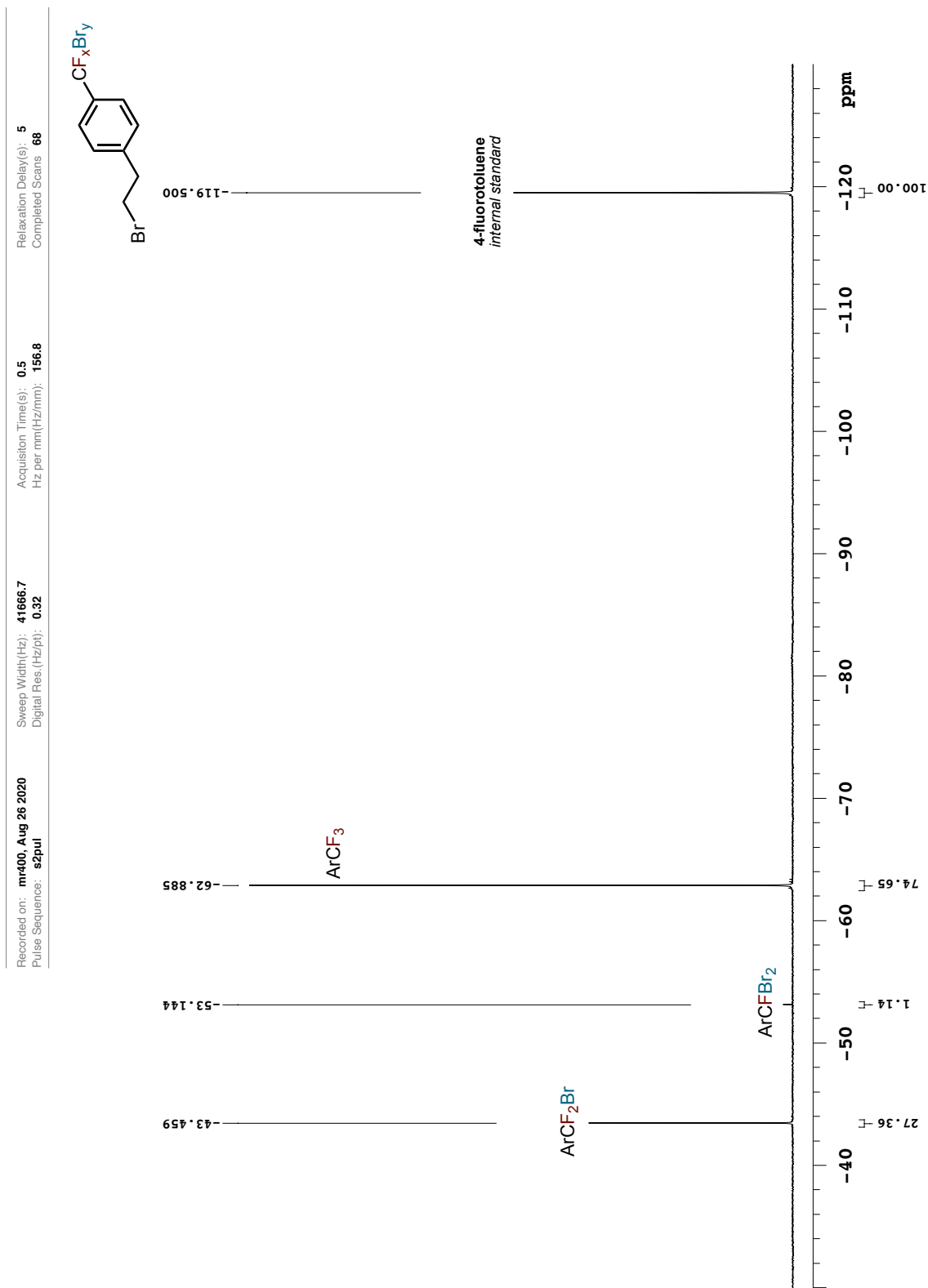


Figure A.29. ^{19}F NMR spectrum of compound **230** reaction II (CDCl_3 , 376.3 MHz)

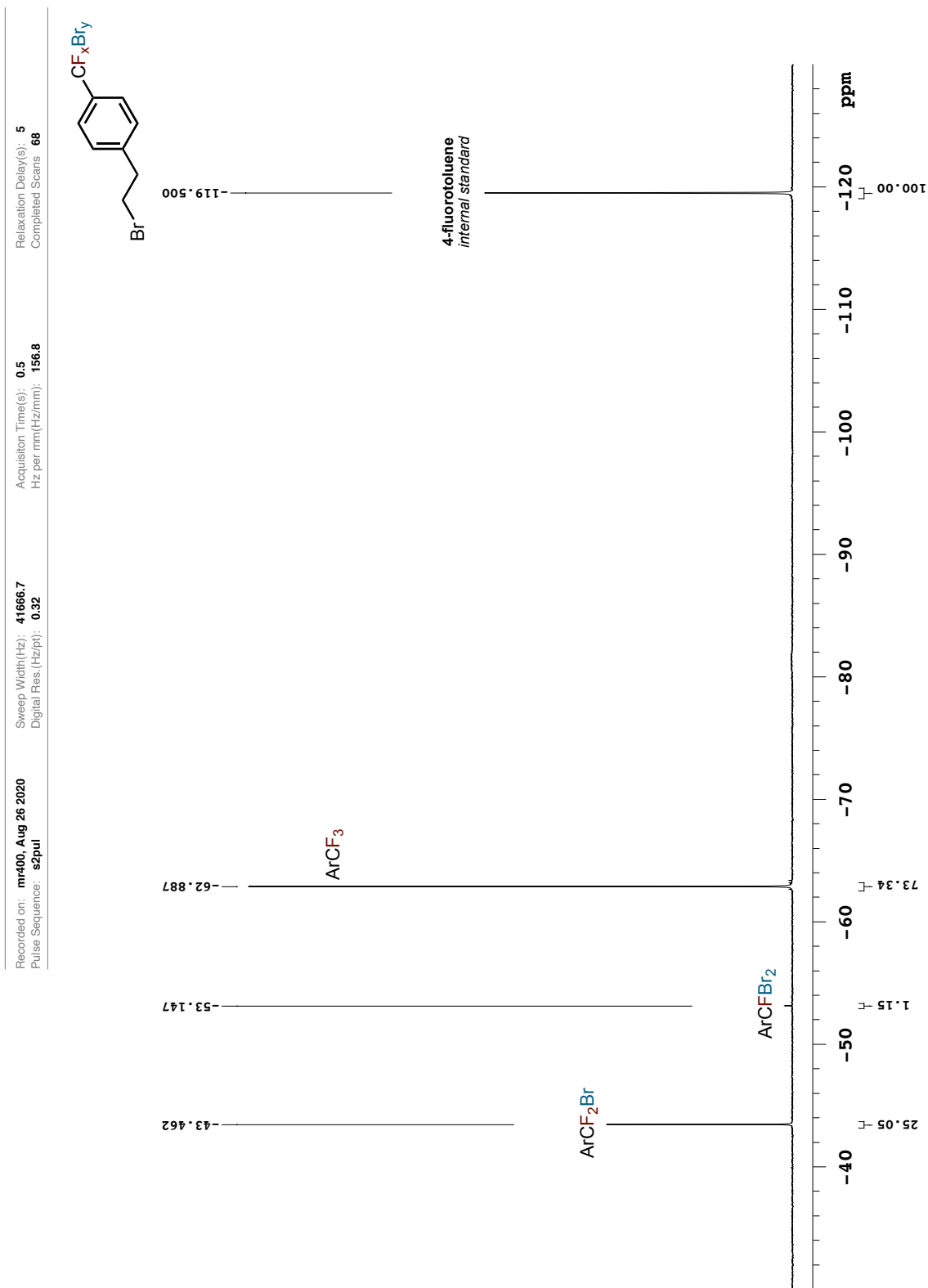


Figure A.30. ^{19}F NMR spectrum of compound 232 reaction I (CDCl_3 , 376.3 MHz)

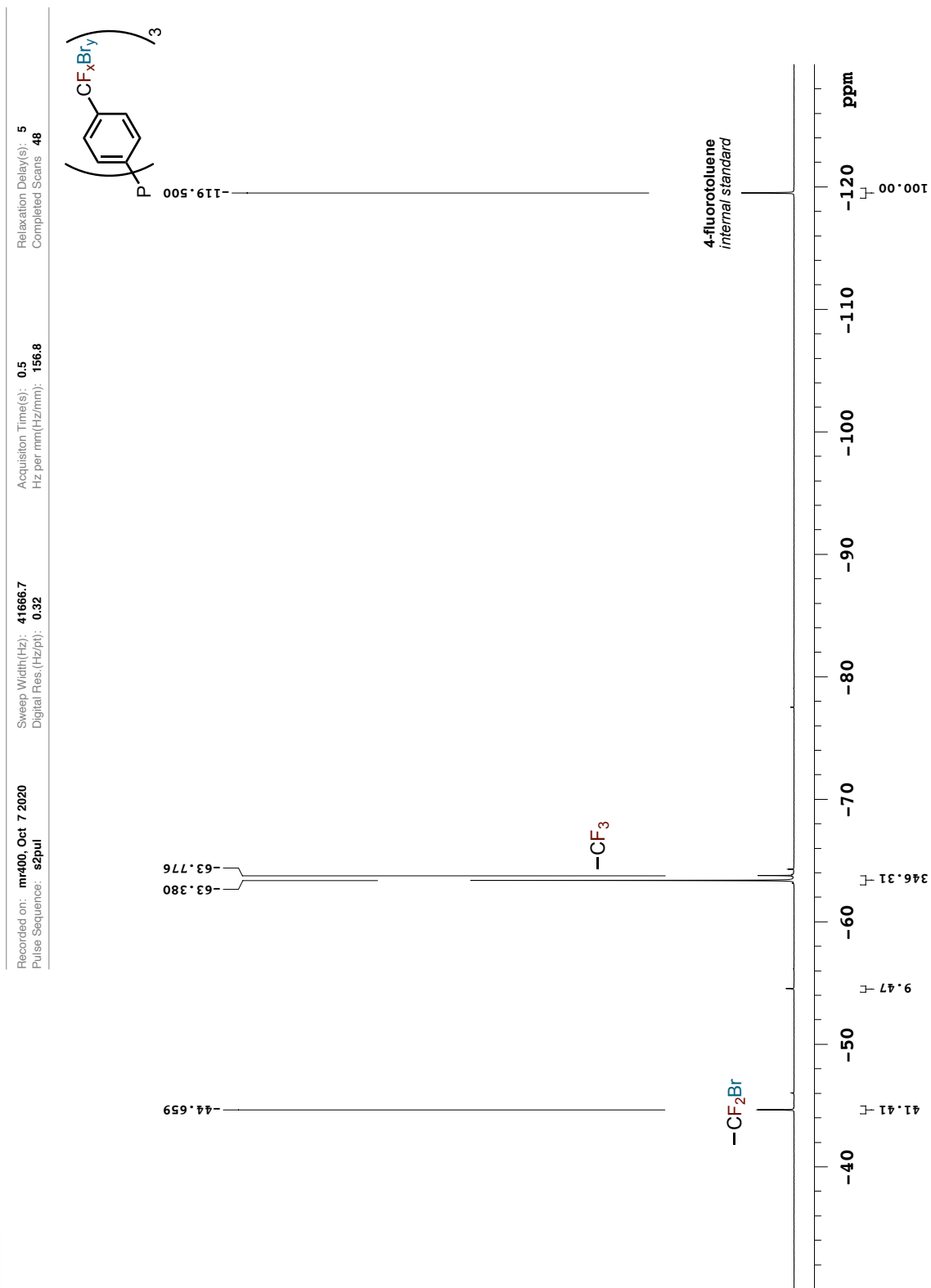


Figure A.3.1. ^{19}F NMR spectrum of compound **232** reaction II (CDCl_3 , 376.3 MHz)

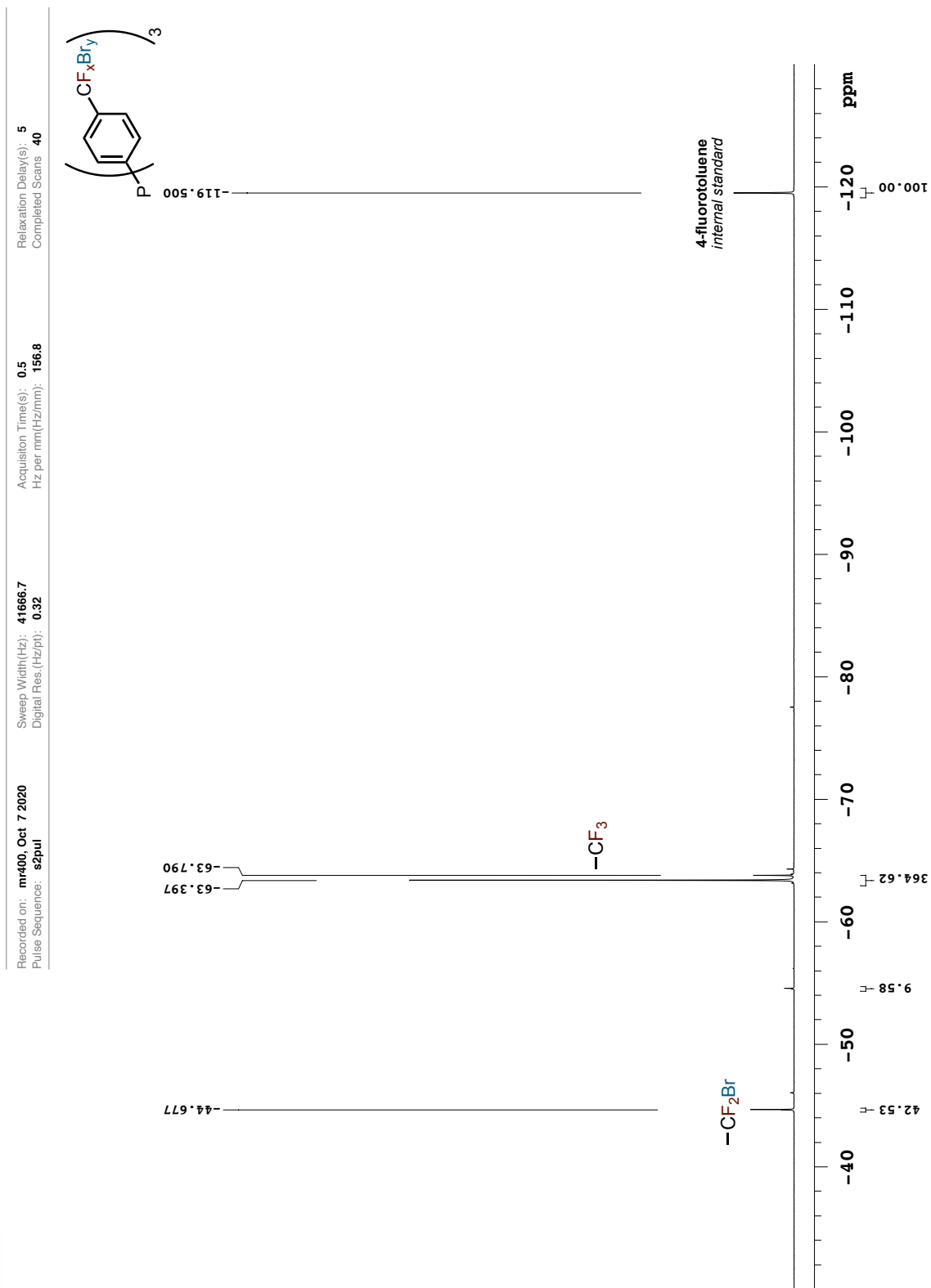


Figure A.3.2. ^{19}F NMR spectrum of compound **234** reaction I (CDCl_3 , 376.3 MHz)

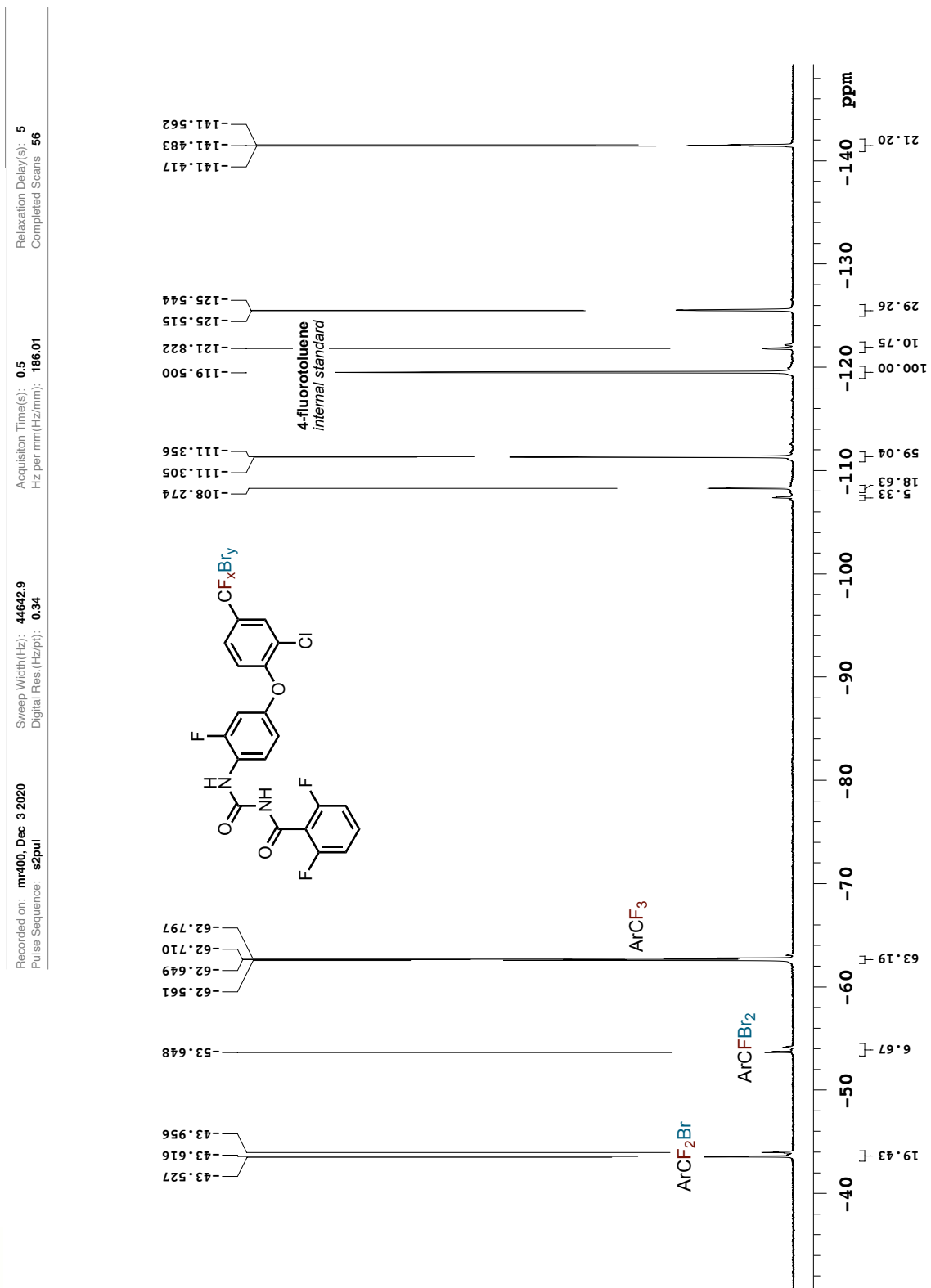


Figure A.33. ^{19}F NMR spectrum of compound **234** reaction II (CDCl_3 , 376.3 MHz)

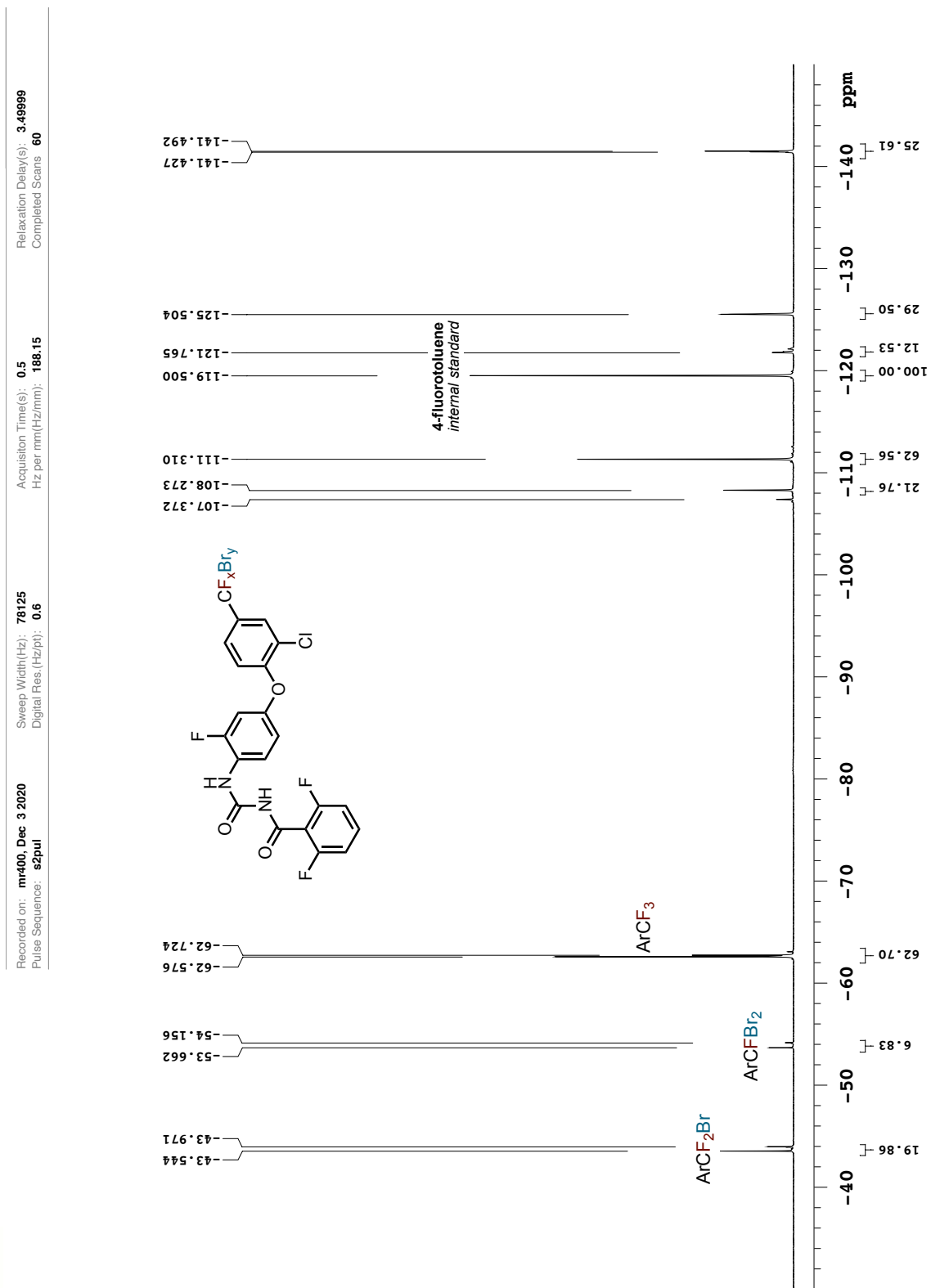


Figure A.34. GCMS chromatogram of compound 210 reaction

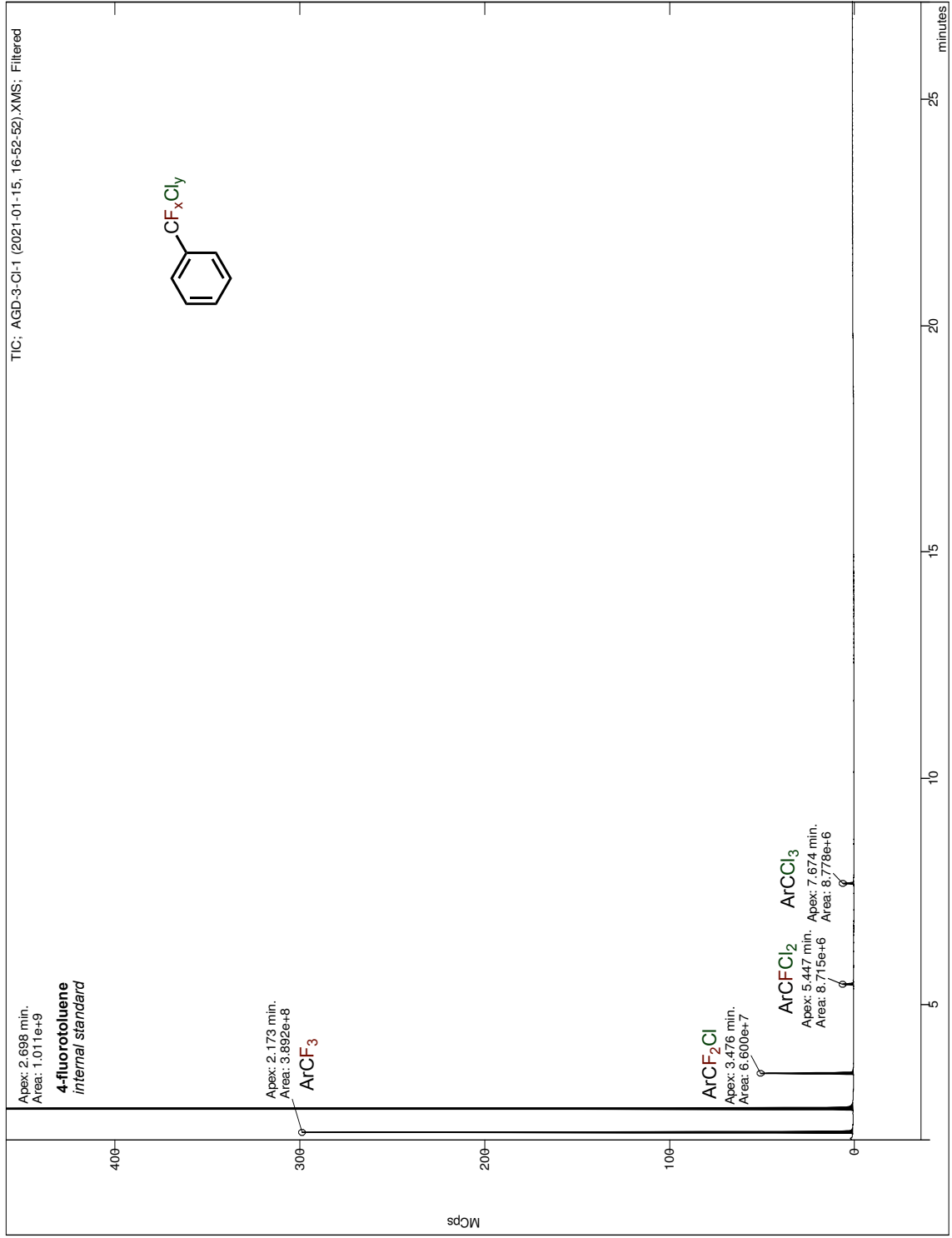


Figure A.35. Mass spectrum for peak at 2.2 minutes (compound 210 reaction)

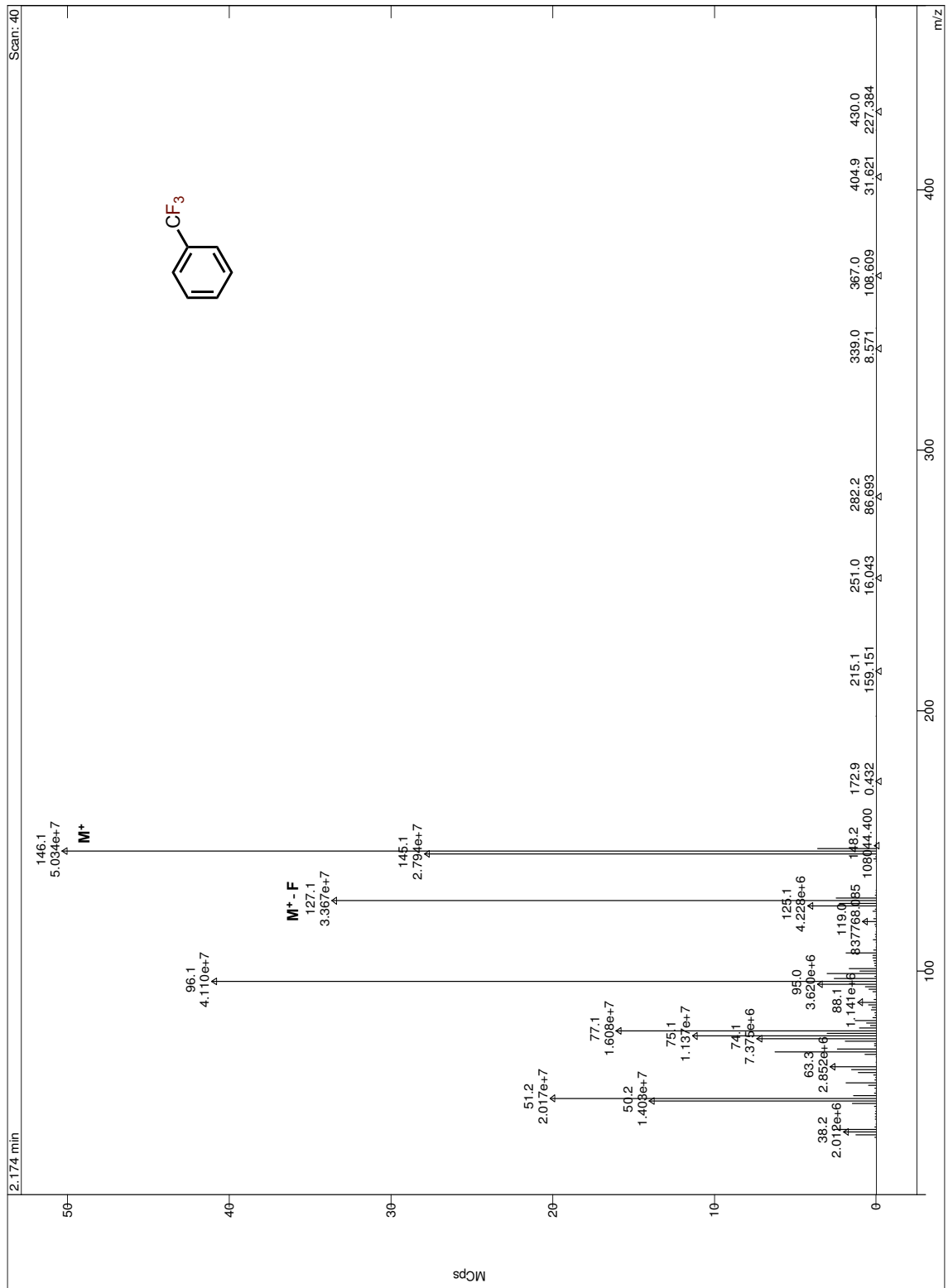


Figure A.36. Mass spectrum for peak at 3.5 minutes (compound 210 reaction)

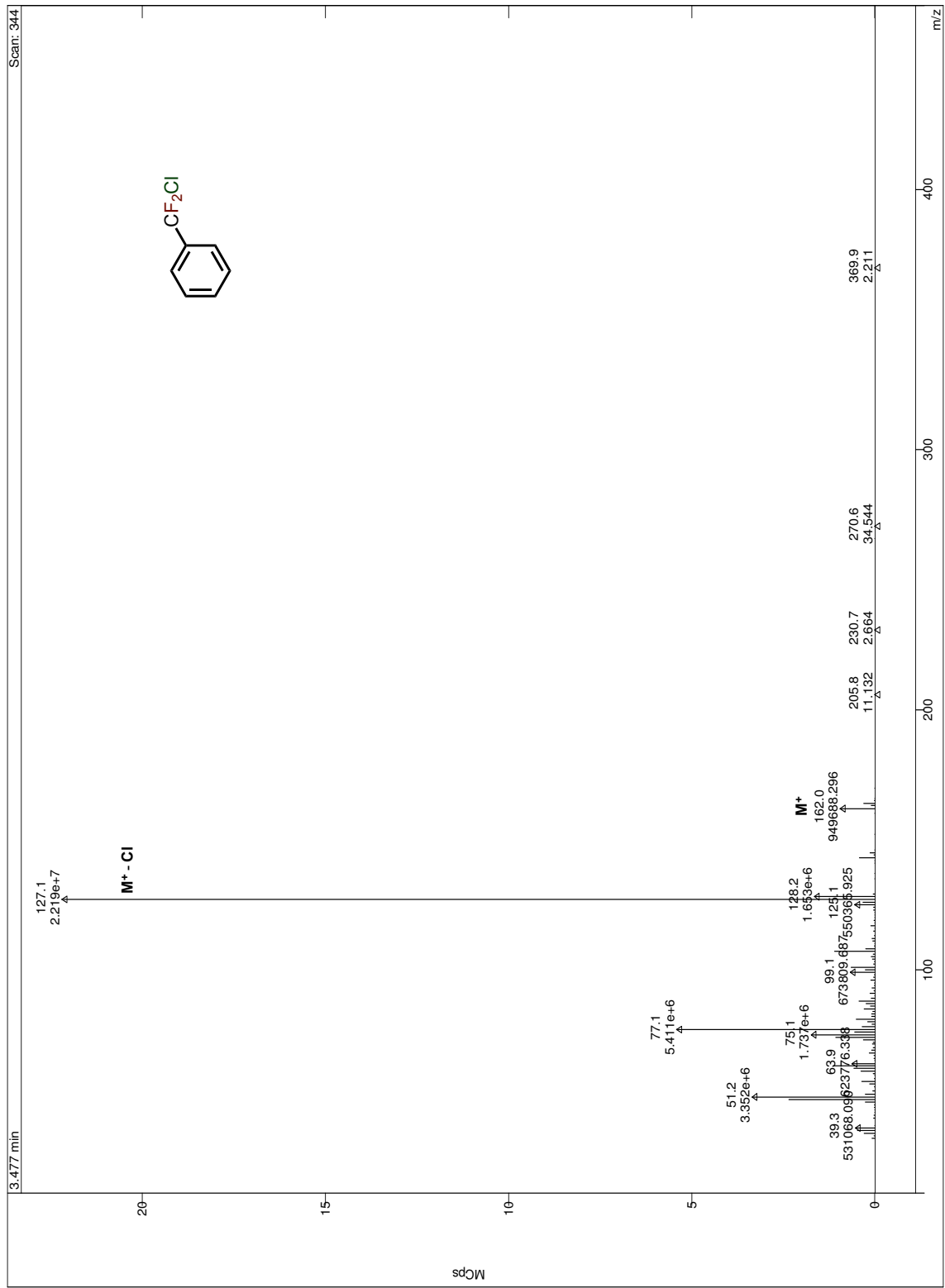


Figure A.37. Mass spectrum for peak at 5.5 minutes (compound 210 reaction)

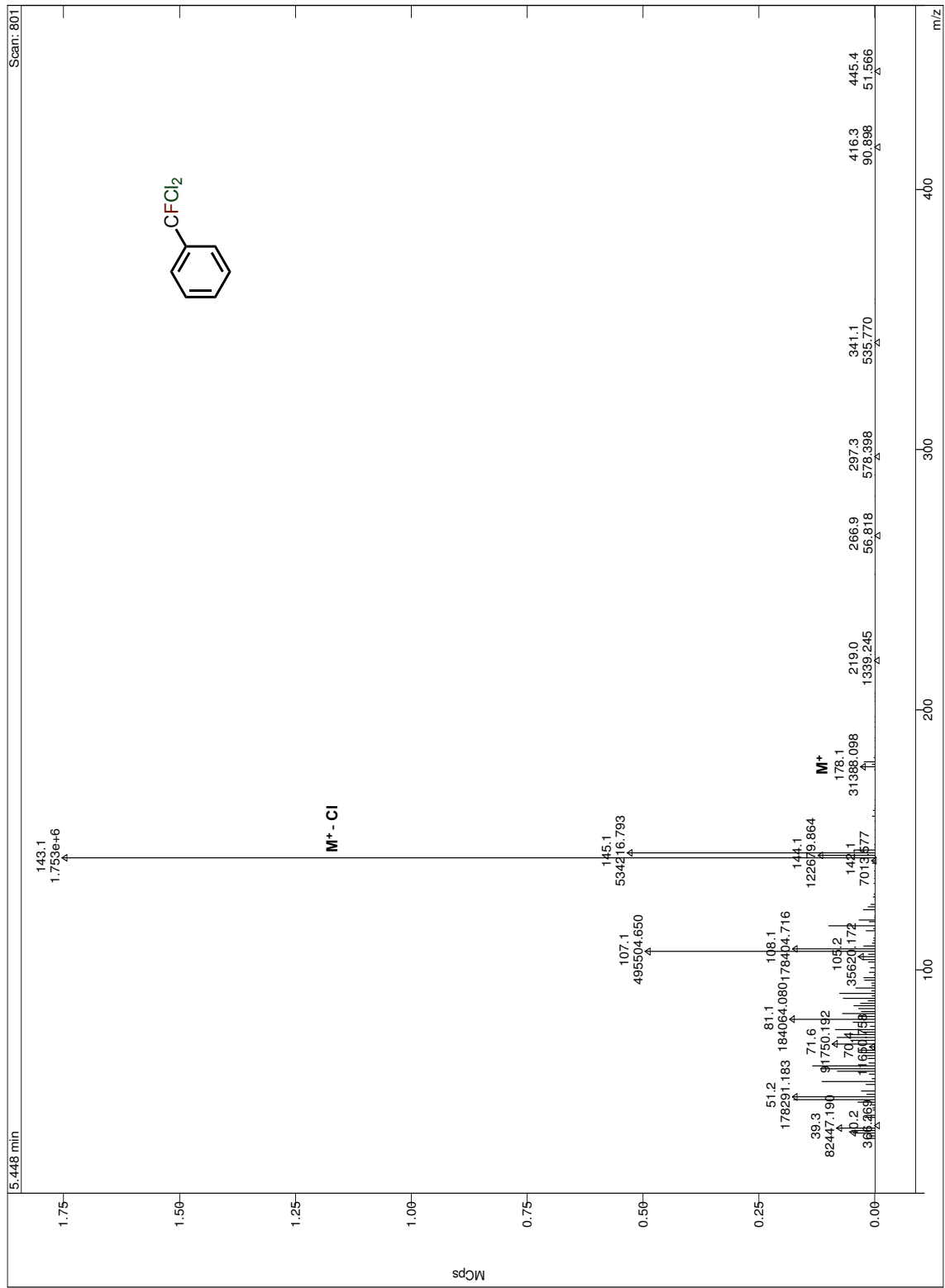


Figure A.38. Mass spectrum for peak at 7.7 minutes (compound 210 reaction)

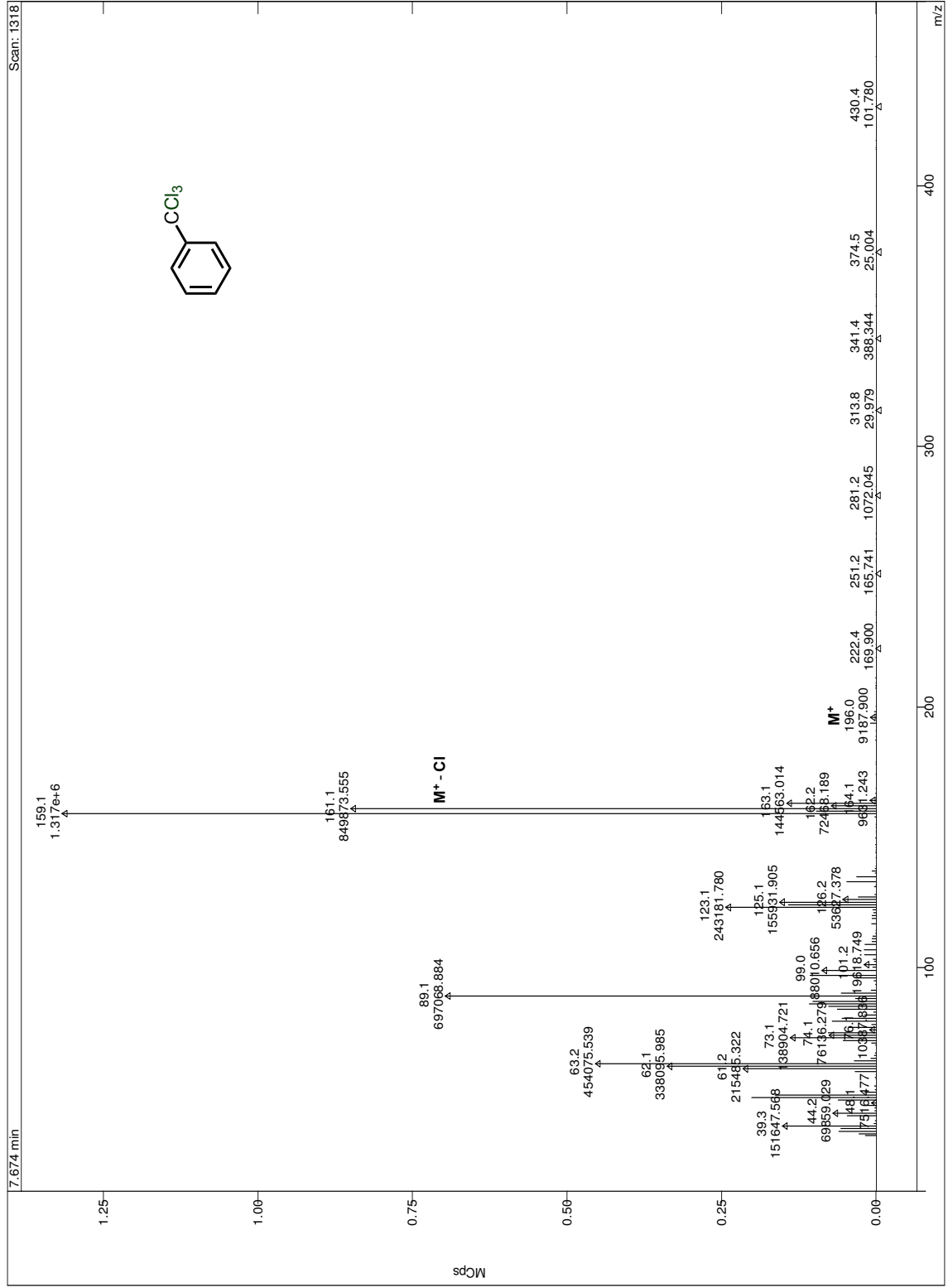


Figure A.39. GCMS chromatogram of compound 218 reaction

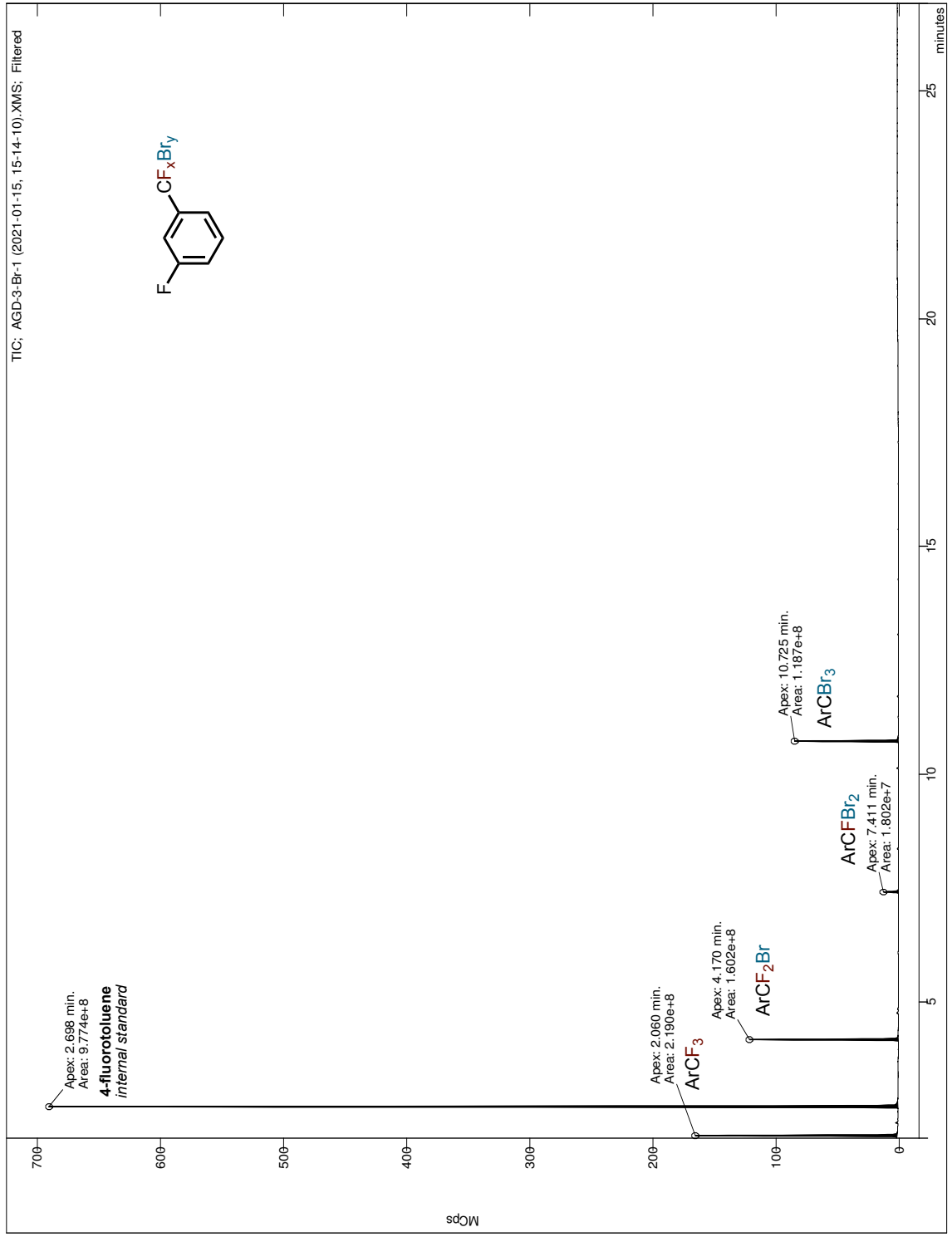


Figure A.40. Mass spectrum for peak at 2.1 minutes (compound 218 reaction)

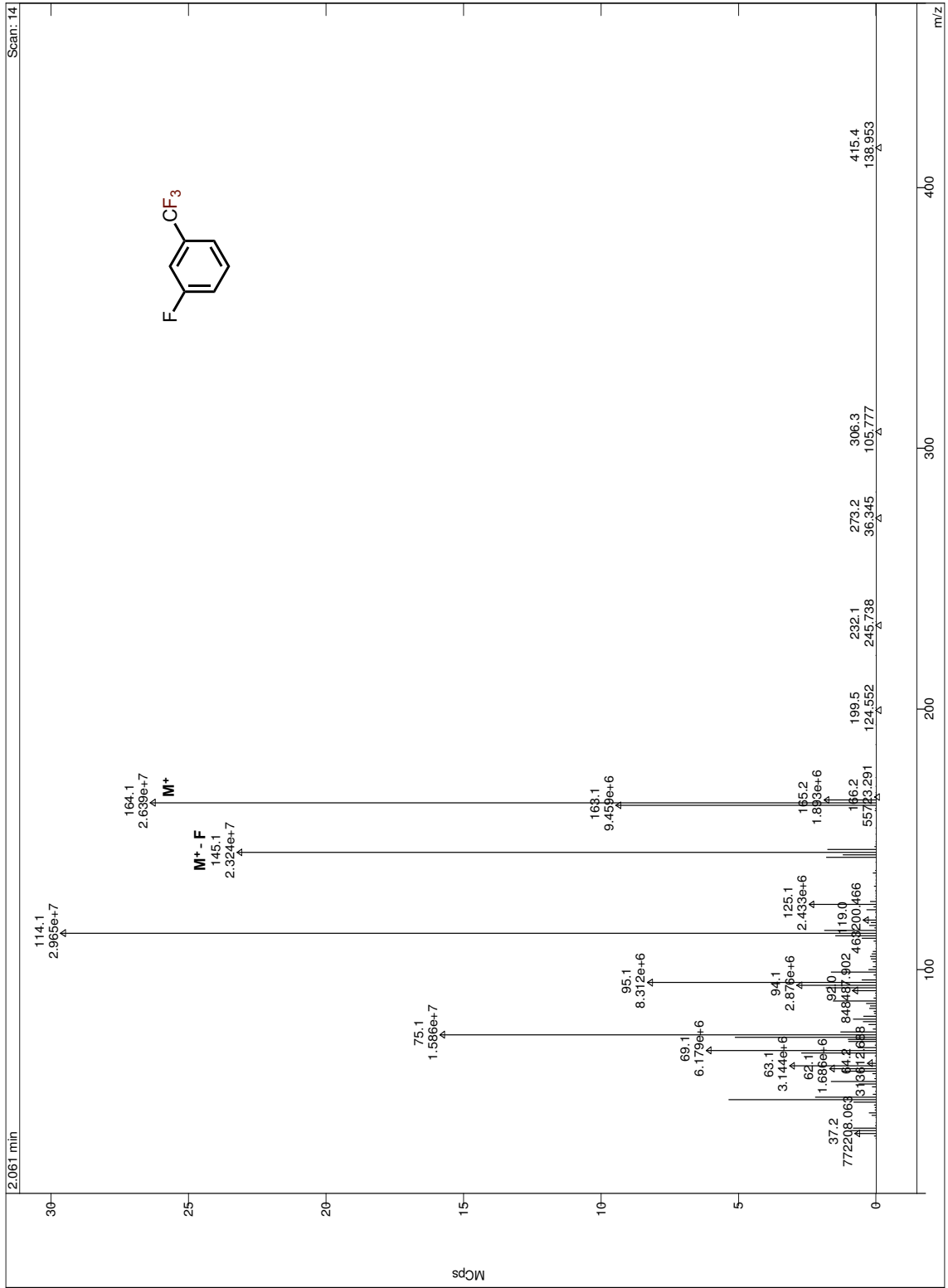


Figure A.41. Mass spectrum for peak at 4.2 minutes (compound 218 reaction)

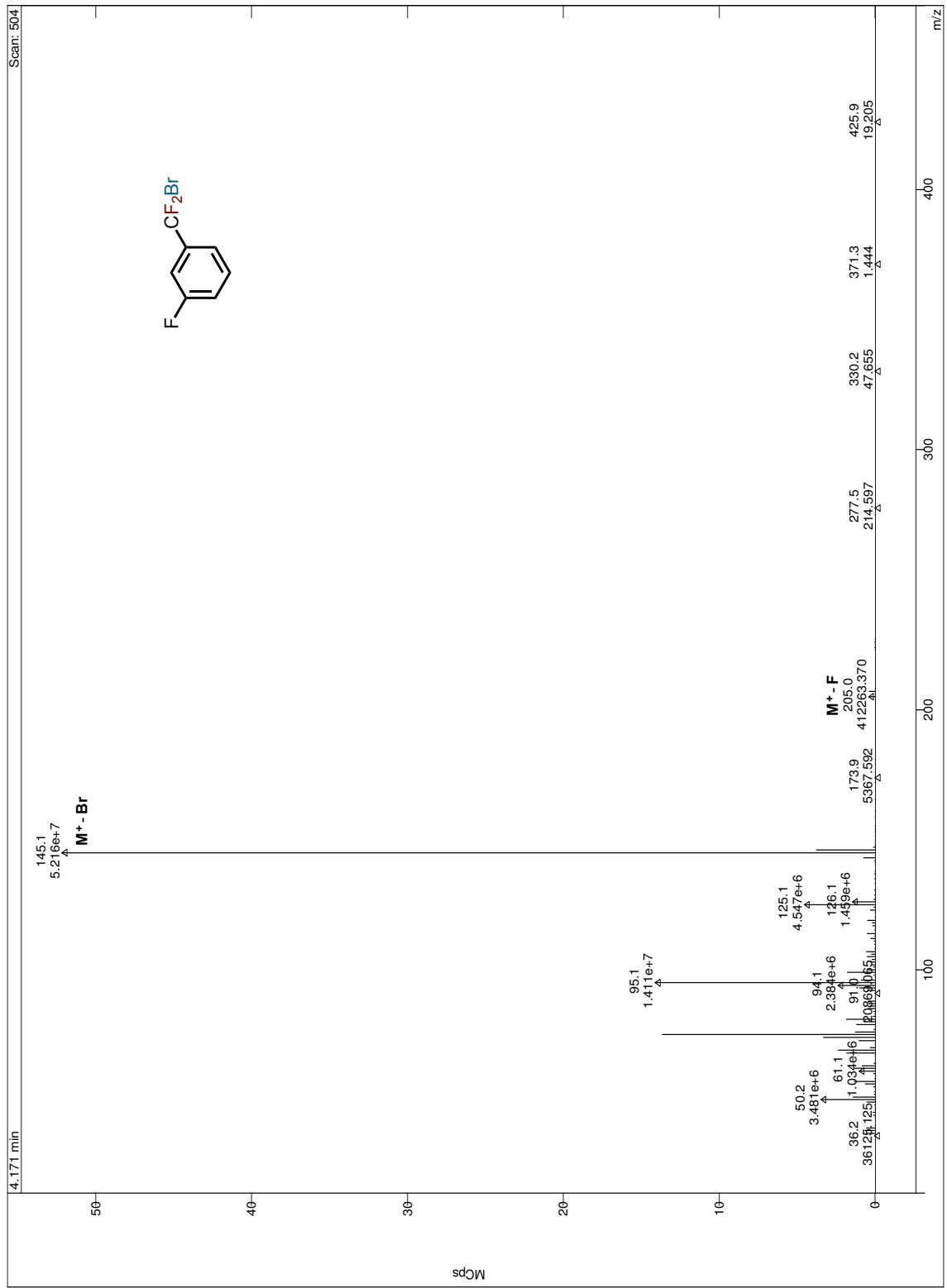


Figure A.42. Mass spectrum for peak at 7.4 minutes (compound 218 reaction)

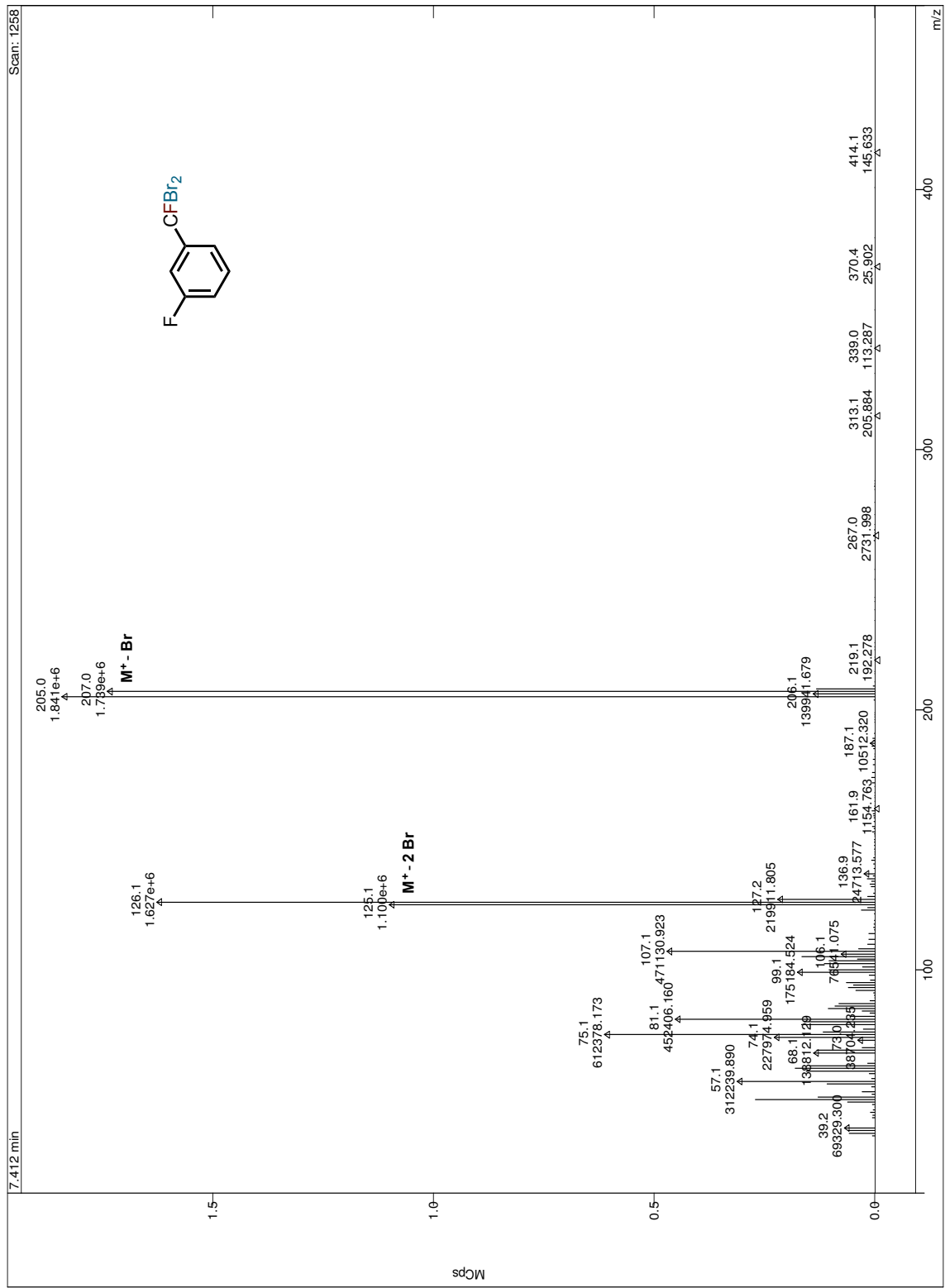


Figure A.43. Mass spectrum for peak at 10.7 minutes (compound 218 reaction)

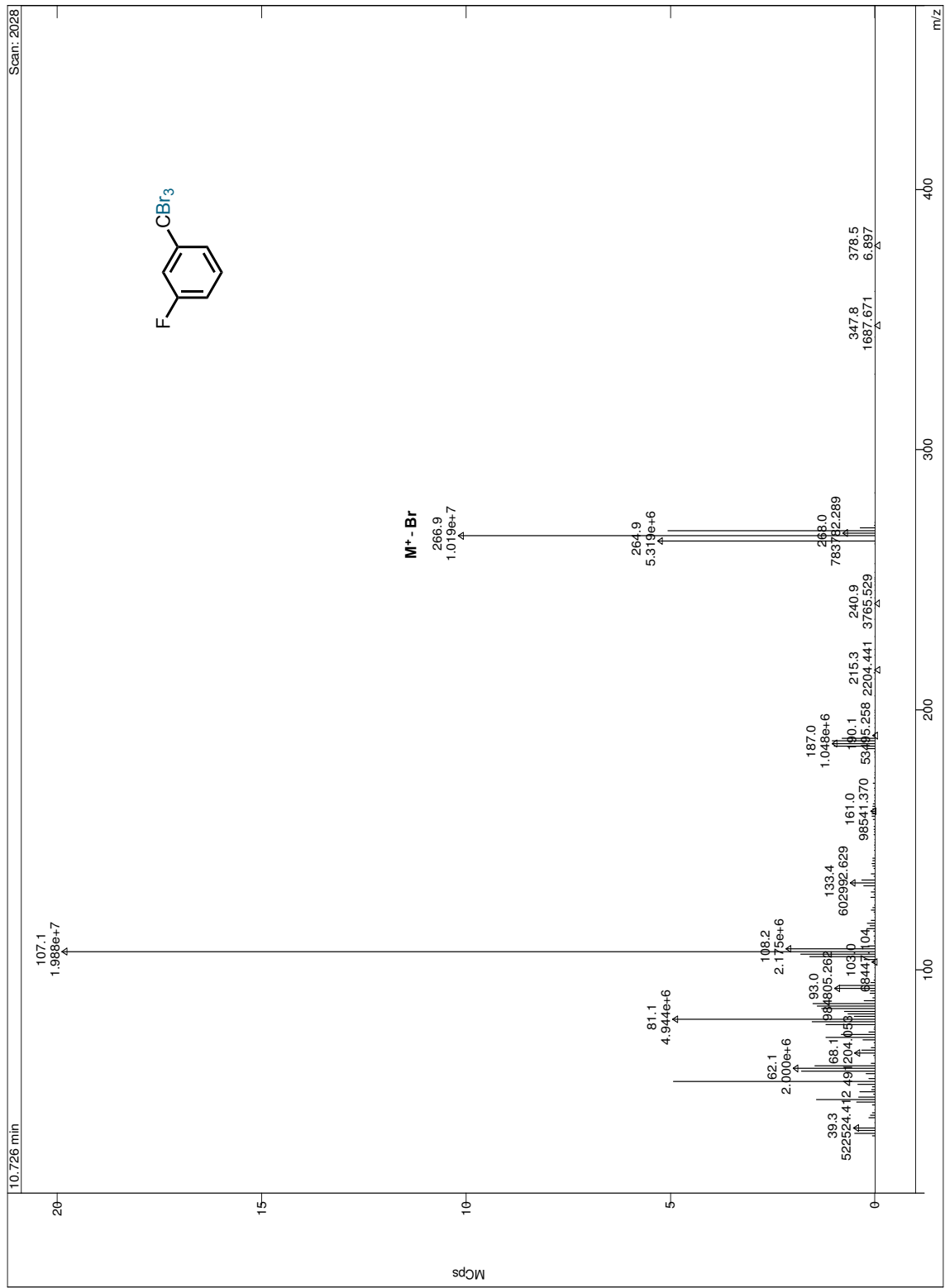


Figure A.44. GCMS chromatogram of compound 224 reaction

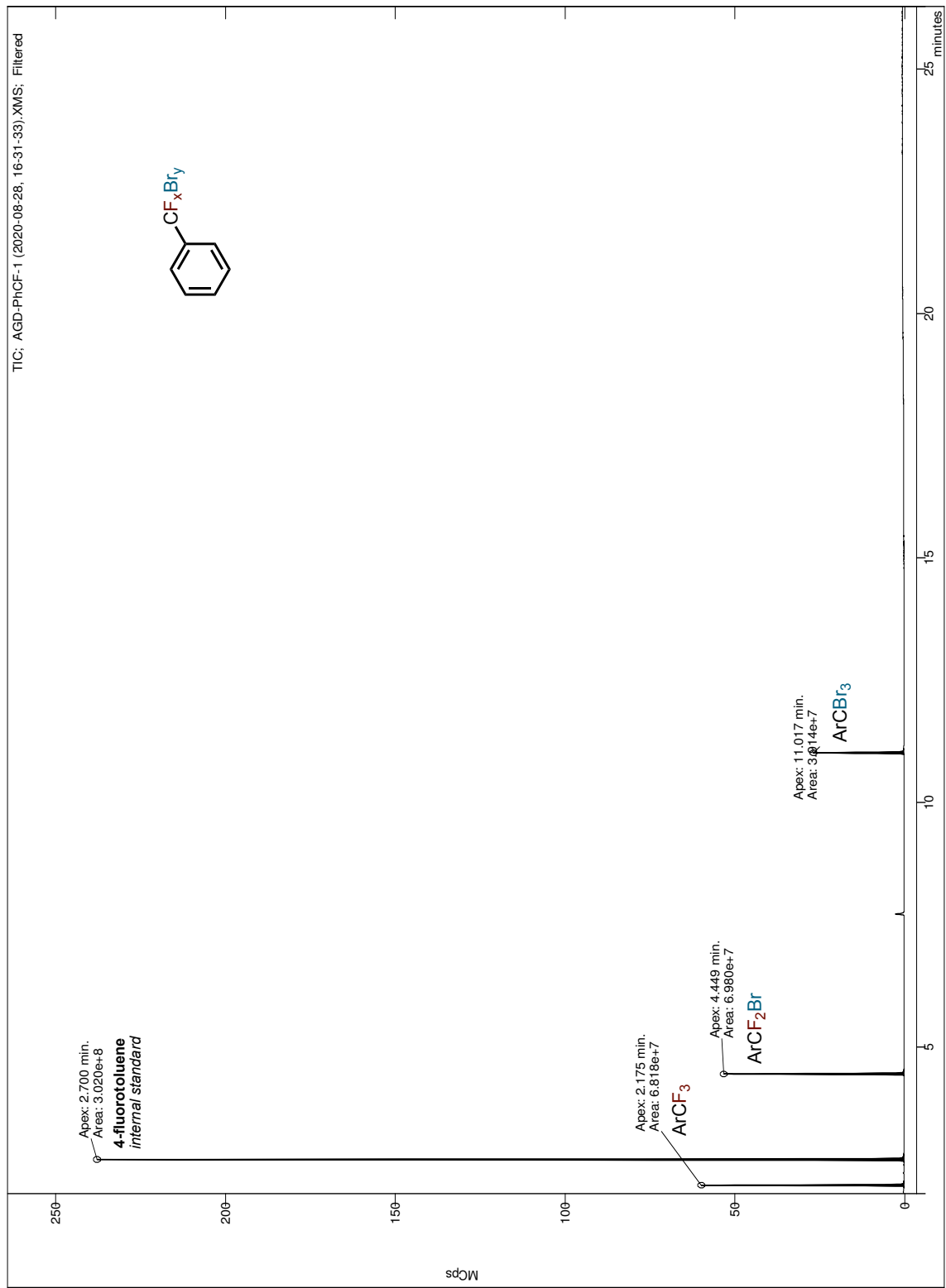


Figure A.45. Mass spectrum for peak at 2.2 minutes (compound 224 reaction)

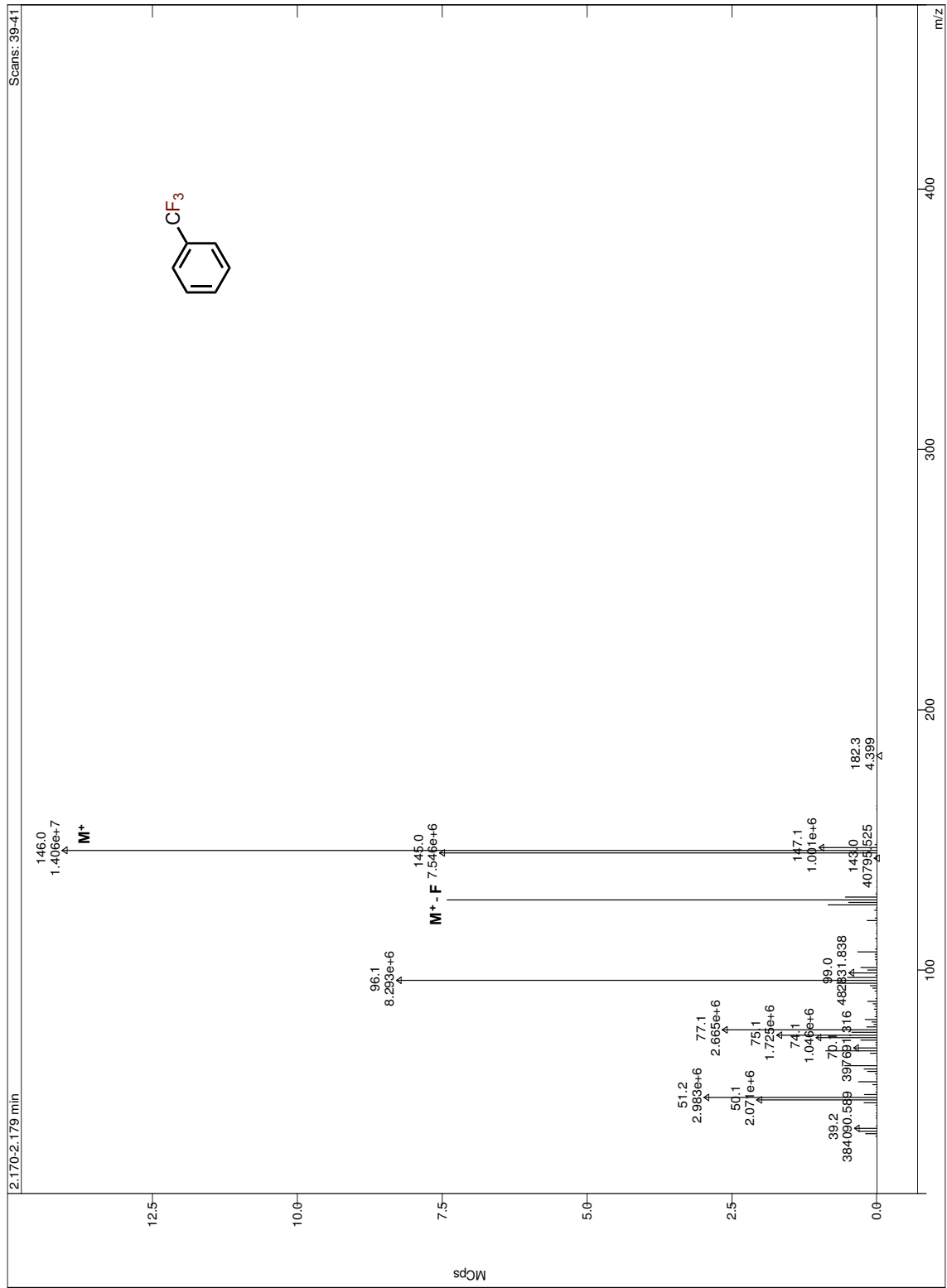


Figure A.46. Mass spectrum for peak at 4.5 minutes (compound 224 reaction)

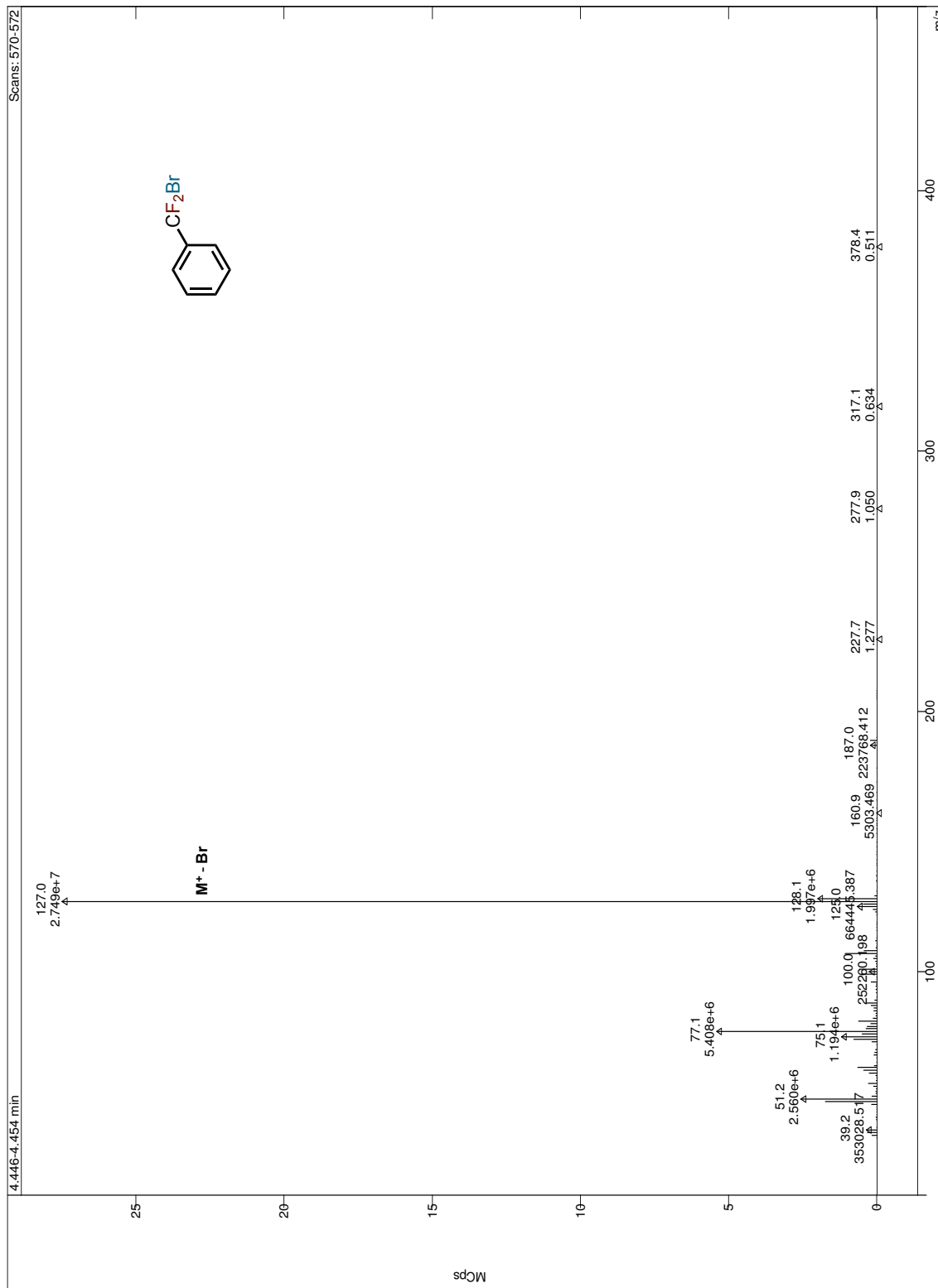


Figure A.47. Mass spectrum for peak at 11.0 minutes (compound 224 reaction)

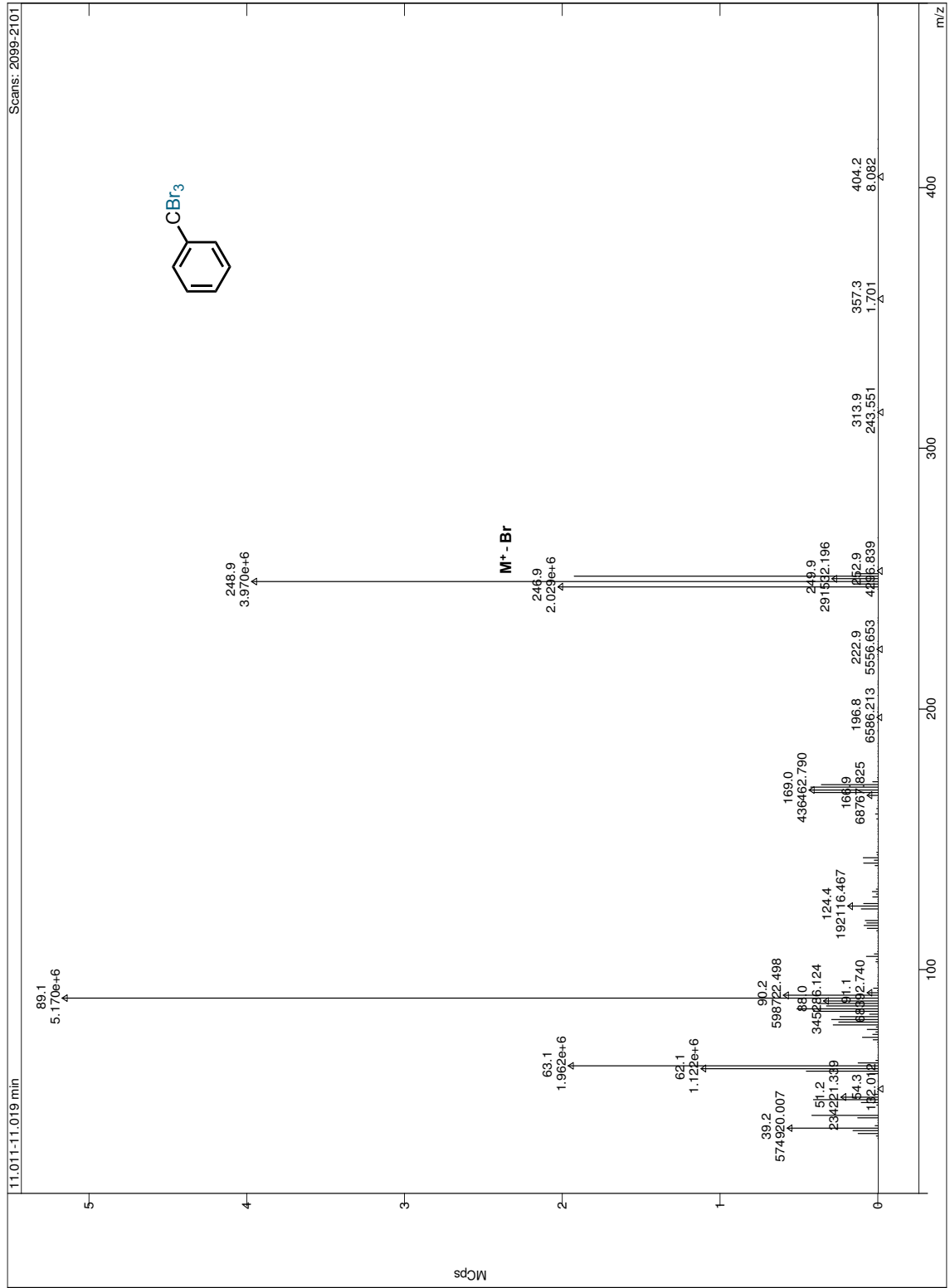


Figure A.48. GCMS chromatogram of compound 225 reaction

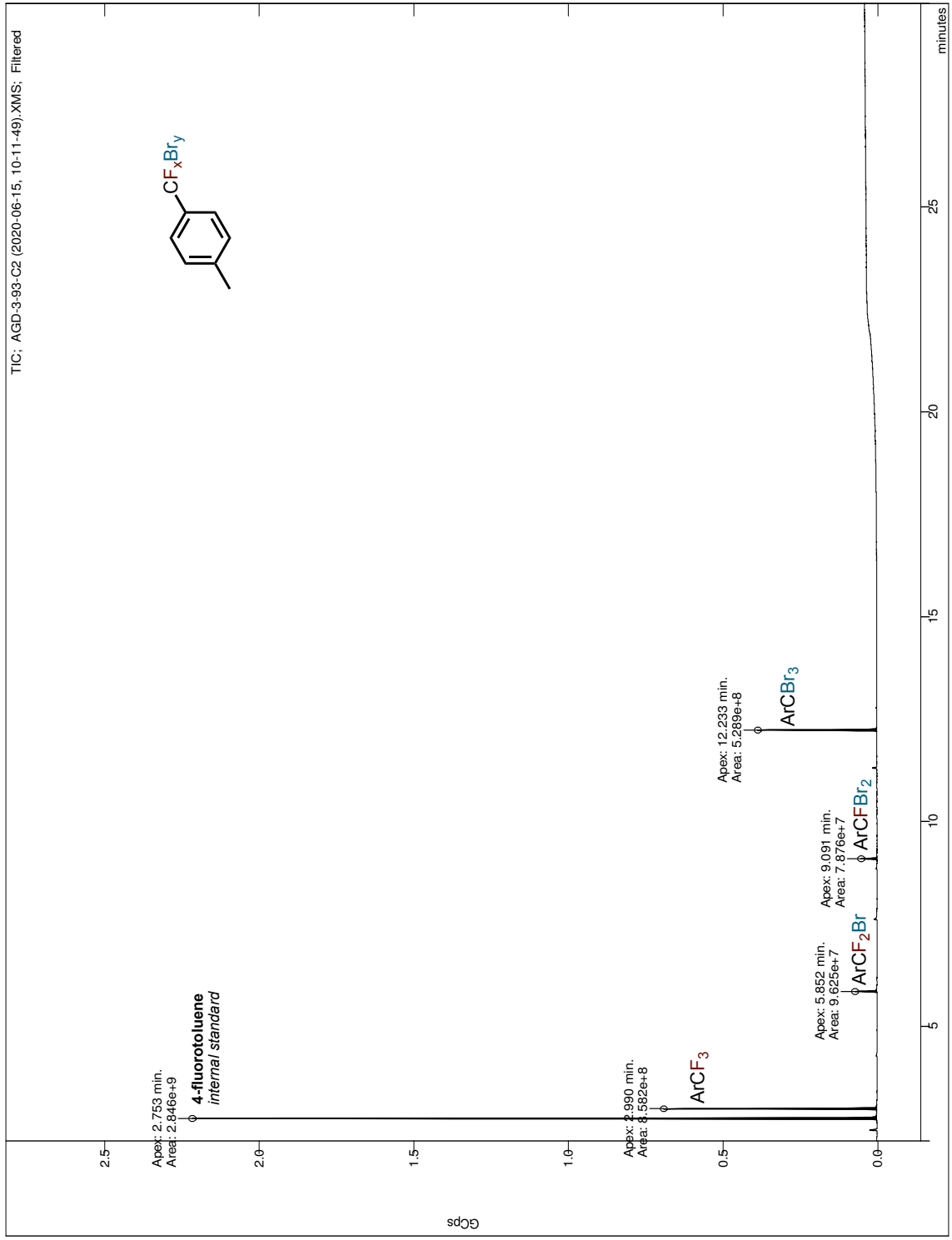


Figure A.49. Mass spectrum for peak at 3.0 minutes (compound 225 reaction)

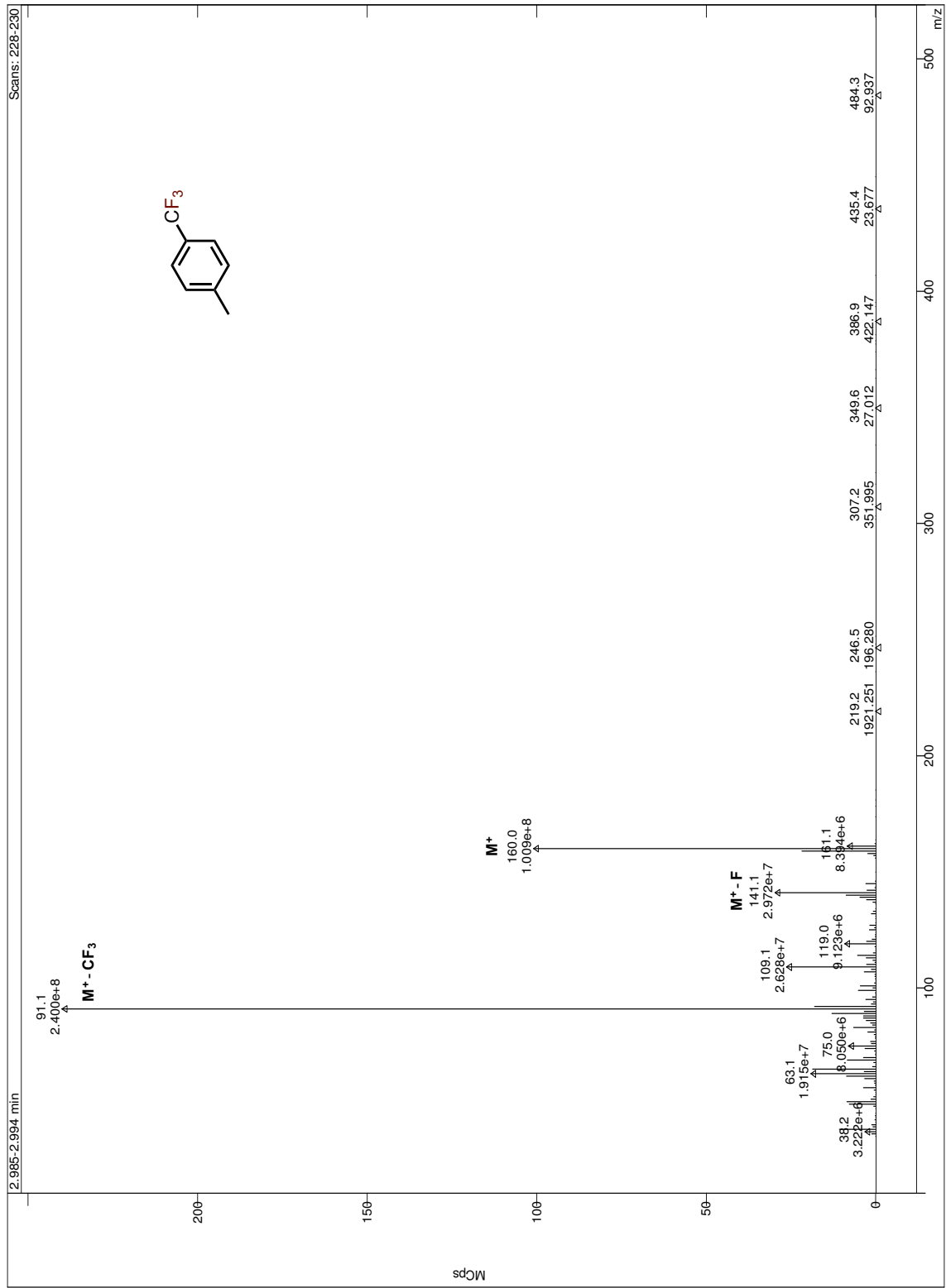


Figure A.50. Mass spectrum for peak at 5.9 minutes (compound 225 reaction)

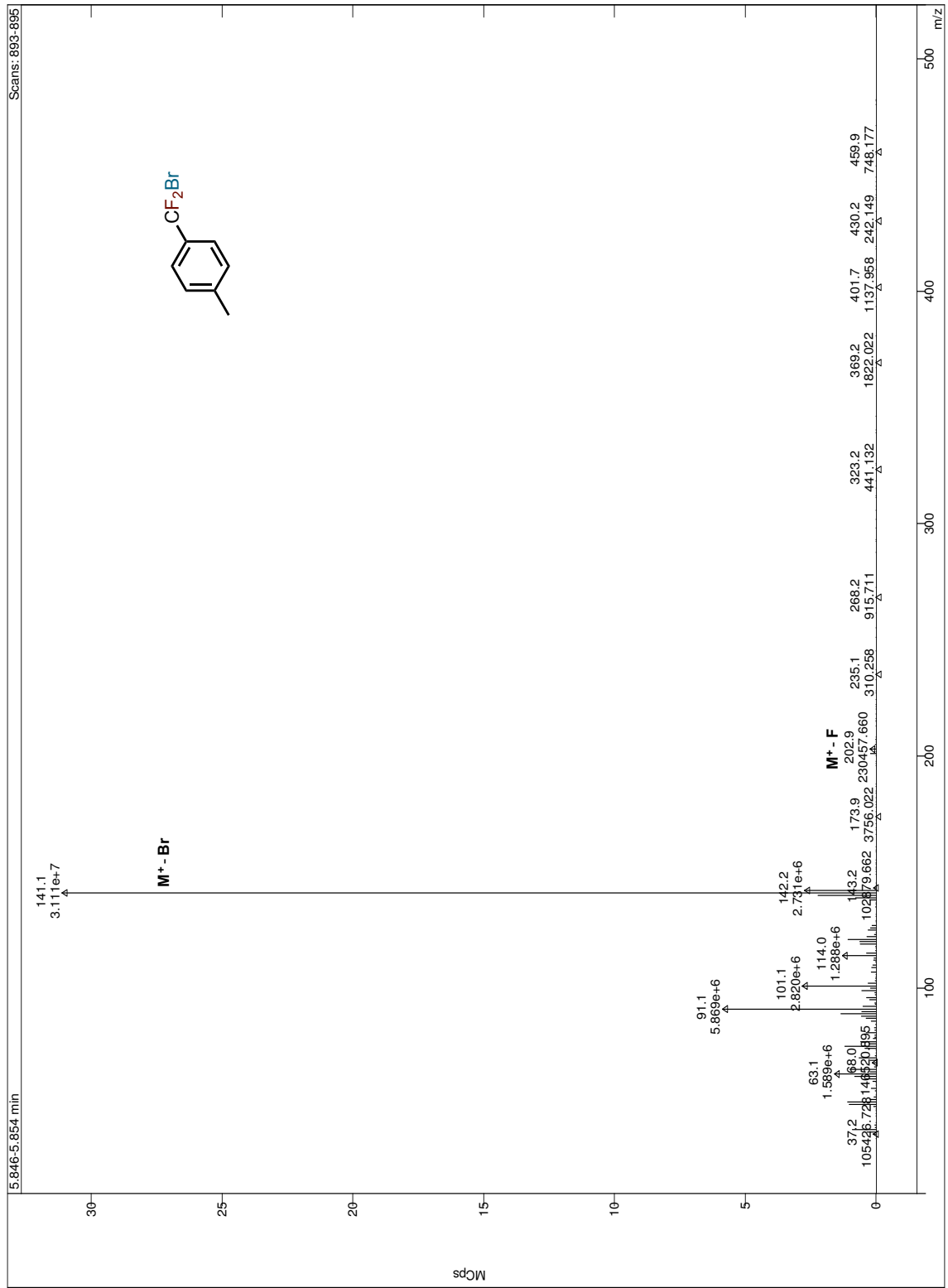


Figure A.5.1. Mass spectrum for peak at 9.1 minutes (compound 225 reaction)

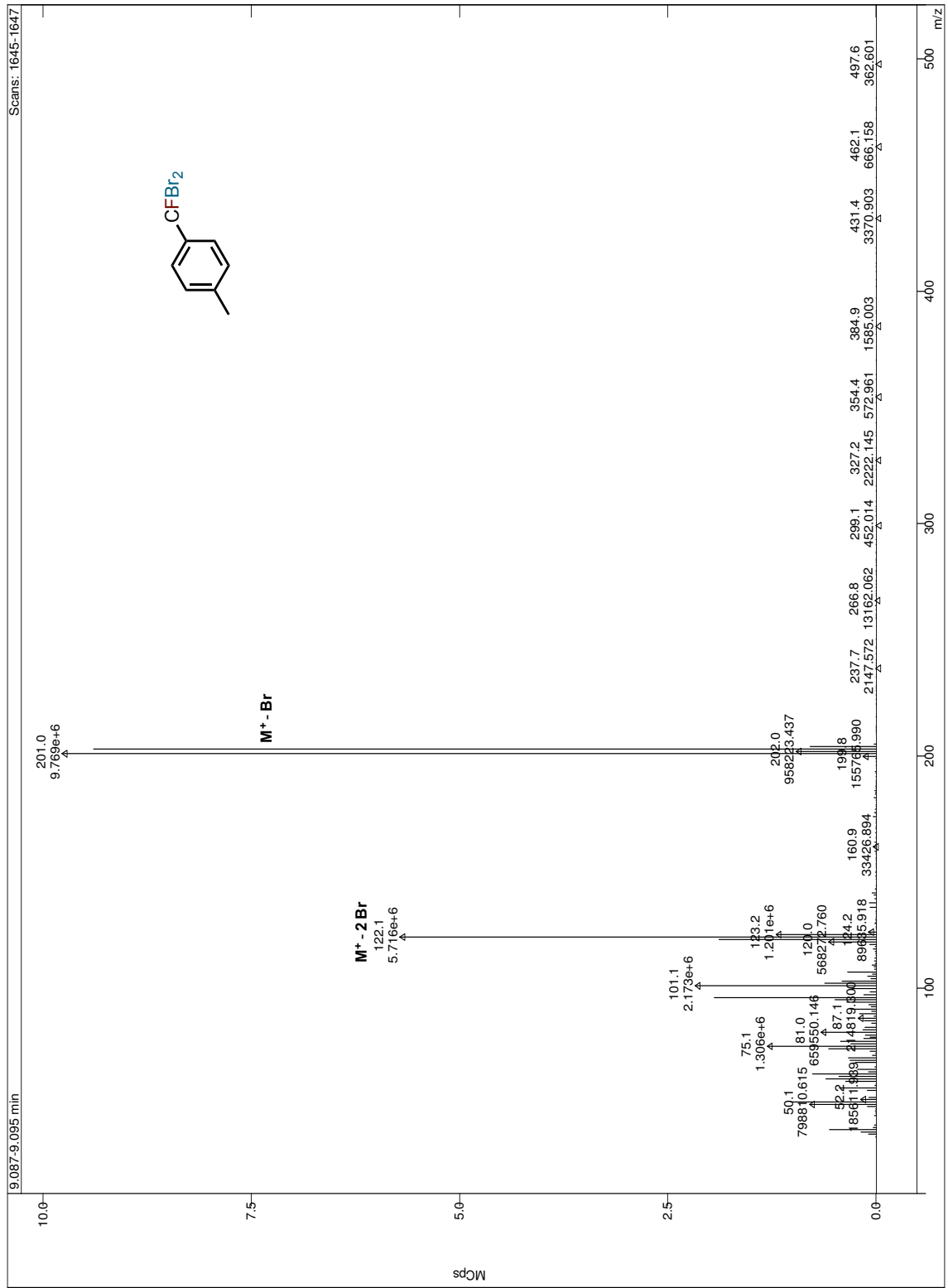


Figure A.5.2. Mass spectrum for peak at 12.2 minutes (compound 225 reaction)

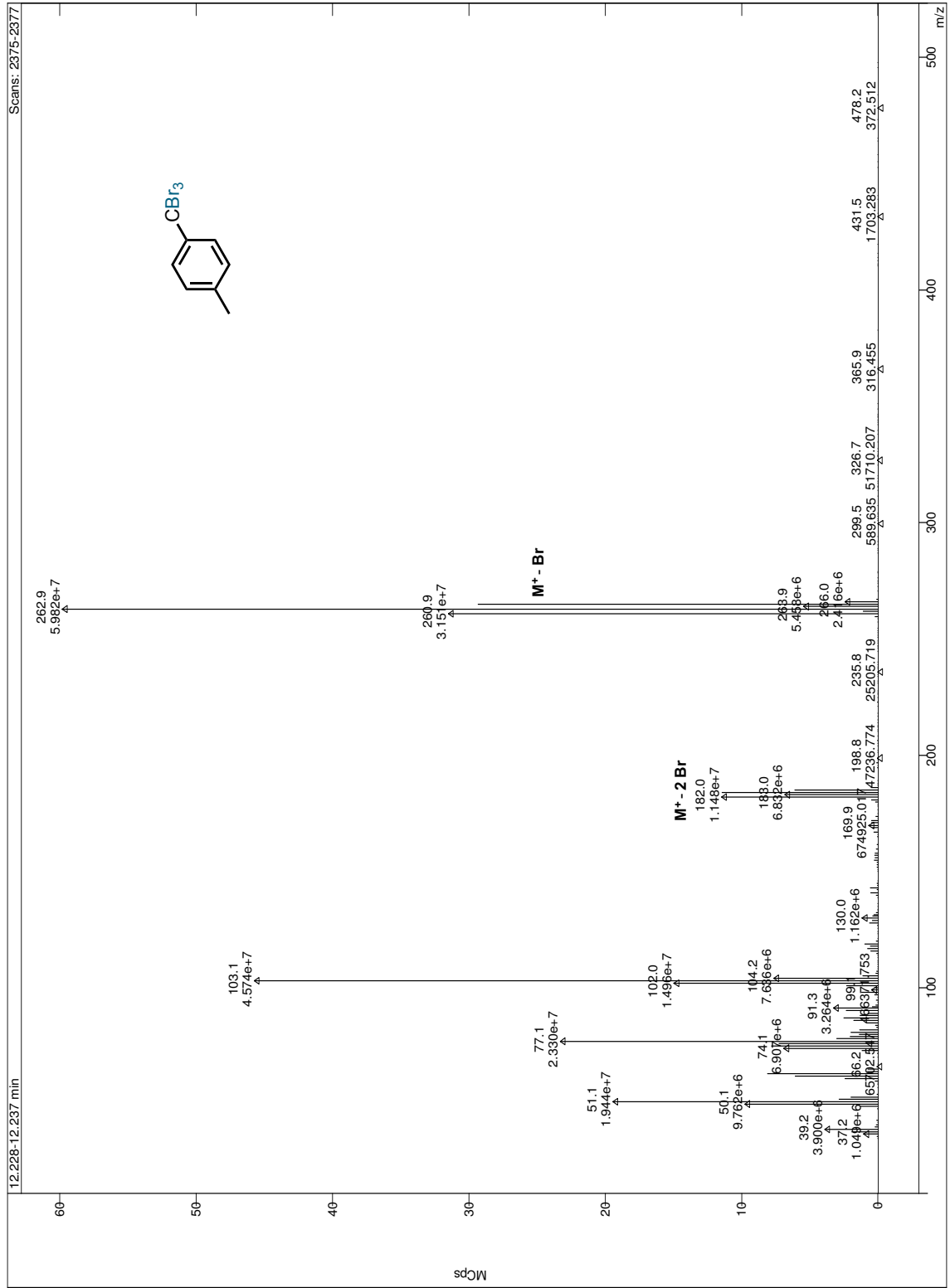


Figure A.53. GCMS chromatogram of compound 226 reaction

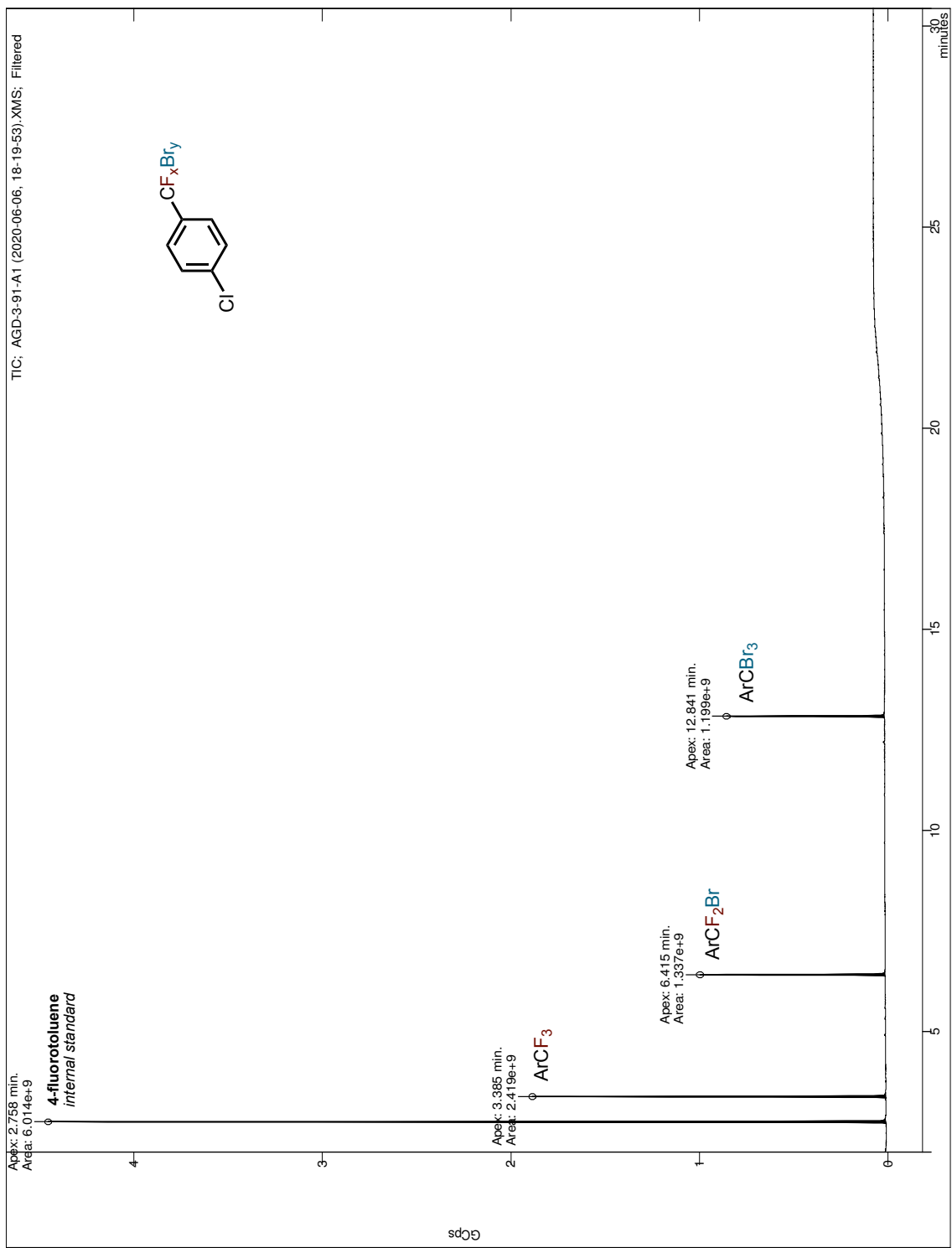


Figure A.54. Mass spectrum for peak at 3.4 minutes (compound 226 reaction)

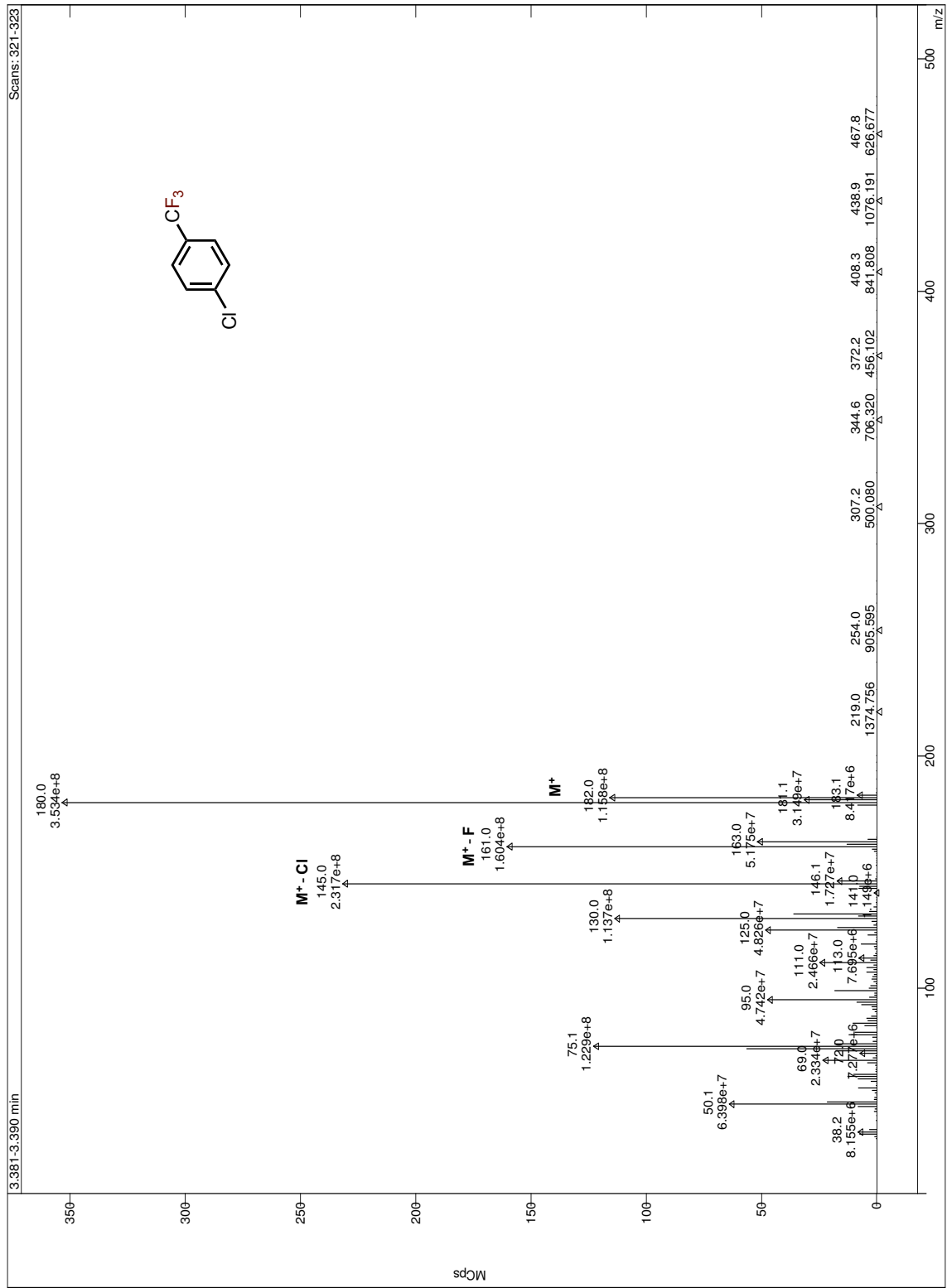


Figure A.55. Mass spectrum for peak at 6.4 minutes (compound 226 reaction)

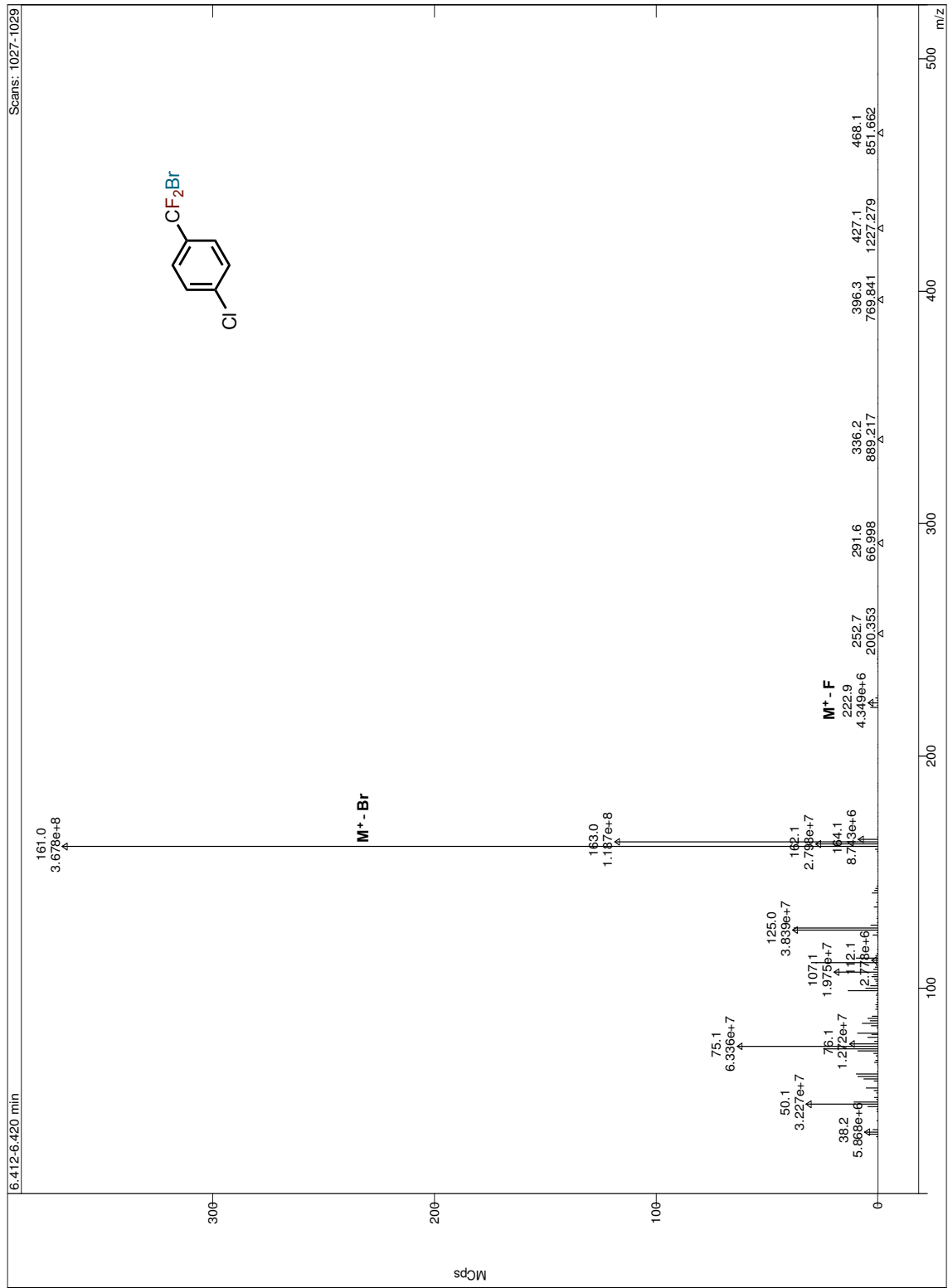


Figure A.56. Mass spectrum for peak at 12.8 minutes (compound 226 reaction)

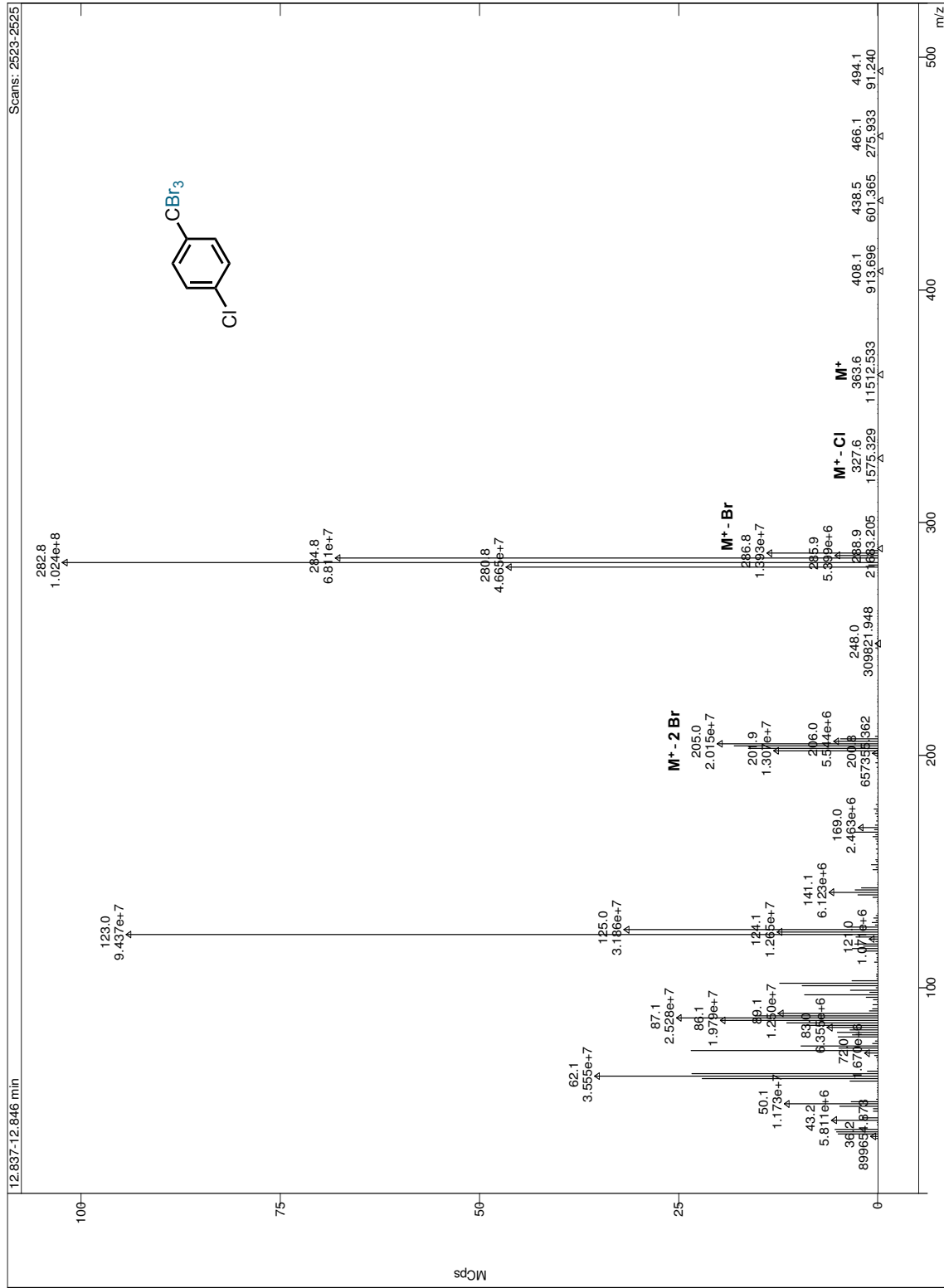


Figure A.57. GCMS chromatogram of compound 227 reaction

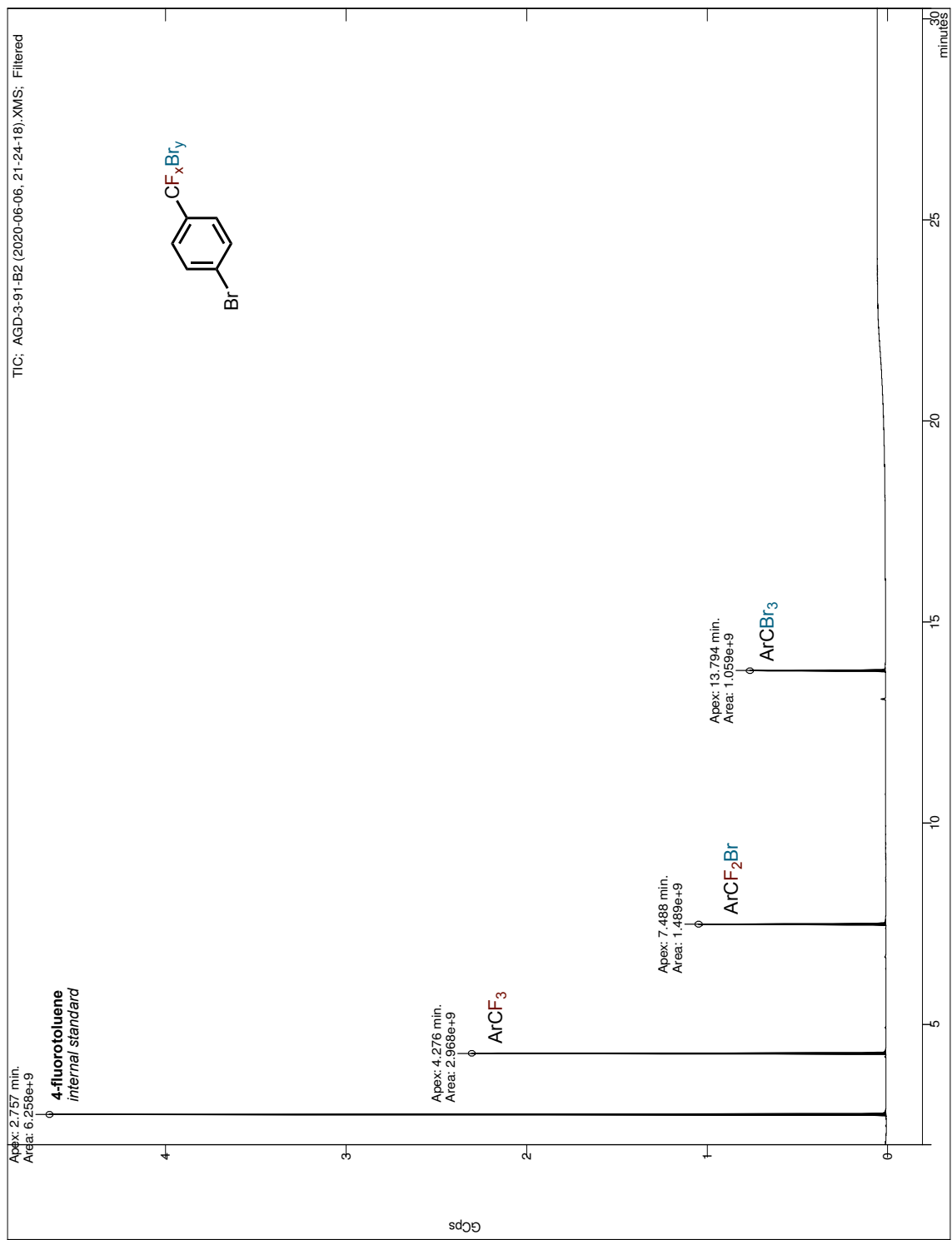


Figure A.58. Mass spectrum for peak at 4.3 minutes (compound 227 reaction)

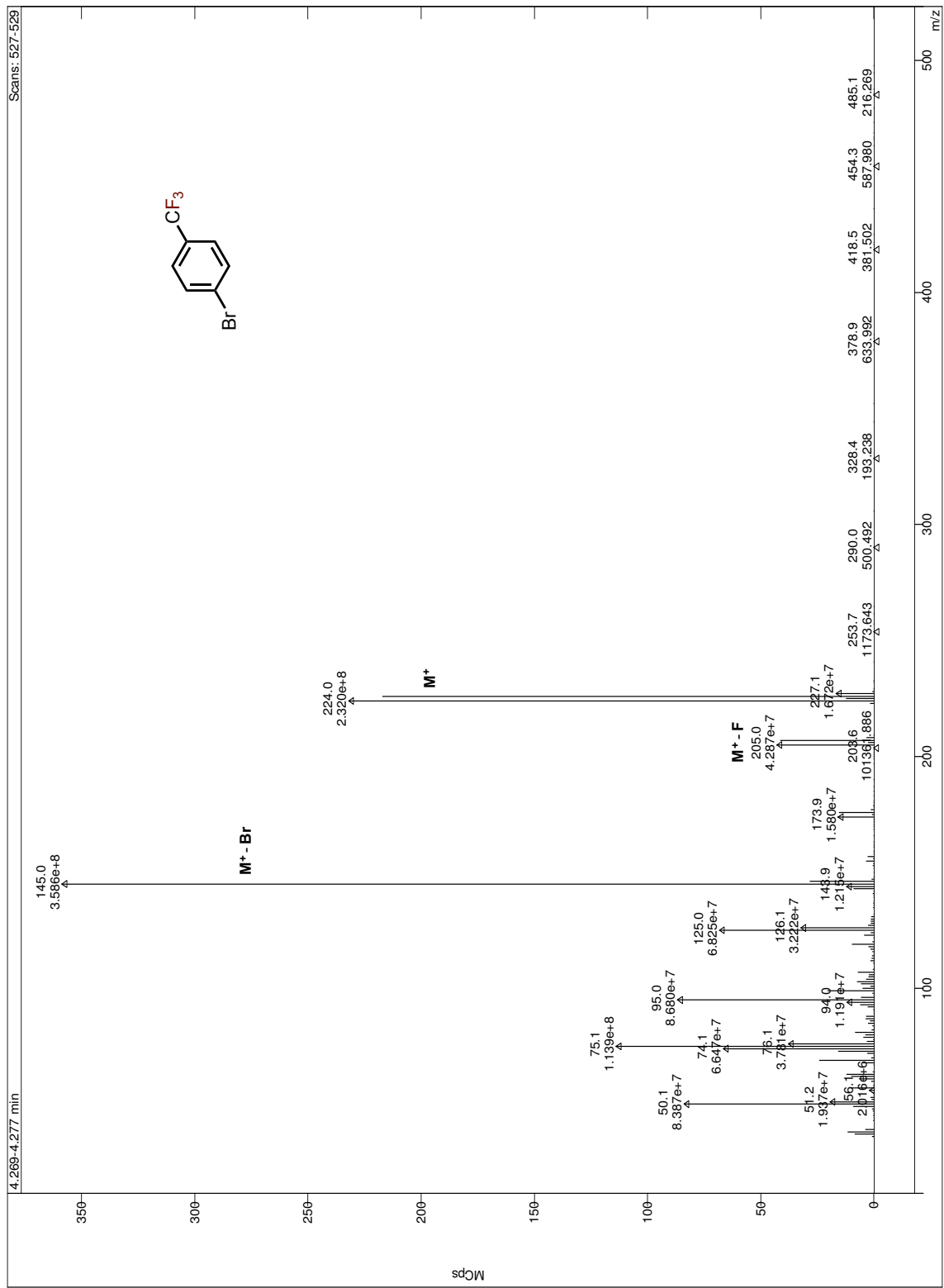


Figure A.59. Mass spectrum for peak at 7.5 minutes (compound 227 reaction)

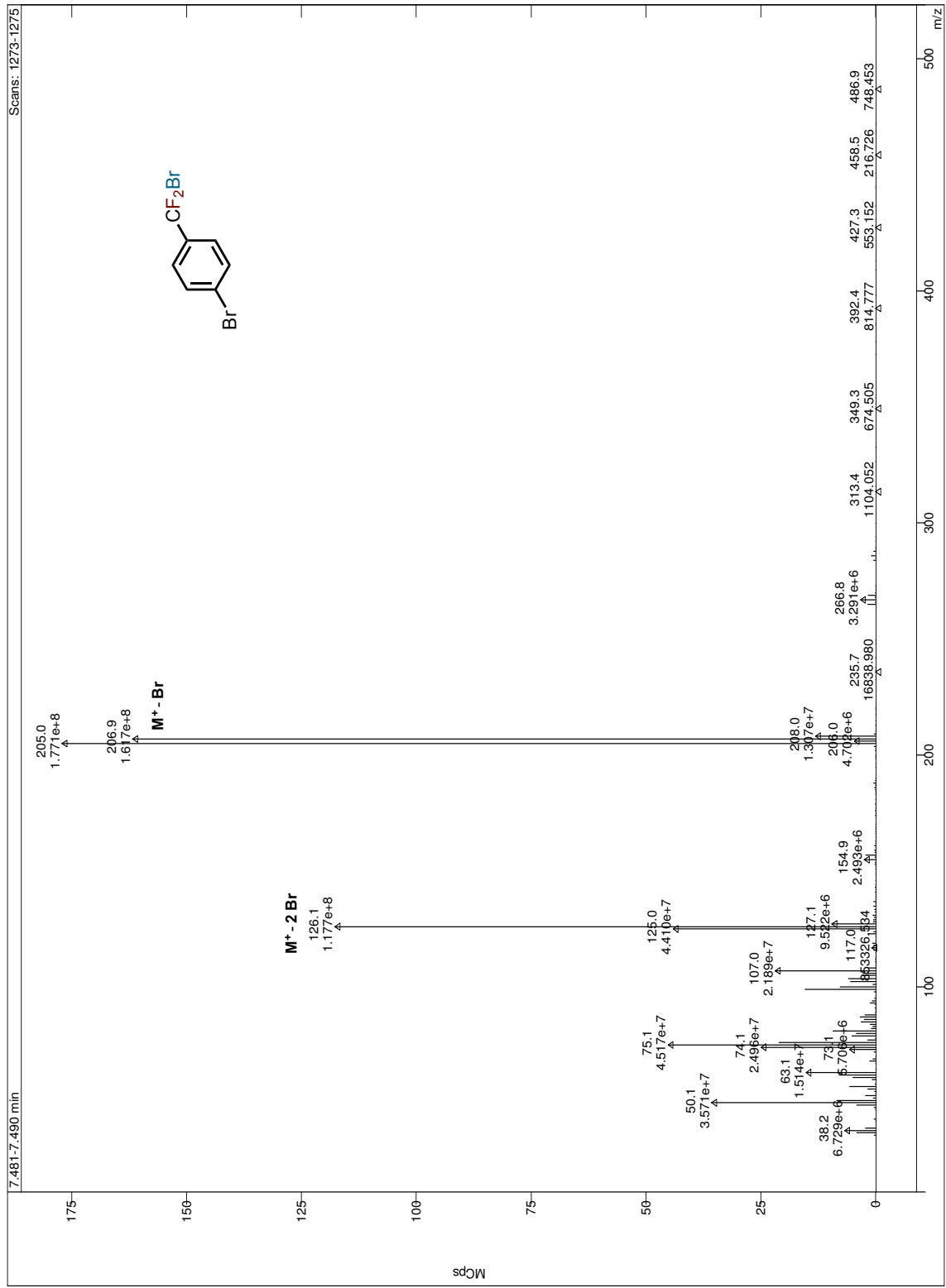


Figure A.60. Mass spectrum for peak at 13.8 minutes (compound 227 reaction)

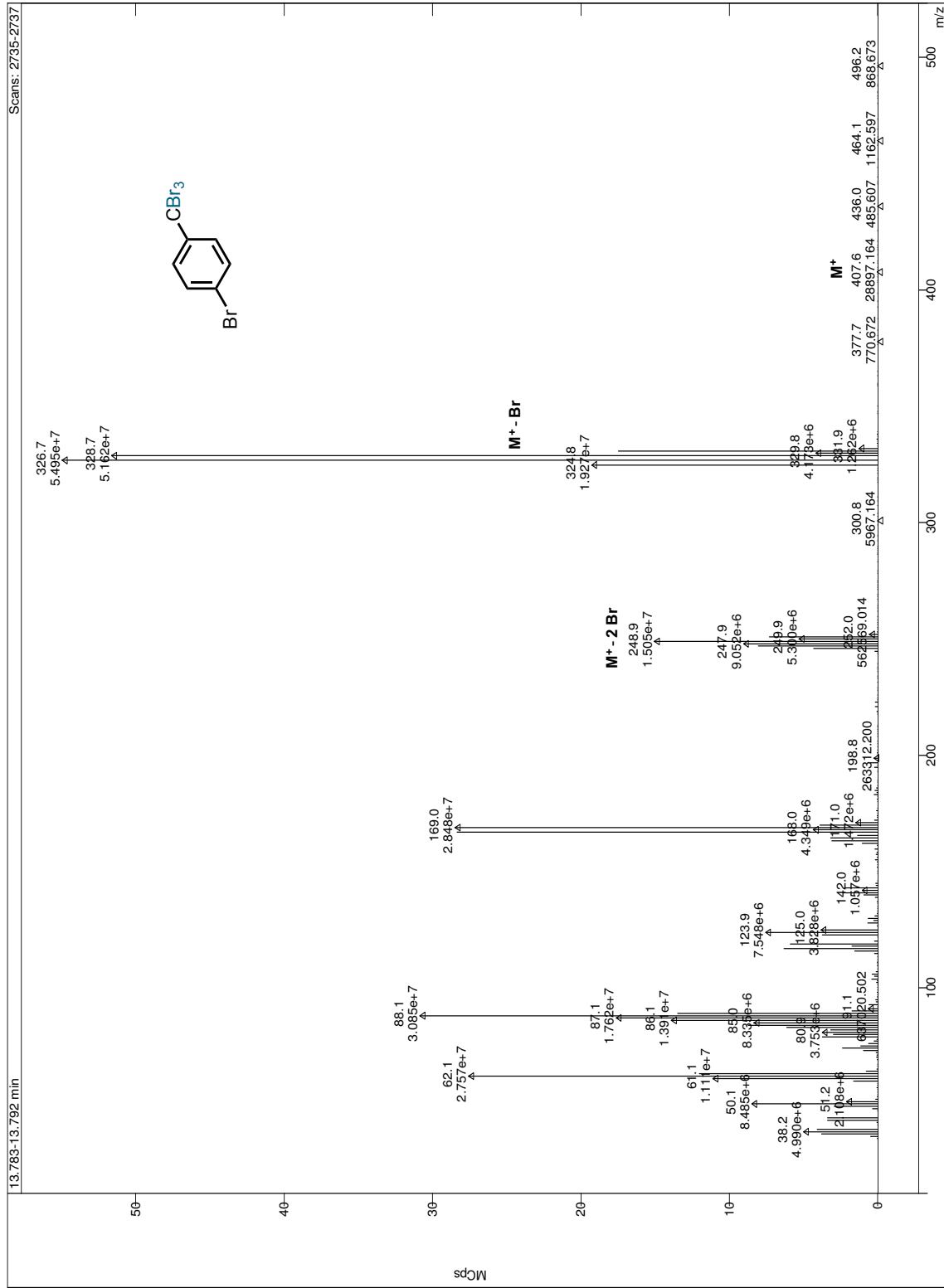


Figure A.61. HPLC chromatogram of compound 228 reaction

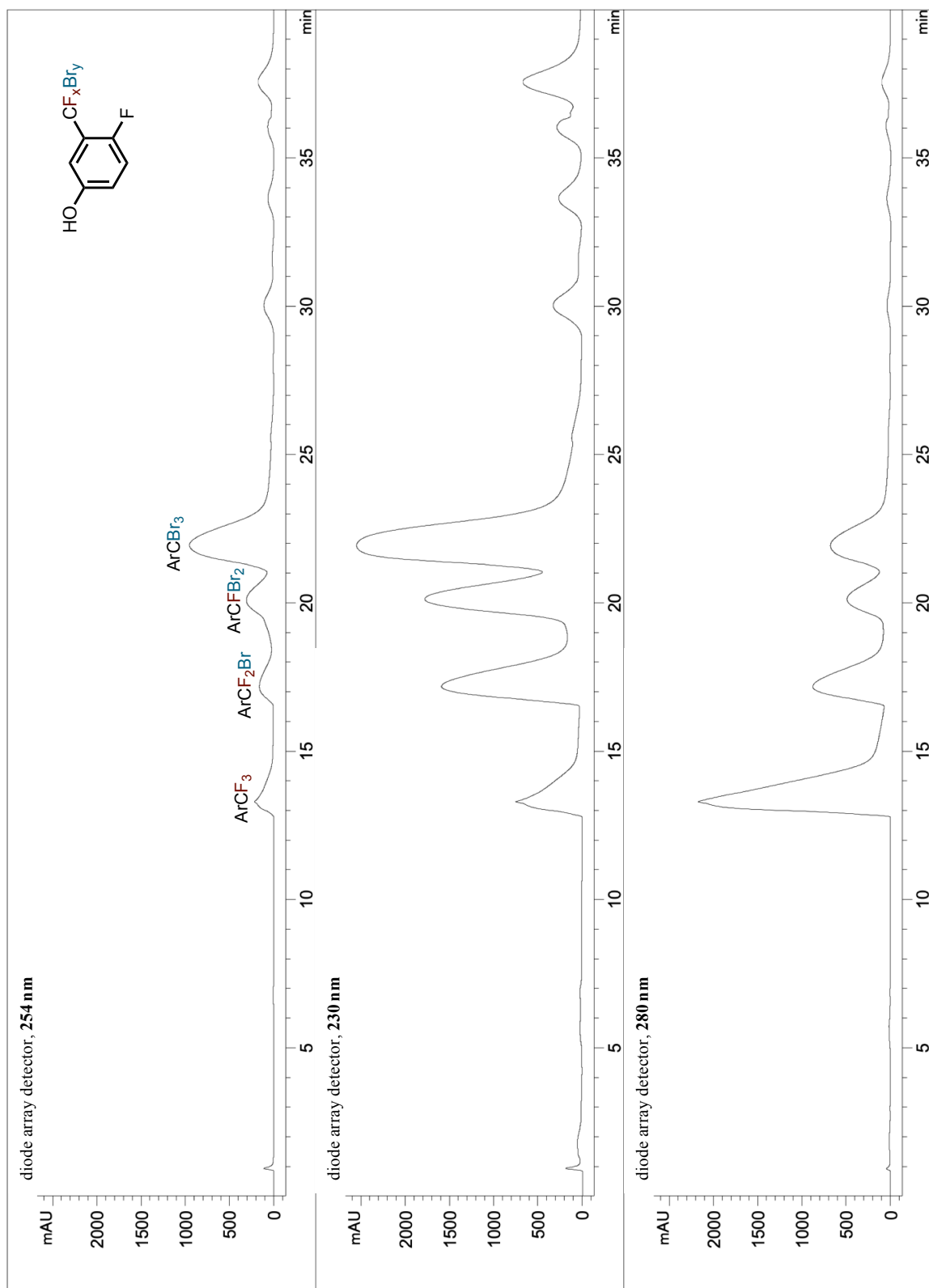


Figure A.62. HPLC chromatogram of compound 229 reaction

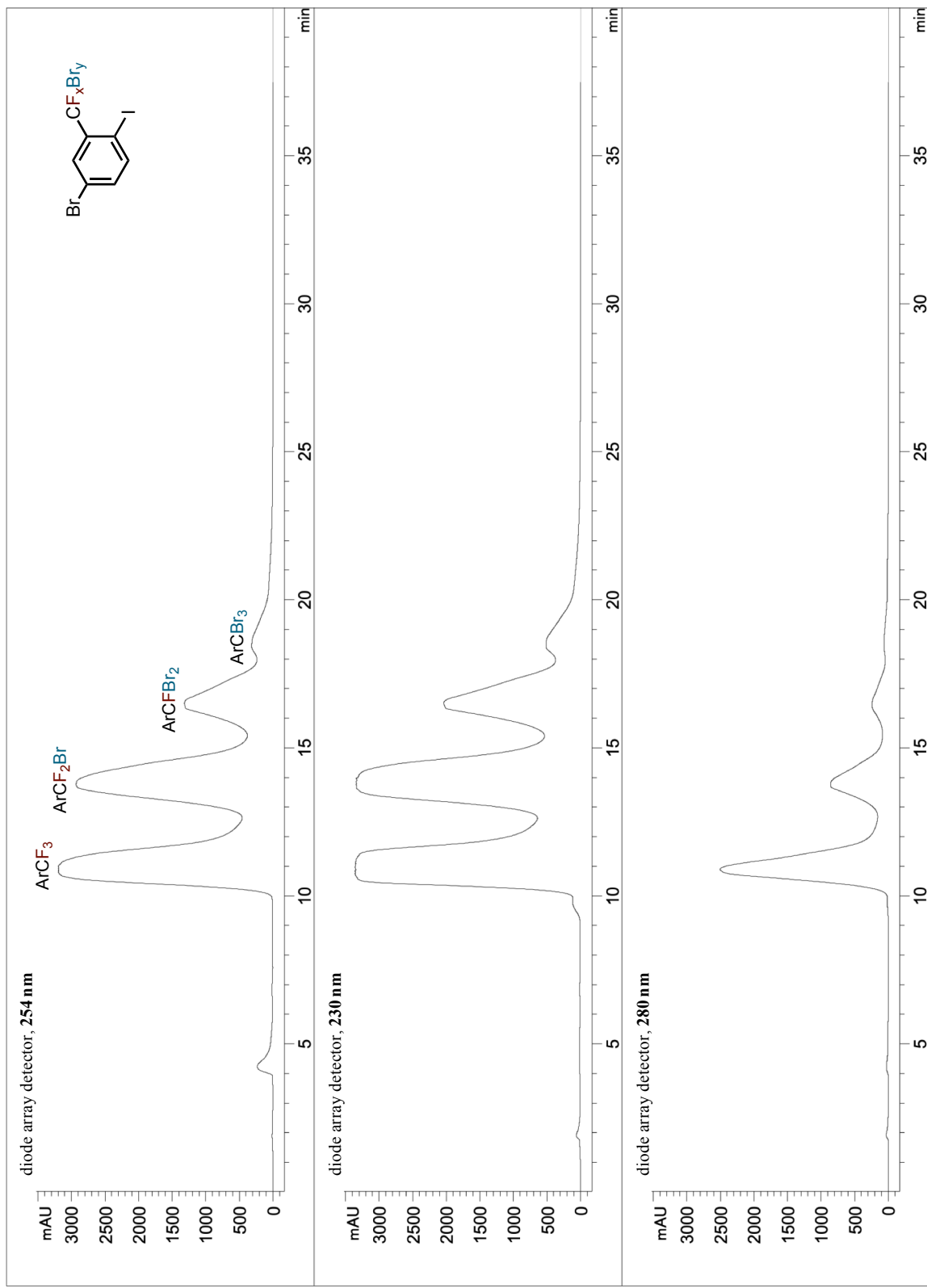


Figure A.63. HPLC chromatogram of compound 230 reaction

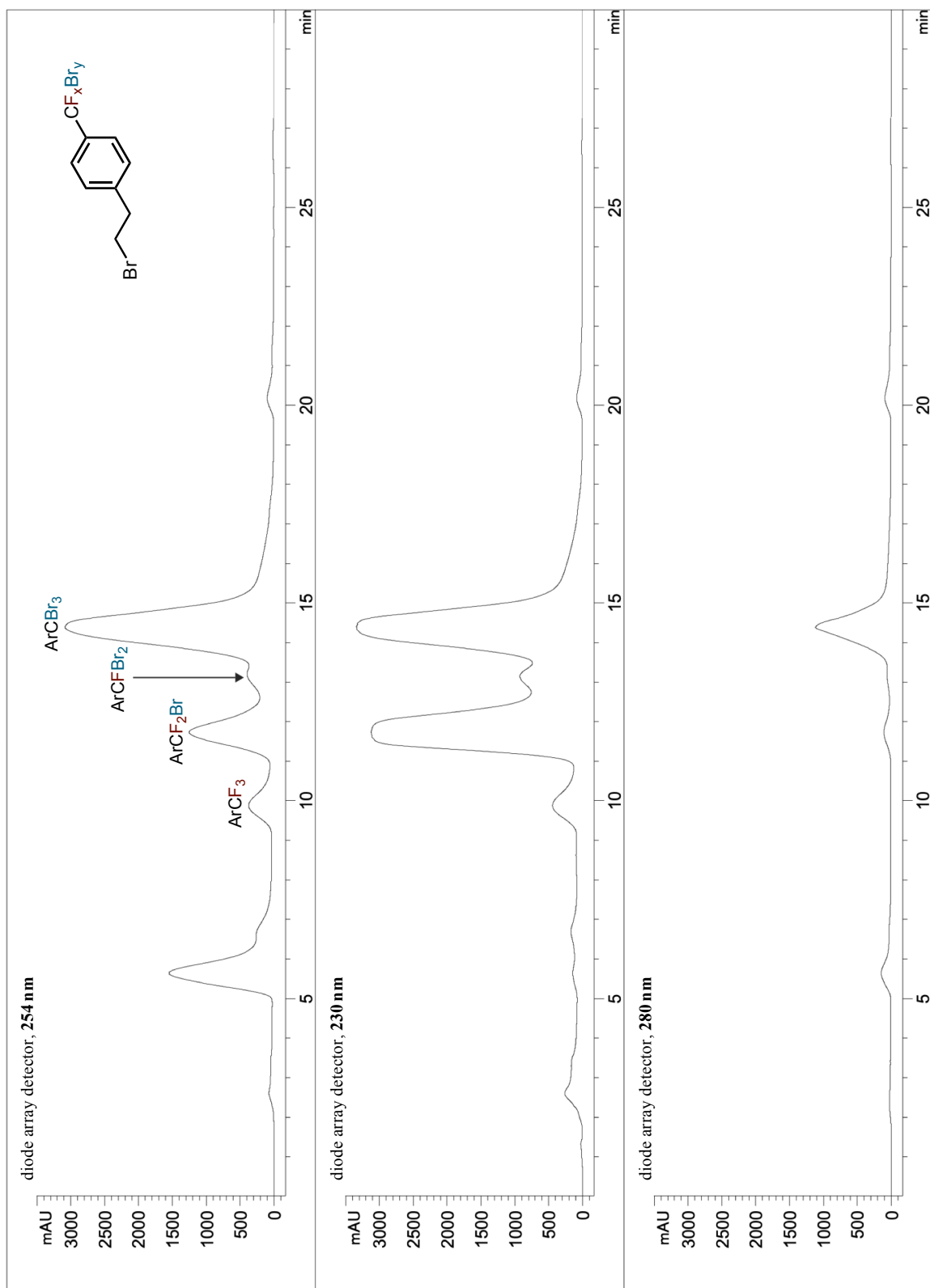


Figure A.64. HPLC chromatogram of compound 232 reaction

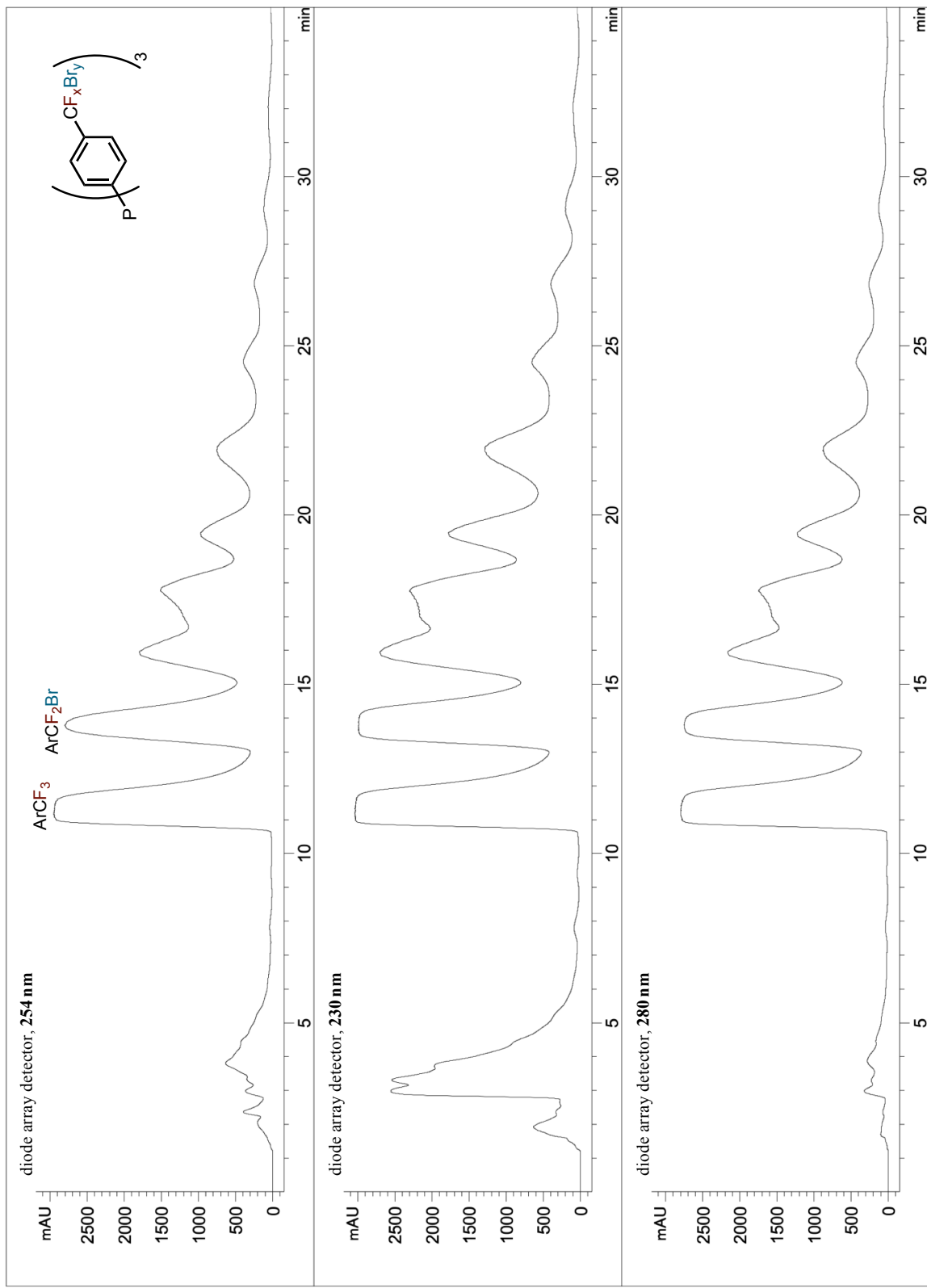


Figure A.65. HPLC chromatogram of compound 234 reaction

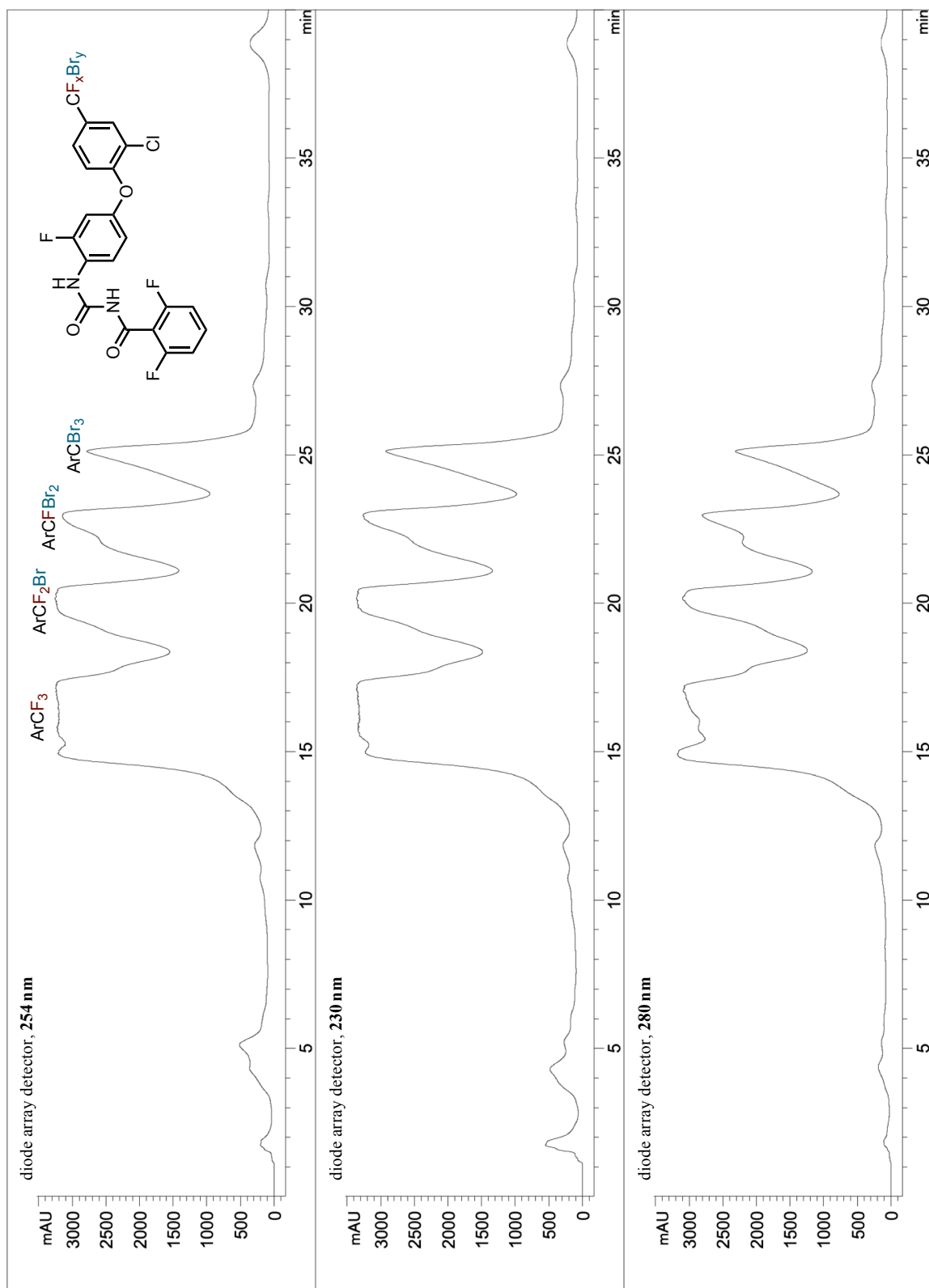


Figure A.66. ¹H NMR spectrum of compound 218 (CDCl₃, 499.8 MHz)

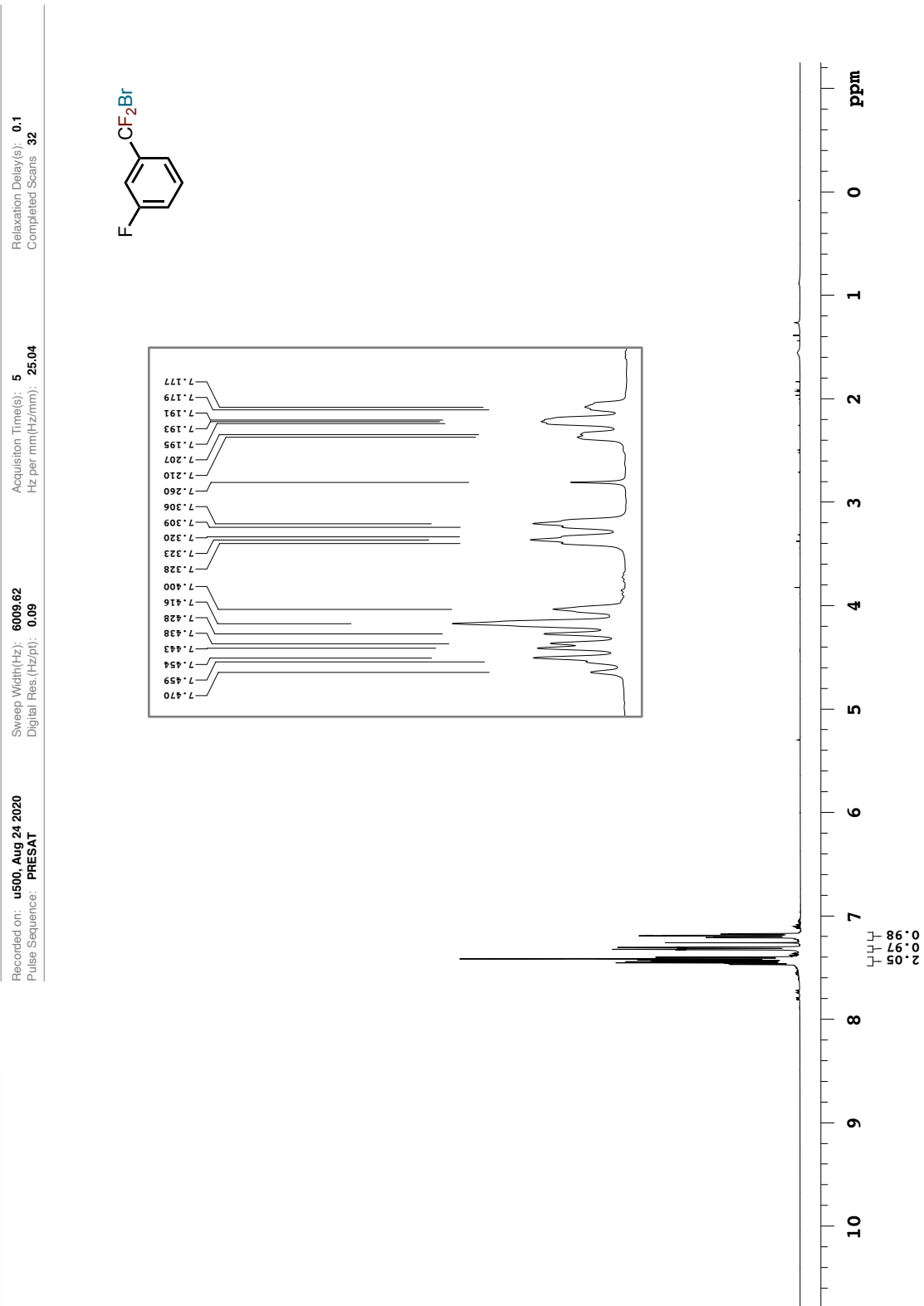


Figure A.67. $^{13}\text{C}\{^1\text{H}\}$ NMR spectrum of compound **218** (CDCl_3 , 125.7 MHz)

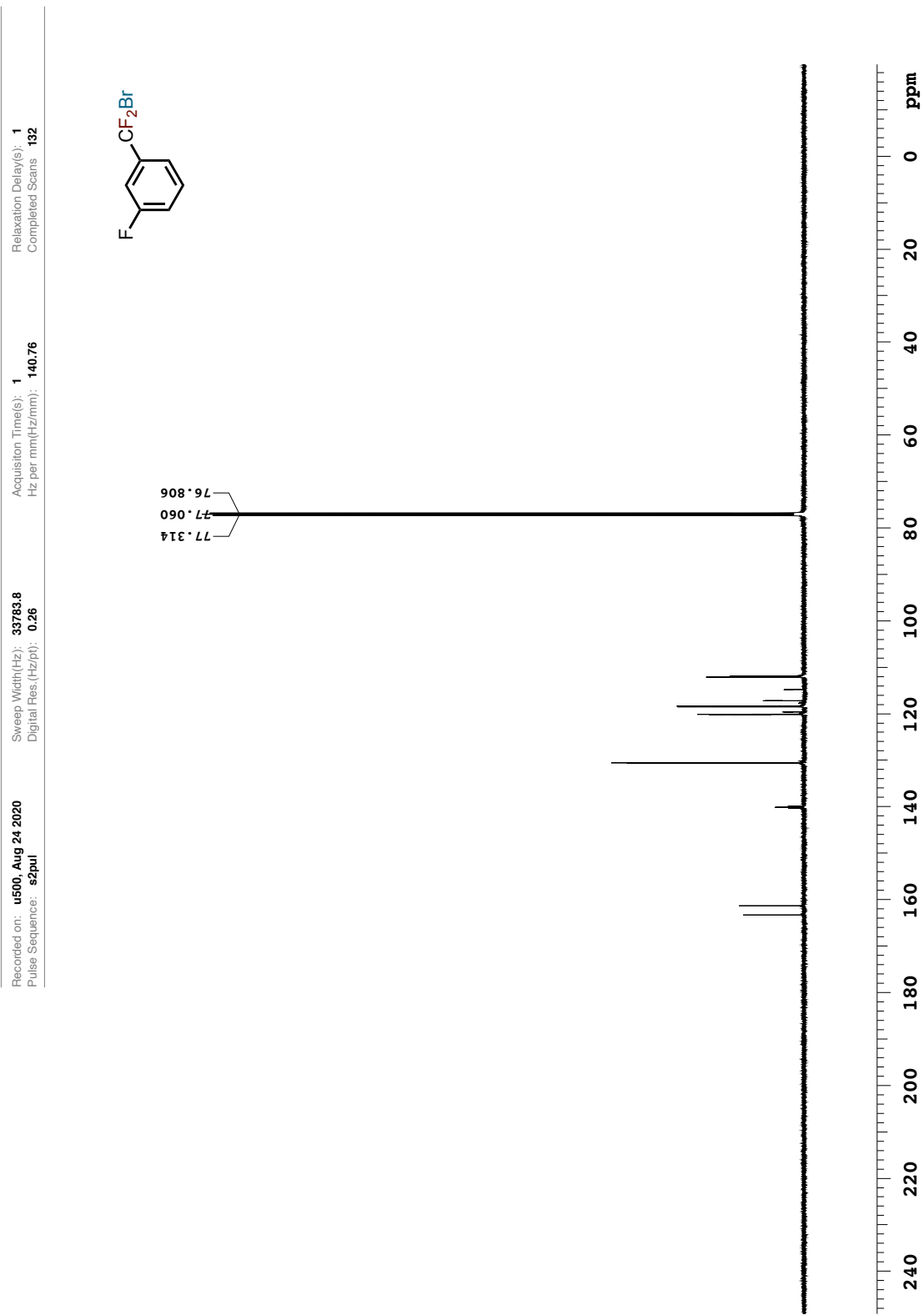


Figure A.68. $^{13}\text{C}\{^1\text{H}\}$ NMR magnified spectrum of compound **218** (CDCl_3 , 125.7 MHz)

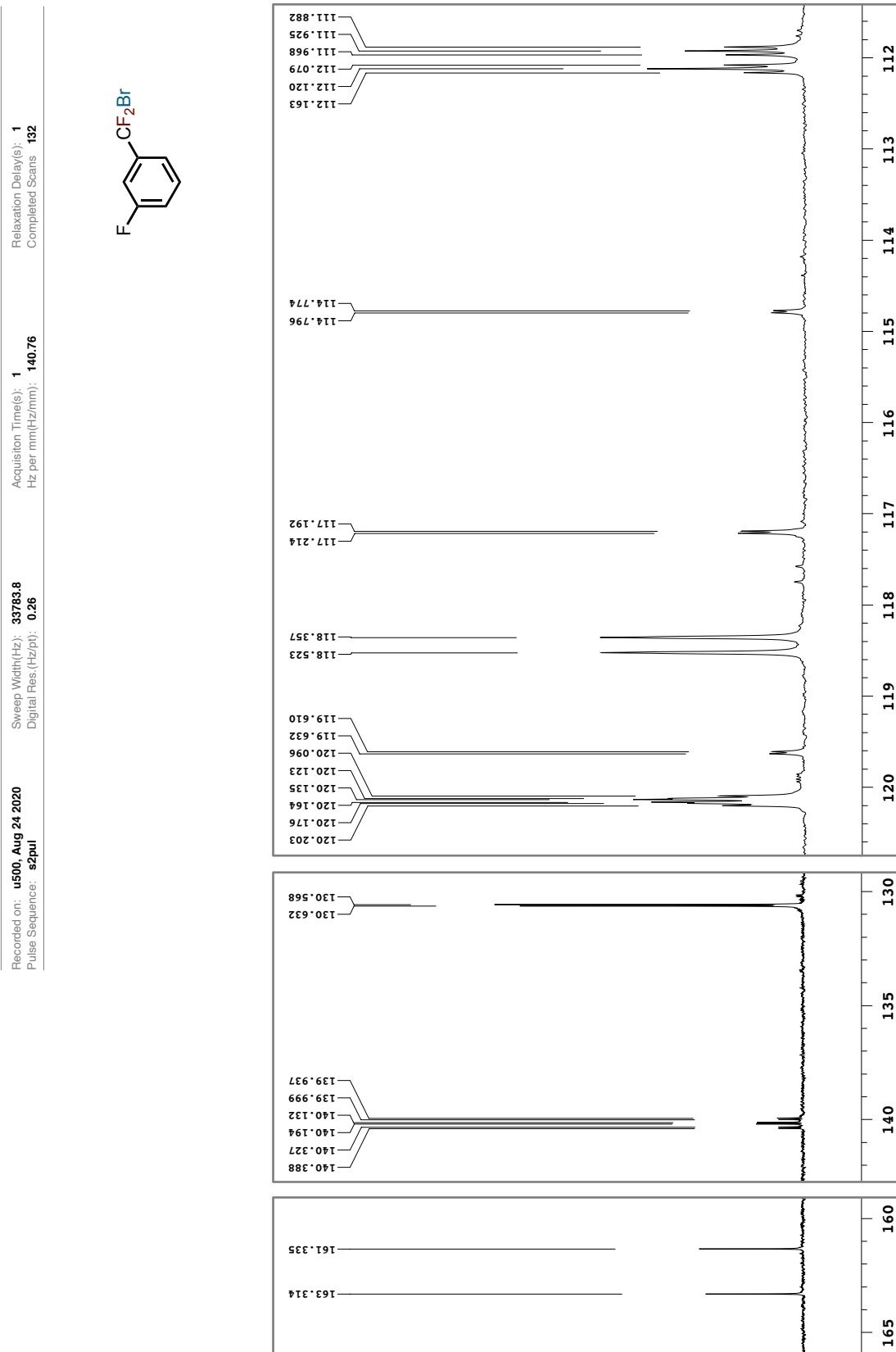


Figure A.69. ^{19}F NMR spectrum of compound **218** (CDCl_3 , 367.3 MHz)

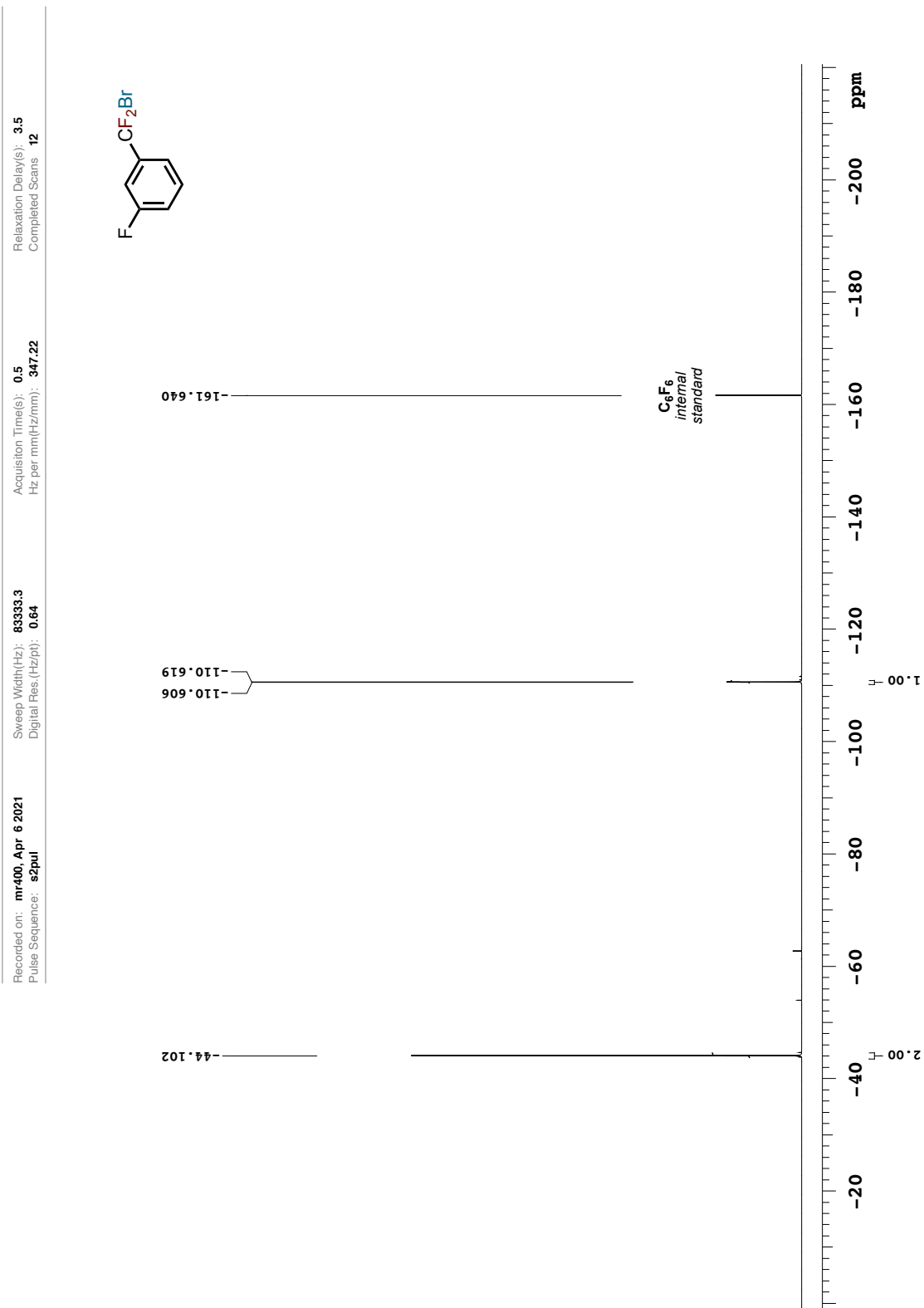


Figure A.70. ¹H NMR spectrum of compound 228 (CDCl₃, 699.8 MHz)

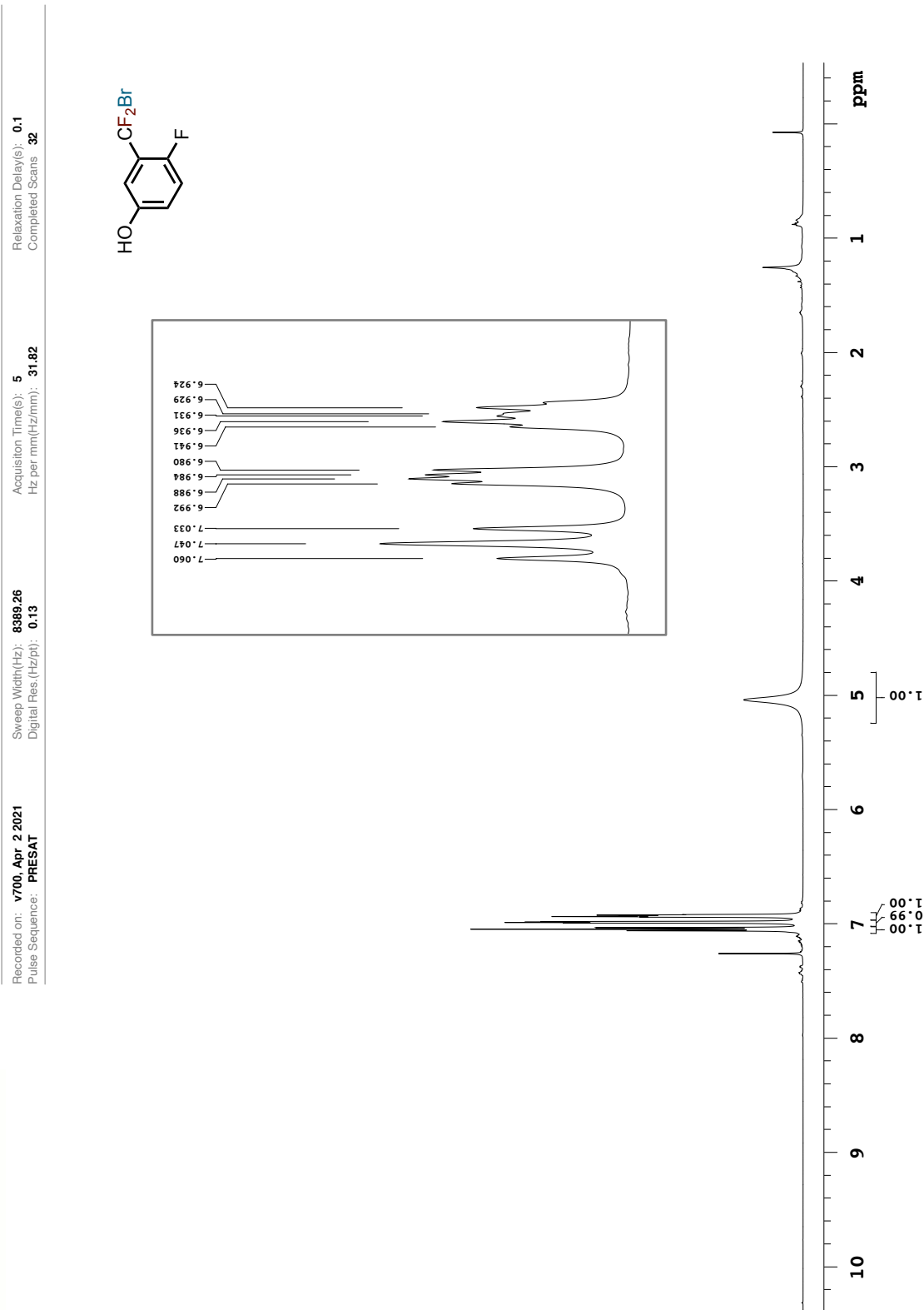


Figure A.71. $^{13}\text{C}\{^1\text{H}\}$ NMR spectrum of compound **228** (CDCl_3 , 125.7 MHz)

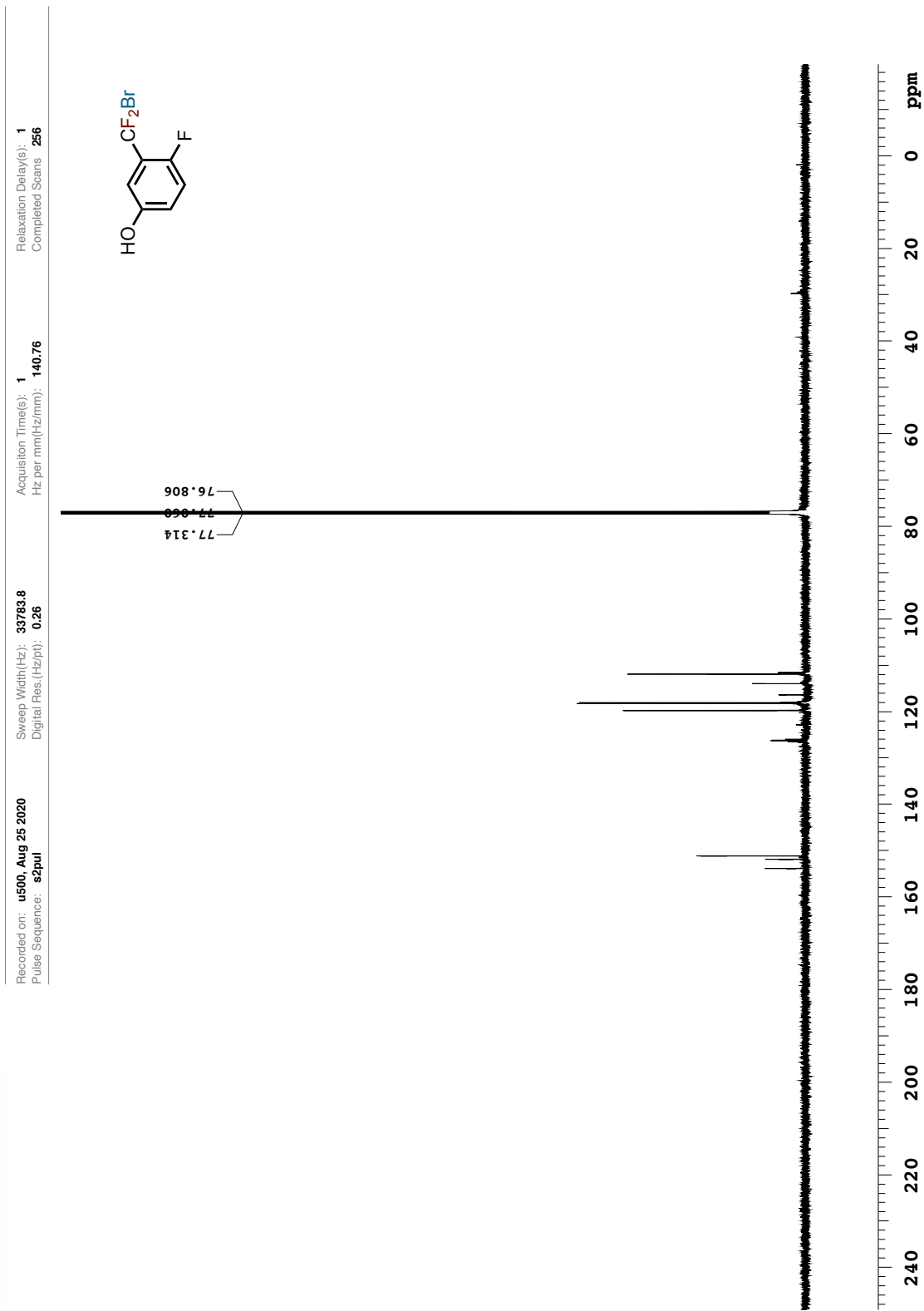


Figure A.72. $^{13}\text{C}\{^1\text{H}\}$ NMR magnified spectrum of compound **228** (CDCl_3 , 125.7 MHz)

Recorded on: **u500, Aug 25 2020** Sweep Width(Hz): **33783.8** Acquisition Time(s): **1** Relaxation Delay(s): **1**
Pulse Sequence: **s2pul** Digital Res. (Hz/pt): **0.26** Hz per mm(Hz/mm): **140.76** Completed Scans: **256**

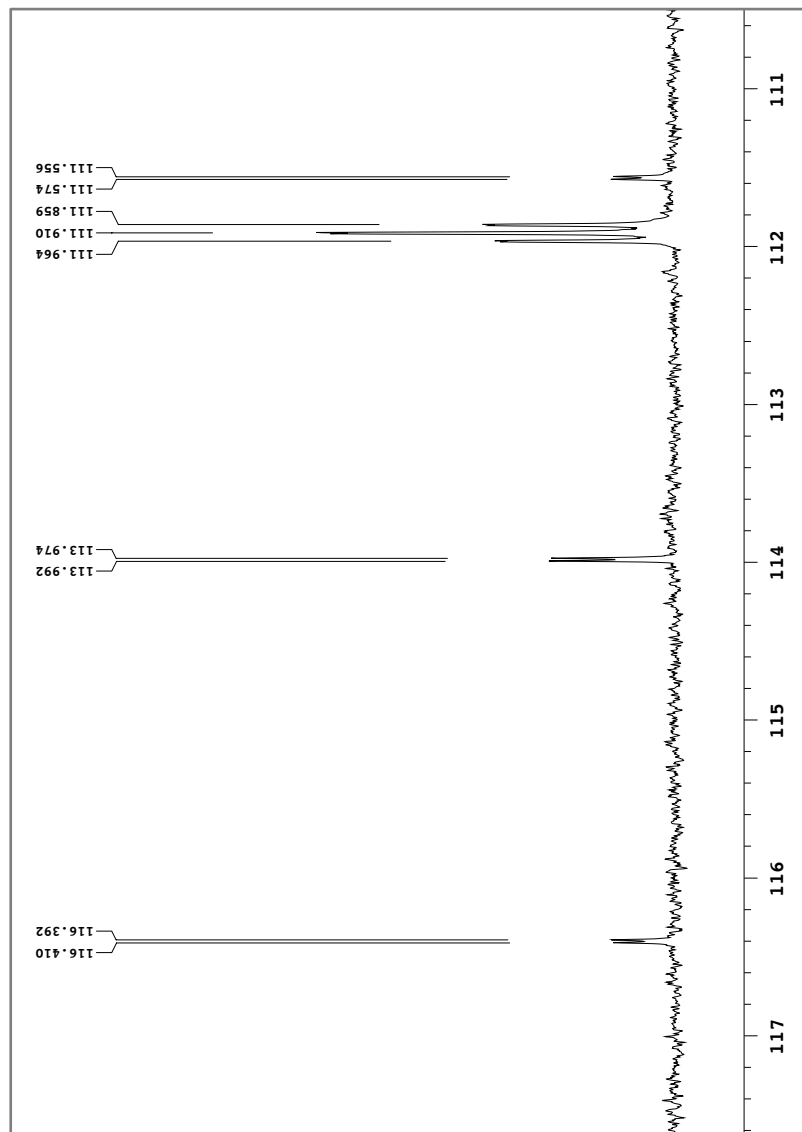
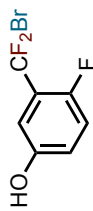


Figure A.73. $^{13}\text{C}\{^1\text{H}\}$ NMR magnified spectrum of compound **228** (CDCl_3 , 125.7 MHz)

Recorded on: **u500, Aug 25 2020** Sweep Width(Hz): **33783.8** Acquisition Time(s): **1** Relaxation Delay(s): **1**
Pulse Sequence: **s2pul** Digital Res. (Hz/pt): **0.26** Hz per mm(Hz/mm): **140.76** Completed Scans: **256**

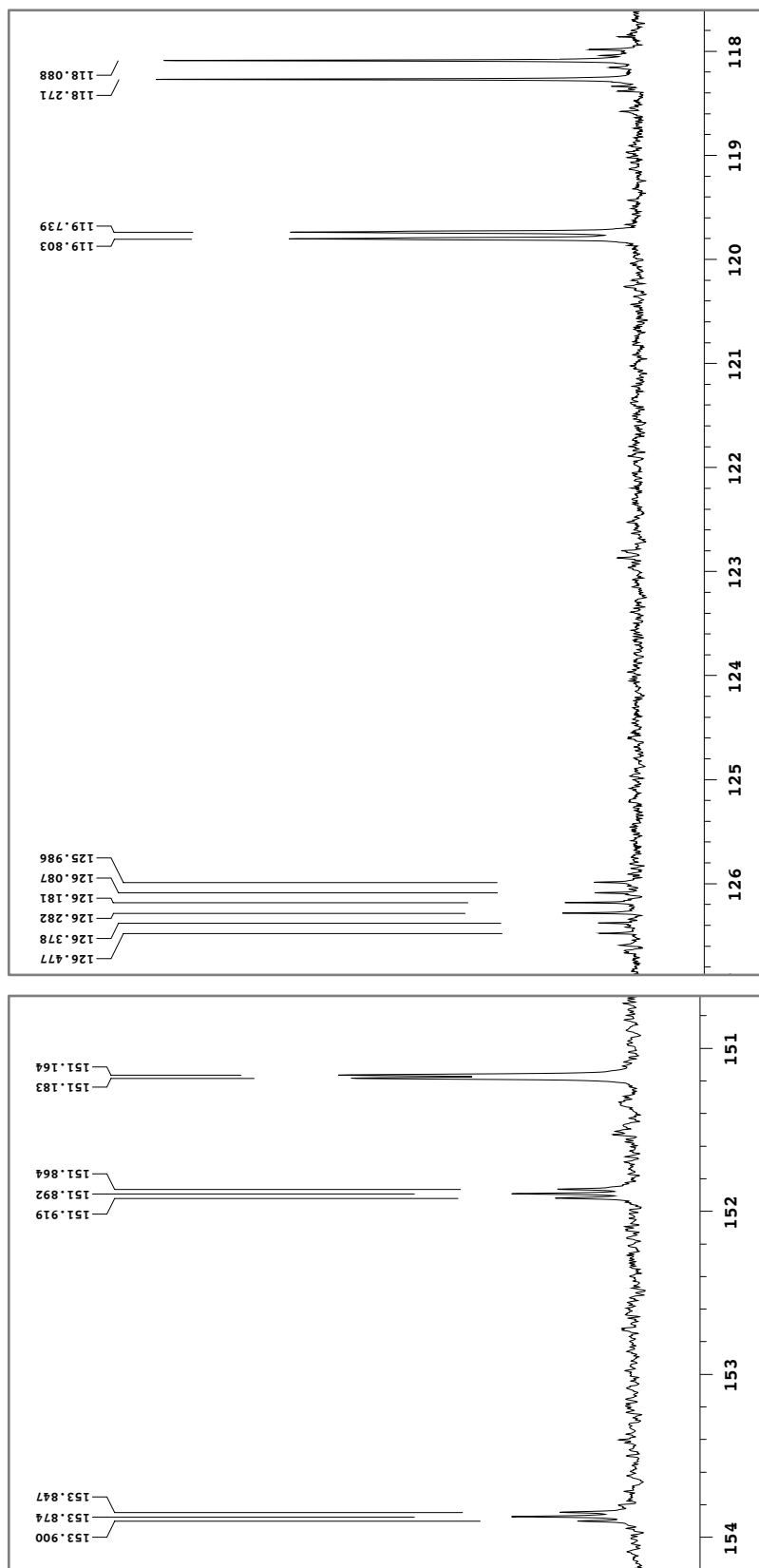
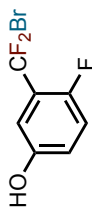


Figure A.74. ^{19}F NMR spectrum of compound **228** (CDCl_3 , 376.3 MHz)

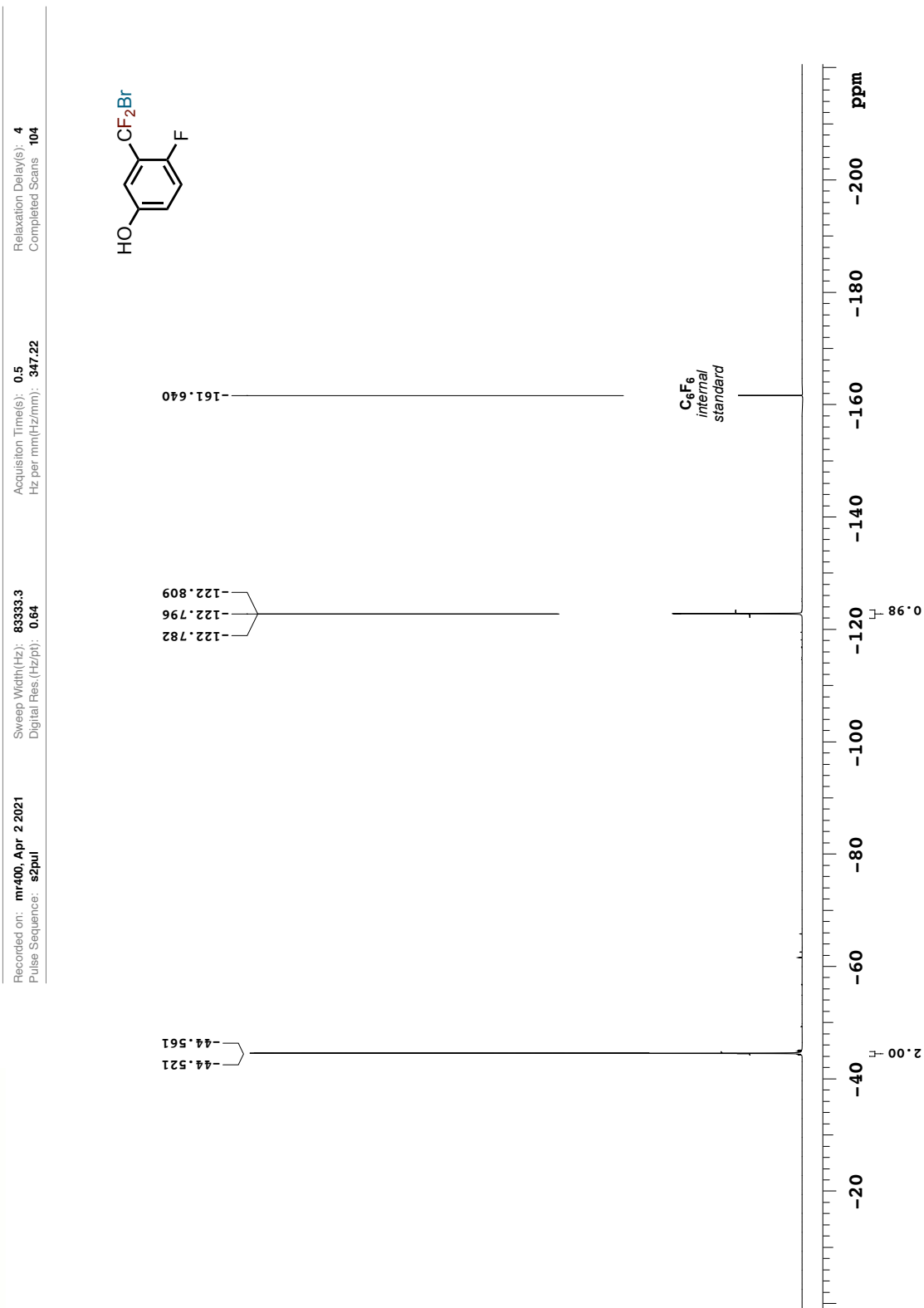


Figure A.75. ^1H NMR spectrum of compound **229** (CDCl_3 , 699.8 MHz)

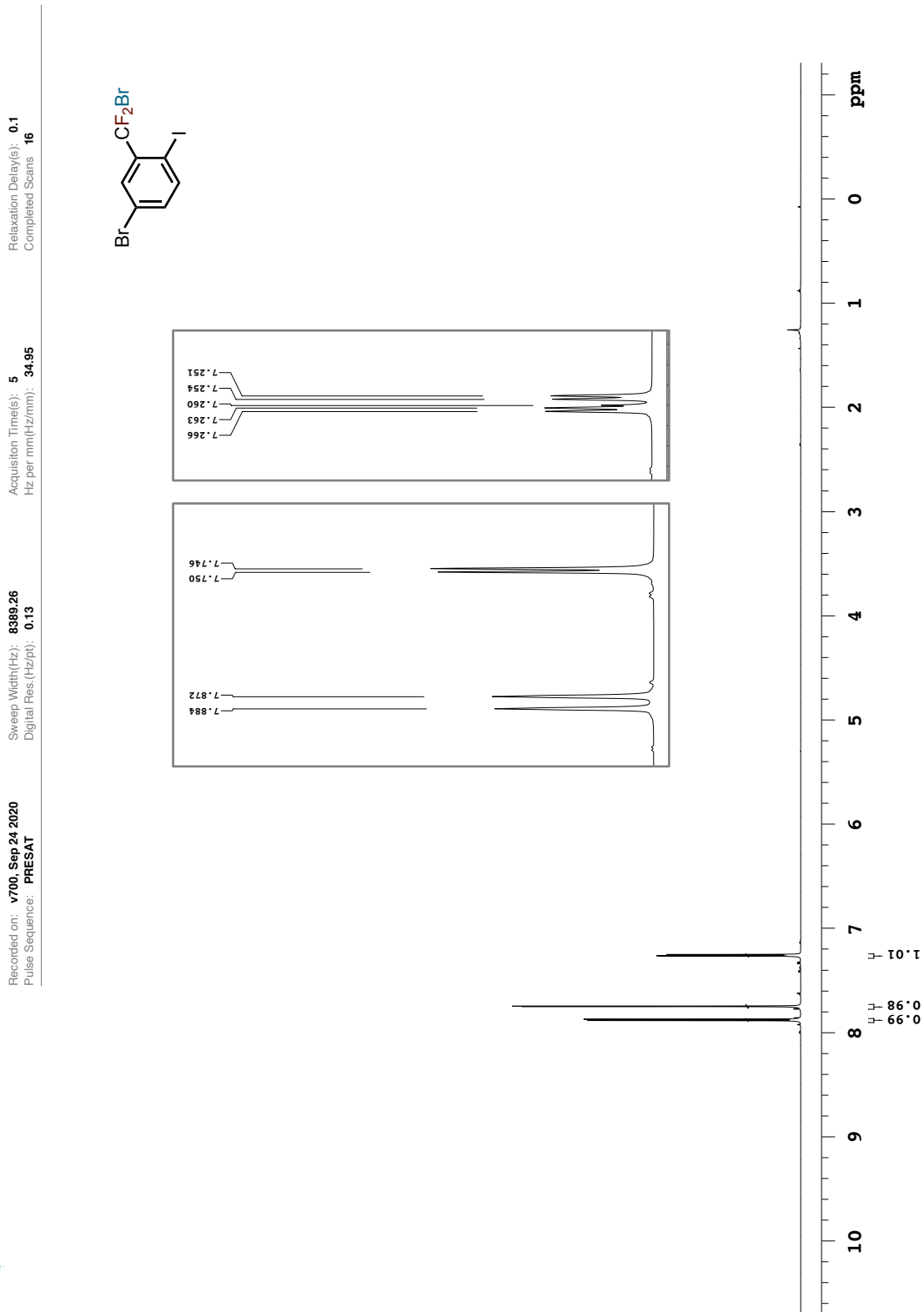


Figure A.76. $^{13}\text{C}\{^1\text{H}\}$ NMR spectrum of compound **229** (CDCl_3 , 176.0 MHz)

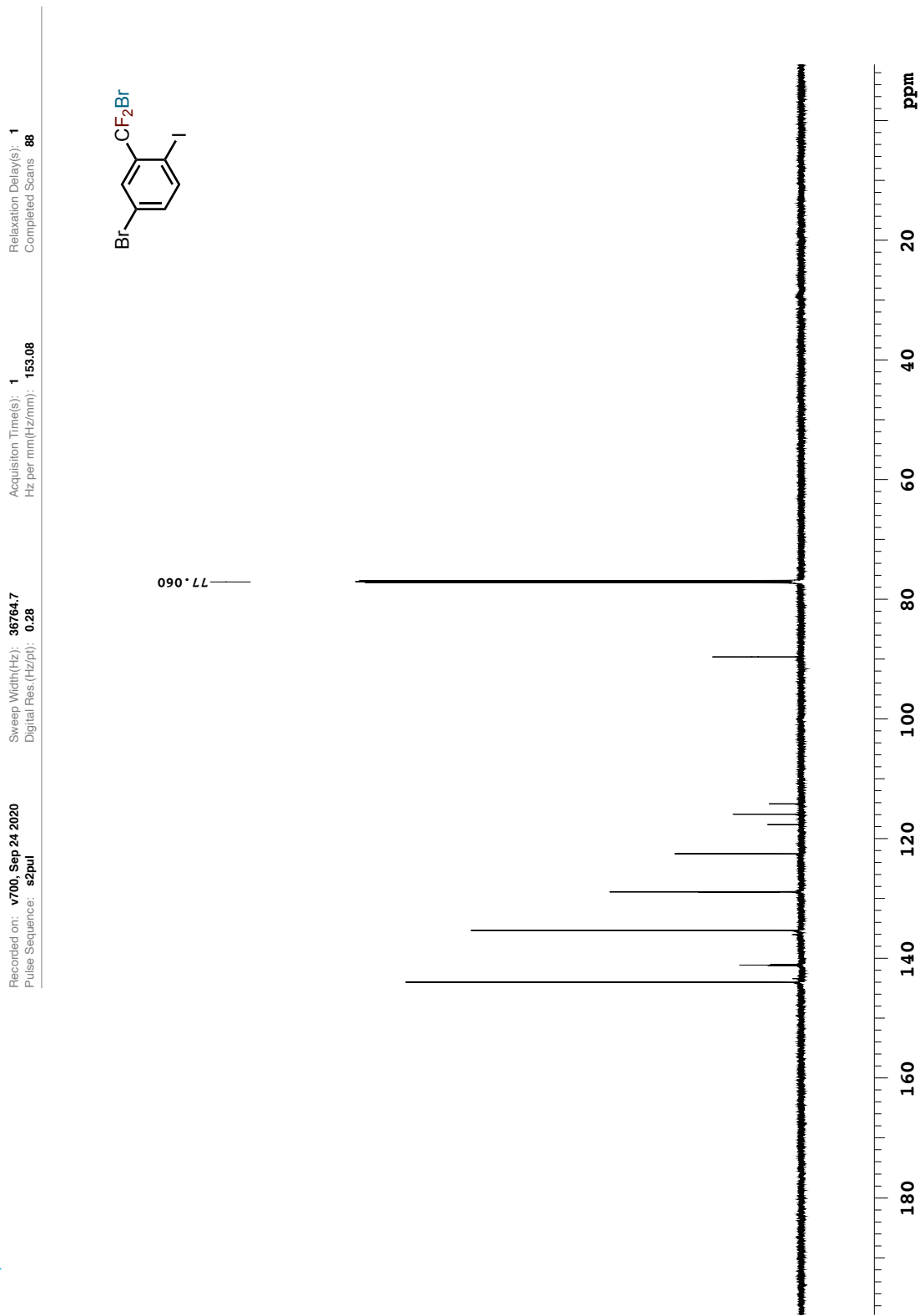


Figure A.77. $^{13}\text{C}\{^1\text{H}\}$ NMR magnified spectrum of compound **229** (CDCl_3 , 176.0 MHz)

Recorded on: **v700, Sep 24 2020** Sweep Width(Hz): **36764.7** Acquisition Time(s): **1** Relaxation Delay(s): **1**
Pulse Sequence: **s2pul** Digital Res. (Hz/pt): **0.28** Hz per mm(Hz/mm): **153.08** Completed Scans: **88**

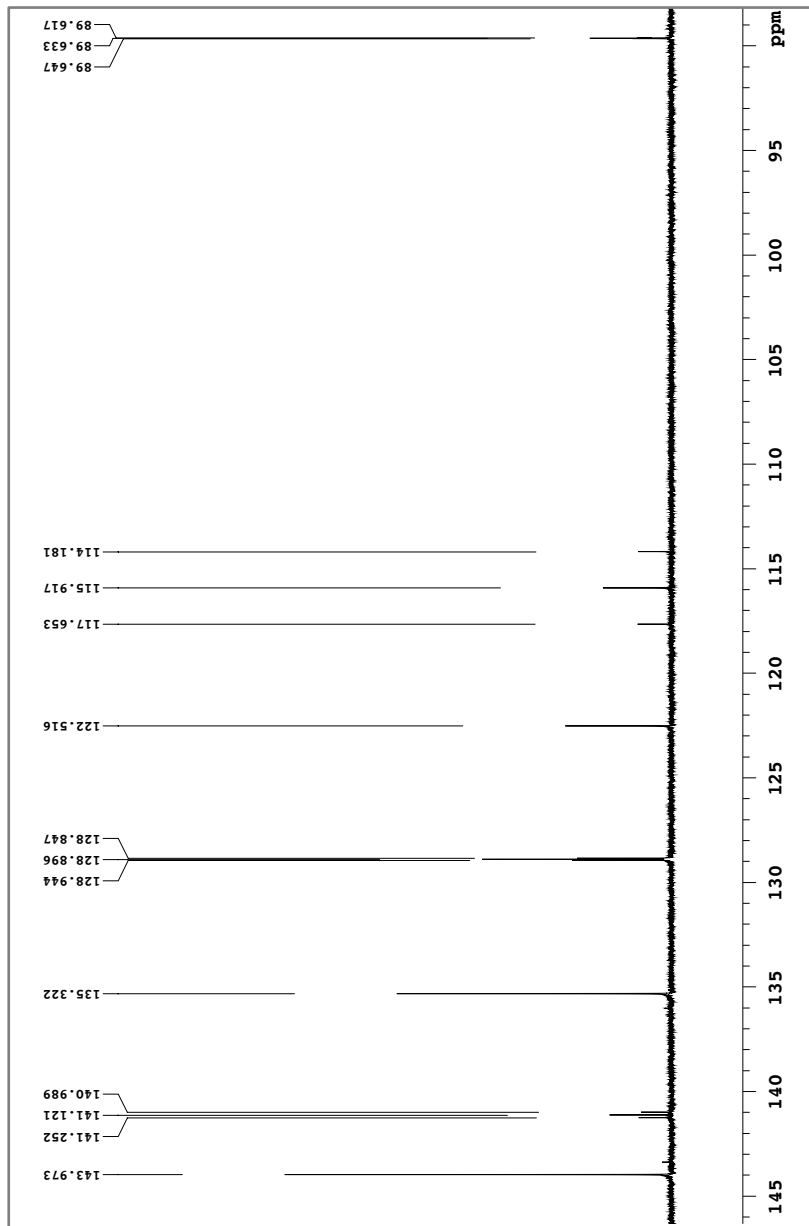
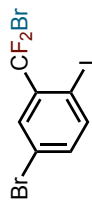


Figure A.78. ^{19}F NMR spectrum of compound 229 (CDCl_3 , 367.3 MHz)

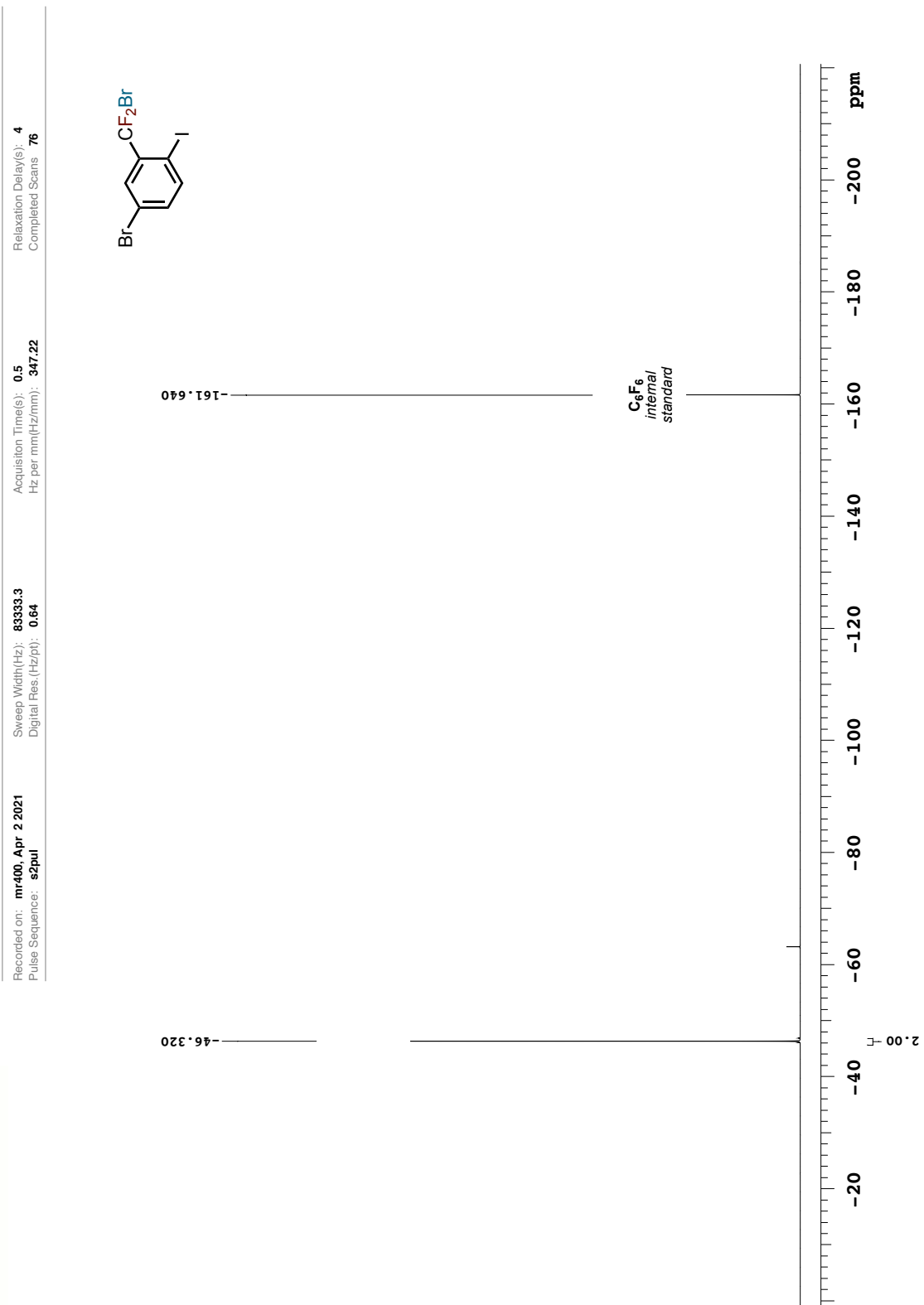


Figure A.79. ¹H NMR spectrum of compound 230 (CDCl₃, 699.8 MHz)

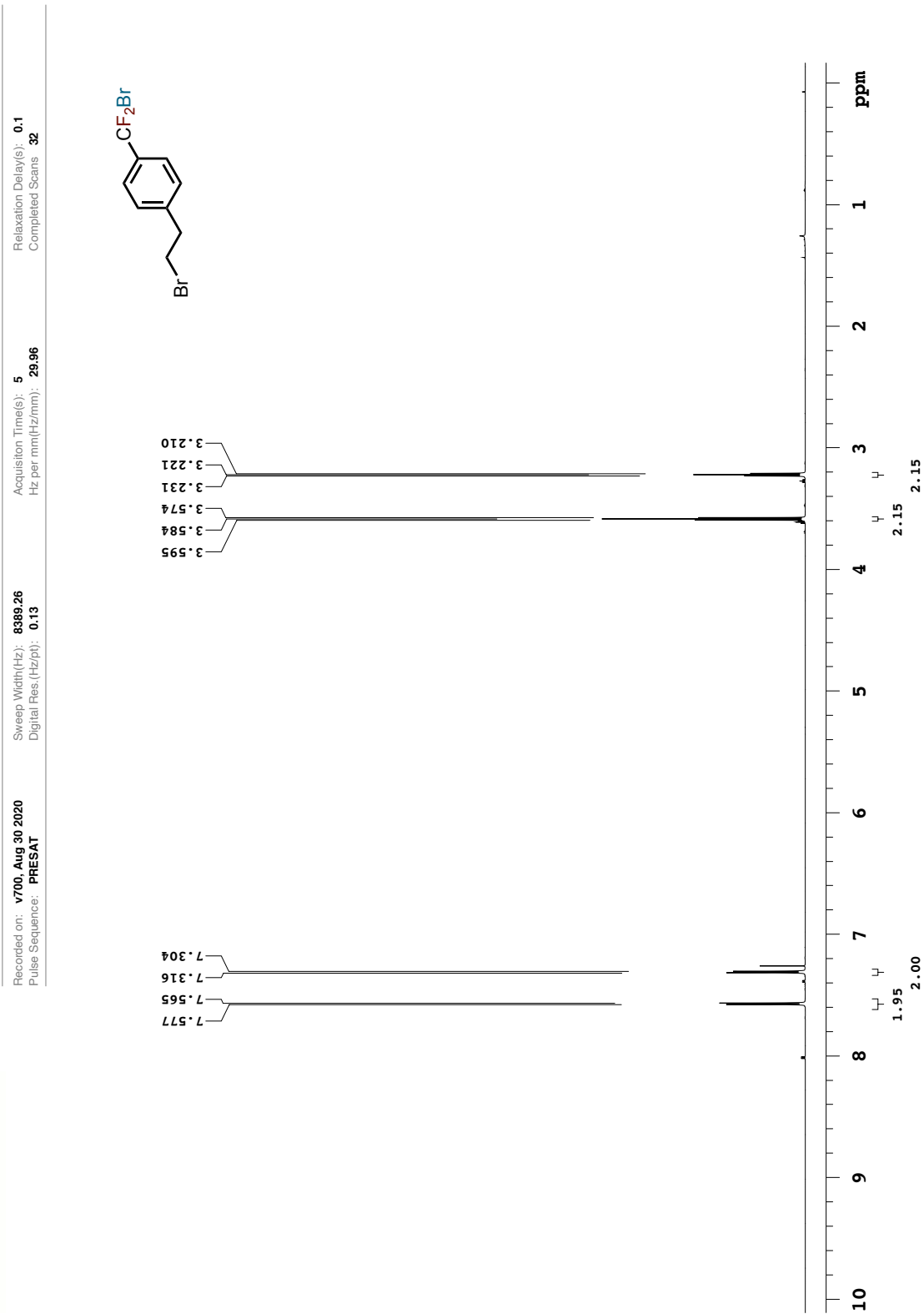


Figure A.80. $^{13}\text{C}\{^1\text{H}\}$ NMR spectrum of compound **230** (CDCl_3 , 176.0 MHz)

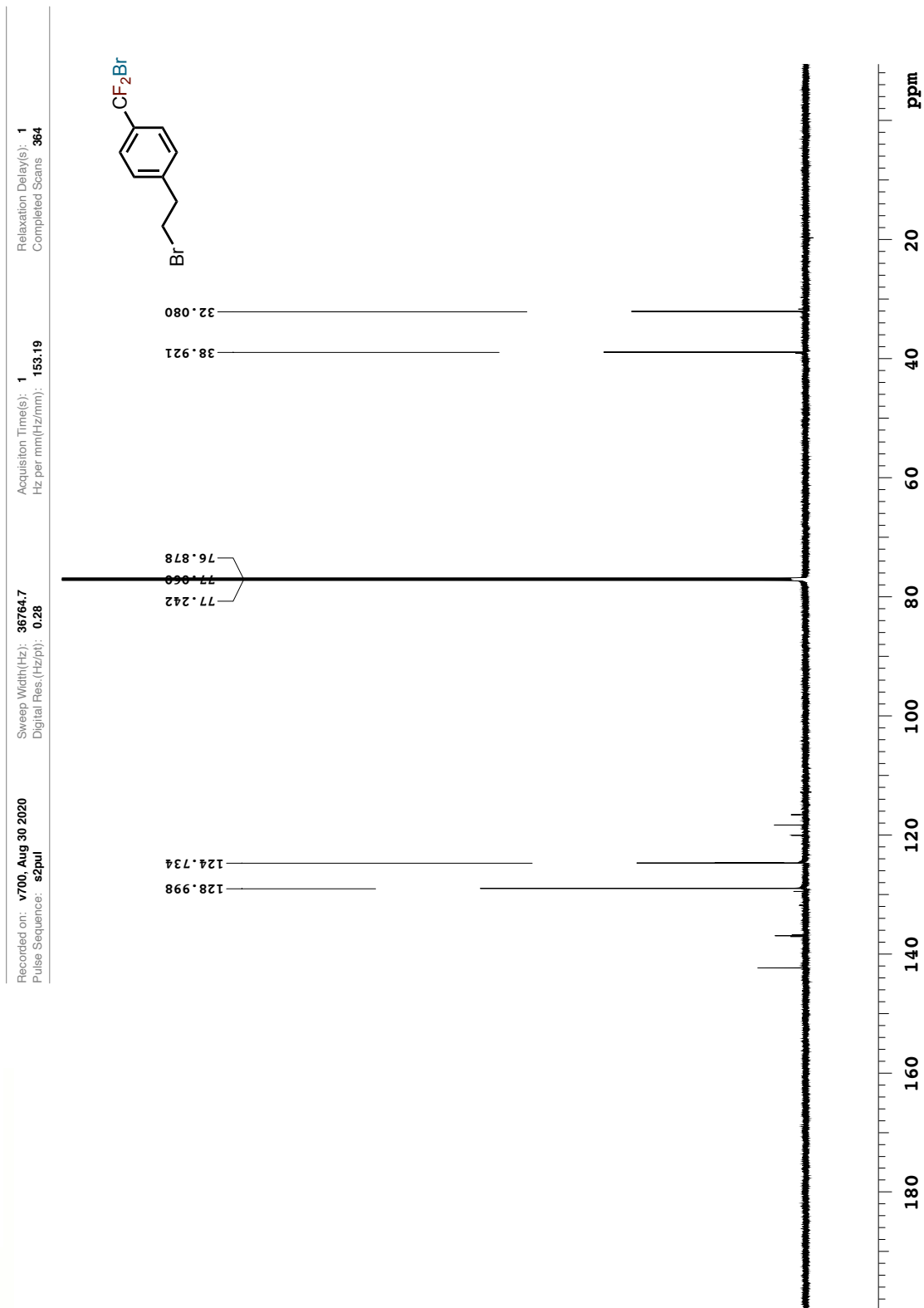


Figure A.81. $^{13}\text{C}\{^1\text{H}\}$ NMR magnified spectrum of compound **230** (CDCl_3 , 176.0 MHz)

Recorded on: **v700, Aug 30 2020** Sweep Width(Hz): **36764.7** Acquisition Time(s): **1** Relaxation Delay(s): **1**
Pulse Sequence: **s2pul** Digital Res. (Hz/pt): **0.28** Hz per mm(Hz/mm): **153.19** Completed Scans: **364**

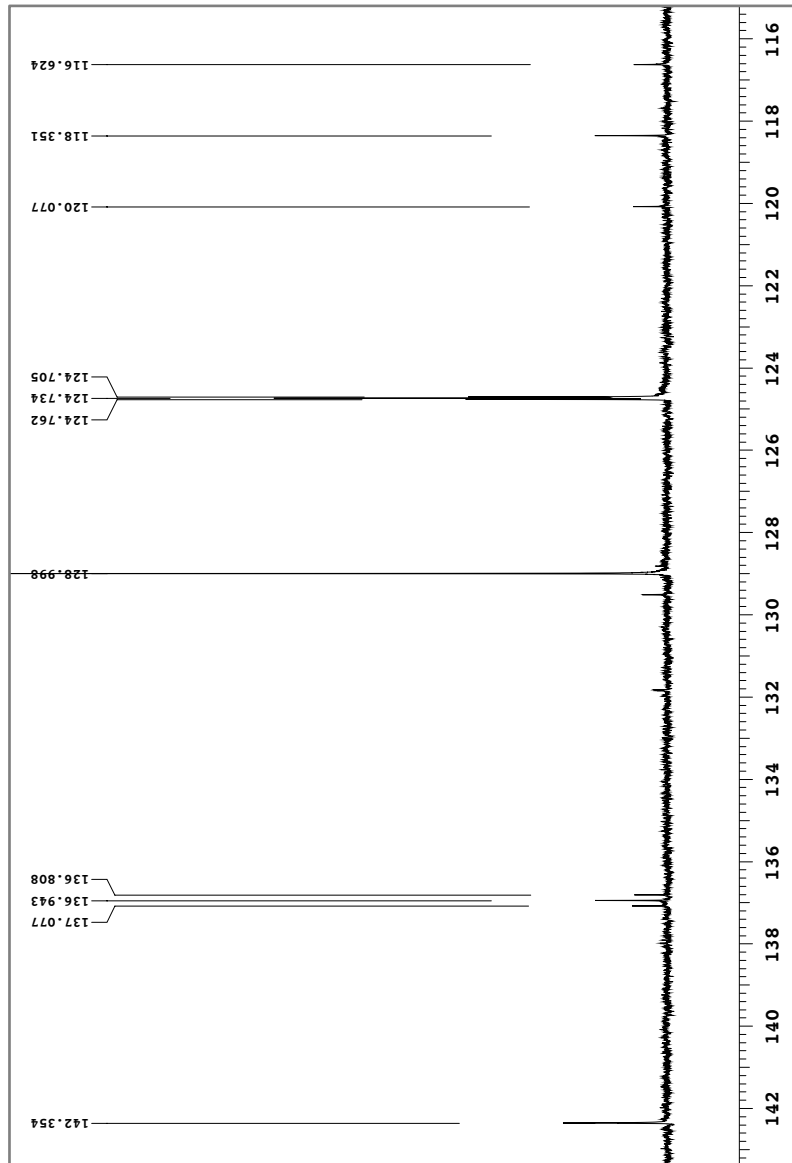
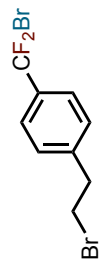


Figure A.82. ^{19}F NMR spectrum of compound **230** (CDCl_3 , 367.3 MHz)

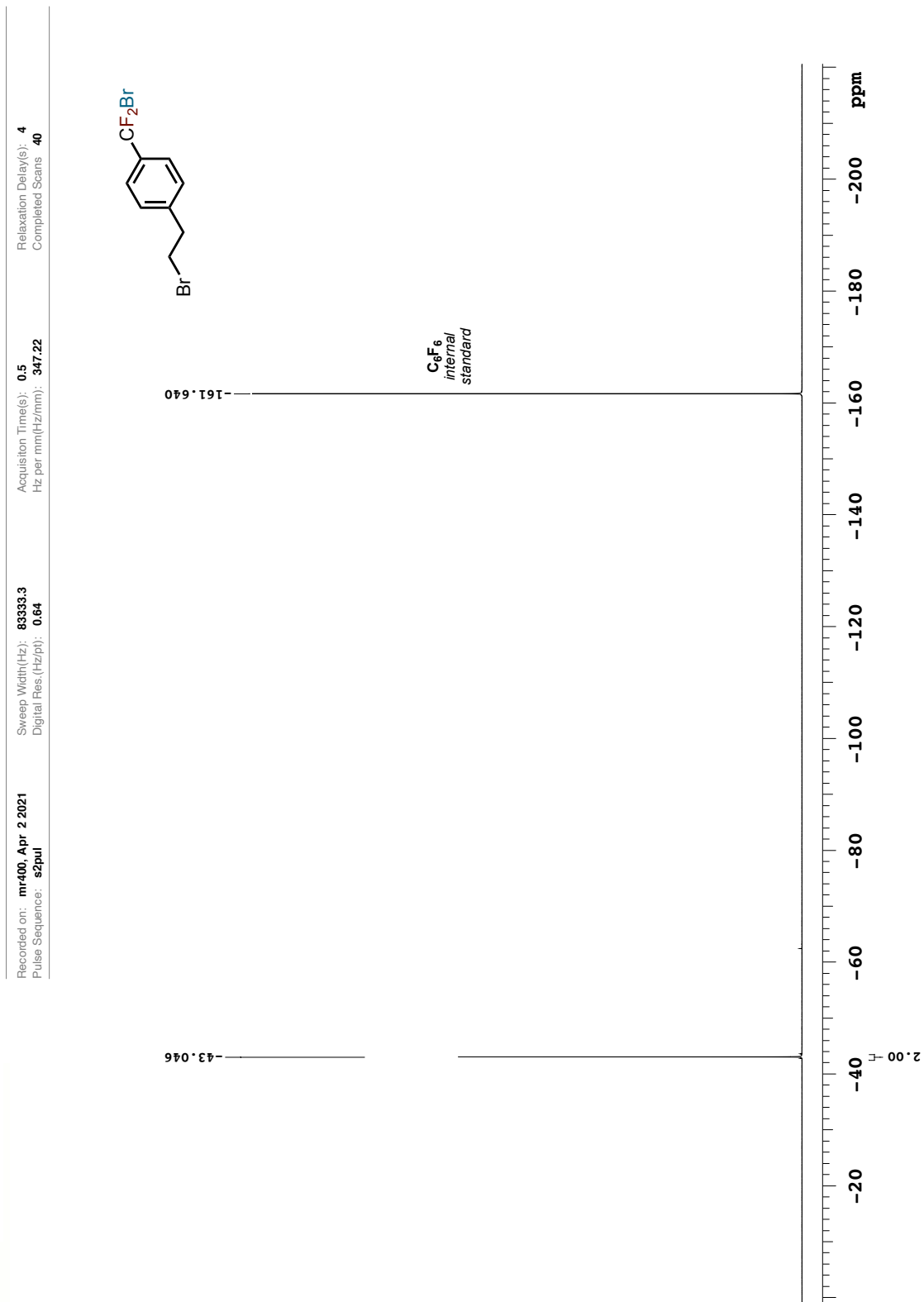


Figure A.83. ^1H NMR spectrum of compound **232** (CDCl_3 , 699.8 MHz)

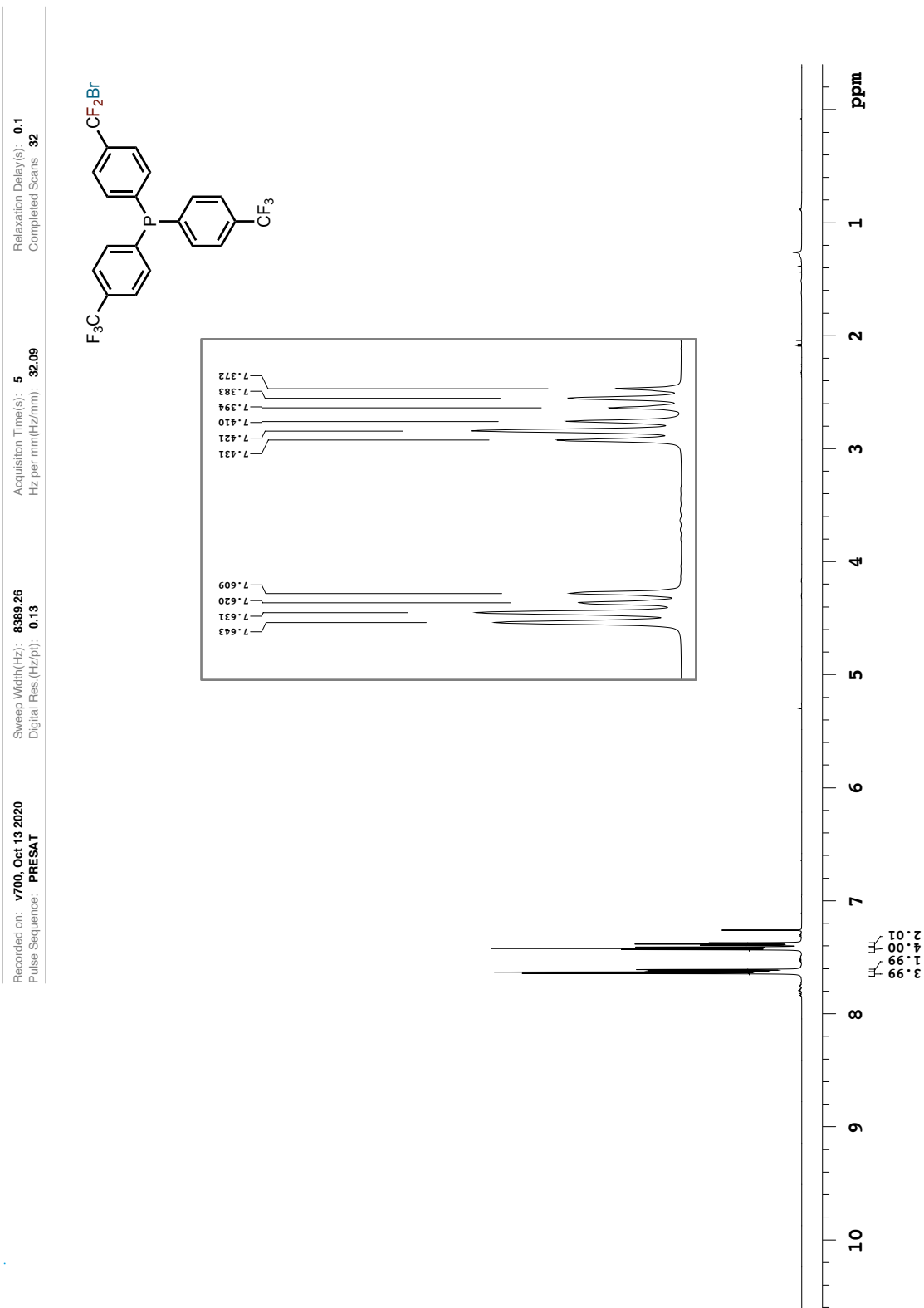


Figure A.84. $^{13}\text{C}\{^1\text{H}\}$ NMR spectrum of compound 232 (CDCl_3 , 176.0 MHz)

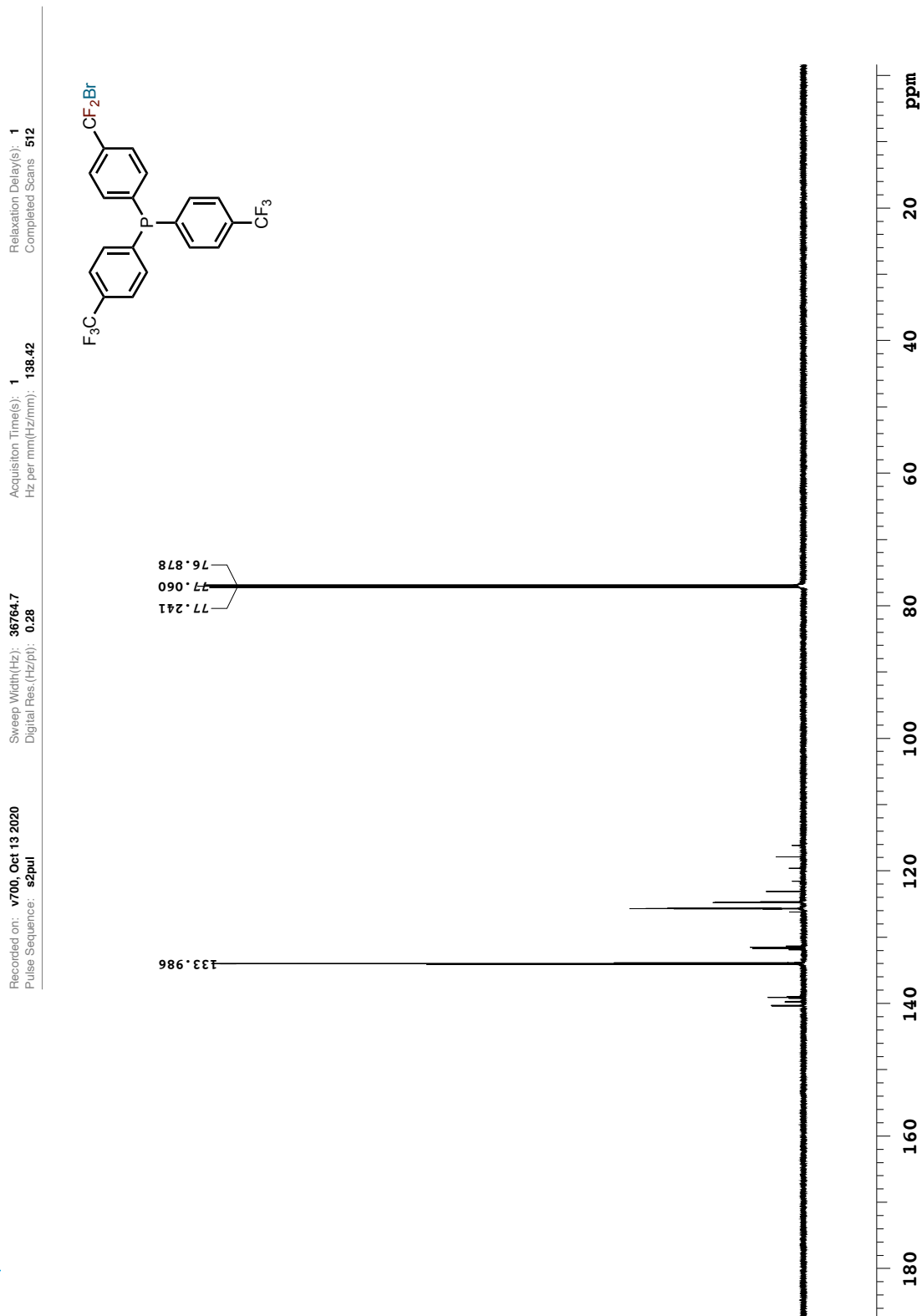


Figure A.85. $^{13}\text{C}\{^1\text{H}\}$ NMR magnified spectrum of compound **232** (CDCl_3 , 176.0 MHz)

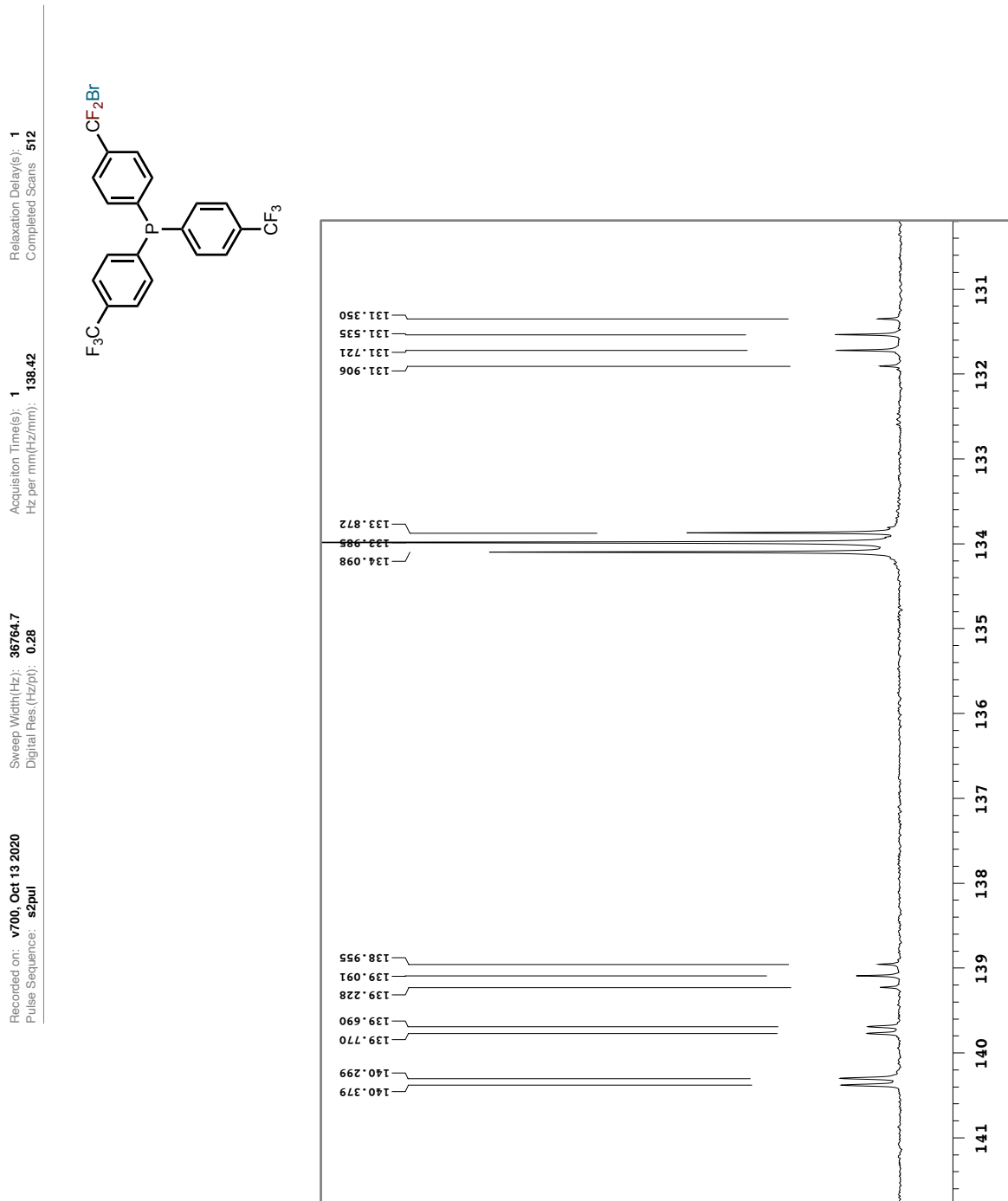


Figure A.86. $^{13}\text{C}\{^1\text{H}\}$ NMR magnified spectrum of compound **232** (CDCl_3 , 176.0 MHz)

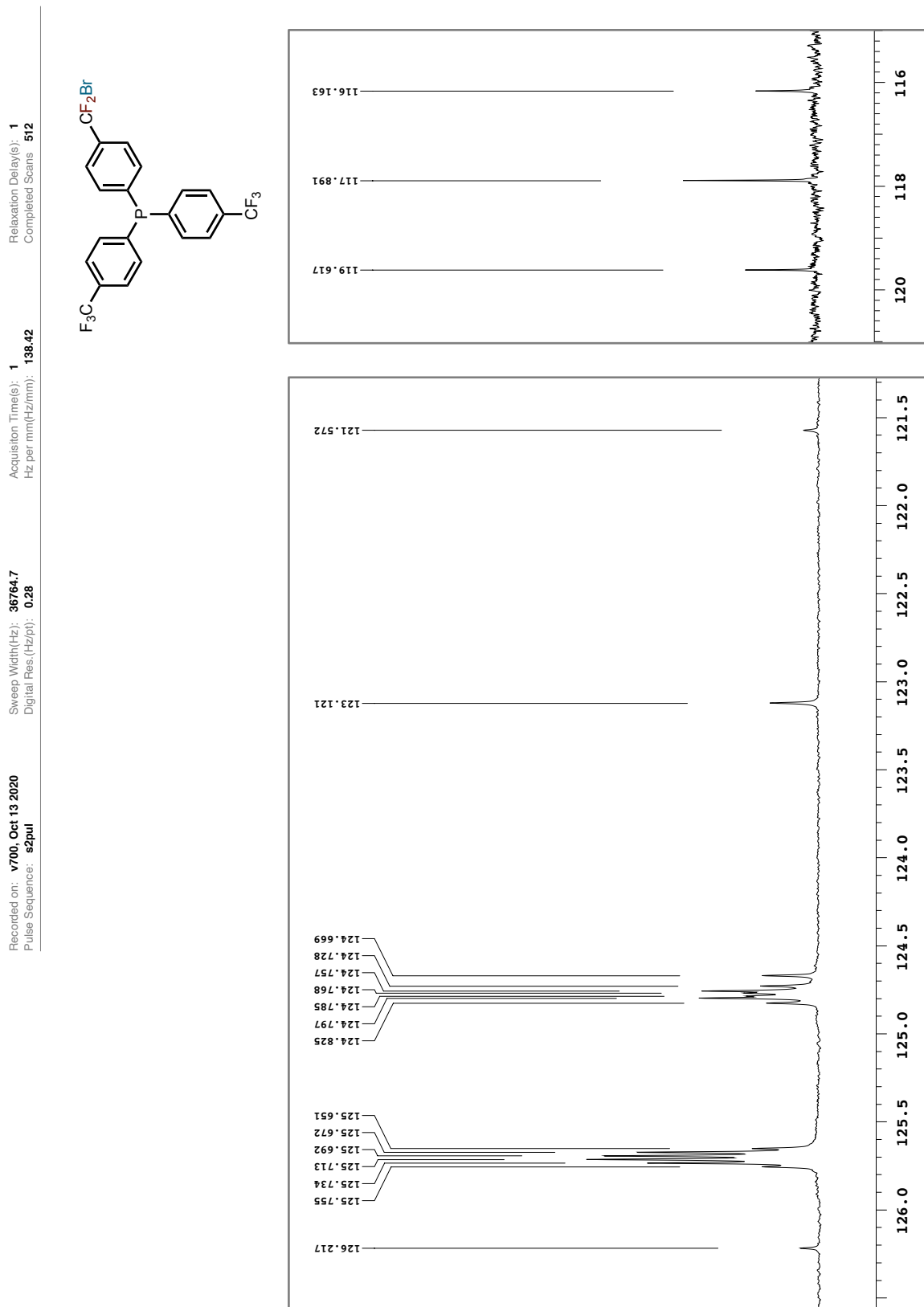


Figure A.87. ^{19}F NMR spectrum of compound **232** (CDCl_3 , 376.3 MHz)

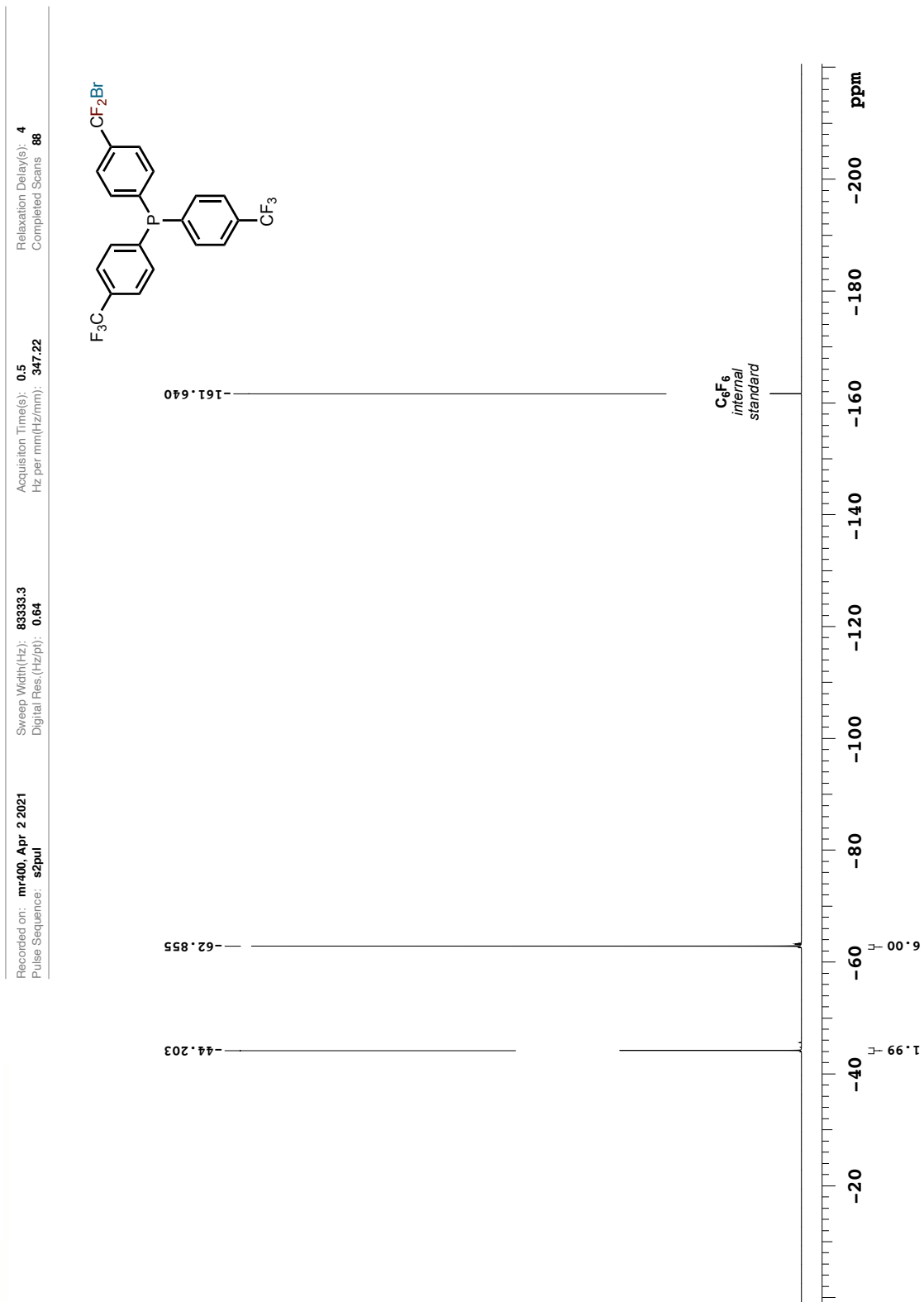


Figure A.88. $^{31}\text{P}\{^1\text{H}\}$ NMR magnified spectrum of compound **232** (CDCl_3 , 161.9 MHz)

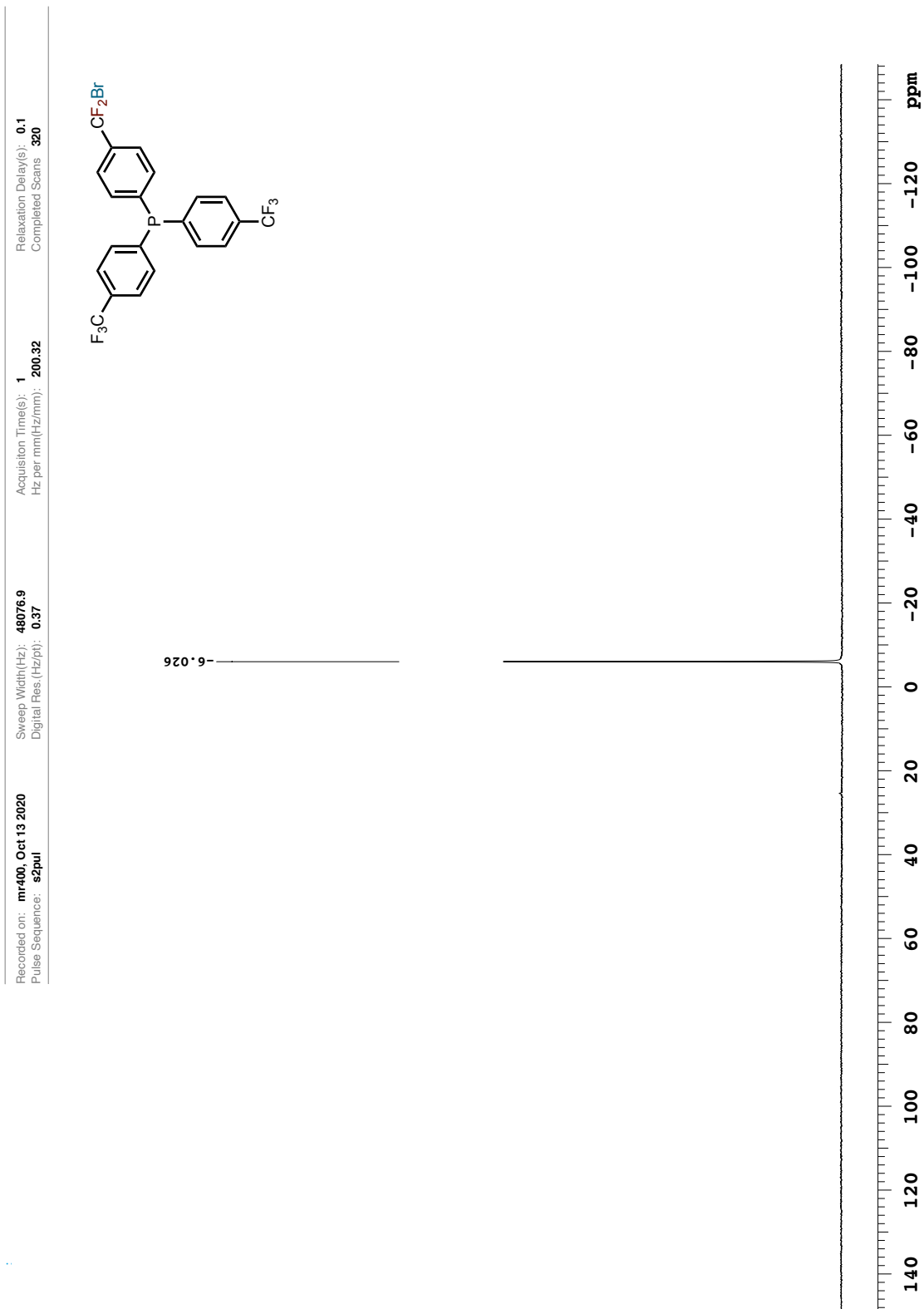


Figure A.89. ^1H NMR spectrum of compound **234** (CDCl_3 , 699.8 MHz)

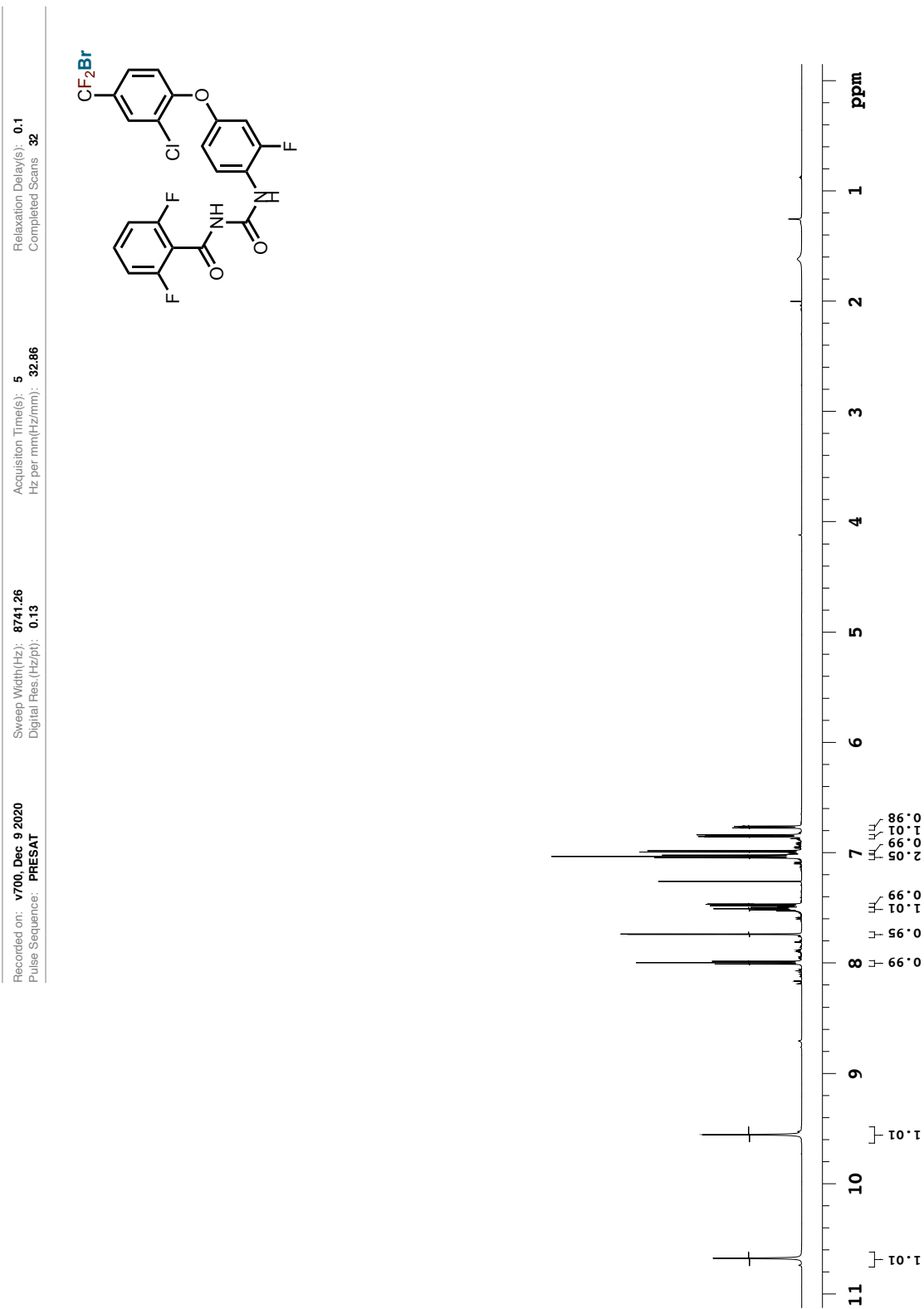


Figure A.90. ¹H NMR magnified spectrum of compound 234 (CDCl₃, 699.8 MHz)

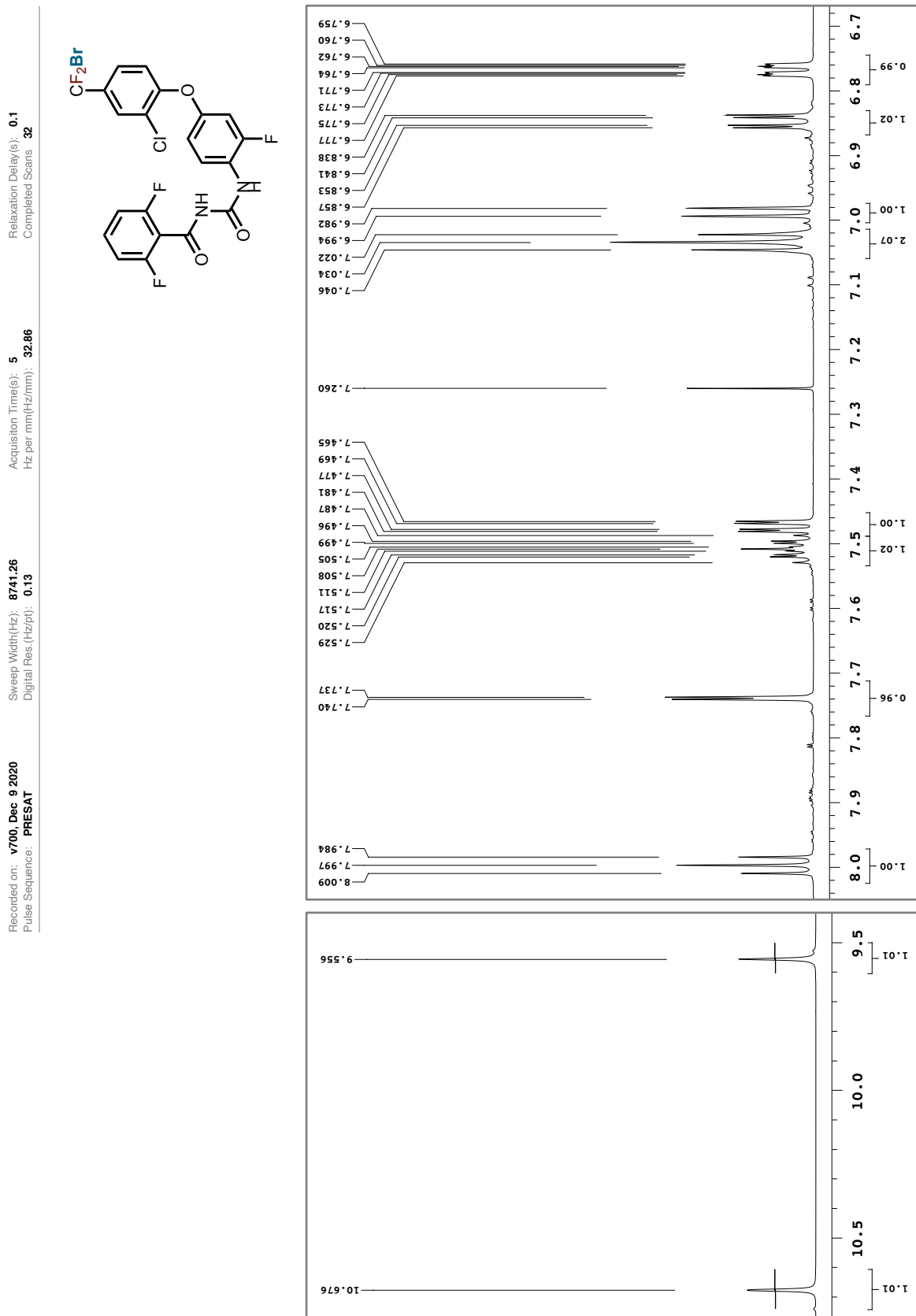


Figure A.91. $^{13}\text{C}\{^1\text{H}\}$ NMR spectrum of compound **234** (CDCl_3 , 176.0 MHz)

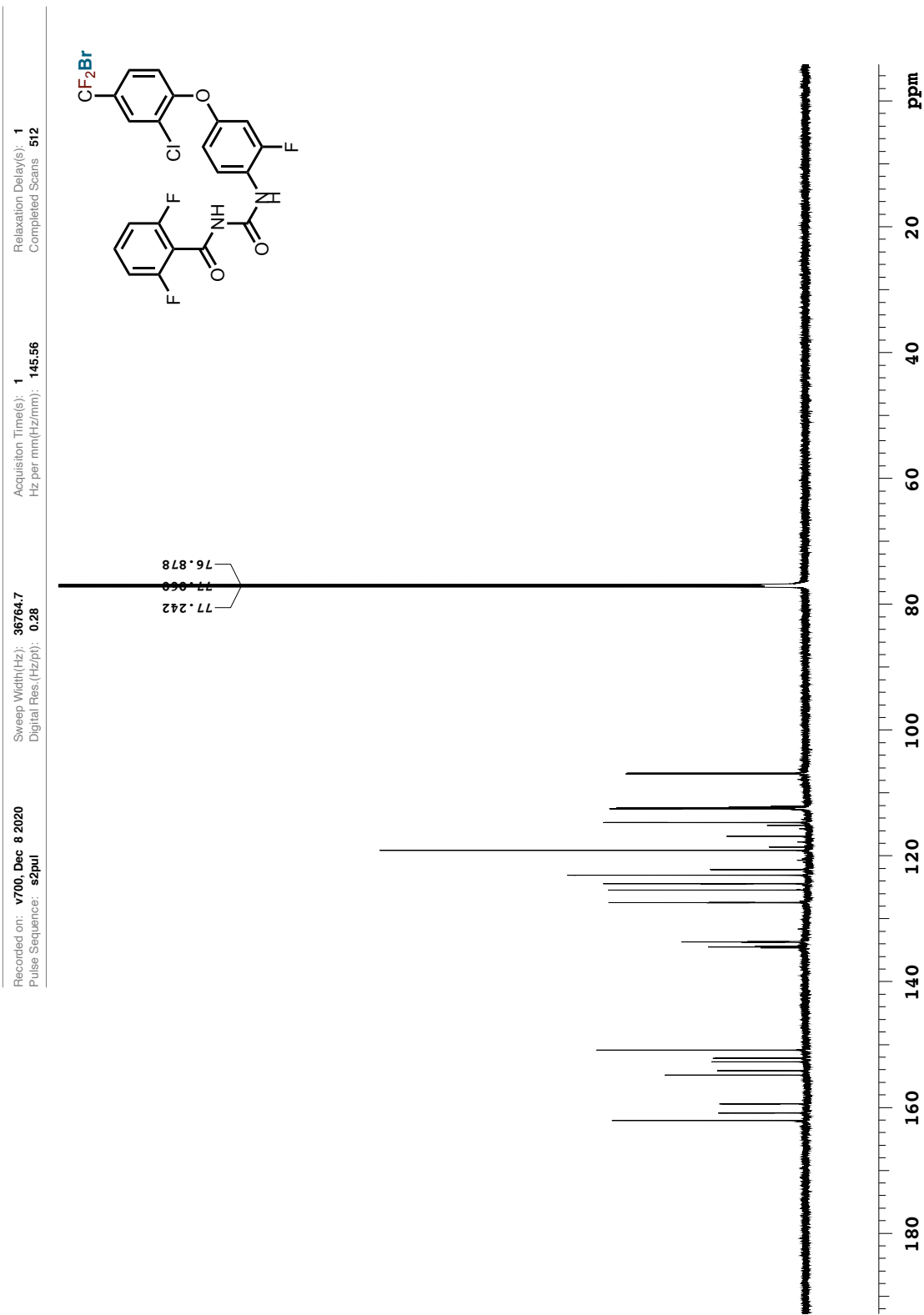


Figure A.92. $^{13}\text{C}\{^1\text{H}\}$ NMR magnified spectrum of compound 234 (CDCl_3 , 176.0 MHz)

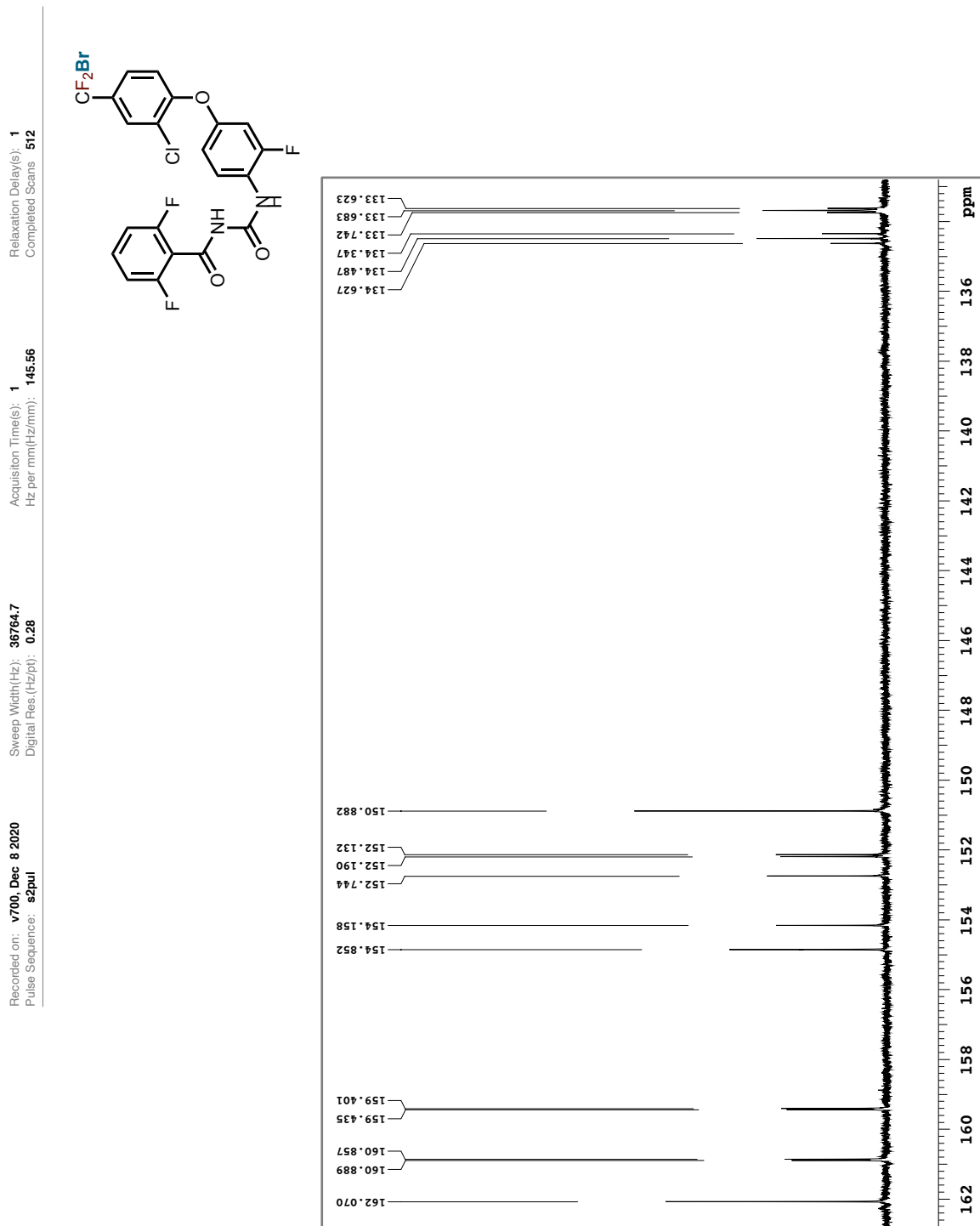


Figure A.93. $^{13}\text{C}\{^1\text{H}\}$ NMR magnified spectrum of compound 234 (CDCl_3 , 176.0 MHz)

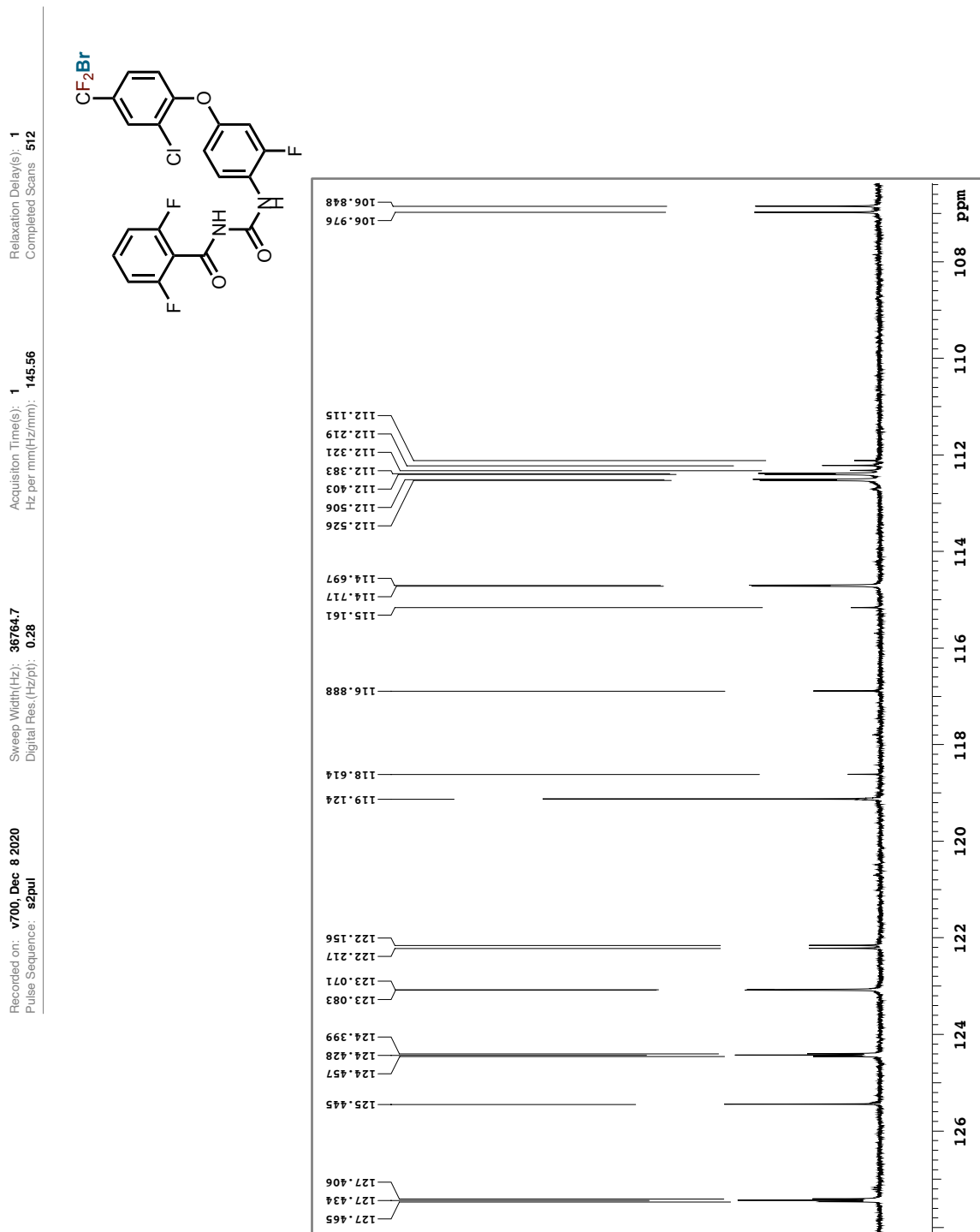


Figure A.94. ^{19}F NMR spectrum of compound **234** (CDCl_3 , 376.3 MHz)

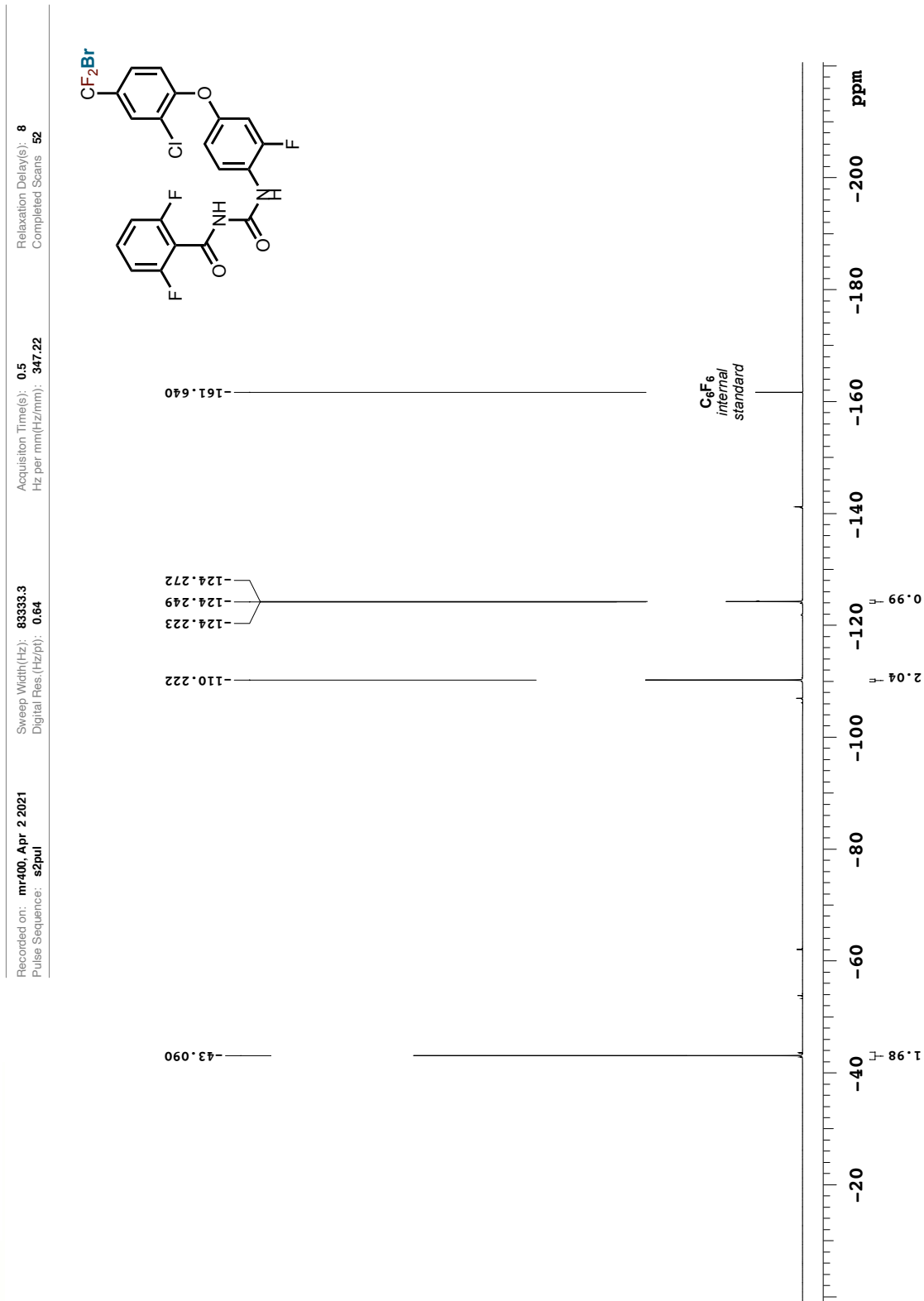


Figure A.95. ¹H NMR spectrum of compound **216** (CDCl₃, 699.8 MHz)

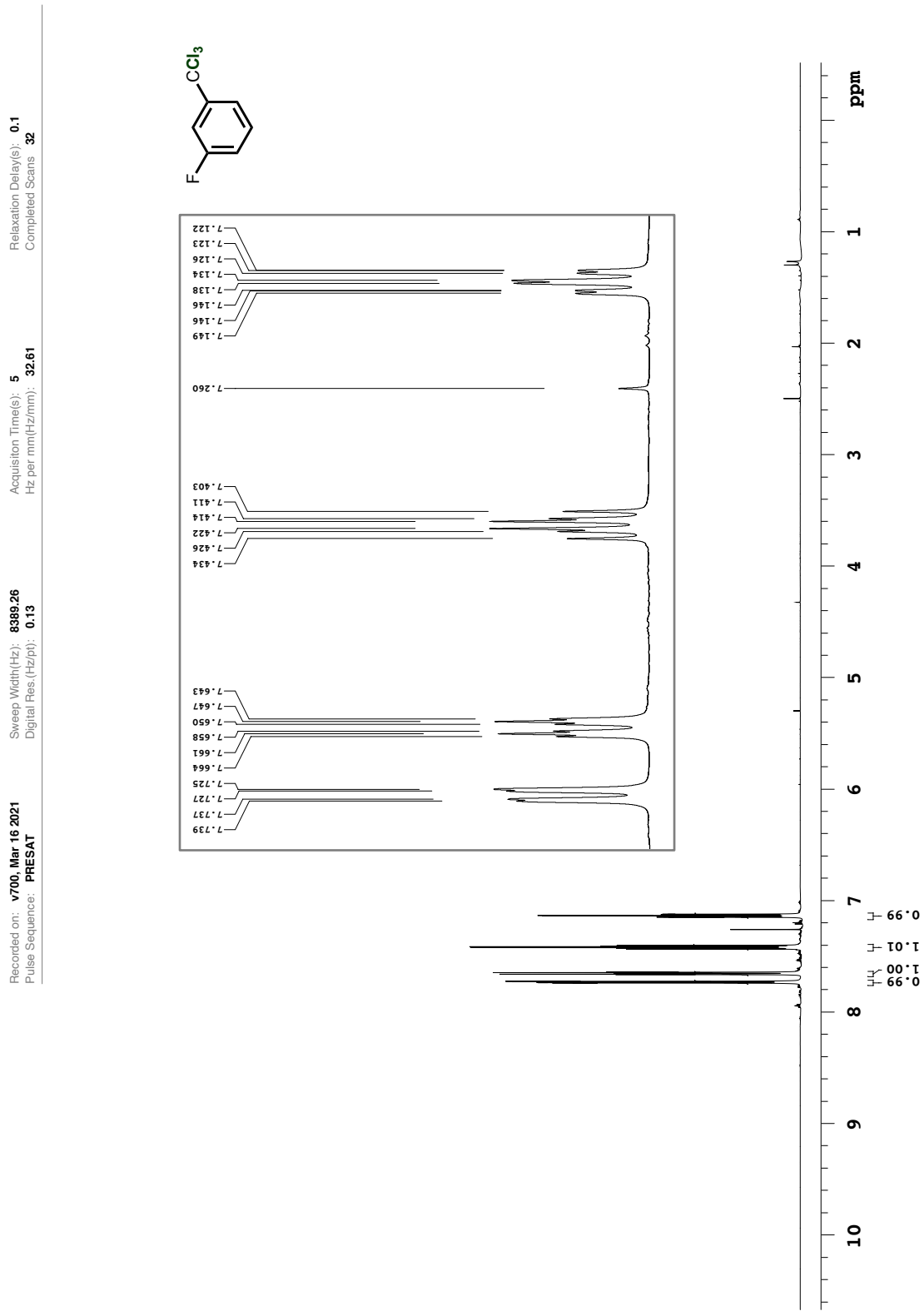


Figure A.96. $^{13}\text{C}\{^1\text{H}\}$ NMR spectrum of compound **216** (CDCl_3 , 176.0 MHz)

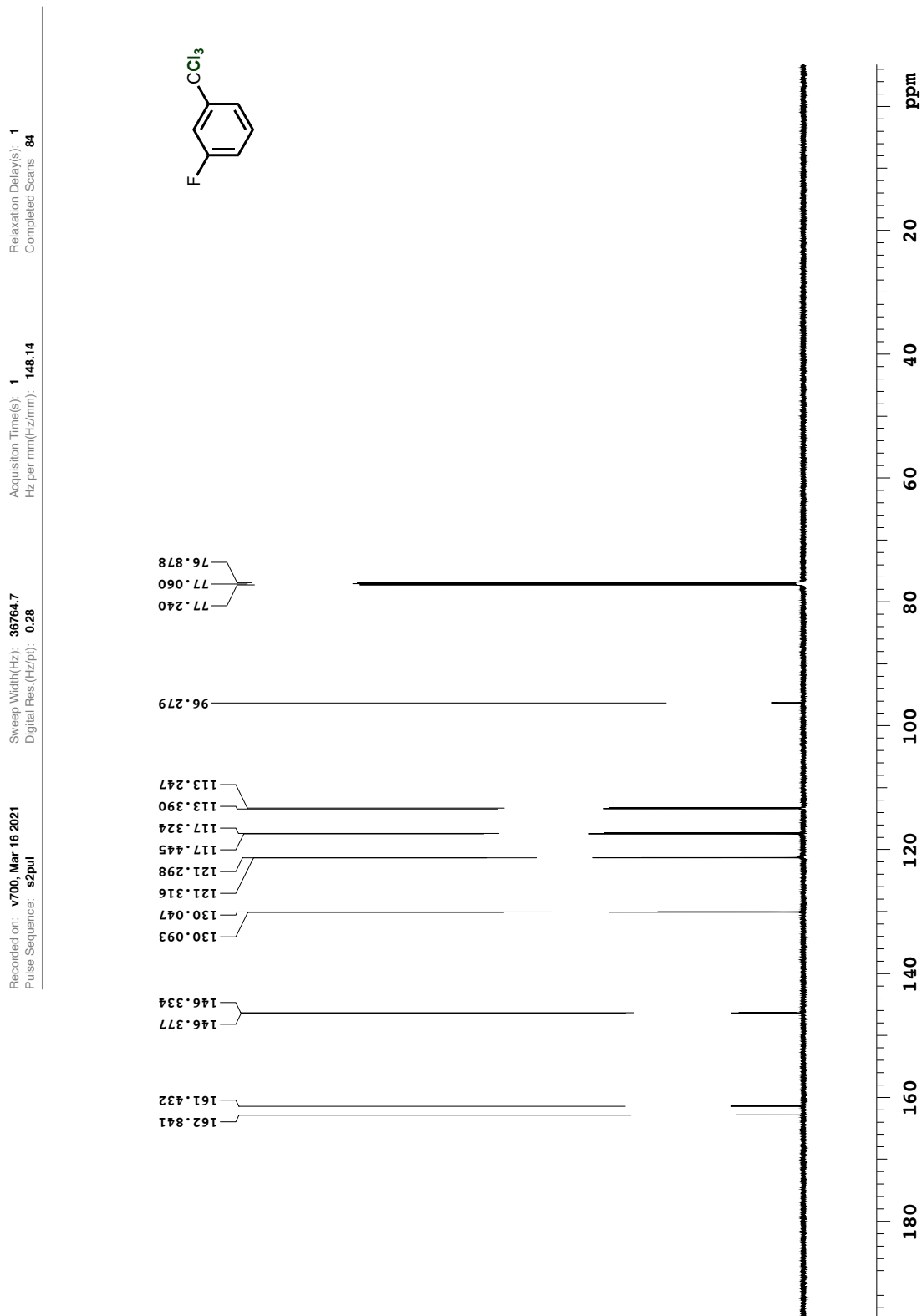


Figure A.97. ^{19}F NMR spectrum of compound **216** (CDCl_3 , 376.3 MHz)

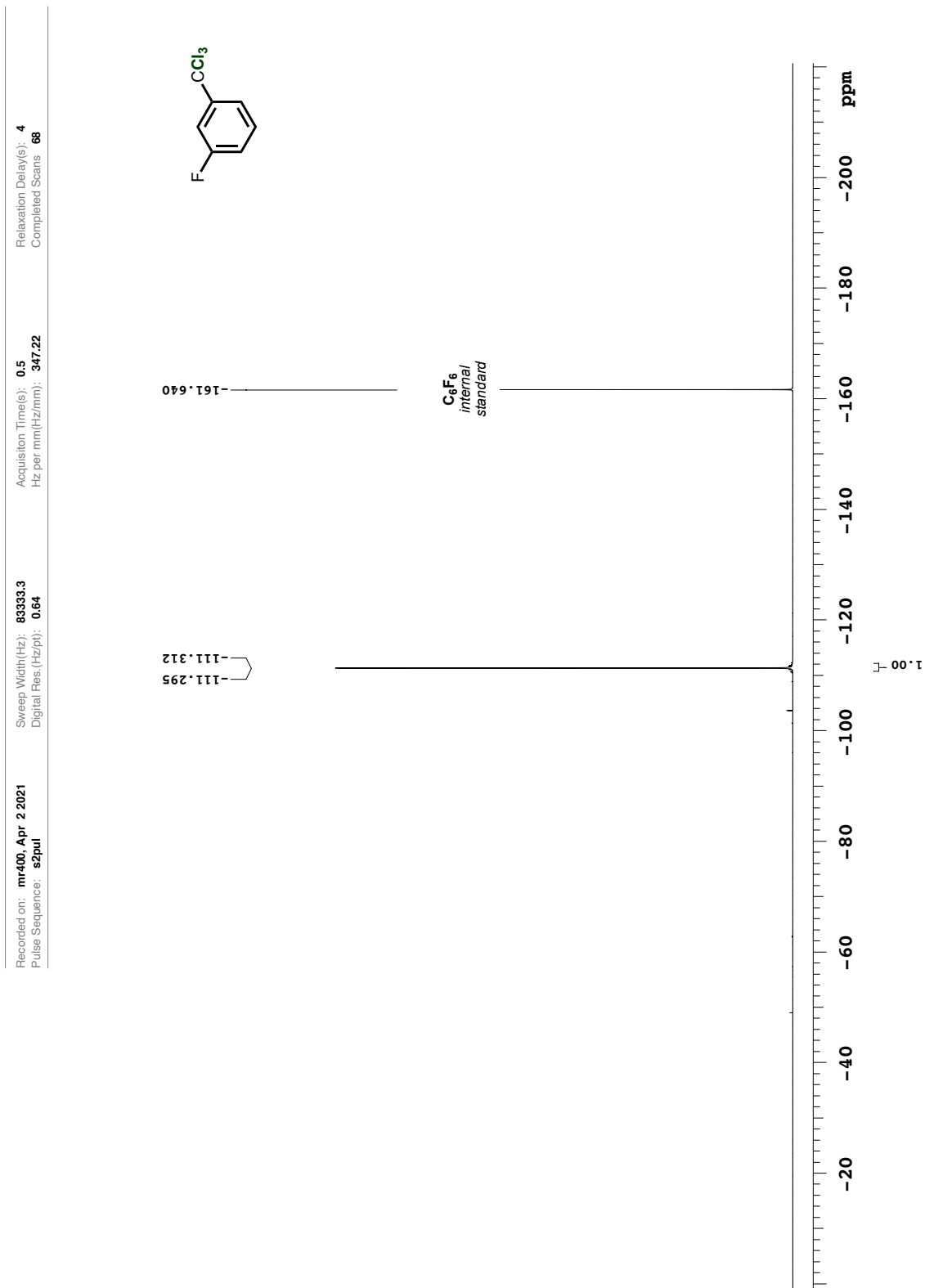


Figure A.98. ¹H NMR spectrum of compound 217 (CDCl₃, 699.8 MHz)

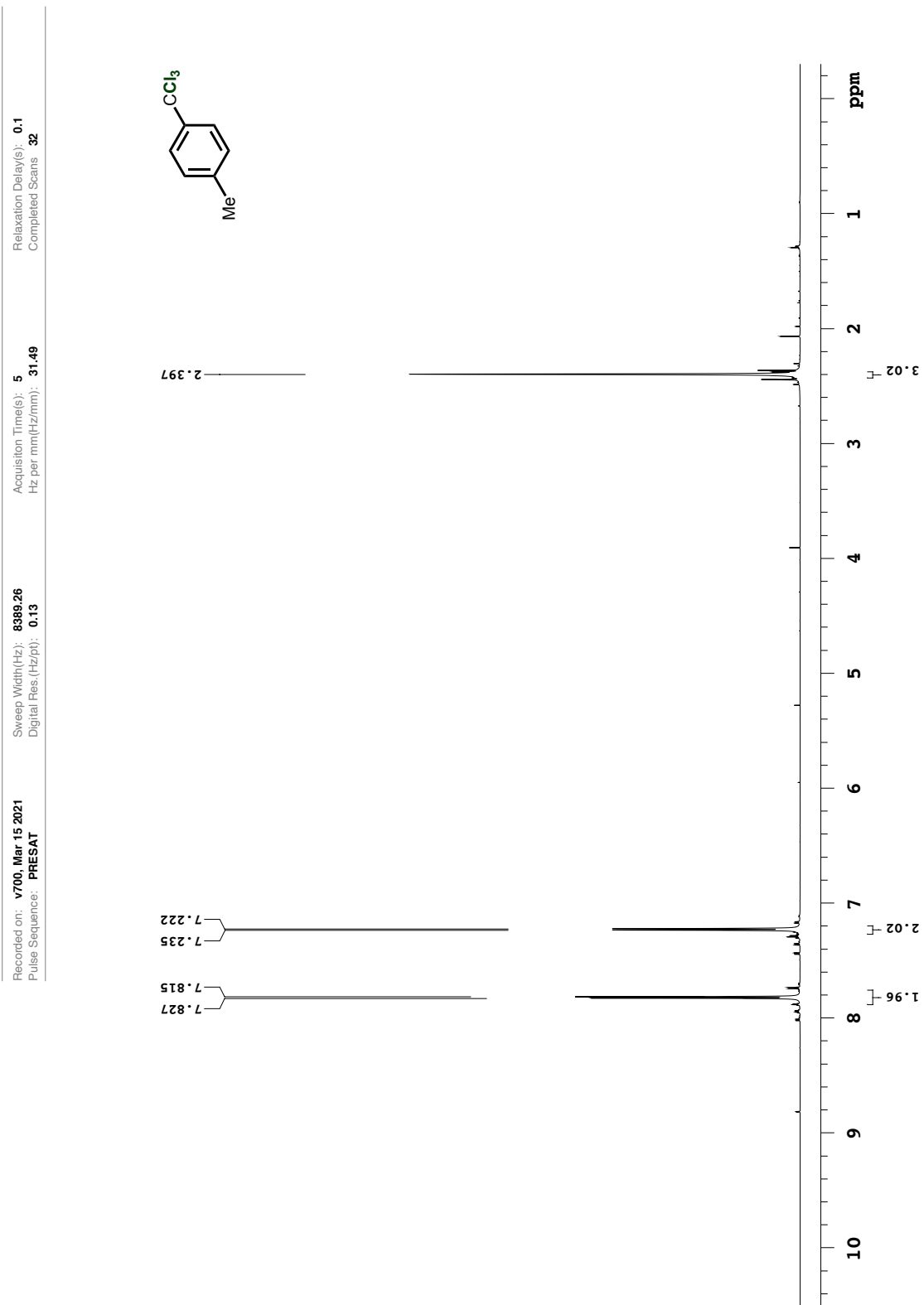


Figure A.99. $^{13}\text{C}\{^1\text{H}\}$ NMR spectrum of compound **217** (CDCl_3 , 176.0 MHz)

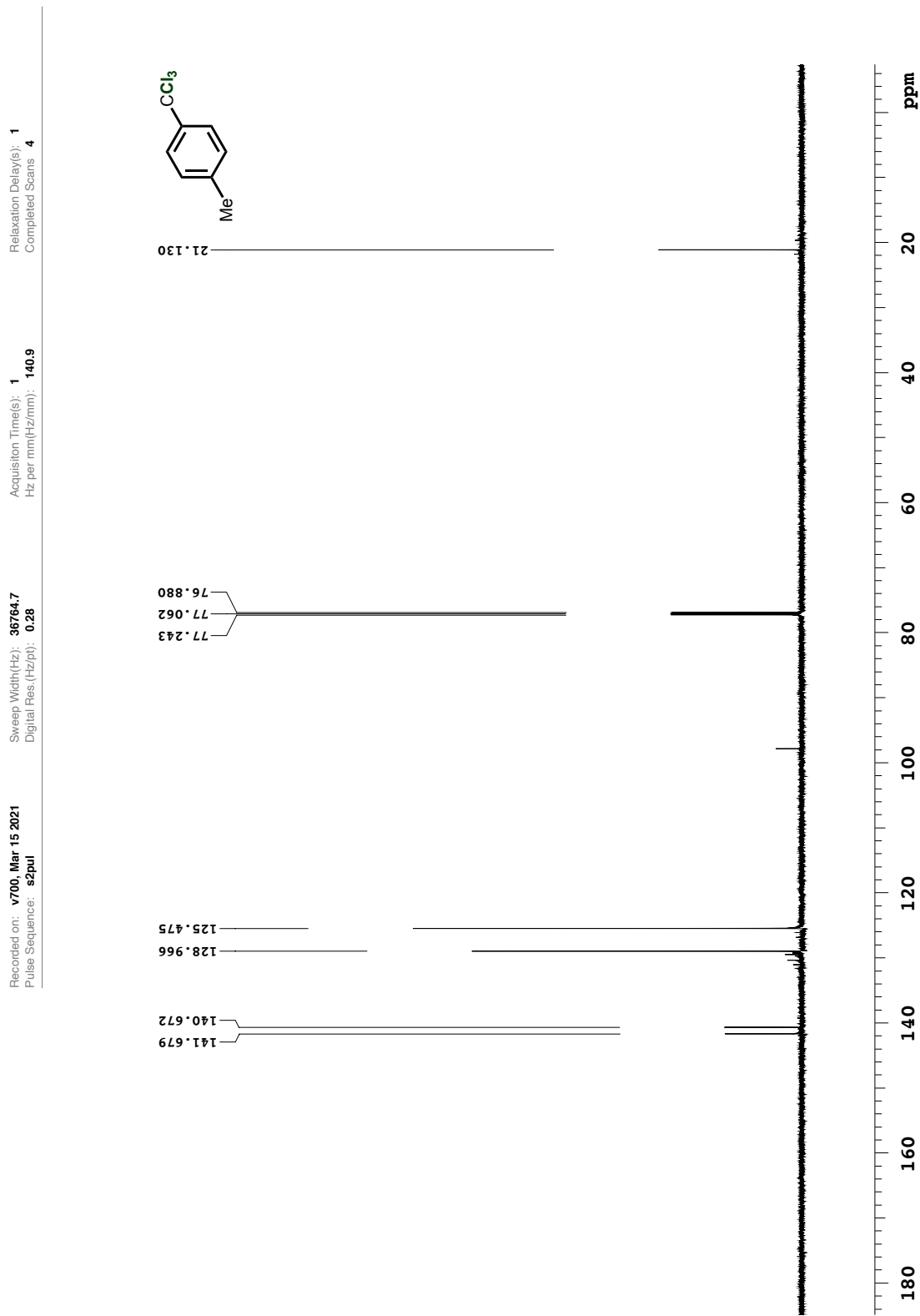


Figure A.100. ¹H NMR spectrum of compound **220** (CDCl₃, 699.8 MHz)

Recorded on: **v700, Dec 13 2020** Sweep Width(Hz): **8389.26** Acquisition Time(s): **5** Relaxation Delay(s): **0.1**
Pulse Sequence: **PRESAT** Digital Res. (Hz/pt): **0.13** Hz per mm(Hz/mm): **32.55** Completed Scans: **32**

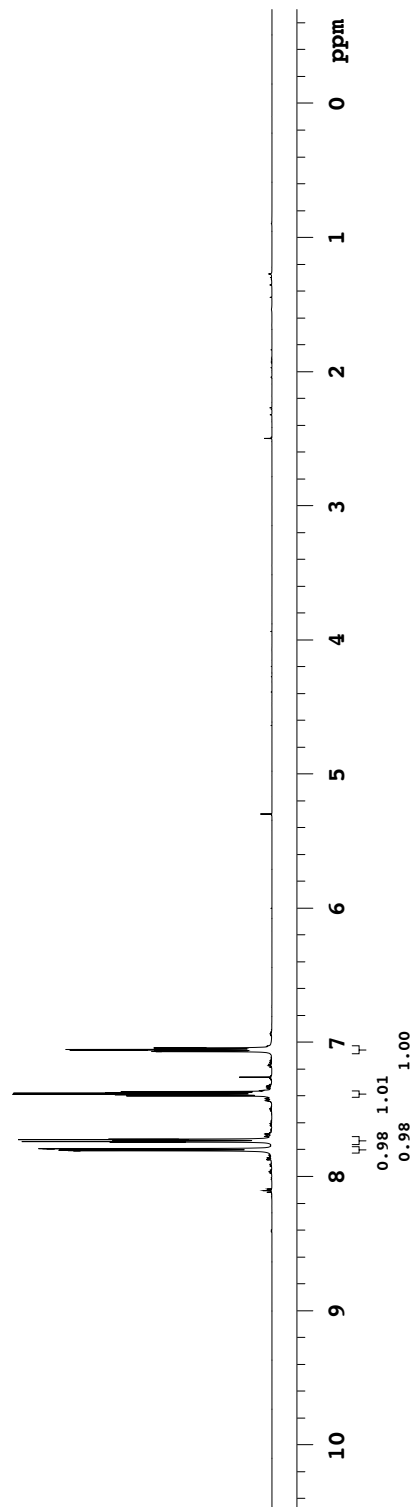
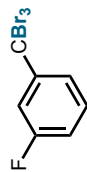


Figure A.101. ¹HNMR magnified spectrum of compound **220** (CDCl₃, 699.8 MHz)

Recorded on: **v700, Dec 13 2020** Sweep Width(Hz): **8385.26** Relaxation Delay(s): **0.1**
Pulse Sequence: **PRESAT** Digital Res. (Hz/pt): **0.13** Hz per mm(Hz/mm): **32.55** Acquisition Time(s): **5** Completed Scans: **32**

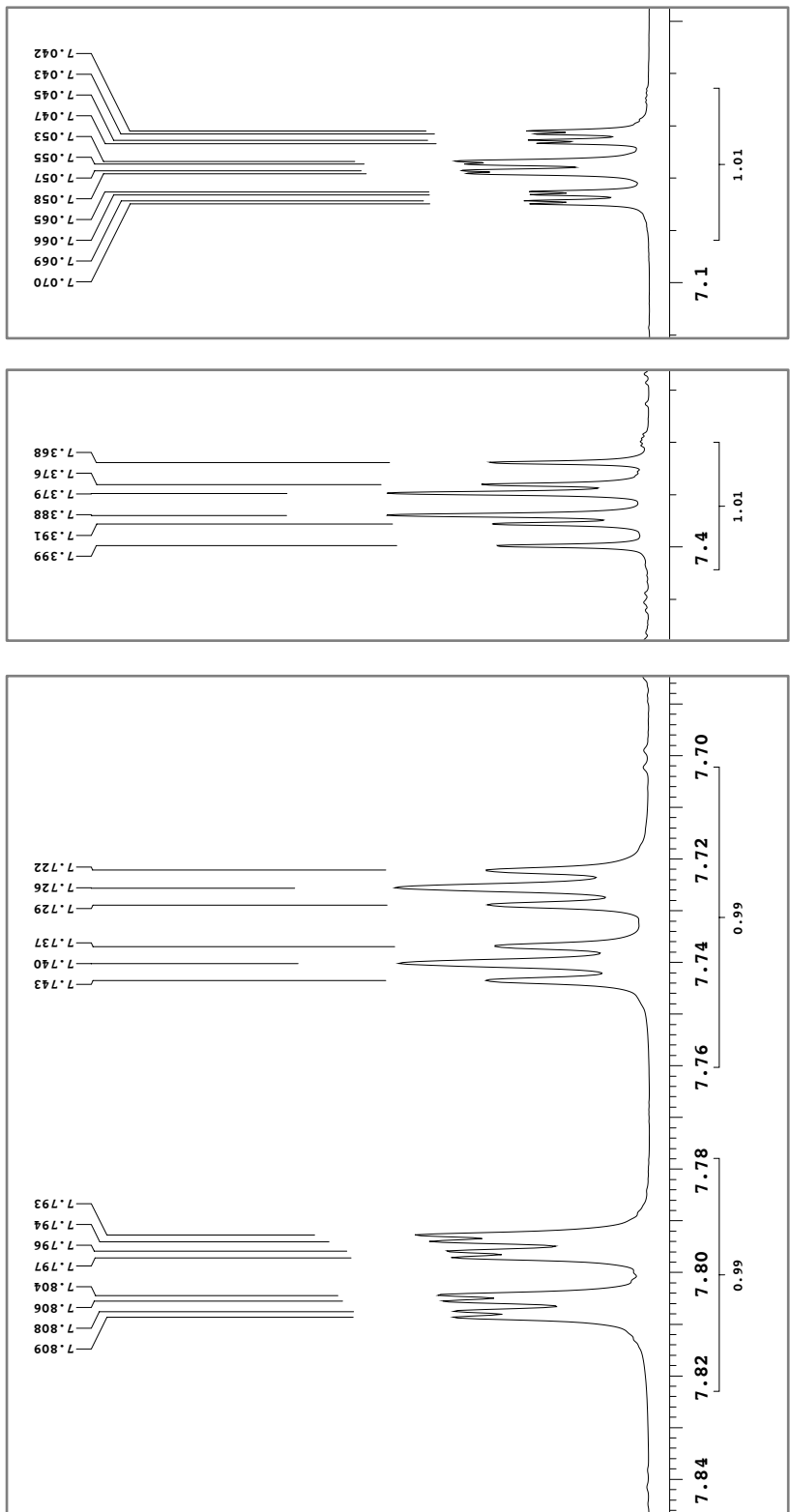
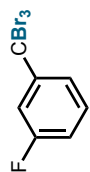


Figure A.102. $^{13}\text{C}\{^1\text{H}\}$ NMR spectrum of compound **220** (CDCl_3 , 176.0 MHz)

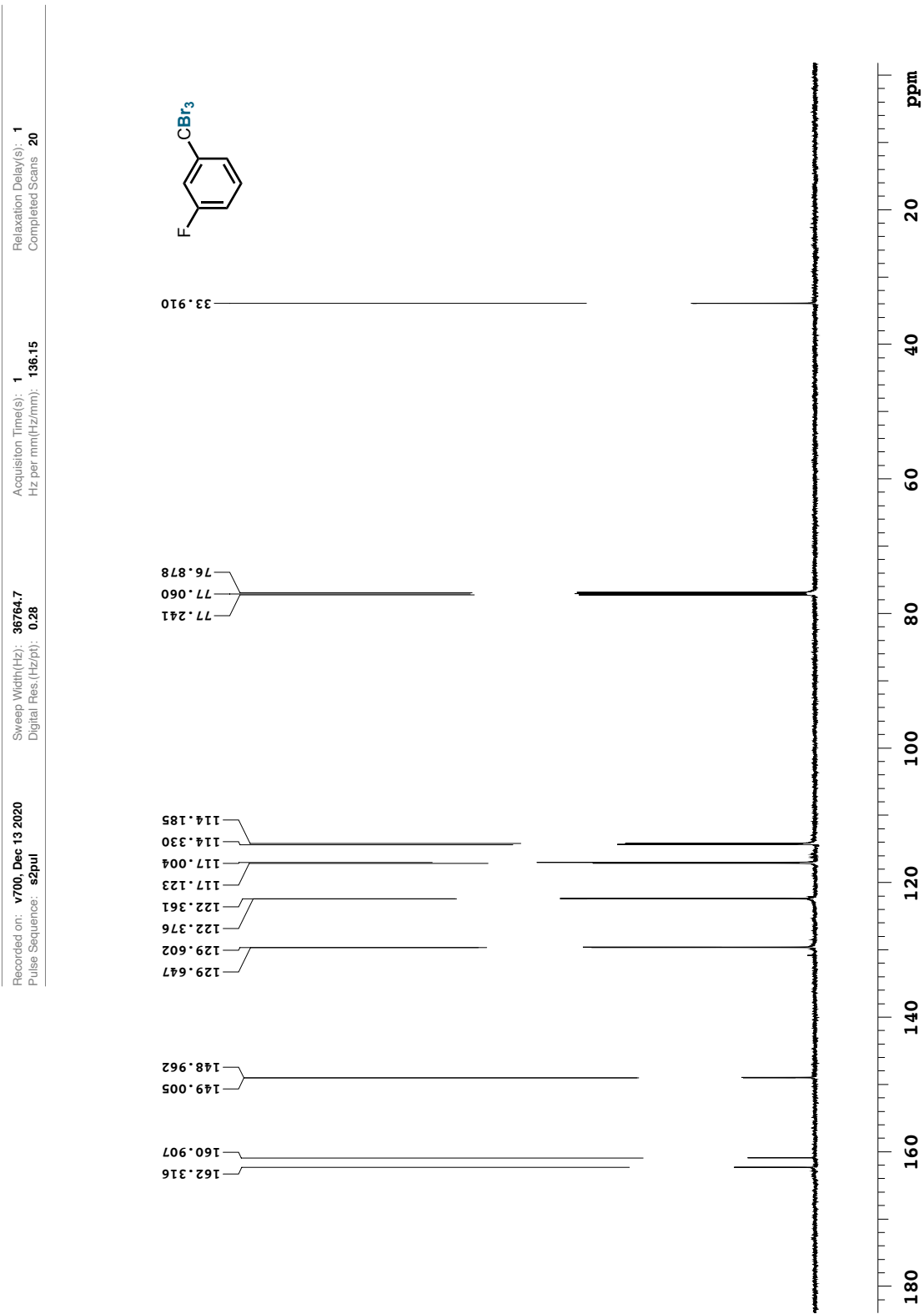


Figure A.103. ^{19}F NMR spectrum of compound **220** (CDCl_3 , 367.3 MHz)

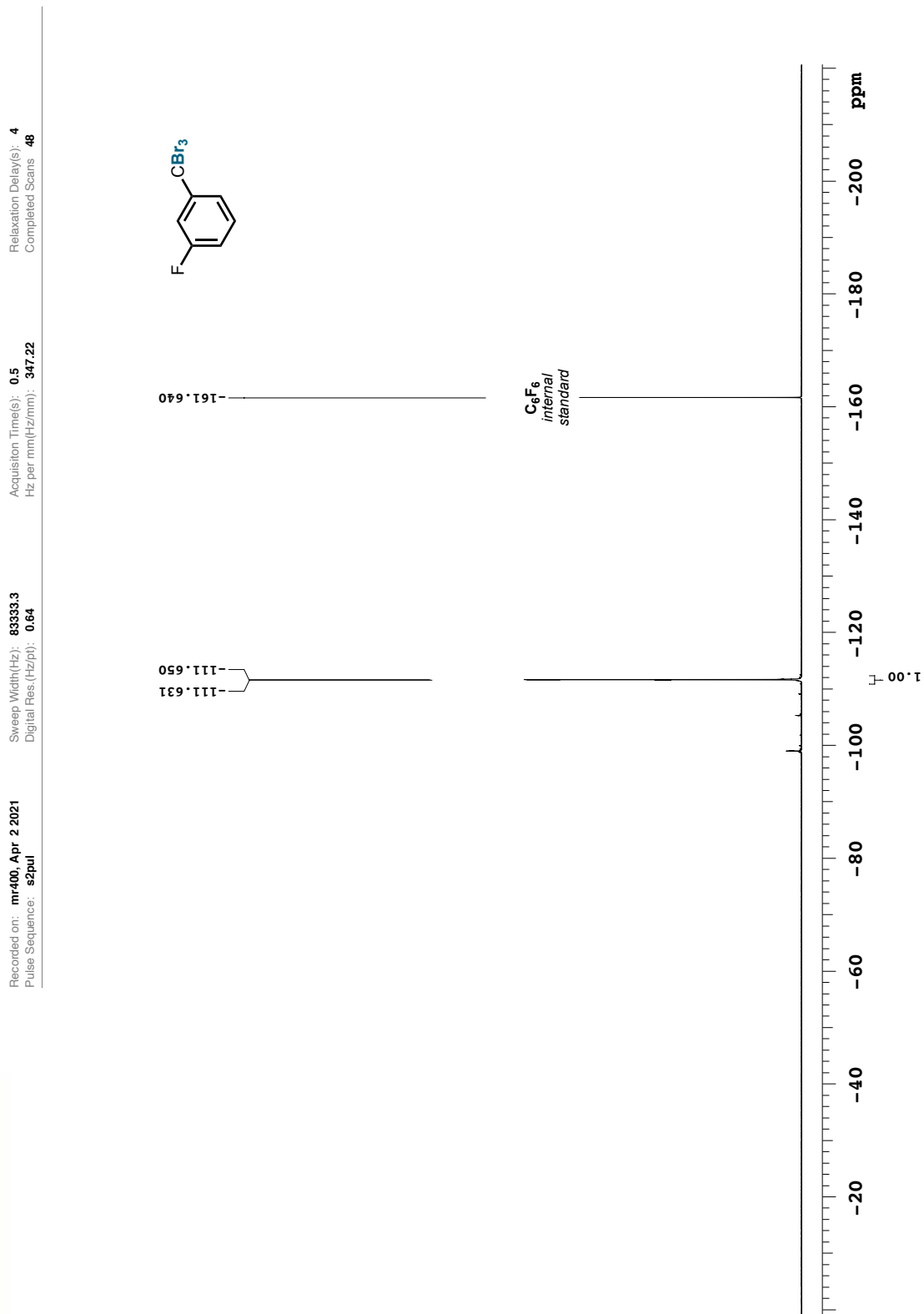


Figure A.104. ¹H NMR spectrum of compound 221 (CDCl₃, 699.8 MHz)

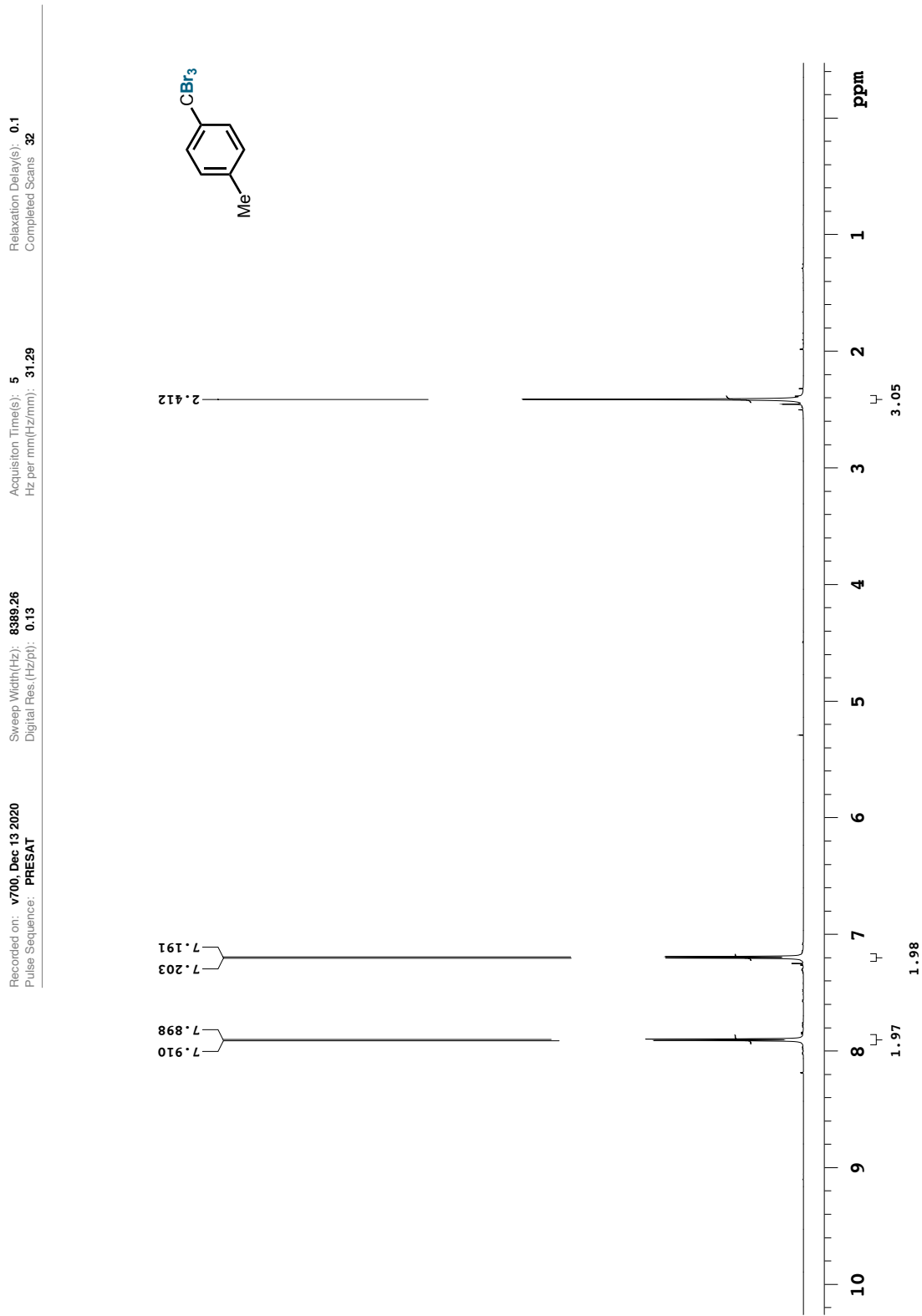


Figure A.105. $^{13}\text{C}\{^1\text{H}\}$ NMR spectrum of compound **221** (CDCl_3 , 176.0 MHz)

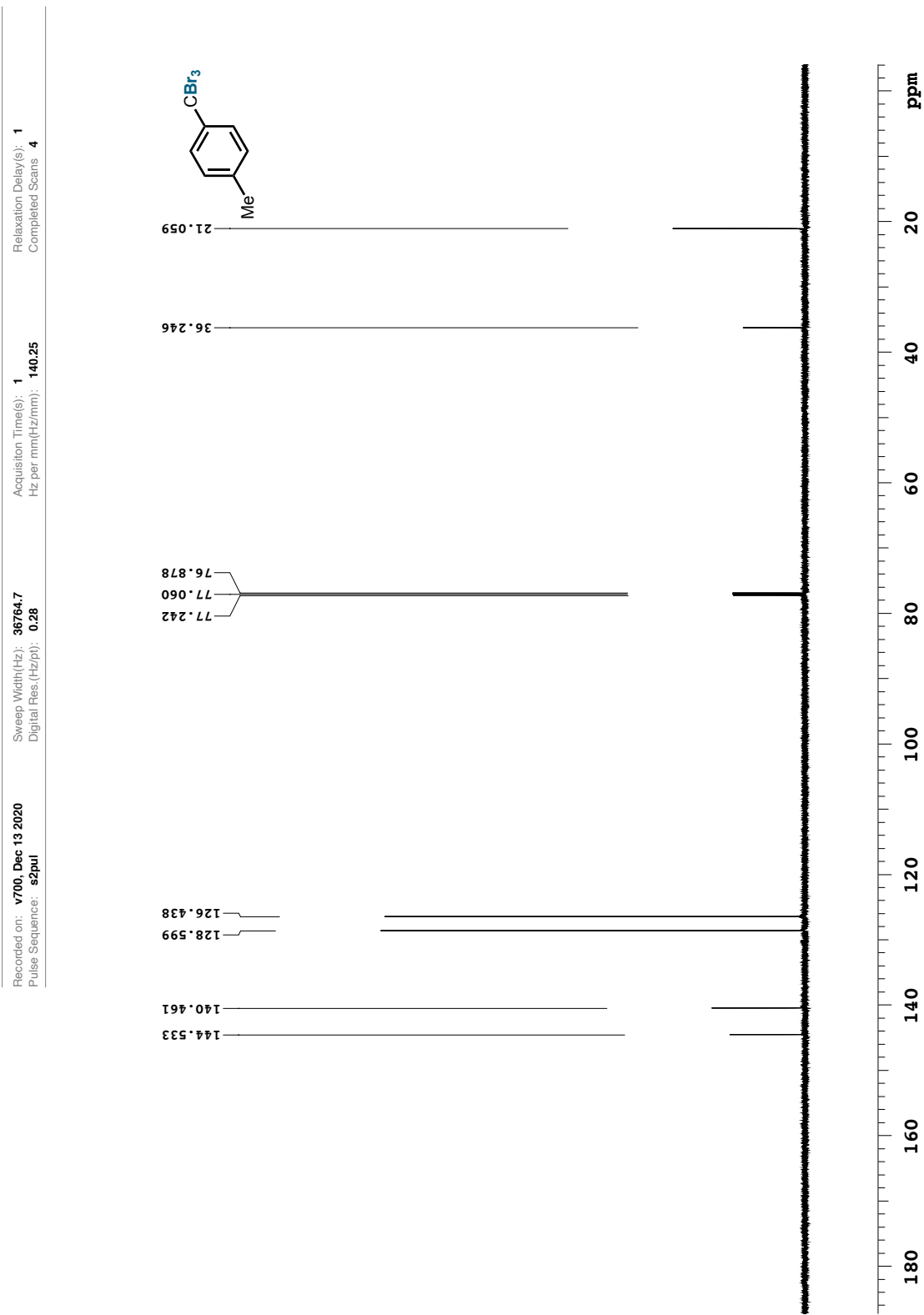


Figure A.106. ¹H NMR spectrum of compound 223 (CDCl₃, 599.9 MHz)

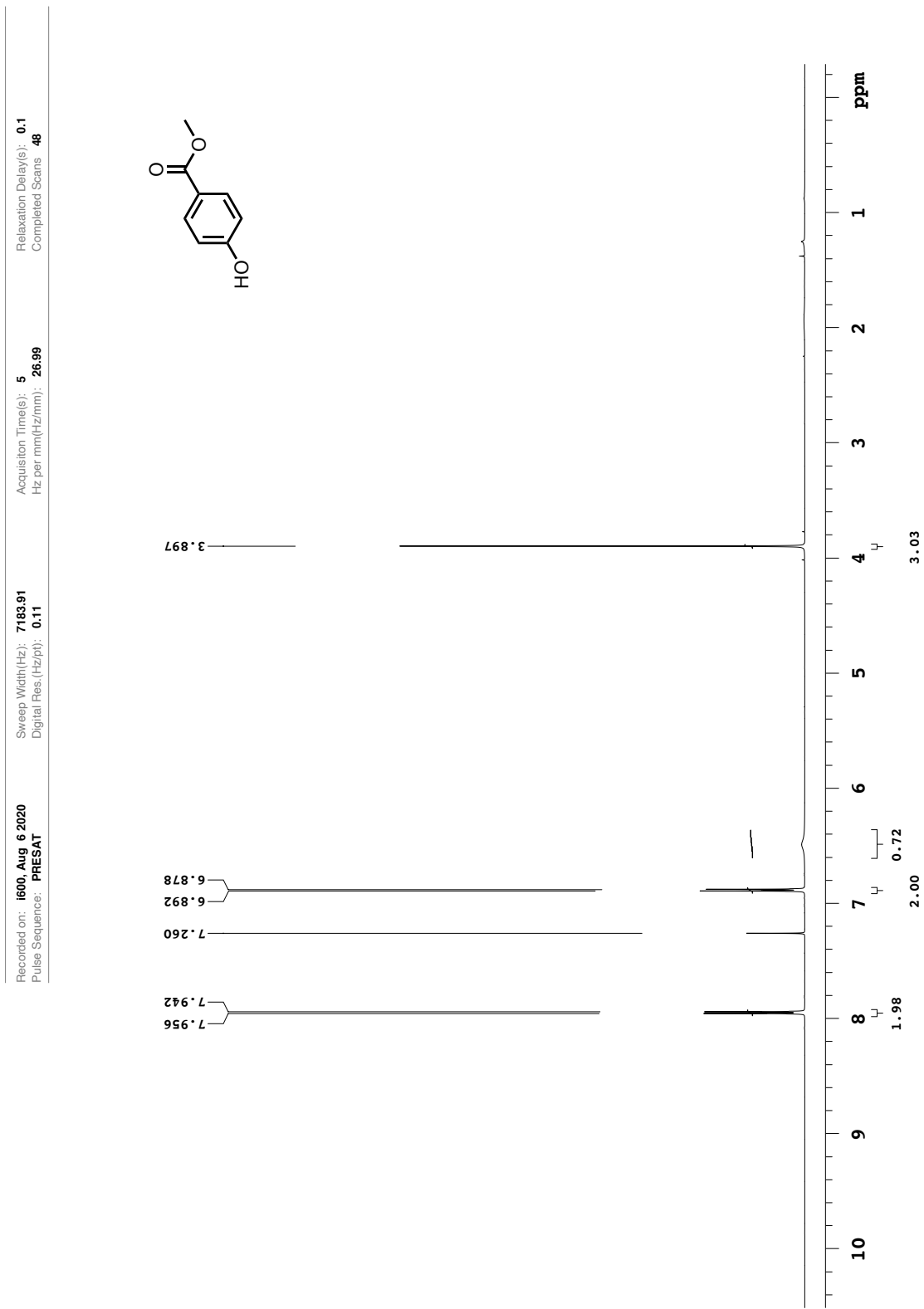


Figure A.107. $^{13}\text{C}\{^1\text{H}\}$ NMR spectrum of compound **223** (CDCl_3 , 150.9 MHz)

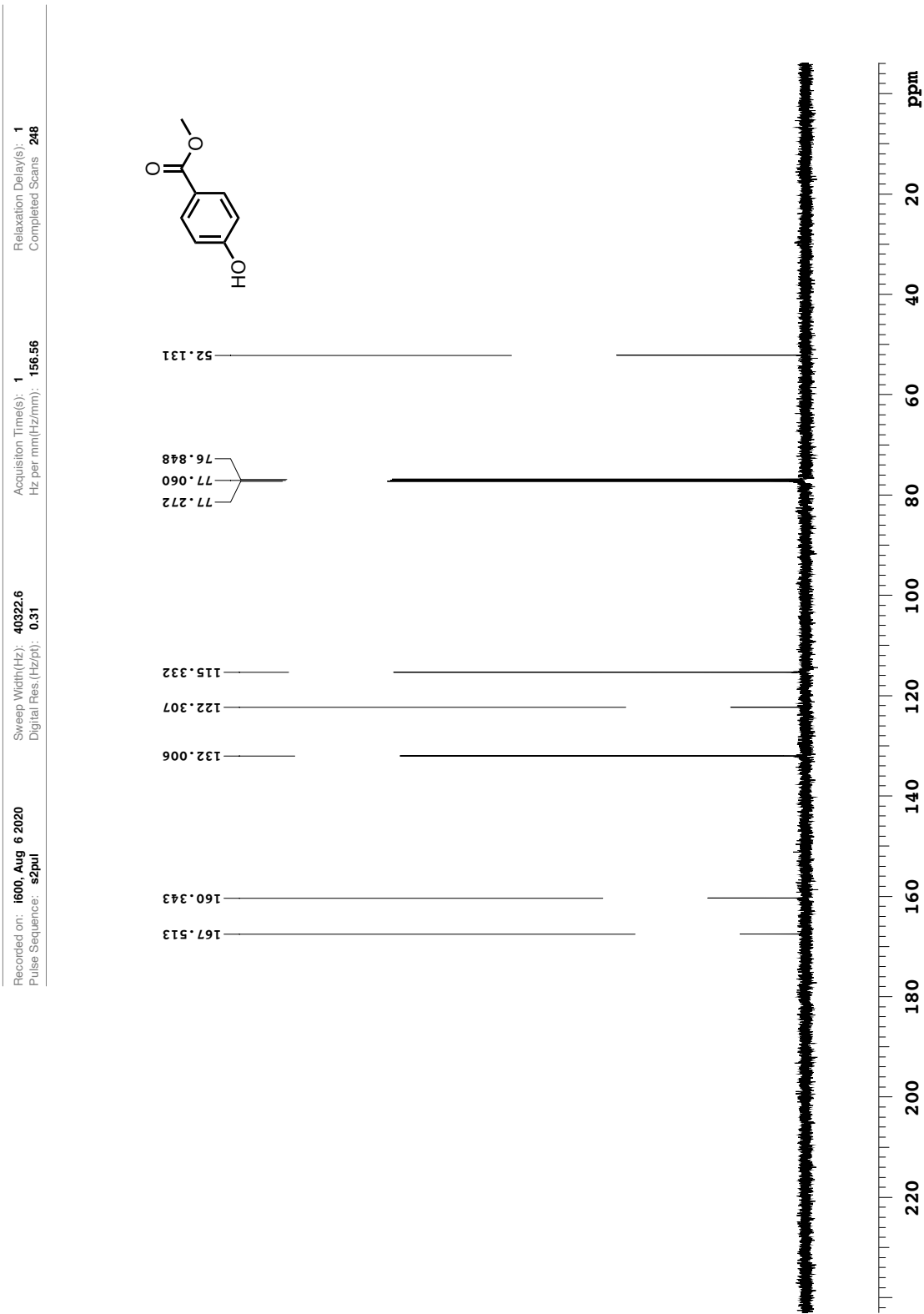


Figure A.108. ¹H NMR spectrum of compound 239 (CDCl₃, 499.8 MHz)

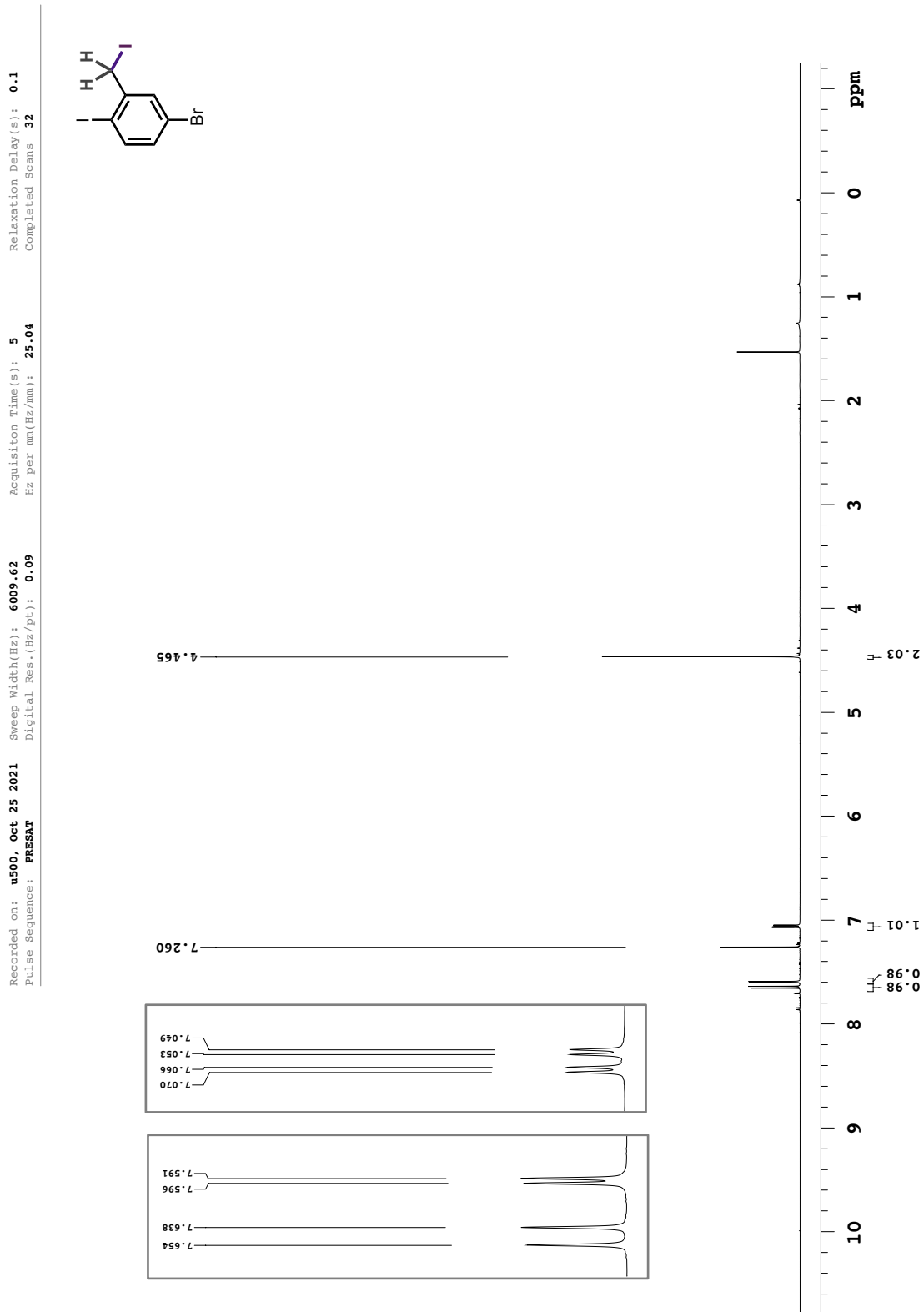


Figure A.109. $^{13}\text{C}\{^1\text{H}\}$ NMR spectrum of compound **239** (CDCl_3 , 125.7 MHz)

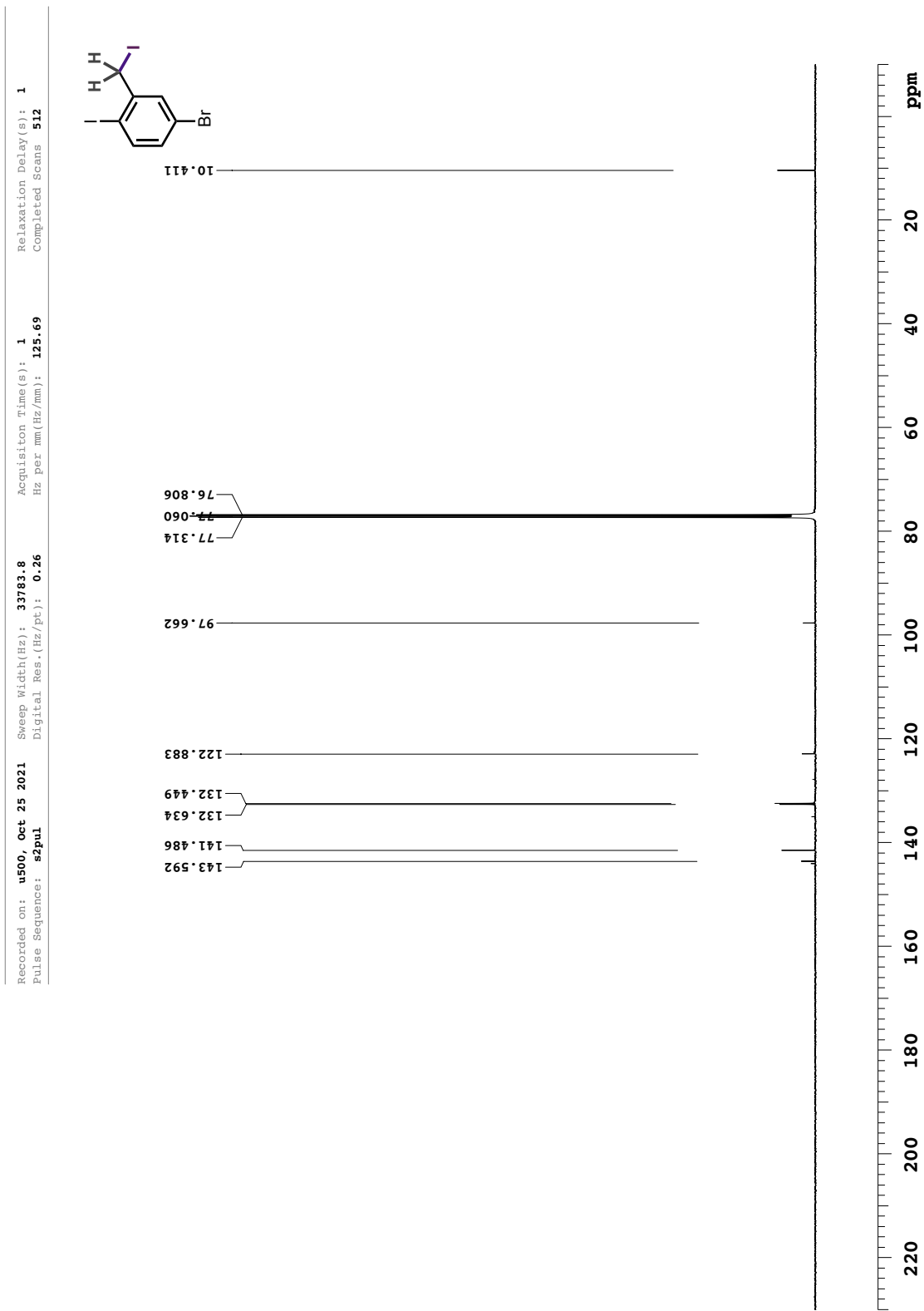


Figure A.110. ¹H NMR spectrum of compound 240 (CDCl₃, 499.8 MHz)

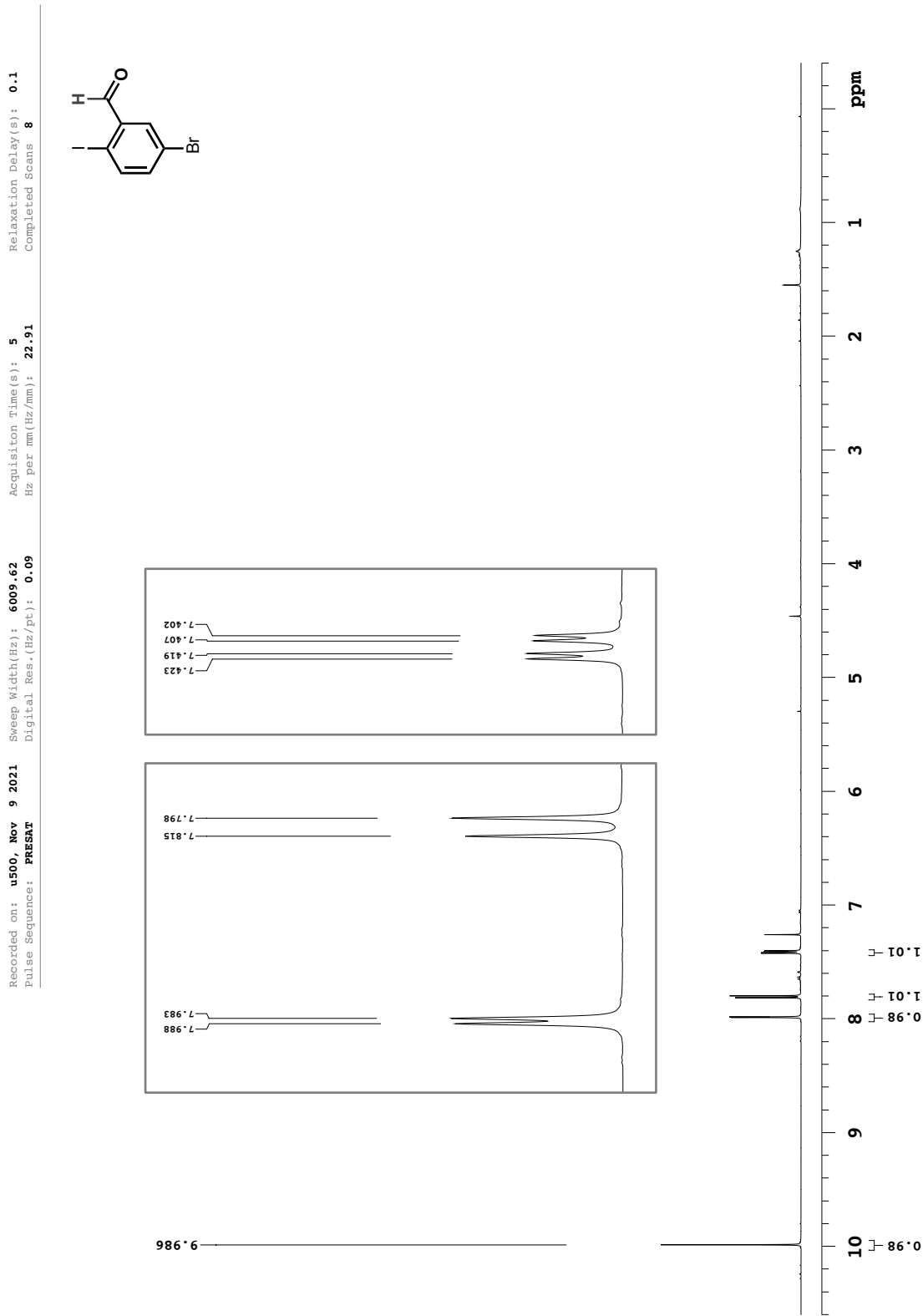


Figure A.111. $^{13}\text{C}\{^1\text{H}\}$ NMR spectrum of compound **240** (CDCl_3 , 125.7 MHz)

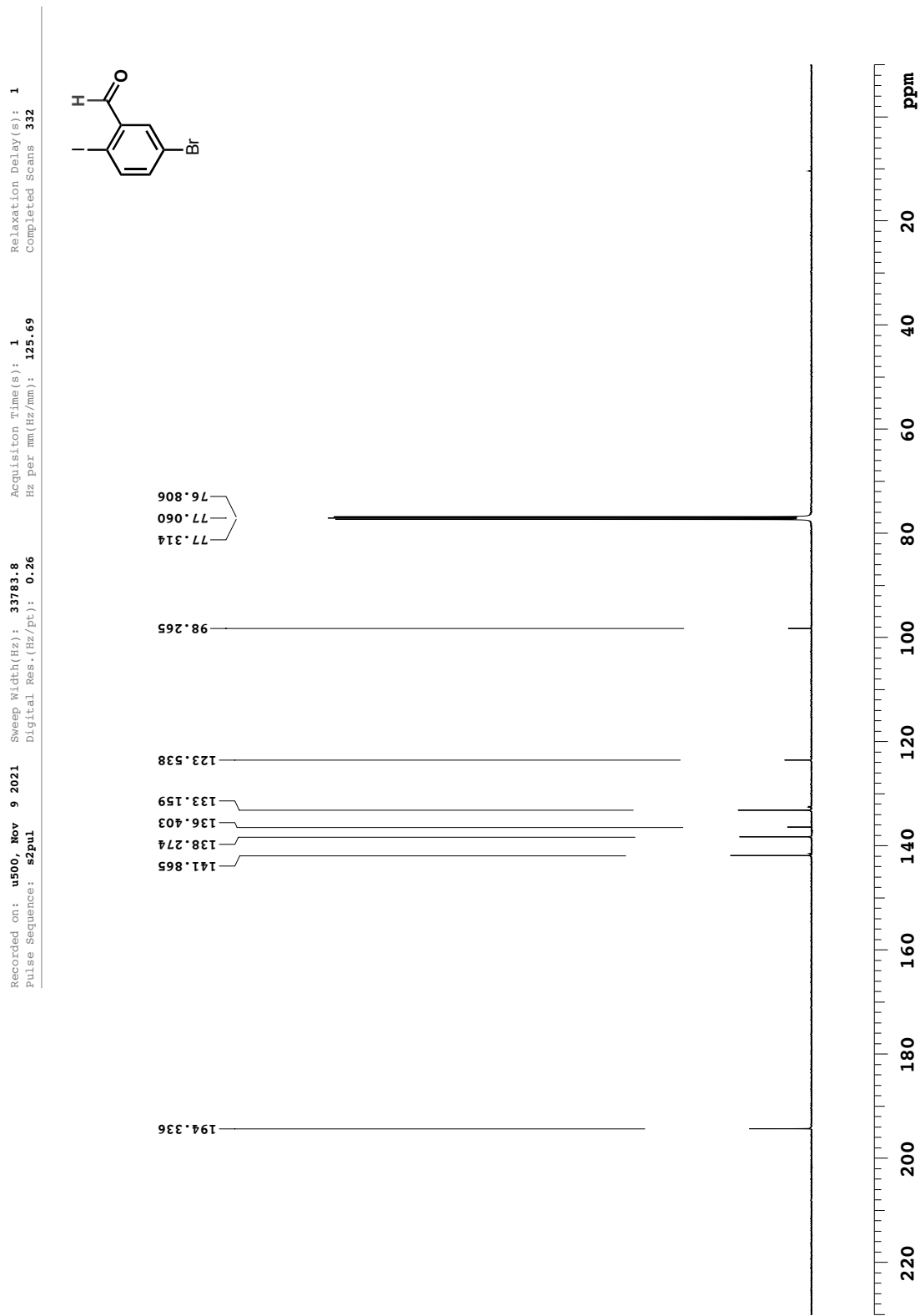


Figure A.112. ¹H NMR spectrum of compound 433 (CDCl₃, 400.0 MHz)

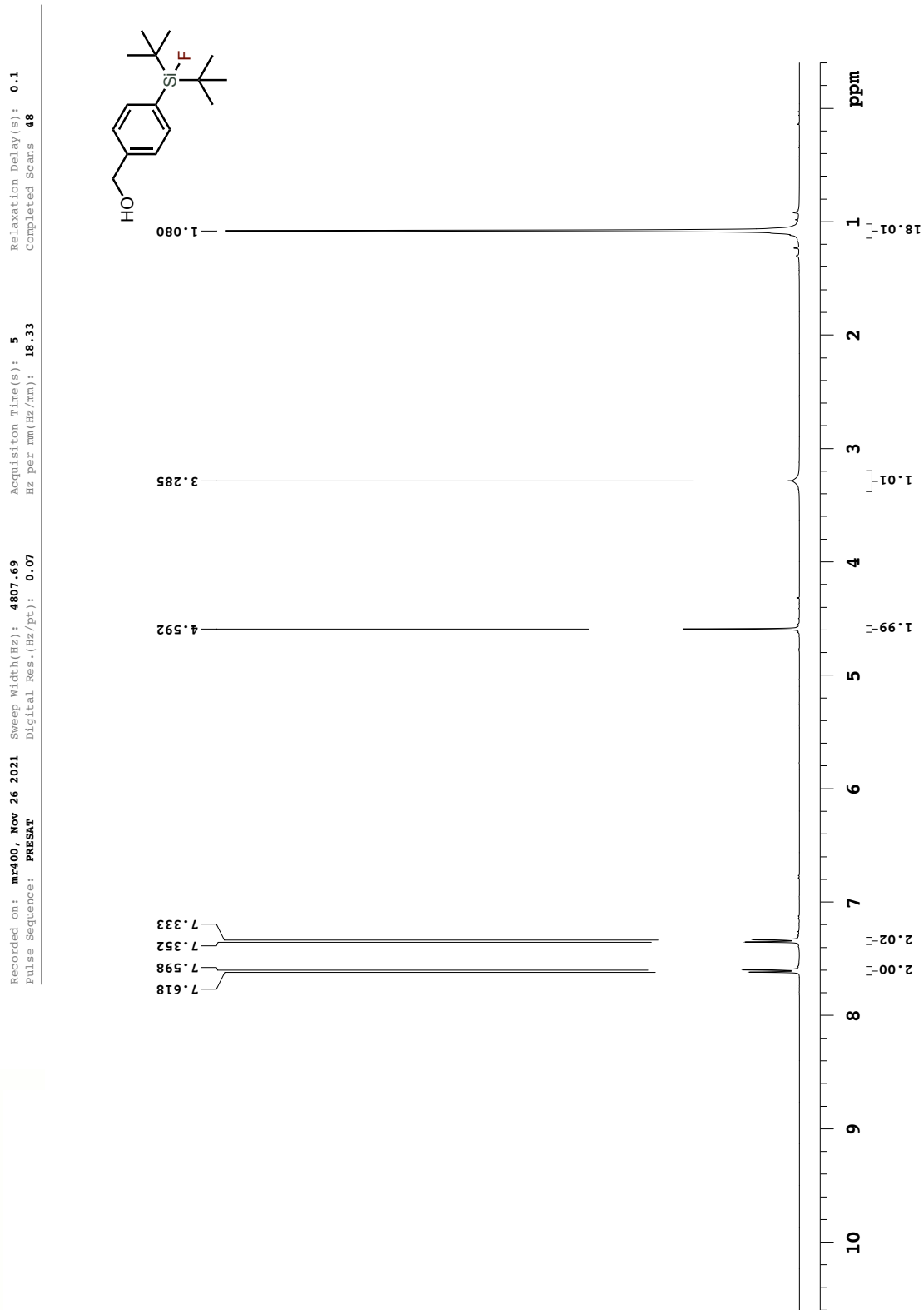


Figure A.113. $^{13}\text{C}\{^1\text{H}\}$ NMR spectrum of compound 433 (CDCl_3 , 125.7 MHz)

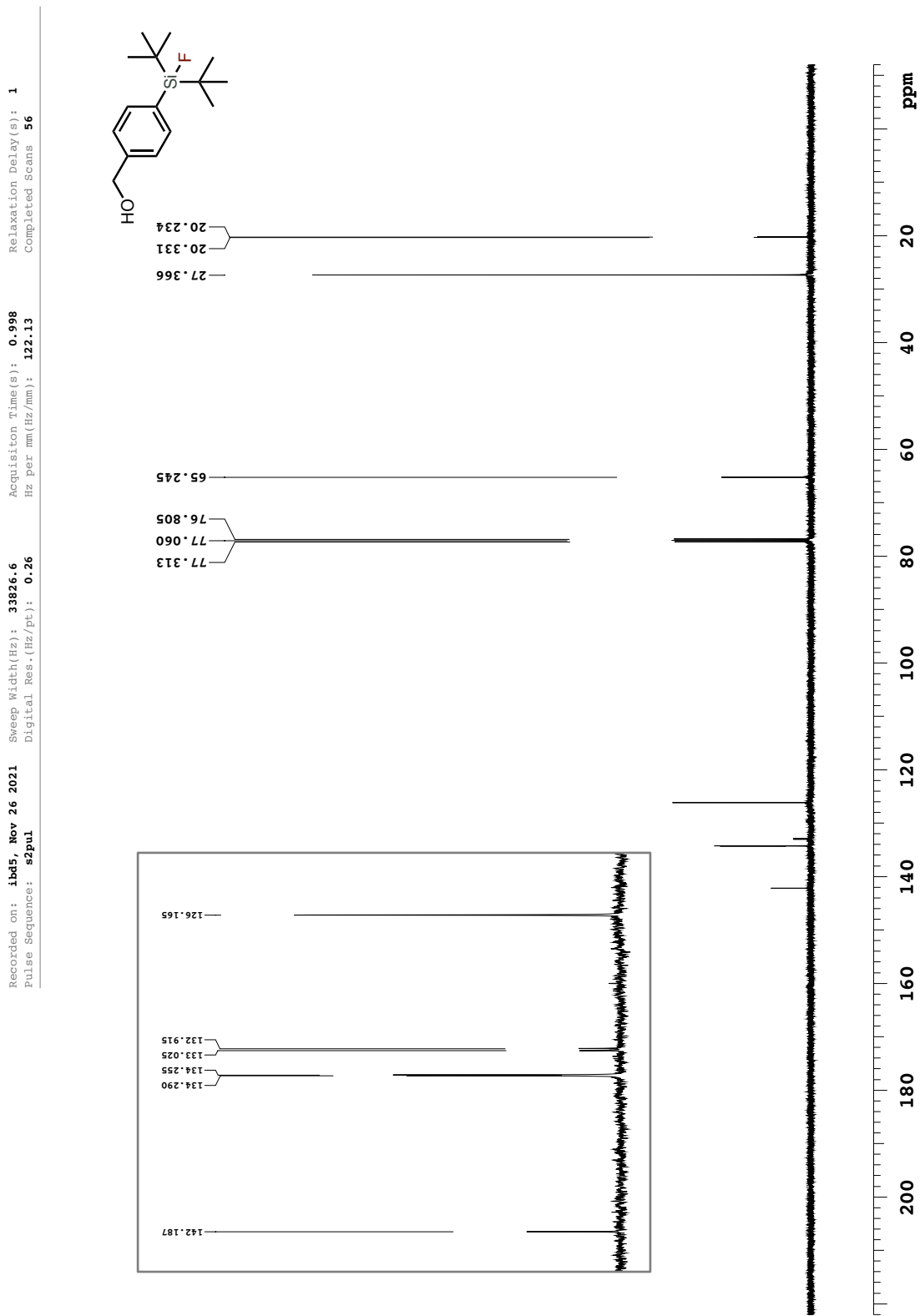
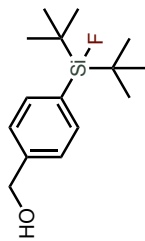


Figure A.114. ^{19}F NMR spectrum of compound 433 (CDCl_3 , 468.6 MHz)

Recorded on: ibd5, Nov 26 2021	Sweep Width (Hz): 98522.2	Acquisition Time(s): 0.5	Relaxation Delay(s): 3.5
Pulse Sequence: s2pul	Digital Res. (Hz/pt.): 1.5	Hz per mm (Hz/mm): 410.5	Completed Scans 16



988.881



Figure A.115. ¹H NMR spectrum of compound 434 (CDCl₃, 498.1 MHz)

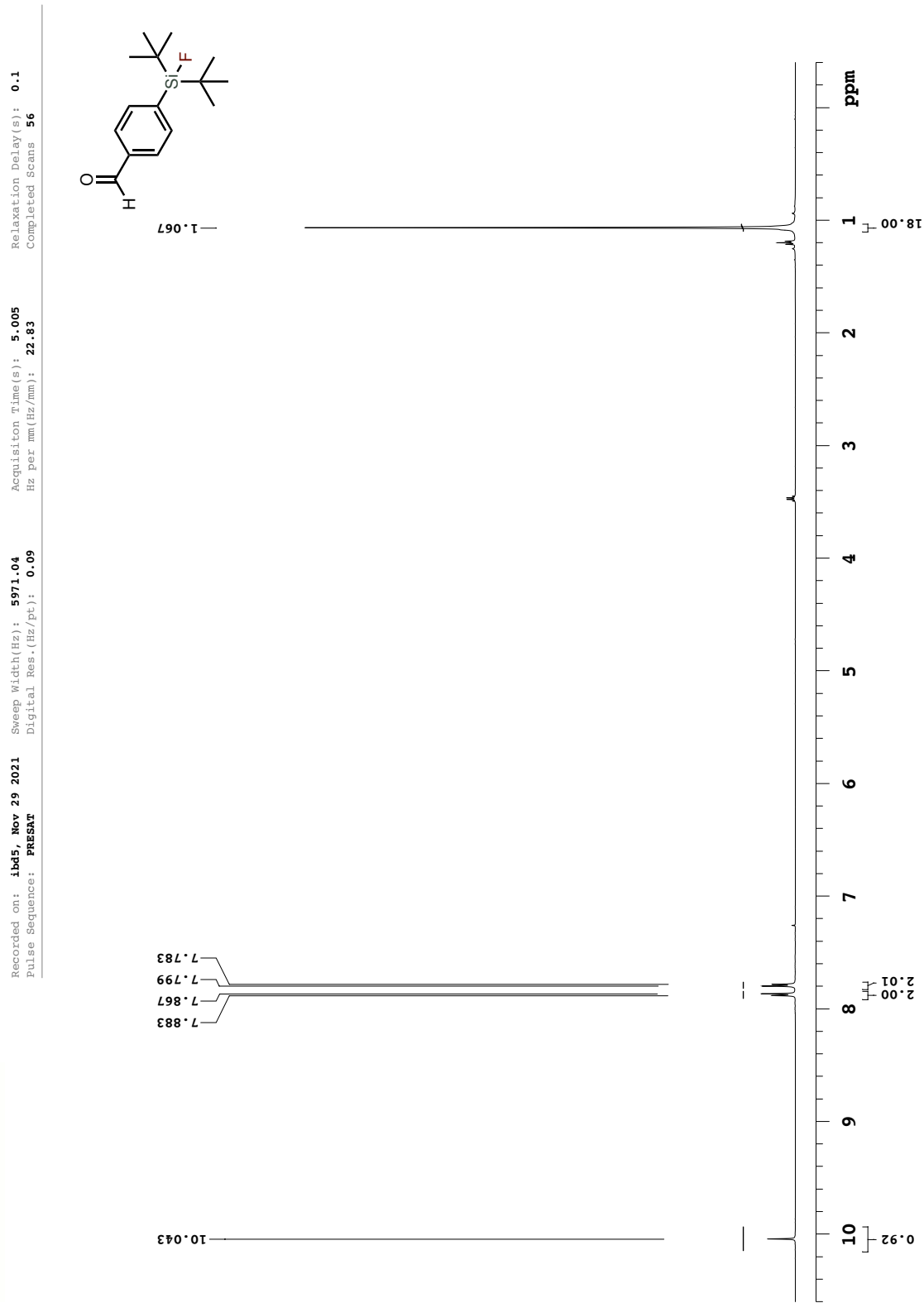


Figure A.116. $^{13}\text{C}\{^1\text{H}\}$ NMR spectrum of compound 434 (CDCl_3 , 125.7 MHz)

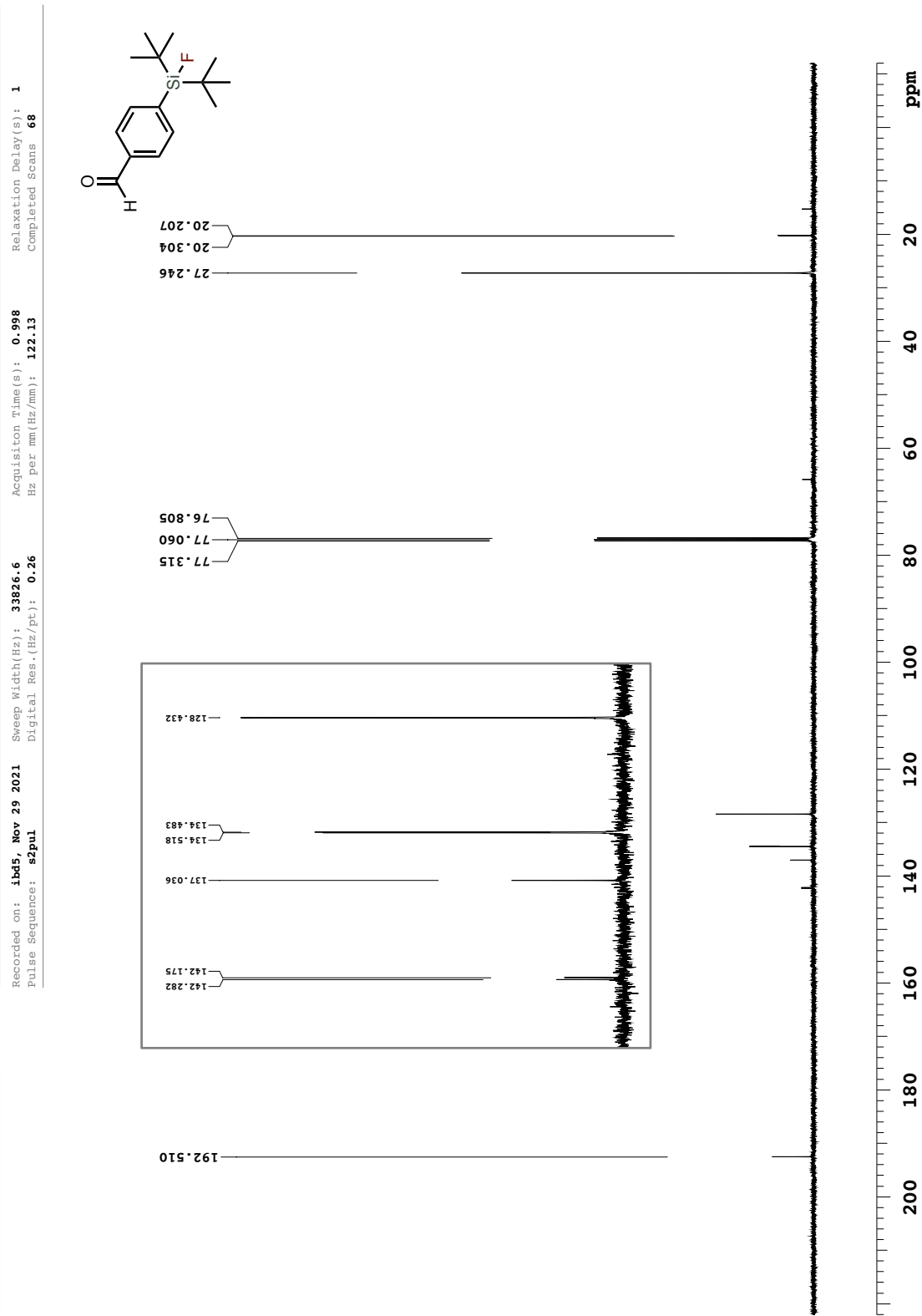


Figure A.117. ¹H NMR spectrum of compound 435 (CDCl₃, 400.0 MHz)

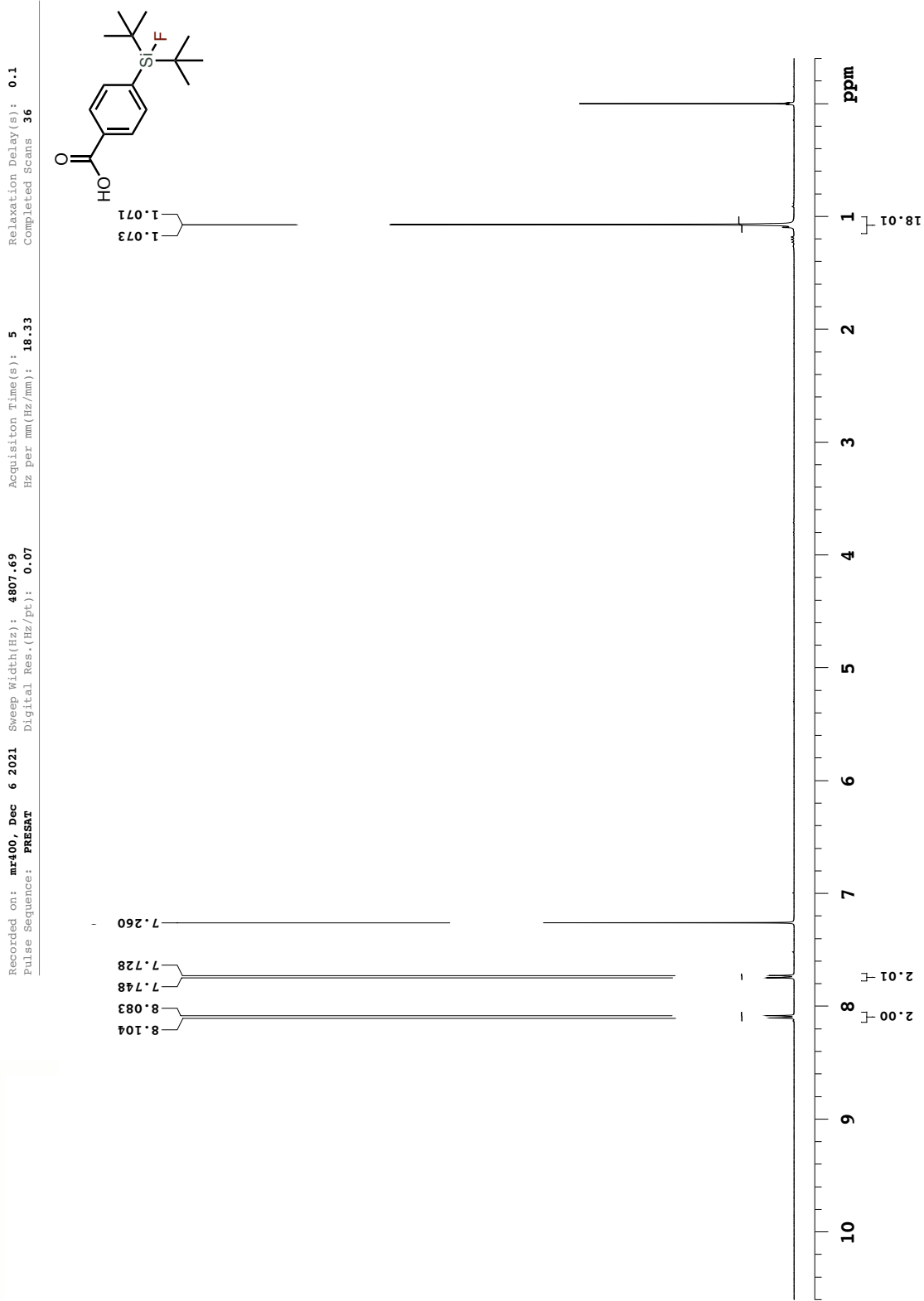


Figure A.118. $^{13}\text{C}\{^1\text{H}\}$ NMR spectrum of compound 435 (CDCl_3 , 100.6 MHz)

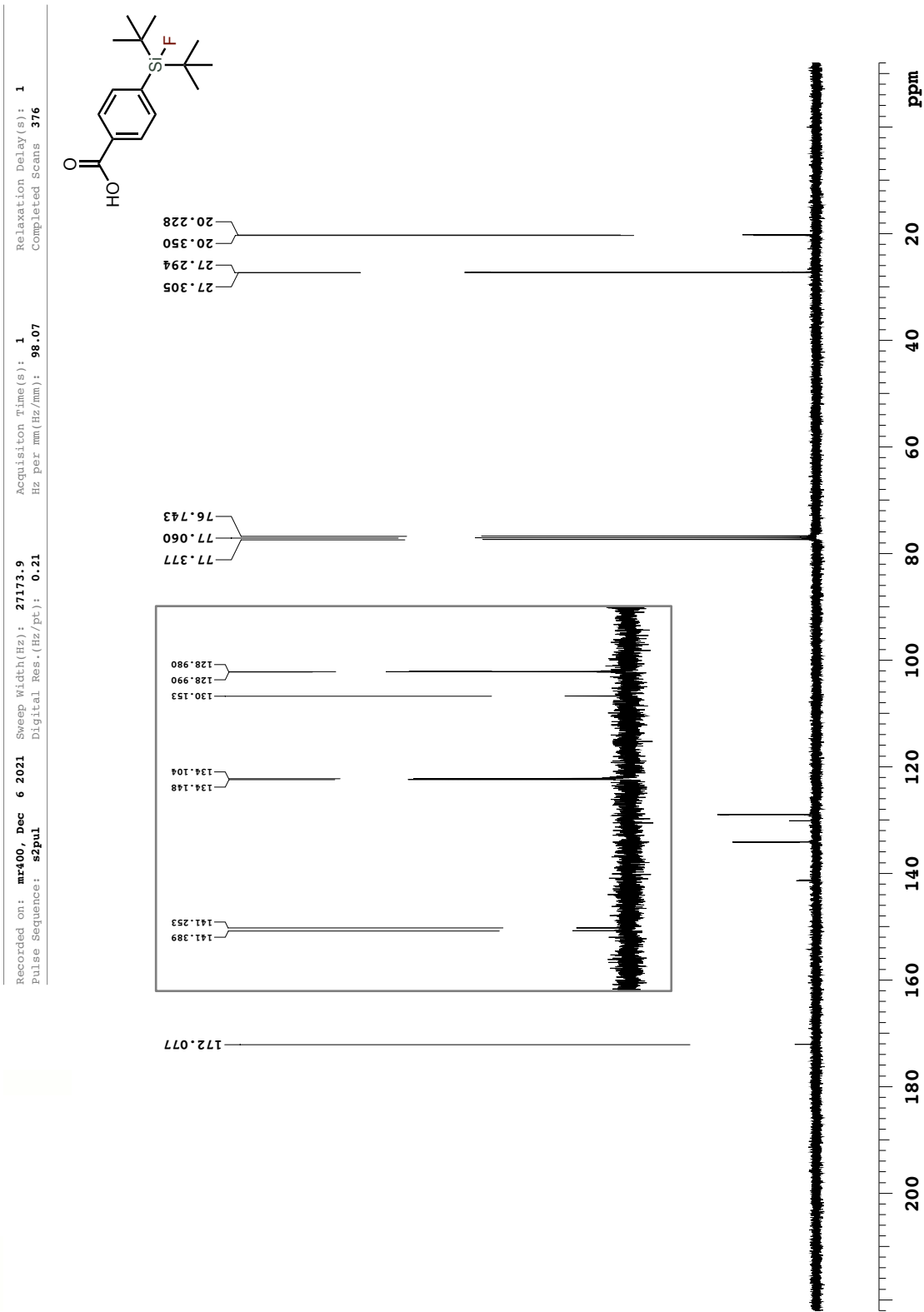


Figure A.119. ¹HNMR spectrum of compound 436 (CDCl₃, 400.0 MHz)

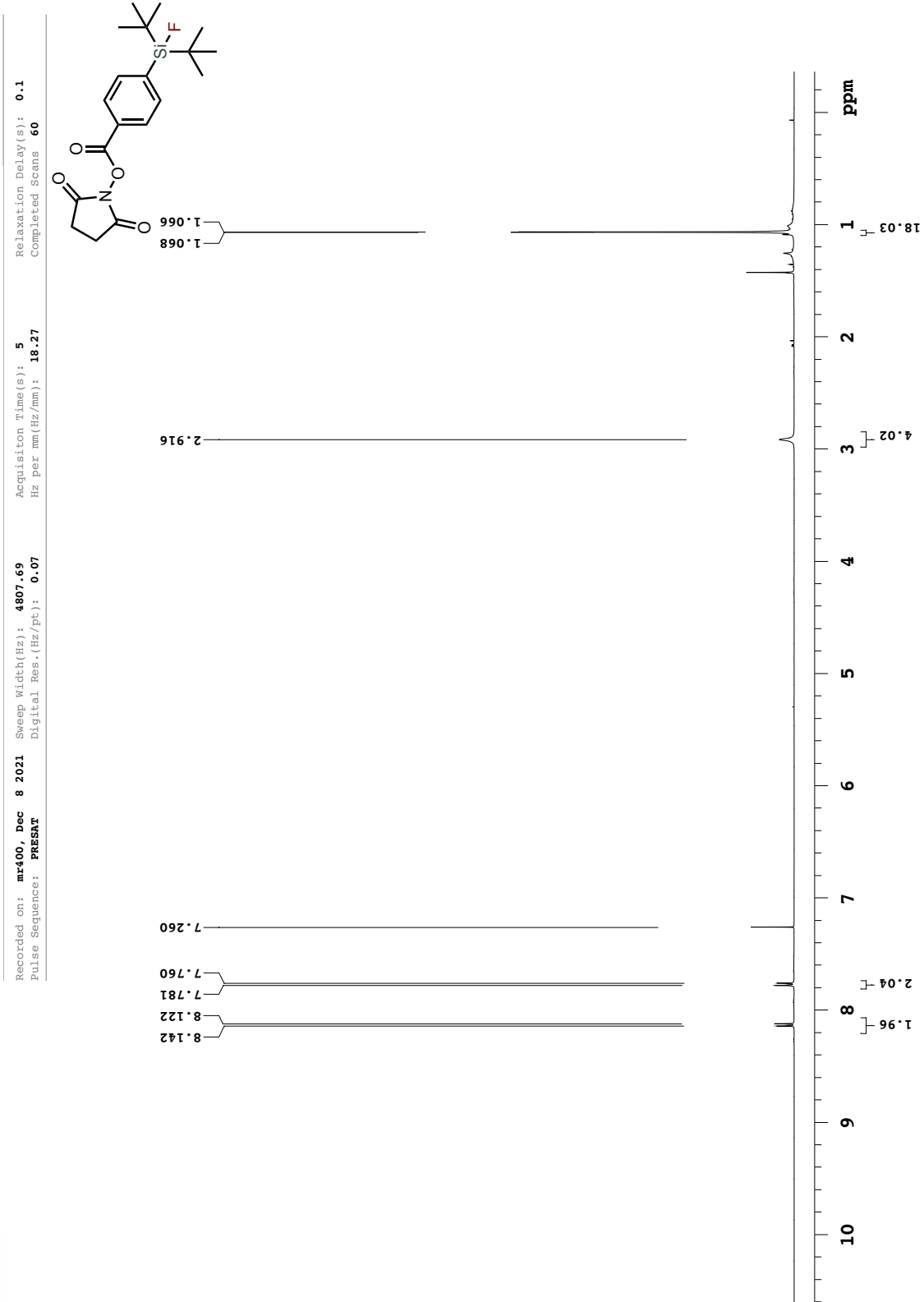


Figure A.120. $^{13}\text{C}\{^1\text{H}\}$ NMR spectrum of compound **436** (CDCl_3 , 176.0 MHz)

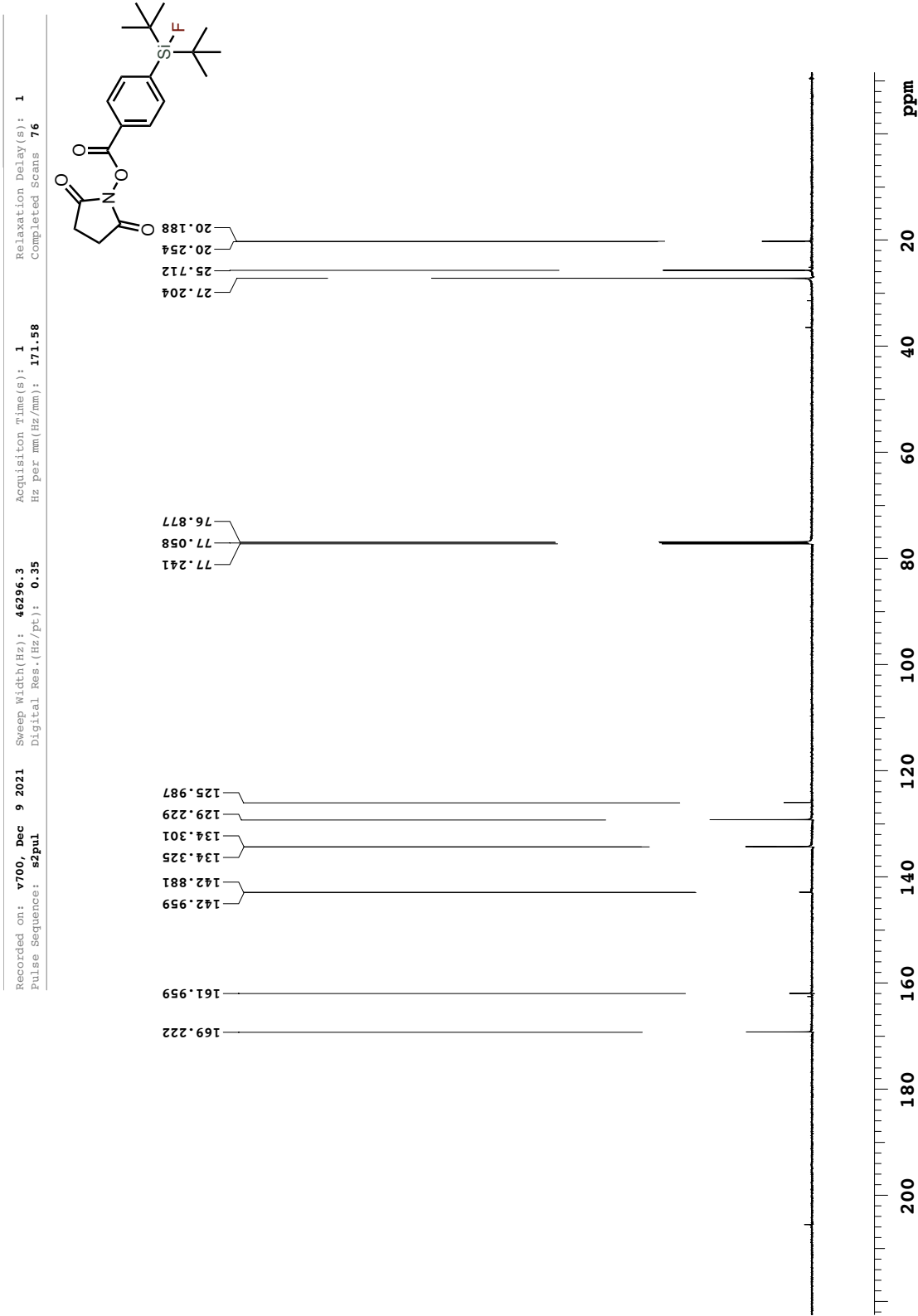


Figure A.121. ^{19}F NMR spectrum of compound 436 (CDCl_3 , 376.3 MHz)

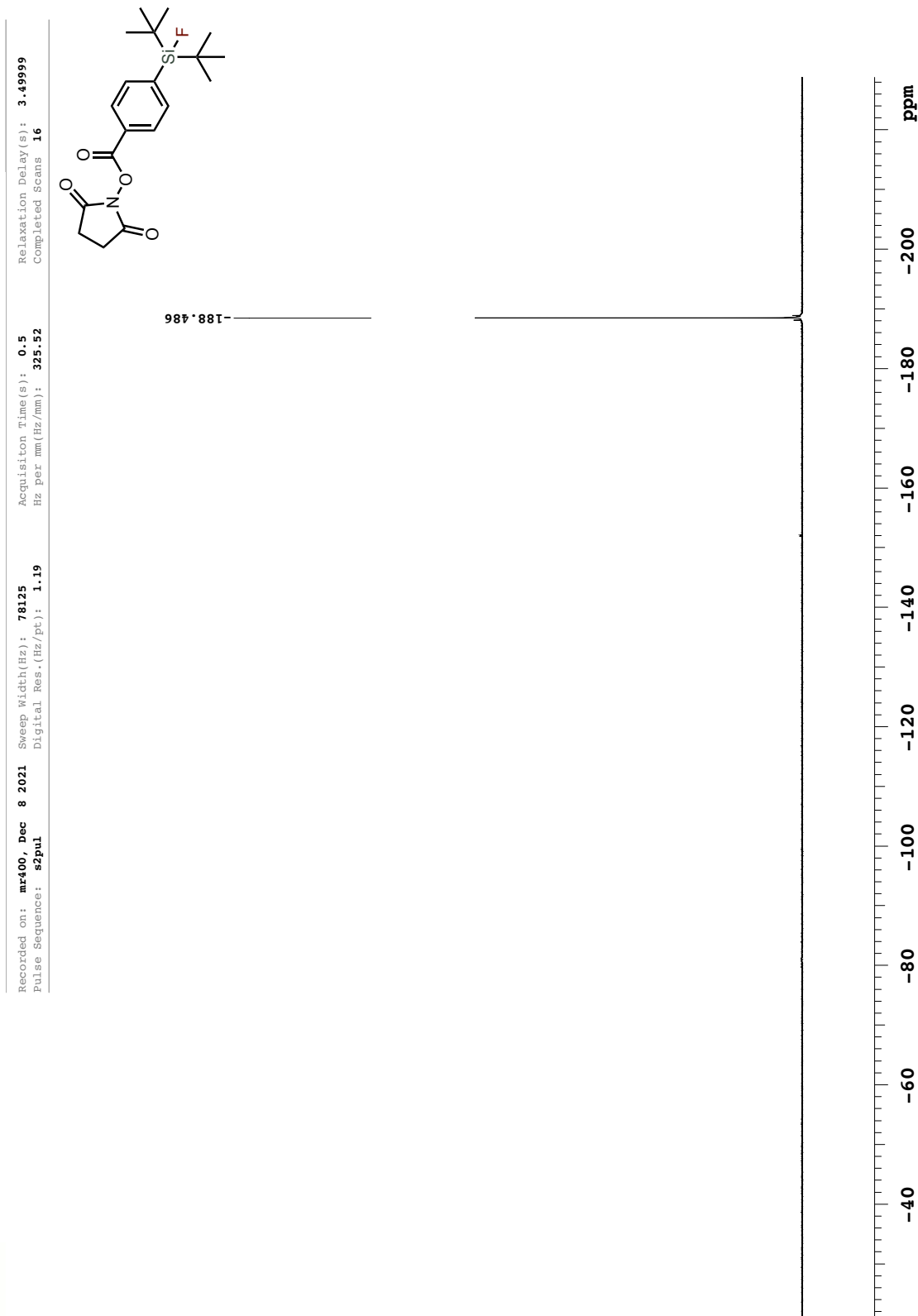


Figure A.122. ¹H NMR spectrum of compound 438 (CDCl₃, 699.8 MHz)

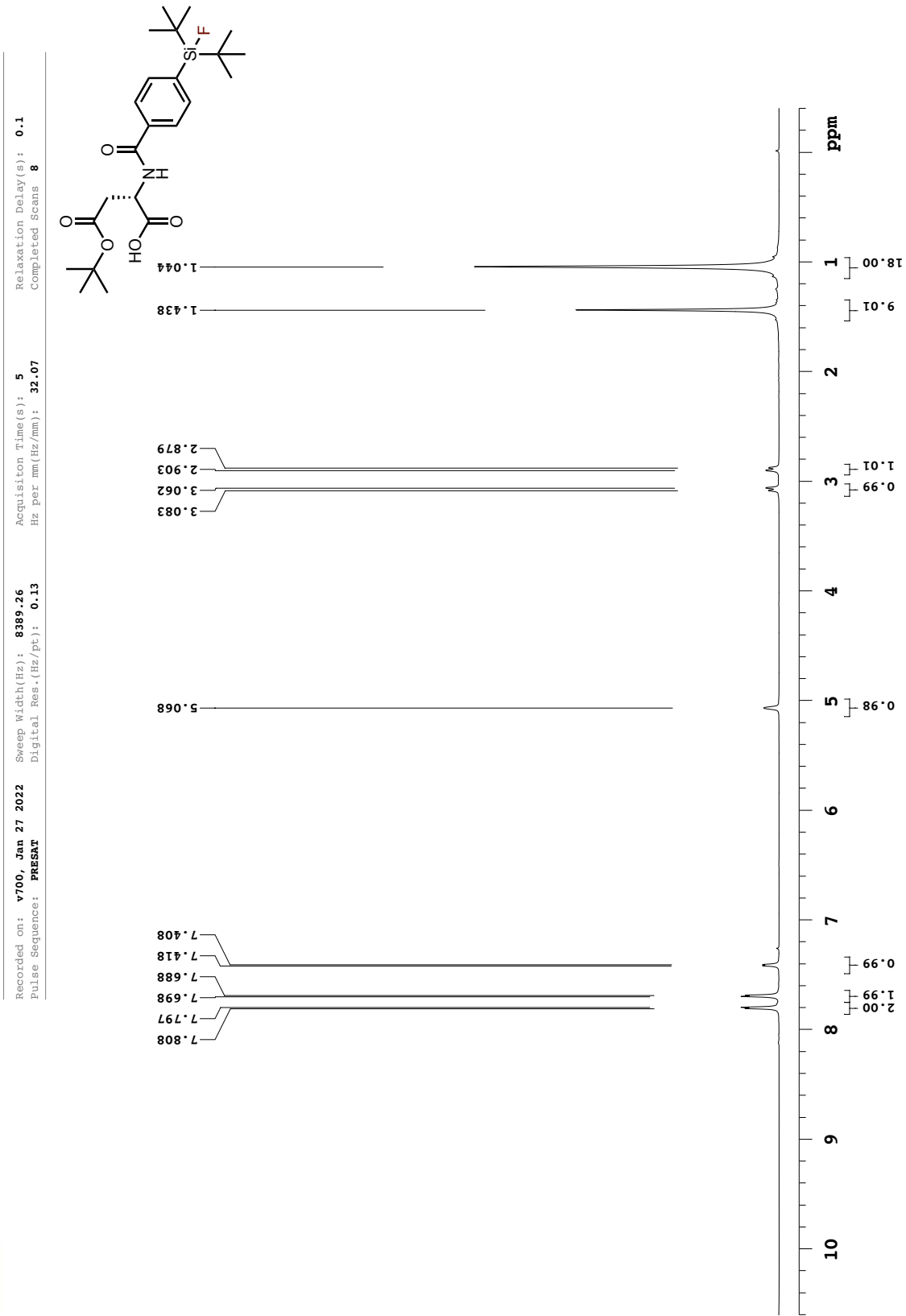


Figure A.123. $^{13}\text{C}\{^1\text{H}\}$ NMR spectrum of compound 438 (CDCl_3 , 176.0 MHz)

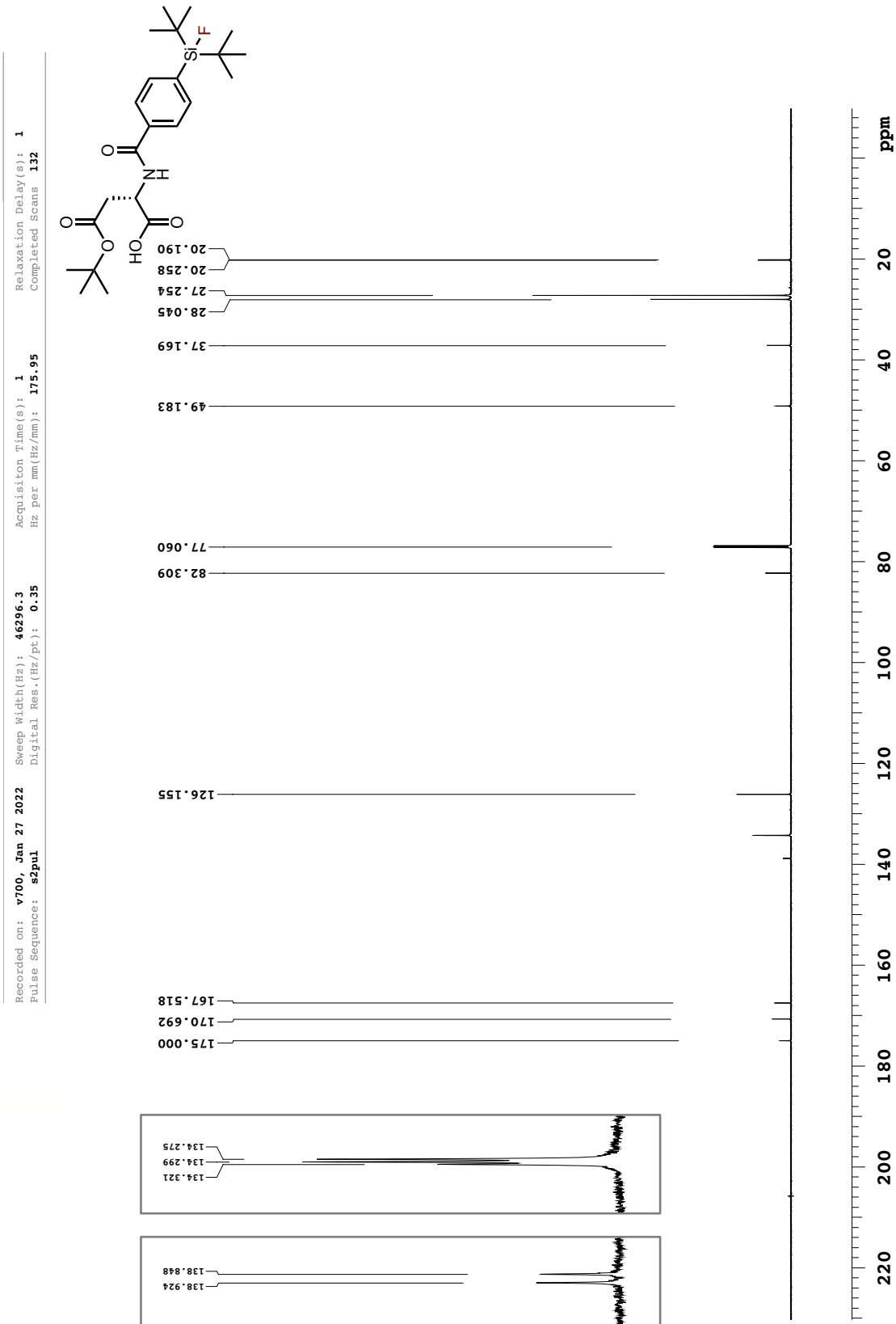


Figure A.124. ¹H NMR spectrum of compound 439 (CDCl₃, 499.8 MHz)

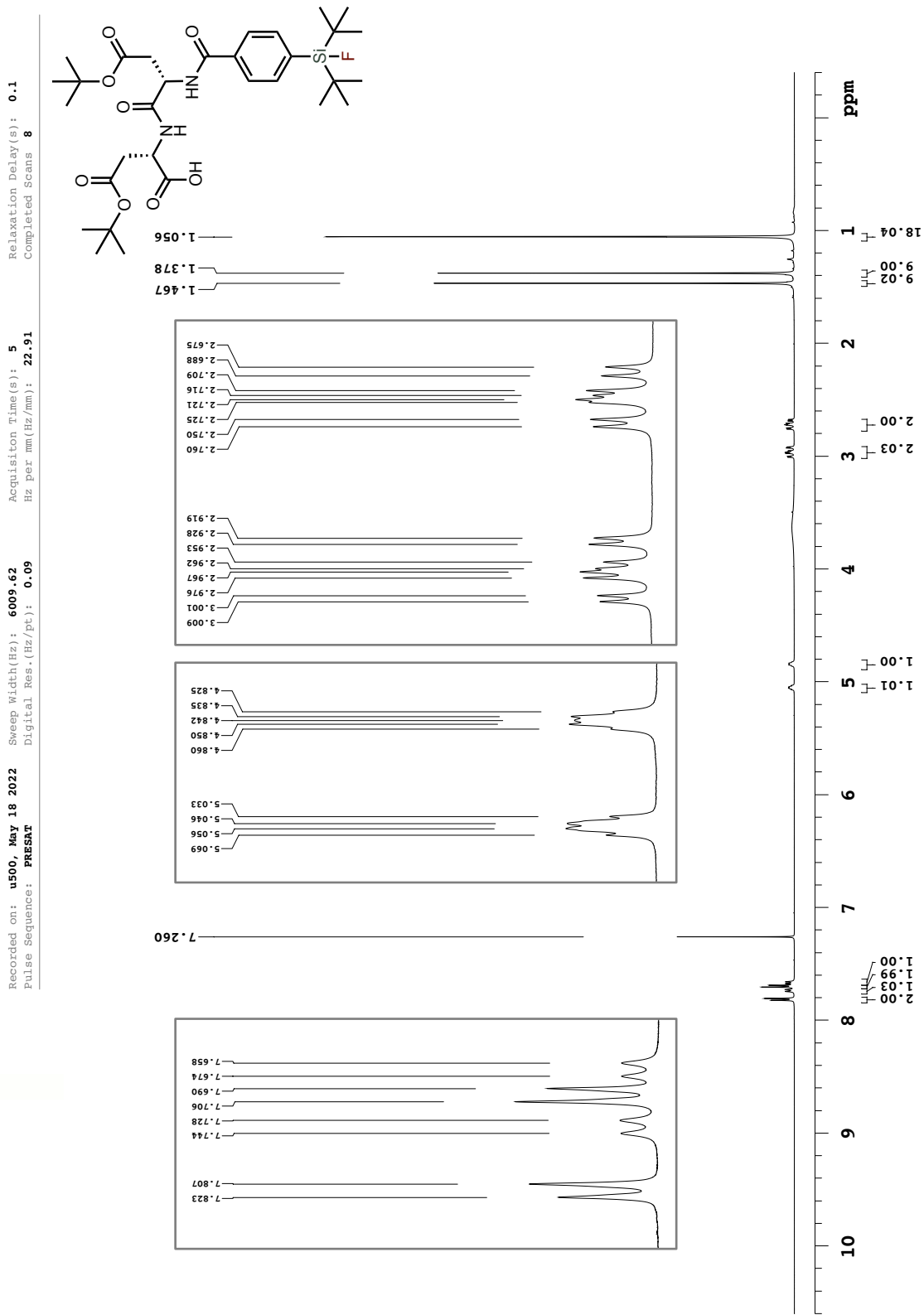


Figure A.125. $^{13}\text{C}\{^1\text{H}\}$ NMR spectrum of compound 439 (CDCl_3 , 125.7 MHz)

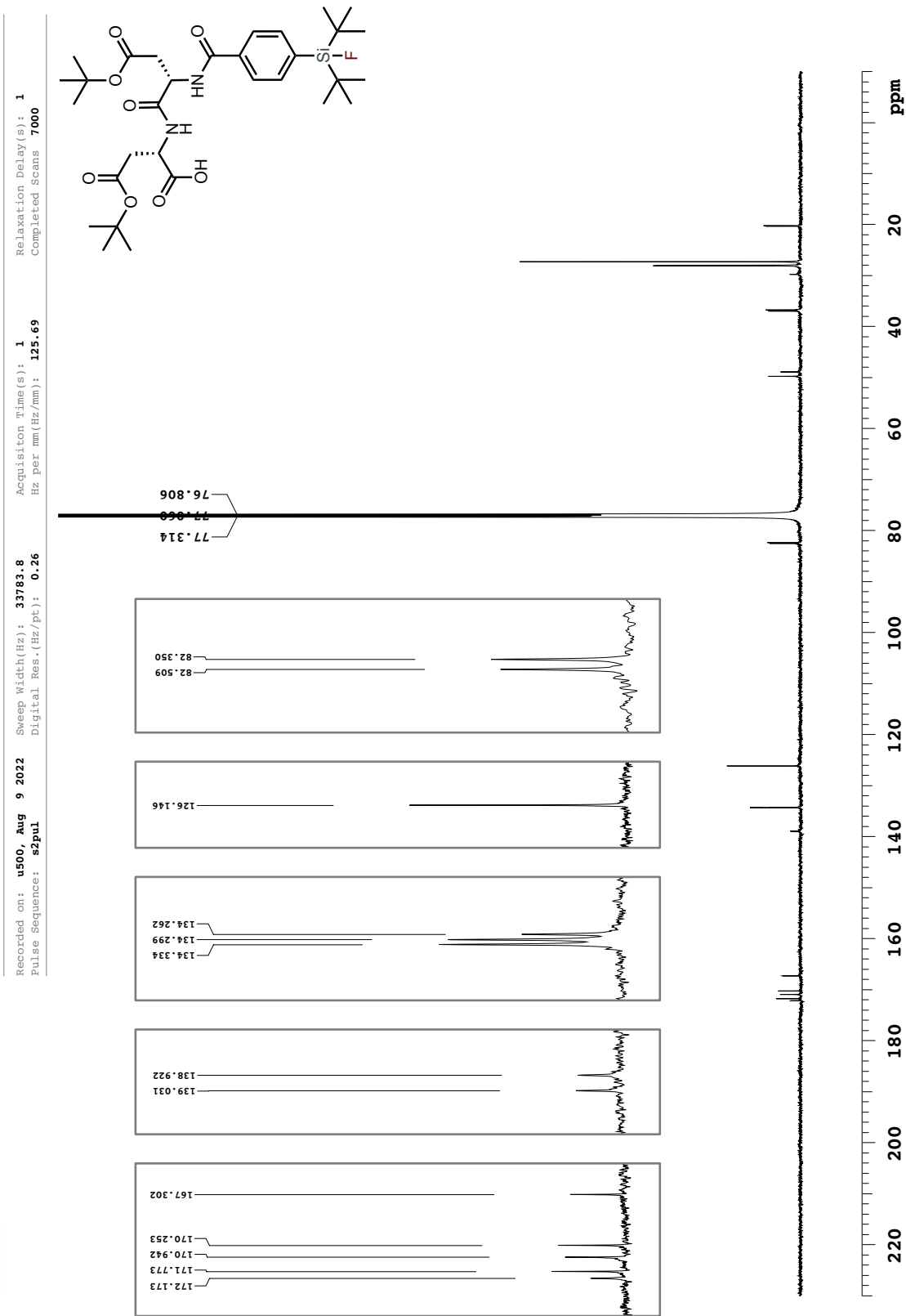


Figure A.126. $^{13}\text{C}\{^1\text{H}\}$ NMR magnified spectrum of compound 439 (CDCl_3 , 125.7 MHz)

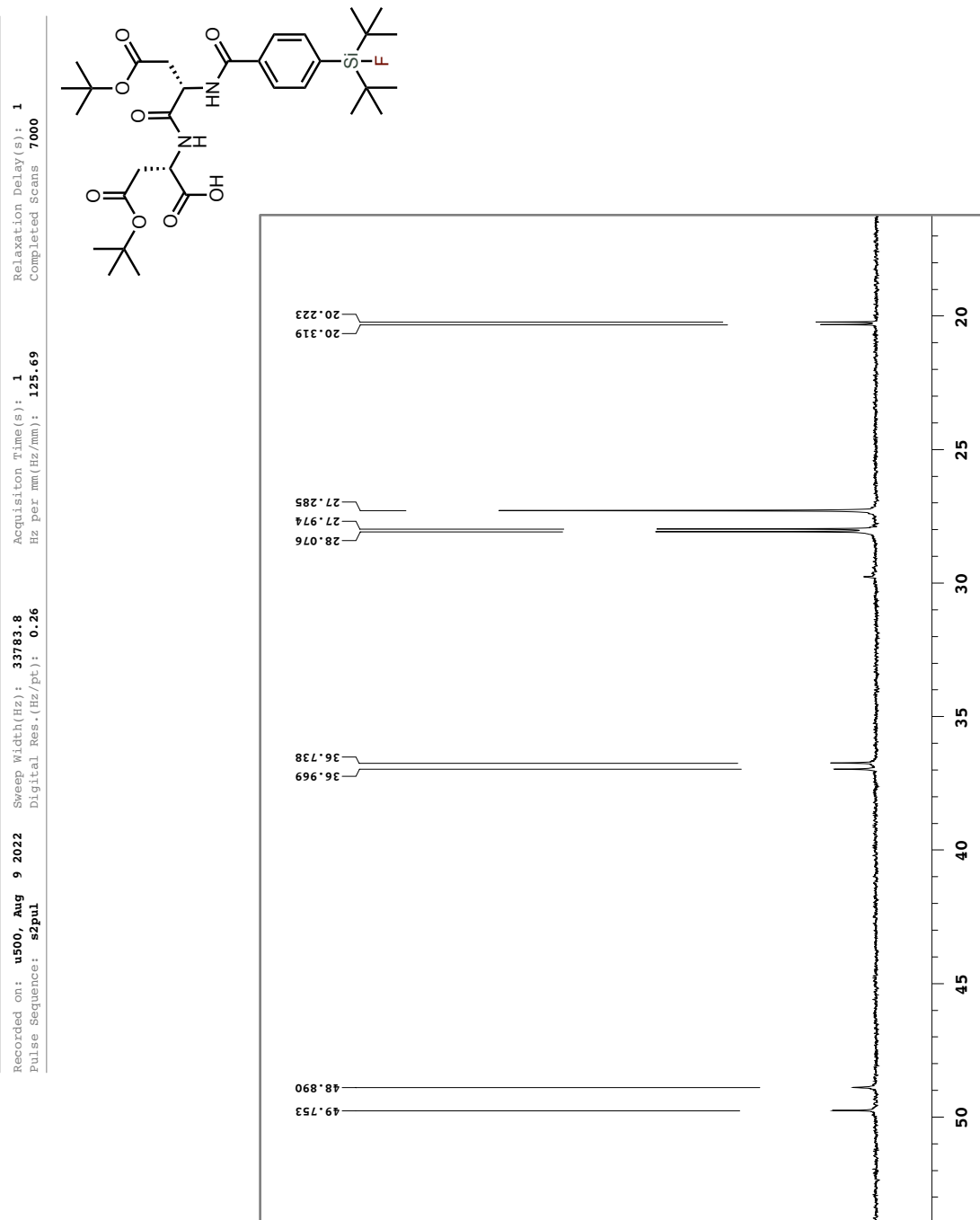


Figure A.127. ^{19}F NMR spectrum of compound 439 (CDCl_3 , 376.3 MHz)

